I. R. IRAN

ISSN: 1728-144X
e-ISSN: 1735-9244

International Journal of Engineering

Journal Homepage: www.ije.ir

MERC

TRANSACTIONS B: APPLICATIONS

Volume 36, Number 02, February 2023

Materials and Energy Research Center

In the Name of God

INTERNATIONAL JOURNAL OF ENGINEERING
Transactions B: Applications

DISCLAIMER

The publication of papers in International Journal of Engineering does not imply that the editorial board, reviewers or publisher accept, approve or endorse the data and conclusions of authors.

International **J**ournal of **E**ngineering *Transactions A: Basics* (ISSN 1728-1431) (EISSN 1735-9244)
International **J**ournal of **E**ngineering *Transactions B: Applications* (ISSN 1728-144X) (EISSN 1735-9244)
International **J**ournal of **E**ngineering *Transactions C: Aspects* (ISSN 2423-7167) (EISSN 1735-9244)
Web Sites: www.ije.ir & www.ijeir.info E-mails: ije.editor8@gmail.com, Tel: (+9821) 88771578, Fax: (+9821) 88773352
Materials and Energy Research Center (MERC)

ISSN: 1728-144X, e-ISSN: 1735-9244

International Journal of Engineering, Volume 36, Number 02, February 2023

CONTENTS

Transactions B: Applications

ISSN: 1728-144X, e-ISSN: 1735-9244

International Journal of Engineering, Volume 36, Number 02, February 2023

IJE TRANSACTIONS B: Applications Vol. 36, No. 02, (February 2023) 191-198

International Journal of Engineering

Journal Homepage: www.ije.ir

Tool Life of Uncoated and Coated Inserts during Turning of Ti6Al4V-ELI under Dry and Minimum Quantity Lubrication Environments

S. R. Nipanikar*[a], G. D. Sonawane[b], V. G. Sargade[c]

[a] *Babasaheb Ambedkar Technological University, Lonere, Maharashtra, India & Department of Mechanical Engineering, Karmaveer Bhaurao Patil College of Engineering, Satara, Maharashtra, India*
[b] *Babasaheb Ambedkar Technological University, Lonere, Maharashtra, India & Sandip Foundation's SITRC, Nashik, India*
[c] *Mechanical Engineering Department, Babasaheb Ambedkar Technological University, Lonere (Maharashtra), India*

PAPER INFO

Paper history:
Received 28 January 2022
Received in revised form 27 February 2022
Accepted 01 November 2022

Keywords:
Ti6Al4V-ELI
Uncoated Insert
PVD AlTiN
PVD TiAlN
Dry
Minimum Quantity Lubrication
Tool Life

ABSTRACT

This paper mainly deals with the tool wear characteristics of uncoated cemented carbide insert and PVD AlTiN, PVD TiAlN coated carbide inserts during turning of Ti6Al4V-ELI (Extra Low Interstitial). To satisfy the sustainability conditions, the experiments have been conducted under dry and minimum quantity lubrication (MQL) environment. To enhance the effectiveness of MQL, palm oil has been used as the cutting fluid. The same machining parameters are employed for all the cutting tool inserts in dry and MQL environments to understand the machining characteristics better. It was found that cutting speed greatly influences average flank wear. Tool life of PVD TiAlN coated tool is more in both MQL, and dry environments as compared to uncoated cemented carbide insert and PVD AlTiN coated insert. Using palm oil under the MQL environment has produced better results while turning by PVD TiAlN insert. The characteristics like good cooling and lubrication provided significantly less average flank wear during machining of Ti6Al4V-ELI under the MQLenvironment.

doi: *10.5829/ije.2023.36.02b.01*

NOMENCLATURE

Vc	Cutting Speed (m/min)	f	Feed (mm/rev)

1. INTRODUCTION

Titanium-based alloys are observed as the most significant materials in the aerospace and biomedical sectors. Titanium alloys cover around 30% of the material in an aerospace engine [1]. Due to this, it is also known as aerospace alloys. Titanium alloys are extensively used in steam turbine blades, superconductors, missiles, marine services, electronic gadgets, biomedical instruments, sports equipment due to their excellent strength and corrosion resistance properties. The high strength-to-weight ratio is one of the reasons for the popularity of these alloys among the numerous sectors. Titanium-based alloys possess high corrosion resistance, hot hardness, and wear resistance [2]. Even though many favourable properties of titanium alloys are still very difficult to machine due to their inherent properties such as high strength and hardness at elevated temperature, low thermal conductivity, low modulus of elasticity, self-induced chatter, work hardening behaviour, and chemical reactivity with various materials at elevated temperatures [3]. Various literature has commented on the poor machining behaviour of titanium alloys. In this concern, Ayed et al. [4] performed machining of titanium alloy Ti17 with uncoated tungsten carbide insert under diverse machining environments. Adhesion wear, abrasion wear, notch wear, and plastic deformation were found to be the main wear mechanism during the machining of Ti17. Bordin et al. [5] studied the tool wear of coated carbide insert observed by adhesive wear mechanism during machining of Ti6Al4V under dry and cryogenic

*Corresponding Author Institutional Email: suresh.nipanikar@kbpcoes.edu.in (S. Nipanikar)

Please cite this article as: S. R. Nipanikar, G. D. Sonawane, V. G. Sargade, Tool Life of Uncoated and Coated Inserts during Turning of Ti6Al4V-ELI under Dry and Minimum Quantity Lubrication Environments, ***International Journal of Engineering, Transactions B: Applications***, Vol. 36, No. 02, (2023), 191-198

environments. Klocke et al. [6] conducted machining of a gamma titanium aluminide alloy with an uncoated carbide insert under dry and MQL environments. Due to the absence of cutting fluid in a dry condition, abrasive wear was the leading wear mechanism. Deng et al. [7] and Pramanik et al. [8] studied diffusion wear during machining titanium alloy Ti6Al4V in a dry environment with WC-Co carbide tools. The results explored that W and Co elements did not significantly penetrate the titanium alloy Ti6Al4V at 400 °C, W and CO diffused into the titanium alloy Ti6Al4V. Armendia et al. [9] studied the machinabilities of Ti54M and Ti6Al4V with an uncoated WC-Co insert. They investigated that adhesion of work material in the form of a built-up edge appeared in all the cutting tools. Chetan et al. [10] observed less flank wear at a higher cutting speed due to the wettability behaviour of Ti6Al4V in the MQL environment. Fan et al. [11] investigated that diffusion, adhesion, and oxidation occurs at the chip-tool interface and accelerates their occurrence with increased cutting speed. Khatri et al. [12] found that abrasion wear was the most dominating tool wear mechanism during machining of Titanium alloy in dry and MQL environments. Guzanova et al. [13] explored that a coating made of powder with a low particle size belonging to the nanopowder coatings has a higher hardness, wear-resistance and almost the same corrosion resistance compared to the coating made up of large particle size. Brezinova et al. [14] found that green carbides coating is an environmentally more friendly replacement for coatings containing CO and Ni without reducing the performance of the coating.

Due to the advances in materials, investigators have now moved their attention to studying the machining behaviour of Ti6Al4V-ELI. It is evident from the available literature, and the author's perception that no systematic study has been conducted to analyze the tool flank wear and tool life of uncoated cemented carbide insert, PVD AlTiN, and PVD TiAlN coated insert during the turning of Ti6Al4V-ELI in dry and MQL environments. The extensive study about the tool life and tool wear during turning Ti6Al4V-ELI with uncoated cemented carbide insert, PVD AlTiN, and PVD TiAlN coated inserts under dry and MQL environments are still not available in the literature. Consequently, the key goal of this study is to find the tool life of uncoated cemented carbide insert, PVD AlTiN, and PVD TiAlN coated inserts in dry and MQL environments is a novelty work. Henceforth, the tool life of uncoated cemented carbide insert, PVD AlTiN, and PVD TiAlN coated inserts during machining Ti6Al4V-ELI in dry and MQL environment is quite innovative.

A comparative study of the machining of Ti6Al4V-ELI with uncoated cemented carbide insert, PVD AlTiN, and PVD TiAlN coated inserts will not only advantage in collecting more data concerning the tool wear characteristics but also help extend the research outputs from uncoated and PVD coated inserts. Moreover, the vegetable oil under the MQL environment during machining Ti6Al4V-With uncoated cemented carbide insert, PVD AlTiN, and PVD TiAlN coated inserts will be significant from economic and environmental aspects.

In the present study, machining of Ti6Al4V-ELI has been carried out under a dry and MQL environment. The cemented carbide uncoated insert, PVD AlTiN, and PVD TiAlN coated inserts have been selected based on the literature review and tool manufacturers' catalogue.

2. EXPERIMENTAL PROCEDURES

2. 1. Workpiece Material The workpiece material (220 mm length and 90 mm diameter) used during the turning process was in the form of a cylindrical bar of titanium alloy Ti6Al4V-ELI. The composition of the Ti6Al4V-ELI (in wt. %) is summarized in Table 1.

The microstructure of a workpiece consisted of an elongated alpha phase surrounded by fine, dark etching of the beta matrix. Ti6Al4V-ELI offers high strength and depth hardenability (32 HRC). The yield strength and ultimate tensile strength of Ti6Al4V-ELI are 795 MPa and 860 MPa, respectively. The modulus of elasticity is 114 GPa. The microstructure of Ti6Al4V- ELI is shown in Figure 1.

The microstructure of Ti6Al4V-ELI shows acicular alpha and aged beta. Alpha platelets at the prior beta grain boundaries. $HF+HNO_3+H_2O$ etchant was used.

2. 2. Cutting Tool A cutting tool inserts with ISO designation CNMG 120408FF KC5010 PVD AlTiN and

TABLE 1. Chemical composition of Ti6Al4V ELI

Composition	C	Si	Fe	Al	N
Wt %	0.08	0.03	0.22	6.1	0.006
Composition	V	S	O	H	Ti
Wt %	3.8	0.003	0.12	0.003	Balance

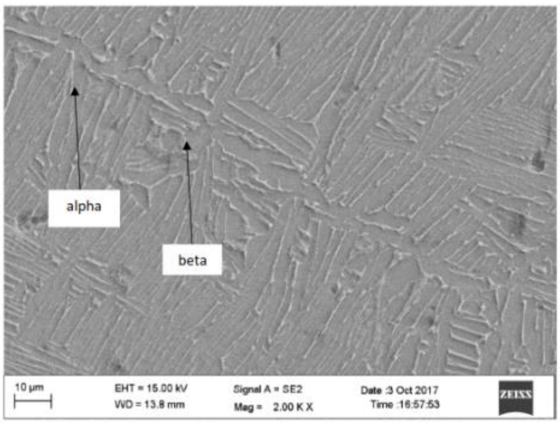

Figure 1. Microstructure of Ti6Al4V ELI

CNMG 120408MS K313 WC/Co uncoated insert Kennametal make CNMG 120408 SF 1105 Sandvik make, we selected for turning of Ti6Al4V-ELI. During experimentation PCLNL 2525 M12 tool holder was used.

The machining performance of the coated tool depends on the quality of both the substrate and the coating. Hence, it is imperative to characterize the selected cutting inserts. It may be noted that the characterization helps in a better understanding of the performance of the coated tool. The uncoated insert was characterized using Scanning Electron Microscopy (SEM). Figure 2 shows the EDAX profile and microstructure of the K313 uncoated cemented carbide insert observed under SEM. SEM image shows a uniform distribution of fine and medium grains. Microstructure and grain size are the most important factors, which govern the properties.

Figure 3 shows a fractured cross-section indicating the coating thickness of the PVD AlTiN and PVD TiAlN coated tools observed under a scanning electron microscope. The average coating thickness is 1.72 µm, and 1.37 µm of PVD AlTiN and PVD TiAlN coated tool, respectively.

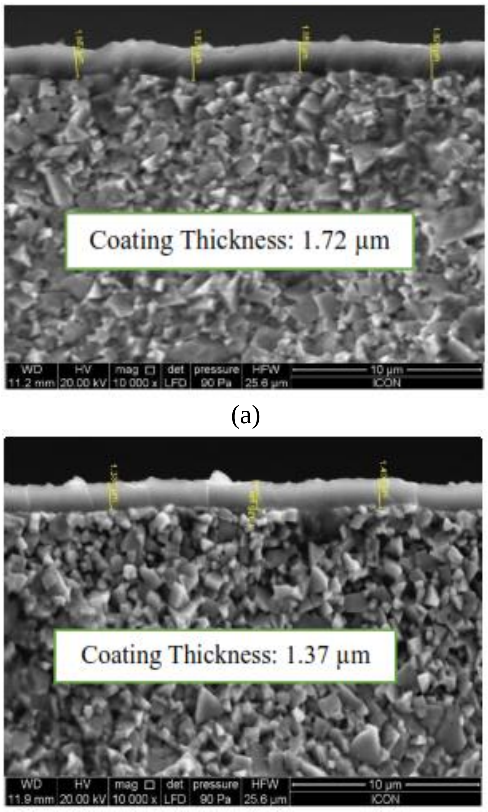

(a)

(b)

Figure 3. Coating Thickness of (a) PVD AlTiN (b) PVD TiAlN Coated Tool

2. 3. MQL Setup Minimum quantity lubrication helps as the substitute for flood cooling by reducing the volume of cutting fluid used during the machining process. In recent years, numerous methods have been developed to control the cutting temperature and increase the cooling process's overall effectiveness during the machining process. Machining in a dry environment is one of the techniques introduced as a new approach to decrease the environmental pollution. Cutting fluids are not supplied during the machining in a dry environment, but this method cannot be applied in all machining processes due to some constraints. All the materials cannot be machined without cutting fluids, and machining in a dry environment reduces tool life and affects the finishing process due to high heat generation. The flood coolant method has been used widely since cutting fluid was introduced in the machining industry. Cutting fluid is delivered excessively to cool and lubricate the cutting tool, and the workpiece subsequently reduces the heat generated at the chip-tool interface. The fast growth in the machine tool industry and the increasing awareness of environmental and health issues lead to near dry machining [15]. In the MQL method, a small amount of cutting fluid is carried by air-jet directly to the cutting zone leading to a decrease in cutting temperature. The photographic view of the experimental setup is shown in Figure 4. The block diagram of the MQL setup is illustrated in Figure 5. The conditions under which MQL is carried out are listed in Table 2.

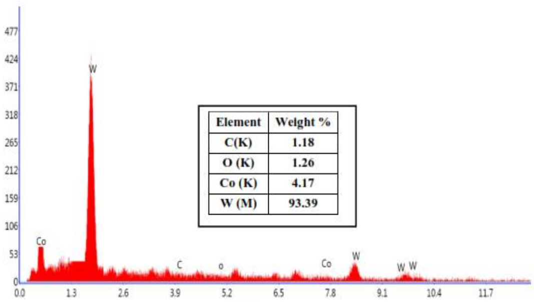

(a)

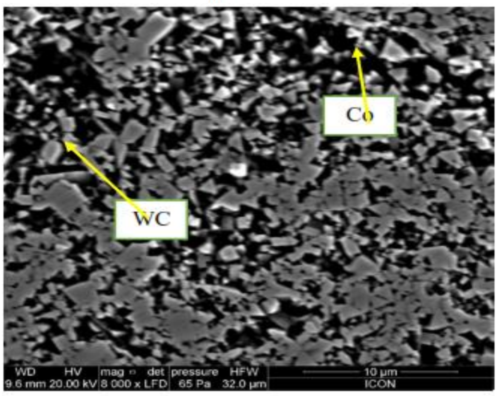

(b)

Figure 2. (a) EDAX Profile (b) SEM Micrograph of K313 Uncoated Cutting Tool

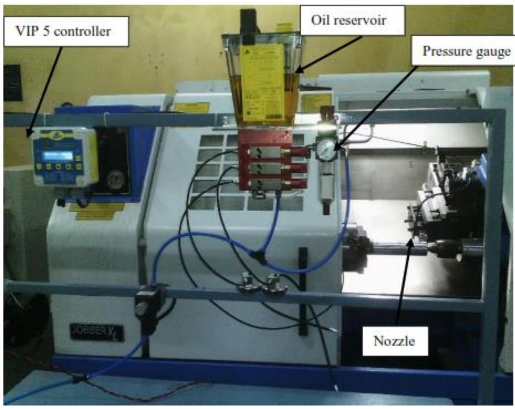

Figure 4. Photographic View of the Experimental Setup

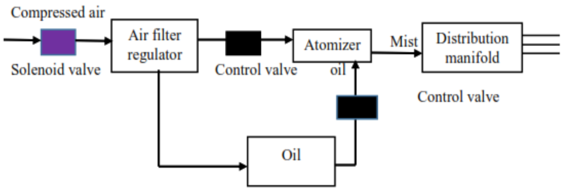

Figure 5. Block Diagram of MQL Setup

TABLE 2. Conditions of MQL System

Cutting Fluid	Palm Oil
MQL Flow Rate	100 ml/h
Air Pressure	5 bar
MQL Nozzle Distance form Contact Zone	20 mm

Working of the MQL setup is as follows:

- Compressed air with a typical air pressure of 5 bars is supplied into the air filter via a solenoid valve.
- The air filter removes any impurities or contaminations that may come along with the supplied air to keep the equipment clean and dirt-free.
- Meanwhile, cutting fluid is supplied to the mixing chamber from the oil reservoir via an oil control valve. The oil control valve is used to control the flow rate of oil to be supplied.
- In the mixing chamber, the compressed air from the filter via an air control valve and the cutting fluid gets mixed to form an aerosol known as oil mist.
- Oil mist is supplied to the machining zone through a nozzle having a very small hole (< 2mm).

2. 4. Measuring Equipment

- Dynamometer and charge amplifier: Kistler piezoelectric dynamometer (model-9257B) was used to measure the cutting forces in all three directions. The charge produced at the dynamometer was amplified using a charge amplifier (Kistler model-5019 B 130). The amplified signal was further processed with the help of Kistler Dynoware software.
- SEM and EDAX: FEI Quanta 200 Scanning Electron Microscope (SEM) was employed to take the worn-out tool's images at higher magnification. This SEM system can easily magnify the image from 5X to 10 X. It was used for elemental analysis work and tool material, measurement of coating thickness of PVD AlTiN and PVD TiAlN inserts, the microstructure of work material.

2. 5. Machining Parameters The machining experiments were conducted on an ACE CNC LATHE JOBBER XL, which FANUC Oi Mate-TC as a controller. The turning process parameter values were designed during the experiments using the experiment's full factorial design. Three levels of cutting speed set the cutting parameters were 80, 125, and 170 m/min, while the three levels of feed were 0.08, 0.15, and 0.2 mm/rev. During the machining process, the depth of cut of 0.5 mm was kept constant. The machining experiments were carried out in a dry and MQL environment. The randomization concept was incorporated to select a sequence of machining parameters. The material was removed to avoid undesirable errors in turning tests. Before machining tests, a thin layer from work material was removed by turning process to remove out of roundness produced due to the earlier operations. A new cutting edge was used for each experiment.

3. RESULTS AND DISCUSSION

3. 1. Tool Wear One of the primary purposes of utilizing cutting fluid in machining is to restrict tool wear and thus increase tool life by minimizing friction, temperature, and cutting forces. Therefore, the study of tool wear is significant for justifying the quantity of cutting fluid used. It is particularly so because cutting fluid has an adverse impact on the operator and the environment in general. Therefore, a detailed study has been undertaken to investigate tool wear under dry machining and MQL using an uncoated cemented carbide insert, PVD AlTiN, and PVD TiAlN single layer coated tool. Tool wear starts at a relatively faster rate due to break-in wear caused by attrition and microchipping at the sharp cutting edges. In the present investigation with the tool, work material, and the machining conditions undertaken, the tool failure modes were mostly gradual wear. In MQL, palm oil and air mixture were sprayed over the tool rake face, as shown in Figure 6.

Flank wear with cutting conditions of uncoated, PVD AlTiN, and PVD TiAlN cutting tool in a dry environment has been illustrated in Figures 7 and 8.

Excellent anti-friction property and wear resistance in combination with the superior thermal stability of TiAlN coating are responsible for the outstanding performance

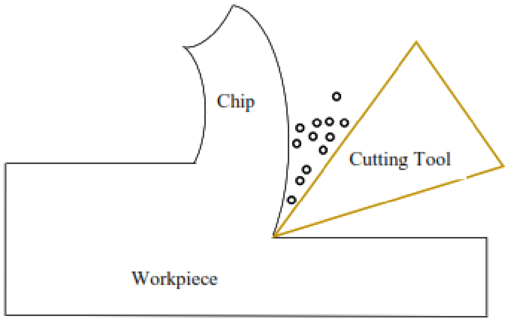

Figure 6. Schematic Diagram of MQL Mechanism at Tool-Work Interface

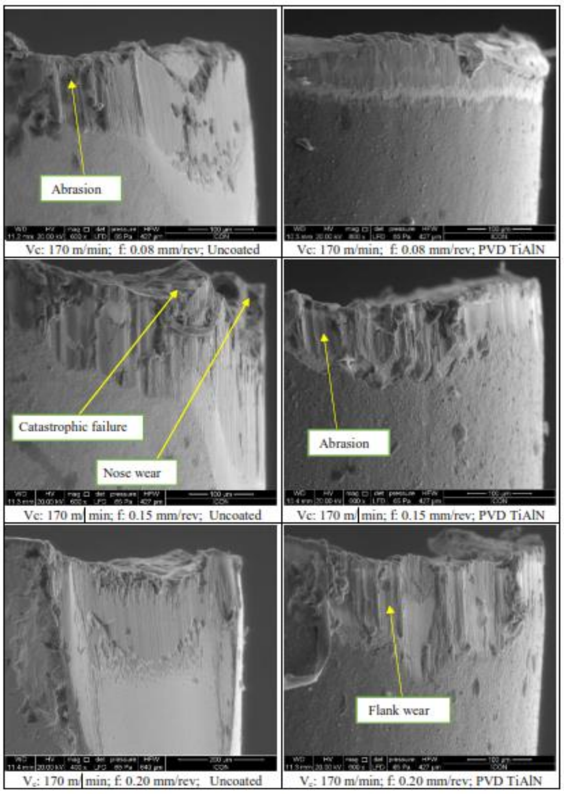

Figure 7. SEM images of tool wear pattern after turning of Ti6Al4V-ELI by using uncoated and PVD TiAlN insert in a dry environment (Turning length = 100 mm)

of PVD coated tool even during machining at such high cutting speed (170 m/min).

Average tool flank wear increases with cutting speed and feed for all the cutting tool inserts. However, cutting speed has a prominent effect on flank wear than feed rate. The PVD TiAlN cutting tool insert is the best for different cutting conditions in terms of low flank wear. The heat generated during cutting is less at low cutting speed and feed rate. As a result, PVD TiAlN coated tool withstands the temperature without affecting the tool geometry showing minimum wear.

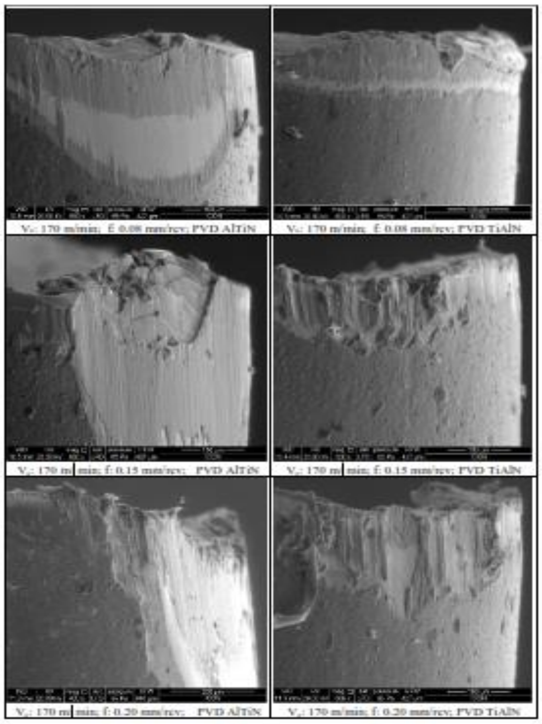

Figure 8. SEM images of tool wear pattern after turning of Ti6Al4V-ELI by using PVD AlTiN and PVD TiAlN insert in a dry environment (Turning length = 100 mm)

The wear rate of PVD AlTiN cutting tool insert is high compared to PVD TiAlN cutting tool insert at all cutting conditions, especially at high cutting speed and feed rate. High "Al" content in the PVD AlTiN tool cannot present better anti-wear properties than PVD TiAlN insert. High "Al" content in PVD AlTiN coating increased the chemical reactivity, which caused severe adhesive wear. Also, oxides of aluminium can increase the brittleness of the layer. Abrasive wear, adhesion wear, oxidation, and brittle failure were the main wear mechanism of the PVD AlTiN cutting tool insert.

3. 2. Tool Life Figures 9 and 10 show the progression of average flank wear plotted against the duration of machining in a dry and MQL environment. Figure 11 shows the tool life of uncoated, PVD AlTiN, and PVD TiAlN coated tools in dry and MQL environments. The SEM images of growth of flank wear of uncoated, PVD AlTiN, and PVD TiAlN tools are shown in Figures 12 through 17, respectively.

The development of flank wear is evaluated in respect of machining time. Figures 9 and 10 show the average principal flank wear progression at the tool edge that encountered the cutting forces, contact stresses, temperature, and friction in a dry and MQL environment. The plots are constructed with the progression of machining time while the cutting speed, feed, and depth of cut were kept constant at 125 m/min; 0.08 mm/rev, and

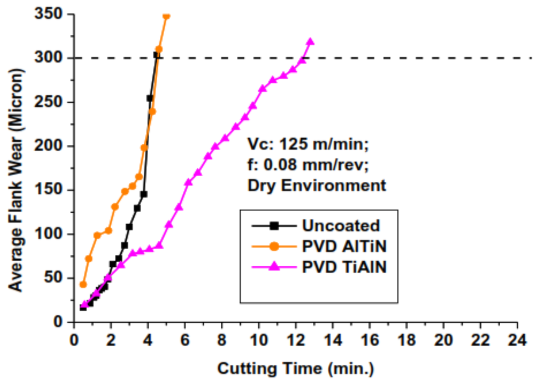

Figure 9. Progression of Average Flank Wear vs. Duration of Machining in a Dry Environment

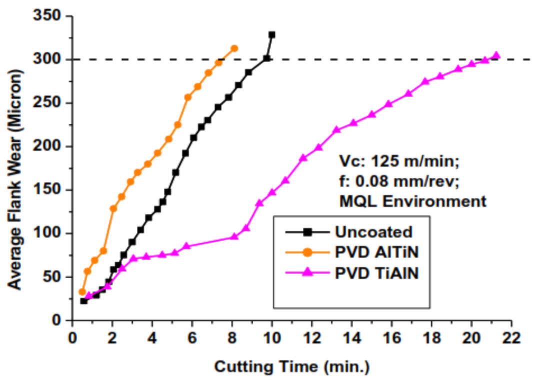

Figure 10. Progression of Average Flank Wear vs. Duration of Machining in MQL Environment

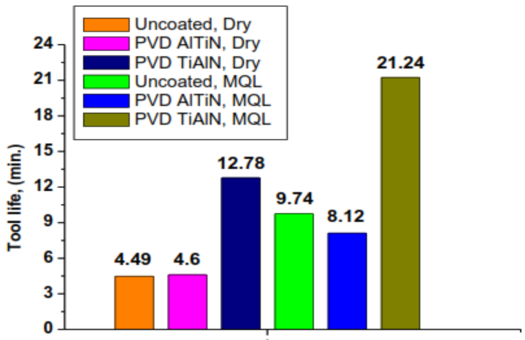

Figure 11. Tool life of Uncoated, PVD AlTiN and PVD TiAlN Coated Tool in dry and MQL Environment

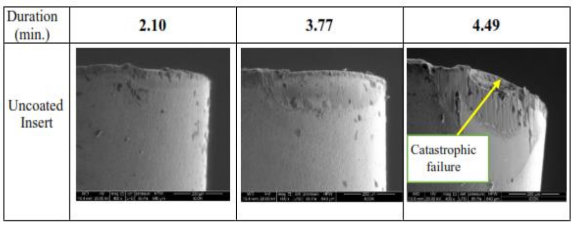

Figure 12. SEM images showing growth of flank wear of uncoated insert at cutting speed of 125 m/min, feed 0.08 mm/rev, and depth of cut 0.5 mm in a dry environment

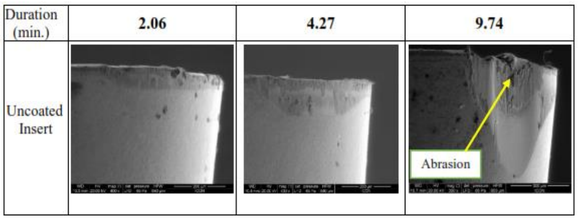

Figure 13. SEM images showing growth of flank wear of uncoated insert at cutting speed of 125 m/min, feed 0.08 mm/rev, and depth of cut 0.5 mm in MQL environment

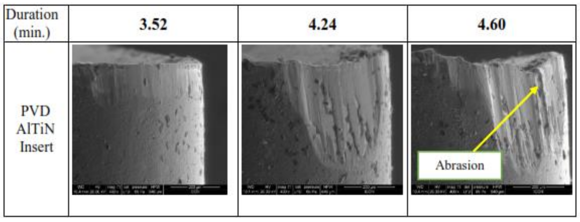

Figure 14. SEM images showing growth of flank wear of PVD AlTiN insert at cutting speed of 125 m/min, feed 0.08 mm/rev, and depth of cut 0.5 mm in a dry environment

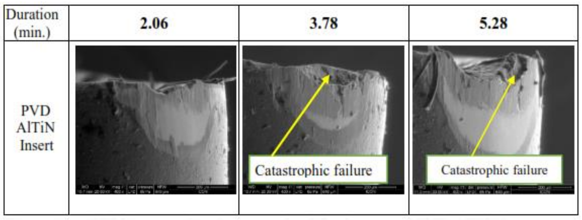

Figure 15. SEM images showing growth of flank wear of PVD AlTiN insert at cutting speed of 125 m/min, feed 0.08 mm/rev and depth of cut 0.5 mm in MQL environment

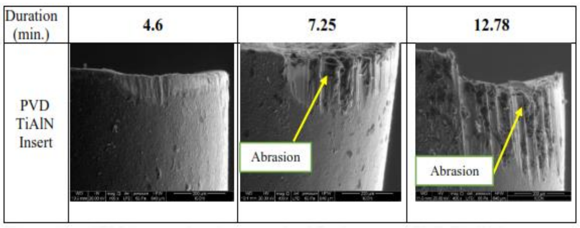

Figure 16. SEM images showing growth of flank wear of PVD TiAlN insert at cutting speed of 125 m/min, feed 0.08 mm/rev, and depth of cut 0.5 mm in a dry environment

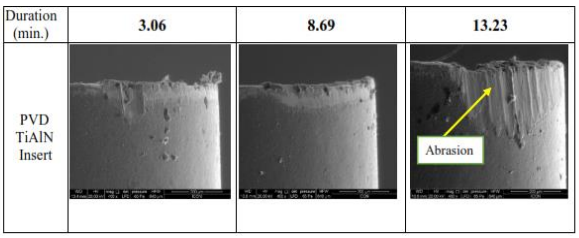

Figure 17. SEM images showing growth of flank wear of PVD TiAlN insert at cutting speed of 125 m/min, feed 0.08 mm/rev, and depth of cut 0.5 mm in MQL environment

0.5 mm, respectively. From Figures 9, it is observed that PVD TiAlN insert showed high tool life, the tool life of PVD AlTiN insert showed slightly more than tool life of uncoated tool in a dry environment at cutting speed 125 m/min, feed rate 0.08 mm/rev and depth of cut 0.5 mm. Also, it is observed that PVD TiAlN insert showed high tool life, the uncoated tool showed intermediated tool life, and PVD AlTiN insert exhibited low tool life. High “Al” content in PVD AlTiN coating increased the chemical reactivity, which aroused severe adhesive wear. Brittleness of the PVD AlTiN coating increases because of the oxide of aluminium. Adhesive wear, oxidation, abrasive wear, and brittle failure are the main wear mechanisms of the PVD AlTiN insert. The application of MQL effectively controls plastic deformation and thus promotes tool life [16]. It can be seen from Figure 10 that the average flank wear, particularly its rate of growth, decreased with MQL by palm oil. The reason behind the decrease in average flank wear observed might reasonably be attributed to a reduction in cutting temperature by MQL, which helped in reducing abrasion wear by retaining tool hardness as well as adhesion and diffusion types of wear which are highly sensitive to cutting temperature. Because of such a reduction in the growth rate of flank wear, the tool life is more in the case of the MQL environment than a dry one [17]. Many abrasion marks were observed on the cutting tool during machining in a dry environment due to a lack of lubrication and coolant. The vegetable oil in the MQL environment formed a lubrication film over the cutting tool and thus reduced the interaction of the workpiece and cutting insert [18]. Continuous adhesion and shearing-off built-up edge from the nose of the tool in a dry environment [19]. Catastrophic tool failure in dry and MQL environment at extreme cutting condition. The tool fracture and abrasion grooves were the major cause of tool wear in both dry and MQL environments. Tool flank wear is a significant criterion to judge the machinability of material because it is directly related to the dimensional accuracy and surface roughness [20].

3. 3. Cutting Force With an increase in cutting speed from 80 to 170 m/min, the cutting force increased from 104 N to 282 N, which contradicts the results mentioned by Fang [20]. As cutting speed increases cutting force increases due to strain gradient induced material strengthening effects. This makes it challenging to increase cutting speed when machining Ti6Al4V-ELI. With an increase in the feed from 0.08 to 0.20 mm/rev, the cutting force was found to increase from 104 N to 282 N. An increase in feed increases cutting force due to an increase in the area of undeformed chip cross-section, which increases the friction between the cutting edge and workpiece. An increase in the feed also increases the chip load, which causes excessive cutting force. Also, the increased deformation due to the increased feed in turning requires a higher cutting force. The cutting force increased from 104 N to 248 N while turning Ti6Al4V-ELI in the MQL environment. The cutting force increased from 128 N to 282 N in a dry environment. Increasing the friction between the cutting edge and workpiece while turning Ti6Al4V-ELI in a dry environment result in more cutting force than the MQL environment. PVD TiAlN coated tool exhibited lower cutting force because coating increases the lubricity and reduces the affinity to the workpiece material and low coefficient of friction of the PVD TiAlN insert.

4. CONCLUSIONS

This research article discussed the tool wear characteristics of uncoated cemented carbide insert, PVD AlTiN, and PVD TiAlN inserts during machining of Ti6Al4V-ELI in dry and MQL environments. The following conclusions can be drawn from the present work:

- The average flank wear increased with cutting speed and feed due to the rise in plastic deformation and temperature. Cutting speed has a dominating effect on tool flank wear.
- Adhesion and cutting-edge chipping were more dominant wear mechanisms for uncoated tools.
- PVD TiAlN tool insert showed low tool flank wear because of good adhesion strength and high thermal conductivity. PVD TiAlN tool exhibited longer tool life than uncoated and PVD AlTiN inserts.
- Flank wear is less in the MQL environment due to the excellent wettability behaviour of Ti6Al4V-ELI. MQL has significantly reduced tool flank wear compared to dry machining due to the effective cooling and lubrication.
- Better penetration of palm oil during machining of Ti6Al4V-ELI provided less crater wear due to less tool-chip contact length.
- Outstanding improvement in resistance to tool wear indicative of superior machinability was consistently obtained with PVD TiAlN coated tool in MQL environment.
- Surface finish enhanced predominantly due to reduction of damage and wear at the tool tip by applying MQL.
- Good adhesion strength, high wear resistance of PVD TiAlN coated tool associated with superior tribological features resulted in increased tool life.
- The tool wear mechanism of the PVD TiAlN coated tool was a combination of abrasive wear, oxidation, and micro-grooves. PVD TiAlN coated tool possesses the lowest wear rate because of the adding of ‘Al.’
- PVD AlTiN coating increased the chemical reactivity because of high ‘Al’ content in PVD AlTiN coated tool results in poor performance compared to PVD TiAlN insert.

5. REFERENCES

1. Ezugwu, E., Bonney, J. and Yamane, Y., "An overview of the machinability of aeroengine alloys", ***Journal of Materials Processing Technology***, Vol. 134, No. 2, (2003), 233-253. https://doi.org/10.1016/S0924-0136(02)01042-7
2. Ezugwu, E., "Key improvements in the machining of difficult-to-cut aerospace superalloys", ***International Journal of Machine Tools and Manufacture***, Vol. 45, No. 12-13, (2005), 1353-1367. https://doi.org/10.1016/j.ijmachtools.2005.02.003
3. Sargade, V., Nipanikar, S. and Meshram, S., "Analysis of surface roughness and cutting force during turning of ti6al4v eli in dry environment", ***International Journal of Industrial Engineering Computations***, Vol. 7, No. 2, (2016), 257-266. http://dx.doi.org/10.5267/j.ijiec.2015.10.004
4. Ayed, Y., Germain, G., Ammar, A. and Furet, B., "Degradation modes and tool wear mechanisms in finish and rough machining of ti17 titanium alloy under high-pressure water jet assistance", ***Wear***, Vol. 305, No. 1-2, (2013), 228-237. https://doi.org/10.1016/j.wear.2013.06.018
5. Bordin, A., Bruschi, S., Ghiotti, A. and Bariani, P., "Analysis of tool wear in cryogenic machining of additive manufactured ti6al4v alloy", ***Wear***, Vol. 328, (2015), 89-99. https://doi.org/10.1016/j.wear.2015.01.030
6. Klocke, F., Settineri, L., Lung, D., Priarone, P.C. and Arft, M., "High performance cutting of gamma titanium aluminides: Influence of lubricoolant strategy on tool wear and surface integrity", ***Wear***, Vol. 302, No. 1-2, (2013), 1136-1144. https://doi.org/10.1016/j.wear.2012.12.035
7. Jianxin, D., Yousheng, L. and Wenlong, S., "Diffusion wear in dry cutting of ti–6al–4v with wc/co carbide tools", ***Wear***, Vol. 265, No. 11-12, (2008), 1776-1783. https://doi.org/10.1016/j.wear.2008.04.024
8. Pramanik, A., Islam, M., Basak, A. and Littlefair, G., "Machining and tool wear mechanisms during machining titanium alloys", in Advanced Materials Research, Trans Tech Publ. Vol. 651, (2013), 338-343. https://doi.org/10.4028/www.scientific.net/AMR.651.338
9. Armendia, M., Garay, A., Iriarte, L.-M. and Arrazola, P.-J., "Comparison of the machinabilities of ti6al4v and timetal® 54m using uncoated wc–co tools", ***Journal of Materials Processing Technology***, Vol. 210, No. 2, (2010), 197-203. https://doi.org/10.1016/j.jmatprotec.2009.08.026
10. Behera, B., Ghosh, S. and Rao, P., "Wear behavior of pvd tin coated carbide inserts during machining of nimonic 90 and ti6al4v superalloys under dry and mql conditions", ***Ceramics International***, Vol. 42, No. 13, (2016), 14873-14885. https://doi.org/10.1016/j.ceramint.2016.06.124
11. Fan, Y., Hao, Z., Zheng, M. and Yang, S., "Wear characteristics of cemented carbide tool in dry-machining ti-6al-4v", ***Machining Science and Technology***, Vol. 20, No. 2, (2016), 249-261. https://doi.org/10.1080/10910344.2016.1165837
12. Khatri, A. and Jahan, M.P., "Investigating tool wear mechanisms in machining of ti-6al-4v in flood coolant, dry and mql conditions", ***Procedia Manufacturing***, Vol. 26, (2018), 434-445. https://doi.org/10.1016/j.promfg.2018.07.051
13. Guzanová, A., Brezinová, J., Draganovská, D. and Maruschak, P., "Properties of coatings created by hvof technology using micro- and nano-sized powder", ***Koroze a Ochrana Materialu***, Vol. 63, No. 2, (2019), 86-93. DOI: 10.2478/kom-2019-0011
14. Brezinová, J., Guzanová, A., Draganovská, D., Maruschak, P.O. and Landová, M., "Study of selected properties of thermally sprayed coatings containing wc and wb hard particles", ***Acta Mechanica et Automatica***, Vol. 10, No. 4, (2016). https://doi.org/10.1515/ama-2016-0046
15. Obikawa, T., Kamata, Y., Asano, Y., Nakayama, K. and Otieno, A.W., "Micro-liter lubrication machining of inconel 718", ***International Journal of Machine Tools and Manufacture***, Vol. 48, No. 15, (2008), 1605-1612. https://doi.org/10.1016/j.ijmachtools.2008.07.011
16. Dearnley, P. and Grearson, A., "Evaluation of principal wear mechanisms of cemented carbides and ceramics used for machining titanium alloy imi 318", ***Materials Science and Technology***, Vol. 2, No. 1, (1986), 47-58. https://doi.org/10.1179/mst.1986.2.1.47
17. Khan, M., Mithu, M. and Dhar, N.R., "Effects of minimum quantity lubrication on turning aisi 9310 alloy steel using vegetable oil-based cutting fluid", ***Journal of Materials Processing Technology***, Vol. 209, No. 15-16, (2009), 5573-5583. https://doi.org/10.1016/j.jmatprotec.2009.05.014
18. Ucun, I., Aslantas, K. and Bedir, F., "An experimental investigation of the effect of coating material on tool wear in micro milling of inconel 718 super alloy", ***Wear***, Vol. 300, No. 1-2, (2013), 8-19. https://doi.org/10.1016/j.wear.2013.01.103
19. Najiha, M., Rahman, M. and Yusoff, A., "Flank wear characterization in aluminum alloy (6061 t6) with nanofluid minimum quantity lubrication environment using an uncoated carbide tool", ***Journal of Manufacturing Science and Engineering***, Vol. 137, No. 6, (2015). https://doi.org/10.1115/1.4030060
20. Fang, N. and Wu, Q., "A comparative study of the cutting forces in high speed machining of ti–6al–4v and inconel 718 with a round cutting edge tool", ***Journal of Materials Processing Technology***, Vol. 209, No. 9, (2009), 4385-4389. https://doi.org/10.1016/j.jmatprotec.2008.10.013

Persian Abstract

چکیده

این مقاله عمدتاً به ویژگی‌های سایش ابزار درج کاربید سیمانی بدون پوشش و درج‌های کاربید پوشش‌داده‌شده (PVD TiAlN ،PVD AlTiN)در هنگام چرخش Ti6Al4V-ELIبینابینی بسیار کم می‌پردازد. برای برآوردن شرایط پایداری، آزمایش‌ها در محیط خشک و حداقل مقدار روانکاری (MQL)انجام شده است. برای افزایش اثربخشی MQL، روغن نخل به عنوان مایع برش استفاده شده است. پارامترهای ماشینکاری یکسان برای همه درج‌های ابزار برش در محیط‌های خشک و MQL به کار گرفته می‌شود تا ویژگی‌های ماشینکاری را بهتر درک کنید. مشخص شد که سرعت برش تا حد زیادی بر سایش متوسط پهلو تأثیر می گذارد. عمر ابزار ابزار پوشش داده شده PVD TiAlN در هر دو محیط MQL و خشک در مقایسه با درج کاربید سیمانی بدون پوشش و درج پوشش دار PVD AlTiN بیشتر است. استفاده از روغن نخل در محیط MQL نتایج بهتری را در حین چرخش توسط درج PVD TiAlN ایجاد کرده است. ویژگی‌هایی مانند خنک‌کاری و روان‌کاری خوب، به طور قابل‌توجهی متوسط سایش جانبی کمتری را در طول ماشینکاری Ti6Al4V-ELI تحت شرایط محیطیMQL ارائه می‌کنند.

International Journal of Engineering

Journal Homepage: www.ije.ir

Fuzzy Logic Control of Maximum Power Point Tracking Controller in an Autonomous Hybrid Power Generation System by Extended Kalman Filter for Battery State of Charge Estimation

K. Sahel Hanane[a], L. Abderrazak*[b], R. Adlene[b], A. Mohamed[a], K. Mohamed[b]

[a] *Mechanical Engineering Department, Automatic Laboratory, University of 20 August 1955, Skikda, Algeria*
[b] *Electrical Engineering Department, Automatic Laboratory, University of 20 August 1955, Skikda, Algeria*

PAPER INFO

Paper history:
Received 07 April 2022
Received in revised form 04 November 2022
Accepted 05 November 2022

Keywords:
Management
Hybrid Photovoltaic System
Stand-alone
DC-DC Converter
State of Charge Estimation
Extended Kalman Filter

ABSTRACT

Autonomous power generation systems are designed to operate independently from the public power grid. Batteries constitute the important element in stand-alone PV system. They are used to store electricity produced by solar energy at overnight or for emergency use during the non-constant load demand. This paper has three major parts.The first pertains the design of an intelligent method for maximum power point tracking based on fuzzy logic controller to improve the efficiency of a standalone solar energy system. The second part describes the battery state of charge (SOC). The proposed model, which better reflects the real SOC response of the lithium battery, is constructed by using the extended Kalman Filter (EKF) states estimator. This proposed method can be considered as a more accurate and reliable method to estimate the battery state of charge. The third part integrates a management system for the above two renewable energy sources. The performance of the proposed management system by using a fuzzy logic controller based maximum power point tracking FLC-MPPT and the EKF estimator have been simulated in Matlab/Simulink at different solar irradiation and temperature for a given no constant load energy request.

doi: *10.5829/ije.2023.36.02b.02*

NOMENCLATURE

q	Electron Charge	v, w	zero-mean white Gaussian
α	Duty cycle	$A_k = \frac{\partial f(x,u)}{\partial x}\Big\|_{x(t),u(t)}$	Linearized System Matrix
x	State variable	$C_k = \frac{\partial f(x,u)}{\partial x}\Big\|_{x(t),u(t)}$	Linearized Output Matrix
u	Control variable	R_{L1} & R_{L2}	Load Resistors
$K_k = P_{k/k-1}C_d^T\left[C_d P_{k/k-1} C_d^T + \Sigma_v\right]^{-1}$	Kalman gain matrix	$P_{k/k-1} = A_d P_{k-1/k-1} A_d^T + \Sigma_w$	Error covariance time update

1. INTRODUCTION

In recent years, solar energy, in particular photovoltaic energy, has seen a significant development as an alternative to meet energy demands, especially in desert areas or for reasons of environmental concern and the fall in the prices of photovoltaic modules [1].

For this purpose, photovoltaic (PV) panels, which are the main technology for converting solar energy into electrical energy, can be installed as stand-alone systems to produce electrical energy in certain isolated areas or be connected to supply the electrical network. Because solar energy is instantaneous and unstable by nature, the PV energy system works in conjunction with storage batteries to provide continuous and stable power in the configuration of hybrid stand-alone power systems photovoltaic generator (GPV)/ batteries. Battery storage can be considered an auxiliary power source to reduce the

*Corresponding Author Institutional Email: a.lachouri@univ-skikda.dz (L. Abderrazak)

Please cite this article as: K. Sahel Hanane, L. Abderrazak, R. Adlene, A. Mohamed, K. Mohamed, Fuzzy Logic Control of Maximum Power Point Tracking Controller in an Autonomous Hybrid Power Generation System by Extended Kalman Filter for Battery State of Charge Estimation, ***International Journal of Engineering, Transactions B: Applications***, Vol. 36, No. 02, (2023), 199-214

risk of PV's irregular power supply, and always ensure the satisfaction of demand [2]. Indeed, to enhance the effectiveness of the PV generation system, DC/DC converters are always used to follow up on the maximal power extracted (MPP) from the PV array system and adapt the connection with an electrical network or battery bank to adjust the power flow route and optimize the whole system performance [3]. In order to retrieve the maximum power delivered by the PV generator, researchers are working on improving MPPT algorithms [4]. In the literature, several algorithms and techniques are developed for calculating the MPPT, such as the perturbation and observation (P&O) algorithm, the incremental conductance algorithm (InCond), the ripple correlation control algorithm (RCC), the fractional voltage/current MPPT, the fuzzy logic controller MPPT algorithm, and the neural network (NN)-based MPPT control [5]. However, the most famous MPPT is the fuzzy logic controller, which is widely adopted because it is the simplest and most robust method among all MPPT ones. The FLC method can be introduced also in other contexts for searching the maximum (or minimum) of a function [6]. Other than an MPPT controller, inverters for PV or grid-connected or stand-alone AC systems, DC/DC converters (buck, boost, buck-boost, Cuk, single-ended primary inductance converter SEPIC etc.) and storage elements such as electrical batteries, which are used to improve the PV efficiency and regulate the output voltage [7].

Hybrid power systems (HPS) based on renewable energy (RE) are a good alternative for conventional systems to guarantee the continuity of electricity supply to customers. In general, batteries are the most common in this context. Many companies are interested in the management and storage of solar energy and providing more intelligent solutions for the solar energy markets, whether for home use or for commercial and industrial use. However, to meet this requirement, we can find that batteries constitute the most attractive energy storage systems because of their high efficiency and low pollution. However, the batteries must be protected against overcharging and deep discharging. This requires continuous monitoring for both the battery state of charge and the energy produced by the photovoltaic panels [8]. Therefore, the battery State of Charge (SOC) which used to estimate its remaining stored charge, is a very important parameter to establish a control strategy [9]. In this context, real-time tracking with an accurate estimate of its SOC can not only protect the battery from overcharging and over discharging and improve its life duration but also allow the applications to make rational control strategies in order to ensure the reliability of the power production system and optimize energy management [10].

There are many types of batteries currently used in the industry: lead-acid batteries, Ni-MH, Ni-Cd and Li-ion batteries. All these batteries have chemical energy storage that cannot be directly accessed and measured. In the literature, evaluation of SOC is essentially based on two methods, physical and electrical:

A. Physical methods: These methods are based on the observation of chemical and physical changes occurring in the battery during charging or discharging in operating mode. Among these methods, one involves measuring the gravity (or specific gravity) of the electrolyte.

B. Electrical methods: These methods are applicable to the majority of batteries. They are calculated from the measurements of the electrical parameters such as the voltage, the current, internal resistance, and impedance. Among these methods: method of charge counting or current integration, Fuzzy logic and ANN-based methods, and recently the Extend Kalman Filter (EKF).

This work presents three main contributions. The first contribution consists of the design of an intelligent method for maximum power point tracking based on fuzzy logic controllers. The second part describes the battery state of charge (SOC). The proposed model, which better reflects the real SOC response of the lithium battery, is constructed by using the extended Kalman Filter (EKF) states estimator realizing a software sensor for the measurement of the battery SOC. The advantage of such a method is that the SOC is optimally estimated even in the presence of wideband measurement noise affecting the system [11]. The paper is structured as follows: section 2 is devoted to the modeling of PV systems. A brief introduction to the control scheme is presented in section 3. Section 4 introduces an EKF-based SOC estimator for the developed model, and the simulation results are provided in section 5.

2. DESCRIPTION OF THE SYSTEM

A stand-alone alternative energy system consists of two or more energy sources, at least one of which is renewable [12]. Solar is a promising power generating source, but it depends on climatic conditions and geographical areas [13]. Generally, the residential PV-battery backup system consisted of a PV generator for the conversion of the solar irradiance to electrical power, deep-cycle flooded lead acid batteries for the storage of the electrical energy, Pulse Width Modulation (PWM) charge controller to regulate the charging operating mode of the battery bank. Also, a power converter is able to operate in two modes: DC/AC and AC/DC conversion. Figure 1 shows a schematic overview of a typical PV/battery Renewable Energy Hybrid System (REHS).

In this section, the PV generator and the storage battery are coupled with the inverter and connected to an AC bus system, which supplies directly the load. In such systems, the battery can be considered as the main source in the case, for instance, of insufficient PV production.

Furthermore, the PV power production has to be exploited with the highest efficiency. Therefore, it is necessary for an operation strategy to design the optimal economic solution for solving this problem. On another side, the capacity of battery has to be large enough to be charged from the power excess provided by the PV generator to cover the power deficit.

2. 1. PV Model In simulations, the literature reveals methods of modeling solar cells, with a major difference between using a single diode solar model or a double diode solar model. They display real system actions with the inclusion of losses [12]. In this paper, a single diode model is used. This model is characterized by its electric diagram, which is illustrated in Figure 2. The power source models the conversion of solar energy into electricity, the resistance shunt reflects the surface quality of the cell periphery, the resistance series refers to the different contact and interaction resistances performed on the cell, and the diode in the PN junction parallel models [13].

The current expression for equivalent solar model is given by Equation (1).

$$I = I_L - I_0\left(e^{\frac{q(V+I\cdot R_S)}{n\cdot k\cdot T}} - 1\right) - \frac{V+I\cdot R_S}{R_{SH}} \tag{1}$$

Generally, for modules in a PV system that are connected in arrays, the cell array contains Np parallel branches, each with Ns modules in series. The total current output can be deduced as follows from Equation (2) [14].

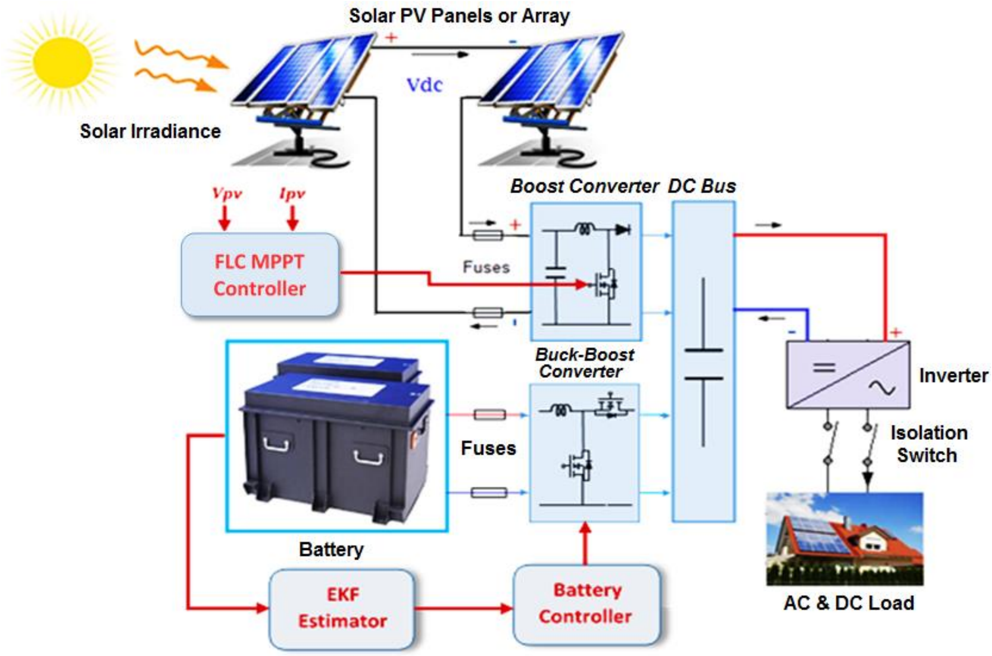

Figure 1. Schematic illustrating the studied REHS configuration

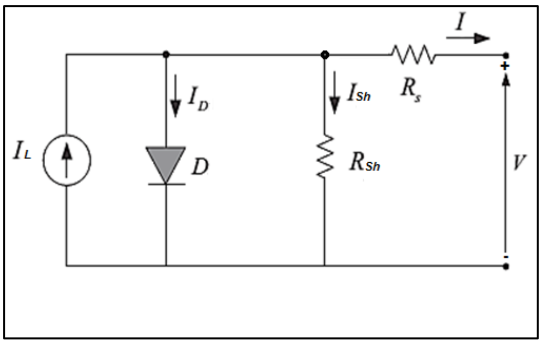

Figure 2. Equivalent Model of Single Diode Solar cell [15]

$$I = N_P\cdot I_L - N_P\cdot I_0\left(e^{\frac{q(V+(N_S/N_P)I\cdot R_S)}{n\cdot k\cdot T\cdot N_S}} - 1\right) - \frac{V+(N_S/N_P)I\cdot R_S}{(N_S/N_P)R_{SH}} \tag{2}$$

where:

- I: is the solar array output current (A).
- I_0: is the cell reverse saturation current (A).
- I_L: is the photo-generated current (A).
- V: is the solar panel output voltage (V).
- q: is the electron charge 1.602*10⁻19 C.
- k: is the Boltzmann constant 1.381* 10^{-23} J/K.
- n: is the p-n junction ideality factor.
- T: is the temperature (K).

2. 2. DC/DC Converter The boost converter is used where a controlled average voltage is required by converting a DC voltage (V_{in}) to another DC voltage (V_0). As shown in Figure 3, it is comprised of a DC input voltage source V_{in}, boost inductor L, controlled switch (MOSFET), diode D, filter capacitor C, and load resistance R. When the switch S is in the on state, the boost inductor stores energy from the PV panel and the current increases linearly. The diode D is reverse biased at the time. However, if the switch S is turned off, the energy stored in the inductor is released through the diode to the input RC circuit. As the name of the converter suggests, the PV panel voltage is added to the inductor voltage (discharge state) to make the output voltage always greater than the input voltage [16].

This converter is modelled as follow [17]:

$$V_0 = \frac{V_{in}}{1-\alpha} \tag{3}$$

$$I_0 = I(1-\alpha) \tag{4}$$

where, α, V_{in} and I, V_0 and I_0 are respectively the duty cycle, PV input voltage, and current, and the output voltage and current of the boost converter.

2. 3. Modeling of Battery The battery is an important element of a stand-alone PV system. The equivalent circuit illustrated in Figure 4 gives the model of the lithium battery. The capacitances C_c and C_{cs} represent the battery storage capacity and the diffusion effects. The resistances R_i and R_t represent the internal and the polarization resistances respectively. The voltages across the bulk capacitor and the surface one are denoted by V_{cb} and V_{cs}. The terminal voltage and current are denoted by V_0 and I, respectivley [18]. For simplicity, the model equations can thus be characterized by the model, which is shown in Figure 4.

$$\dot{V}_{cb} = \frac{I}{C_{cb}} \tag{5}$$

$$\dot{V}_{cs} = \frac{1}{R_t C_{cs}} V_{cs} + \frac{1}{C_{cs}} I \tag{6}$$

$$V_0 = V_{cb} + V_{cs} + IR_i \tag{7}$$

It seems that the relationship between open circuit terminal voltage (OCV) and State of Charge SOC is only

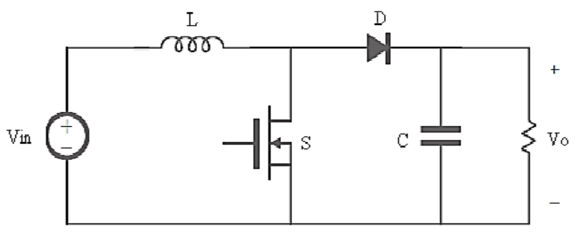

Figure 3. DC-DC Boost converter

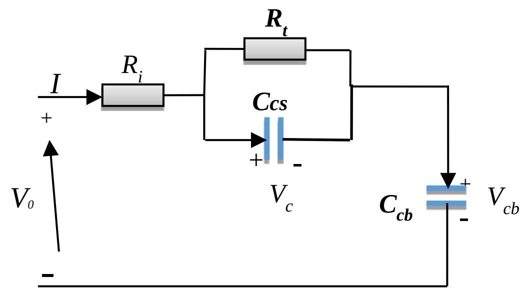

Figure 4. Equivalent circuit model for a lithium battery

piecewisely linear and static [19], one can define:

$$V_{cb} = kSoc + d \tag{8}$$

where k and d ≠ 0, (k and d are not constants and vary with battery SOC and the ambient temperature). Here, SOC represents the battery's State Of Charge. By substituting Equation (8) into Equation (5) ~ Equation (7), the equations describing the battery characteristics can be defined as:

$$\begin{bmatrix} \dot{Soc} \\ \dot{V}_{cs} \end{bmatrix} = \begin{bmatrix} \frac{I}{kC_{cb}} \\ -\frac{1}{R_t C_{cs}} V_{cs} + \frac{1}{C_{cs}} I \end{bmatrix} \tag{9}$$

$$V_0 = kSoc + V_{cs} + IR_i + d \tag{10}$$

3. CONTROL STRATEGIES

The literature has suggested several MPPT techniques to improve MPP algorithms that have been published, such as: P&O MPPT algorithm, Fractional Open-Circuit Voltage-Based MPPT, Incremental Conductance Based MPPT Technique, Fuzzy Logic Control Based MPPT, Neural Network Based MPP. Out of which, due to several advantages like fast operation, simple implementation, Fuzzy Logic Control Based MPPT is preferred [20-22].

3. 1. Fuzzy MPPT Control The MPPT fuzzy logic controller has been developed to extract the maximum solar energy by forcing the PV panel to operate at its maximum power point (MPP). This control is considered a crucial element for improving the efficiency of the PV system [23]. Fuzzy control is a method that allows the construction of nonlinear controllers from heuristic information that comes from the knowledge of an expert. In the MPPT configuration, Fuzzy Logic Controller (FLC) is used to determine the duty cycle of the DC-DC boost converter. In this study, the fuzzy logic controller was developed with two inputs and one output functions such as PV voltage, PV current, and duty cycle of the PV boost converter. Figure 5 shows the diagram of the FLC MPPT algorithm. The power produced by the

PV panels is calculated from the measured values of the current and voltage sensors [24]. The main parts of the FLC include: fuzzification, system inference, rule base, and defuzzification.

The fuzzy logic controller has been developed with two inputs and one output function, such as, dV_{pv}, dP_{pv} and duty cycle of the PV boost converter, as shown in Figure 6(a). The fuzzy dV_{pv} input membership function is classified into seven ranges, namely negative dV_{pv}, negative medium dV_{pv}, negative small dV_{pv}, zero dV_{pv}, positive small dV_{pv}, positive medium dV_{pv} and positive dV_{pv} as presented in Figure 6(b). The fuzzy PV dP_{pv} input membership function is classified into seven ranges, namely negative dP_{pv}, negative medium dP_{pv}, negative small dP_{pv}, zero dP_{pv}, positive small dP_{pv}, positive medium dP_{pv} and positive dP_{pv} as presented in Figure 6(c). The fuzzy duty cycle output membership function is classified into seven ranges that are negative Duty Cycle, negative medium Duty Cycle, negative small Duty Cycle, zero Duty Cycle, positive small Duty Cycle, positive medium Duty Cycle and positive Duty Cycle as presented in Figure 6(d). The fuzzy rules surface waveform presented in Figure 6(e).

3. 2. Battery Charge Controller Based on simulation work done for a stand-alone PV system, a strategy for ON/OFF-switching control signals can be generated through a PID-type controller where the battery and the PV generator never simultaneously power the load. When the energy produced by the PV is not enough to meet the load demand, the secondary power supply (battery) takes over and supplies the load. This control strategy aims to adjust the phase between the system bus voltage (Vdc) and the battery voltage according to the state of charge (BAT_SOC). Figure 7(a) shows the ON/OFF-switching set points (or thresholds) for the battery and PV panel power contributions. When the power produced by the solar panels falls below the load demand, or the threshold, the battery is switched ON

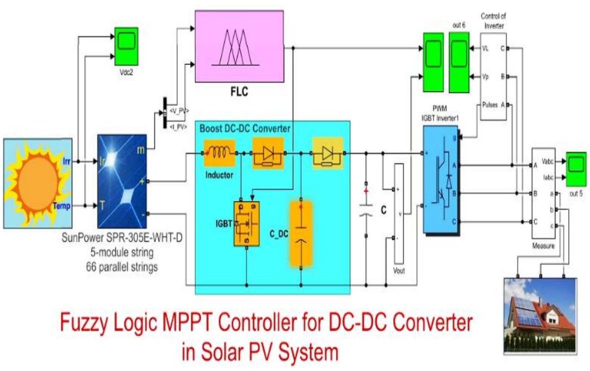

Figure 5. Fuzzy based MPPT controller simulation model for PV system Design of Fuzzy Logic Controller

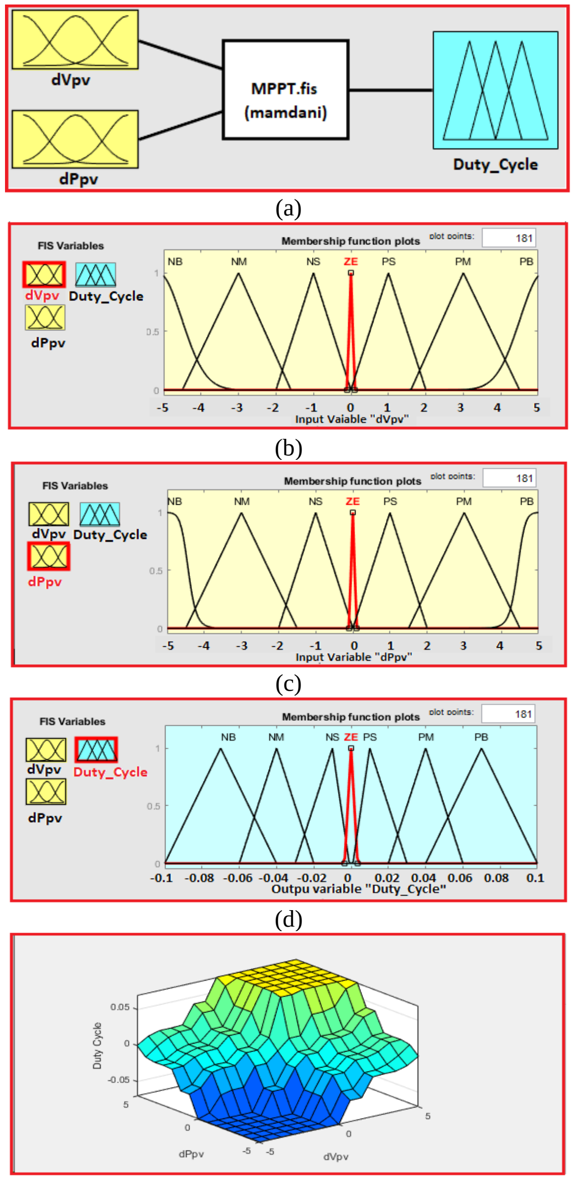

Figure 6. (a) Design of Fuzzy Controller for DC-DC converter (b) Input dV_{pv} Membership function (c) Input dP_{pv} Membership function, (d) Output Duty Cycle Membership function and (e) The fuzzy rules surface waveform

and kept on until BAT_SOC falls below the threshold. The two variables S1 and S2 are used to put the battery either in charging mode or in energy source mode according to Table 1.

The battery's operating mode is directly related to the DC-DC converter's functioning. In the case that the GPV energy production is insufficient, the battery takes over as an emergency power supply. Switching between the PV source and the battery is ensured by the gate control output, provided by a PI regulator Figure 7(b).

TABLE 1. Battery operating mode

S2	S1	Operating mode
0	0	Disconnected
0	1	Source
1	0	Loading
1	1	Disconnected

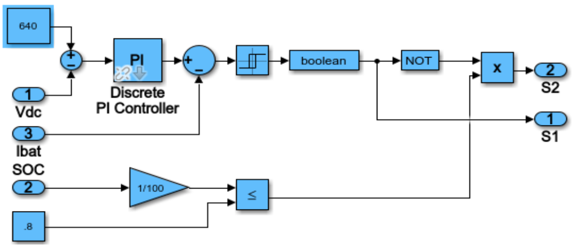

(a)

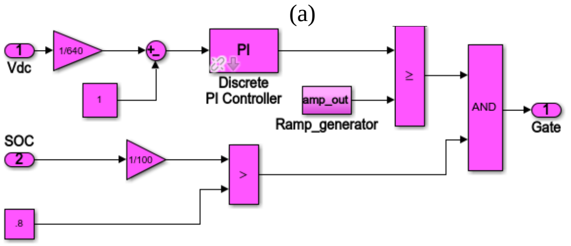

(b)

Figure 7. (a) Battery/electrolyzer Controller (b) PI Controller for Switching between the PV source and the battery

4. EKF-BASED SOC ESTIMATION

The EKF considers the noise characteristics of the current and voltage sensors, and effectively overcomes the effect of random errors. There exist several alternatives to the Kalman filter, depending to whether the mathematical model is linear, nonlinear, discrete or continuous. In this work, the battery is the dynamic model, and the state of charge constitutes the state variable to estimate. If the model is nonlinear, then we may use a linearization process at every time step to approximate the nonlinear system with a linear time varying (LTV) system. This LTV system is then implemented by Kalman filter, resulting in an Extended Kalman Filter (EKF) on the true nonlinear system. Note that although EKF effectiveness has been validated in many works [10, 25-27]. In this study, the EKF, based on dynamic equations, is used to estimate the battery state of charge [28] Figure 7.

The nonlinear system is presented as follows:

$$\dot{x}(t) = f(x,u) + w \tag{11}$$

$$y(t) = g(x,u) + v \tag{12}$$

where, w and v are zero-mean white Gaussian stochastic processes with covariance matrices Σ_w and Σ_v respectively. Now, $f(x,u)$ is a nonlinear dynamics function and $g(x,u)$ is a nonlinear measurement function. The input is expressed as $u(t) = I$ and the output is $y = V_0$.

$$f(x,u) = \begin{bmatrix} \frac{u}{kC_{cb}} \\ -\frac{1}{R_tC_{cs}}x_2 + \frac{1}{C_{cs}}u \end{bmatrix} \tag{13}$$

$$g(x,u) = kx_1 + x_2 + R_iu + d \tag{14}$$

At each time step, $f(x,u)$ and $g(x,u)$ are linearized by a first-order Taylor-series expansion. The linearized model is:

$$\delta\dot{x} = A_k\delta x + B_k\delta u \tag{15}$$

$$y = C_k\delta x + D_k\delta u \tag{16}$$

where:

$$A_k = \frac{\partial f(x,u)}{\partial x}\bigg|_{x(t),u(t)} = \begin{bmatrix} 0 & 0 \\ 0 & -\frac{1}{R_tC_{cs}} \end{bmatrix}$$

$$B_k = \frac{\partial f(x,u)}{\partial u}\bigg|_{x(t),u(t)} = \begin{bmatrix} \frac{1}{kC_{cs}} & \frac{1}{C_{cs}} \end{bmatrix}$$

$$C_k = \frac{\partial f(x,u)}{\partial x}\bigg|_{x(t),u(t)} = \begin{bmatrix} k & 1 \end{bmatrix}$$

and $D_k = \frac{\partial g(x,u)}{\partial x}\Big|_{x(t),u(t)} = R_i$

The model represented by Equations (15)-(16) can be discretized as follows:

$$x_{k+1} = A_dx_k + B_du_k \tag{17}$$

$$y_{k+1} = C_dx_k + D_du_k \tag{18}$$

where:

$A_d \approx E + T_sA_k$,

$B_d \approx T_sB_k$,

$C_d \approx C_k$, and $D_d \approx D_k$, E is the unit matrix and T_s is the sampling period.

The algorithm of the EKF has three distinct phases: *Initialization, Prediction and upgraded* [28]:

Initialization: for k = 0, given the initial state values x_0, covariance matrix P, noise variance Σ_w and Σ_v.

Prediction: The step of prediction consists to using the state estimated of the previous moment to calculate an estimate of the current state.

The state estimate update:

$$\bar{x}_{k/k-1} = f\left(\bar{x}_{k-1/k-1}, u_{k-1}\right)$$

Error covariance time update:

$$P_{k/k-1} = A_dP_{k-1/k-1}A_d^T + \Sigma_w$$

Upgraded and correction: In this step, the current measurements are used to correct the state predicted to obtain a more precise estimate of the state.

Kalman gain matrix:

$$K_k = P_{k/k-1}C_d^T\left[C_dP_{k/k-1}C_d^T + \Sigma_v\right]^{-1}$$

State estimate measurement update:

$$\bar{x}_{k/k} = \bar{x}_{k/k-1} + K_k\left[y_k - g\left(\bar{x}_{k/k-1}, I_k\right)\right]$$

Error covariance measurement update:

$$P_{k/k} = (E - K_kC_d)P_{k/k-1}$$

5. MATLAB/SIMULINK SIMULATION AND RESULTS

The solar panel model is made in *Matlab/Simulink* software, the model is simulated under STC, and the *I*–*V* and *P*–*V* characteristics are presented in Figure 8. These curves change depending on the temperature and solar irradiance variation Figure 9.

Simulation is the simplest and most efficient technique used today for the evaluation of engineering solutions. The MATLAB-SIMULINK model was designed, as depicted in Figure 9, to explore the performance of the integrated PV/Battery/AC & DC Load system and the control strategy. However, the components of the proposed stand-alone PV system are: The solar panels and storage batteries are connected to the DC bus by a DC/DC boost converter and DC/DC buck-boost converter consecutively. Then we find a three-phase inverter that is supervised by its own controller and it is used to convert from DC to AC voltage. Finally, two loads are connected / disconnected to the AC voltage side by the inverter controller, with Load 1 representing the critical one and Load 2 represents the less priority loads. The conventional fuzzy logic MPPT controller, is proposed and the calculation of the SOC status is evaluated by EKF observer. The PV module considered in the simulation is the Array type: SunPower SPR-305E-WHT-D (with a capacity of 100 kW); 5 series modules; 66 parallel strings in which the model parameters are given in Table 2.

A Stand-alone system involves no interaction with a utility grid. Many scenarios are considered to simulate the autonomous hybrid power system with local load variations. Firstly, we consider a constant temperature with varying irradiation and secondly a constant irradiance with varying temperature applied to the solar panel SunPower SPR-305E-WHT-D. For the 100 kW solar array block, we used 330 SunPower SPR-305E-WHT-D modules, connected in a combination of 66 cells in-parallel by 5 cells in-series. A series connection of cells results in higher voltages, while a parallel connection results in higher current. This array generates 100.7 kW at an irradiance of 1 kW/m^2 at a temperature of 25°C. Its MPP voltage varies approximately from 250.2 V to 296.6 V up to given environmental conditions. The DC-DC Converter operates at a switching frequency of 5 kHz and provides an output at 640 V DC. The DC link

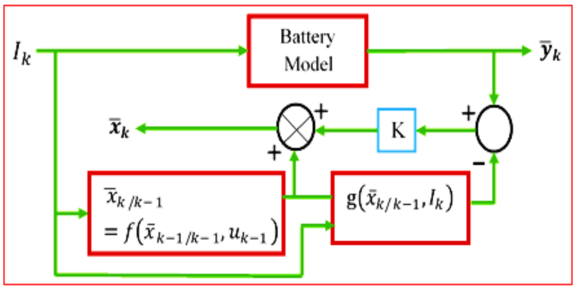

Figure 8. Structure of the Extended Kalman Filter

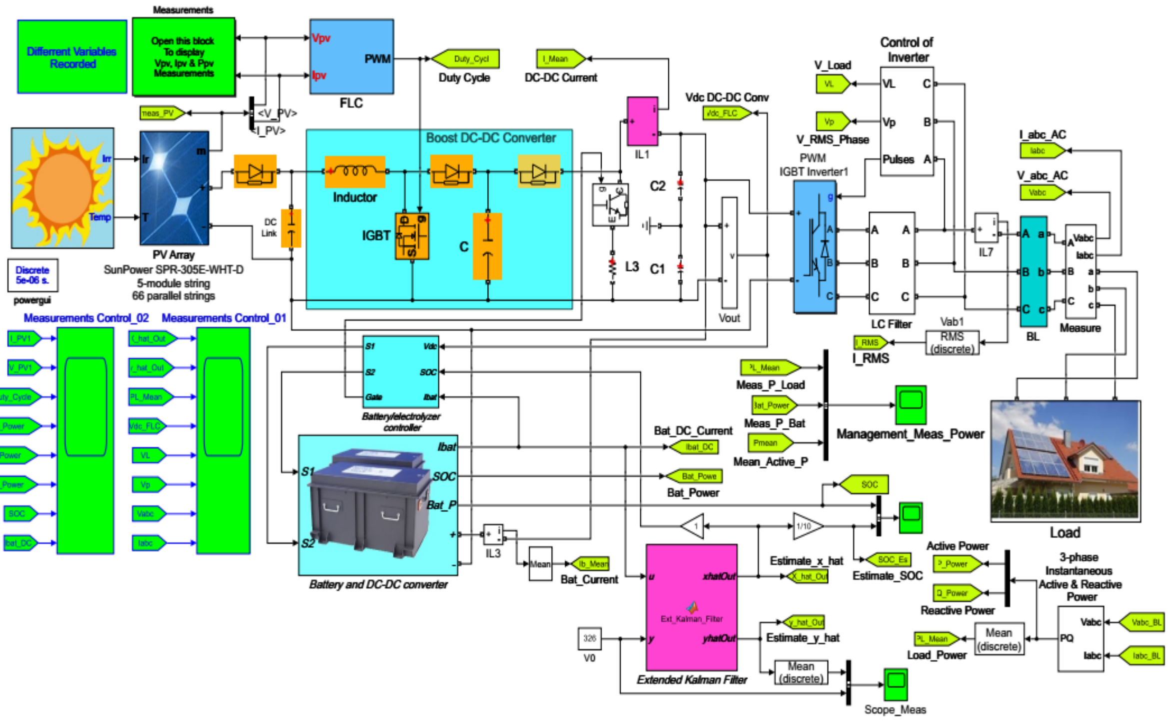

Figure 9. Simulink model of proposed control of the system

capacitors C1 and C2 play a damping role in order to maintain the stability of the MPPT during these transitory disturbances. This aspect is important because this ripple is directly perceived as electrical pollution at the output voltage of the PV module. By making step variations in the solar radiation S and the temperature T, the proposed power generation system of Figure 7 provided the I–V and P–V characteristics as shown in Figure 8. Hence, as shown, the sampling time T_s is 50 µs and the simulated data are in accordance with the characteristics mentioned in Table 2.

The DC link capacitors C1 and C2 play a damping role in order to maintain the stability of the MPPT during these transitory disturbances. This aspect is important because this ripple is directly perceived as electrical pollution at the output voltage of the PV module. By making step variations in the solar radiation S and the temperature T, the proposed power generation system of Figure 9 provided the I–V and the P–V characteristics as shown in Figure 10. Hence, as shown, the sampling time T_s is 50 µs and the simulated data are in accordance with the characteristics mentioned in Table 2.

5. 1. Effects of Changing Irradiance

As the irradiance increases short circuit current also increases along with the open circuit voltage. Because of both increasing of V and I, the P_{max} is also increases according the irradiance.

Case Study 01: Irradiance and Temperature variation

For the first case study applied to the PV array type SunPower SPR-305E-WHT-D, the supervisory control

TABLE 2. PV module M/s SunPower SPR-305E-WHT-D Paramaters at STC (25°C & 1000W/m^2)

Designation	Value
Parallel String	66
Series-connected modules per string	5
No. of cells per module	96
Number not of modules	330
PV module power	305.226W
Isc of PV array	5.96 A
Voc of PV array	64.2 V
MPP Voltage at 25 ◦C Vmpp	54.7 V
MPP Current at 25 ◦C Impp	5.58 A
Temperature coefficient of Voc (%/deg.C)	-0.27269
Temperature coefficient of Isc (%/deg.C)	0.061745
Parallel resistance (Rp)	269.5934Ω
Series resistance (Rs)	0.37152 Ω
Diode ideality factor	0.94504

considers the forecast energy demand of the end-users and makes instantaneous decisions about stand-alone energy production. The main goal of stand-alone system management is to satisfy the loads energy needs.

Simulation inputs for the solar panel model are the incident solar irradiance and the ambient temperature. These parameters are updated at each time interval, and they are subject to the variability of the data. The simulation outputs of the solar panel array at each time step are the current, voltage and power generated. The PV array generates the maximum amount of power at around 100KW within the given irradiation (1000W/m^2,25°C). An R load (constant impedance) model is used to examine the PV system behavior under the FLC MPPT algorithm. Loads in a stand-alone system are commonly categorized into fixed and flexible ones, depending on the comfort choices defined by the user. The simplified R no constant load model consists of a resistor R connected in parallel (R_{L1} & R_{L2}) with values of 30000Ω and 10000Ω respectively. The load profile adopted in this study is as follow:

- ✓ *From 0 to 1.25s : load1* = 30000Ω,
- ✓ *From 1.25 to 2.5s : load1+load2* = 40000Ω,
- ✓ *From 2.5 to 3s : load1* = 30000Ω,

The obtained simulation results are summarized in Figures 11-17. Figure 11 shows the incident solar irradiance and the ambient temperature profile. Figure 12 depicts the PV array voltage $V_{pv}(t)$ (Figure 12(a)) and current $I_{pv}(t)$ (Figure 12(b)) responses, respectively.

The plots of results in Figure 13 show the duty cycle (d), calculated from a conventional FLC MPPT controller, and its effect on the promising performance and accurate tracking of the stand-alone system according to the profile change of irradiance and temperature, this figure also illustrates the DC-DC voltage and current respectively. Figure 13(a) shows the duty cycle temporal evolution calculated from the PWM signal, then Figure 13(b) gives the DC-DC converter voltage and the Figure 13(c) illustrates the currents generated by the DC-DC converter, the mean and the rms currents respectively. Simulation results are obtained as shown in Figure 14, which shows the SOC and current battery. Figure 14(a) shows that the estimate SOC curve follows the measured SOC closely. Therefore, Figure 14(b) depicts the measured and estimated battery current with its *zoomed-in views*. Figure 14 shows clearly how the real SOC reflects precisely the battery operation, whether in charging or discharging mode.

Figure 15 shows the inverter output voltage before filtering, which contains the harmonic components. In addition, we can easily see that the stability of the inverter output voltage is always assured even with the load variation. However, Figure 16 shows the Inverter output *Vabc* Voltage (a) and *RMS(Vabc)* (b) with varying

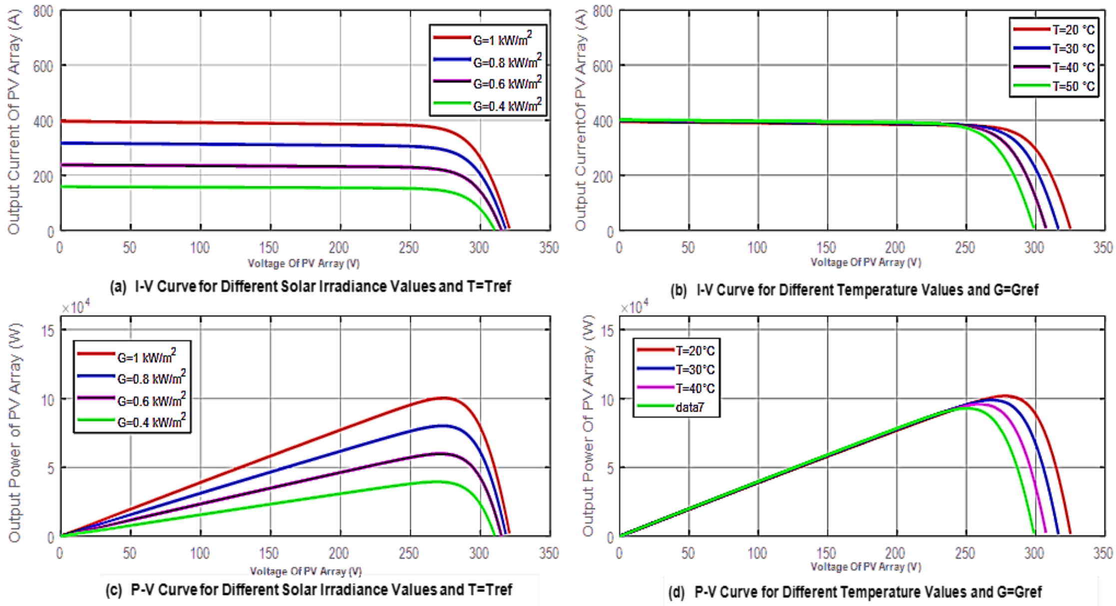

Figure 10. I-V and P-V characteristics of PV array under various temperatures and solar irradiation levels

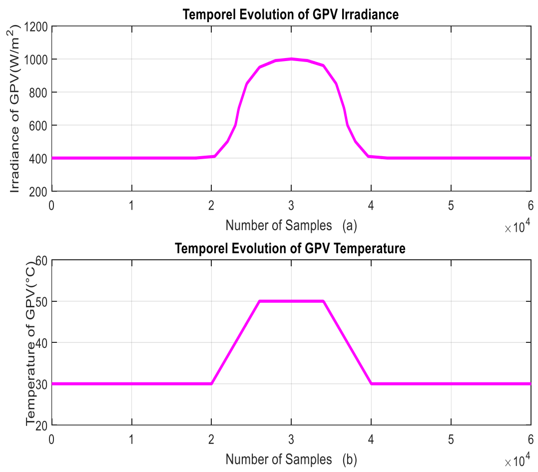

Figure 11. The incident solar irradiance (a) and the ambient temperature (b) profile

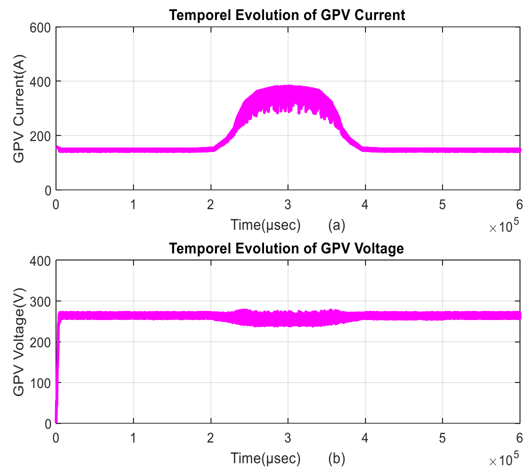

Figure 12. GPV ($\mathbf{I_{pv}}$ & $\mathbf{V_{pv}}$) behavior during sudden full load Temporal Evolution of $\mathbf{I_{pv}}$ (a) and $\mathbf{V_{pv}}$ (b)

irradiance and temperature values with no constant. Then the figure (Figure 17) shows the produced power trajectories for all three stand-alone alone components, PV panels, battery and the load. The main goal of hybrid system management is to satisfy the battery and load needs. For this assumption, the control algorithm starts with the selection of the mode connection, and then it checks the battery SOC, after that it passes to the comparison between the panel power and that required by the load demands. These comparisons are done according to the following main cases:

Case 1: The solar power covers the load demand, and charges the battery banks.
Case 2: The battery helps the PV generator to supply the load demand.
As Figure 17 shows, the PV panel generates the energy according to the given climatic conditions (Irradiation, Temperature). The resulting graphs will be discussed according to time intervals, as follows:
From 0 to $\boldsymbol{1.8520s}$***:*** During this period, the PV energy is greatere than load demand, and the battery is fully charged.

From $\mathbf{1.8520}$***s to*** $\mathbf{2.5165}$***s:*** The PV energy can't cover the power needs despite the increased load demand. The storage battery delivers the lacking power in order to supply the load.

From $\mathbf{2.5165}$***s to*** $\mathbf{3}$***s:*** During this interval time, the PV energy covers the load power needs. The battery is fully charged and the energy supplied by the battery must be zero.

Case Study 02: variable Irradiance and constant Temperature

Simulations depicted in Figures 18-24 illustrate the case with variable Irradiance, constant Temperature and no constant Load. All the waveforms of these figures illustrate the response of PV array type SunPower SPR-305E-WHT-D. However, we can easily conclude that the PV generator is very sensitive to rapid environmental changes and, it is well known that an irradiance change has a much greater effect on array characteristics than does the temperature change. When the irradiance is changed, the power-voltage characteristic of the PV panel and its MPP are simultaneously reformulated. Therefore, the FLC MPPT controller must track the changed MPP rapidly. Figure 18 presents PV panel inputs, irradiance and ambient temperature fixed at 25°C. The signal is drawn to vary from 1000 W/m^2 to 250 W/m^2 and returns to its initial value until the end. Therefore, the Figure 19 shows the I_{pv} and V_{pv} output PV array. These two parameters have the same behavior then the case_01. Figure 20 gives the duty cycle control signal (Figure 20 (a)) Vdc Voltage (Figure 20(b)) and I_{dc} Current (Figure 20(c)) of the DC-DC converter. The control signal (duty cycle) generates adaptive values within the climatic conditions and no constant load. The Dc voltage is around 640V. The Figure 21 shows the SOC measured and estimated by using the Extended Kalman Filter (EKF). This estimator is adopted to introduce a senseless technique to estimate the storage battery SOC. The figures (Figures 22 and 23) illustrate the three-phase inverter response, currents, voltages and rms value. For the power balance between the PV generator and Battery, we can easily see the efficiency of the proposed strategy control. Figure 24 depicted the behavior of the hybrid stand-alone power systems management against the irradiance variation and no constant load demand.

In conclusion, the rapid changing weather should challenge the MPPT algorithm and it does so. However, the reaction of the MPPT controller is quick; by looking at Figures 20(a) and 20(b) it can be seen how fast the MPPT responds to the irradiance change. At the end of this research work, we can conclude that the obtained results are satisfactory and that the objective to maintain the maximum power possible from a PV generator, during different climatic conditions of the solar insolation and temperature, was realized. This controller makes a shorter time to find the point of maximum power.

The obtained results can be compared with other research works using the same context concerning the power management applied to hybrid systems. In our case, despite the very severe operating conditions, a non-constant load and variable climatic conditions, the proposed controller gives very efficient results compared with those cited in [28, 29]. The chattering phenomenon is damped and the voltage Vdc is almost constant even in the presence of fluctuations during the operating mode. The efficiency of this controller is proven especially during the switching of the power produced by the different sources.

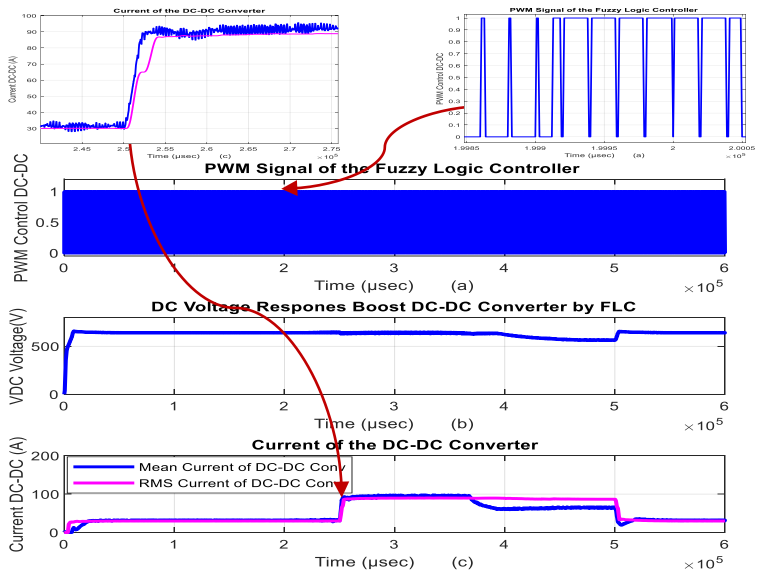

Figure 13. The Cycle duty control signal (a), **Vdc** Voltage (b) and **Idc** Current (c) of the **DC-DC** converter

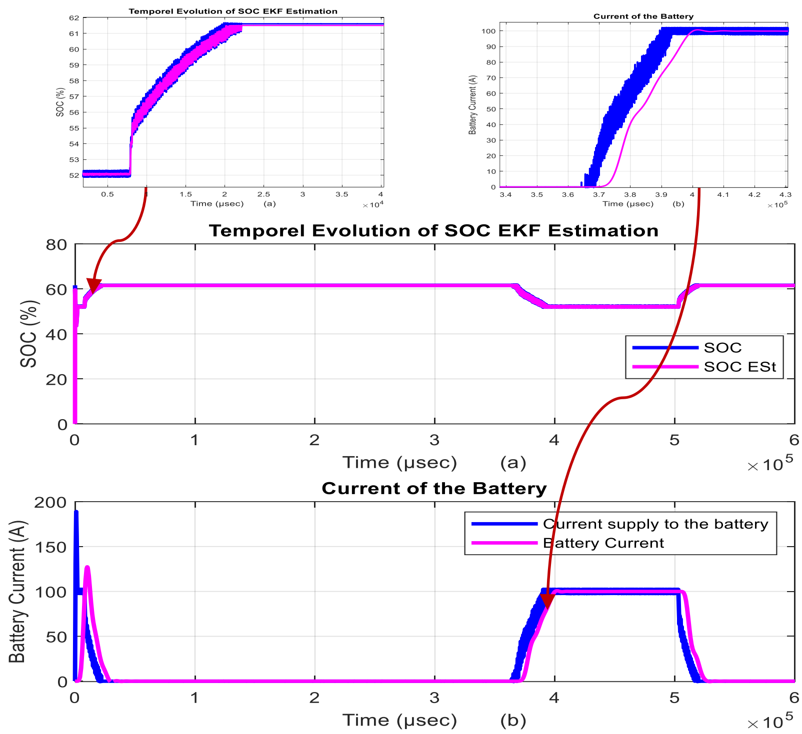

Figure 14. Measurement and Estimate SOC (a), Current supply and generate current (b) of the battery

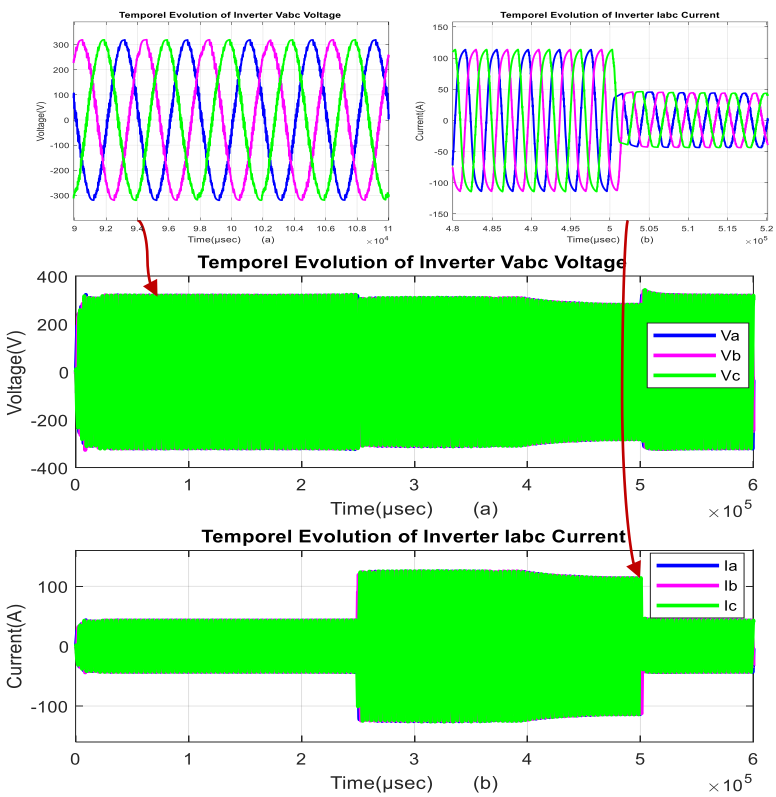

Figure 15. Inverter three phase sinusoidal voltage (a) and current (b) during no constant load according solar irradiance and the ambient temperature condition

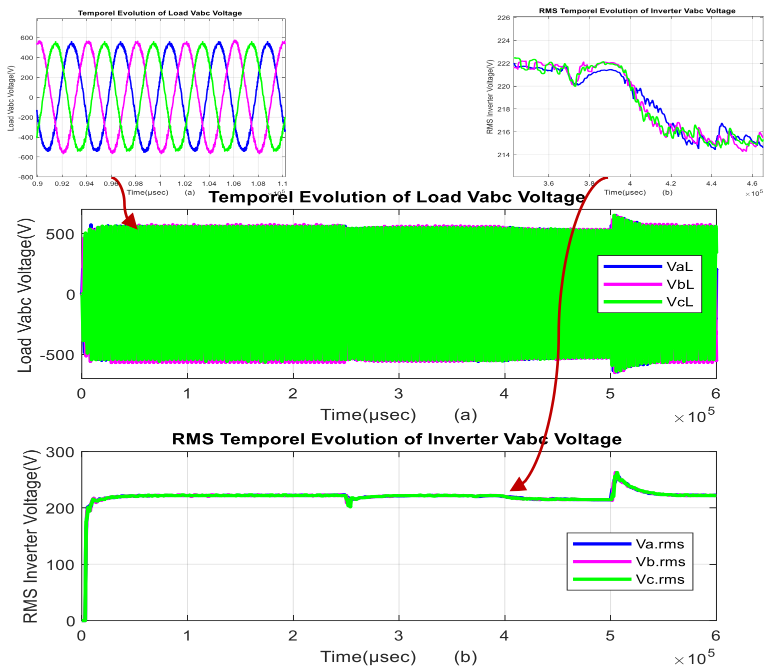

Figure 16. Inverter **Vabc** Phase to Phase Voltage (a) and (b) RMS (**Vabc**) with varying irradiance and temperature values with no constant Load

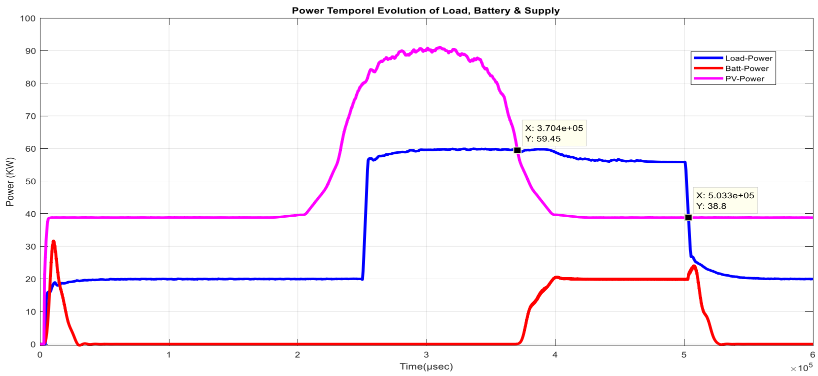

Figure 17. Power balance during integration of PV system and Battery by using a no constant Load

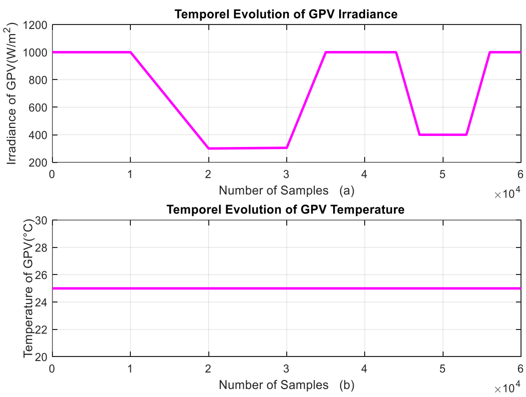

Figure 18. The incident solar irradiance (a) and the ambient temperature (b) profile

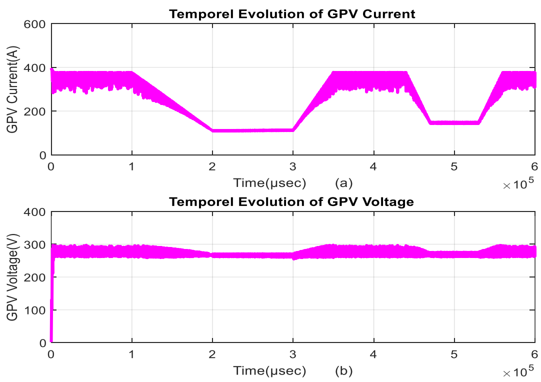

Figure 19. GPV ($\mathbf{I_{pv}}$ & $\mathbf{V_{pv}}$) behavior during sudden full load, temporal evolution of $\mathbf{I_{pv}}$ (a) and $\mathbf{V_{pv}}$ (b)

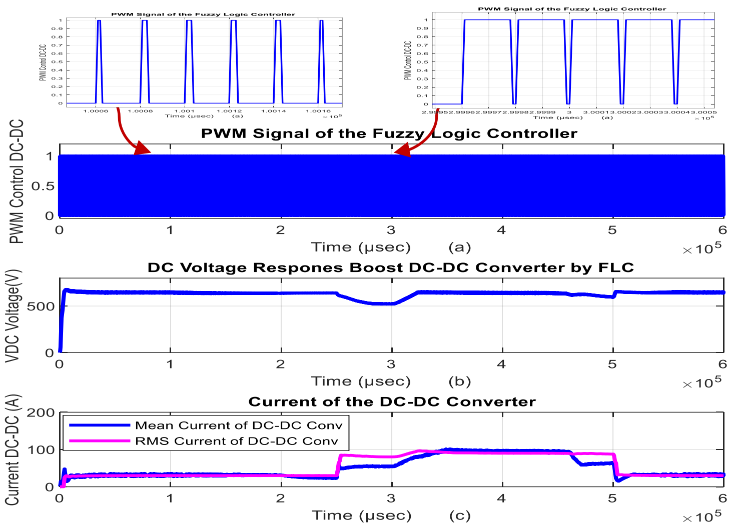

Figure 20. The Cycle duty control signal (a), **Vdc** Voltage (b) and **Idc** Current (c) of the **DC-DC** converter

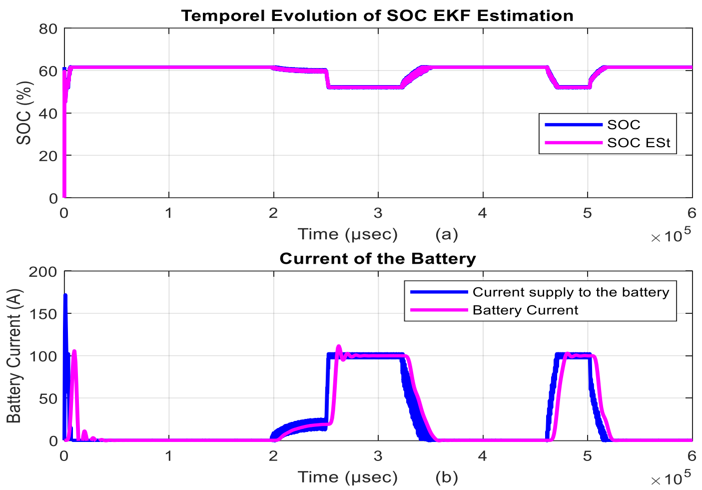

Figure 21. Measurement and Estimate SOC (a), Current supply and generate current (b) of the battery

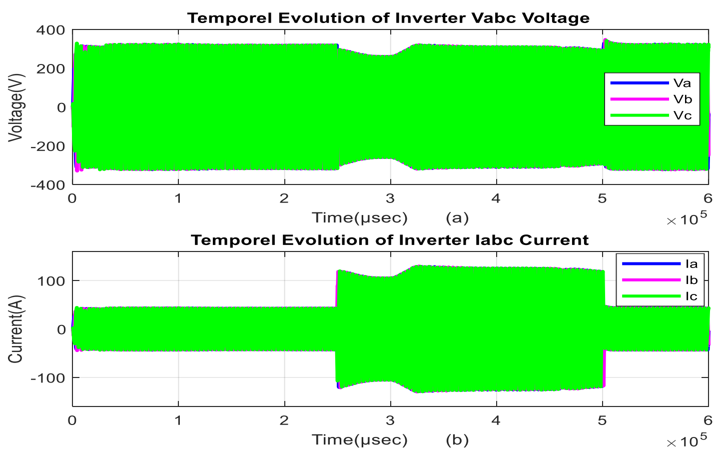

Figure 22. Inverter **Vabc** voltage and current during no constant load according solar irradiance and constant Temperature

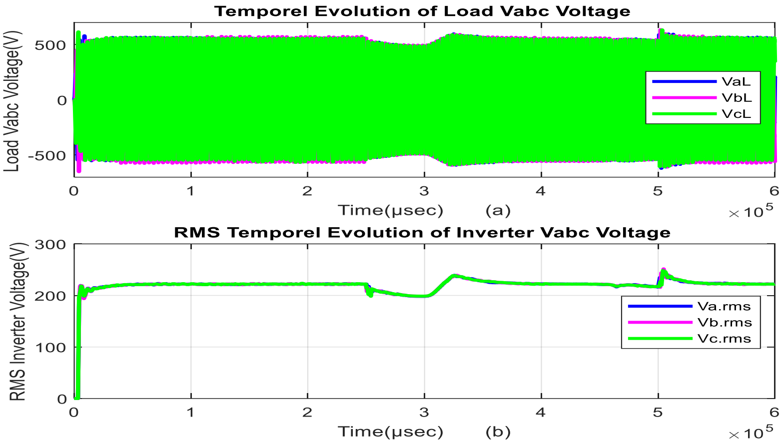

Figure 23. Inverter **Vabc** Phase to Phase Voltage (a) and (b) **RMS(Vabc)** with varying irradiance and temperature values with no constant Load

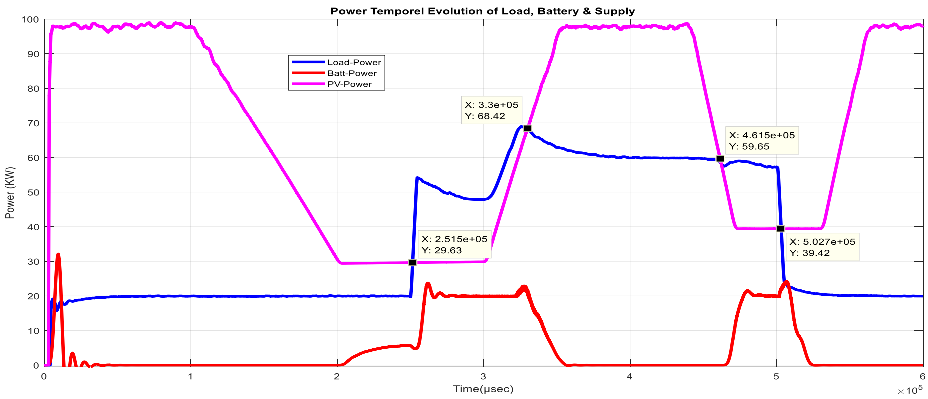

Figure 24. Power balance during integration of PV system and Battery by using a no constant Load

6. CONCLUSION

The purpose of this research work has mainly focused on the development of an autonomous hybrid power system and its energy management unit in variable climatic conditions. To sum up, firstly, the PV array type SunPower SPR-305E-WHT-D is considered in this study, where the developed mathematical model, the boost converter with the FLC MPPT algorithm used to track the given power, the battery charging\discharging, and the EKF algorithm have been explained in deep detail. The fuzzy membership functions are designed based on the triangle method for the fuzzification process and used centroid method for the defuzzification process. The DC-link voltage has been converted to AC voltage by three phase voltage source inverter and applied to no constant load. The EKF algorithm is used to the estimate SOC of a lithium battery pack, with the assumption that the relationship between battery OCV and SOC is piecewise linear and varies with the ambient temperature. The performance of the system at various input conditions is studied with the proposed control. The optimal load sharing has been achieved proportionally among the solar and proper charging and discharging modes of batteries at particular load conditions. The proposed management system conducts to attain the targeted objectives, despite the climatic conditions and load variation, in order to maintain the power demand at satisfactory levels satisfactory and to protect the battery against deep discharging\overcharging. The simulation results show that SOC estimation by using the EKF method is effective and can estimate battery SOC accurately.

7. REFERENCES

1. Necaibia, S., Kelaiaia, M.S., Labar, H., Necaibia, A. and Castronuovo, E.D., "Enhanced auto-scaling incremental conductance mppt method, implemented on low-cost

microcontroller and sepic converter", ***Solar Energy***, Vol. 180, (2019), 152-168. https://doi.org/10.1016/j.solener.2019.01.028

2. Wu, Z., Tazvinga, H. and Xia, X., "Demand side management of photovoltaic-battery hybrid system", ***Applied Energy***, Vol. 148, (2015), 294-304. https://doi.org/10.1016/j.apenergy.2015.03.109
3. Tang, L., Zhang, Y., Xu, W. and Zeng, C., "Novel variable step-size maximum power point tracking control strategy for pv systems based on contingence angles", in 2013 IEEE Energy Conversion Congress and Exposition, IEEE., (2013), 3904-3911.
4. Eldahab, Y.E.A., Saad, N.H. and Zekry, A., "Enhancing the design of battery charging controllers for photovoltaic systems", ***Renewable and Sustainable Energy Reviews***, Vol. 58, (2016), 646-655. https://doi.org/10.1016/j.rser.2015.12.061
5. Jiang, Y., Qahouq, J.A.A. and Haskew, T.A., "Adaptive step size with adaptive-perturbation-frequency digital mppt controller for a single-sensor photovoltaic solar system", ***IEEE Transactions on Power Electronics***, Vol. 28, No. 7, (2012), 3195-3205. doi: 10.1109/TPEL.2012.2220158.
6. Manganiello, P., Ricco, M., Petrone, G., Monmasson, E. and Spagnuolo, G., "Optimization of perturbative pv mppt methods through online system identification", ***IEEE Transactions on Industrial Electronics***, Vol. 61, No. 12, (2014), 6812-6821. doi: 10.1109/TIE.2014.2317143.
7. Deveci, O. and Kasnakoğlu, C., "Performance improvement of a photovoltaic system using a controller redesign based on numerical modeling", ***International Journal of Hydrogen Energy***, Vol. 41, No. 29, (2016), 12634-12649. https://doi.org/10.1016/j.ijhydene.2016.05.149
8. Hassani, H., Zaouche, F., Rekioua, D., Belaid, S., Rekioua, T. and Bacha, S., "Feasibility of a standalone photovoltaic/battery system with hydrogen production", ***Journal of Energy Storage***, Vol. 31, (2020), 101644. https://doi.org/10.1016/j.est.2020.101644
9. Chan, C., Lo, E. and Weixiang, S., "The available capacity computation model based on artificial neural network for lead–acid batteries in electric vehicles", ***Journal of Power Sources***, Vol. 87, No. 1-2, (2000), 201-204. https://doi.org/10.1016/S0378-7753(99)00502-9
10. Zhang, F., Liu, G. and Fang, L., "A battery state of charge estimation method with extended kalman filter", in 2008 IEEE/ASME International Conference on Advanced Intelligent Mechatronics, IEEE., (2008), 1008-1013.
11. Zhang, F., Liu, G. and Fang, L., "A battery state of charge estimation method using sliding mode observer", in 2008 7th world congress on intelligent control and automation, IEEE., (2008), 989-994.
12. Uddin, M.H., Baig, M.A. and Ali, M., "Comparision of 'perturb & observe'and 'incremental conductance', maximum power point tracking algorithms on real environmental conditions", in 2016 International Conference on Computing, Electronic and Electrical Engineering (ICE Cube), IEEE., (2016), 313-317.
13. Sera, D. and Baghzouz, Y., "On the impact of partial shading on pv output power", ***Proceedings of RES'08***, (2008). https://www.researchgate.net/publication/259786752
14. Khelif, M., M'raoui, A. and Malek, A., "Simulation, optimization and performance analysis of an analog, easy to implement, perturb and observe mppt technique to be used in a 1.5 kwp photovoltaic system", in 2013 International Renewable and Sustainable Energy Conference (IRSEC), IEEE. (2013), 10-17.
15. Sera, D., Valentini, M. and Raducu, A., "Real time photovoltaic array simulator for testing grid-connected pv inverters", in 2008 IEEE International Symposium on Industrial Electronics, ISIE 2008, IEEE., (2008).
16. Motahhir, S., Aoune, A., El Ghzizal, A., Sebti, S. and Derouich, A., "Comparison between kalman filter and incremental conductance algorithm for optimizing photovoltaic energy", ***Renewables: Wind, Water, and Solar***, Vol. 4, No. 1, (2017), 1-10. https://doi.org/10.1186/s40807-017-0046-8
17. Aoune, A., Motahhir, S., El Ghzizal, A., Sebti, S. and Derouich, A., "Determination of the maximum power point in a photovoltaic panel using kalman filter on the environment psim", in 2016 International Conference on Information Technology for Organizations Development (IT4OD), IEEE., (2016), 1-4.
18. Vasebi, A., Partovibakhsh, M. and Bathaee, S.M.T., "A novel combined battery model for state-of-charge estimation in lead-acid batteries based on extended kalman filter for hybrid electric vehicle applications", ***Journal of Power Sources***, Vol. 174, No. 1, (2007), 30-40. https://doi.org/10.1016/j.jpowsour.2007.04.011
19. Rahimi Mirazizi, H. and Agha Shafiyi, M., "Evaluating technical requirements to achieve maximum power point in photovoltaic powered z-source inverter", ***International Journal of Engineering, Transactions C: Aspects*** Vol. 31, No. 6, (2018), 921-931. doi: 10.5829/ije. 2018.31.06c.09.
20. Rupesh, M. and Vishwanath, T., "Intelligent controllers to extract maximum power for 10 kw photovoltaic system", ***International Journal of Engineering, Transactions A: Basics*** Vol. 35, No. 4, (2022), 784-793. doi: 10.5829/ije.2022.35.04a.18.
21. Al-Majidi, S.D., Abbod, M.F. and Al-Raweshidy, H.S., "A novel maximum power point tracking technique based on fuzzy logic for photovoltaic systems", ***International Journal of Hydrogen Energy***, Vol. 43, No. 31, (2018), 14158-14171. https://doi.org/10.1016/j.ijhydene.2018.06.002
22. Senthil, R., "Global mppt control algorithms for solar pv systems under non-uniform solar radiation", ***International Journal of Recent Technology and Engineering***, Vol. 7, (2019), 2102-2105.
23. Boutabba, T., Drid, S., Chrifi-Alaoui, L. and Benbouzid, M., "A new implementation of maximum power point tracking based on fuzzy logic algorithm for solar photovoltaic system", ***International Journal of Engineering, Transactions A: Basics*** Vol. 31, No. 4, (2018), 580-587. doi: 10.5829/ije.2018.31.04a.09.
24. Plett, G.L., "Extended kalman filtering for battery management systems of lipb-based hev battery packs: Part 3. State and parameter estimation", ***Journal of power sources***, Vol. 134, No. 2, (2004), 277-292. https://doi.org/10.1016/j.jpowsour.2004.02.033
25. Bhangu, B., Bentley, P., Stone, D. and Bingham, C., "Observer techniques for estimating the state-of-charge and state-of-health of vrlabs for hybrid electric vehicles", in 2005 IEEE Vehicle Power and Propulsion Conference, IEEE., (2005), 780-789,
26. Vikhe, P., Sabale, A., Kadu, C., Mandhare, V. and Jondhale, A., "Pv generation with battery storage supplying a variable load–supervision and control strategy", Vol. 27, No. 12, (2021).
27. Soliman, M.S., Belkhier, Y., Ullah, N., Achour, A., Alharbi, Y.M., Al Alahmadi, A.A., Abeida, H. and Khraisat, Y.S.H., "Supervisory energy management of a hybrid battery/pv/tidal/wind sources integrated in dc-microgrid energy storage system", ***Energy Reports***, Vol. 7, (2021), 7728-7740. https://doi.org/10.1016/j.egyr.2021.11.056
28. Anagreh, Y.N., Alnassan, A. and Radaideh, A., "High performance mppt approach for off-line pv system equipped with storage batteries and electrolyzer", ***International Journal of Renewable Energy Development***, Vol. 10, No. 3, (2021). doi: 10.14710/ijred.2021.34131.

Persian Abstract

چکیده

سیستم های تولید برق مستقل به گونه ای طراحی شده اند که مستقل از شبکه برق عمومی کار کنند. باتری ها عنصر مهم در سیستم PV مستقل را تشکیل می دهند. آنها برای ذخیره برق تولید شده توسط انرژی خورشیدی در یک شب یا برای استفاده اضطراری در طول تقاضای بار غیر ثابت استفاده می شوند. این مقاله دارای سه بخش اصلی است. اولی مربوط به طراحی یک روش هوشمند برای ردیابی نقطه حداکثر توان مبتنی بر کنترل کننده منطق فازی برای بهبود کارایی یک سیستم انرژی خورشیدی مستقل است. بخش دوم وضعیت شارژ باتری (SOC)را توضیح می دهد. مدل پیشنهادی، که پاسخ SOC واقعی باتری لیتیومی را بهتر منعکس می‌کند، با استفاده از تخمین‌گر حالات فیلتر کالمن (EKF)ساخته شده است. این روش پیشنهادی را می توان به عنوان روشی دقیق تر و قابل اعتمادتر برای تخمین وضعیت شارژ باتری در نظر گرفت. بخش سوم یک سیستم مدیریت برای دو منبع انرژی تجدید پذیر فوق را یکپارچه می کند. عملکرد سیستم مدیریت پیشنهادی با استفاده از کنترل‌کننده منطق فازی مبتنی بر ردیابی نقطه حداکثر توان FLC-MPPT و برآوردگر EKF در Matlab/Simulink در تابش خورشیدی و دمای متفاوت برای درخواست انرژی بدون بار ثابت شبیه‌سازی شده‌اند.

International Journal of Engineering

Journal Homepage: www.ije.ir

Artificial Neural Network-based Fault Location in Terminal-hybrid High Voltage Direct Current Transmission Lines

A. Hadaeghi*[a], M. M. Iliyaeifar[a], A. Abdollahi Chirani[b]

[a] *Department of Electrical Engineering, Ahrar Institute of Technology and Higher Education, Rasht, Iran*
[b] *Department of Electrical Engineering, University of Guilan, Rasht, Iran*

PAPER INFO

Paper history:
Received 11 March 2022
Received in revised form 15 November 2022
Accepted 16 November 2022

Keywords:
Fault Location
High Voltage Direct Current
Hybrid-High Voltage Direct Current
Artificial Neural Network
Wavelet Transform

ABSTRACT

In this article, a fault location technique based on artificial neural networks (ANN) for Terminal-Hybrid LCC-VSC-HVDC has been assessed and scrutinized. As is known, in conventional HVDC systems (LCC-based and VSC-based HVDCs), the same type of filter is used on both sides due to the use of similar converters in both sender and receiver terminals. In this article, it is concluded that due to the use of two different types of converters at the both ends of the utilized Terminal-hybrid LCC-VSC-HVDC system, and the use of different DC filters on both sides, fault location using positive and negative pole currents of the rectifier side has much better results than the rest of input signals. Therefore, it will be finalized that by increasing and designing suitable DC filters on the transmission line of HVDC systems, fault localization matter will be remarkably and surprisingly facilitated. Nowadays, the fault location of HVDC transmission lines with a value of more than 1% is generally discussed in most articles. In this research, the fault location with a value of 0.0045%, i.e., a distance of 22.5 meters from the fault point in the most satisfactory case is obtained, which shows the absolute feasibility of the ANN along with the wavelet transform. To validate the proposed method, a ±100 KV, Terminal-hybrid LCC-VSC-HVDC system is simulated via MATLAB. The outcomes verify that the proposed technique works perfectly under various fault locations, resistances, and fault types.

doi: *10.5829/ije.2023.34.02b.03*

1. INTRODUCTION

High-voltage direct current (HVDC) networks are extensively employed for power dispatch over long distances. There are generally two classes of HVDC systems: (i) line commutated converter-based HVDC (LCC-HVDC) systems and (ii) voltage source converter-based HVDC (VSC-HVDC) systems. The LCC-HVDC systems have such advantages as high transmission capability, long transmission extent, high transmission proficiency, and lower manufacturing costs than the latter; but the thyristors used in them are semi-controlled switches that do not have the turn-off ability. This problem has caused the LCC-HVDC systems to suffer from commutation failure for a long time and also made them unable to power a passive grid [1-3]. In contrast, VSC-HVDC systems do not experience commutation failure due to fully controlled power switches such as IGBTs and can also supply passive networks. But, compared to LCC-HVDC, they suffer from higher manufacturing costs, lower transmission efficiency, and higher losses. On the other hand, the hybrid-HVDC transmission system, which uses LCC as a rectifier and VSC as an inverter, has overcome the above problems with superiorities such as high transmission aptitude and proficiency and long transmission expanse. Besides, it does not face the problem of commutation failure and can also supply passive networks [4-7].

Recently, many fault location strategies have been suggested for HVDC systems; however, few pieces of research have been done to solve the fault location problem of LCC-VSC-HVDC transmission lines. Due to the different structures of the hybrid-HVDC systems, there would be different fault characteristics and

*Corresponding Author Institutional Email: Hadaeghi.a@shirazu.ac.ir (A. Hadaeghi)

Please cite this article as: A. Hadaeghi, M. M. Iliyaeifar, A. Abdollahi Chirani, Artificial Neural Network-based Fault Location in Terminal-hybrid High Voltage Direct Current Transmission Lines, ***International Journal of Engineering, Transactions B: Applications***, Vol. 36, No. 02, (2023), 215-225

attributes on the transmission line under various types of faults. Therefore, re-evaluation and reanalysis of the existing fault location methods are of tremendous importance, especially artificial intelligence-based strategies that have not been preached. The following are some works done in the context of hybrid HVDC systems. Wang et al. [1] offerred a traveling wave-based directional pilot protection strategy for hybrid LCC-VSC-HVDC transmission lines, in which, by dissecting the TW dispersion features alongside the HVDC transmission line and melding the instantaneous power and current on both rectifier and inverter sides, a new criterion for fault direction discrimination is presented. Wang et al. [2] suggests a directional pilot protection method based on traveling waves for hybrid LCC-MMC-HVDC transmission lines. This procedure can detect internal and external faults and does not require any particular data synchronization system. Xing et al. [8] proposed a fault localization technique for hybrid LCC-MMC-HVDC systems. In this approach, using fault attributes analysis at the rectifier station and clamp double submodule modular multilevel converter (CDSM-MMC) on the inverter station, the authors have tried to avoid the effects of transient resistance and dispersed capacitance to achieve high accuracy in fault location. Wang and Hou [9] presented a TW fault location strategy for hybrid LCC-MMC-HVDC transmission systems based on the Hilbert-Huang transform. Wang et al. [10] suggested a TW fault location method for LCC-MMC-HVDC hybrid DC transmission lines established on a capacitance-divided electronic voltage transformer (C-EVT), in which by analyzing the TW transmission characteristic of C-EVT, an algorithm is proposed based on the secondary differential voltage traveling wave (D-VTW). Wang et al. [11] presented a fault localization approach suited for hybrid HVDC systems in which the fault location is obtained based on the functional association between the fault distance and the inverter side DC bus equivalent characteristic impedance. Wang and Hou [12] offerred a traveling wave fault location method, which is established on the secondary differential current traveling wave (D-CTW) output signal of Rogowski coil electronic current transformer (R-ECT), fitting for multi-terminal hybrid LCC-MMC-HVDC transmission cables. Zhang et al. [13] deliverred a single-ended protection scenario for hybrid three-terminal LCC-VSC-HVDC systems in which internal and external faults are discovered by scrutinizing the amplitude-frequency features of the wave impedance. Gao et al. [14] suggestted a TW fault localization procedure for a hybrid three-terminal HVDC network founded on improved Local Mean Decomposition (LMD) that is not influenced by wave velocity. Wang and Zhang [15], at first, analyzed the reflection and refraction attributes of the fault traveling wave in DC buses and the defective point of LCC-MMC hybrid HVDC systems. They proposed a procedure for locating pole-to-ground and pole-to-pole faults, which does not need to detect the wave polarity and value of the wave velocity. As is common knowledge, the issue of fault localization in HVDC systems with an average error of typically more than 1% is usually debated in the majority of articles [16]. The main work of this paper is to propose and assess an artificial intelligence-based strategy for fault location in hybrid LCC-VSC-HVDC transmission lines, with the ability if locating the fault with an average percentage error of less than 1%. To do so, at first, the required voltage and current fault signals are measured from the terminals of the hybrid HVDC system. Next, wavelet transform (WT) is employed to extract high-frequency components from the input signals and improve fault location precision. Then the energy of the extracted high-frequency components is calculated and provided to the artificial neural network (ANN) as train data. Finally, the output of ANN will represent the exact location of the fault point with an accuracy of 0.0045% and 0.0943%, i.e., 22.5 and 471.5 meters from the defective spot in the lowest and highest possibilities, respectively. Additionally, it is conceivable that enhancing the DC transmission line filters will significantly reduce the average percentage error of fault location.

The remnant of this article is organized as follows. In section 2, four system-level hybrid-HVDC topologies and the theory of traveling wave-based fault location are briefly explained. In section 3, the fundamental of the utilized tools is described and given in short. In section 4, a fault location strategy based on a double-layer ANN is proposed and assessed for LCC-VSC-HVDC transmission lines. In section 5, simulations and results confirm that the offered procedure works correctly with various fault locations, fault resistances, and sorts of faults. At last, section 6 summarizes and concludes the paper.

2. LITERATURE REVIEW

In this division, four system-level hybrid HVDC topologies and traveling wave-based fault location theory will be introduced and briefly recapitulated.

2. 1. System-level Hybrid-HVDC Topologies

Xiao et al. [17] discussed four system-level hybrid-HVDC topologies in detail and resemble them in terms of DC fault ride-through strategy, PQ operating zone, and power flow reversal strategy. These four hybrid-HVDC topologies will be briefly introduced and described in this section.

2. 1. 1. Terminal-hybrid HVDC System Figure 1 depicts the basic structure of the Terminal-hybrid

HVDC topology. In this arrangement, each terminal uses a dissimilar converter. One terminal uses LCC, and the other one embraces VSC. In this topology, the VSC is usually employed on the receiving side. In this case, and due to the VSC's turn-off aptitude, it can be operated as a passive inverter, which makes it attainable to provide isolated loads without commutation failure on the receiving terminal. On the other hand, active and reactive power can be managed individually by VSC. This means the hybrid-terminal HVDC system can provide active and reactive power to intensify voltage resilience when faults appear [18].

2. 1. 2. Pole-hybrid HVDC System Figure 2 illustrates the main structure of the Pole-hybrid HVDC system. In this configuration, each terminal consists of two poles. One pole embraces LCC, and the other employs VSC, which is connected in series to assemble a bipolar arrangement. In this topology, the LCC provides part of the active power required by the system, and the rest is supplied by the VSC. The VSC is also responsible for controlling the reactive power needed for the LCC. Generally, the pole-hybrid HVDC system has high control flexibility and good dynamic performance. Furthermore, it deals with a great start-up and sufficient fault recovery. It can also be mentioned that the system can operate stably in various operating conditions [19].

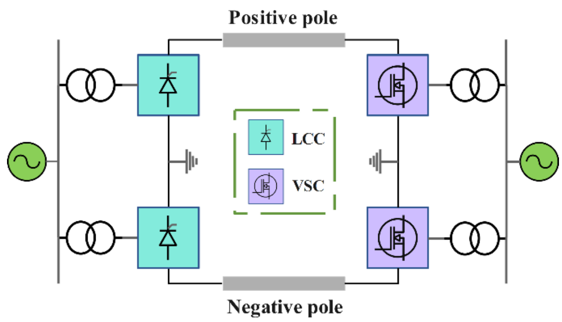

Figure 1. Main structure of the Terminal-hybrid HVDC topology

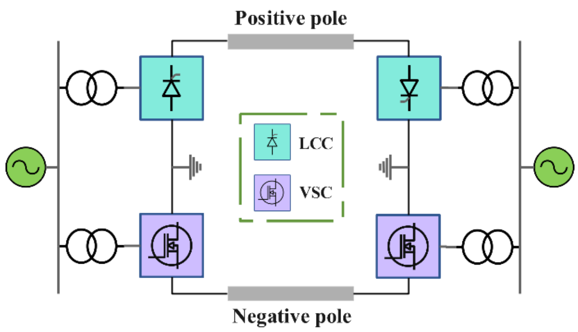

Figure 2. Main structure of the Pole-hybrid HVDC topology

2. 1. 3. Series Converter-hybrid HVDC System Figure 3 illustrates the main configuration of the series converter-hybrid HVDC system. As can be seen, in this topology, each terminal consists of several poles, each consisting of LCCs and VSCs in series connection. Due to this arrangement, the same current flows through the converters, but their voltages are different; hence their conveyed power will be disparate. The poles are also connected symmetrically to the transmission lines in this structure. Since the VSC is widely employed in rectifiers or inverter stations, the system deals with flexible active and reactive power management. Furthermore, due to the control collaboration between the LCC and VSC, there would not be any current cut-off under AC faults on the rectifier side. Besides, if an AC fault arises on the inverter side, the transmitted power can be preserved to some extent [20].

2. 1. 4. Parallel Converter-hybrid HVDC System Figure 4 shows the rudimentary arrangement of the Parallel converter-hybrid HVDC system. Each terminal

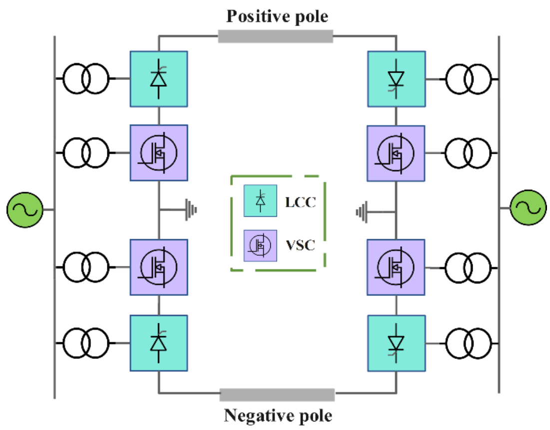

Figure 3. Main structure of the Series converter-hybrid HVDC topology

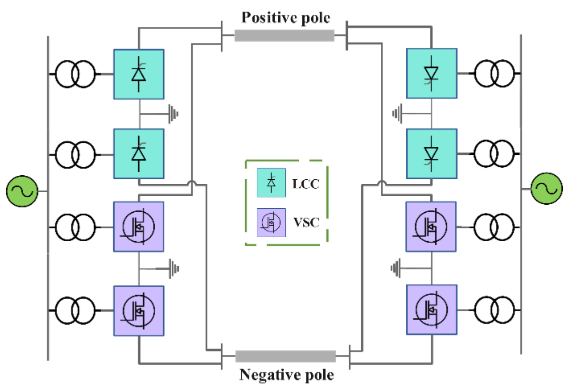

Figure 4. Main structure of the Parallel converter-hybrid HVDC topology

is composed of LCCs and VSCs connected in parallel in this topology. As can be seen, both LCC and VSC portion an identical transmission line and retain equal DC voltage, but the flowing current is different; hence, they provide dissimilar power ratings. Overall, this topology has many potentials, such as bulk-power transmission capability, power reversal capability, reactive power compensation, and fault ride-through ability. Furthermore, if either LCCs or VSCs are halted, the rest of the system can operate smoothly without any problem [21].

2. 2. Travelling Wave-based Fault Location Theory

When a fault appears in a power system transmission line, the traveling waves propagate along the line in the form of electromagnetic pulses in both directions from the fault point to the system terminals. These waves spread along the line and experience reflections and refractions as they propagate. Then the energy of these traveling waves is gradually reduced according to the fault and system characteristics until it is completely dissipated [22]. These waves contain information about the fault, including its location and its distance from the system terminals, which can be used to detect and locate the faulty point. By accurately measuring the arrival time and propagation speed of two consecutive peaks of these traveling waves that are heading to the system's terminals, the exact location of the faulty point can be determined.

The following partial differential equations pertain to the voltage and current measurements taken at any point x:

$$\frac{\partial e}{\partial x} = -L\frac{\partial \mathrm{i}}{\partial \mathrm{t}} \quad \text{and} \quad \frac{\partial \mathrm{i}}{\partial x} = -C\frac{\partial e}{\partial t} \tag{1}$$

where L and C represent the line's inductance and capacitance, respectively, for each unit of the line's length. It is presumed that there will be a negligible amount of resistance. These equations have the following answers as their solutions:

$$e(x,t) = e_f(x-vt) + e_r(x+vt) \tag{2}$$

$$i(x,t) = \frac{1}{z}e_f(x-vt) - \frac{1}{z}e_r(x+vt) \tag{3}$$

where $Z = \sqrt{(L/C)}$ denotes the transmission line characteristic impedance and $V = 1/\sqrt{(LC)}$ indicates the velocity at which the signal is propagating. Both forward (e_f and i_f) and backward (e_r and i_r) waves, as shown in Figure 5, depart the disturbed area "x" heading in various directions at the speed of "v," which is a tiny bit smaller than the light speed, toward the transmission line extremities. The terminations of transmission lines constitute a discontinuity or a change in impedance, and as a result, some of the wave's energy will be reflected back to the source of the disturbance. The remainder of the power will be distributed across the system via

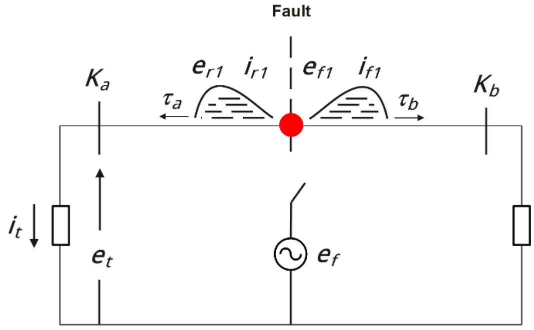

Figure 5. Voltage and current traveling waves

transmission lines or other power system components. Figure 6 depicts the numerous waves created at the ends of the line using a Bewley Lattice diagram. Reflection coefficients k_a and k_b, which are based on characteristic impedance ratios at the discontinuities, are used to express the amplitudes of waves. Time intervals, τ_α and τ_b, are used to illustrate how much time it takes for a fault to reach the discontinuity point. The distance (x) from substation A to the defective point can be determined by just using the line length (l) and the duration of the arrival discrepancy $(\tau_\alpha - \tau_b)$ as follows:

$$x = \frac{1-c(\tau_\alpha-\tau_b)}{2} \tag{4}$$

In Equation (4), C denotes the wave propagation of 299.79 µm/µsec (≅1ft/ns) [23].

3. FUNDAMENTALS OF THE UTILIZED TOOLS

This part will briefly explain the basic principles of the utilized implements, including wavelet transforms and artificial neural networks.

3. 1. Artificial Neural Network Artificial neural networks (ANNs) are conventional machine learning

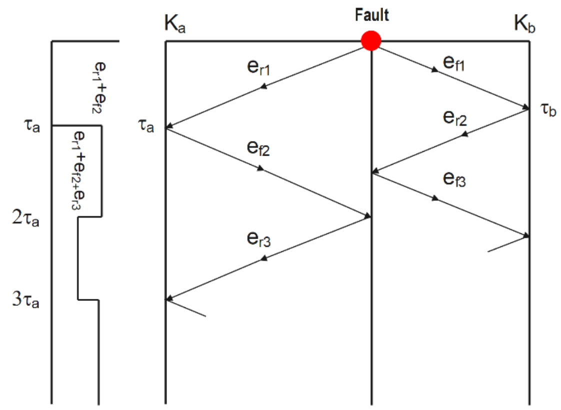

Figure 6. Bewley Lattice Diagram

strategies that simulate the learning mechanism of the human brain. ANN is a new way to predict and model time series that are not linear and can't be solved easily or accurately [24, 25].

Artificial neural networks are generally divided into two categories: (i) single-layer neural networks and (ii) multilayer neural networks. A single-layer neural network is the simplest type of neural network that consists of an input layer and an output node. In this network, data is transferred directly from the input layer to the output layer, and all operations are visible to the user. This network is also called a perceptron. Figure 7(a) shows a single-layer neural network. A multilayer neural network, on the other hand, has multiple computational layers in which neurons are arranged in a layered structure. In this network, the input and output layers are split by a group of layers called "hidden layers," as their executed operations are not visible to the user. Multilayer neural networks are also referred to as feed-forward networks [26, 27]. Figure 7(b) illustrates a multilayer neural network.

ANN is generally a fast and accurate method for fault localization. One of the most prominent features of ANN is that its process follows a very simple set of operations. Typically, in a power system, the values of voltage and current are very unstable and change under various types of faults. Hence, an artificial neural network would be a great choice for detecting, classifying, and locating the transmission line faults of HVDC systems, as a neural network is basically able to incorporate dynamic changes in power systems [28-32].

3. 2. Wavelet Transform Processing non-static signals is difficult and requires specific tools for analysis. Nowadays, the wavelet transform is widely employed in the field of transmission line fault localization in HVDC systems due to its high ability for fault transient analysis as discussed in literature [33-36]. In this paper, the wavelet transform is utilized in order to improve fault location accuracy as well as extract high-frequency components from the input voltage and current fault signals.

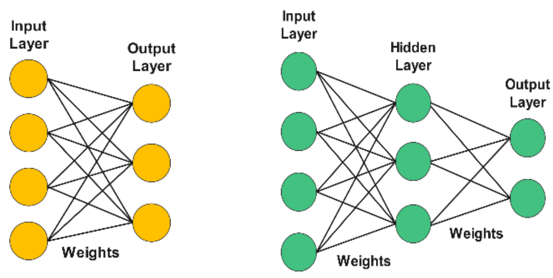

(a) (b)

Figure 7. The architecture of neural networks. (a) single-layer neural network. (b) multilayer neural network

In general, the wavelet transform of a function *v(t)* can be defined as the following relationship [37]:

$$WT_{\psi(\alpha.b)}v(t) = \int_{-\infty}^{+\infty} V\,(t)\Psi_{a.b}^{*}(t)dt \quad (5)$$

where $\Psi_{a.b}^{*}(t)$ is the daughter wavelet and is defined as follows:

$$\Psi_{a.b}^{*}(t) = \frac{1}{\sqrt{\alpha}}\Psi\left(\frac{t-b}{a}\right) \quad (6)$$

In Equation (6), α is the binary dilation and is responsible to scale the mother wavelet $\psi_{a.b}(t)$. b is the binary position by which the mother wavelet is translated (shifted). The daughter wavelet is indeed a translated and dilated version of the mother wavelet [38, 39].

Wavelet transforms can generally be divided into two categories: (i) continuous wavelet transform (CWT) and (ii) discrete wavelet transform (DWT). Basically, CWT detects wave time more accurately than DWT, but DWT is computationally faster and considered by researchers to be more suitable for protective applications.

In this paper, as mentioned before, the wavelet transform has been utilized in order to extract high-frequency components from fault signals as well as to increase fault location accuracy. There are several mother wavelets that can be used in the proposed method, including Haar, Daubechies, Symlets, Biorthogonal, etc. In this paper, the Daubechies mother wavelet (db4) is employed to decompose fault signals into 15 levels. The simulation results confirm that the 15-level decomposition has the best outcome among the selected levels for WT in the proposed algorithm.

4. THE PROPOSED METHOD

Due to their high proficiency in pattern detection and classification, artificial neural networks are considered an excellent apparatus for the localization of faults in power transmission lines. In this paper, an artificial neural network is employed to locate the transmission line fault of the studied Terminal-hybrid LCC-VSC-HVDC system. For this purpose, the Levenberg-Marquardt backpropagation algorithm (trainlm) has been hired as the train function in MATLAB software. Besides, according to Equation (7), the hyperbolic tangent sigmoid transfer function (tansig) is employed for the input and hidden layers, and the linear transfer function (purlin) is utilized for the output layer.

$$tansig(s) = \frac{2}{1+e^{-2s}} - 1 \quad (7)$$

In addition, 70% of the total input data is considered training data, 15% validation data, and 15% test data. Finally, in order to evaluate the network performance according to Equation (8), the mean squared normalized error performance function (MSE) is exploited. It can also be noted that the single input data, which are a total of eight different types of signals, are employed as intake data.

$$MSE = \frac{1}{n}\sum_{i=1}^{n}(Y_i - \hat{Y}_i)^2 \quad (8)$$

where n is the number of data points and Y_i and $\hat{Y}_i$ represent the observed and predicted values, respectively. The closer the MSE value is to zero, the more accurately the artificial neural network can specify the fault location.

To obtain the train patterns needed for the artificial neural network, all types of faults, including positive pole to ground (PG), negative pole to ground (NG), positive pole to negative pole (PN), and positive pole to negative pole to ground (PNG), are applied to 500 different points along the entire DC transmission line with varying fault resistances (0.1, 1, 20, 70, and 100 Ω). The fault distance starts at 0.5 km from the rectifier terminal and continues with a step of 1 km to a distance of 499.5 km from the same terminal. The duration of the fault is also set to be 20 milliseconds. It is to be mentioned that, in this stage, a total of 10000 samples (4 types of faults × 5 individual fault resistances × 500 different points) are collected from the terminals of the employed Terminal-hybrid LCC-VSC-HVDC system to verify the proposed fault location strategy. Then, using the wavelet transform, the high-frequency components of these 10000 samples are extracted into 15 levels. Furthermore, in order to obtain the required test data, all four types of faults (PG, NG, PN, and PNG) with fault resistances of (2, 5, 25, 80, and 120 Ω) were applied to 50 random points throughout the entire length of the DC transmission line. Then, like the train data, the high-frequency components of test data are also decomposed into 15 levels by the use of wavelet transform. It has to be noted that, the Daubechies mother wavelet of type (db4) is indeed employed in order to increase the fault localization preciseness as well as to extract high-frequency components from the train and test fault signals. In the next step, according to Equation (9), the energy of all 15 levels of the decomposed high-frequency components of both train and test signals will be calculated and given to a double-layer artificial neural network as intake data. To do this, a double-layer artificial neural network with 20 neurons in the first hidden layer and 4 neurons in the second hidden layer is adopted. Finally, according to Equation (10), the output of ANN will determine the exact location of the faulty point with an average percentage error of about 0.0045%, which is a distance of 22.5 meter from defective spot. The flowchart of the main steps of the evaluated fault location method is shown in Figure 8.

$$E_{X_n} = \int_{t_1}^{t_1+\Delta t} X_n^2(t)dt \quad (9)$$

$$\text{percentage error (\%)} = \frac{|X_1 - X_2|}{\text{L}} \times 100 \quad (10)$$

In Equation (9), t_1 and Δt stand for the start time and the length of the sampling window, while n stands for the level of data decomposition. In Equation (10), X_1 and X_2 represent the actual fault location and the estimated fault location, respectively, while L stands for the total length of the transmission line.

5. SIMULATION AND RESULTS

5. 1. System Specification The structure of the exerted hybrid HVDC system is depicted in Figure 9. In order to test and validate the proposed algorithm, a Terminal-hybrid LCC-VSC-HVDC system is implemented and simulated by MATLAB software. In this topology, the rectifier side uses a twelve-pulse LCC, and the inverter side adopts a conventional two-level VSC. Besides, The SPWM control strategy is used for the VSC side. The switching frequency is also set to be 10 kHz. The main specifications of the utilized system are listed in Table 1.

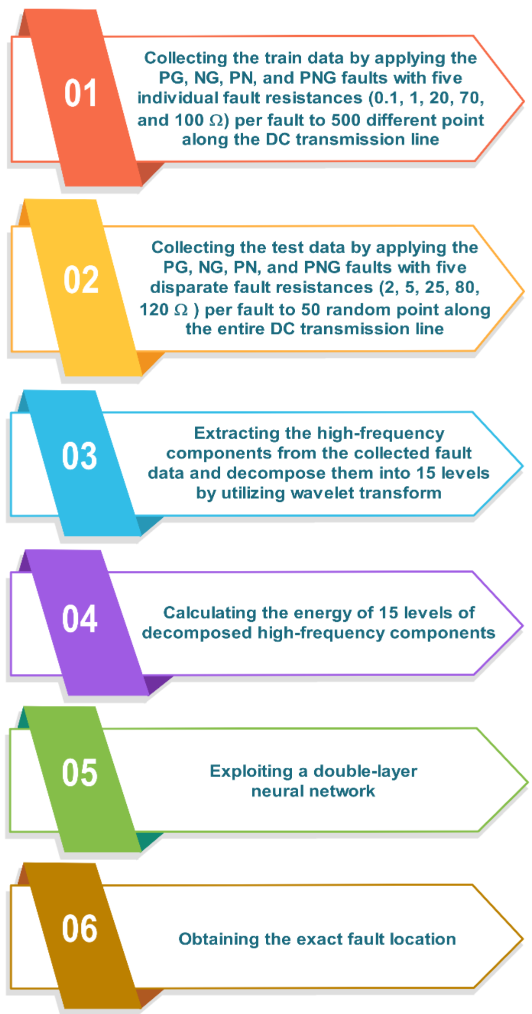

Figure 8. The flowchart of the proposed fault location method's principal steps

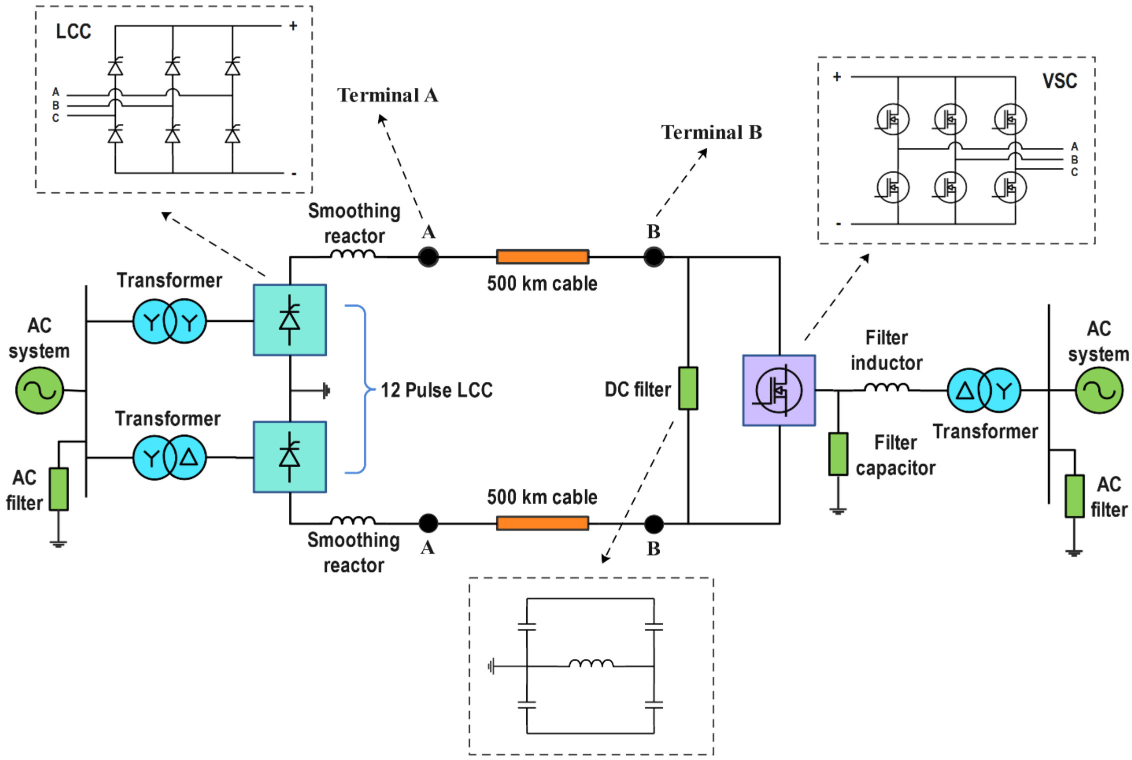

Figure 9. The main configuration of the utilized Terminal-hybrid LCC-VSC-HVDC system

TABLE 1. The main specification of the Terminal-hybrid LCC-VSC-HVDC system

Real power (P)	1100 MW
AC voltage	230 kV
Nominal frequency	50 Hz
Transmission line DC voltage (v_{dc})	±100 kV
Transmission line DC current (i_{dc})	2 kA
Cable length	500 km
Cable resistance	0.0139 Ω/km
Cable inductance	0.159 mH/km
Cable capacitance	231 nF/km

5. 2. Fault Location Results Using a Double-layer Artificial Neural Network In this paper, a total of eight measuring probes are embedded to gauge the transmission line voltage and current signals during the fault circumstance, which includes rectifier side (terminal A), positive pole current (IP1), negative pole current (IN1), positive pole to ground voltage (VP1), negative pole to ground voltage (VN1), and inverter side (terminal B) positive pole current (IP2), negative pole current (IN2), positive pole to ground voltage (VP2), and negative pole to ground voltage (VN2). Furthermore, a double-layer artificial neural network is exploited to achieve the best network performance with 20 and 4 neurons for the first and second hidden layers, respectively. According to Equation (10), the average percentage error of fault location using a double-layer artificial neural network under 4 different types of faults with 5 disparate fault resistances (0.1, 1, 20, 70, and 100 Ω for train data) and (2, 5, 25, 80, and 120 Ω for test data) based on both the type of fault and the type of signal along with the graph are displayed in Table 2, Figures 10 and 11, respectively.

Moreover, in order to prove the sufficiency of the selected levels for wavelet transform decomposition, 5 different levels, including 5, 10, 15, 20, and 25, have been chosen to be analyzed. The test was performed under the PG fault type with the same fault resistances (0.1, 1, 20, 70, and 100 Ω for train data) and (2, 5, 25, 80, and 120 Ω for test data). Besides, the same double-layer neural network was employed with 20 and 4 neurons for the first and second hidden layers, respectively. The experimental results are shown in Table 3 and Figure 12, respectively. The results indicate that the 5-level decomposition eventually culminated in a far less beneficial outcome, and this can be seen to be the case right off the bat. However, as the number of levels of decomposition is increased, the results continue to get better and better until they reach a point where they converge relatively around the 15-level decomposition. As a matter of fact, 15-level decomposition has the best result among the selected levels for the wavelet transform.

TABLE 2. The average percentage error of fault location using a double-layer ANN with the number of neurons [20 4] in the hidden layers under four different types of faults and five particular fault resistances

Type of data	Type of fault				Average percentage error (%)
	PG	NG	PN	PNG	
IP1	0.0024	0.0003	0.0115	0.0121	**0.0066**
IN1	0.0008	0.0028	0.0074	0.0069	**0.0045**
VP1	0.0323	0.0083	0.1660	0.1104	**0.0544**
VN1	0.0068	0.0248	0.1639	0.1705	**0.0915**
IP2	0.0319	0.0037	0.0916	0.0679	**0.0488**
IN2	0.0038	0.0267	0.0820	0.0835	**0.0490**
VP2	0.0164	0.0065	0.1797	0.1533	**0.0890**
VN2	0.0061	0.0172	0.1530	0.2009	**0.0943**
Average percentage error (%)	**0.0126**	**0.0113**	**0.1069**	**0.1007**	

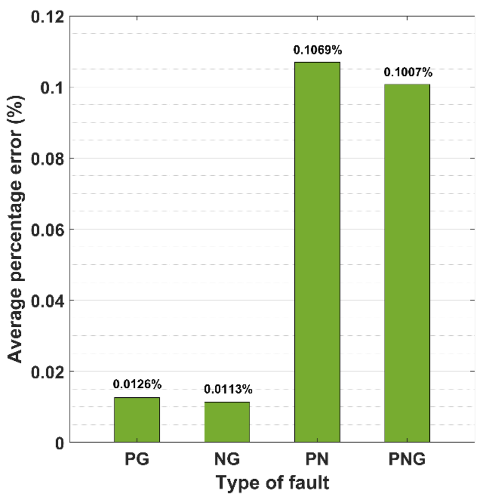

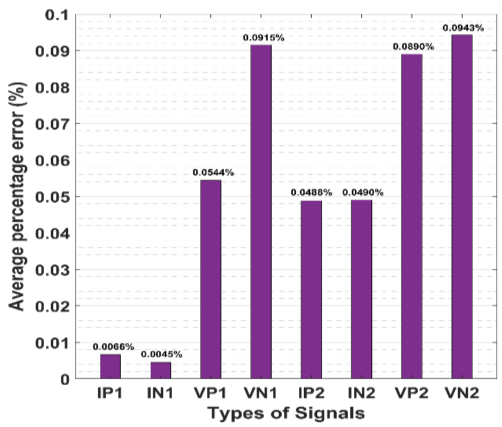

Figure 10. The average percentage error of fault location using a double-layer ANN with the number of neurons [20 4] in the hidden layers and five particular fault resistances based on different types of faults

TABLE 3. The average percentage error of fault location using different decomposition levels of the wavelet transform under the PG fault type and five disparate fault resistances

Type of data	Levels of decomposition				
	5	10	15	20	25
IP1	0.2891	0.1407	0.0024	0.0062	0.0037
IN1	0.0146	0.0034	0.0008	0.0018	0.0075
VP1	0.7877	0.1949	0.0323	0.1139	0.0918
VN1	0.9161	0.2412	0.0068	0.0447	0.0457
IP2	0.7605	0.2103	0.0319	0.0354	0.0618
IN2	0.3728	0.1260	0.0038	0.0092	0.0955
VP2	0.6975	0.1755	0.0164	0.1070	0.2095
VN2	0.4393	0.2244	0.0061	0.0554	0.2024
Average percentage error (%)	**0.5347**	**0.1646**	**0.0126**	**0.0467**	**0.0897**

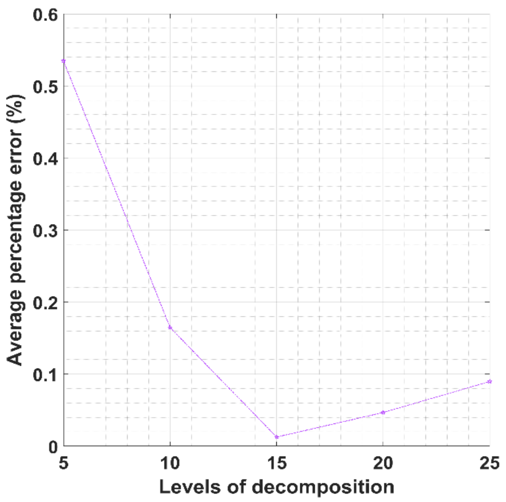

Figure 11. The average percentage error of fault location using a double-layer ANN with the number of neurons [20 4] in the hidden layers and five particular fault resistances based on different types of signals

As can be inferred from Table 2 and Figure 11, the proposed fault location algorithm using the positive and negative pole current signals of the rectifier side (IP1 and IN1) has the best results among others. It can be seen that PN and PNG fault localization using positive and negative pole currents of the inverter side (IP2 and IN2) as well as positive and negative pole to ground voltages of both sides (VP1, VN1, VP2, and VN2) have a notably higher error rate than the two aforementioned signals. The fact that there are two large smoothing reactors in the rectifier terminal would be the only reason that can be taken into account, since they basically prevent sharp pulses and sudden changes in the current when a fault emerges, hence making it more appropriate for the rectifier side positive and negative pole current signals (IP1 and IN1) to be effectively used for transmission line fault localization of the utilized Terminal-hybrid LCC-VSC-HVDC system.

Because of the symmetrical nature of the system's terminals and the use of the same kind of converter on both ends of the transmission line, identical DC filters are utilized on both sides of the transmission line in tradditional high-voltage direct current (HVDC) systems, as is common knowledge. On the other hand, the Terminal-hybrid HVDC system incorporates disparate filters with various values on both ends due to the presence of two different types of converters on both substations. In addition, any increase in the value of the DC transmission line capacitor filters on the inverter side (VSC), will result in a considerable rise in the amount of time required for the transmission line voltages and currents to transition from one state to another. As a result, capacitor filters with an average value of roughly 70μF are implemented in this research for the VSC side transmission line in order to circumvent the problem with the transient period. On the rectifier side (LCC), in contrast, there are two huge smoothing reactors each with a value of 200mH. Because of such a preference, the fault currents of the positive and negative poles of the rectifier side (LCC) (IP1 and IN1) were kept to a minimum, which significantly reduced the potential of sharp pulses and rapid changes occurring during the fault scenario. Over this, the process of learning of the artificial neural network has been drastically enhanced. Correspondingly, the positive and negative pole currents of the rectifier side (IN1 and IP1) have become more appropriate for the fault location of the employed Terminal-hybrid LCC-VSC-HVDC transmission system. Therefore, the transmission line failures of Terminal-hybrid LCC-VSC-HVDC networks may be satisfactorily identified through the utilization of these two signals, all of which were described earlier in the argument. It is possible to draw the conclusion that by designing appropriate DC filters to be installed on the DC Power line, not only is it possible to alleviate the ripple voltage and current of the HVDC transmission line as well as enhance the reliability of the conveyed power, but it is also feasible to efficiently expedite the fault location problem in a way that is both surprising and novel.

6. CONCLUSION

This paper uses artificial neural network to evaluate the transmission line fault location issue of Terminal-hybrid LCC-VSC-HVDC systems. To do so, all types of faults, including PG, NG, PN and PNG faults with 5 individual fault resistances (0.1, 1, 20, 70, and 100 Ω for train data) and (2, 5, 25, 80, and 120 Ω for test data) are applied to 500 different points along the DC transmission line and voltage and current fault signals are measured from the hybrid system terminals. These signals are then decomposed and their high frequency components are extracted to 15 levels by the use of wavelet transform. In the next step, the energy of all 15 levels of the extracted high-frequency components is calculated and provided to a double-layer artificial neural network with neurons in the hidden layers as input train and test data. Finally, the exact location of the fault is determined by using the artificial neural network.

As a result of this research, the average percentage error was found to have a value of 0.0045%, which corresponds to a range of 22.5 meters from the faulty spot in the most sufficient scenario. This demonstrates that the ANN, in conjunction with the wavelet transform, is utterly feasible in the field of fault localization in hybrid-HVDC networks. According to the simulation results and due to the different structure of the studied Terminal-hybrid LCC-VSC-HVSC system in compare to conventional HVDC systems (LCC-HVDC and VSC-HVDC) and also the use of two large smoothing reactors on the rectifier side, it can be observed that the positive and negative pole current signals of the rectifier side (IP1 and IN1) achieve the best results in the proposed fault location algorithm. In other words, it is best to understand the significance of the role that DC filters play throughout the transmission line of HVDC networks and the influence that they already have in terms of fault location. It is undeniable that a well-designed DC filter for the DC transmission line can ameliorate the ripple voltage and current of the HVDC transmission line, enhance the integrity of the power being transferred, and significantly mitigate the fault location difficulties. Hence, the authors will suggest the use of the two aforementioned signals for transmission line fault localization in Terminal-hybrid LCC-VSC-HVDC systems.

7. REFERENCES

1. Wang, D., Hou, M., Gao, M. and Qiao, F., "Travelling wave directional pilot protection for hybrid hvdc transmission line", ***International Journal of Electrical Power & Energy Systems***, Vol. 107, (2019), 615-627. doi: 10.1016/j.ijepes.2018.12.028
2. Wang, D., Hou, M., Gao, M. and Qiao, F., "Travelling wave directional pilot protection for hybrid lcc-mmc-hvdc transmission line", ***International Journal of Electrical Power & Energy Systems***, Vol. 115, (2020), 105431. doi: 10.1016/j.ijepes.2019.105431
3. Zare, H., Khanalizadeh Eini, M. and Esmaeili, A., "Stabilization of voltage and current in the distribution networks using apf and tsc", ***International Journal of Engineering, Transactions B: Applications***, Vol. 35, No. 5, (2022), 1064-1073. doi: 10.5829/IJE.2022.35.05B.21
4. Xiao, H., Xu, Z., Tang, G. and Xue, Y., "Complete mathematical model derivation for modular multilevel converter based on successive approximation approach", ***IET Power Electronics***, Vol. 8, No. 12, (2015), 2396-2410. doi: 10.1049/iet-pel.2014.0892
5. Farshad, M. and Karimi, M., "Intelligent protection of csc-hvdc lines based on moving average and maximum coordinate difference criteria", ***Electric Power Systems Research***, Vol. 199, (2021), 107439. doi: 10.1016/j.epsr.2021.107439
6. Tavassoli, F., Ghoreishy, H., Adabi, J. and Rezanejad, M., "An advanced modulation technique featuring common mode voltage suppression for three-phase neutral point clamped back to back converters", ***International Journal of Engineering, Transactions B: Applications***, Vol. 35, No. 11, (2022), 2220-2228. doi: 10.5829/IJE.2022.35.11B.17
7. Abbasghorbani, M., "Prioritization of transmission network components based on their failure impact on reliability of composite power systems", ***International Journal of Engineering, Transactions C: Aspects***, Vol. 35, No. 3, (2022), 502-509. doi: 10.5829/IJE.2022.35.03C.02
8. Xing, C., Li, S. and Xi, X., "Research on a fault location method for a pole-to-pole short-circuit fault in an lcc-mmc hybrid dc transmission system", ***IEEE Access***, Vol. 8, (2020), 165683-165692. doi: 10.1109/ACCESS.2020.3022717
9. Wang, D. and Hou, M., "Travelling wave fault location algorithm for lcc-mmc-mtdc hybrid transmission system based on hilbert-huang transform", ***International Journal of Electrical Power & Energy Systems***, Vol. 121, (2020), 106125. doi: 10.1016/j.ijepes.2020.106125
10. Wang, D., Yang, H., Hou, M. and Guo, Y., "Travelling wave fault location principle for hybrid multi-terminal lcc-mmc-hvdc transmission lines based on c-evt", ***Electric Power Systems Research***, Vol. 185, (2020), 106402. doi: 10.1016/j.epsr.2020.106402
11. Wang, J., Zhang, Y. and Li, T., "Equivalent characteristic impedance based hybrid-hvdc transmission line fault location", ***Electric Power Systems Research***, Vol. 194, (2021), 107055. doi: 10.1016/j.epsr.2021.107055
12. Wang, D. and Hou, M., "Travelling wave fault location principle for hybrid multi-terminal lcc-vsc-hvdc transmission line based on r-ect", ***International Journal of Electrical Power & Energy Systems***, Vol. 117, (2020), 105627. doi: 10.1016/j.ijepes.2019.105627
13. Zhang, D., Wu, C., He, J. and Liang, C., "A new protection scheme for transmission line of three-terminal hybrid hvdc system", ***International Journal of Electrical Power & Energy Systems***, Vol. 134, (2022), 107446. doi: 10.1016/j.ijepes.2021.107446
14. Gao, S., Xu, Z., Song, G., Shao, M. and Jiang, Y., "Fault location of hybrid three-terminal hvdc transmission line based on improved lmd", ***Electric Power Systems Research***, Vol. 201, (2021), 107550. doi: 10.1016/j.epsr.2021.107550
15. Wang, J. and Zhang, Y., "Traveling wave propagation characteristic-based lcc-mmc hybrid hvdc transmission line fault location method", ***IEEE Transactions on Power Delivery***, (2021). doi: 10.1109/TPWRD.2021.3055840
16. Roy, N.B., "Fault identification and determination of its location in a hvdc system based on feature extraction and artificial neural network", ***Journal of The Institution of Engineers (India): Series B***, Vol. 102, No. 2, (2021), 351-361. doi: 10.1007/s40031-021-00541-5
17. Xiao, H., Sun, K., Pan, J., Li, Y. and Liu, Y., "Review of hybrid hvdc systems combining line communicated converter and voltage source converter", ***International Journal of Electrical Power & Energy Systems***, Vol. 129, (2021), 106713. doi: 10.1016/j.ijepes.2020.106713
18. Li, G., Li, G., Liang, H., Yin, M. and Zhao, C., "Operational mechanism and characteristic analysis of novel hybrid hvdc system", in 2006 International Conference on Power System Technology, IEEE., (2006), 1-6. doi: 10.1109/ICPST.2006.321914
19. Qahraman, B. and Gole, A., "A vsc based series hybrid converter for hvdc transmission", in Canadian Conference on Electrical and Computer Engineering, 2005., IEEE., (2005), 458-461. doi: 10.1109/CCECE.2005.1556970
20. Xu, Z., Wang, S. and Xiao, H., "Hybrid high-voltage direct current topology with line commutated converter and modular multilevel converter in series connection suitable for bulk power overhead line transmission", ***IET Power Electronics***, Vol. 9, No. 12, (2016), 2307-2317. doi: 10.1049/iet-pel.2015.0738
21. Xiao, H., Sun, K., Pan, J. and Liu, Y., "Operation and control of hybrid hvdc system with lcc and full-bridge mmc connected in parallel", ***IET Generation, Transmission & Distribution***, Vol. 14, No. 7, (2020), 1344-1352. doi: 10.1049/iet-gtd.2019.1336
22. Wijaya, G. and Abu-Siada, A., "Review of transmission line fault location using travelling wave method", in 2018 Conference on Power Engineering and Renewable Energy (ICPERE), IEEE., (2018), 1-6. doi: 10.1109/ICPERE.2018.8739752
23. Packard, H., "Traveling wave fault location in power transmission systems", ***Application Note***, Vol. 1285, (1997).

24. Hadaeghi, A., Samet, H. and Ghanbari, T., "Multi extreme learning machine approach for fault location in multi-terminal high-voltage direct current systems", ***Computers & Electrical Engineering***, Vol. 78, (2019), 313-327. doi: 10.1016/j.compeleceng.2019.07.022

25. Abderrazak, L., Hanane, K.S., Adlene, R., Mohamed, A. and Mohamed, K., "Fuzzy logic control of mppt controller in autonomous hybrid power generation system by using extended kalman filter for battery soc estimation", ***International Journal of Engineering, Transactions B: Applications***, Vol. 36, No. 2, (2023).

26. Aggarwal, C.C., "Neural networks and deep learning", ***Springer***, Vol. 10, (2018), 978-973. doi: 10.1007/978-3-319-94463-0

27. Tzelepis, D., Mirsaeidi, S., Dyśko, A., Hong, Q., He, J. and Booth, C.D., "Intelligent fault location in mtdc networks by recognizing patterns in hybrid circuit breaker currents during fault clearance process", ***IEEE Transactions on Industrial Informatics***, Vol. 17, No. 5, (2020), 3056-3068. doi: 10.1109/TII.2020.3003476

28. Nagar, K. and Shah, M., "A review on different ann based fault detection techniques for hvdc systems", I***nternational Journal of Innovative Research in Engineering & Management***, Vol. 3, No. 6, (2016), 477-481. doi: 10.21276/ijirem.2016.3.6.5

29. Hussain, M., Dhimish, M., Titarenko, S. and Mather, P., "Artificial neural network based photovoltaic fault detection algorithm integrating two bi-directional input parameters", ***Renewable Energy***, Vol. 155, (2020), 1272-1292. doi: 10.1016/j.renene.2020.04.023

30. Ankar, S. and Yadav, A., "Wavelet-ann based fault location scheme for bipolar csc-based hvdc transmission system", in 2020 First International Conference on Power, Control and Computing Technologies (ICPC2T), IEEE., (2020), 85-90. doi: 10.1109/ICPC2T48082.2020.9071450

31. Xiang, W., Yang, S. and Wen, J., "Ann-based robust dc fault protection algorithm for mmc high-voltage direct current grids", ***IET Renewable Power Generation***, Vol. 14, No. 2, (2020), 199-210. doi: 10.1049/iet-rpg.2019.0733

32. Khan, N.M., Mansoor, M., Moosavi, S.K.R., Zafar, M.H., Khan, U.A. and Shahzad, M., "A novel search and rescue optimization algorithm based artificial neural network for identification, classification and location of dc fault in two terminal hvdc transmission systems", in 2022 International Conference on Emerging Trends in Smart Technologies (ICETST), IEEE. (2022), 1-6. doi: 10.1109/ICETST55735.2022.9922910

33. Ye, X., Lan, S., Xiao, S.j. and Yuan, Y., "Single pole-to-ground fault location method for mmc-hvdc system using wavelet decomposition and dbn", ***IEEJ Transactions on Electrical and Electronic Engineering***, Vol. 16, No. 2, (2021), 238-247. doi: 10.1002/tee.23290

34. Ravesh, N.R., Ramezani, N., Ahmadi, I. and Nouri, H., "A hybrid artificial neural network and wavelet packet transform approach for fault location in hybrid transmission lines", ***Electric Power Systems Research***, Vol. 204, (2022), 107721. doi: 10.1016/j.epsr.2021.107721

35. Rohani, R., Koochaki, A. and Siahbalaee, J., "Fault location in vsc-hvdc systems based on nsga-ii and discrete wavelet transform", ***International Journal of Renewable Energy Research (IJRER)***, Vol. 12, No. 3, (2022), 1347-1361. doi: 10.20508/ijrer.v12i3.13050.g8519

36. Yi, L., Liu, Y., Lu, D., Nie, Y. and Zheng, X., "Hvdc line fault location using wavelets to mitigate impact of frequency dependent line parameters", in 2022 IEEE Power & Energy Society General Meeting (PESGM), IEEE., (2022), 1-5. doi: 10.1109/PESGM48719.2022.9916742

37. Hadaeghi, A., Samet, H. and Ghanbari, T., "Multi svr approach for fault location in multi-terminal hvdc systems", ***International Journal of Renewable Energy Research (IJRER)***, Vol. 9, No. 1, (2019), 194-206. doi: 10.20508/ijrer.v9i1.8868.g7576

38. Tzelepis, D., Dyśko, A., Fusiek, G., Niewczas, P., Mirsaeidi, S., Booth, C. and Dong, X., "Advanced fault location in mtdc networks utilising optically-multiplexed current measurements and machine learning approach", ***International Journal of Electrical Power & Energy Systems***, Vol. 97, (2018), 319-333. doi: 10.1016/j.ijepes.2017.10.040

39. Pourafzal, A., Fereidunian, A. and Safarihamid, K., "Chaotic time series recognition: A deep learning model inspired by complex systems characteristics", ***International Journal of Engineering, Transactions A: Basics***, Vol. 36, No. 1, (2023). doi: 10.5829/IJE.2023.36.01A.01

Persian Abstract

چکیده

در این مقاله، یک تکنیک مکان‌یابی خطا براساس شبکهٔ عصبی مصنوعی (ANN) برای سیستمهای HVDC هایبریدی-ترمینالی از نوع LCC-VSC-HVDC مورد بررسی و ارزیابی قرار گرفته است. در سیستم‌های HVDC متداول (سیستمهای HVDC مبتنی بر LCC و یا مبتنی بر VSC)، به دلیل استفاده از مبدل‌های مشابه در پایانه‌های فرستنده و گیرنده، از فیلترهای یکسان در هر دو سمت خط انتقال استفاده می‌گردد. در این مقاله نتیجه گرفته می‌شود که با توجه به استفاده از دو نوع مبدل مختلف در هر دو انتهای سیستم هایبریدی-ترمینالی مورد استفاده از نوع LCC-VSC-HVDC و استفاده از فیلترهای DC مختلف در هر دو طرف، مکان‌یابی خطا با استفاده از جریان‌های قطب مثبت و منفی سمت یکسوساز نتایج بسیار بهتری نسبت به بقیه سیگنال‌های ورودی خواهد داشت. بنابراین، مشخص خواهد شد که با افزایش و طراحی فیلترهای DC مناسب بر روی خط انتقال سیستم‌های HVDC هایبریدی، مسالهٔ مکان‌یابی خطا به طور قابل‌توجه و شگفت انگیزی تسهیل خواهد یافت. امروزه مکان‌یابی خطا در خطوط انتقال HVDC با مقداری بیش از ۱ ٪ به طور کلی در اکثر مقالات مورد بحث قرار می‌گیرد. در این تحقیق، مکان دقیق خطا با مقدار ۰.۰۰۴۵ ٪ یعنی فاصلهٔ ۲۲.۵ متری از نقطهٔ خطا در رضایتبخش‌ترین حالت بدست آمده است که عملکرد بی‌نظیر شبکهٔ عصبی مصنوعی را در کنار تبدیل موجک نمایش می‌دهد. به منظوراعتبارسنجی روش پیشنهادی، یک سیستم هایبریدی-ترمینالی از نوع LCC-VSC-HVDC از طریق نرم‌افزار MATLAB شبیه‌سازی شده است. نتایج تایید می‌کنند که روش پیشنهادی به طور کامل تحت موقعیت‌های مختلف، مقاومت‌های مختلف و انواع متفاوت خطا به درستی عمل می‌کند.

IJE TRANSACTIONS B: Applications Vol. 36, No. 02, (February 2023) 226-235

International Journal of Engineering

Journal Homepage: www.ije.ir

Coordination of Load and Generation Sides to Reduce Peak Load and Improve Arbitrage of Smart Distribution Grid

M. K. Al-Saadi*

Electromechanical Engineering Department, University of Technology-Iraq, Baghdad, Iraq

PAPER INFO

Paper history:
Received 23 May 2022
Received in revised form 30 October 2022
Accepted 12 November 2022

Keywords:
Microgrids Optimization
Load Management
Energy Storage
Emission Cost

ABSTRACT

This paper proposes an approach to improve the system arbitrage and reduce peak load by managing both the generation and load sides simultaneously. The peak load reduction is achieved using a load control program, while the arbitrage is enhanced by minimizing the operating and emission costs. The load management and minimization of operating cost are combined in an optimization approach in a multi-objective framework. The storage battery is utilized to contribute in the shaving of the peak load and reducing the operating and emission cost, where the battery aging is taken into account in the proposed model. The management of load sides is considered as decision variables in the approach. A mixed-integer quadratic program is employed to formulate the optimization approach. The proposed approach is applied to a smart low-voltage distribution grid. The results show that the management of both the demand and generation sides reduces the operating and emission costs and improves the load factor of the system.

doi: *10.5829/ije.2023.36.02b.04*

1. INTRODUCTION

Balancing the generation and demand in microgrid (MG) is challenging because the intermittent nature of renewable energy resources (wind, solar). These sources are uncontrolled and their generation changes with weather condition. So, it is difficult to make these sources follow the load changes. Therefore, managing both the generation and demand sides play a vital role in the balance demand and generation. Besides, the reduction of peak load improves the overall energy efficiency and reduces the total cost.

In the open literature, the researchers proposed a peak load management and its integration with the operating of MGs. Wang and Huang [1] presented the demand response technique which is contributed to economic operation of MG, where end-user responses to the energy price. Aghajani et al. [2] proposed a formula to reduce the total cos of a MG, which includes renewable energy and mixed generation sources. The load management was considered in the model to reduce the total cost and balance the load and generation, where different types of loads are participated in the load management shifting program.

Huang and Billinton [3] presented a load algorithm on seven different load sectors and studied the effects of load management on the load shape and the system reliability. Hamidian and Sedighi [4] pointed out time of use strategy to smooth the load. They analyzed the impacts of load control to reduce losses and improve reliability. However, Huang and Billinton [3] Hamidian and Sedighi [4] ignored the impact of load management on system cost and other benefits of the load control on system operation and they also neglected the reactive load. Fotuhi-Firuzabad and Billinton [5] suggested the impact of a peak clipping, load shifting and load interrupting on the system cost function and system reliability; however, they ignored many important constraints and other benefits of load control. Logenthiran et al. [6] proposed a demand side technique that brought the load curve close to the objective load curve. The load cutting to reduce the operating cost of

*Corresponding Author Institutional Email: 50055@uotechnology.edu.iq (M. K. Al-Saadi)

Please cite this article as: M. K. Al-Saadi, Coordination of Load and Generation Sides to Reduce Peak Load and Improve Arbitrage of Smart Distribution Grid, ***International Journal of Engineering, Transactions B: Applications***, Vol. 36, No. 02, (2023), 226-235

MG was argued by Parisio et al. [7]. The load cut was applied to the total load and ignored other load management techniques. Olamaei and Ashouri [8] analyzed the impact of load response on the cost of MG and the load response presented as a load shifting. The algorithm was applied to low voltage MG which consists of micro turbines, wind turbines, and storage devices. However, they ignored the emission cost and many important constraints and other benefits of load management and they applied load control program on active load only. The energy management from both generation, the total cost and demand were investigated by Wang et al. [9]. The problem was formulated by using receding horizon strategy. This algorithm applied on single residential home. They ignored the cost of storage device, the on/off and maintenance cost and they ignored the reactive production cost. Shi et al. [10] suggested a management algorithm to improve the total cost of a MG and the demand side management integrated with problem modelling and it is applied to total MG load; however, they override the emission cost, reactive cost, on/off cost and benefits of load response on operation of grid. Liu et al. [11] proposed an optimization approach to reduce the total cost of the MG and the load response program integrated with optimization problem and its applied on total MG load. They did not consider storage device and reactive power, emission cost, start up and shutdown cost. They also ignored the system constraints and the ramp rate constraints and load management were applied only on active load. Wu et al. [12] applied load management program on the system includes only photovoltaic and battery to minimize the cost of the system. Kinhekar et al. [13] applied load shifting technique on industrial load and they investigated the effect of load management on the whole system cost. The reactive and emission cost, other benefits of load management, and the cost of battery operation were not taken into account in the model. Jafari et al. [14] proposed an optimal operation approach of MG, where the demand response was considered as shifting technique in responding to energy market price. The optimal management and control of the microgrid is a hierarchical structure, where the optimal operation and unit commitment (UC) strategy is within the tertiary level [15, 16].

In this paper, a novel optimization approach with managing both the load and generation is presented to improve the arbitrage of the smart distribution grid and to shave a peak load. Both the active and reactive loads are managed and integrated with the optimization approach as decision variables. The load-shifting program is developed and integrated with the proposed optimization approach to analyze the effects of load management program on the total cost of MG and on the load factor. The UC is employed to consider the real and imaginary parts of the output generation of the generators. The battery is employed to reduce the peak load and improve the total cost, where the aging of battery is taking into account in the proposed approach. Furthermore, the isolated mode constraints are considered in the formulation of approach to ensure seamless transition when the connection with utility grid is lost.

In comparing with the previous papers in the literature, this paper develops an approach to manage both generation and load sides with taken into account the active and reactive loads, whereas majority of papers investigate the management of the generation side as given by Al-saadi and Luk [17]. This impacts on the results and the fidelity of the model. Besides, this paper considers the UC technique for both active and reactive power, while other papers consider only active power. Considering both generation and load side management with taken into account different constraints to reduce operating and emission cost makes the proposed model closed to real scenario.

2. MATHMATICAL MODELS

To model and formulate the proposed approach, the following models should be considered.

2. 1. Distributed Generators Model The cost of fuel of the distributed generators (DGs) at each time interval $\boldsymbol{t}$ is modelled as [18, 19]:

$$C_P^t = a + b.P_g^t + c.{P^2}_g^t \tag{1}$$

where a (\$/h), b (\$/kWh), and c (\$/kW^{2}h) are the parameters of the cost function, and P_g^t is the real power of the generators.

2. 2. Cost Function of inactive Power This cost is determined using the following equation [17]:

$$C_Q^t = aq + bq.Q_g^t + cq.{Q^2}_G^t \tag{2}$$

where aq (\$/h), bq (\$/kVArh), and cq (\$/kVAr^{2}h) are the parameters of the expense of inactive power, and Q_g^t is the output inactive power of the generators.

2. 3. Maintenance Cost of the Generators This cost is formulated as follows:

$$K_g^t = K_g.P_g^t \tag{3}$$

where K_g (\$/kWh) is the parameter of the maintenance expense of the generators.

2. 4. Storage Device Model The following equation is employed to represent the operation of storage battery in the proposed optimization approach:

$$E_b^t = E_b^{t-1} + \Delta t.\ P_{bch}^t.\eta_{ch} - \Delta t.\left(\frac{P_{bdis}^t}{\eta_{dis}}\right) \quad (4)$$

where E_b^t , E_b^{t-1} are the capacity of the storage device at $t$and $t-1$ period. P_{bch}^t and $P_{bdis}^t$are the absorbing and delivering power of the battery, while η_{ch} and η_{dis} are the efficiencies.

The battery aging cost is converted to the monetary concept by employing the following equations:

$$C_b^t = C_d\ .P_b^t.\Delta t \quad (5)$$

where C_d is the aging expense of battery ($/kWh), $P_b^t$is absorbing or delivering power. The C_d is determined as follows [20, 21].

$$C_d = \frac{c_b}{L_b} \quad (6)$$

where c_b is the purchasing cost ($) of the battery, L_b is the actual life (kWh), which is determined using the following equation:

$$L_b = DoD.E_b.L_c \quad (7)$$

where DoD is the depth of discharge, L_c is the battery cycle life.

2. 5. Trading Energy with the Upstream Grid MG can exchange power with the upstream grid in case of connected mode. The expense of trading power with the upstream system is determined as follows:

$$C_{UP}^t = c_{UP}^t P_U^t \quad (8)$$

$$C_{UQ}^t = c_{UQ}^t Q_U^t \quad (9)$$

where c_{UP}^t in ($/kW) and c_{UP}^t in ($/kVAr) are the active and inactive price of exchanging energy with the upstream grid (OMPs). P_U^t is the real trading power and Q_U^t is the reactive trading power.

2. 6. Environmental Cost The emission of CO_2, SO_2, NO_x, and PM are considered as greenhouse gases. The emission of $\boldsymbol{j^{th}}$ greenhouse gas from $\boldsymbol{i^{th}}$ DG is determined as follows:

$$C_e^t = \sum_{j=1}^{M}\sum_{i=1}^{N} E_{j,i}\ .C_j.P_g^t \quad (10)$$

where C_j ($/kg) is the expense of emission of j^{th} pollutant gases, and $E_{j,i}$ (kg/kWh) is the emitted amount of the harm gases from the generators. M is the number of gases and N is the number of generators.

3. PROPOSED MODELS of the DIRECT LOAD CONTROL

The different types of loads are taken into account in this paper, residential (R), commercial (C) and industrial (I) consumers. All these kinds of loads are taken into consideration in the proposed optimization framework. The direct load control program is applied individually on different load sectors: residential, industrial and commercial. The load control strategy is also applied simultaneously on three types of loads. peak clipping and load shifting are considered as demand control program in this paper.

3. 1. Proposed Mathematical Model of the Peak Clipping and Load Shifting The moving of the load changes the pattern of the original load profile according to the load management program. This technique aims to limit the maximum demand to a specified value, where the load is moved from high to low hours load demand. The following mathematical equation are employed to simulate the peak clipping and load shifting for active and reactive loads.

For active load

$$L^{-t}_{\ p} = \{L_p^t - (L_p^t - P_p^t).\delta_c^t\} + A_p^t \quad (11)$$

$$A_p^t = a_p.\left\{\frac{\sum_{t\in\Omega}(L_p^t - P_p^t).\delta_c^t}{h_p}\right\}.\delta_f^t \quad (12)$$

For reactive load

$$L^{-t}_{\ q} = \{L_q^t - (L_q^t - P_q^t).\delta_c^t\} + A_q^t \quad (13)$$

$$A_q^t = a_p.\left\{\frac{\sum_{t\in\Omega}(L_q^t - P_q^t).\delta_c^t}{h_p}\right\}.\delta_f^t \quad (14)$$

where A_p^t and A_q^t are active and reactive loads moved to low-peak hours, a_p and a_q are the percentage of the reduced active and reactive power during the on-peak hour and recovered during off-peak hours, h_p and h_q are the number of off-peak hours (h), L_p^t and $L_q^t$are active and reactive base loads (kW) and (kVAr), $L^{-t}_{\ p}$ and $L^{-t}_{\ q}$ are modified active and reactive loads, P_p^t, P_q^t are peak active and reactive loads, Ω is the set of on-peak hours during which the energy is reduced.

$$\delta_c^t = 1 \text{ for } L_p^t > P_p^t\ and\ L_q^t > P_q^t \quad (15)$$

$$\delta_c^t = 0 \text{ for } L_p^t \le P_p^t\ and\ L_q^t \le P_q^t \quad (16)$$

$$\delta_f^t = 1 \text{ for } t_1 \le t \le t_2 \quad (17)$$

$$\delta_f^t = 1 \text{ for other value of t} \quad (18)$$

$$0 \le a_p \le 1 \quad (19)$$

$$0 \le a_q \le 1 \quad (20)$$

3. 2. Load Management for Multi-load The shaping of the load curve that is obtained from the load management programs can be achieved at the same time in many sectors or areas of the distribution grid. It assumes that there are N sectors or areas in the system. The aggregated effects of load management are formulated as follows:

For active load

$$L^{-k}_{T-P} = L^{-k}_{1-P} + L^{-k}_{2-P} + \cdots L^{-k}_{NL-P} \quad (21)$$

For reactive load

$$L^{-k}_{T-Q} = L^{-k}_{1-Q} + L^{-k}_{2-Q} + \cdots L^{-k}_{NL-Q} \quad (22)$$

where L^{-k}_{T-P} and L^{-k}_{Tq} are the total modified active and reactive loads model, L^{-k}_{NL-P} and L^{-k}_{NL-Q} are the modified active and reactive loads model of NL load sectors.

3. 3. Load Factor The load factor (LD) is determined as follows:

$$LD = \frac{average\ load}{peak\ load} \quad (23)$$

4. FORMULATION OF OBJECTIVE FUNCTION

The proposed approach aims to reduce the peak load and minimize the total cost of the MG. The proposed approach involves the aforementioned costs. Besides, the objective function involves the expense of loads cutting. Based on the aforementioned mode of costs, the cost function is formulated as follows:

$$F = Min \sum_{t=1}^{T}\{\sum_{i=1}^{N}[[C^t_{Pi} + C^t_{Qi} + C^t_{gi}]\delta^t_{gi} + ST^t_{gi} + SD^t_{gi}] + C^t_e + C^t_b + C^t_{UP} + C^t_{UQ} + (1 - a_p).\rho_p.\sum_{h=1}^{NL} X^t_{h-p} + (1 - a_q).\rho_q.\sum_{h=1}^{NL} X^t_{h-q}\} \quad (24)$$

where X^t_{h-p} and X^t_{h-q} are the active and reactive power reduced during the on-peak hour and not recovered, NL is the number of load sectors, ρ_p and ρ_q are the penalty of active and reactive uncovered loads ($), i is i^{th} DG, δ^t_{gi} is the state of the i^{th} DG.

5. FORMULATION OF CONSTRAINTS

The proposed cost function undergoes to the following constraints.

5. 1. Power Balance Constraints The following constraints are expressed as follows for the active and reactive power.

$$\sum_{t=1}^{T}\{\sum_{i=1}^{N} \delta^t_{gi}.P^t_g + \sum_{i1=1}^{N1} P^t_{Wi1} + \sum_{i2=1}^{N2} P^t_{PVi2} + P^t_b + P^t_U = (L^t_p - (L^t_p - P^t_p).\delta^t_c + A^t_p)\} \quad (25)$$

$$\sum_{t=1}^{T}\{\sum_{i=1}^{N} \delta^t_{gi}.Q^t_g + Q^t_U = (L^t_q - (L^t_q - P^t_q).\delta^t_c + A^t_q)\} \quad (26)$$

5. 2. Generating Limits These constraints are formulated as follows:

$$\delta^t_{gi}.P^t_{gmin} \le P^t_g \le \delta^t_{gi}.P^t_{gmax} \quad (27)$$

$$\delta^t_{gi}.Q^t_{gmin} \le Q^t_g \le \delta^t_{gi}.Q^t_{gmax} \quad (28)$$

where P^t_{gmin} and P^t_{gmax} are the low and high possible output power of the genertors. Q^t_{gmin} and Q^t_{gmax} are the low and high possible reactive power of generators.

5. 3. Trading Power with the upstream Grid Constraints Trading energy with the upstream grid at period normally either delivering or taking power. There are also possibilities that no exchanging power occurs between the MG and the upstream grid at a certain period. Therefore, two binary variables $\boldsymbol{\delta^t_{Up}} \in [\mathbf{0},\mathbf{1}]$ and $\boldsymbol{\delta^t_{Us}} \in [\mathbf{0},\mathbf{1}]$, are assigned to represent this operation and the following equation $\boldsymbol{\delta^t_{Up} + \delta^t_{Us} \le 1}$ is defined to prevent purchasing or selling power at the same time. The exchanging power constraints are formulated as follows:

$$\delta^t_{Up}.P^t_{Upmin} \le P^t_{Up} \le \delta^t_{Up}.P^t_{Upmax} \quad (29)$$

$$\delta^t_{Up}.Q^t_{Upmin} \le Q^t_{Up} \le \delta^t_{Up}.Q^t_{Upmax} \quad (30)$$

$$\delta^t_{Us}.P^t_{Usmin} \le P^t_{Us} \le \delta^t_{Us}.P^t_{Usmax} \quad (31)$$

$$\delta^t_{Us}.Q^t_{Usmin} \le Q^t_{Us} \le \delta^t_{Us}.Q^t_{Usmax} \quad (32)$$

where P^t_{Usmax}, Q^t_{Usmin}, Q^t_{Usmax}, and power from are sold power from the upstream grid, P^t_{Upmin}, P^t_{Upmax}, Q^t_{Upmin}, Q^t_{Upmax} are purchasing power from the upstream grid.

5. 4. Constraints of the Battery The operating constraints of the batteries are formulated as follows [22].

5. 4. 1. Battery State of Charge Constraint

$$E^t_{bmin} \le E^t_b \le E^t_{bmax} \quad (33)$$

where E^t_{bmin} is the minimum state of charge and E^t_{bmax} is the maximum state of charge at time t.

5. 4. 2. Constraints of Battery Operation The status of the battery at each time interval is explained with three possible states: absorbing, delivering and idle. Therefore, two binary variables, $\boldsymbol{\delta^t_{bch}} \in [\mathbf{0},\mathbf{1}]$ and $\boldsymbol{\delta^t_{bdis}} \in [\mathbf{0},\mathbf{1}]$, which are assigned and formulated the status of the battery operation. $\boldsymbol{\delta^t_{bch} + \delta^t_{bdis} \le 1}$ is considered to avoid absorbing or delivering power simultaneously. The operation constraints of the battery are formulated as follows:

$$\delta^t_{bch}.P^t_{bchmin} \le P^t_{bch} \le \delta^t_{bch}.P^t_{bchmax} \quad (34)$$

$$\delta^t_{bdis}.P^t_{bdismin} \le P^t_{bdis} \le \delta^t_{bdis}.P^t_{bdismax} \quad (35)$$

where P_{bchmin}^{t} and P_{bchmax}^{t} are the minimum and maximum possible absorbing, while $P_{bdismin}^{t}$ and $P_{bdismax}^{t}$ are the low and high delivering power of the storage device.

5. 5. Emission Limitation Constraints The constraints that limit the emission of pollutant gases in the area of the MG is formulated as follows:

$$\sum_{i=1}^{N} E_{j\,i} \,.\, P_{g}^{t} \leq L_{j} \tag{36}$$

where L_j (kg/h) is the acceptable level of emission of the pollutant j in the MG, where $(j = 1, 2, 3 \ldots \ldots . M)$

5. 6. Isolated Mode Constraints The following constraints are determined using the following equations:

$$\sum_{i=1}^{T}\{\sum_{i=1}^{N} \delta_{gi}^{t} . P_{gmax}^{t} \geq \left(L_{p}^{t} - \left(L_{p}^{t} - P_{p}^{t}\right). \delta_{c}^{t} + A_{p}^{t}\right)\} \tag{37}$$

$$\sum_{i=1}^{T}\{\sum_{i=1}^{N} \delta_{gi}^{t} . Q_{gmax}^{t} \geq (L_{q}^{t} - \left(L_{q}^{t} - P_{q}^{t}\right). \delta_{c}^{t} + A_{q}^{t})\} \tag{38}$$

6. PROPOSED MG FOR CASE STUDY

The proposed approach is applied to the standard multi-feeder low voltage distribution grid with voltage 0.4 kV as depicted in Figure 1. This grid is a standard multi-feeder LV microgrid which is taken from literature [17, 23, 24], where all the parameters are on the standard LV feeder. In this study, the microgrid impact is considered in all scenarios. The proposed MG encompasses of three feeders and seventeen bus bars. The power factor is presumed to be 0.9. Besides, the MG encompasses mixed of distributed generators technologies including three diesel engines (DE), two Micro turbines (MTs), one fuel cell (FC), one wind turbine, and PV panels. The cost functions parameters and the emission levels of the DGs are taken from the following sources [25-29]. Moreover, the grid involves a battery. The capacity of the battery is 50 kWh and the maximum charging and discharging power is 25 kWh. The operating efficiency is presumed to be 0.9. The hourly spectrums for a wind and PV output, OMPs and loads are summarized in Table 1.

7. RESULTS AND DISCUSSION

The optimization problem is solved by employing of IMB ILOG CPLEX version 12.6, where Microsoft Excel is interfaced with CPLEX to show the results [30]. Firstly, the direct load control program is applied to the residential, industrial, and commercial sectors separately. Secondly, the load control program is conducted on the all loads simultaneously. The LF without load control is 0.68.

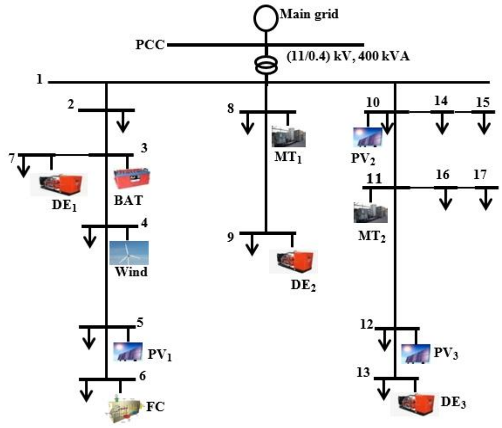

Figure 1. The MG under study

TABLE 1. Spectrum of wind turbine and solar panels, OMPs and total loads

Time (h)	WT power (m/s)	PV power (kW)	Active power price ($/kW)	Inactive power price ($/kVAr)	Total load (kW)
1	12	0	0.065	0.013	76.45
2	8	0	0.058	0.0116	70.01
3	8	0	0.048	0.0096	67.68
4	6.5	0	0.05	0.01	63.44
5	10	0	0.052	0.0104	69.64
6	12	0	0.07	0.014	80.08
7	14.25	0	0.087	0.0174	109.21
8	13.5	0.5	0.09	0.018	149.78
9	16	1.4	0.14	0.028	178.23
10	17	2	0.195	0.039	201.32
11	16	2.2	0.15	0.03	211.05
12	13.25	2.25	0.14	0.028	205.54
13	12.6	2.4	0.126	0.0252	223.24
14	13	2.5	0.0105	0.021	229.26
15	10.3	2.25	0.1	0.02	218.54
16	8.25	2	0.09	0.018	208.16
17	10.5	1.5	0.098	0.0196	193.91
18	16.2	0.6	0.098	0.0196	208.77
19	18	0.5	0.11	0.022	207.96
20	14	0	0.109	0.0218	212.31
21	11.6	0	0.098	0.0196	188.61
22	14	0	0.088	0.0176	159.30
23	13	0	0.064	0.013	129.07
24	15	0	0.045	0.009	79.87

7. 1. Case 1: Applying Load Control on the Residential Sector Figures 2 and 3 show the effect of the load shifting on the R load and the accumulated load. The demand is shifted from peak load to off-peak hours. These figure show that the peak of the total load is unaffected by demand side management (DSM) on residential load because the residential peak load occurs at a different time from peak load of total grid load. In this case, the load factor does not affect. Figures 4 and 5 depict the planning of the generators and power of the storage device and the trading power with the upstream system. These figure show that the highest generation from DGs occurs at 10 pm. This is because of the OMPs reach the highest values at this hour. Therefore, the MG delivers power to the main grid to reduce its cost. Besides, the MG purchases the possible highest power from the upstream grid during hours 14 to 18 because the load has the highest value and the OMPs arrive to low values and lower than the cost of power generation of the DGs. However, the DEs provide the lowest output power to fulfill the isolated mode constraints. In addition, the DEs uncommitted from hour 1 to 6 because they have the highest generation cost, where other generators can satisfy the isolated mode constraints and meet the demand with buying power from the upstream system. Moreover, at hour 24 solely the DE3 and MT2 supply their minimum output generation to fulfill the isolated mode constraints, where the load is met from purchasing power from the main grid and storage battery. This is because the OMPs reach the lowest value. The MG spends 425.445 $ per day with load management while it spends 428.872 $ per day without load management. This leads to cost reduction by 0.8% per day.

7. 2. Case 2: Applying Load Control on the Industrial Sector Figures 6 and 7 show the impact of load shifting on the industrial loads and the total loads, where the demand is shifted from peak load to off-peak

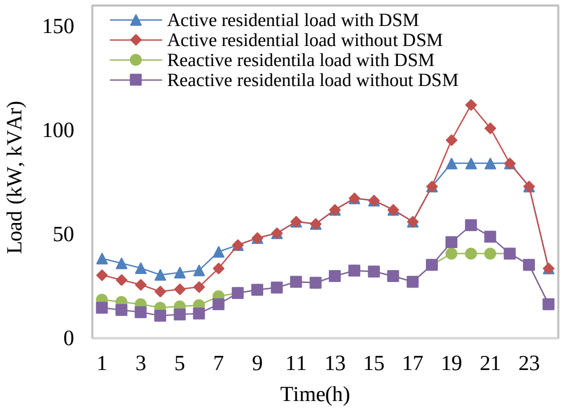

Figure 2. The profile of the residential load with and without load control

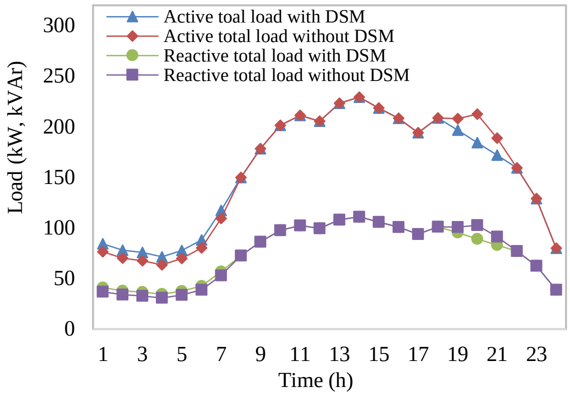

Figure 3. The profile of the total load with and without load control

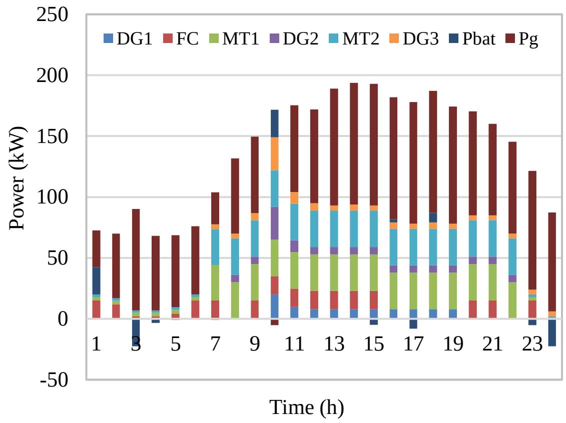

Figure 4. Optimal active power scheduling

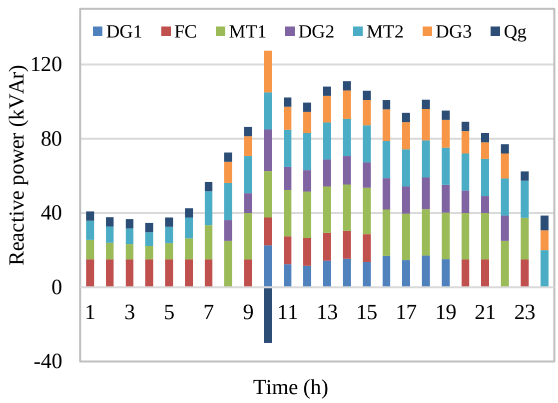

Figure 5. Optimal reactive power scheduling

hours. It can be noticed that the applied the DSM program on industrial load make significant reduction in the peak of the total load because the industrial peak load coincides with the peak of the total load. The new peak of load moved to hour 20. The decreasing of the peak of total load increases the load factor to 0.734 Figures 8 and 9 displays the optimal planning of the generators, battery

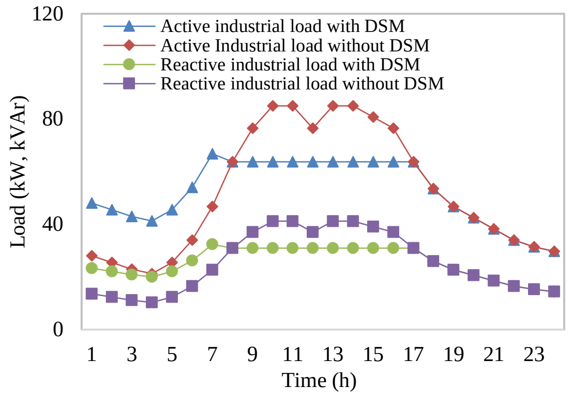

Figure 6. The profile of the industrial load with and without load control

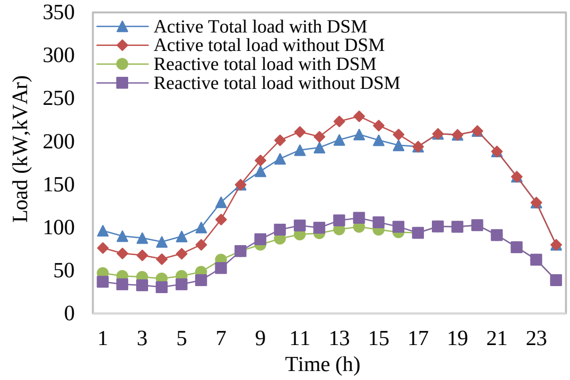

Figure 7. The profile of the total load with and without load control

and trading power with the upstream system. These figures show that at hour 10 the DGs generate the highest power and the battery discharges the highest discharging power to sell power to the upstream system because at this hour the price of selling power to utility grid has the highest value and the load at these hours is reduced as shown in Figures 8 and 9. The MG delivers power to the upstream grid at hour 10 because the power generation obtained from the DGs is less than the trading power with the main grid. The MG, in this case, sells higher power than in the previous case because the total load is reduced at this hour. Furthermore, at hour 24 only the DE3 and MT2 provide their minimum output power to satisfy the Isolated mode constraints, where the load is met from purchasing power from the main grid, storage battery, and renewable energy resources for exactly the same reason of the previous case. The total cost of load management is $418.726 per day. Therefore, the cost reduction, in this case, is 2.4% per the scheduling day.

7. 3. Case 3: Applying Load Control on the Commercial Sector

Figures 10 and 11 show the impact of load management on the commercial loads and the total grid loads. It can be seen that the applying of load management on the commercial load leads to a decrease in the peak of total MG load because the peak loads on the commercial sector coincides with the peak of the total load. This leads to increase the load factor to 0.728. However, the new peak load of the total load is still at hour 14. Figures 12 and Figure 13 depict the optimal scheduling of the generators, battery and trading power with the upstream system. It is observed that the

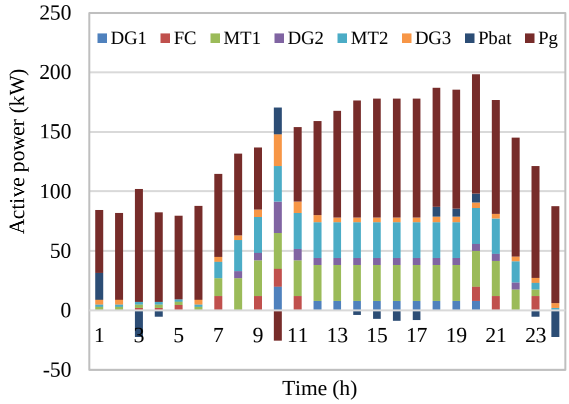

Figure 8. Optimal active power scheduling

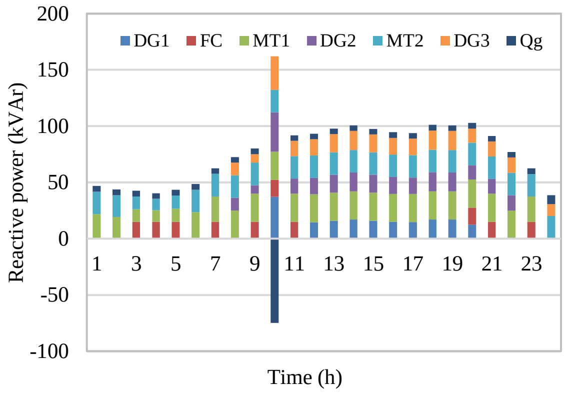

Figure 9. Optimal reactive power scheduling

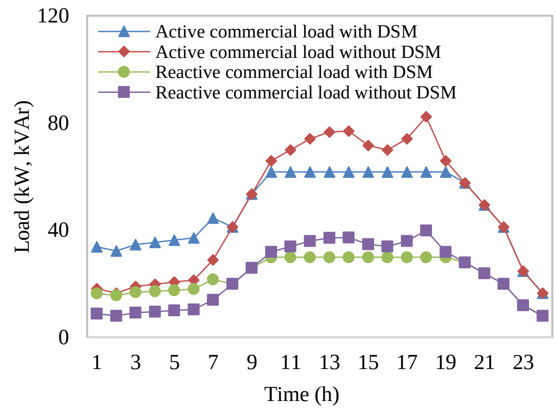

Figure 10. The profile of the commercial load with and without load control

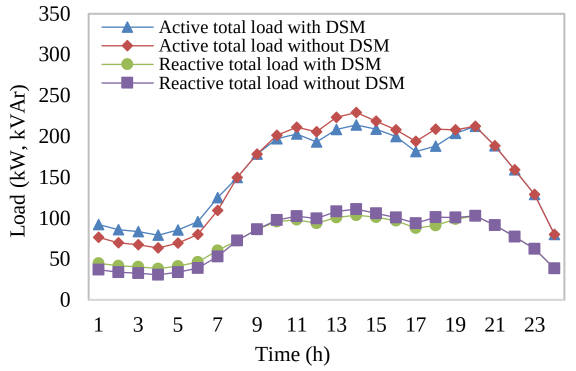

Figure 11. The profile of the total load with and without load control

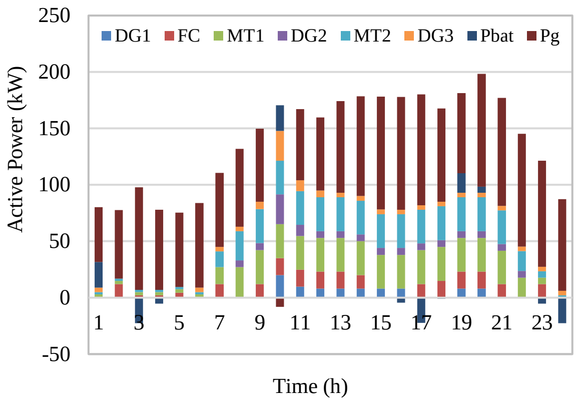

Figure 12. Optimal active power scheduling

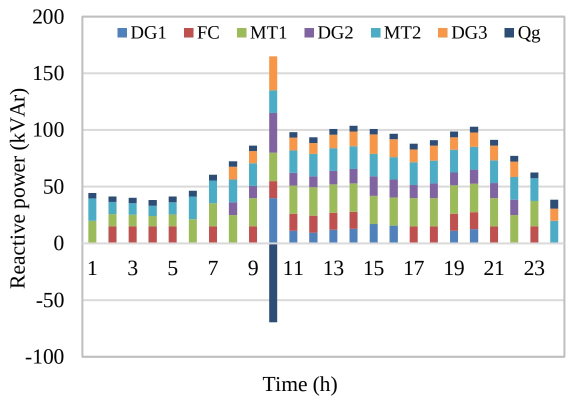

Figure 13. Optimal reactive power scheduling

MG delivers power to the upstream grid at hour 10 for the same reason as the previous cases. Besides, at hours 17 and 18 the MG sells less power from the upstream grid comparing with the previous two cases because in this case the load is reduced at this hour, while the total loads are not reduced. The MG spends $422.963 per day. Therefore, the cost reduction, in this case, is 1.4% per scheduling day.

7. 4. Case 4: Applying Load Control on the Residential, Industrial, and Commercial Sectors Simultaneously

Figure 14 shows the impact of the load management program on the accumulated loads of the grid. It is observed that the new peak of total loads is reduced by amount higher than the three previous cases because the reduction results from both the industrial and commercial sectors. This leads to reduce the load factor, where the increasing of load factor improves secure operation of the system. Figures 15 and 16 show the active and reactive optimal scheduling of the DGs and trading power with the upstream grid and the battery. It can be observed that the MG sells power to the main grid at hour10 to minimizes the cost because the OMPs reach the highest price at this hour. Therefore, the battery discharges its maximum power at this hour to sell more power to the main grid because the selling power at this hour is higher than the generation cost and charging cost. Furthermore, the MG purchases the possible highest power from the main grid at hours 13 and 14 and the committed DGs supply minimum output power. This is because the OMPs have quite low values at these hours. The total cost is 410.932 $ and the cost reduction is 4.18% per scheduling day. The LF increases to 0.808.

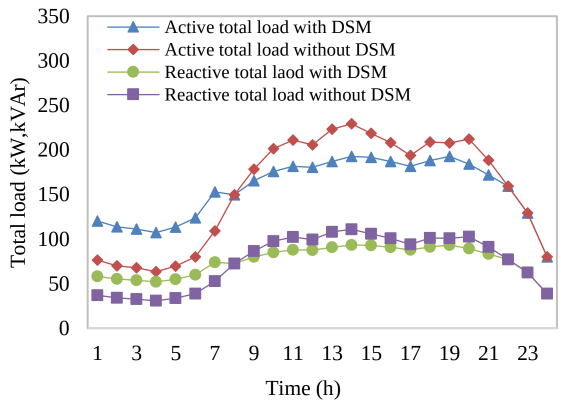

Figure 14. The profile of the total load with and without load control

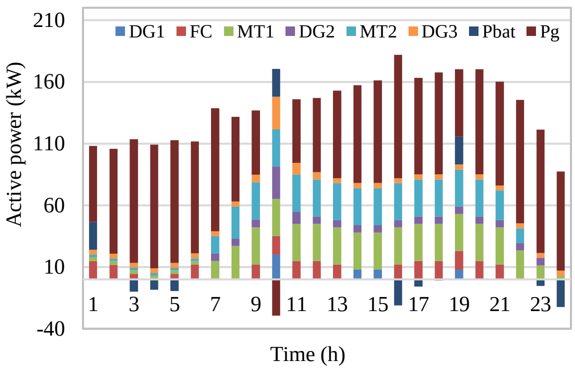

Figure 15. Optimal active power scheduling

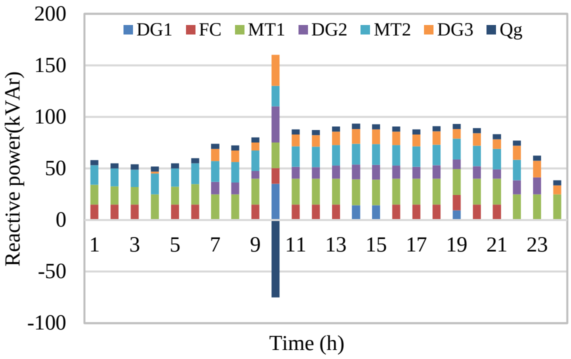

Figure 16. Optimal reactive power scheduling

It can be summarized that the highest cost reduction occurs at applying the load control on the residential, industrial and commercial loads simultaneously because in this case the highest load factor and peak loads reduction have the highest values, where the increase of the load factor leads to decrease the peak load and improving the security of supply. Besides, the high load factor postpones the investment of distribution grids. The highest peak loads reduction leads to improve the secure operation of MG. The lowest cost reduction in case of applying load control program on residential load because of the reduction of peak loads equal to zero.

8. CONCLUSIONS

An optimal management approach with integrating of load control program is proposed, where the load shifting program is conducted to the all types of loads. The load management is considered as decision variable in the proposed approach. The impacts of the load control on the economic planning of the generators, system peak load and load factor are analyzed and the system is validated through systematic testing in the low voltage distribution grid. The model considers solely the quadratic cost function. The results show that the proposed load management technique decreases not only the total cost but also decreases the peak of the total loads. This peak reduction of the total loads results in increasing the load factor. This leads to avoid of investment in terms of generation capacity. Furthermore, the security of supply and the spinning reserve are also improved.

9. REFERENCES

1. Wang, Y., Huang, Y., Wang, Y., Li, F., Zhang, Y. and Tian, C., "Operation optimization in a smart micro-grid in the presence of distributed generation and demand response", ***Sustainability***, Vol. 10, No. 3, (2018), 847. https://doi.org/10.3390/su10030847.

2. Aghajani, G., Shayanfar, H. and Shayeghi, H., "Demand side management in a smart micro-grid in the presence of renewable generation and demand response", ***Energy***, Vol. 126, (2017), 622-637. https://doi.org/10.1016/j.energy.2017.03.051

3. Huang, D. and Billinton, R., "Effects of load sector demand side management applications in generating capacity adequacy assessment", ***IEEE Transactions on Power Systems***, Vol. 27, No. 1, (2011), 335-343. https://doi.org/10.1109/TPWRS.2011.2164425

4. Sedighi, A.R. and Hamidian, M., "A novel method for implementing of time-of-use to improve the performance of electric distribution systems: A case study", ***International Journal of Engineering, Transactions C: Aspects,*** Vol. 30, No. 3, (2017), 357-365.

5. Fotuhi-Firuzabad, M. and Billinton, R., "Impact of load management on composite system reliability evaluation short-term operating benefits", ***IEEE Transactions on Power Systems***, Vol. 15, No. 2, (2000), 858-864. https://doi.org/10.1109/59.867185

6. Logenthiran, T., Srinivasan, D. and Shun, T.Z., "Demand side management in smart grid using heuristic optimization", ***IEEE Transactions on Smart Grid***, Vol. 3, No. 3, (2012), 1244-1252. https://doi.org/10.1109/TSG.2012.2195686.

7. Parisio, A., Rikos, E. and Glielmo, L., "A model predictive control approach to microgrid operation optimization", ***IEEE Transactions on Control Systems Technology***, Vol. 22, No. 5, (2014), 1813-1827. https://doi.org/10.1109/TCST.2013.2295737

8. Olamaei, J. and Ashouri, S., "Demand response in the day-ahead operation of an isolated microgrid in the presence of uncertainty of wind power", ***Turkish Journal of Electrical Engineering and Computer Sciences***, Vol. 23, No. 2, (2015), 491-504. https://doi.org/10.3906/elk-1301-164

9. Wang, X., Palazoglu, A. and El-Farra, N.H., "Operational optimization and demand response of hybrid renewable energy systems", ***Applied Energy***, Vol. 143, (2015), 324-335. https://doi.org/10.1016/j.apenergy.2015.01.004

10. Shi, W., Xie, X., Chu, C.-C. and Gadh, R., "Distributed optimal energy management in microgrids", ***IEEE Transactions on Smart Grid***, Vol. 6, No. 3, (2014), 1137-1146. https://doi.org/10.1109/TSG.2014.2373150

11. Liu, Y., Yuen, C., Hassan, N.U., Huang, S., Yu, R. and Xie, S., "Electricity cost minimization for a microgrid with distributed energy resource under different information availability", ***IEEE Transactions on Industrial Electronics***, Vol. 62, No. 4, (2014), 2571-2583. https://doi.org/10.1109/TIE.2014.2371780

12. Wu, Z., Tazvinga, H. and Xia, X., "Demand side management of photovoltaic-battery hybrid system", ***Applied Energy***, Vol. 148, (2015), 294-304. https://doi.org/10.1016/j.apenergy.2015.03.109

13. Kinhekar, N., Padhy, N.P., Li, F. and Gupta, H.O., "Utility oriented demand side management using smart ac and micro dc grid cooperative", ***IEEE Transactions on Power Systems***, Vol. 31, No. 2, (2015), 1151-1160. https://doi.org/10.1109/TPWRS.2015.2409894

14. Jafari, E., Soleymani, S., Mozafari, B. and Amraee, T., "Optimal operation of a micro-grid containing energy resources and demand response program", ***International Journal of Environmental Science and Technology***, Vol. 15, No. 10, (2018), 2169-2182. https://doi.org/10.1007/s13762-017-1525-6

15. Mobashsher, M.M., Keypour, R. and Savaghebi, M., "Distributed optimal voltage control in islanded microgrids", ***International Transactions on Electrical Energy Systems***, Vol. 31, No. 11, (2021), e13045. https://doi.org/10.1002/2050-7038-13045

16. Feng, X., Shekhar, A., Yang, F., E. Hebner, R. and Bauer, P., "Comparison of hierarchical control and distributed control for microgrid", ***Electric Power Components and Systems***, Vol. 45,

No. 10, (2017), 1043-1056. https://doi.org/10.1080/15325008.2017.1318982

17. Al-Saadi, M.K., Luk, P.C., Fei, W. and Bati, A., "Security constrained active and reactive optimal power management of microgrid in different market policies", in 2016 UKACC 11th International Conference on Control (CONTROL), IEEE., (2016), 1-6.
18. Puspitasari, K.M.D., Raharjo, J., Sastrosubroto, A.S. and Rahmat, B., "Generator scheduling optimization involving emission to determine emission reduction costs", ***International Journal of Engineering***, ***Transactions B: Applications,*** Vol. 35, No. 8, (2022). https://doi.org/10.5829/IJE.2022.35.08B.02
19. Al-Saadi, M.K., Dakheel, H.S. and Abdullah, Z.B., "Impact of the weather on the combined economic and emission optimization problem of mg", in IOP Conference Series: Materials Science and Engineering, IOP Publishing. Vol. 765, (2020), 012012.
20. Zhou, C., Qian, K., Allan, M. and Zhou, W., "Modeling of the cost of ev battery wear due to V2G application in power systems", ***IEEE Transactions on Energy Conversion***, Vol. 26, No. 4, (2011), 1041-1050. https://doi.org/10.1109/TEC.2011.2159977
21. Tomić, J. and Kempton, W., "Using fleets of electric-drive vehicles for grid support", ***Journal of Power Sources***, Vol. 168, No. 2, (2007), 459-468. https://doi.org/10.1016/J.JPOWSOUR.2007.03.010
22. Al-Saadi, M.K., Luk, P.C. and Fei, W., "Impact of unit commitment on the optimal operation of hybrid microgrids", in 2016 UKACC 11th International Conference on Control (CONTROL), IEEE., (2016), 1-6.
23. Papathanassiou, S., Hatziargyriou, N. and Strunz, K., "A benchmark low voltage microgrid network", in Proceedings of the CIGRE symposium: power systems with dispersed generation, CIGRE., (2005), 1-8.
24. Bharti, D., "Graph theoretic loss allocation method for microgrids having variable generation", ***International Journal of Engineering***, ***Transactions C: Aspects,*** Vol. 34, No. 9, (2021), 2060-2069. https://doi.org/10.5829/IJE.2021.34.09C.03
25. T. Logenthiran, D. Srinivasan, Khambadkone, A.M. and H. N. Aung, "Multiagent system for real-time operation of a microgrid in real-time digital simulator", ***IEEE Transactions on Smar Grid***, Vol. 3, No. 2, (2012), 925-933. https://doi.org/ 10.1109/TSG.2012.2189028
26. Hatziargyriou, N., Jenkins, N., Strbac, G., Lopes, J.P., Ruela, J., Engler, A., Oyarzabal, J., Kariniotakis, G. and Amorim, A., "Microgrids–large scale integration of microgeneration to low voltage grids", ***CIGRE C6-309***, Vol. 1, (2006).
27. Kamel, R.M., Chaouachi, A. and Nagasaka, K., "Carbon emissions reduction and power losses saving besides voltage profiles improvement using micro grids", ***Low Carbon Economy***, Vol. 1, No. 1, (2010), 1. https://doi.org/ 10.1109/TSG.2012.2189028
28. di Valdalbero, D.R., "External costs and their integration in energy costs", in European Sustain. Energy Policy Seminar INFORSE-Europe., (2006).
29. García-Gusano, D., Cabal, H. and Lechón, Y., "Evolution of no x and SO_2 emissions in spain: Ceilings versus taxes", ***Clean Technologies and Environmental Policy***, Vol. 17, No. 7, (2015), 1997-2011. https://doi.org/10.1007/s10098-015-0923-z
30. Corporation, I., *Ibm ilog cplex optimization studio cplex user's manual v12. 8*. 2018, IBM Corporation New York.

Persian Abstract

چکیده

ین مقاله رویکردی را برای بهبود آربیتراژ سیستم و کاهش بار پیک با مدیریت هر دو طرف تولید و بار به طور همزمان پیشنهاد می‌کند. کاهش اوج بار با استفاده از یک برنامه کنترل بار حاصل می شود، در حالی که آربیتراژ با به حداقل رساندن هزینه عملیاتی و انتشار بهبود می یابد. مدیریت بار و به حداقل رساندن هزینه عملیاتی در یک رویکرد بهینه سازی در یک چارچوب چند هدفه ترکیب شده است. باتری ذخیره سازی برای کمک به پیک سایی بار اوج و کاهش هزینه عملیات و انتشار استفاده می شود، جایی که طول عمر باتری در مدل پیشنهادی در نظر گرفته شده است. مدیریت سمت های بار به عنوان متغیرهای تصمیم گیری در رویکرد در نظر گرفته می شود. یک برنامه درجه دوم عدد صحیح مختلط برای فرمول‌بندی رویکرد بهینه‌سازی استفاده می‌شود. رویکرد پیشنهادی بر روی یک شبکه توزیع ولتاژ پایین هوشمند اعمال می‌شود. نتایج نشان می دهد که مدیریت هر دو طرف تقاضا و تولید باعث کاهش هزینه های عملیاتی و انتشار و بهبود ضریب بار سیستم می شود.

International Journal of Engineering

Journal Homepage: www.ije.ir

Adaptive Polynomial Coding of Multi-base Hybrid Compression

G. K. AL-Khafaji[a], M. H. Rasheed*[b], M. M. Siddeq[b], M. A. Rodrigues[c]

[a] *Department of Computer Science, College of Science, University of Baghdad, Iraq*
[b] *Computer Engineering Department, Technical College/Kirkuk, Northern Technical University, Iraq*
[c] *GMPR-Geometric Modelling and Pattern Recognition Research Group, Sheffield Hallam University, Sheffield, UK*

PAPER INFO

Paper history:
Received 04 August 2022
Received in revised form 11 October 2022
Accepted 15 October 25, 2022

Keywords:
Image Compression
Lossless/Lossy
Polynomial Coding
Iterative Based Technique

ABSTRACT

With increasing demand for the intensive use of images, especially linked to online applications as well as the massive, continuous revolution of mobile phone technology, the need has emerged for efficient, standard image compression techniques that ensure simplicity and speed. These must be compatible with user needs, but also meet the challenges of improving compression techniques. Polynomial coding is one such techniques still under development, based on a modelling concept of deterministic and probabilistic coding bases. This paper introduces a new mathematical iterative polynomial model to represent both coding bases. The model proposes an efficient hybrid way where coefficients are represented as lossless while residuals are presented as a lossy but with minimum loss, which ensures effective performance in terms of compression ratios and quality. Results show that while the technique has some limitations, the proposed system achieves equivalent compression ratios as the standard JPEG technique, but with superior quality for the same compression ratio.

doi: *10.5829/ije.2023.36.02b.05*

1. INTRODUCTION

Today the number of people that are active online exceeds 2.5 billion. The vast majority use instant messaging (e.g., Viber, WhatsApp) and social media (e.g., Facebook, Twitter, Instagram), which can change our lives, relations, and even political views. Since we digitally communicate through data streams, conveying events (news), broadcasting TV, cinema and other media in cheap and effortless ways has become a must. The basic elements of these electronic communications are text messages, audio, video and images, and these need to be compressed to save excessive byte consumption (storage) and overcome limited bandwidths.

Generally, image compression reduces the required bits to represent an image through efficient exploitation of redundancy in the image itself. Redundancy utilization can be purely statistical or combined with psycho-visual effects [1] implying lossy and lossless techniques. To remove redundancy from the data implies transform coding (TC) and spatial coding (SC) along with mixtures of both called hybrid coding (HC). The background information related to compression basics can be found in literature [2-5], also reviews of various image compression techniques are described in literature [6-10]. Each technique has its own characteristics in terms of performance which is normally optimized for compression ratios and/or preserving image quality.

Today, due to their high performance, the dominant standard image compression techniques are the joint photographic expert group (JPEG) and JPEG2000 (JP2). Both employ lossy approaches that effectively utilize the TC of discrete cosine transform (DCT) and discrete wavelet transform (DWT), respectively [11, 12]. However, the need for efficient compression techniques means that this field is not yet mature and still represents an attractive research area. Techniques that use SC may compete with these standards. Predictive coding (PC), also referred to as auto-regression (AR), or differential pulse code modulation (DPCM) are used by a large number of research projects characterized by their simplicity, but still faces a number of inherent problems

*Corresponding Author Institutional Email:
Mohammed.rasheed@ntu.edu.iq (M. H. Rasheed)

Please cite this article as: G. K. AL-Khafaji, M. H. Rasheed, M. M. Siddeq, M. A. Rodrigues, Adaptive Polynomial Coding of Multi-base Hybrid Compression, ***International Journal of Engineering, Transactions B: Applications***, Vol. 36, No. 02, (2023), 236-252

that can be summarized as: the difficulty of choosing an appropriate model, where the model is composed of three elements termed by order (number of neighbours), structure (1D/2D), causality (causal/acausal), the way of estimating the coefficients (linear/nonlinear) and the seed values (initial condition).

Polynomial coding solves the above-mentioned problems related to predictive coding techniques using *Taylor series*, where the model and the estimation coefficients methods are determined either by linear or non-linear models. It solves the approximation base with no use of seed values which can be considered the most pressing problem. Currently, polynomial coding is utilized to compress both lossy or lossless images [13-18], but still suffers from large residuals (prediction errors) and large number of coefficients.

This paper introduces a novel adaptive technique for lossy polynomial base to efficiently represent the coefficients and residuals applied independently to each image plane demonstrated as grey images. In other words, the work implies investigation into an innovative approach to model the deterministic and stochastic polynomial parts effectively using fewer required number of bytes using an iteration base scheme of high precision techniques, where a mathematical model is generated based on subtraction and division for coefficients (a0, a1, a2) and residual, respectively ensures the effectiveness in compression ratios and quality. The rest of the paper is organized as follows: section 2 reviews related work, section 3 describes the proposed technique, section 4 delivers experimental results with discussion, while conclusions are presented in section 5.

2. RELARED WORK

Polynomial coding is one of the modern techniques that overcome the inherited problems of predictive coding which is characterized by simplicity and symmetry, but still suffering from large byte consumption. Here we concentrate on a linear lossy polynomial approach used to compress greyscale images efficiently. The works surveyed here can be classified into two major classes: the enhancement-based polynomial which aims to improve the standard techniques with an adaptation process, and a residual-based technique which is concentrated on utilizing various residual quantization methods, where the residual can be considered the largest and main problem related to polynomial coding.

The first type of enhancement-based polynomial approach includes Ghadah [14], utilizing variable block sizes ($n \times m$) using the quadtree scheme instead of a fixed partitioning process of ($n \times n$). Variable square block sizes are adopted after determining the minimum and maximum block sizes, with a homogeneity measure and quantization step of coefficients. Concerning residuals, results are promising for standard natural images compared to traditional polynomial coding of fixed block size (4×4). Using smaller blocks of variable sizes ($Min=2$ and $Max=16$) the same performance is obtained in terms of quality and compression ratios. Athraa [12], exploited the hierarchical scheme of interpolation base, where the multi-resolution principle was adopted for three layers. Through enlarging or shrinking of nearest neighbour interpolation technique, a quarter of the image is compressed instead of the full image (i.e., quarter size of coefficients and residuals). Results were shown to be adequate and improved almost four times on the traditional model. Rasha [7], adopted three improvement techniques to enhance the polynomial coding. First, a hierarchal scheme was used in which the polynomial coefficients of the first layer were utilized efficiently to construct the second layer polynomial coding. Second, a fixed predictor was used to remove the spatial redundancy before utilizing the polynomial coding, and lastly the residual reduction was achieved using the discrete wavelet transform (DWT). All these adaptations aimed to overcoming the polynomial problems of redundancy embedded within the image itself, the coefficients, and residuals. The results show high performance compared to traditional polynomial based techniques with at least two times improvement in compression ratios on average while preserving high image quality. Murooj [13], used various fixed predictor models of certain order with different structures (1D/2D) on a causality basis to remove the inherited spatial redundancy embedded within the image, before using the polynomial coding to lossy compress a natural standard image. The approach also exploited the selective predictor model where each block utilized different predictors according to residuals. The results indicated improvements of four-fold increase in compression ratios while preserving image quality.

The second type of enhancement-based polynomial approach relates to the quantization process of the residual image, where block size is of 4×4 and the quantization coefficients is of scalar uniform base. These include: Ghadah [14], which quantized the residual image using block truncation coding (BTC) of binary representation, namely two levels of a quantization scheme technique. The results for four standard square images exceeded eight times compression ratios compared to the original image with a good image quality. Ghadah et al. [15], adopted multi-resolution representation of two-level DWT, with all the details sub bands of the two layers quantized using the absolute block truncation coding (ABTC). The polynomial coding was applied to the second level approximation sub band, while the residual was first mapped to positive then sliced into its layers by applying bit plane slicing techniques (BPS). The least significant layers from layer 1 to layer 4 were ignored, while the most significant layers from layer 5 to layer 8 were quantized uniformly differently (each layer quantized with a scalar quantization step) and coded. The results were of high compression ratio with acceptable quality. Ghadah and Noor [16], utilized the one level decomposition residual based on DWT, with the hard or soft quantization process adopted for details sub bands, while the approximation sub band was quantized uniformly. The results showed the superiority of soft techniques for higher image quality compared to hard techniques for high compression ratios and lower quality. Ghadah and Sara [17], utilized the two-stage multiple description scalar quantizer (TSMDSQ) principle to efficiently quantize the residual image. The results are effective in terms of quality and compression performance. Ghadah [18], adopted the midtread adaptive quantizer to quantize the approximation sub band, along with soft quantization for the details sub bands, where the one level decomposition of DWT was used. Results were efficient and indicated high performance. Ghadah [19], utilized selected hard thresholding techniques of single or multiple base(s) to quantize the details sub-bands, while the approximation sub-band of one-layer DWT hierarchal scheme coded with the traditional linear polynomial coding. The results are of better performance compared to the traditional linear model where a higher compression ratio is achieved while preserving high image quality. Ghadah and Loay [20], introduced 1-D linear polynomial coding techniques that utilized two coefficients (a0, a1) for the deterministic part instead of the traditional model that used three coefficients (a0, a1, a2) for each segmented block, along incorporating a non-uniform quantization method for the probabilistic part (residual). Experimental results were promising in terms of performance (compression ratio, PSNR quality) for natural and medical grayscale images. Samara et al. [21] exploited the introduced 1-D polynomial coding techniques with matrix minimization algorithm of six values to efficiently compress residuals. The system achieved superior results than that adopted by Zhou et al. [22] using the same test images. The compression ratio was increased threefold compared to the first introduced 1-D scheme, with PSNR values converging to the compared mentioned work.

3. ADAPTIVE POLYNOMIAL CODING OF ITERATIVE BASED TECHNIQUES

As mentioned above, polynomial coding has been adopted by previous researches and can be considered as an extended revised version of predictive coding. This technique still suffers from residual and coefficients consumption, where actually the residual can be considered the main obstacle or difficulty compared to coefficients. In this paper we introduce a new method to efficiently represent polynomial coding of coefficients and residuals using an iterative based scheme. Figure 1 depicts the adaptive model, where the main contributions of the proposed system are:

1. This paper develops models for deterministic (coefficients) and probabilistic parts (residual).
2. It shows the effectiveness in terms of quality and compression ratios for spatial modelling techniques compared to the well-known standards techniques of JPEG and JPEG-2000.

The main steps of the algorithm are described as follows:

3. 1. Load the Original uncompressed image plane I of size N×N, where I corresponds to an input image of N=256.

3. 2. Partition I Into Non-overlapping fixed sized blocks of size n×n. The partition exploits the local dependency (correlation) embedded within image neighbourhoods, where no global correlation can be captured as a whole. In general, the fixed partition is utilized for simplicity without considering the homogeneity of blocks; the number of the fixed blocks equals to $(N/n)^2$, where here n = 4, so the number of blocks equals to $(256/4)^2$ = 64×64 blocks.

3. 3. Compute the Coefficients of the linear polynomial coding according to Equations (1-4) [1, 6, 13, 15, 19], which implies three coefficients, where a_0 corresponds to the mean value of each block of size n×n, a_1 and a_2 represent ratios of cumulative distances to both coordinates, and x_c, y_c correspond to the centre of the block.

$$a_0 = \frac{1}{n \times n}\sum_{i=0}^{n-1}\sum_{j=0}^{n-1} I(i,j). \tag{1}$$

$$a_1 = \frac{\sum_{i=0}^{n-1}\sum_{j=0}^{n-1} I(i,j)\times(j-x_c)}{\sum_{i=0}^{n-1}\sum_{j=0}^{n-1}(j-x_c)^2} \tag{2}$$

$$a_2 = \frac{\sum_{i=0}^{n-1}\sum_{j=0}^{n-1} I(i,j)\times(i-y_c)}{\sum_{i=0}^{n-1}\sum_{j=0}^{n-1}(i-y_c)^2} \tag{3}$$

$$xc = yc = \frac{n-1}{2} \tag{4}$$

Here we have three arrays of the three computed coefficients each of size 64×64 blocks.

3. 4. Represent the Computed a_0 Coefficients of mean block values using iteration-based techniques. In other words, we introduce a new technique to model the a_0 coefficient values, which can be considered as adaptive

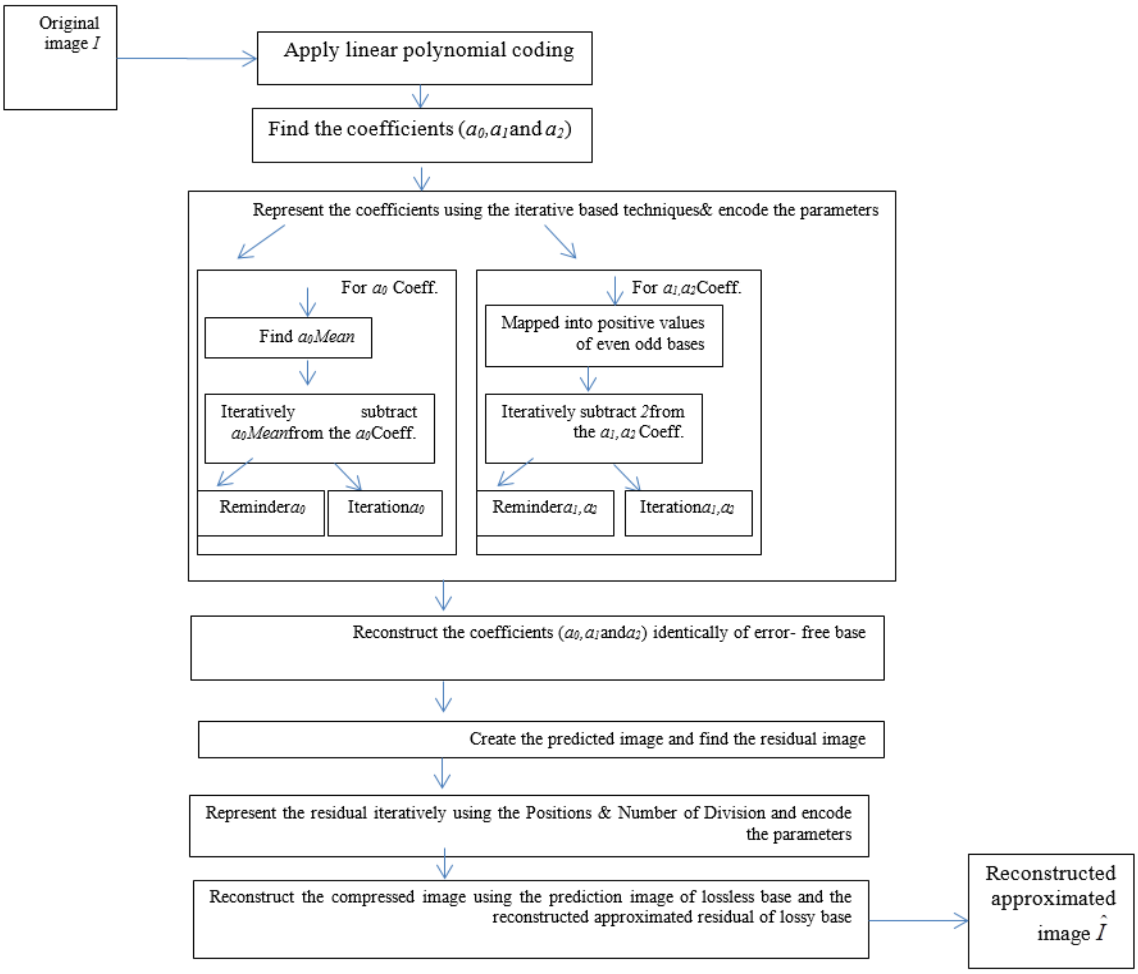

Figure 1. The proposed compression and decompression method

of the DPCM used in JPEG to encode the DC values, but with a recursive base of computed mean seed values. Put simply, start by computing the mean value of a_0 coefficients such as a_0M_{ean} according to Equation (5). Initially we compare each value in the a_0 coefficients array with the computed a_0M_{ean}: if the value is less than or equal to a_0M_{ean} then we keep the values as it is in Remainder with Iteration equal to zero, then for the values greater than the a_0M_{ean} we compare it recursively; namely for every iteration we subtract the mean value a_0M_{ean} from the a_0 coefficients with increments the iteration by one, until a_0 coefficient value becomes less than the threshold computed mean value a_0M_{ean}. Table 1 illustrates the steps using an example of one-dimension a_0 values with eight mean values; also, Algorithm (1) summarizes the techniques.

$$a_0M_{ean}(n,n) = \frac{1}{n \times n}\sum_{i=0}^{n-1}\sum_{j=0}^{n-1} a_0(i,j) \tag{5}$$

3. 5. Represent the Other Computed Coefficients (a_1 and a_2) effectively using the iteration principle, though here the scenario is different from a_0, since these values (a_1 and a_2) may be either negative or positive. Consequently, the first step is to map them into positive numbers of even and odd bases using Equation (6) [13].

$$Mapi_{Values} = \begin{cases} 2Coff_i & \text{if Coffi} \geq 0 \\ 2|Coffi| - 1 & \text{else} \end{cases} \tag{6}$$

Here $Coff$ corresponds to (a_1&a_2) values, $Mapi_{Values}$ mapped positive values, where positive values are mapped into even bases, while negative values are mapped into odd bases. Basically, the idea is to iteratively subtract a number – here we use base 2 since 2 is easily distinguished either even or odd base –from each value, which results in a binary representation of zeros and ones along the iteration number. It is important to remember to initially check these values in case the values are equal

TABLE 1. Example of a_0 recursive representation of Remainder and Iteration values, where the mean values of the eight a_0 values here equals to 62.

	$a_0(1)$	$a_0(2)$	$a_0(3)$	$a_0(4)$	$a_0(5)$	$a_0(6)$	$a_0(7)$	$a_0(8)$
***a₀* original values**	12	13	67	163	3	34	114	90
Remaindera_0	12	13	5	101 39	3	34	52	28
Iteration a_0	0	0	1	2	0	0	1	1

Algorithm (1). Recursive differencing a_0 coefficients encoding of mean-based techniques

```
Input: a0 coefficient image of size (N/n)^2 (i.e., 64x64 for N=256, n=4)
 Sm = 0; a0Mean = 0;
  Output: Remaindera0, Iterationa0 each of size (N/n)^2 and a0Mean
  Begin
    //1- find size of a0 image
      [Rows, Cols] = size (a0)
    //2-  calculate the mean (average)  of a0 image
for i = 1 : Rows
   for j = 1 : Cols
     Sm = Sm +a0 (i,j)
  End
End
    a0Mean=Sm/(Rows x Cols)
//3-  Initialize the two-output array (Remaindera0 and Iterationa0) each of size (N/n)^2 with values equal to zeros
  Iterationa0(N/n)^2 =0 ,   Remaindera0(N/n)^2 =0
//4- Apply the proposed differencing technique
for i = 1 : Rows
   for j = 1 : Cols
      if    a0(i,j)<=floor(a0Mean)    Remaindera0(i,j)=a0(i,j)    , Iterationa0(i,j) =0.
          if a0(i,j)- a0Mean >=1
           begin
              If    Remaindera0(i,j)<=a0Mean    Remaindera0(i,j)= a0(i,j)  ,Iterationa0(i,j) =Iterationa0(i,j)+1.
            Else     a0(i,j)=Remaindera0(i,j),     Iterationa0(i,j =Iterationa0(i,j)+1.
         End if
       End if
    End if
 End
End
End
```

to zeros or ones, with iteration number equal to zero. Table 2 illustrates an example of one-dimension a_1 values of eight mean values; also, Algorithm (2) summarizes the techniques.

3. 6. Encode/Decode the Compressed Information

of coefficients representation (*Remainder* a_0 ,a_1, a_2, *Iteration* a_0, a_1, a_2) along the extra information (a_0Mean, *2*) using different coding techniques (Huffman coding/LZW) according to the parameter's nature.

3. 7. Reconstruct the Coefficients

identically using the equations below, also illustrated in Tables 3 and 4:

$$a_0 = Remainder\ a_0 + (a_0Mean \times Iteration\ a_0) \tag{7}$$

$$a_1, a_2 = Remainder\ a_1, a_2 + (2 \times Iteration a_1\ , a_2) \tag{8}$$

For the reconstructed coefficients of (a_1&a_2) bases the de-mapping process is required, such as described in literature [13]:

$$DeMap_i = \begin{cases} \mathrm{Re}c(a_1\ , a_2)/\,2 & \text{if even} \\ -(\mathrm{Re}ca_1, a_2 + 1)/\,2 & \text{else} \end{cases} \tag{9}$$

where Reca_1,a_2 corresponds to reconstructed coefficients of even/odd bases.

3. 8. Create the Predicted Image $\tilde{I}$

using the original coefficient values of lossless base coding

TABLE 2. Example of a_1 recursive representation of Remainder and Iteration values.

	$a_1(1)$	$a_1(2)$	$a_1(3)$	$a_1(4)$	$a_1(5)$	$a_1(6)$	$a_1(7)$	$a_1(8)$
***a₁* original values**	0	-3	-2	5	4	8	3	-1
***a₁* values after mapping**	0	5	3	10	8	16	6	1
Differencing		3 1	1	8 6 4 2 0	6 4 2 0	14 12 10 8 6 4 2 0	4 2 0	
Iteration a_1	**0**	**2**	**1**	**5**	**4**	**8**	**3**	**0**
Remainder a_1	**0**	**1**	**1**	**0**	**0**	**0**	**0**	**1**

TABLE 3. Example of a_0 construed using the representation of Remainder and Iteration values along the mean

Remainder a_0	**12**	**13**	**5**	**39**	**3**	**34**	**52**	**28**
Iteration a_0	0	0	1	2	0	0	1	1
Use the encoded/decoded information using equation7								
***a_0* error-free reconstructed values**	12	13	67	163	3	34	114	90

TABLE 4. Example of a_1 construed using the representation of Remainder and Iteration values along the base of 2 value

Iteration a_1	**0**	**2**	**1**	**5**	**4**	**8**	**2**	**0**
Remainder a_1	0	1	1	0	0	0	1	1
Use the encoded/decoded information using equation8								
a_1 error-free reconstructed values before demapping	0	5	3	10	8	16	5	1
Use the encoded/decoded information using equation9								
***a_1*error-free reconstructed values after demapping**	0	-3	-2	5	4	8	-3	-1

Algorithm (2): Recursive differencing a_1, a_2 coefficients encoding proposed technique.

```
Input: a1,a2 coefficient images each of size (N/n)^2 (i.e., 64x64 for N=256, n=4)
Output: Remainder a1,a2, Iteration a1,a2 each of size (N/n)^2
Begin
//1- find size of a1 images
[Rows, Cols] = size (a1)
// 2- Mapped the values of a1,a2 images into even and odd values
 for i = 1 : Rows
  for j = 1 : Cols
    if (a1 (i,j) or a2 (i,j))>=0 Mapi_Values=(2x a1 (i,j)) or Mapi_Values= (2x a2 (i,j))
      else Mapi_Values=(2x abs(a1 (i,j))-1) or Mapi_Values=(2x abs(a2 (i,j))-1)
   End if
 End
End
//3- Initialize the two-output array (Remainder a1,a2 and Iteration a1,a2) each of size (N/n)^2 with values equal to zeros
Iteration a1,a2 (N/n)^2 =0 ,  Remainder a1,a2 (N/n)^2 =a0(i,j)
//4- Apply the proposed differencing technique
 for i = 1 : Rows
   for j = 1 : Cols
     If Mapi_Values(i,j) =0 or Mapi_Values (i,j)=1    Iteration a1,a2=0 , Remainder a1,a2=Mapi_Values(i,j)
      if Mapi_Values (i,j)- 2>=1
      begin
       If Remainder a1,a2 (i,j)<=2 , Remainder a1,a2 (i,j)= a1,a2 (i,j), Iteration a1,a2 (i,j) =Iteration a1,a2 (i,j)+1.
       Else a1,a2 (i,j) =Remainder a1,a2 (i,j)  ,Iteration a1,a2 (i,j) =Iteration a1,a2 (i,j)+1.
       End if
     End if
   End if
  End
End
End
```

(Namely create the predicted image using the deterministic part), such as in literature [13,15]:

$$\tilde{I} = a_0 + a_1(j - x_c) + a_2(i - y_c) \quad (10)$$

3. 9. Find the Residual (Difference) between original image I and the predicted one from the step above, this part corresponding to the probabilistic part in literature [13, 15]:

$$I\,\mathrm{Re}\,s(i,\, j) = I(i,\, j) - \tilde{I}(i,\, j) \quad (11)$$

The residual is the vital part of the modelling process due to the prediction limitation (insufficiency) of capturing all the image characteristics using the same or various models for an image of varying details. Hence all the unpredicted information found in the residual which is essential for reconstructing the image, and in the same way is the core of the excessive bytes due to large uncorrelated data values that are difficult to manipulate directly, is traditionally solved using the lossy encoder of quantizer base, either of scalar base, which means the uniform/non-uniform techniques, or of vector base followed by a symbol encoder.

3. 10. Represent the Lossy Residual and iteratively using the scalar uniform base with predetermined thresholds of minimum and maximum values; this is necessary to preserve the quality of a minimum loss. In other words, each residual value is divided by 2 iteratively while it is within the quality range limited by maximum and minimum values. Each time, the remainder is kept with an increasing number of iterations. The main reason of using the value of 2 for division is the ability to exploit the values bit by bit (i.e., forcing the least significant bit to be the remainder until having forced all the other bits). Figure 2 illustrates an example of the residual iterative base; also, Algorithm (3) summarizes the techniques.

3. 11. Encode/Decode the Residual iterative representation, where the Number of Division parameter is coded using the popular Huffman coding, while the Position parameter which corresponds to the precision

Algorithm (3): Recursive division of residual based encoding techniques.

Input: *Residual* image of size (*N*×*N*) (*256×256*), *QuantizationFactor*=2
Output: Positions and Number of Division each of size (*N*×*N*)
Begin
//1- find size of a_1 images
[Rows, Cols] = size (Residual)
//2- Initialize the two-output array (Positions, Number of Division) each of size (N×N) with values equal to zeros values
Positions(*Rows*, *Cols*)=0 , Number of Division(*Rows*, *Cols*) =0

//3- Check if the residual values equals to zero
for i = 1 : Rows
for j = 1 : Cols
if (Residual (i,j) =0) Positions(i,j)=0 , Number of Division(i,j) =0
End if
End
End
Step 4:// Apply the proposed technique for non- zero residual values
While (all value in Residual not zero)
Matrix = Residual./QuantizationFactor; // Dot Division matrix by 2 ….
Iteration ++ ; // Increment iteration
If (Residual (i,j) >=MinimumQuality and <MaximumQuality)
Positions(i,j)=Residual , Number of Division(i,j) = Iteration
End if
End
End

matrix of floating-point values is subject to arithmetic coding. Our goal is to retain high accuracy with minimum degradation which is essential for conversion into integer number of preserving values, such as:

$$Positions = integer(Positions \times 10) \tag{12}$$

Here we convert the *Position* matrix into integer by keeping one significant digit after the decimal point. The integer position matrix is then coded using efficient arithmetic coding techniques.

3. 12. Reconstruct the Approximated Residual

image values based on iterative lossy using the equations below. The coded data illustrated in Figure 2 is recovered and illustrated in Figure 3.

$$Positions = \frac{Positions}{10} \tag{13}$$

$$Values = 2^{Number\ of\ Divisions} \tag{14}$$

$$I\widehat{Res} = round(Values \times Positions) \tag{15}$$

3. 13. Rebuild the Compressed Image $\hat{I}$ by

adding the approximated reconstructed residual image from the step above to the predicted the image from step 8, such as in [13, 15].

100 -64 - 12 78 23 24 65 90 34 76 56 -80 9 17 30 33	50.0 -32.0 -6.0 39.0 11.5 12.0 32.5 45.0 17.0 38.0 28.0 -40.0 4.5 8.5 15.0 16.5	25.0 -16.0 -3.0 19.5 5.75 6.0 16.25 22.5 8.5 19.0 14.0 -20.0 2.25 4.25 7.5 8.25
Iteration #0 (Original)	Iteration #1 (Divide by 2)	Iteration #2 (Divide by 2)
12.5 -8.0 -1.5 9.75 2.87 3.0 8.12 11.2 4.25 9.5 7.0 -10.0 1.12 2.12 3.75 4.12	6.25 -4.0 **0** 4.87 1.43 1.5 4.06 5.62 2.12 4.75 3.5 - 5.0 **0** 1.06 1.87 2.062	3.12 -2.0 **0** 2.43 **0** **0** 2.03 2.81 1.06 2.37 1.75 -5 **0** **0** **0** 1.03
Iteration #3 (Divide by 2) Save RED values in matrix called Position (according to their X,Y)	Iteration #4 (Divide by 2) Save RED values in matrix called Position (according to their X,Y)	Iteration #5 (Divide by 2) Save RED values in matrix called Position (according to their X,Y)
1.56 -1.0 **0** 1.21 **0** **0** 1.01 1.4 **0** 1.18 **0** -1.25 **0** **0** **0** **0**	**0 0 0 0** **0 0 0 0** **0 0 0 0** **0 0 0 0**	
Iteration #6 (Divide by 2) Save RED values in matrix called Position (according to their X,Y)	Iteration #7 (Stop)	
1.5 -1.0 -1.5 1.2 1.4 1.5 1.0 1.4 1.0 1.1 1.7 -1.2 1.1 1.0 1.8 1.0	6 6 3 6 4 4 6 6 5 6 5 6 3 4 4 5	
Position Matrix (corresponds to precision matrix of remainder base that is limited between maximum and minimum quality measures)	Number of Divisions (comes from the number of iterations; at each stage when data are zero means stop counting for that data, replace it by iteration value)	

Figure 2. Example of residual image block of size 4x4 with quality measures of maximum=2 and minimum=1

15 -10 -15 12	1.5 -1.0 -1.5 1.2	
14 15 10 14	1.4 1.5 1.0 1.4	
10 11 17 -12	1.0 1.1 1.7 -1.2	
11 10 18 10	1.1 1.0 1.8 1.0	
Converted into integer numbers by multiplying by 10	Original Position matrix (precision values of real numbers)	
64 64 8 64	96 -64 -12 77	100 -64 - 12 78
16 16 64 64	22 24 64 90	23 24 65 90
32 64 32 64	32 70 54 -77	34 76 56 -80
8 16 16 32	9 16 29 32	9 17 30 33
Values according to Equation (13)	Reconstructed residual values of minimum loss using the iterative based technique	Original residual values

Figure 3. Example of reconstructed residual image block of size 4x4 using the iterative lossy technique

4. EXPERIMENTAL RESULTS

In the experiments described here, we report on the amount of compression (number of bytes) compared using Huffman, Arithmetic Coding and the LZW-Lempel-Ziv-Welch algorithm. Concerning image quality, we use the objective fidelity criteria of PSNR (peak-signal to noise ratio) and NRMSE (normalized root mean squared error) (see Equations (17)-(18)), for simplicity, speed, and to facilitate comparisons with other related work. Test images of different types are shown in Figure 4. This includes natural, medical, and

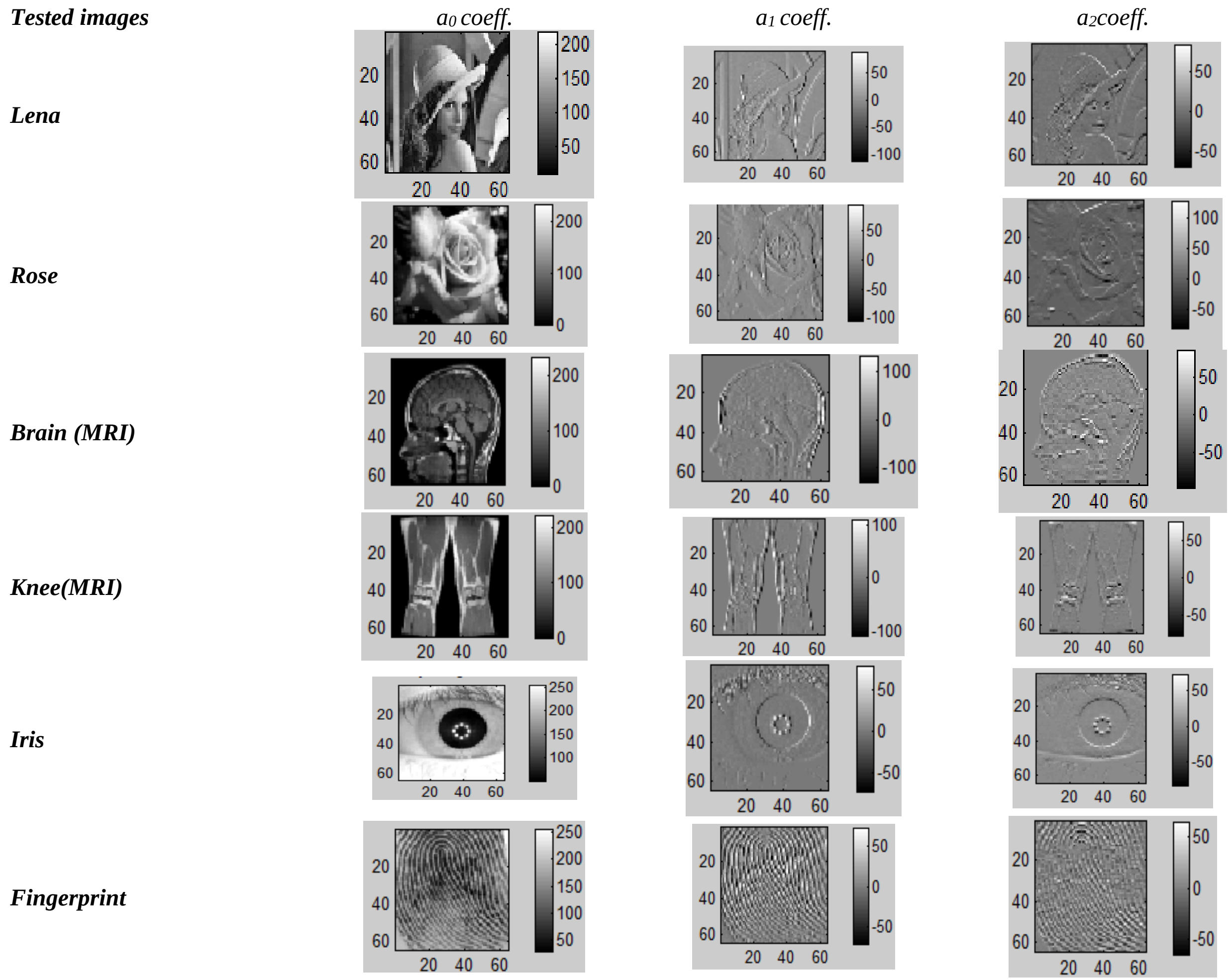

Figure 4. Test image coefficients (a_0, a_1, a_2) with range values

biometric images of varying details. All images are greyscale (8bits/pixels) of square size (256×256), and the block size used is 4×4. The proposed compression method was tested on a laptop computer with a processor Intel Corei 5-2450 CPU at 2.50GHz, 6 GB or RAM, using Matlab programming language. The fidelity measures defined as [1, 3-6]:

$$NRMSE(I,\hat{I}) = \sqrt{\frac{\sum_{x=0}^{N-1}\sum_{y=0}^{N-1}[\hat{I}(x,y) - I(x,y)]^2}{\sum_{x=0}^{N-1}\sum_{y=0}^{N-1} I(x,y)^2}} \quad (18)$$

$$PSNR(I,\hat{I}) = 10\log_{10}\left(\frac{(255)^2}{\frac{1}{N\times N}\sum_{x=0}^{N-1}\sum_{y=0}^{N-1}[\hat{I}(x,y) - I(x,y)]^2}\right) \quad (17)$$

where I represents the original uncompressed image and $\hat{I}$ represents the decoded compressed image.

4. 1. Experiment 1 The first experiment tested our proposed technique to lossless encoding polynomial coefficients (a_0, a_1, a_2), and comparing it to the traditional techniques of Huffman, arithmetic coding and LZW. Figure 5 shows the coefficients of the test images. Generally, for each of the coefficients (a_0, a_1, a_2) one byte was required (i.e., 64×64=4096 bytes for each coefficient). Tables 4 and 5 illustrate the size in bytes for the (a_0,a_1,a_2) coefficient values for the test images using the selected traditional techniques. In our proposed method, we use Huffman coding for iteration parameters and LZW for remainder parameters. This is because despite high repetition of iteration values meaning that

$$\hat{I}(x,y) = \tilde{I}(x,y) + I\widehat{Res}(x,y) \quad (16)$$

arithmetic coding would perform better than Huffman coding, the latter is simpler and, moreover, results showed that there are only small differences between them. Results clearly show that the proposed method has higher compression efficiency, which exceeds more than 2 times on average for all coefficient representations parameters. Tables 3, 4 and Figure 5 demonstrate the total number of bytes required for polynomial coefficients (a_0, a_1, a_2) using the Huffman coding and the adopted techniques. Figure 6 shows the performance comparison for the coefficients between the traditional coding techniques (Huffman coding, Arithmetic coding, LZW) and the proposed iterative techniques of error-free based.

4. 2. Experiment 2 Figure 7 shows the predicted and residual images of the test images. The second experiment results are shown in Tables 5-7 and Figure 8 which measuring the amount of residual image information before utilizing the representation of the iterative process of lossy base using the popular objective quantitative measure of root mean square error as follows [1]:

$$RMSE\,\mathrm{Res} = \frac{1}{N^2}\sqrt{\sum_{x=0}^{N-1}\sum_{y=0}^{N-1} I\,\mathrm{Res}(x,y)^2} \quad (19)$$

The *RMSE Res* simply measures the amount of uncaptured image information due to the limitation of the prediction model which is directly affected by the image details or characteristic, around the edges of non-smooth details.

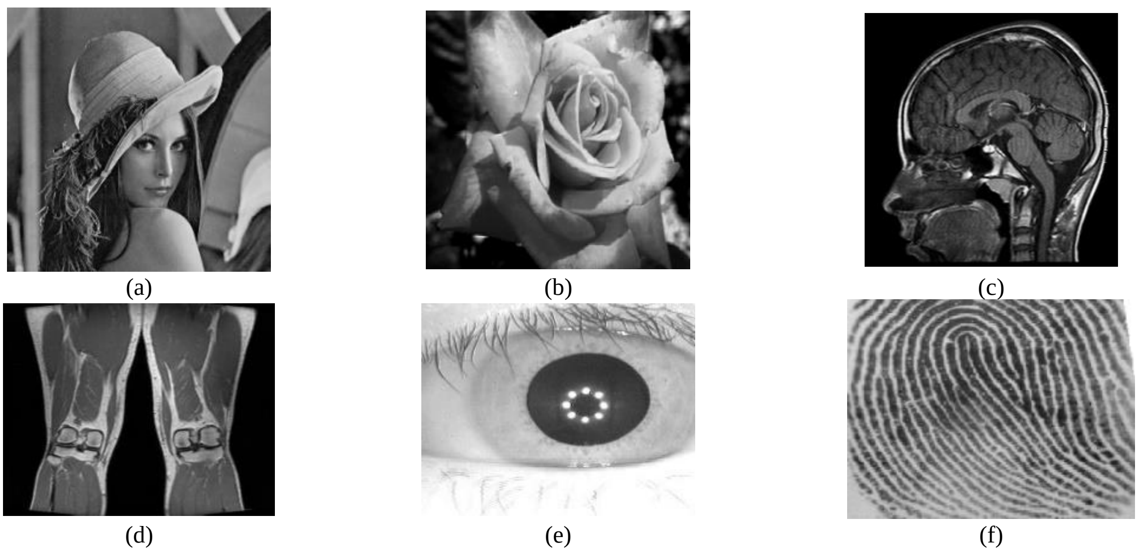

Figure 5. Test images are categorized into three groups, where (a) Lena and (b) Rose correspond to natural images, (c) Brain and (d) Knee correspond to medical images, and(e) Iris and (f) Fingerprint correspond to biometric images

TABLE 5. A comparison between coded techniques of *a1, a2* coefficients using traditional techniques and iterative base techniques

Tested Images	Coefficients	Number of bytes	Lossless encoding of the a_1, a_2 coefficients values			Lossless encoding of the a_1,a_2 coefficients for iteration based techniques		
			Huffman	Arithmetic coding	LZW	Remainder parameter	Iteration parameter	Total
Lena	a_1	4096	2796	2779	2612	863	490	1353
	a_2	4096	2392	2380	2152	790	348	1138
Rose	a_1	4096	2680	2668	2527	948	410	1358
	a_2	4096	2582	2566	2355	779	380	1159
Brain	a_1	4096	2566	2547	2337	986	358	1344
	a_2	4096	2462	2442	2350	840	352	1192
Knee	a_1	4096	2486	2462	2220	652	415	1067
	a_2	4096	2008	1978	1791	715	356	1071
Iris	a_1	4096	2286	2270	2256	862	466	1328
	a_2	4096	2268	2254	2012	866	356	1222
Fingerprint	a_1	4096	3440	3428	2987	1060	367	1427
	a_2	4096	3078	3064	2780	865	467	1332

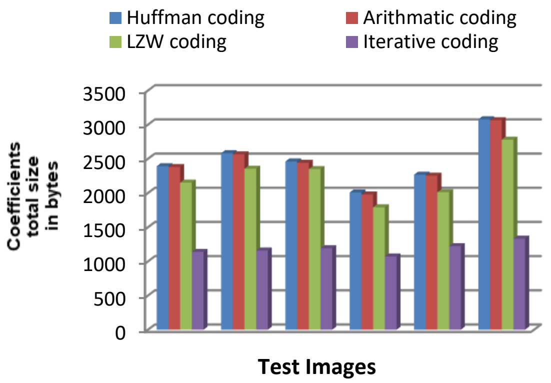

Figure 6. Comparison performance of the coefficients encoding techniques of traditional base (Huffman, arithmetic, LZW) and iterative base techniques

TABLE 6. Total number of bytes for the coefficients using the Huffman coding techniques and the proposed iterative based system for the test images

Tested images	Huffman coding	Proposed techniques
Lena	8958	3617
Rose	9186	3701
Brain	8136	3794
Knee	7660	3407
Iris	8112	3686
Fingerprint	10212	4113

4. 3. Experiment 3 This experiment is conducted to test how the parameters affects the residual iterative

TABLE 7. The size of residual or prediction error for the tested images

Tested images	RMSE Res
Lena	12.0464
Rose	7.2657
Brain	14.1352
Knee	8.7756
Iris	8.6346
Fingerprint	13.4981

process of lossy base, namely the quality that is limited between maximum and minimum values. Here, three quality parameters were adopted that range between 1 and 2, 1 and 10, and 1 and 20, respectively. The PSNR (Equation (16)) between the original residual image and the reconstructed image was adopted, as shown in Table 8 and Figure 9(a) and (b). Additionally, SSIM measurement used to calculate the quality between residual image and the reconstructed image.

Certainly, the quality of residual images and byte consumption improves as the range of maximum and minimum values decrease; it is a trade-off between them, namely the higher the quality, the larger number of bytes related by a small range of values, and vice versa.

4. 4. Experiment 4 The last experiment was concerned with measuring the performance in terms of quality, compression time and compression ratio, which meant measuring the amount of encoded information in bytes which should be smaller than the original image.

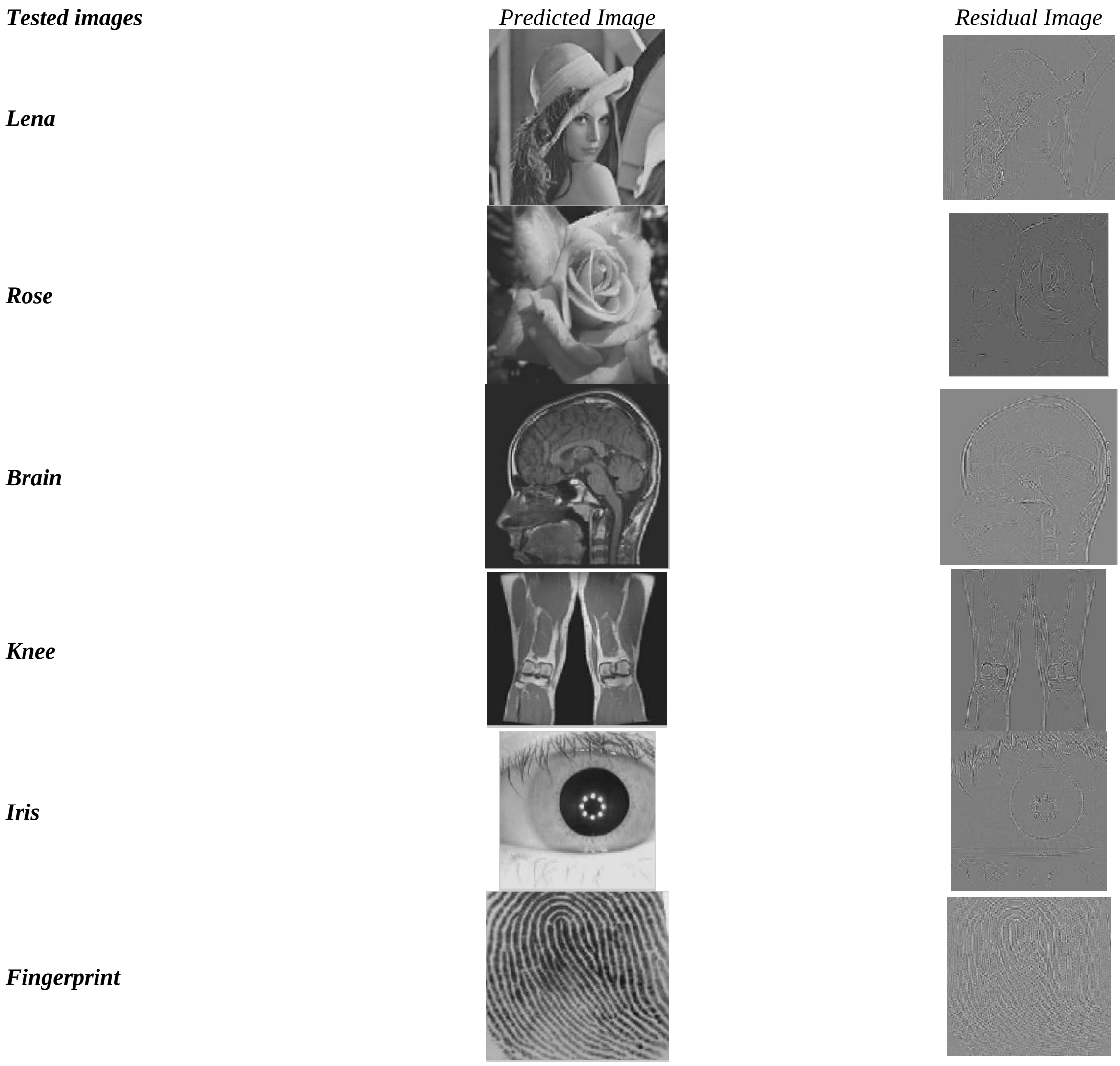

Figure 7. Tested prediction and residual images with block size of 4x4

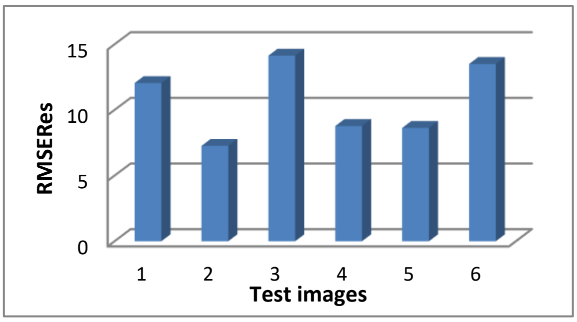

Figure 8. The amount of residual image information for each tested image in terms of RMSE

The compressed image size depends on the size of coefficients of lossless base and size of the residual of lossy base, along with the overhead information (a_0M_{ean}, base$_2$ for a_1, a_2 and the base$_2$ for division) of three extra bytes. So, the size of compressed information can be formulated such as in [1]:

$$Size_{Compressed} = Size_{Coefficients} + Size_{Residual} + Size_{ExtraInfo} \quad (20)$$

Table 9 and Figure 10(a) and (b) demonstrates the compression ratio versus the PSNR and NRMSE respectively for the tested images. Figure 11 shows the original and compressed tested images of high and low quality.

As expected, results showed an inverse relation between compression ratio and quality that is directly affected by the image details (characteristics) along with the effect of the quality residual measure minimum and maximum values. Also, the results illustrate that the total

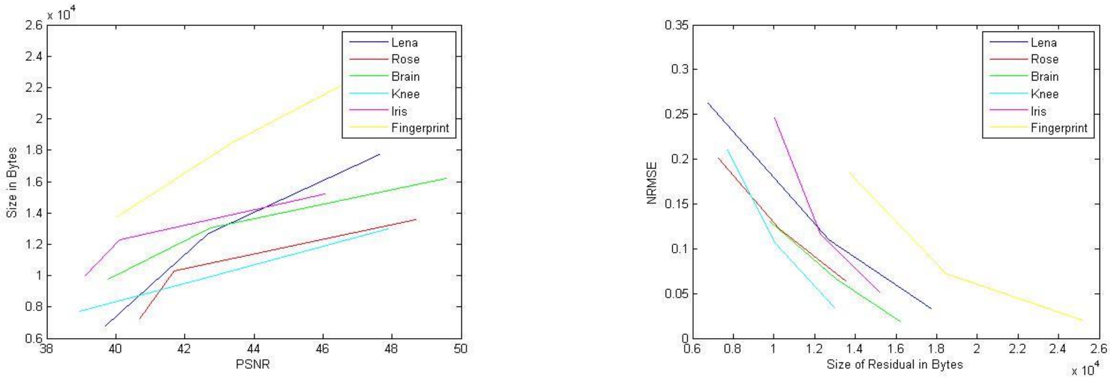

(a) (b)

Figure 9. Total size of the residual versus (a)PSNR and (b) NRMSE

TABLE 9. Compression performance for tested images

Tested Images	Coeff, in bytes	Limited by Quality Min.	Limited by Quality Max.	Position, in bytes	Total size, in bytes (eq. 20)	CR	PSNR (I, $\hat{I}$)	Quality NRMSE (I, $\hat{I}$)	SSIM (I, $\hat{I}$)	Total time in sec
		1	2	17749	21369	3.0669	52.6356	0.0178	0.972	7.0512
Lena	3617	1	10	12686	16306	4.0191	48.7623	0.0584	0.866	7.0356
		1	20	6768	10388	6.3088	46.2578	0.0755	0.892	6.9264
		1	2	13548	17252	3.7989	53.8307	0.0215	0.876	7.3164
Rose	3701	1	10	10279	13983	4.6869	49.8702	0.0614	0.811	7.1760
		1	20	7254	10958	5.9807	46.3887	0.0847	0.833	6.8660
		1	2	16195	19992	3.2781	55.6287	0.0145	0.931	5.9436
Brain	3794	1	10	13071	16868	3.8852	51.9552	0.0496	0.895	5.8344
		1	20	9798	13595	4.8206	49.0311	0.0737	0.877	5.7865
		1	2	12984	16394	3.9976	53.9435	0.0207	0.934	6.1308
Knee	3407	1	10	10087	13497	4.8556	51.0609	0.0557	0.953	6.0020
		1	20	7749	11159	5.8729	48.0721	0.0848	0.833	5.9804
		1	2	15211	18900	3.4676	52.0969	0.0199	0.812	6.9732
Iris	3686	1	10	12304	15993	4.0978	49.1702	0.0555	0.864	6.8640
		1	20	10020	13709	4.7805	47.1879	0.07933	0.798	6.6371
		1	2	25208	29324	2.2349	56.0829	0.0118	0.941	6.1528
Fingerprint	4113	1	10	18476	22592	2.9009	52.3889	0.0429	0.953	6.0996
		1	20	13722	17838	3.6739	50.4090	0.0695	0.875	5.9592

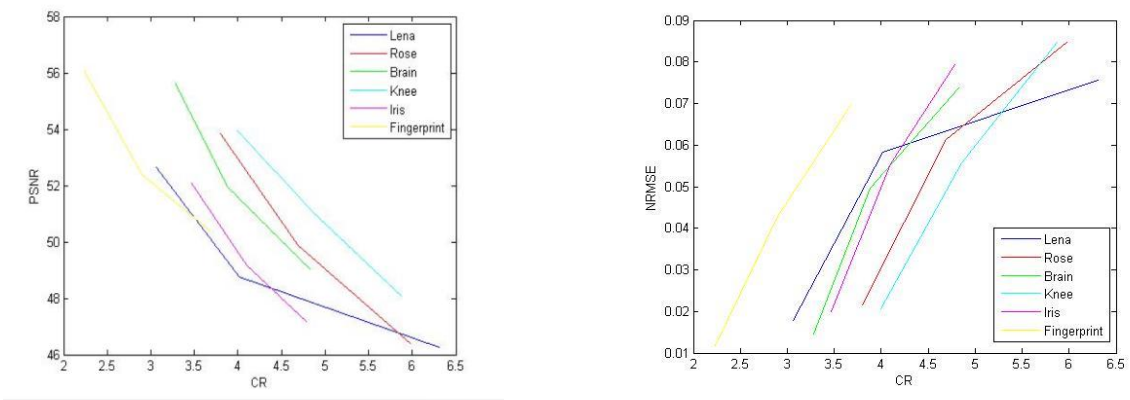

(a) (b)

Figure 10. Compression ratio versus the (a) PSNR and (b) NRMSE for the tested images

(a) (b) (c)

Figure 11. Other tested natural images, where (a) Card and (b) Apple correspond to natural images, and (c) Guitar images. Each image is 1200x1200 pixels, 1.37MB.

compression time- encoding of iterative based techniques and direct decoding process – is inversely related to the range of the residual quality measures; a small range has a large number of division iterations, and as the range increases the division iteration numbers decrease, with decreasing time. The interesting point is the excellent near perfect quality of the decoded compressed images. It is subjectively impossible to differentiate between the compressed image and the original one. This is due to preserving image information in terms of lossless coefficients causing minimum degradation or minimum residual loss.

Finally, the comparison with the well-known standard techniques JPEG and JPEG2000 is given in Table 10, based on measuring the compression ratio and the quality in terms of PSNR for the test images shown in Figure 4. Also, other test natural images added for comparative analysis of performance are shown in Figure 12. They follow the same criteria adopted for the previous images, namely they are greyscale square images of size (256×256). Figures 13 and 14 show a direct comparison of JPEG and JPEG-2000 set at the highest image quality with our technique compressed at lower quality. The decoded images in JPEG/JPEG2000

TABLE 10. PSNR of JPEG set on the highest quality compared to the original image.

Tested Images	JPEG				JPEG-2000			
	Total size in bytes	**CR**	**PSNR**	**SSIM**	**Total size in bytes**	**CR**	**PSNR**	**SSIM**
Lena	11366	5.7659	38.8708	0.761	10879	6.0240	41.3328	0.901
Rose	10762	6.0895	41.0337	0.721	8704	7.5294	43.7361	0.987
Brain	11858	5.5267	39.8728	0.812	10137	6.4650	42.4219	0.954
Knee	9728	6.7394	41.2240	0.952	9113	7.1914	45.0710	0.899
Iris	8908	7.3567	40.3316	0.912	10235	6.4031	43.9751	0.879
Fingerprint	15698	4.1747	38.8799	0.912	11035	5.9389	40.1820	0.946
Card	14336	4.5614	34.5320	0.871	10822	6.0558	36.7908	0.932
Apple	13207	4.9622	41.0911	0.911	11666	5.6176	44.8534	0.923
Guitar	11288	5.8085	39.8915	0.991	9830	6.6669	43.1997	0.988

Test Image ***Original image*** ***Compressed at higher quality*** ***Compressed at lower quality***

Lena

Rose

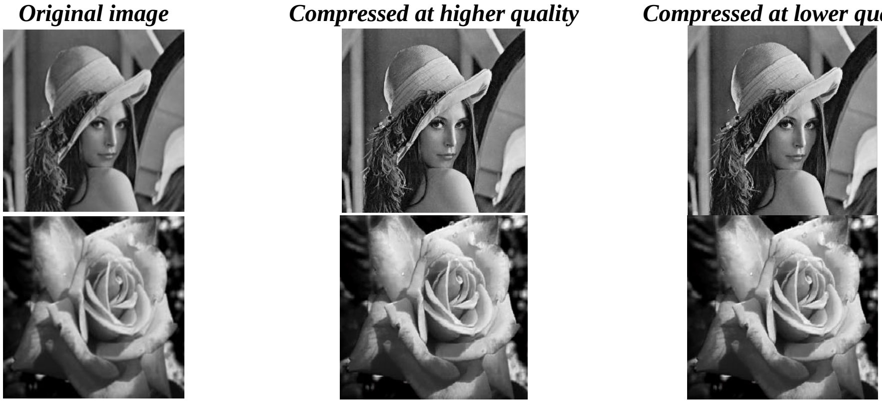

Brain

Knee

Iris

Fingerprint

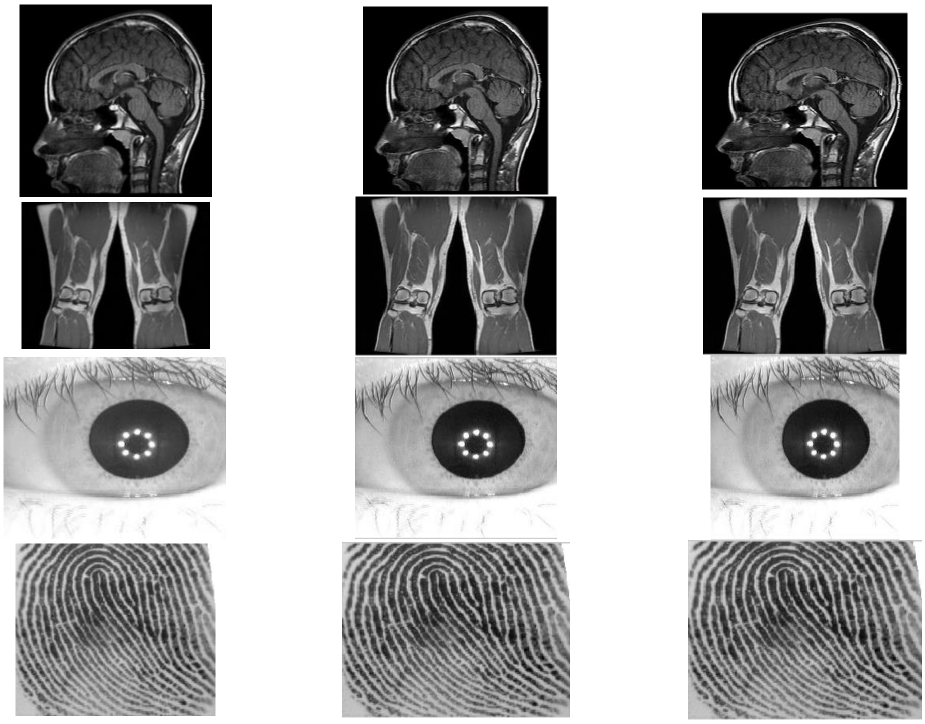

Figure 12. Examples of original test images and compressed images of high/low quality by our proposed method. Each image is 256x256 pixels, 65 KB

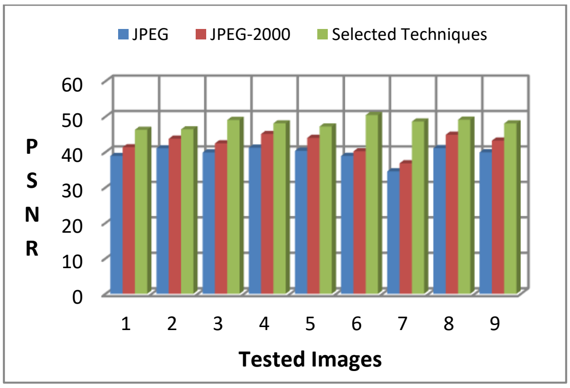

Figure 13. PSNR of JPEG/JPEG2000 versus the proposed technique for the tested images

are inferior to our method, even when our method is set to low quality (to yield similar compression ratios as JPEG/JPEG2000). Therefore, it is demonstrated the superior performance of our method with higher PSNR values as compared to JPEG/JPEG2000, for similar compression ratios. Also, the other comparison performed with traditional polynomial and two adaptive works relied on the Lena/Rose test images is given in Tables 11 and 12; where superior higher quality is achieved compared to litrature. Even with high compression ratios performed , still our results are promising with a clear trade-off between quality and compression ratio.

Image *JPEG reconstructed* *JPEG-2000 reconstructed* *Our method set at low image quality*

Lena

Rose

Brain

Knee

Iris

Fingerprint

Card

Apple

Guitar

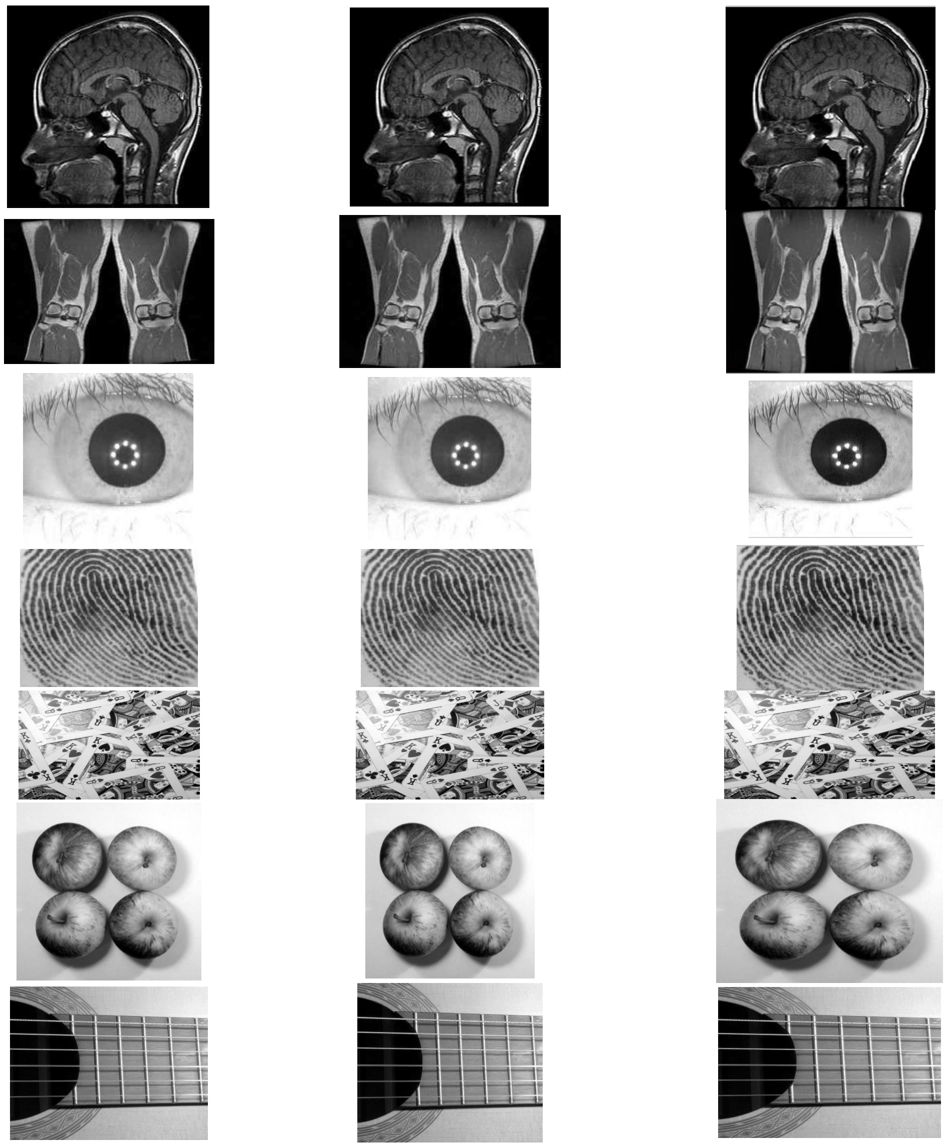

Figure 14. Examples of original tested images and compressed images of JPEG technique set at the highest quality and the suggested technique set at low quality

TABLE 11. Comparison with traditional polynomial, adaptive techniques and the proposed system for Lena image

Image Compression Techniques of traditional coding, adaptive coding and the proposed	**Performance for Lena Tested image**		
	CR	**PSNR**	**SSIM**
Traditional polynomial coding block size *4x4*, Quantization Coeff.*1,2,2*, and Quantization Res *5*	3.3227	45.0201	0.889
Traditional polynomial coding of 2D base, block size *4x4*, Quantization Coeff.*1,2,2*, and Quantization Res *40*	4.4329	31.1426	0.432
adaptive polynomial coding of 2D hard thresholding base, block size *4x4*, Quantization Coeff.*1,2,2*, and thresholding of subbans coding *20,20,40* and approximation subband *2* [23]	5.1312	29.9972	0.219
adaptive polynomial coding of 2D soft thresholding base, block size *4x4*, Quantization Coeff.*1,2,2*, and thresholding of subbans coding *20,20,40* and approximation subband *2* [23]	4.9201	33.3726	0.495
Adaptive polynomial with Quantization Steps of Coefficients are *1,2,2*, *LHThr=21,HLThr=36,HHThr=32*, Using the Seven Midtread Quantization base adopted by Burget & Das that utilized the minimum standard deviation value of residual image	8.5556	31.7175	0.456
Proposed system with quality between *1*to *2*	3.0669	52.6356	0.972
Proposed system with quality between *1*to *10*	6.3088	46.2578	0.892

TABLE 12. Comparison with traditional polynomial, adaptive techniques and the proposed system for Rose tested image

Image Compression Techniques of traditional coding, adaptive coding and the proposed	Performance for Rose Tested image		
	CR	**PSNR**	**SSIM**
Traditional polynomial coding block size *4x4*, Quantization Coeff.*1,2,2*, and Quantization Res *5*	3.7186	45.4949	0.828
Traditional polynomial coding of 2D base, block size *4x4*, Quantization Coeff.*1,2,2*, and Quantization Res *40*	4.4783	33.2660	0.638
Adaptive polynomial with Quantization Steps of Coefficients are *1,2,2, LHThr=21, HLThr=36, HHThr=32,* Using the Seven Midtread Quantization base adopted by Burget & Das that utilized the minimum standard deviation value of residual image	9.6718	35.5568	0.532
Proposed system with quality between *1*to *2*	3.7989	53.8307	0.876
Proposed system with quality between *1*to *10*	5.9807	46.3887	0.833

5. CONCLUSION

This paper proposed a novel iterative image coding technique based on an efficient hybrid lossy technique. The significance of our proposed methods is that they are convenient for a variety of image types including natural, medical and biometric grey level images. For the latter two types compression is critical, and is normally coded in lossless manner (error-free) as priority is given to keeping all information from the image. The experiments shown here demonstrate our proposed technique to a wide range of images where the quality of all tested images in terms of PSNR exceeds the well-known standard techniques of JPEG and JPEG-2000.

The iterative part constitutes the core of the paper and uses two different schemes, a lossless followed by a lossy method. First, the lossless method is based on a set of polynomial coefficients a_0 and (a_1,a_2) where a_0 is characterized by efficiently embedding correlations by subtracting the mean value at each iteration and keeping the number of iterations with the remainder. The mapping/de-mapping process is essential for converting the coefficients (a_1,a_2) values from negative and positive values into even/odd base to overcome the sign problem of negative numbers which requires a large number of bytes. The iterative process applies base2 differential techniques with superior representational performance converting uncorrelated, large byte consuming values into efficient representation of number of iterations and remainder parameters. Second, the lossy method is based on the residual that represents the number of divisions along the remainder. It is used to reconstruct an approximated value with minimum loss controlled by a maximum and minimum quality range that resembles the non-uniform quantization process.

The considerations above highlight the main limitations of our proposed method in relation to complexity, which may represent obstacles to its wide use. The average time complexity of the methods is estimated as O (n log n). Before the methods can be widely adopted (at par with other techniques such JPEG/JPEG2000) the following aspects are required to be addressed:

1. Standardization/practical issues: the proposed system produces high quality images with good compression ratios, but is still complex and needs to be optimized.
2. Performance issues: the polynomial coding is promising and simple to implement, however, there are a number of related issues that need to be developed further:
- The simplicity of the utilized symbol encoder techniques.
- Extending the system to utilize a hybrid system of the transform coding, by incorporating frequency techniques such as discrete wavelet transforms (DWT) or discrete cosine transform (DCT).
- Extending the system by mixing between the linear and the non-linear polynomial based techniques allowing the block nature to efficiently reduce the residual.
- Exploiting the region of interest (ROI) based segmentation process, especially in medical or frontal face images, to use the lossy background effectively.
3. Extending the proposed system to work with colour images; an initial solution could be simply repeat the method for each image plane.

Research on the above issues is under investigation and results will be reported in related works

6. REFERENCES

1. Al-Khafaji, G., "Intra and inter frame compression for video streaming", ***Computer Science***, (2012).
2. Shi, Y.Q. and Sun, H., "Image and video compression for multimedia engineering: Fundamentals, algorithms, and standards, CRC press, (1999).
3. Gonzales, R.C. and Woods, R.E., "Digital image processing, 2-nd edition", Prentice Hall, New Jersey, 2nd edition January, Vol. 15, No. 2002, (2002), 793.

4. Ghanbari, M., "Standard codecs: Image compression to advanced video coding, Iet, (2003).
5. Sayood, K., "Introduction to data compression, Morgan Kaufmann, (2017).
6. Kaur, M. and Kaur, G., "A survey of lossless and lossy image compression techniques", ***International Journal of Advanced Research in Computer Science and Software Engineering***, Vol. 3, No. 2, (2013), 323-326. https://doi.org/10.23851/mjs.v29i2.242
7. Setyaningsih, E. and Harjoko, A., "Survey of hybrid image compression techniques", ***International Journal of Electrical and Computer Engineering***, Vol. 7, No. 4, (2017), 2206. doi: 10.11591/ijece.v7i4.pp2206-2214.
8. Hussain, A.J., Al-Fayadh, A. and Radi, N., "Image compression techniques: A survey in lossless and lossy algorithms", ***Neurocomputing***, Vol. 300, (2018), 44-69. doi: 10.1016/j. neucom.2018.02.094.
9. Rahman, M.A. and Hamada, M., "Lossless image compression techniques: A state-of-the-art survey", ***Symmetry***, Vol. 11, No. 10, (2019), 1274. doi: 10.3390/sym11101274.
10. Kotha, H.D., Tummanapally, M. and Upadhyay, V.K., "Review on lossless compression techniques", in Journal of physics: conference series, IOP Publishing. Vol. 1228, (2019), 012007.
11. Siddeq, M.M. and Al-Khafaji, G., "Applied minimized matrix size algorithm on the transformed images by dct and dwt used for image compression", ***International Journal of Computer Applications***, Vol. 70, No. 15, (2013). doi: 10.5120/12040-8000.
12. Siddeq, M. and Rodrigues, M., "A new 2d image compression technique for 3d surface reconstruction", International Conference on Circuits, Systems, Communications and Computers, Santorin Island, Greece, (2014), 379-386.
13. George, L.E. and Sultan, B., "Image compression based on wavelet, polynomial and quadtree", ***Journal of Applied Computer Science & Mathematics***, Vol. 11, No. 5, (2011), 15-20. doi: 10.5120/13229-0658.
14. George, L. and Dhannon, B., "Image compression using polynomial and quadtree coding techniques", ***International Journal of Scientific & Engineering Research***, Vol. 4, No. 11, (2013), 2229-5518. https://doi.org/10.47577/technium.v4i6.7008
15. Rasha, A.-T., "Image compression using enhancement polynomial prediction coding", Master thesis, University of Baghdad, Iraq, (2015),
16. Al-Khafaji, G. and Al-Mahmood, H., "Lossless compression of medical images using multiresolution polynomial approximation model", ***International Journal of Computer Applications***, Vol. 76, No. 3, (2013).
17. Al-Khafaji¹, G. and Bassim, M., "Color image compression of inter-prediction base", ***International Journal of Computer Science and Mobile Computing***, Vol. 8, No. 11, (2019), 65-70.
18. Al-Khafaji, G. and Al-Kazaz, H.B., "Adaptive color image compression of hybrid coding and inter-differentiation based techniques", ***International Journal of Computer Science and Mobile Computing*** Vol. 8, No. 11, (2019), 65-70.
19. Al-Khafaji, G., "Image compression based on quadtree and polynomial", ***International Journal of Computer Applications***, Vol. 76, No. 3, (2013). doi: 10.5120/13229-0658.
20. Al-Khafaji, G. and George, L., "Grey-level image compression using 1-d polynomial and hybrid encoding technique", ***Journal of Engineering Science and Technology***, Vol. 16, No. 6, (2021), 4707-4728. doi. https://jestec.taylors.edu.my/V16Issue6.htm
21. AL-Hadithy, S.S., "Adaptive 1-d polynomial coding of c621 base for image compression", ***Turkish Journal of Computer and Mathematics Education (TURCOMAT)***, Vol. 12, No. 13, (2021), 5720-5731. https://www.turcomat.org/index.php/turkbilmat/article/view/9823
22. Wang, Z., Bovik, A.C., Sheikh, H.R. and Simoncelli, E.P., "Image quality assessment: From error visibility to structural similarity", ***IEEE Transactions on Image Processing***, Vol. 13, No. 4, (2004), 600-612. doi: 10.1109/TMM.2011.2152382.
23. Al-Khafaji, G. and Mahdi, N.S., "Image compression based on adaptive polynomial coding of hard & soft thresholding", ***Iraqi Journal of Science***, Vol. 57, No. 2B, (2016), 1302-1307. https://ijs.uobaghdad.edu.iq/index.php/eijs/article/view/7392

Persian Abstract

چکیده

با افزایش تقاضا برای استفاده فشرده از تصاویر، به ویژه مرتبط با برنامه های کاربردی آنلاین و همچنین انقلاب عظیم و مداوم فناوری تلفن همراه، نیاز به تکنیک های فشرده سازی کارآمد و استاندارد که سادگی و سرعت را تضمین می کند، پدیدار شده است. اینها باید با نیازهای کاربر سازگار باشند، اما با چالش‌های بهبود تکنیک‌های فشرده‌سازی نیز مواجه شوند. کدگذاری چند جمله‌ای یکی از این تکنیک‌ها است که هنوز در حال توسعه است، بر اساس مفهوم مدل‌سازی مبانی کدگذاری قطعی و احتمالی. این مقاله یک مدل چند جمله ای تکراری ریاضی جدید را برای نشان دادن هر دو پایه کدگذاری معرفی می کند. این مدل یک روش ترکیبی کارآمد را پیشنهاد می‌کند که در آن ضرایب به‌عنوان بدون تلفات نشان داده می‌شوند در حالی که باقیمانده‌ها به‌عنوان تلفات اما با حداقل تلفات ارائه می‌شوند، که عملکرد مؤثر را از نظر نسبت تراکم و کیفیت تضمین می‌کند. نتایج نشان می‌دهد که در حالی که این تکنیک دارای محدودیت‌هایی است، سیستم پیشنهادی به نسبت‌های فشرده‌سازی معادل تکنیک JPEG استاندارد دست می‌یابد، اما با کیفیت برتر برای نسبت فشرده‌سازی مشابه.

IJE TRANSACTIONS B: Applications Vol. 36, No. 02, (February 2023) 253-263

International Journal of Engineering

Journal Homepage: www.ije.ir

A Novel 19-Level Boost Type Switched-capacitor Inverter with Two DC Sources and Reduced Semiconductor Devices

F. Sagvand, J. Siahbalaee*, A. Koochaki

Department of Electrical Engineering, Aliabad Katoul Branch, Islamic Azad University, Aliabad Katoul, Iran

PAPER INFO

Paper history:
Received 11 October 2022
Received in revised form 08 November 2022
Accepted 09 November 2022

Keywords:
Multilevel Inverter
Switched-Capacitor
Voltage Boosting
Nearest Level Control

ABSTRACT

In this paper, a novel voltage-boosting switched-capacitor multilevel inverter (SCMLI) capable of producing 19 voltage levels using a combination of only 10 switches, 4 diodes, 2 capacitors, and 2 DC sources has been proposed. The main features of the proposed topology are 1) utilization of a very low number of devices, 2) very low Total Standing Voltage (TSV) equal to 6.55 and 3) self-balance property of the capacitors' voltages. In order to provide the IGBTs of the circuit with the desired switching signals, the Nearest Level Control (NLC) method has been adopted. To clarify the benefits of the designed topology as to the total quantity of switches, DC sources, capacitors as well as the total standing voltage (TSV), and converter boosting, a thorough comparison has been carried out versus the recently published 19-level topologies. Also, for the purpose of performance evaluation and validation, the suggested topology has been tested against various loads through an experimental setup in the laboratory using TMS320F28379D DSP as the processor. The comparative, simulation, and experimental results all imply the superiority of the proposed topology against its predecessor counterparts.

***doi**: 10.5829/ije.2023.36.02b.06*

1. INTRODUCTION

In recent years, multilevel inverters (MLIs) have been developed in form of DC to AC converters for numerous applications including renewable energy conversion systems, electric vehicles, AC tractions, high-voltage direct current (HVDC) transmission systems, distributed power generation systems, etc. [1-3]. Compared to two-level inverters, the primary benefits of MLIs are smaller dv/dt tensions, larger operational voltage using devices of a lower rating, reduced total harmonic distortion (THD), low switching frequency, and improved efficiency [4]. For powers of medium and higher ranges, the conventional two-level inverters are now substituted by such elementary MLIs as the flying capacitor (FC) inverters, neutral point clamped (NPC) inverters, modular multilevel converters (MMC), and cascaded H-bridge (CHB) inverters. Nevertheless, in order to attain a high number of output voltage levels, these conventional MLIs require more semiconductors (switches and diodes), capacitors, and DC sources [5-7]. To overcome these issues, researchers have proposed several switched-source (SSMLI) and switched capacitor multilevel inverters (SCMLI) which need a lower quantity of devices to provide more voltage levels [8-14]. Although SSMLI topologies can give rise to structures consisting of only a few devices they are not able to provide a voltage boost on the output inverter. Lately, designs founded on the SCMLI technology, in which serial/ parallel arrangements of electrical and electronic modules are utilized, have been the focus of attention, especially where voltage boost is a necessary feature. Naik et al. [13] designed a 7-level inverter using ten switches and one capacitor which could raise the output voltage up to 1.5 times. Khoun Jahan et al. [15] considered a CHB and substituted several of its DC sources with capacitors which led to the usage of only one DC source in the inverter's structure. Hussan et al. [16] came up with a boost inverter of gain 6, however, it cost 29 switches and a Total Standing Voltage (TSV) equal to 34. As an improvement, Taghvaie et al. [17] lowered this number to 19 switches for the same voltage

*Corresponding Author Institutional Email: ja_siah@yahoo.com (J. Siahbalaee)

Please cite this article as: F. Sagvand, J. Siahbalaee, A. Koochaki, A Novel 19-Level Boost Type Switched-capacitor Inverter with Two DC Sources and Reduced Semiconductor Devices, ***International Journal of Engineering, Transactions B: Applications***, Vol. 36, No. 02, (2023), 253-263

gain at the cost of a TSV equal to 39. A new inverter design with 55 voltage levels using 7 capacitors and 3 asymmetrical DC sources was suggested by Taghvaie et al. [18]. However, the existence of many modules, in this case, means risking the circuit reliability. Samadaei et al. [14] introduced a 7-level voltage inverter of high voltage gain using 2 capacitors along with 12 switches. More examples of SCMLI topologies with a low number of devices and self-balancing capabilities can be found in literature [19-23]. This article proposes an SCMLI design based upon fewer number of components which provides a quite low TSV. Here, 10 switches are combined to keep the TSV of the circuit as low as 6.55. A modest version of the Nearest Level Control (NLC) method is adopted for switching signals provisioning of the IGBTs. The primary findings of the suggested inverter design can be summarized as,

a) 19 voltage levels using only 10 switches and two DC sources.

b) A 19-level voltage on load gives a multilevel inverter with high-power quality and low cost function.

c) A voltage gain of 2.25 at the output.

d) Self-balance of the two capacitor voltages which makes the control circuitry as simple as possible.

The rest of the paper is as follows. The suggested topology along with its different operational modes have been presented in section 2. The charge and discharge modes of the capacitors, which are to be maintained in balance, suitable measures for choosing the capacitors, and power losses study will be brought in section 3. In section 4, the NLC technique as the intended switching method for IGBTs will be explained. A comparison of the suggested topology against a number of recently published MLIs has been conducted in section 5, regarding the utilized components, voltage gain, TSV, and cost function. Simulation as well as experimental results, aimed to provide illustrations of the suggested topology's feasibility and performance under different loading conditions, will be given in section 6. Finally, section 7 concludes the paper.

2. THE SUGGESTED INVERTER TOPOLOGY

Figure 1 illustrates the suggested scheme. This structure is combined of two capacitors (C_1, C_2), two DC voltage sources (u_1, u_2), ten switches (S_1, S_2, S_3, S_4, S_5, S_6, T_1, T_2, T_3, T_4) and four power diodes (D_1, D_2, D_3, D_4). The capacitors maintain their balance against each other. They will be charged up to the intended level for numerous instances of a fundamental cycle according to the series-shunt balancing rule of voltage. Here, electric charges of C_1 and C_2 must be Vdc and 4Vdc, respectively to achieve 19 levels of voltage from -9Vdc to +9Vdc. The projected turning on/off order of switches as well as the charge and discharge states of the capacitors' are summarized in Table 1.

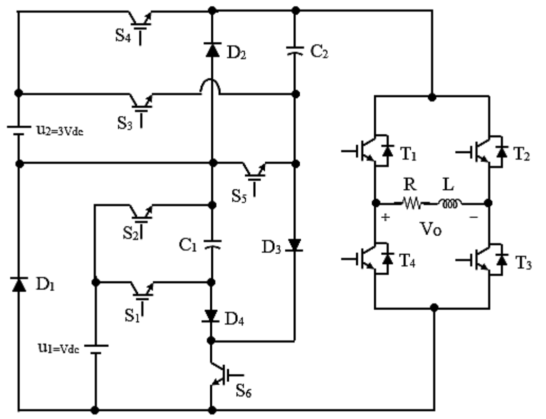

Figure 1. The suggested topology for the 19-level inverter

The current flow path towards load (red lines) throughout the positive half cycle and level zero are given in Figure 2. The voltage of level zero would be resulted by switching D_1, D_2, T_1, and T_3 on, as depicted in Figure 2(a). The level +Vdc is formed by turning on the S_2, T_1, and T_3 through diode D_2; at this moment, tuning the S6 on will raise the C1's voltage by Vdc, as shown in Figure 2(b). According to Figure 2(e), when the voltage of level +4Vdc is transferred to the load, the capacitor C2 will be charged to the sum voltage of the DC sources (+4Vdc) through S_2, S_4, D_3, and S_6. The remaining states will be analyzed in a similar way. In order to create the negative levels, switches T_2 and T_4 must be turned on instead of T_1 and T_3. It should be noted that, while diodes D_3 and D_4 maintain the capacitors' charges through a closed loop path, diodes D_1 and D_2 will transfer the voltage levels over to the output.

3. CAPACITOR SIZING AND POWER LOSSES ANALYSIS

3. 1. Capacitor Sizing Within the suggested SCMLI, there are two capacitors as well as two DC sources to provide 19 levels of voltages. As maintained before, the capacitors' voltages are leveled up with each other to the intended potential via the parallel linkage of the voltage source and capacitor over the interval of a fundamental cycle of switching. While C_1 maintains the same potential as the source u_1 (V_{dc}), C_2's potential will raise to the sum of the sources' voltages (4Vdc). The charge and discharge stages of C_1 and C_2 are depicted in Figure 3. The ideal capacitor sizing, then, is determined by their Largest Discharge Cycle (LDC) and load current (i_L). Over the duration of LDC, the charge variations of C_1 and C_2 are as:

TABLE 1. The Switching Orders and Capacitors States in the Suggested 19-level designed inverter

State	S_1	S_2	S_3	S_4	S_5	S_6	T_1	T_2	T_3	T_4	D_1	D_2	D_3	D_4	C_1	C_2	V_{out}
1	0	0	0	0	0	0	1	0	1	0	on	on	off	off	---	---	0
2	0	1	0	0	0	0	1	0	1	0	off	on	off	on	---	---	$+V_{dc}$
3	1	0	0	0	0	0	1	0	1	0	off	on	off	off	D	---	$+2V_{dc}$
4	0	0	0	1	0	0	1	0	1	0	on	off	off	off	---	---	$+3V_{dc}$
5	0	1	0	1	0	1	1	0	1	0	off	off	on	off	C	C	$+4V_{dc}$
6	0	1	0	0	0	0	1	0	1	0	off	off	off	off	---	D	$+5V_{dc}$
7	1	0	0	0	1	0	1	0	1	0	off	off	off	off	D	D	$+6V_{dc}$
8	0	0	1	0	0	0	1	0	1	0	on	off	off	off	---	D	$+7V_{dc}$
9	0	1	1	0	0	0	1	0	1	0	off	off	off	off	---	D	$+8V_{dc}$
10	1	0	1	0	0	0	1	0	1	0	off	off	off	off	D	D	$+9V_{dc}$
11	0	1	0	0	0	0	0	1	0	1	off	on	off	on	---	---	$-V_{dc}$
12	1	0	0	0	0	0	0	1	0	1	off	on	off	off	D	---	$-2V_{dc}$
13	0	0	0	1	0	0	0	1	0	1	on	off	off	off	---	---	$-3V_{dc}$
14	0	1	0	1	0	1	0	1	0	1	off	off	on	off	C	C	$-4V_{dc}$
15	0	1	0	0	0	0	0	1	0	1	off	off	off	off	---	D	$-5V_{dc}$
16	1	0	0	0	1	0	0	1	0	1	off	off	off	off	D	D	$-6V_{dc}$
17	0	0	1	0	0	0	0	1	0	1	on	off	off	off	---	D	$-7V_{dc}$
18	0	1	1	0	0	0	0	1	0	1	off	off	off	off	---	D	$-8V_{dc}$
19	1	0	1	0	0	0	0	1	0	1	off	off	off	off	D	D	$-9V_{dc}$

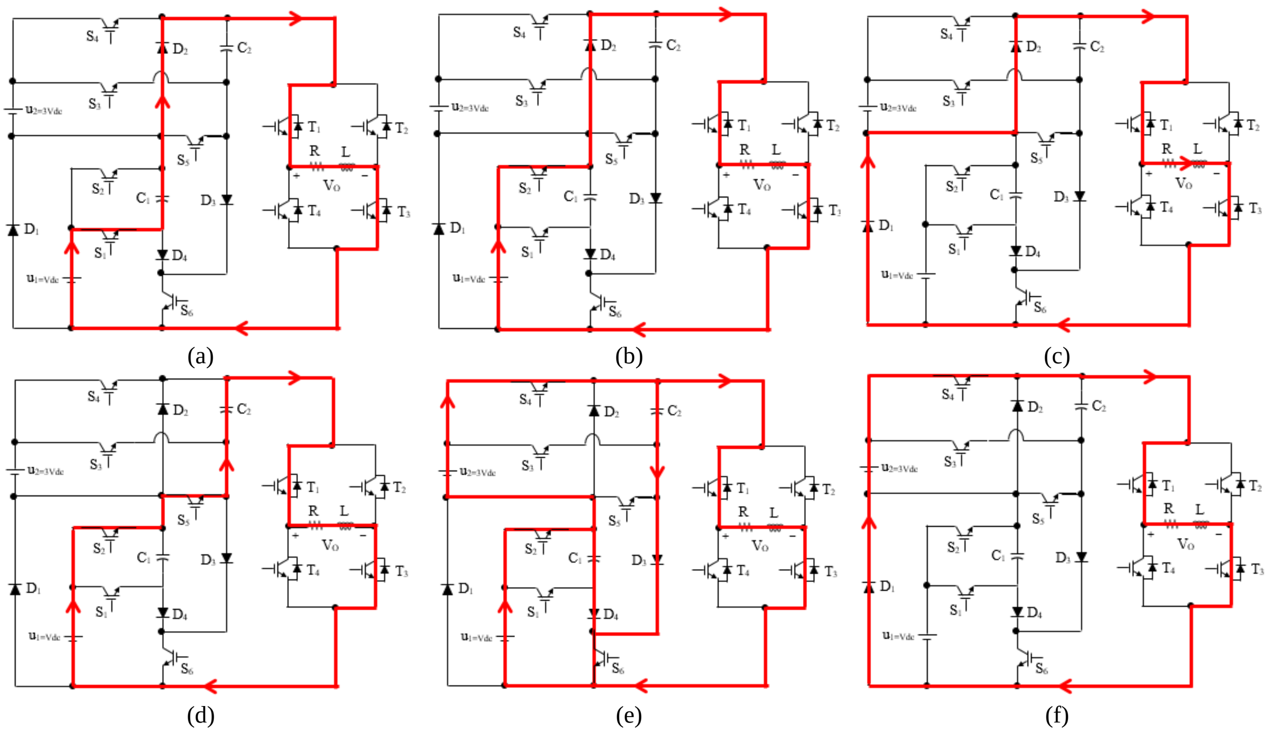

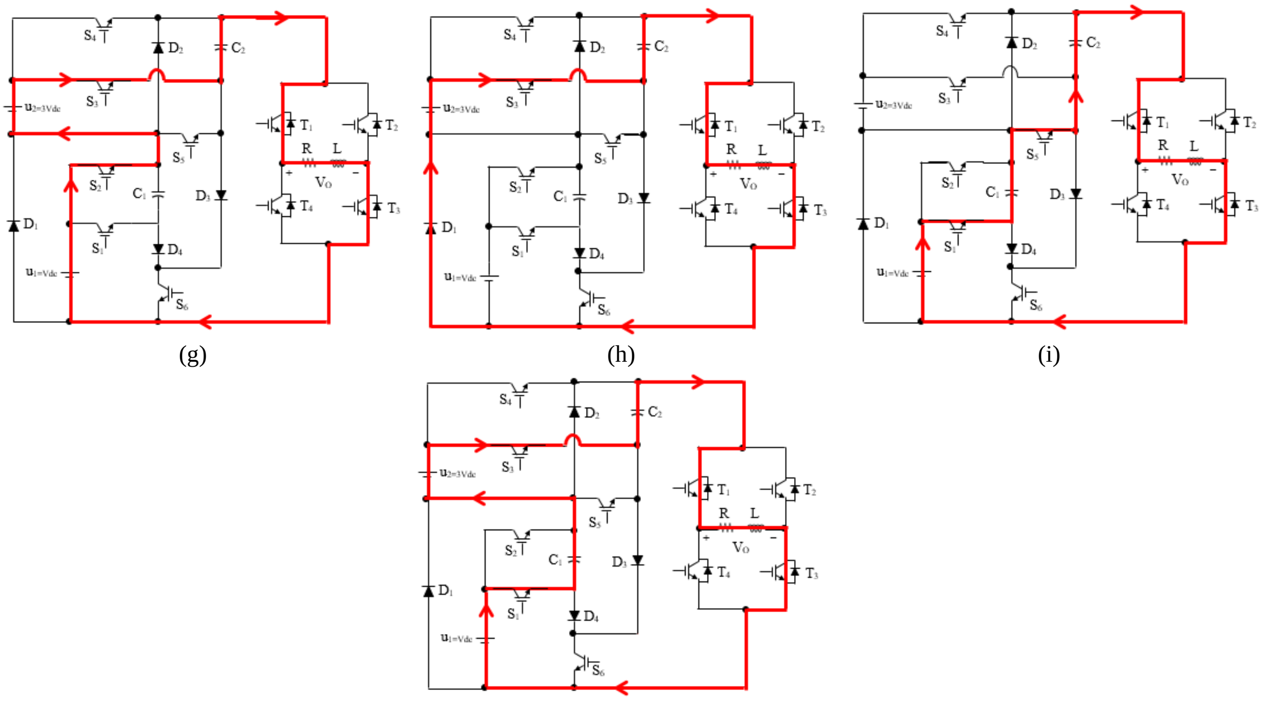

Figure 2. Schematic of switching states for generating different positive and zero levels on the load. (see Table 1): (a) state 1 for $V_O = 0V_{dc}$, (b) state 2 for $V_O = +V_{dc}$, (c) state 3 for $V_O = +2V_{dc}$, (d) state 4 for $V_O = +3V_{dc}$, (e) state 5 for $V_O = +4V_{dc}$, (f) state 6 for $V_O = +5V_{dc}$, (g) state 7 for $V_O = +6V_{dc}$, (h) state 8 for $V_O = +7V_{dc}$, (i) state 9 for $V_O = +8V_{dc}$, (j) state 10 for $V_O = +9V_{dc}$

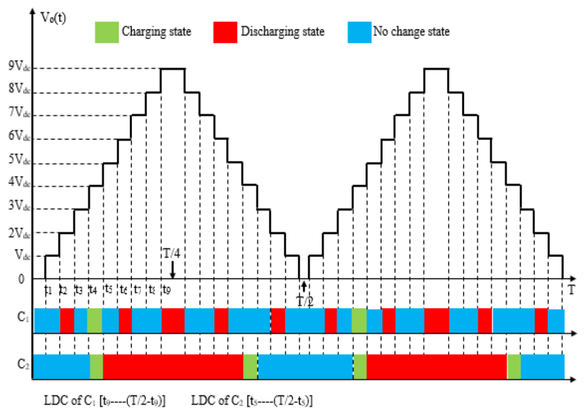

Figure 3. The Charge and Discharge Sequence of Capacitors

$$\Delta Q_{C_1} = \int_{t_9}^{T/2-t_9} i_L(t)dt \tag{1}$$

$$\Delta Q_{C_2} = \int_{t_5}^{T/2-t_5} i_L(t)dt \tag{2}$$

Using Equtions (1) and (2), sizes of C_1 and C_2 can be calculated by:

$$C_1 = \frac{1}{\Delta V_{C_1}} \int_{t_9}^{T/2-t_9} i_L(t)dt \tag{3}$$

$$C_2 = \frac{1}{\Delta V_{C_2}} \int_{t_5}^{T/2-t_5} i_L(t)dt \tag{4}$$

Considering the value of u_1= 20v and u_2=60v (to obtain the maximum output voltage V_{out} = 180V), the C_1 and C_2 voltages will be raised up to 20v and 60v, respectively. Therefore, the voltage differences ΔV_{C1} and ΔV_{C2}, usually considered as 10% of the corresponding capacitor voltage, will be equal to 2V and 8V, respectively. The time instances t_1-t_9 can also be found as:

$$v(t) = v_m \sin(\omega t) \tag{5}$$

$$t_i = \frac{1}{\omega}\sin^{-1}\left(\frac{2i-1}{N-1}\right) \quad ,i = 1,2,3,...,9 \tag{6}$$

in which, N is the dimension of the output levels. Using Equation (6), then t_is, i = 1, .. ,9 are calculated as 0.17 ms, 0.53 ms, 0.89 ms, 1.3 ms, 1.7 ms, 2.1 ms, 2.6 ms, 3.1 ms, and 3.9 ms, respectively. For a load of strict resistance, the current would be:

$$i_L(t) = i_m \sin(\omega t) \tag{7}$$

For a maximum load current im = 2A, the solution of Equation (3) gives the optimal size of C1,

$$C_1 = \frac{2 \times i_m \cos(\omega t_9)}{2\pi f \times \Delta V_{C_1}} \tag{8}$$

Similarly, the precise size of C_2 can be obtained from Equation (4) as:

$$C_2 = \frac{2 \times i_m \cos(\omega t_5)}{2\pi f \times \Delta V_{C_2}} \tag{9}$$

Combining Equations (8) and (9), the ultimate sizes of C_1 and C_2 would be 2156 µF and 1369 µF, respectively. For these capacitors, the closest existing size in the lab is 4700 µF. For this reason, in the experimental setup, they are both chosen equal to $C_1 = C_2 = 4700$µF.

3. 2. Power Losses Analysis There are three types of power losses in the proposed SCMLI topology. These are switching loss, conduction loss, and ripple losses of capacitors.

3. 2. 1. Switching Losses The switching losses are caused by delays during the turning on/off of switches and the reverse recovery time of the diodes. As shown in Figure 4, when the pulse reaches the gate terminal of the switch at α_1, it takes a t_{on} for the collector-emitter voltage and collector current to reach their final values. Moreover, when the pulse is removed from the gate terminal at α_3, the switching-off process will take t_{off} seconds. These delays are the source of the switching losses.

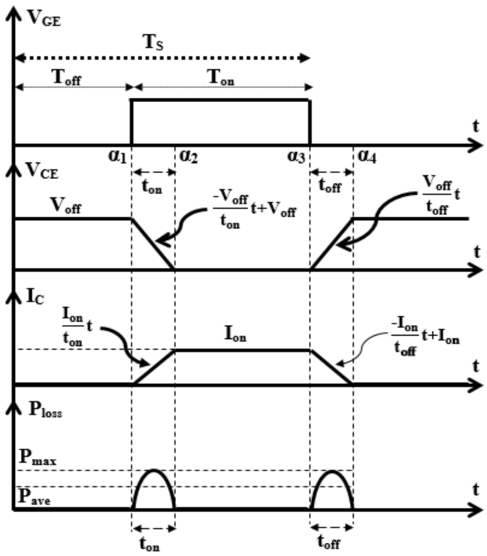

Figure 4. Instantaneous changes of voltage, current, and power on the switches

The switching losses during the ON ($P_{sw,on}$) and OFF ($P_{sw,off}$) states of a typical switch can be calculated by inferred from Equations (10) and (11), respectively, as:

$$P_{sw,on} = \frac{f_s.V_{off}.I_{on}.t_{on}}{6} \tag{10}$$

$$P_{sw,off} = \frac{f_s.V_{off}.I_{on}.t_{off}}{6} \tag{11}$$

where f_s is the frequency of switching,V_{off} , the switch's nominal voltage, and I_{on}, the average load current. Additionally, the switching losses on the diodes will be:

$$P_{sw,D} = \frac{f_s.V_{RM}.I_{RM}.t_B}{6} \tag{12}$$

where V_{RM} and I_{RM} are, respectively, the maximum voltage and current of reverse recovery and t_B, the time delay of the reverse current. The total switching losses can be calculated by:

$$P_{sw,total} = \sum_{i=1}^{N_{sw}} \left(\sum_{j=1}^{N_{on}} \left(P_{sw,on,ij} \right) + \sum_{j=1}^{N_{off}} P_{sw,off,ij} \right) + \sum_{k=1}^{N_D} \left(\sum_{h=1}^{N_{off}} \left(P_{sw,D,kh} \right) \right) \tag{13}$$

where N_{sw} and N_D denote the numbers of switches and diodes, respectively; N_{on} and N_{off} are also the number of ON and OFF states of the switches and diodes during a fundamental cycle (1/Ts).

3. 3. 2. Conduction Losses Conduction losses are due to the resistances and voltage drops across the switches and diodes during turning-ON states. In multilevel inverters, each voltage level contributes to the conduction losses since there is a different current path for each voltage level. The conduction losses of a switch ($P_{cond,sw}$) and a diode ($P_{cond,D}$) can be written as:

$$P_{cond,sw} = V_{on,sw}.I_{sw,ave} + R_{on,sw}.I_{sw,rms}{}^2 \tag{14}$$

$$P_{cond,D} = V_{on,D}.I_{D,ave} + R_{on,D}.I_{D,rms}{}^2 \tag{15}$$

in which, R_{on} and V_{on} denote, respectively, the resistance of the switch and diode and their voltages during the turning-ON state; I_{rms} and I_{ave}, are also the RMS and average currents of semiconductors, respectively. According to Figure 2, for voltage levels of 0 to $\pm 9V_{dc}$, the conduction losses will be:

$$
\begin{aligned}
&P_{cond,(+9V_{dc})} = (4V_{on,sw}.I_{load,ave} + 4R_{on,sw}.I_{load,rms}{}^{2}) \\
&+(0 \times V_{on,D}.I_{load,ave} + 0 \times R_{on,D}.I_{load,rms}{}^{2}) \\
&P_{cond,(+8V_{dc})} = (4V_{on,sw}.I_{load,ave} + 4R_{on,sw}.I_{load,rms}{}^{2}) \\
&+(0 \times V_{on,D}.I_{load,ave} + 0 \times R_{on,D}.I_{load,rms}{}^{2}) \\
&\vdots \\
&\vdots \\
&P_{cond,(-8V_{dc})} = (4V_{on,sw}.I_{load,ave} + 4R_{on,sw}.I_{load,rms}{}^{2}) \\
&+(0 \times V_{on,D}.I_{load,ave} + 0 \times R_{on,D}.I_{load,rms}{}^{2}) \\
&P_{cond,(-9V_{dc})} = (4V_{on,sw}.I_{load,ave} + 4R_{on,sw}.I_{load,rms}{}^{2}) \\
&+(0 \times V_{on,D}.I_{load,ave} + 0 \times R_{on,D}.I_{load,rms}{}^{2})
\end{aligned} \tag{16}
$$

For example, for the level $+9V_{dc}$, according to Figure 2(j), there are 4 switches and 0 diode in the current commutation path; thus, a correct relationship of the conduction loss must take care of the individual number of switches and diodes for each possible path. The total conduction loss, then, will be the sum of losses overall voltage levels,

$$
\begin{aligned}
P_{cond,total} &= P_{cond,(+9V_{dc})} + P_{cond,(+8V_{dc})} + \cdots\cdots \\
&+ P_{cond,(-8V_{dc})} + P_{cond,(-9V_{dc})}
\end{aligned} \tag{17}
$$

3. 3. 3. Ripple Losses of Capacitors

When capacitors are in charging mode, the potential difference between the DC sources and capacitors results in ripples of capacitor voltages. This, in turn, creates ripple losses, which can be calculated as follows:

$$
P_{loss,cap} = \frac{f_{ref}}{2} \sum_{i=1}^{N_C} C_i \Delta V_{Ci}{}^{2} \tag{18}
$$

where NC denotes the number of capacitors. Taking all the losses into account, then, the efficiency of the proposed 19-level topology can be calculated as:

$$
\begin{aligned}
\eta &= \left(\frac{P_{out}}{P_{out} + P_{loss}} \right) \times 100 \\
&= \left(\frac{\dfrac{\left(V_{out(rms)}\right)^2}{R_{load}}}{\dfrac{\left(V_{out(rms)}\right)^2}{R_{load}} + P_{sw,total} + P_{cond,total} + P_{loss,cap}} \right) \times 100
\end{aligned} \tag{19}
$$

4. NEAREST LEVEL CONTROL (NLC)

The suggested topology of the inverter is well suited to work at a couple of switching frequencies including the fundamental as well as higher ones. Among the available modulation schemes for the switching operation, PWM has many advantages such as lower power loss with respect to switching and snubber while maintaining the dv/dt rating quite small. As for the fundamental frequency, there are two well-known switching techniques, one is Selective Harmonic Elimination (SHE) [24] and the other is NLC [25-30]. In the SHE technique, increasing the number of output levels creates a large volume of offline computational costs with respect to switching angles and their storage. Therefore, here, the NLC has been adopted as the switching control technique. For the purpose of switching, a sampled and quantized waveform is needed. In NLC, this waveform is obtained through the comparison of two waveforms: the reference sinusoidal and the desired output. In order to provide the desired switching signals for IGBTs switches, the resulting waveform of this comparator must be quantized to the nearest level and subsequently compared with the given switching plan in Table 1. Figure 5 illustrates the operating principle of the NLC method.

5. COMPARATIVE ASSESSMENT

In this section, the suggested inverter topology will be compared with those of the recent studies which have the same number of output levels. The comparison will be accomplished based upon such measures as the number of (semiconductor) power switches (N_{sw}), diodes (N_d), capacitors (N_C), gate drivers (N_{gd}), voltage gain (V_G), total standing voltage (TSV) and cost function (CF).

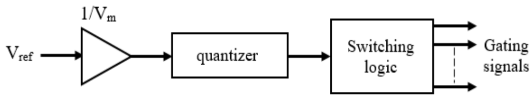

(a)

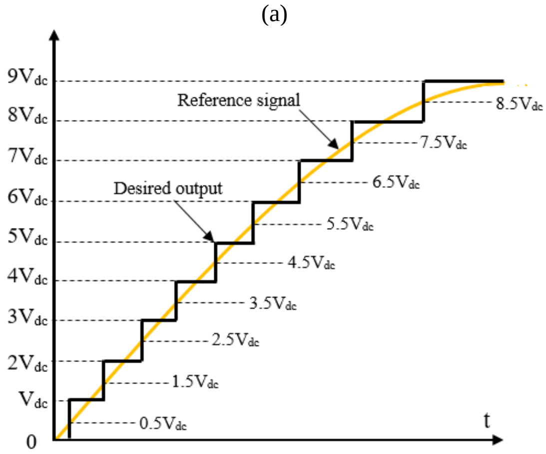

(b)

Figure 5. The NLC Switching Method: (a) Schematic Block Diagram (b) Graph-Based Functional Illustration

The total standing voltage is defined as the total peak inverse voltage (PIV) across the semiconductor devices when they are turned off. In the case of TSV per-unit, the total TSV will be divided by the maximum voltage level on the output. Table 2 illustrates the results of this comparison. As it can be seen, the suggested topology is evidently more successful than its other predecessors as to the number of components used per level, especially compared to topologies of the same number of levels.
For the monetary comparison of the given inverter topologies, here, the following cost function (CF) has been considered,

$$CF = \left(N_{sw} + N_{gd} + N_d + N_C + \alpha \times TSV^{pu}\right) \tag{20}$$

$$NCF = \frac{CF}{N_L} \tag{21}$$

According to Table 2, the suggested SCMLI topology gives an acceptable NCF, especially for α = 0.5, which implies the cost-related effectivity of the suggested design when a large number of voltage levels can be produced using very a low number of components.

TABLE 2. Comparison of the Suggested MLI with its Latest Counterparts

Top.	N_L	N_{sw}	N_d	N_C	N_{gd}	V_G	TSV^{pu}	NCF
[18]	11	11	0	1	11	1.6	4.4	4.66
[19]	13	14	0	2	11	2	5.33	4.56
[20]	17	10	2	2	10	2	5.5	3.14
[21]	17	10	2	2	10	2	5.5	3.14
[22]	13	11	1	1	10	1.5	6.3	4.18
[23]	13	18	0	2	15	2	5	5.76
[31]	17	18	2	4	14	2	6	4.82
[32]	19	12	6	4	12	2.2	5.8	3.85
[24]	19	12	1	2	10	1.8	6.66	3.02
Pro.	19	10	4	2	10	2.2	6.55	3.08

6. RESULTS AND DISCUSSION

6. 1. Simulation Results Simulations are done for the suggested topology and the corresponding results are shown in Figure 6. The simulation parameters are given in Table 3. The voltage waveforms of the output, capacitor C_1 (V_{C1}), capacitor C_2 (V_{C2}) as well as the load current waveform of the suggested design are shown in Figure 6(a) for a load of an exclusive resistance (R = 90 Ω). For the sake of clarity, the vertical axis of the currents are all multiplied by 50. According to Figure 6(a), for a load R=90 Ω, the peak of the current reaches 2A (180v/90Ω). Figure 6(b) illustrates the output waveforms for a variable load between Z=90 Ω at 0 < t < 0.05s and Z=180 Ω at 0.05 < t < 0.1s. For this load, the peak current is equal to 1A. In Figure 6(c), the load has changed from a pure resistance into a mixed impedance, respectively equal to Z=90 Ω at 0 < t < 0.05s and Z=90 Ω + 100 mH at 0.05 < t < 0.1s. As can be seen, here, the output current is nearly sinusoidal due to the filtering nature of the inductor. For all the cases, the output voltage has maintained its steady state while voltages of the capacitors C1 and C2 are in balance with acceptable ripple. According to Table 3, the mean value of capacitors C1 and C2 voltages are approximately equal to 20v and 60v, respectively. Figure 7, also, illustrates the harmonic spectrum analysis of the suggested scheme. As this figure shows, the voltage THD at the inverter output is 4.39%, which is less than 8% complying with the IEEE-519 standards.

6. 2. Results of Experimental Setup In order to back up the theoretical results as well as those of simulations for the proposed 19-level inverter, as shown in Figure 8, an experimental setup corresponding to a single-phase, low-power version of the inverter, was provided. Using a TMS320F28379D DSP, the NLC switching control method was digitally programmed with code composer studio 8.1.0. For the IGBTs switches and SCHOTTKY diodes, IRG4IBC30S and MBRF20100C are used, respectively. In order to isolate the power circuit

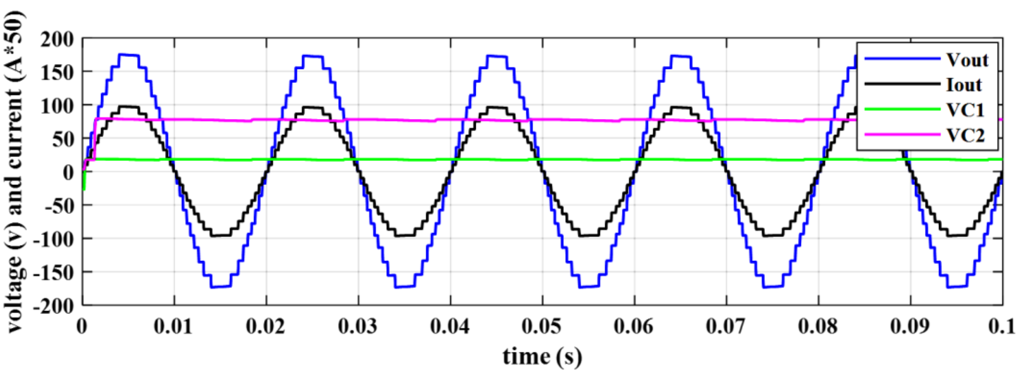

(a)

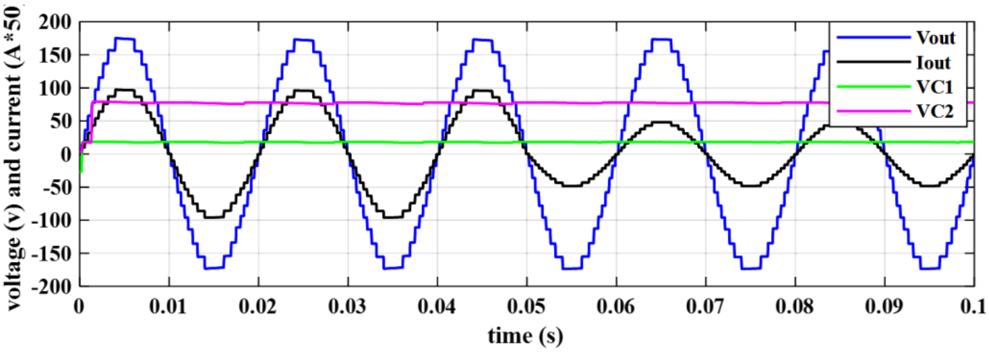

(b)

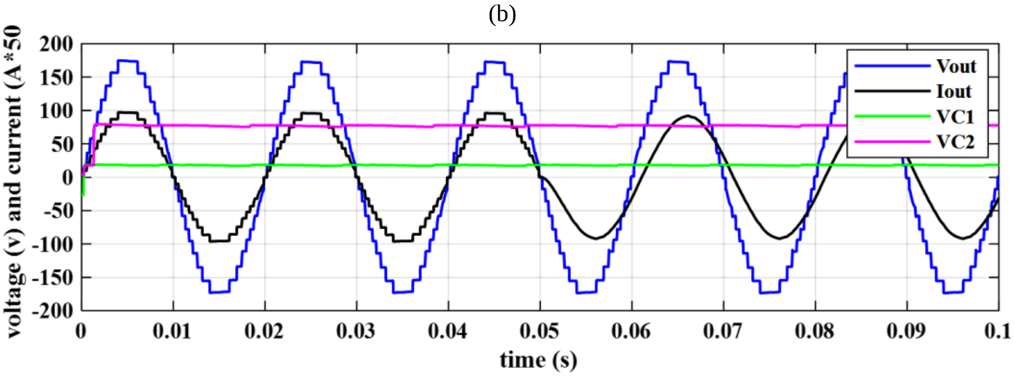

(c)

Figure 6. Simulation results with various loads. (a) Z=90 Ω. (b) Z=90Ω at 0<t<0.05s and Z=180 Ω at 0.05<t<0.1s. (c) Z=90 Ω at 0<t<0.05s and Z=90Ω + 100mH at 0.05<t<0.1s. In all figures, for more clear observation, the current wave has been multiplied by 50

TABLE 3. Components of the 19-Level inverter in the experimental setup

First input DC-source	u_1= 20 v
Second input DC-source	u_2= 60 v
Peak output voltage	180 v
Processor	DSP TMS320F28379D
Capacitors	C_1=C_2= 4700 µF
IGBT	IRG4IBC30S
Diode	MBRF20100CT
Driver/optocoupler	HCPL-3120
Current sensor	Resistive divider (1/7 Ω, 40 w)
Voltage sensor	Resistive divider (15×100 kΩ)
Sample time	10 µs
Output frequency	50 Hz
Resistive load	R= 180 Ω, 90 Ω
Resistive-Inductive load	R= 180 Ω, L= 22 mH

from the rest, the HCPL3120 driver was used, which aside from isolation, provides the necessary amplifications, too. The resulting setup was tested against several loads, both resistive and inductive using the following components: R=90 Ω, R=180Ω, and L=22mH.

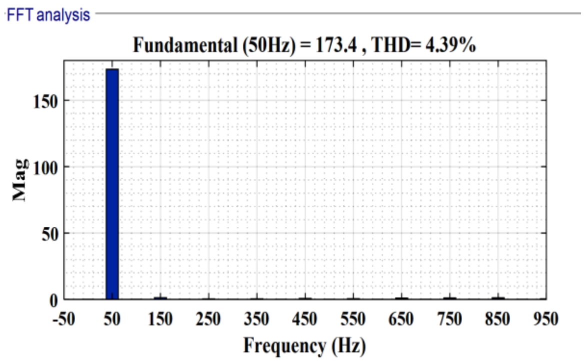

Figure 7. Harmonic Spectrum of Output Voltage of the Proposed 19-level Topology for a Pure Resistive Load (Z=90 Ω)

For the practical implementation, the following must be taken into account,

a) To avoid electrical interference, all gate driver power supplies should be isolated from each other.
b) A high-power resistor should be placed parallel with each capacitor for discharging and safety upon the completion of the test.
c) It is better off to use a PNP- type IGBT for switch S3 (see Figure 1) since S3 and S5 have a common emitter. The parameters related to the laboratory implementation are listed in Table 3.

Figure 8. Experimental Set-up in the laboratory

Figure 9 depicts the output voltage of the 19-level inverter (150V). According to the smallest selected voltage level, i.e., 20V, the maximum voltage level must be 180V, however, due to the voltage drop across the switches and diodes, it was reduced to 150V. Figure 10 displays the voltage and current of the inverter's output for a load combined of an exclusive resistance equal to 180Ω. For this load, the current peak is equal to 0.8 A. In Figure 11, the scenario of Figure 10 has been repeated except that, here, the load changes from 180Ω to 90Ω. As shown in this figure, the current amplitude has changed from 0.8A to 1.6A. Figure 12 displays the load's voltage and current when its value changes from 180 Ω to 180 Ω+22mH. According to Figure 12, the current approximately mimics a sinusoidal with a peak of 0.8 A. Figure 13 depicts the capacitors' voltages. In order to measure the capacitors' voltages, a voltage divider with a factor of 1/3 has been considered. From Figure 13, capacitors C_1 and C_2 are charged up to about 15.6V and 65V, respectively. Given the values of the DC sources as u_1=20v and u_2=60v, the capacitors C_1 and C_2 were expected to be charged up to 20V and 80V, respectively. The difference between the two, again, is due to the voltage drop across the switches and diodes. In the laboratory results, according to Figure 13 below, the

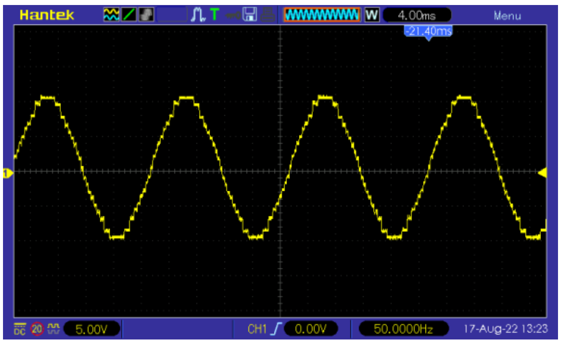

Figure 9. Output Voltage of the 19-Level Inverter (To obtain the actual values, the vertical axis must be multiplied by 15 factor)

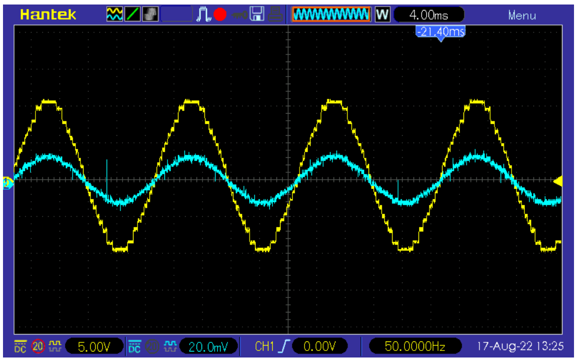

Figure 10. Output Voltage (yellow wave) and Current (blue wave) of the 19-Level Inverter for a Constant Pure Resistive Load of 180Ω. For actual values of voltage and current, the vertical axes must be multiplied by 15 and 7, respectively (see Table 3). The Corresponding oscilloscope probes for voltage and current are set on the ×1 and ×10, respectively

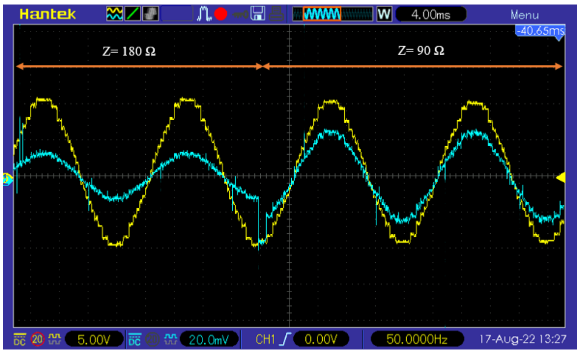

Figure 11. Voltage (yellow wave) and current (blue wave) of the 19-level inverter's output when its load changes from R=180 Ω to R=90 Ω. For the actual voltage and current, the vertical axes must be multiplied by 15 and 7, respectively (see Table 3). (The oscilloscope probes for voltage and current are set to ×1 and ×10, respectively)

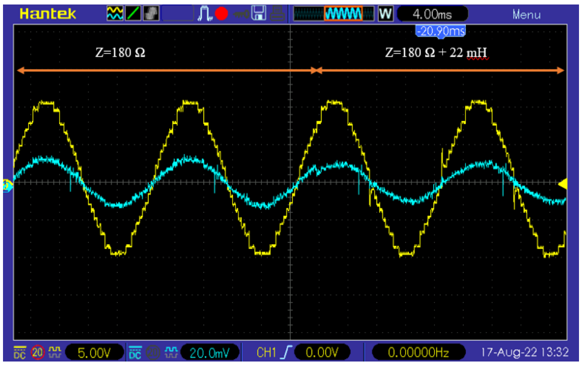

Figure 12. Output voltage (yellow wave) and current (blue wave) of the 19-level inverter when its load changes from Z=300 Ω to Z=300 Ω + 22mH. For actual voltage and current, the vertical axes must be multiplied by 15 and 7, respectively. (Probes of the oscilloscope for voltage and current are set to ×1 and ×10, respectively)

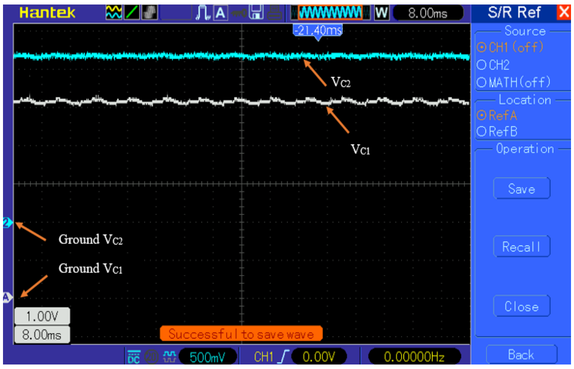

Figure 13. (a) Voltages of Capacitors C1 and C2. (For the actual values of the capacitors' voltage, the vertical axis must be multiplied by 8 for the V_{c2}. The probes of the oscilloscope for capacitors voltage C1 and C2 are set to ×1 and ×10, respectively)

voltage ripple of the first capacitor is equal to $\Delta V_{C1}=0.1\times0.5\times8=0.4V$, where 0.1 is the ripple voltage on the oscilloscope page, 0.5 is the channel2 scale and 0.8 is the resistor divider in the hardware experimental. Moreover, the voltage ripple of the second capacitor is equal to $\Delta V_{C2}=0.2\times1\times10=2V$, where 0.2 is the ripple voltage on the oscilloscope page, 1 is the channel1 scale and 10 is the probe factor of channel1. The capacitor voltage of C_1 and C_2 have been obtained as 15.6 and 65v, respectively. It means that the percent of ripple voltage on the capacitors C_1 and C_2 is 2.5% and 3%, respectively. So, we expect that a 19-level voltage is produced on the output with very low distortion harmonics.

7. CONCLUSIONS

This paper suggested a novel topology for a 19-level inverter, consisting of 10 switches, two DC sources, four diodes, and two capacitors. Besides the low number of components in the inverter circuit, it was designed in a way so that its capacitors are naturally in balance with respect to the voltage without further need for auxiliary circuits. Detailed simulation backed up by an experimental set-up against numerous constant as well as variable resistive and mixed resistive-inductive loads verified the performance of the suggested design. The TSV and NCF of the suggested inverter were, respectively, 6.55 and 3.08, which is comparable to its recent counterparts. The voltage gain was 2.25 with an output THD equal to 4.39%, from which, the latter is within the acceptable limit of IEEE-519 standard. As a suggestion for future research, the proposed inverter can be upgraded to a bi-directional inverter to eliminate the H-bridge. We can also mention the research to find new applications, especially in low voltage photovoltaic systems connected to the grid.

8. REFERENCES

1. Bhukya, M.N., Kota, V.R. and Depuru, S.R., "A simple, efficient, and novel standalone photovoltaic inverter configuration with reduced harmonic distortion", ***IEEE Access***, Vol. 7, (2019), 43831-43845. doi: 10.1109/ACCESS.2019.2902979.
2. Dhanamjayulu, C., Khasim, S.R., Padmanaban, S., Arunkumar, G., Holm-Nielsen, J.B. and Blaabjerg, F., "Design and implementation of multilevel inverters for fuel cell energy conversion system", ***IEEE Access***, Vol. 8, (2020), 183690-183707. doi: 10.1109/ACCESS.2020.3029153.
3. Chen, J., Song, Q., Yin, S. and Chen, J., "On the decentralized energy management strategy for the all-electric apu of future more electric aircraft composed of multiple fuel cells and supercapacitors", ***IEEE Transactions on Industrial Electronics***, Vol. 67, No. 8, (2019), 6183-6194. doi: 10.1109/TIE.2019.2937069.
4. Sunddararaj, S.P. and Srinivasarangan Rangarajan, S., "An extensive review of multilevel inverters based on their multifaceted structural configuration, triggering methods and applications", ***Electronics***, Vol. 9, No. 3, (2020), 433. https://doi.org/10.3390/electronics9030433
5. Palanisamy, R., Aravindh, P. and Vijayakumar, K., "Effectual svpwm for 3-level npc-mli with grid connected pv system", ***International Journal of Electrical Engineering and Technology***, Vol. 11, No. 3, (2020). https://ssrn.com/abstract=3635208
6. Celikovic, J., Das, R., Le, H.-P. and Maksimovic, D., "Modeling of capacitor voltage imbalance in flying capacitor multilevel dc-dc converters", in 2019 20th Workshop on Control and Modeling for Power Electronics (COMPEL), IEEE., (2019), 1-8.
7. Yang, K., Lan, X., Zhang, Q. and Tang, X., "Unified selective harmonic elimination for cascaded h-bridge asymmetric multilevel inverter", ***IEEE Journal of Emerging and Selected Topics in Power Electronics***, Vol. 6, No. 4, (2018), 2138-2146. doi: 10.1109/JESTPE.2018.2808539.
8. Wang, L., Wu, Q. and Tang, W., "Novel cascaded switched-diode multilevel inverter for renewable energy integration", ***IEEE Transactions on Energy Conversion***, Vol. 32, No. 4, (2017), 1574-1582. doi: 10.1109/TEC.2017.2710352.
9. Vahedi, H., Sharifzadeh, M. and Al-Haddad, K., "Modified seven-level pack u-cell inverter for photovoltaic applications", ***IEEE Journal of Emerging and Selected Topics in Power Electronics***, Vol. 6, No. 3, (2018), 1508-1516. doi: 10.1109/JESTPE.2018.2821663.
10. Tashiwa, I.E., Dung, G.D. and Adole, B.S., "Review of multilevel inverters and their control techniques", ***European Journal of Engineering and Technology Research***, Vol. 5, No. 6, (2020), 659-664. https://doi.org/10.24018/ejeng.2020.5.6.1707
11. Gallaj, A., Beiraghi, M., Fallah Ardashir, J. and Ghanizadeh, R., "New switched-capacitor multilevel converter with reduced elements", ***Journal of Energy Management and Technology***, Vol. 4, No. 4, (2020), 12-20. doi: 10.22109/JEMT.2020.199538.1193.
12. Khan, M.N., Barzegarkhoo, R., Siwakoti, Y., Khan, S., Li, L. and Blaabjerg, F., "A new switched-capacitor multilevel inverter with soft start and quasi resonant charging capabilities", ***International Journal of Electrical Power & Energy Systems***, Vol. 135, (2022), 107412. https://doi.org/10.1016/j.ijepes.2021.107412
13. Naik, B.S., Suresh, Y., Venkataramanaiah, J. and Panda, A.K., "A hybrid nine-level inverter topology with boosting capability and reduced component count", ***IEEE Transactions on Circuits and Systems II: Express Briefs***, Vol. 68, No. 1, (2020), 316-320. doi: 10.1109/TCSII.2020.2998496.

14. Samadaei, E., Kaviani, M. and Bertilsson, K., "A 13-levels module (k-type) with two dc sources for multilevel inverters", ***IEEE Transactions on Industrial Electronics***, Vol. 66, No. 7, (2018), 5186-5196. doi: 10.1109/TIE.2018.2868325.

15. Jahan, H.K., Abapour, M. and Zare, K., "Switched-capacitor-based single-source cascaded h-bridge multilevel inverter featuring boosting ability", ***IEEE Transactions on Power Electronics***, Vol. 34, No. 2, (2018), 1113-1124. doi: 10.1109/TPEL.2018.2830401.

16. Hussan, M.R., Sarwar, A., Siddique, M.D., Iqbal, A. and Alamri, B., "A cross connected asymmetrical switched-capacitor multilevel inverter", ***IEEE Access***, Vol. 9, (2021), 96416-96429. doi: 10.1109/ACCESS.2021.3093826.

17. Taghvaie, A., Adabi, J. and Rezanejad, M., "A self-balanced step-up multilevel inverter based on switched-capacitor structure", ***IEEE Transactions on Power Electronics***, Vol. 33, No. 1, (2017), 199-209. doi: 10.1109/TPEL.2017.2669377.

18. Taghvaie, A., Adabi, J. and Rezanejad, M., "A multilevel inverter structure based on a combination of switched-capacitors and dc sources", ***IEEE Transactions on Industrial Informatics***, Vol. 13, No. 5, (2017), 2162-2171. doi: 10.1109/TII.2017.2710265.

19. Babaie, M., Mehrasa, M., Sharifzadeh, M. and Al-Haddad, K., "Floating weighting factors ann-mpc based on lyapunov stability for seven-level modified puc active rectifier", ***IEEE Transactions on Industrial Electronics***, Vol. 69, No. 1, (2021), 387-398. doi: 10.1109/TIE.2021.3050375.

20. Rawa, M., Siddique, M.D., Mekhilef, S., Mohamed Shah, N., Bassi, H., Seyedmahmoudian, M., Horan, B. and Stojcevski, A., "Dual input switched-capacitor-based single-phase hybrid boost multilevel inverter topology with reduced number of components", ***IET Power Electronics***, Vol. 13, No. 4, (2020), 881-891. https://doi.org/10.1049/iet-pel.2019.0826

21. Siddique, M.D., Mekhilef, S., Sarwar, A., Alam, A. and Mohamed Shah, N., "Dual asymmetrical dc voltage source based switched capacitor boost multilevel inverter topology", ***IET Power Electronics***, Vol. 13, No. 7, (2020), 1481-1486. https://doi.org/10.1049/iet-pel.2019.1567

22. Shalchi Alishah, R., Hosseini, S.H., Babaei, E., Sabahi, M. and Zare, A., "Extended high step-up structure for multilevel converter", ***IET Power Electronics***, Vol. 9, No. 9, (2016), 1894-1902. https://doi.org/10.1049/iet-pel.2015.0893

23. Zamiri, E., Vosoughi, N., Hosseini, S.H., Barzegarkhoo, R. and Sabahi, M., "A new cascaded switched-capacitor multilevel inverter based on improved series–parallel conversion with less number of components", ***IEEE Transactions on Industrial Electronics***, Vol. 63, No. 6, (2016), 3582-3594. doi: 10.1109/TIE.2016.2529563.

24. Fahad, M., Tariq, M., Faizan, M., Ali, A., Sarwar, A., Dehghani Tafti, H., Ahmad, S. and Shah Noor Mohamed, A., "A dual source switched-capacitor multilevel inverter with reduced device count", ***Electronics***, Vol. 11, No. 1, (2021), 67. https://doi.org/10.3390/electronics11010067

25. Yaqoob, M.T., Rahmat, M.K. and Maharum, S.M.M., "Modified teaching learning based optimization for selective harmonic elimination in multilevel inverters", ***Ain Shams Engineering Journal***, Vol. 13, No. 5, (2022), 101714. https://doi.org/10.1016/j.asej.2022.101714

26. Nguyen, M.H. and Kwak, S., "Nearest-level control method with improved output quality for modular multilevel converters", ***IEEE Access***, Vol. 8, (2020), 110237-110250. doi: 10.1109/ACCESS.2020.3001587.

27. Sarwar, M.I., Sarwar, A., Farooqui, S.A., Tariq, M., Fahad, M., Beig, A.R. and Alamri, B., "A hybrid nearest level combined with pwm control strategy: Analysis and implementation on cascaded h-bridge multilevel inverter and its fault tolerant topology", ***IEEE Access***, Vol. 9, (2021), 44266-44282. doi: 10.1109/ACCESS.2021.3058136.

28. Rahimi Mirazizi, H. and Agha Shafiyi, M., "Evaluating technical requirements to achieve maximum power point in photovoltaic powered z-source inverter", ***International Journal of Engineering, Transactions C: Aspects,***, Vol. 31, No. 6, (2018), 921-931. doi: 10.5829/IJE.2018.31.06C.09.

29. Alemi-Rostami, M. and Rezazadeh, G., "Selective harmonic elimination of a multilevel voltage source inverter using whale optimization algorithm", ***International Journal of Engineering, Transactions B: Applications***, Vol. 34, No. 8, (2021), 1898-1904. doi: 10.5829/IJE.2021.34.08B.11.

30. Arehpanahi, M. and Paknia, D., "A new single-phase symmetrical cascade multilevel inverter with low number of power switches", ***International Journal of Engineering, Transactions B: Applications***, Vol. 31, No. 8, (2018), 1228-1233. doi: 10.5829/ije.2018.31.08b.10.

31. Lee, S.S., Lee, K.-B., Alsofyani, I.M., Bak, Y. and Wong, J.F., "Improved switched-capacitor integrated multilevel inverter with a dc source string", ***IEEE Transactions on Industry Applications***, Vol. 55, No. 6, (2019), 7368-7376. doi: 10.1109/TIA.2019.2893850.

32. Barzegarkhoo, R., Moradzadeh, M., Zamiri, E., Kojabadi, H.M. and Blaabjerg, F., "A new boost switched-capacitor multilevel converter with reduced circuit devices", ***IEEE Transactions on Power Electronics***, Vol. 33, No. 8, (2017), 6738-6754. doi: 10.1109/TPEL.2017.2751419.

Persian Abstract

چکیده

در این مقاله ، یک اینورتر چند سطحی جدید افزاینده نوع خازن سوئیچ شده که قادر به تولید ۱۹ سطح ولتاژ با استفاده از تنها ۱۰ سوئیچ ، ٤ دیود ، ۲ خازن و ۲ منبع DC است ارائه شده است. ویژگی های اصلی توپولوژی پیشنهادی عبارتند از: ۱) استفاده از تعداد بسیار کمی ازعناصر نیمه هادی ، ۲) ولتاژ ایستایی (تحمل) بسیار پایین برابر با ٦.٥٥ و ۳) خاصیت خود متعادلی ولتاژهای خازن‌ها. به منظور ارائه سیگنال‌های سوئیچینگ مورد نظر به سوئیچ ها ، روش کنترل نزدیکترین سطح بکارگرفته شده است. برای ارزیابی مزایای توپولوژی طراحی شده اینورتر ۱۹ سطحی جدید، از دیدگاه تعداد سوئیچ ها ، تعداد منابع DC ، تعداد خازن ها و همچنین ولتاژ ایستایی ، یک مقایسه در مقابل آخرین توپولوژی های ارائه شده انجام شده است. همچنین ، به منظور ارزیابی عملکرد اینورتر پیشنهاد شده و اعتبار سنجی آن ، چندین آزمایش در بارهای مختلف با استفاده از پردازشگر TMS320F28379D DSP مورد آزمایش قرار گرفته است. نتایج شبیه سازی و آزمایشگاهی همگی حاکی از برتری توپولوژی پیشنهادی در برابر ساختارهای قبلی خود است.

IJE TRANSACTIONS B: Applications Vol. 36, No. 02, (February 2023) 264-275

International Journal of Engineering

Journal Homepage: www.ije.ir

Application of Random Radial Point Interpolation Method to Foundations Bearing Capacity Considering Progressive Failure

S. Hashemi, R. Naderi*

Civil Engineering Department, Shahrood University of Technology, Shahrood, Iran

PAPER INFO

Paper history:
Received 16 July 2022
Received in revised form 15 October 2022
Accepted 23 October 2022

Keywords:
Bearing Capacity of Foundation
Radial Point Interpolation Method
Probabilistic Analysis
Monte Carlo Simulation
Progressive Failure

ABSTRACT

In conventional analyzes of foundations failure, strengh parameters are assumed constant. However, during the failure, soil resistance exhibits maximum and residual amounts, and its strength decreases prematurely by increasing the plastic strain. In addition to change soil strengh parameters in the progressive mechanism, the non-uniform nature of the soil also causes spatial variations of these parameters. Therefore, geotechnical systems should be considered in terms of the uncertainty of soil parameters values, uncertainly using the concepts of statistics and probabilities. The purpose of this study is to investigate foundations in meshless method. In this article, radial point interpolation method (RPIM), a meshless method is proposed for simulation of soil foundation. Difficulties of methods related to mesh are solved by using this method. A code has been developed based on this method and some examples are solved for analyzing the code. In this research, a RPIM in combination with a random field was used to model the spatial variations of soil strengh properties and foundation bearing capacity analysis. For probabilistic analysis, random field is also used to determine the cohesion and the friction angle as well as the dilation angle based on their mean values and standard deviation. In order to investigate the application of the point interpolation method with randomized radial functions, a foundation with definite geometry has been analyzed deterministic and probabilistic and its safety factor has been investigated. Based on the analysis of the progressive failure modeling, it is concluded that the actual failure of the soil and the occurrence of continuous displacements occur simultaneously with the formation of a progressive mechanism of soil failure and the arrival of the slipping path to the ground. In the following, probabilistic distribution functions of the safety factor were determined by probabilistic analysis and the production of random fields, and then the statistical parameters are calculated.

***doi**: 10.5829/ije.2023.36.02b.07*

NOMENCLATURE

κ^{ps}	development of stiffness strain	c'_p	maximum cohesion
$\Delta\varepsilon_1^{ps}\ \Delta\varepsilon_3^{ps}$	development of the plastic strain along the direction of maximum and minimum stress are the main	c'_r	residual cohesion
$\Delta\varepsilon_m^{ps}$	development of the volumetric plastic shear strain correction factor	φ'_p	maximum internal friction angle
$\kappa_r^{ps}\ \ \kappa_p^{ps}$	strain values are threshold	φ'_r	residual internal friction angle

1. INTRODUCTION

Analysis of soil bearing capacity under foundations is always one of the challenging problems that has been remained in geotechnical engineering and it has been the subjected by numerous researches over the past years [1]. In such issues, the occurrence of soil rupture and design failure can be caused by not paying attention to locative changes in soil properties and complexity of the deterioration mechanism. Or it can be caused due to the problems and limitations of the modeling tools under consideration, which could leads to financial and fatality loss in engineering projects.

*Corresponding Author Institutional Email: rz_naderi@yahoo.com (R. Naderi)

Please cite this article as: S. Hashemi, R. Naderi, Application of Random Radial Point Interpolation Method to Foundations Bearing Capacity Considering Progressive Failure, ***International Journal of Engineering, Transactions B: Applications***, Vol. 36, No. 02, (2023), 264-275

Numerous studies had been done in the field of numerical modeling soil interaction and behavior at failure and analysis of its deterioration mechanism [2, 3]. However, the real concept of soil failure mechanism is not fully understood and its modeling is always accompanied by ambiguities and uncertainties. In most studies, it is assumed that the failure occurs simultaneously along the slip surface in the soil mass. However, the plastic strains were not uniform due to an increase in loading or decrease in soil strength and thereby the process of failure will be progressive. In addition, in most studies it was assumed that the soil parameters remain unchanged even at large strains. Considering this assumption in issues such as analysis soil bearing capacity under foundations is incorrect, Because soil strengh parameters show maximum and residual values, also soil strength process decreases with increasing plastic strain. According to this concept, numerical analyzes of progressive failure has been used in various geotechnical issues, until now [4-6].

In addition to changes of soil strengh parameters during the progressive mechanism, the non-uniform nature of the soil causes spatial changes in these parameters. Soil has always been recognized as heterogeneous material and its spatial specification changes has important role in soil behavior. Therefore concepts of statistics and probabilities should be used in geotechnical systems which have uncertainty in soil parameters values. In purpose of checking the locative changes of soil strengh parameters effects on soil behavior, soil modeling done in form of one multidimensional process along with several random parameters in probabilistic analysis. Random field theory is the basis of providing such model. Details of random field theory and its application in geotechnical engineering are fully described by Zdravkovic et al. [7]. By use of this theory numerous researchers have examined the impact of spatial changes in soil parameters [8, 9].

It should be noted that deterministic and probabilistic analysis of the progressive failure process are only possible by using numerical techniques such as finite elements method that are able to simulate the creation and development of a shear zone with a focus on strain. Although finite elements method (FEM) widely used at analysis of foundation bearing capacity. However, this method has problems like stress discontinuity at boundary element and low accuracy at analysis of large deformations and weakness in convergence caused by entanglement elements. This category of finite elements method problems basically related to meshing.

In the context of deformation problems, the finite elements method suffers from several problems, which are mainly caused by its complexity of mesh element. In fact, main weakness of methods which is perform their analysis based on mesh is by every changes in the geometry of the problem, mesh needs to regenerated and this is a time-consuming task and in addition it increases complexity and decreases the accuracy of results. Other problem of these methods include low accuracy in stress calculation, especially in the case of complex phenomena such as crack propagation or phase change (due to severe discontinuities).

Therefore one suitable way to get ride of this difficulties is using meshless methods (MFMs) to analysis the stability issues with enough accuracy. Meshless methods developed by Lucy [10] using the smoothed particle hydrodynamics (SPH) method for the modeling physical astronomy phenomena. Nowadays, this method is known as an effective numerical tool for analyzing various engineering problems and several studies have been conducted on the application of this method in various branches such as geotechnical engineering [11-13].

Another issue in analysis of instability of soil problems is necessity of combining desire numerical method by concepts of statistics and probability. Soil in its natural is considered as a material with the most changes in behavioral characteristics among engineering materials. Therefore, uncertainty in geotechnical engineering and soil mechanics is considered a reality and considering it has made the engineering perspective more open in analysis of stability issues.

In this research, it has been used point interpolation method with radial functions in combination with random field for modeling locative variations of soil strengh parameters and analysis of soil bearing capacity under foundations. In order to consider the progressive failure of soil, the elastoplastic solution method has been used with the extended Mohr-Coulomb model in terms of strain-softening behaviour. Firstly, strengh parameters such as cohesion and internal friction angle are considered indefinitely with mean values and standard deviation to perform this analysis. Then random fields of indefinite parameters are generated by examining the correlation between domain points. These data along with other parameters values use as input to point interpolation method with radial functions in analysis of soil bearing capacity of foundations. Probabilistic analysis of this method is placed in combination with Monte Carlo simulation. In other words, stability analysis is repeated as much as the number of random fields created. The output of this process is probabilistic distributions for soil bearing capacity safety factor.

In meshless method, due to creation of large number of unknowns in equation that should solved simultaneously, the volume calculations is large. So first step in using this method is using computer programming to control this system of equations. In this research, MATLAB programming software is used as a matrix calculator for analysis in combination with elastoplastic theory and progressive failure model to analyze instability in soil problems. Key features of using MATLAB are simplicity and ease of working with it, a huge library of predefined functions, high ploting power and finally, having a comprehensive and complete guide on how to execute commands.

In this paper authors focused on analyzing the influence of some relevant aspects of random characterization of soil by means of numerical algorithm, as follows:

• the rule of anisotropy in random field approach to soil parameters, implemented by analyzing different values of correlation length along vertical and horizontal direction;

• to investigate random variability of soil properties based on progressive failure data resulting.

Hereinafter is organized as follows. The next sections briefly describes the progressive rupture. Then formulations of RPIM method are described and random field is explained. In following sections, we perform numerical model, deterministic and probabilistic analysis of foundation bearing capacity which are described. Then results of the analysis are presented. We finalized this article by the conclusions section.

2. PROGRESSIVE FAILURE IN SOIL

The failure caused by large displacements in soil problems is made by the progressive expansion of inelastic shear bands. Over time, many efforts have been made to identify the spread of failure in soil, and until now, non-uniform distribution of strain is known as one of main causes of progressive failure. Suitable conditions of progressive failure provides by reduction of shear strength in proportion to shear plastic strain, from its maximum to residual value. Analysis of such issues is possible by applying a model considering strain-softening behaviour. Some of complex problems in geotechnical engineering are analyzing the slope, bearing capacity and other soil problems in regard to strain-softening behavior. In such problems, specificity of material is changed at different stages from maximum to residual value, and failure is occured by applying strength reduction technique with increasing the strain. In general, this type of failure, failing happen in part of soil in which strains are locally formed. Soil strength decreases from a maximum value to residual value by increasing strain in this area. The application of reprocessing stress method causes expansions on shear zone and its penetration into adjacent soil. Therefore, the slip surface is following progressive expansion along with area by mean strength between maximum and residual value.

Various strain-softening behaviours have always been proposed to calculate soil strength parameters during strain changes. Among these, we can refer to extended model of Mohr-Columbus, which allows materials to behave with strain-softening. In this model, the properties are defined as linear functions of a piece of plastic shear strain κ^{ps}. The development of hardening strain is also presented as follows:

$$\Delta\kappa^{ps} = \frac{1}{\sqrt{2}}\sqrt{(\Delta\varepsilon_1^{ps} - \Delta\varepsilon_m^{ps})^2 + (\Delta\varepsilon_m^{ps})^2 + (\Delta\varepsilon_3^{ps} - \Delta\varepsilon_m^{ps})^2} \tag{1}$$

where $\Delta\varepsilon_1^{ps}$ and $\Delta\varepsilon_3^{ps}$ represented plastic strain of maximum and minimum main stress. $\Delta\varepsilon_m^{ps}$ is development of the volumetric plastic shear strain that is defined as follows:

$$\Delta\varepsilon_m^{ps} = (\Delta\varepsilon_1^{ps} + \Delta\varepsilon_3^{ps})/3 \tag{2}$$

According to studies in soil problems, a model with three-component partial linear function with strain-softening behaviour according to Figure 1 is often used [7].

The characteristics of this model are presented in the form of following relations:

$$c' = \begin{cases} c'_p & \kappa^{ps} \le \kappa_p^{ps} \\ c'_r + \dfrac{\kappa^{ps} - \kappa_r^{ps}}{\kappa_p^{ps} - \kappa_r^{ps}}(c'_p - c'_r) & \kappa_p^{ps} \le \kappa^{ps} \le \kappa_r^{ps} \\ c'_r & \kappa^{ps} \le \kappa_r^{ps} \end{cases} \tag{3}$$

$$\varphi' = \begin{cases} \varphi'_p & \kappa^{ps} \le \kappa_p^{ps} \\ \varphi'_r + \dfrac{\kappa^{ps} - \kappa_r^{ps}}{\kappa_p^{ps} - \kappa_r^{ps}}(\varphi'_p - \varphi'_r) & \kappa_p^{ps} \le \kappa^{ps} \le \kappa_r^{ps} \\ \varphi'_r & \kappa^{ps} \le \kappa_r^{ps} \end{cases} \tag{4}$$

In these relations c'_p, c'_r are the maximum and residual cohesion, as well as φ'_p and φ'_r which is the maximum and residual internal friction angle, respectively. Also κ_r^{ps}, κ_p^{ps} are threshold strain values. The values of these parameters are obtained by performing conventional tests [7, 14].

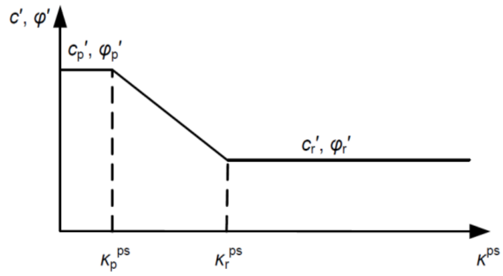

Figure 1. Strain-softening model

3. POINT INTERPOLATION METHOD WITH AMPLIFIED RADIAL FUNCTION

Point interpolation method is one of kind meshless methods that uses finite series form to represent the approximation function. For this purpose the scalar function u(x,y) is considered in two-dimensional space created by a bunch of scattered nodes. The point interpolation relationship of the function u(x,y) at the point (x,y) is given as follows:

$$u(x,y)=\sum_{i=1}^{m} B_i a_i \qquad (5)$$

In this relation Bi(x,y) is base function in two-dimensional coordinates, m is the number of the base function and ai is the coefficient related to the base function. In the point interpolation method, basic functions can be selected as polynomial functions. As a result, derivation shape functions are easily performed. Simplicity and appropriate accuracy of results are key features of this method. However, point interpolation method with polynomial basic functions always suffers from solvation of individual torque matrix. For fixing this, interpolation method used radial functions. On the other hand, in order to take advantage of polynomial functions, we can strengthen the model by adding polynomial phrase as basic functions until desire order. In this case, point interpolation equation with the amplified radial basis functions for u(x,y) is written as follows:

$$u(x,y)=\sum_{i=1}^{n} R_i(x,y)a_i+\sum_{j=1}^{m} P_i(x,y)b_i=\mathbf{R}^T(x,y)\mathbf{a}+\mathbf{P}^T(x,y)\mathbf{b} \qquad (6)$$

In this equation, R and P are radial basic functions and polynomial of n number points nodes at local support domain point with (x,y) coordinates and m is a number of polynomial phrase items use to basic functions. The phrases of polynomial functions in specific spatial coordinates are selected using the Pascal triangle [15]. To determine the values of ai and bj, it is necessary to form n + m equation. In this regard, n equations are created by applying node values to the function u(x,y) as follows:

$$u_k=u(x_k,y_k)=\sum_{i=1}^{n} R_i(x_k,y_k)a_i+\sum_{j=1}^{m} p_j(x_k,y_k)b_j \quad k=1,2,\ldots,n \qquad (7)$$

Equation (7) rewrite in Matrix form as follows:

$$\mathbf{U_s}=\mathbf{R_Q a}+\mathbf{P_m b} \qquad (8)$$

In this equation, RQ and Pm are from matrices in the following form in two-dimensional space, respectively:

$$\mathbf{R_Q}=\begin{bmatrix} R_1(x_1,y_1) & R_2(x_1,y_1) & \ldots & R_n(x_1,y_1) \\ R_1(x_2,y_2) & R_2(x_2,y_2) & \ldots & R_n(x_2,y_2) \\ \vdots & \vdots & \ddots & \vdots \\ R_1(x_n,y_n) & R_2(x_n,y_n) & \ldots & R_n(x_n,y_n) \end{bmatrix} \qquad (9)$$

$$\mathbf{P_m}=\begin{bmatrix} p_1(x_1,y_1) & p_2(x_1,y_1) & \cdots & p_m(x_1,y_1) \\ p_1(x_2,y_2) & p_2(x_2,y_2) & \cdots & p_m(x_2,y_2) \\ \vdots & \vdots & \ddots & \vdots \\ p_1(x_n,y_n) & p_2(x_n,y_n) & \cdots & p_m(x_n,y_n) \end{bmatrix} \qquad (10)$$

In radial functions, the only available variable is ri , which is distance between two spatial coordinates (x,y) and (xi,yi). Different radial functions provided for performing analysis. In this research, Multiquadratics radial function with following form of equation has been used:

$$R_i(x,y)=(r_i^2+c^2)^q=[(x-x_i)^2+(y-y_i)^2+c^2]^q \qquad (11)$$

In this relation, c and q are shape parameters. The best value for these parameters is obtained based on type of problem and performing numerical tests. In this study, according to analysis on shape parameters in solid mechanics, the values of 1.42 and 0.98 have been used for c and q , respectively [15]. The m remaining equation will be obtained from unique actions conditions answer as follows:

$$\sum_{i=1}^{n} p_j(x_i,y_i)a_i=0 \quad j=1,2,\ldots,m \qquad (12)$$

Or in matrix form:

$$\mathbf{P_m^T}a=0 \qquad (13)$$

Therefore, Equation (8) is rewritten in the following form:

$$\mathbf{\bar{U}_s}=\begin{Bmatrix}\mathbf{U_s}\\ \mathbf{0}\end{Bmatrix}=\begin{bmatrix}\mathbf{R_Q} & \mathbf{P_m}\\ \mathbf{P_m^T} & \mathbf{0}\end{bmatrix}\begin{Bmatrix}\mathbf{a}\\ \mathbf{b}\end{Bmatrix}=\mathbf{Ga_0} \qquad (14)$$

In this regard:

$$\mathbf{a_0}=[a_1\ \ a_2\ \ \ldots\ \ a_n\ \ b_1\ \ b_2\ \ \ldots\ \ b_m] \qquad (15)$$

$$\mathbf{\bar{U}_s}=[u_1\ \ u_2\ \ \ldots\ \ u_n\ \ 0\ \ 0\ \ \ldots\ \ 0] \qquad (16)$$

Therefore, according to Equation (14), we can write:

$$\mathbf{a_0}=\begin{Bmatrix}\mathbf{a}\\ \mathbf{b}\end{Bmatrix}=\mathbf{G^{-1}\bar{U}_s} \qquad (17)$$

Finally, by combination of Equations (17) and (6) we have:

$$u(x)=\{\mathbf{R}^T(x)\ \ \mathbf{P}^T(x)\}\mathbf{G^{-1}\bar{U}_s}=\mathbf{\bar{\Phi}^T}(x)\mathbf{\bar{U}_s} \qquad (18)$$

In this regard:

$$\mathbf{\bar{\Phi}^T}=\{\varphi_1(x)\ \varphi_2(x)\cdots\varphi_n(x)\ \varphi_{n+1}(x)\ \varphi_{n+2}(x)\cdots\varphi_{n+m}(x)\} \qquad (19)$$

After calculating vector of shape functions, for desire domain of support with n number of nodes in it, the vector of main shape function is considered as follows:

$$\mathbf{\Phi^T}=\{\varphi_1(x)\ \varphi_2(x)\cdots\varphi_n(x)\} \qquad (20)$$

4. RANDOM FIELD

Soil is one of the materials in which its characteristics are related to the location. In other words, properties of these materials vary from one place to other place. So it is not possible to use usual methods of statistics and probability, which are based on independence observations of samples. On the other hand, during soil exploration operations, its characteristics are obtained only in sampled places. However, values of these specifications remain unknown in other parts of the area. In this regard, random field theory is known solution used to obtain random values in different parts of the domain area to deal with uncertainty [16]. Random field theory can effectively explain the spatial variation of soil properties by correlation function. In fact, this theory is a forecasting method to predict desired characteristics of other points based on limited available information. In this method, a specific soil feature is almost identical at very close points and will not be related at distant points. According to this purpose, relationship between the points in domain area are defined by the correlation function. Among the existing correlation functions. We can mention Gaussian, triangular, etc. correlation functions. In this research, exponential correlation function is used to construct a correlation matrix as follows:

$$\rho = \exp(-\frac{\tau_x}{\theta_x} - \frac{\tau_y}{\theta_y}) \quad (21)$$

In this equation, τx and τy are distances in x and y directions between two points under consideration and θx and θy are correlation lengths in the x and y directions, respectively. The length of correlation represents the threshold distance that shows effect of parameters correlation. The correlation function is applied to all points in relation to other points and the correlation matrix for n points system is performed as follows:

$$\boldsymbol{\rho} = \begin{bmatrix} \rho_{11} & \rho_{12} & \cdots & \rho_{1n} \\ \rho_{21} & \rho_{12} & \cdots & \rho_{2n} \\ \vdots & \vdots & \ddots & \vdots \\ \rho_{n1} & \rho_{n2} & \cdots & \rho_{nn} \end{bmatrix} \quad (22)$$

In next step, by decomposing this matrix using Cholesky method, a top and bottom triangular matrix is obtained:

$$\boldsymbol{\rho} = \mathbf{L}\mathbf{L}^{\mathbf{T}} \quad (23)$$

Then, desire values of constructing a random field are obtained by multiplying the lower triangular matrix L and normal random values of standard Z that generated by random numbers in standard norm with mean values of zero and standard deviation of one, as follows:

$$\mathbf{G} = \mathbf{L} \times \mathbf{Z} \quad (24)$$

Finally, by using G matrix values and using the following equation, random field for variable x is obtained by the following expresion:

$$\mathbf{X}_{\mathbf{R.F}} = \mu(x) + \mathbf{G}.\sigma(x) \quad (25)$$

In this equation, $\mu(x)$ and $\sigma(x)$ are mean and standard deviation of the random field of x respectively.

5. NUMERICAL MODELING AND ANALYSIS METHOD

The intended specifications for soil behavior at maximum and residual conditions are given in Table 1. The soil under the foundation including a layer of soil with the characteristics of conventional parameters are stated in Table 2. In this research, the bearing capacity of the foundation is investigated in the form of plain strain conditions. In this type of analysis, geometry, problem properties, and field variables are defined in terms of two spatial coordinates, x and y.

5. 1. Geometry and Boundary Conditions

In order to investigate the application of point interpolation method with random radial functions, a foundation with the geometry shown in Figure 2 was analyzed deterministic and the probabilistic. The soil under the foundation with a depth of 5 meters and a radius of 10 meters from the center of the foundation is examined. This geometry is determined based on formation of a failure wedge under foundation and depth of its stress impact [17]. The boundary conditions are as follows: the bottom of soil domain (BD) is fixed in both directions, while on other sides of domain (AB and CD), horizontal

TABLE 1. Values of soil resistance parameters at maximum and residual state

Parameter	Maximum amount	Residual amount
Internal friction angle (°)	20	15
Cohesion (kN / m 2)	20	5
Dilation angle (°)	10	0.0005

TABLE 2. Values of definite soil parameters

Parameter	The amount of
Modulus of elasticity (kN/m^2)	100000
Specific gravity (kN/m^3)	16
Poisson ratio	0.3

displacements are fixed only which is allowing nodes for a vertical displacement.

5. 2. Methodology The first step in analyzing point interpolation method with radial functions is to define domain of problem by distributing its node. The number and arrangement of nodes are chosen so that simulated body is as close to reality as possible. The choice of node arrangement is often dictated by the geometry of problem and number of independent points needed to define the scope of problem. In order to perform problem analysis, soil amplitude under the studied foundation is modeled by nodes according to Figure 3 by point interpolation method with radial functions.

Integration with surface or volume is required in order to estimate stiffness and force matrix. Therefore, it is necessary to use appropriate numerical integration method to calculate relationships in problem domain. In this research, stress point method due to high convergence power has been used to perform numerical integration. For this purpose, we defined points in domain problem between nodes of point interpolation method with radial functions. Then voronoi cells are created around these points, so that area allocated to each stress point by each cell represents the integral weight of that stress point. Figure 4 shows defined stress points along with their Voronoi cells.

The result of bearing capacity of foundation analysis is safety factor parameter. This quantity is equal to coefficient on which main parameters of strengh, c and φ , are divided and thus decreased shear strength under a constant weight force, resulting in failure. For this purpose, during analysis, weight load is obtained by integral of each support domain according to considered value of specific gravity of materials and applied to problem during its development. Then a strength reduction loop is considered in program, which gradually reduces the soil strength to perform failure by performing elastoplastic analysis of soil. Accordingly, multiplied resistance parameters of soil are expressed as follows:

$$\begin{aligned} \varphi_f &= \arctan(\tan\varphi/srf) \\ c_f &= c/srf \end{aligned} \tag{26}$$

The second step is to perform probabilistic analysis, choosing appropriate distribution for the input parameters, which in this research are cohesion, internal friction angle and dilation angle, which are considered as probabilities with specified mean values and standard deviation.

Correlation between different points of domain is checked in third step of this method. In fact, at this stage, relationship between different points can be created to desire parameter based on their spatial distance defined by building a correlation matrix on a suitable random field . In this research, integral points or stress points are used in meshless method to define correlation. We should mention that these points represent specified region of corresponding Voronoi cell. Based on these by using the appropriate correlation function such as the Markov function, the correlation matrix is created and random field related to each parameter is created as described.

In the next step, Monte Carlo simulation method is used after constructing a random field for selected non-deterministic parameters. In fact, constructed random fields used as input of numerical solution method. After analysis, a value is calculated for considered output parameter, which is used as safety factor in this research. Based on Monte Carlo method concepts, this process is repeated 5000 times and according to repetitions number, different values are obtained for the desired output. In other words, by using Monte Carlo method, according to repetitions number of solution process for different input random fields, the final output of problem will be different values for which a probability distribution that can be obtained after statistical analysis.

In last step, after determining probability distribution value of random variable of safety factor, performing a probability analysis in form of calculating target parameters such as reliability index, probability of failure or coefficient of variation are examined.

Figure 5 shows methodology flowchart.

6. DETERMINISTIC ANALYSIS OF FOUNDATION BEARING CAPACITY

In this section, soil under desired foundation is definitively analyzed using parameters of Table 2 and

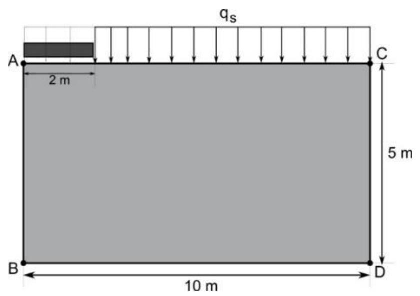

Figure 2. The geometry and boundary conditions foundation

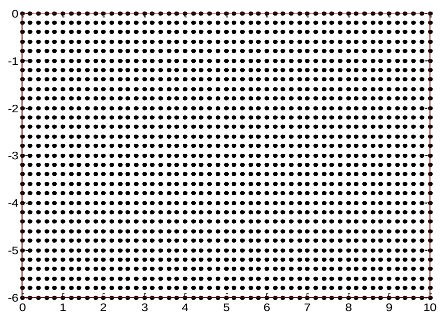

Figure 3. Domain separated by knot

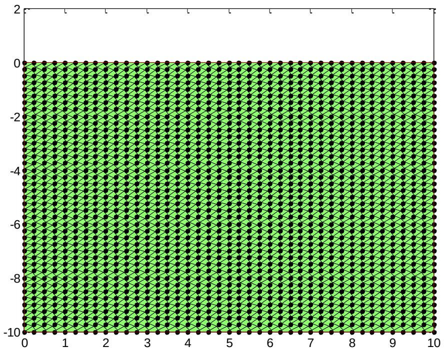

Figure 4. View stress points and related Voronoi cells

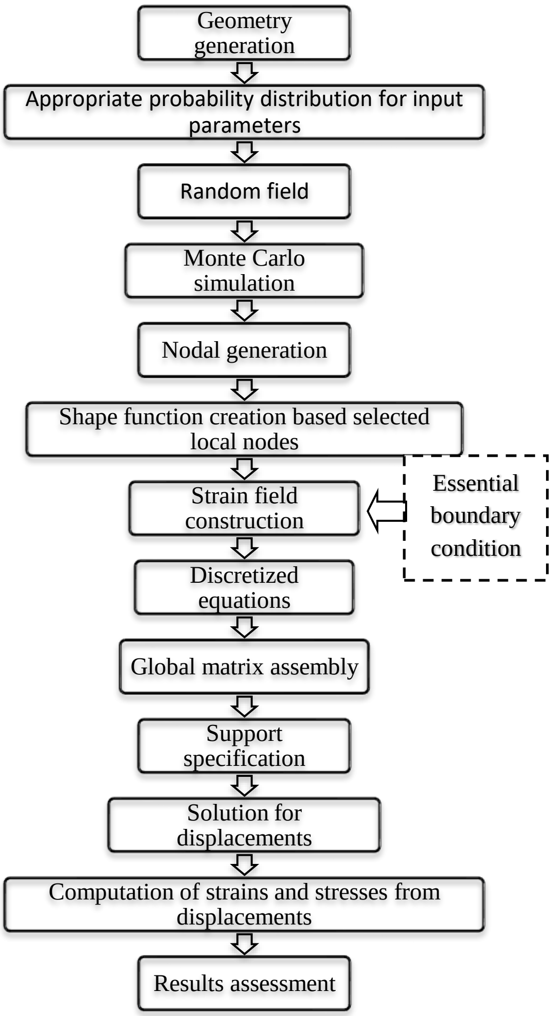

Figure 5. Methodology flowchart

soil parameters in maximum and residual conditions presented in Table 1 separately. The safety factors related to analysis of bearing capacity of desired foundation have been done separately using point interpolation method with radial functions using soil parameters in maximum and residual state without considering progressive failure.

In continuation of deterministic problem analysis on desired foundation is examined in terms of progressive failure model. According to model with strain-softening behaviour in simulation of progressive failure, values of strengh parameters (friction angle and cohesion) are modified using Equations (3) and (4) with a value between maximum and minimum. Figures 6(a) to 6(h) show progression of a deviant plastic strain during repetition of elastoplastic solution in soil slope under foundation. According to Figure 6(a), it is observed that approximately in repetition number 10, plastic strains have formed in edge of foundation area. Also, it shows increasing repetition in soil area under foundation in proportion to failure mechanism on slip path (Figure 6(b)). The plastic strains according to Figure 6(c) in repetition number less than 30 is to a depth of 3 meters under foundation formed failure mechanism. Then, according to Figures 6(d) to 6(y), it expands with increasing repetition failure advances, so that large displacements occur in different parts of soil under foundation.

6. 1. Verification The desired foundation has been investigated by the finite elements method using Plaxis software and results are presented in Table 3 in order to

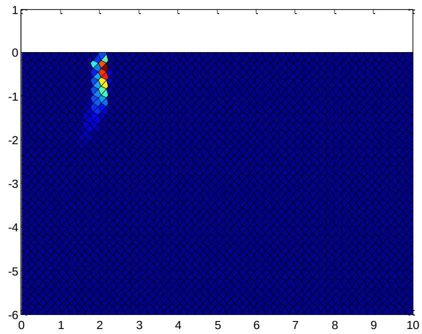

(a) 10 Repetition

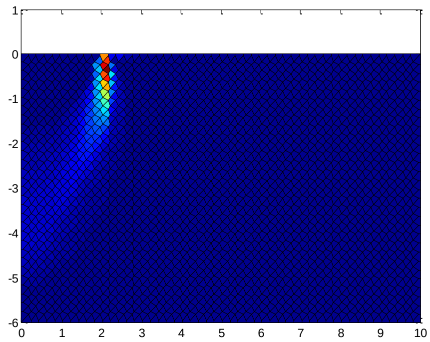

(b) 20 Repetition

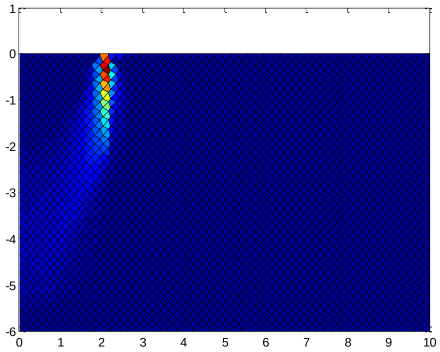

(c) 30 Repetition

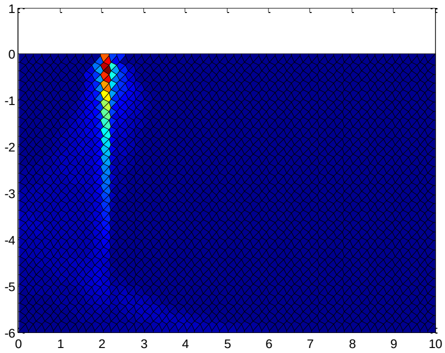

(d) 50 Repetition

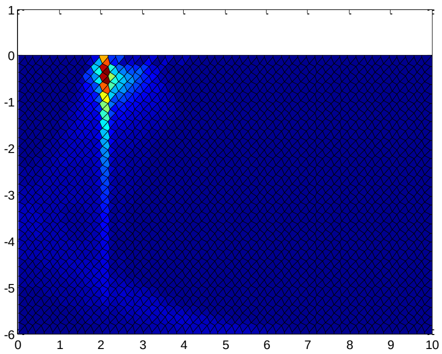

(e) 80 Repetition

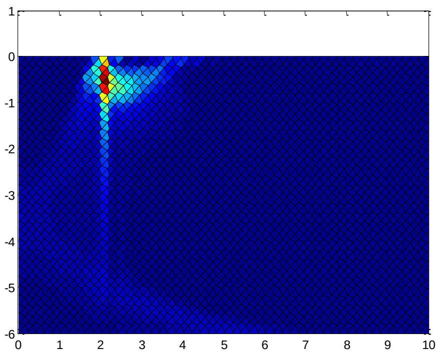

F) 150 Repetition

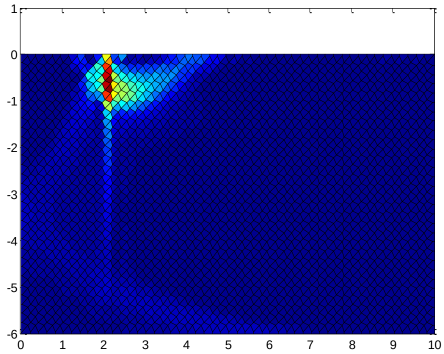

G) 200 Repetition

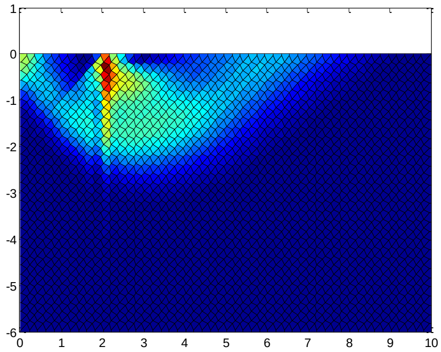

H) 400 Repetition

Figure 6. progressive shear plastic strain at levels of elastoplastic solution

validate numerical program of solution by point interpolation method with radial functions. The deformed amplitude of soil under foundation is shown in Figure 7 by performing analysis on maximum soil parameters. According to safety factors presented in Table 3, it is possible to compare results of above methods. According to results presented in table, it can be seen that safety factor changes obtained from point interpolation method with radial functions are in a more limited range than finite elements method. It is also known that safety factor of foundation bearing capacity decreases by changing values of parameters from maximum to residual state. Therefore, type of failure in soil under investigated foundation is progressive.

TABLE 3. Comparison of values of safety factors obtained by point interpolation methods with radial functions and finite elements

Method of analysis	Maximum mode	Residual mode
Interpolation with radial functions	4.08	2.18
Finite elements	4.31	1.97

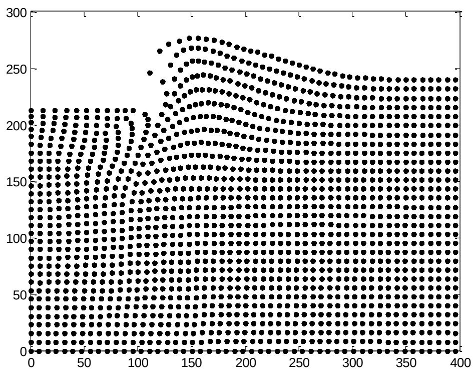

Figure 7. Domain change shape found soil under foundation

7. PROBABILISTIC ANALYSIS OF FOUNDATION BEARING CAPACITY

Influential parameters in process of modeling soil problems have inherent uncertainties. Therefore, using only one value will not represent changes in these parameters. Therefore, solution to this problem is generating random field using statistical distribution for each parameter as a input of computational algorithm in stability problem analysis. Hence, in order to perform probabilistic analysis using point interpolation method with random radial functions, appropriate distribution for input parameters is selected, which is considering by mean value and standard deviation. Soil parameters are often defined using constrained normal distributions or normal logs. Table 4 shows mean values and standard deviation of probabilistic parameters. In this research, definition of correlation between used domain points under integral points or so called stress points used in point interpolation method with radial functions. It should be noted that these points represent identified region of Voronoi cell. Next, a correlation matrix is constructed by using Markov correlation function and a random field corresponding to each parameter is generated.

TABLE 4. Mean values and standard deviation of probabilistic soil parameters

Parameter	Average	Standard deviation
Maximum internal friction angle (°)	20	2
Residual internal friction angle (°)	15	2
Maximum cohesion (kN/m ^{2})	20	2
Residual cohesion (kN/m ^{2})	5	2
Maximum dilation angle (°)	10	2
Residual dilation angle (°)	0.0005	2

Figures 8 to 13 show random field generated of Monte Carlo iteration on parameters of internal friction angle, cohesion and dilation angle of both maximum and residual modes, respectively. Random fields in this analysis are generated in terms of correlation length of 10 meters. As shown in Figures 8 and 9, the values of friction angle in random field of maximum state in range between 16 to 22 degrees and in random field of residual state in range between 13 to 19 degrees. The difference between values of generated fields between maximum and residual state of cohesion parameter was greater according to Figures 10 and 11. This is related to significant reduction of cohesion parameter during progressive failure.

8. RESULTS

Finally, appropriate distribution of calculated safety factors is obtained and main necessary parameters of

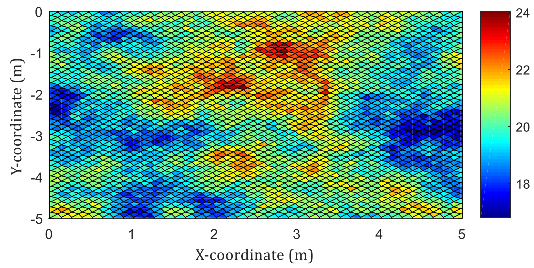

Figure 8. Square by accident angle friction internal maximum (°)

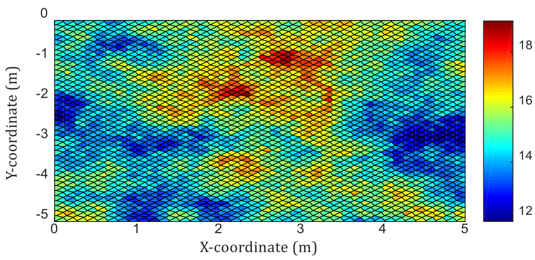

Figure 9. Square by accident angle friction internal residual (°)

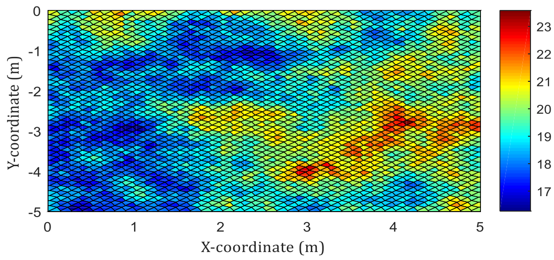

Figure 10. Square by accident cohesion maximum (kN/m^2)

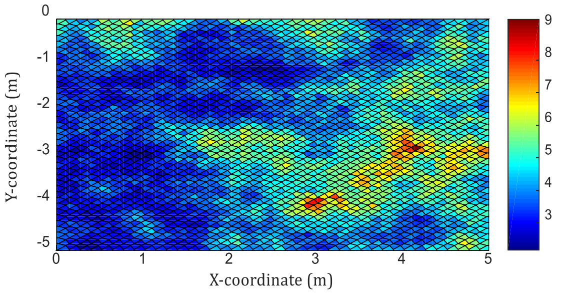

Figure 11. Square by accident cohesion residual (kN/m^2)

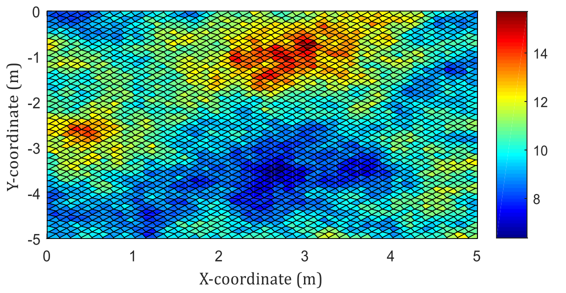

Figure 12. Square by accident dilation angle maximum (°)

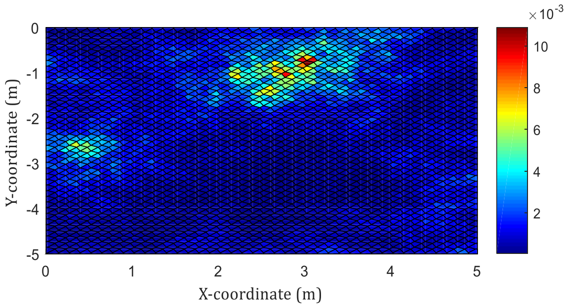

Figure 13. Square by accident dilation angle residual (°)

analysis can be obtained by applying statistical concepts. After determining probability distribution for target value of random variable (safety factor), performing probability analysis in form of calculating parameters such as reliability index, failure probability or coefficient of variation are examined.

After repeating the steps of stability analysis 5000 times, histogram diagram of the 5000 reliability numbers obtained is drawn according to Figure 14.

According to the figure, results obtained from random field are often associated with fluctuation. Therefore, continuous distribution function is obtained through curve fitting and makes probabilistic analysis possible. Since all uncertain parameters are assumed to be normal log input distribution, probability density function of safety factor follows the same distribution and fits histogram. By determining probability density function, cumulative distribution function can also be determined according to Figure 15. It can be concluded that probability of safety factor used for bearing capacity of foundation in terms of progressive failure and spatial variation of strengh parameters is less than 3 will be about 14% by using this diagram. This number actually indicates probability of foundation failure under consideration. Then, according to probabilistic distribution functions, statistical parameters of problem such as mean, standard deviation, reliability index, failure probability and coefficient of variation are determined and presented in Table 5.

It should be noted that coefficient of variation represents dispersion of probability distribution function related to random variable and reliability index (β) indicates distance of average distribution to failure threshold.

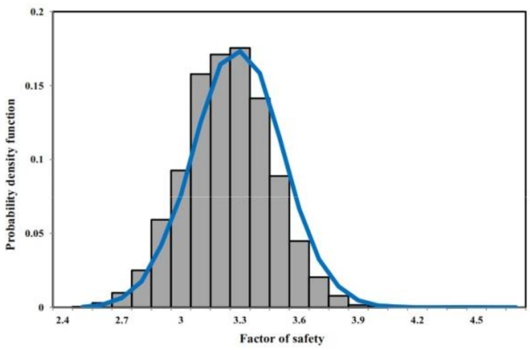

Figure 14. Density probability density function

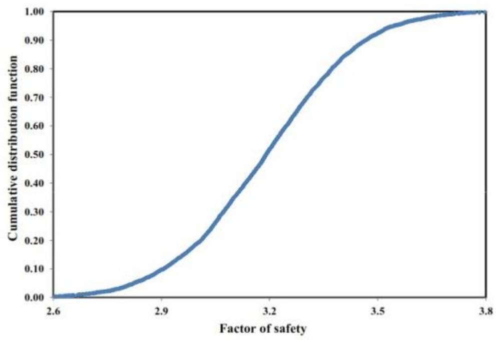

Figure 15. Cumulative reliability distribution function

TABLE 5. Probabilistic parameters of reliability distribution

Average	3.19
Standard deviation	0.22
Coefficient of change	0.07
Probability of failure	0.14
Reliability	0.19

9. CONCLUSION

In this paper, point interpolation method with random radial functions has been used to analyze failure of soil under foundation by modeling spatial variation of soil strengh properties to taking into account progressive failure. In order to evaluate application of this method, The foundation with definite geometry is analyzed deterministic and probabilistic. Then, its safety factor is calculated. According to presented results, it can be seen that safety factor changes obtained from point interpolation method with radial functions are in a more limited range than other methods. Also, values of this safety factor are reduced by changing values of the parameters from maximum to residual state. Therefore, in this study, progressive failure in soil is occured. Based on results obtained in progressive failure, when failure mechanism is formed and has advanced to ground, large deformations have been occurred in different points under foundation, which always will increase with increasing repetition. In other words, actual failure of soil and occurrence of continuous displacements arises simultaneously with formation of progressive mechanism of soil failure and arrival of slip surface to ground. In this study, it can be concluded that by increasing value of correlation length parameter, probability of failure under foundation decreases by examining effect of correlation length on probability analysis. In other words, not considering dispersion of soil properties under problem can lead to conservative results. It should be noted that in this analysis, same correlation length is considered for all uncertain parameters. Therefore, according to all presented results, point interpolation method with random radial functions can be used as a suitable numerical tool with possibility of probabilistic modeling of changes in main soil parameters in various geotechnical problems.

10. REFERENCES

1. Farid, Z., Lamdouar, N. and Ben Bouziyane, J., "A method of strip footings design for light structures on expansive clays", ***International Journal of Engineering, Transactions A: Basics***, Vol. 35, No. 1, (2022), 248-257. doi: 10.5829/ije.2022.35.01a.24.
2. Tarrad, A.H., "3d numerical modeling to evaluate the thermal performance of single and double u-tube ground-coupled heat pump", ***HighTech and Innovation Journal***, Vol. 3, No. 2, (2022), 115-129. doi: 10.28991/HIJ-2022-03-02-01.
3. Tarrad, A.H., "Development of analytical model for a vertical single u-tube ground-coupled heat pump system", ***Global Journals of Research in Engineering***, Vol. 20, No. J3, (2020), 1-14.
4. Troncone, A., "Numerical analysis of a landslide in soils with strain-softening behaviour", ***Geotechnique***, Vol. 55, No. 8, (2005), 585-596.
5. Conte, E., Donato, A. and Troncone, A., "Progressive failure analysis of shallow foundations on soils with strain-softening behaviour", ***Computers and Geotechnics***, Vol. 54, (2013), 117-124. https://doi.org/10.1016/j.compgeo.2013.07.002
6. Wang, B., Vardon, P. and Hicks, M., "Investigation of retrogressive and progressive slope failure mechanisms using the material point method", ***Computers and Geotechnics***, Vol. 78, (2016), 88-98. https://doi.org/10.1016/j.compgeo.2016.04.016
7. Zdravković, L., "Finite element analysis in geotechnical engineering: Theory, Thomas Telford, (1999).
8. Griffiths, D. and Fenton, G.A., "Probabilistic slope stability analysis by finite elements", ***Journal of Geotechnical and Geoenvironmental Engineering***, Vol. 130, No. 5, (2004), 507-518. https://doi.org/10.1061/(ASCE)1090-0241(2004)130:5(507)
9. Zhang, D.-Y., Xie, W.-C. and Pandey, M.D., "A meshfree-galerkin method in modelling and synthesizing spatially varying soil properties", ***Probabilistic Engineering Mechanics***, Vol. 31, (2013), 52-64. https://doi.org/10.1016/j.probengmech.2012.12.004
10. Lucy, L.B., "A numerical approach to the testing of the fission hypothesis", ***The Astronomical Journal***, Vol. 82, (1977), 1013-1024.
11. Binesh, S., Hataf, N. and Ghahramani, A., "Elasto-plastic analysis of reinforced soils using mesh-free method", ***Applied Mathematics and Computation***, Vol. 215, No. 12, (2010), 4406-4421. https://doi.org/10.1016/j.amc.2010.01.004
12. Bui, H.H., Fukagawa, R., Sako, K. and Wells, J.C., "Slope stability analysis and discontinuous slope failure simulation by elasto-plastic smoothed particle hydrodynamics (SPH)", ***Geotechnique***, Vol. 61, No. 7, (2011), 565-574.
13. Nonoyama, H., Moriguchi, S., Sawada, K. and Yashima, A., "Slope stability analysis using smoothed particle hydrodynamics (SPH) method", ***Soils and Foundations***, Vol. 55, No. 2, (2015), 458-470. https://doi.org/10.1016/j.sandf.2015.02.019
14. Conte, E., Silvestri, F. and Troncone, A., "Stability analysis of slopes in soils with strain-softening behaviour", ***Computers and Geotechnics***, Vol. 37, No. 5, (2010), 710-722. https://doi.org/10.1016/j.compgeo.2010.04.010
15. Liu, G., "A point assembly method for stress analysis for two-dimensional solids", ***International Journal of Solids and Structures***, Vol. 39, No. 1, (2002), 261-276. https://doi.org/10.1016/S0020-7683(01)00172-X
16. Vanmarcke, E., "Random fields: Analysis and synthesis, World scientific, (2010).
17. Fenton, G.A. and Griffiths, D.V., "Risk assessment in geotechnical engineering, John Wiley & Sons New York, Vol. 461, (2008).

Persian Abstract

چکیده

در تحلیل‌های مرسوم گسیختگی در زیر پی، پارامترهای مقاومتی بدون تغییر و به‌صورت قطعی فرض می‌شوند. این در حالی است که در حین گسیختگی، مقاومت خاک مقادیر بیشینه و پسماند از خود نشان داده و استحکام آن به‌صورت پیش‌رونده با افزایش کرنش خمیری کاهش می‌یابد. علاوه بر تغییرات پارامترهای مقاومتی خاک طی مکانیسم پیش رونده، ماهیت غیریکنواخت خاک نیز سبب ایجاد تغییرات مکانی این پارامترها می‌شود. ازاین‌رو، بایستی با لحاظ عدم قطعیت مقادیر پارامترهای خاک به‌صورت غیرقطعی و با استفاده از مفاهیم آمار و احتمالات بررسی شوند. در این تحقیق از روش درون‌یابی نقطه‌ای با توابع شعاعی در ترکیب با میدان تصادفی جهت مدل‌سازی تغییرات مکانی خصوصیات مقاومتی خاک و تحلیل ظرفیت باربری پی استفاده‌شده است. برای انجام تحلیل احتمالاتی، میدان تصادفی پارامترهای چسبندگی و زاویه اصطکاک و همچنین کرنش خمیری حد آستانه بر اساس مقادیر میانگین و انحراف معیار آن‌ها تولید می‌شوند. به‌منظور بررسی کاربرد روش درون‌یابی نقطه‌ای با توابع شعاعی تصادفی، یک پی با هندسه مشخص به‌صورت قطعی و غیرقطعی مورد تحلیل قرارگرفته و ضریب اطمینان مربوط به آن بررسی‌شده است. بر اساس تحلیل به‌واسطه مدل‌سازی گسیختگی پیش‌رونده، نتیجه می‌شود که گسیختگی واقعی خاک و وقوع جابجایی‌های ادامه‌دار به‌طور هم‌زمان با شکل‌گیری مکانیسم پیش‌رونده زوال خاک و رسیدن مسیر لغزش به سطح زمین به وقوع می‌پیوندند. در ادامه با انجام تحلیل احتمالاتی و تولید میدان‌های تصادفی، توابع توزیع احتمالاتی ضریب اطمینان تعیین‌شده و پس‌ازآن پارامترهای آماری محاسبه‌شده‌اند.

IJE TRANSACTIONS B: Applications Vol. 36, No. 02, (February 2023) 276-288

International Journal of Engineering

Journal Homepage: www.ije.ir

Analytical Modeling of Heat Transfer Coefficient Analysis in Dimensionless Number of an Electric Parking Brake Using CFD

V. Agrawal*[a], H. P. Khairnar[b]

[a] Research Scholar of Mechanical Engineering, Veermata Jijabai Technological Institute, Matunga (E), Mumbai, India
[b] Faculty of Mechanical Engineering, Veermata Jijabai Technological Institute, Matunga (E), Mumbai, India

PAPER INFO

Paper history:
Received 16 June 2022
Received in revised form 28 July 2022
Accepted 31 July 2022

Keywords:
Brake Mass
Heat Dissipation
Nusselt Number
Clamp Pressure
Emmisivity

ABSTRACT

The present study intends the development of an electric parking brake (EPB) for commercial vehicles (CVs). CVs with EPB applications are currently available in an entirely different set of issues than EPB applications on passenger cars, which are presently widely used. Safe parking requires much more focus with an order of magnitude, more thermal capacity, brake mass, and clamp pressures. In the first instance, heat loss from the brake disc was estimated. The investigations also allowed for precise prediction of radiative heat loss by defining surface emissivity. The parameters of air movement, convective heat transfer coefficients, and velocities were investigated, and validation was done with the CFD model. When the temperature dropped to 252 °C, the maximum estimated value of the Nusselt number was 72.25. Nusselt number pattern that looks identical over the arc surface yields 13.38 percent better results. Nu values at maximum temperature were calculated to be 80.5 and 82.6 at 251.8 °C. The "h_{conv}" value was 4.1 percent lower than in the arc region, with the highest value at 400°C being 11.5 W/m^{2}K. The present study adopted unique approach and obtained brake disc temperature and the coefficient of convective heat transfer on disc friction surfaces and hat regions. CFD modeling was done during the cooling phase to evaluate flow patterns and "h_{conv}" fluctuation across the entire disc brake surface area. The mathematical modeling and adopted methodology for computing heat transfer coefficients for different disc regions have helped to better understand of a CV brake disc heat dissipation.

doi: *10.5829/ije.2023.36.02b.08*

NOMENCLATURE

CFD	Computational fluid dynamics	*Nu*	Nusselt number
CV	Commercial vehicle	*Pr*	Prandtl number
EPB	Electric parking brake	*Ra*	Rayleigh number
HTC	Heat transfer coefficient	*Re*	Reynolds number
FE	Finite Element	*T*	Temperature
OD	Outer diameter	*v*	Velocity
C_p	Specific heat capacity	r	Radius
A	Surface area	**Greek Symbols**	
D	Disc diameter	ρ	Density (kg/m^3)
y_r	Wall characterstic length	μ	Dynamic viscosity (kg/ms^2)
Gr	Grashof number	ν	Kinematic viscosity (m^2/s)
h	Heat transfer coefficient	t	time (s)
k	Thermal conductivity	V	Kinematic viscosity (m^2/s)
l	Length	*L*	Characterstic length (m)
m	Mass	**Subscripts**	
p	Pressure	α	Thermal diffusity
Q	Cooling power	ε	Emmisivity
Q	Cooling power	ε	Emmisivity

*Corresponding Author Institutional Email: vkagrawal_p18@me.vjti.ac.in (V. Agrawal)

Please cite this article as: V. Agrawal, H. P. Khairnar, Analytical Modeling of Heat Transfer Coefficient Analysis in Dimensionless Number of an Electric Parking Brake Using CFD, ***International Journal of Engineering, Transactions B: Applications***, Vol. 36, No. 02, (2023), 276-288

1. INTRODUCTION

The objective is to contribute to the development of commercial vehicle (CV) electric parking brakes (EPB). Despite being widely used in passenger cars today, EPB applications on CVs present entirely different challenges. In the research process, typical dimensionless air properties were used to investigate over a simplified brake disc friction surface, deviation in mean local convective heat transfer coefficients. For the entire cooling process, a nonlinear equation was used to calculate the average convective heat transfer coefficient at the surface fluctuation when it comes to temperature reduction. First-order differential equations were built based on fundamental principles of bulk disc temperature. A good correlation with observed values was attained, to within 10%, by including variations during the cooling period. Heat is dissipated through convection and radiation. Until now, there has not been much research on geometric shape heat dissipation from a stationary disc. In the same way, there is not a lot of research on the cooling of stationary brake discs. Due to the task's relative design robustness, this was formerly assumed to be a technical issue that received little attention. The electrification of braking systems, as well as recent breakthrough in automotive development, however, is necessary to gain a better understanding of thermal brake characteristics in stationary settings. This knowledge will undoubtedly aid in predicting temperature in a variety of driving situations. Brake temperatures at the disc interface have a significant impact based on friction coefficient and pad wear. It has been explored chiefly for moving vehicles in the past. For city buses, stationary brake cooling is very crucial, and they spend a significant amount of time waiting at bus stops, traffic lights, and other such sites.

It was discovered that the stationary disc brake had the highest coefficient of heat transfer. It is obvious that the presence of disc has increased the air flow and turbulence in the rotor, resulting in a higher value of coefficient of heat transfer. A rise in thermal conductivity with temperature prevents the appearance of the apex h_{conv} value, as it does the Nusselt number. It was observed that the value of h_{conv} was higher along with the value of maximum heat transfer coefficient.

Figure 1 depicts the research methodology adopted in heat transfer analysis of the stationary disc brake. In the analytical-numerical modeling is the topic of research on the heat dissipation using conduction, convection and radiation of the discs over an extended period. Investigates the brake disc of outboard and inboard view of the disc brake, and computed the temperature and convective heat transfer coefficients based on CFD modeling.

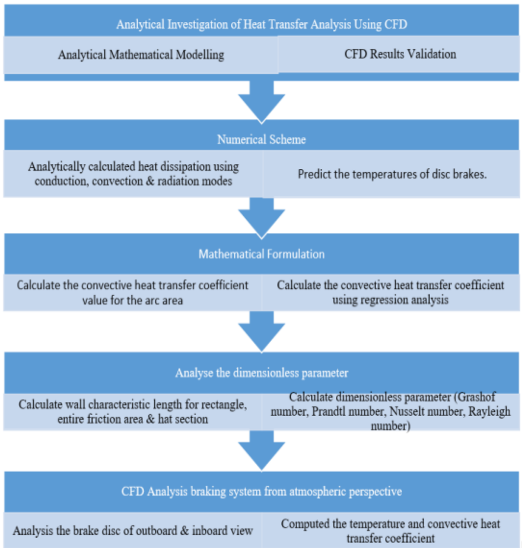

Figure 1. Research methodology adopted in heat dissipation

2. LITERATURE REVIEW

Most current EPB research publications focus on the EPB's motor control system. For example, sensorless position and velocity monitoring enable more precise EPB actuation control [1]. However, the motor response time of a fuzzy-type numerical controller is faster than that of typical PID controllers [2]. If any frequent EPB errors occur, to transmit driver notifications, a technique for detecting faults has been developed [3]. Therefore, friction coupling cooling is integral to any braking system's thermal concerns.

Many vane arrangements have been used in convective cooling by optimizing air movement across the disc [4]. Because the air is driven through the vanes at a greater rate as the vehicle speed increases, convection significantly affects brake cooling. The flow of air quality is equally as crucial as the speed with which it moves. The vanes produce recirculation zones, which diminish the convection process [5]. Brake designers and academics have turned to CFD modeling procedures to understand better the convective heat transfer coefficients and the resulting flow field. Flow separation straight vane rotors have a leading-edge surface that has been effectively demonstrated using CFD. Resulting in a lower convective heat transfer coefficient [6]; the leading edge, in contrast to the trailing edge, a steady air flow can be seen down the vane.

Brake temperature levels can be reliably predicted subject to properly stated boundary conditions using finite element (FE) methods [7]. Both disc temperatures were computed using a linked thermo-mechanical FE model, and thermal strains induced in the event of a complex braking situation further demonstrated the utility of FE analysis and enabled researchers to predict the occurrence of thermal cracks in the rotors [8]. Nusselt number pattern looks identical over the arc surface using his correlation equation [9, 10].

The vertical friction surfaces provide the majority of convective cooling because the rotor section's thickness is significantly less than the OD [11]. The correlation approach provides values that are closer to experimental data. Several relationships have been found within the confines of a buoyant fluid flowing across a solid surface [12-22].

The non-Fourier heat conduction in a semi-infinite body was examined. The heat wave non-Fourier heat conduction model was used for thermal analysis. Thermal conductivity was assumed temperature-dependent, which resulted in a nonlinear equation [23]. The temperature gradient and thermal conductivity compute the heat flux through the interface. The uncertainty in the heat flux computation may be examined by comparing the differences in the calculated values of heat flux for both the hot and cold specimens in the steady-state condition [24]. The aero-thermal environment of a TSTO flying test bed has been assessed both from the engineering-based and CFD-based approaches. Computations with the air modeled as perfect gas highlight that vehicle aero heating is more severe than existing reentry vehicles [25].

The approximation order of the optimal control issue for the spatial process of heat conduction. An algorithm for solving the difference problem is explained, and an estimate of the value of the difference functional divergence from the continuous functional is obtained using the methods of integral inequalities and the method of difference approximation [26]. All heavy metals found, with the exception of Fe, (Zn, Ni, Cu, Cr, and Pb), have a close relationship with road traffic, according to the level of heavy metal contamination of roadside soils exposed to road traffic on a major road and the results attained [27, 28].

The research issues currently being explored are summarized in work discussed above. They were all done in dynamic conditions, primarily on passenger automobiles. However, there has been relatively little research on static brake qualities published. Thermal considerations, on the other hand, are critical in hot parking scenarios. The lack of vehicle motion causes only airflow-natural convection results in a significant reduction in cooling rate and a substantial shift in heat flow patterns. Thermal contraction requires more investigation into the impacts of heat transmission by conduction, convection, and radiation.

Because of their reduced size and lower load requirements, they are more popular; passenger vehicle EPBs offer the advantage of over-clamp the brake without causing damage to the brake caliper fatigue life to mitigate the brake disc and pad thermal contraction effects. Three minutes after the original application, a passenger vehicle EPB re-energizes the brake by applying a second-stage clamp force. On the other hand, CV brakes offer a substantially higher clamp force and thermal capacity, allowing for much more thermal expansion. Longer cooling durations are expected, with increased thermal capacity during the parked brake cooling period. However, higher development induces increased contraction, resulting in brake performance uncertainty. As a result, EPBs have not yet been fully integrated into CVs. The introduction of EPB to CVs spurred this research into several aspects and influencing parameters on static disc cooling. The ultimate goal is to create reliable and accurate prediction models that shorten the time to market.

3. MATHEMATICAL MODEL

It has been shown to be more challenging to model stationary disc brakes heat transfer than to model heat transfer in dynamic situations. Short braking periods and disc rotation, symmetry around constant heat transfer coefficients for constant heat transfer coefficients (HTC) for each vane channel are reasonable assumptions. Because natural convection is the only source of airflow, cooling times are substantially longer in stationary parking conditions. Coefficients of heat transmission can no longer be thought of as constant. The disc brake's convective heat transmission variability must be understood to provide an accurate temperature forecast technique. All the modelings were done with the brake disc shown in Figure 1, and the purpose of testing was to obtain this knowledge. The disc is constructed of grey cast iron and features a straight vane vented shape that prevents it from coming (Figure 2).

Table 1 provides more information about the braking disc used. The disc has an anti-coning shape, meaning the friction face on the inboard side is not concave. As the word implies, there is no considerable coning due to the thermal expansion, specifically, a difference in axial

Figure 2. Brake disc analysed: a) Outboard view; b) Inboard view

TABLE 1. Characteristics of disc brake

Specification	Dimension
Outside friction diameter (mm)	434
Inside friction diameter (mm)	234
Thickness of the rotor (mm)	45
Weight (N)	380
Number of vanes	30

displacement between the outer and inner diameter of the disc. Since friction surfaces are kept level, this disc type has a lower risk of brake judder caused by uneven pad wear. The air enters through the side that faces outward, passing through a small gap between the inner diameters of the hub and disc before turning 90 degrees and flowing radially via the channels towards the disc's outer diameter. Furthermore, this disc is subjected to more significant thermal stresses in the disc transition zone than the standard disc design. The disc features 30 straight radial vanes and an overall thickness of 45 mm, channel width with two 14 mm thick walls separated by a 17 mm gap.

The brake disc was heated consistently to a higher temperature in all of the analyses in this study. Figure 3 and Table 2 show the heat dissipation zones and their associated modes. The disc ventilation system was shut down by using temperature-resistant tape to block the channel entry and exit points (Figure 2). Reduce noise; an insulating gasket was installed between the disc hat and the wheel carrier flange to analyze efficiently, and precisely all modes of heat transport have been investigated and adequately modeled.

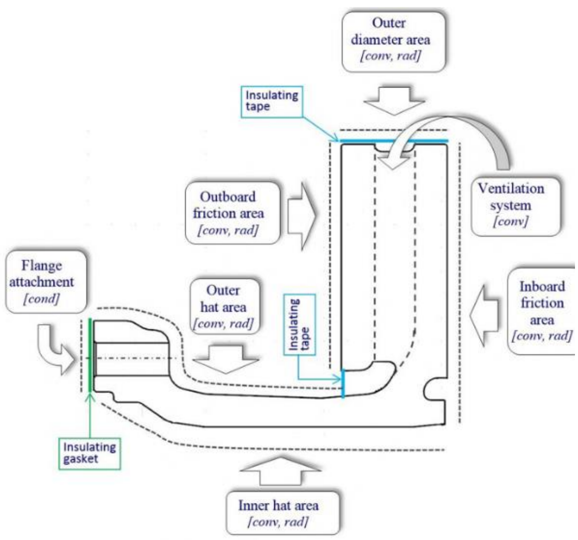

Figure 3. Areas of the discs and the heat dissipation modes [21]

TABLE 2. Modes of heat dissipation and their associated locations

	Total convective area (m^2) = 0.658				
Total conductive area (m^2) =0.025	Outer hat	Friction outboard	Friction inboard	Outside diameter	Ventilation system
	0.104	0.105	0.119	0.0166	0.313
	Total radiative area (m^2) = 0.35				

4. ANALYTICAL INVESTIGATION

Conduction transports heat from the wheel carrier to the disc through the contact zone, as depicted in Figure 3: Flange attachment. In the vehicle installation, 10 M16 bolts with a torque of 330 N-m are used for fastening. Heat can move in either direction, but because the disc is usually at a greater temperature, the conductive transfer is primarily from the disc to the wheel carrier. Thermal contact resistance will inevitably exist due to imperfections in the surfaces in contact, inhibiting heat transmission and producing temperature differences between the interfaces.

In practice, the thermal conductance parameter, as many writers employ, is the best way to explain this phenomenon. Heat is transported through conduction according to Equation (1).

$$Q = h_{cond}A_{cond}(T_d - T_c) \quad (1)$$

The conditions of interface surfaces, the material employed, and the force clamp used to determine thermal conductance. If the conductance, interface temperature, and contact area differential are all high, the heat transfer rate will be faster. Tirovic and Voller [9] devised an experiment to determine heat conductivity for this sort of material (spheroidal cast iron wheel carriage and grey cast iron disc), surface coatings, and the state of the contact surface. Since the pressure at the interface determines conductance, these values will vary depending on which side of the interface, Equation (2) average values in engineering calculations for bulk heat transfer:

$$h_{conv} = 800P_{avg} + 2300 \quad (2)$$

The previous calculation yields h_{cond} (avg) in [W/m^2 K]. Calculate the average interface pressure and total clamping force (due to 10 bolts) divided by the region of the user interface. The bolt tightening torque can be used to estimate clamp force. Heat transmission to and during protracted cooling periods, the temperature of the wheel carrier may fluctuate, and conduction will be challenging to incorporate into simplified models. This effect is unlikely to be significant when considering small conductive elements due to the short contact area. As a result, it was determined that at this time, it would be preferable to use a thermal insulating gasket at the disc interface to reduce bolt clamping force.

In most braking circumstances, convection is the primary heat transfer method, and it is highly dependent on vehicle speed. Therefore, it requires special attention. The minimum feasible convective heat transfer that will be used in the rotating disc speed is zero in the case under investigation. Furthermore, in driving situations, the disc's temperature has a minor effect on the convective heat transfer coefficient. Because the surface is given fresh air, when the temperature rises, only a slight decrease in the convective heat transfer coefficient occurs. Only natural convection occurs in stationary conditions. Therefore, the scenario is fundamentally different. The temperature difference between the disc-air is the only driving force, and the hotter, more excellent disc is the h_{conv}, resulting in the total heat released. Convective cooling power is identical to conductive cooling power in Equation (3).

$$Q_{conv} = h_{conv} A_{conv} (T_d - T_a) \quad (3)$$

Convective heat transfer coefficient values will differ throughout disc areas, and T_d temperatures will almost certainly differ over broad disc surfaces. As a result, convective cooling becomes much more difficult, and the required 'averaging' is more susceptible to assumptions, simplifications, and mistakes. The disc ventilation system's heat transport (channels and vanes), as well as air temperatures near the disc and coefficients of local convective heat transfer will be studied in Part 2 of this paper using CFD modelling. The first stage is focused towards achieving this. The ventilation system was turned off at the channel entry (inside disc diameter) and exit for this preliminary stage of analysis (outside disc diameter). Although radiant heat dissipation is usually associated with extreme heat and is often overlooked, In the case of a fixed disc, since convective cooling is minimal. Radiative heat dissipation's basic formula in Equation (4).

$$Q_{rad} = \left(T_d^4 - T_a^4\right) \quad (4)$$

An average emissivity value of 0.92 was found in the investigation of this research and will be used as a parameter in the simulation of this specific disc under test conditions. Because the ventilation system has no radiative heat loss to the environment, the disc area emitting heat via radiation is substantially lower than the convective area. Boundary conditions become significantly more difficult when the brake is mounted within the wheel cavity due to radiative transmission. The conductive and convective modes can be represented in Equation (5).

$$Q_{rad} = h(T_d - T_a) \quad (5)$$

The coefficient of convective heat transfer on disc friction surfaces and hat regions was determined using analytical methods. Numerical models were then used to predict the temperatures of disc brakes. The investigations also allowed for precise prediction of radiative heat loss by defining surface emissivity. Finally, temperatures were measured and calculated, and the results were compared.

Since there has been no previous work on analytical modeling of the geometry of a CV brake disc, no precedent for establishing accurate temperature forecasts has been established. A series of local h_{conv} values were created using a reduced brake disc design, which was then averaged throughout the entire friction surface. As illustrated in Figure 4, dimensionless parameters were derived using well-known literature equations, and friction surface geometry partitions were then projected as sections of the simplified friction surface geometry. After averaging these values throughout the total surface area, for the temperature range pertinent to CV parking applications, an equation for average h_{conv} was derived. Finally, the hat region was subjected to the same analytical procedure; the concept of horizontal cylinder heat dissipation was employed instead of the vertical wall theory. The cylindrical area at disc OD can be handled in the same way, but it can be ignored because it is insulated and much smaller. The process is easier to understand, and all cooling is supposed to proceed with only a tiny amount of energy delivered to the wheel carrier by conduction. The wheel carrier is heated by convection and radiation. The cylindrical area at disc OD can be handled similarly, but it can be ignored because it is insulated and much smaller. The analytical results will be compared to observed values during validation.

Heavy braking applications can cause brake disc temperatures to exceed 500°C, though it's unlikely that a CV would be parked as a result of an application, reaching and exceeding 400°C regularly. As a result, a parking simulation was planned to start with a 400°C disc brake surface temperature.

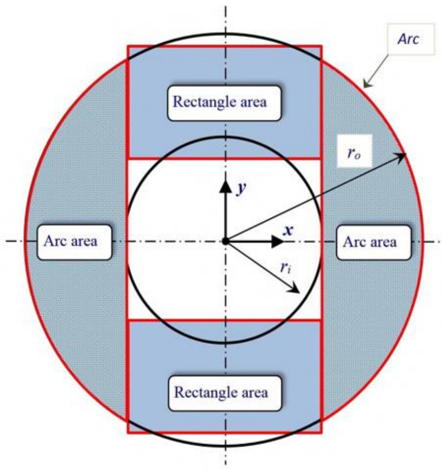

Figure 4. Disc friction surfaces are divided into simpler geometric portions

Natural convection transmission of heat research has been done on bodies of basic geometry throughout history. McAdams [10] showed how a vertically and horizontally positioned flat plate in open-air might produce thermal and hydrodynamic boundary layers. In cylindrical geometry, Morgan [11] demonstrated the same. The vertical friction surfaces provide the majority of convective cooling because the rotor section's thickness is significantly less than the OD. As a result, two vertical plates can be used to approximate the disc in free air. It would be difficult to justify just using McAdams [10] and Churchill and Chu [12] traditional formulae because they were calculated using rectangular plates with constant characteristic lengths in open air. Flow across a known characteristic length local vertical surface is believed to be independent of flow horizontally adjacent to it, and Gr values are calculated accordingly. The air parallel to the surface is unlikely to be affected by the turbulent flow's eddy currents toward the turbulent region lateral flow motion, which will impact parts of the laminar flow areas as they approach the laminar r_0. Because the mathematical calculations have become more complicated and because of the project's time constraints, this effect cannot be examined further without CFD. For the time being, any turbulence flow will be found on the disc brake surface and be restricted to a direction perpendicular to the horizontal. When examining a single point along the horizontal center line, the size of the Grashof number increases as temperature falls, peaking at 255.6°C. When there is not a temperature gradient, the Grashof number decreases until it reaches zero at room temperature. The temperature change is directly proportional to the Grashof number; the occurrence of the peak Grashof number value is linked to a change in kinematic viscosity. The thermal expansion causes a fluid's density to decrease as its temperature rises. Lowering the kinematic viscosity of a fluid with a lower density reduces during a frictional flow. The viscosity kinematic effects exceed thermal gradient at a temperature of 255.6°C or higher, lowering the Gr value.

The Rayleigh number, Grashof, and Prandtl numbers are multiplied to get the result. Regarding heat transmission from a body in a buoyancy-driven flow, Equation (6) is used instead of the Grashof number. It expresses the proportion of conductive to convective heat transfer. Conduction is the primary heat transport method below the critical temperature, which switches to convection. Ra's critical value varies based on the surroundings and geometry of solid surfaces. An essential factor in a horizontal flat plate, according to McAdams [10], is as low as 10^7; in open air, the critical value for vertically stacked cylinders is as high as 10^9, according to Necati Ozisik [13].

$$\mathrm{Ra} = \mathrm{Pr} * \mathrm{Gr} \tag{6}$$

They consider that Rayleigh number is a Grashof number function. However, the fact that the observed findings are similar is not surprising. McAdams [10] states that at 400°C, turbulent flow is represented by a value of 3.5 x10^8. The results reveal that the airflow only 8 mm from the OD gets turbulent. Necati Ozisik [13] proposed a crucial Ra value for a different shape, indicating that the flow parallel to the arc surface is laminar throughout. Neither of the calculated values was for a character with the same geometry as the arc. Numerical calculations cannot determine whether or not the flow is entirely in a turbulent state. The heat dissipation conclusion cannot be drawn with precision due to the ambiguity of the airflow state. Research suggests that when the disc is at its hottest, the flow will have crossed the boundary between the laminar and turbulent flow.

The fluid characteristics for flow across an arc surface have recently been discovered; the Nusselt number was calculated to better explain the flow will have crossed the boundary between the laminar and turbulent flow. Since the numbers in Equation (6) are not always known, it is not always as straightforward as in the Nusselt number. Small changes in shape have an impact on the buoyant flow's intensity and subsequent parameter values. When it comes to the Nusselt number, it's common to employ approximation formulae derived from analytical data and correlation analysis. Compared to theoretically calculated equations, Necati Ozisik [13] showed that the correlation approach provides values closer to experimental data. Several relationships have been found within the confines of a buoyant fluid flowing across a solid surface. Churchill and Chu [12] proposed a vertical wall correlation equation, when isothermal wall conditions are considered, Rayleigh numbers between 10^{-1} and 10^{12} are valid.

$$\mathrm{Nu} = \frac{\mathrm{h_{conv}L}}{\mathrm{k}} \tag{7}$$

As a ratio of convection to conduction, the Nusselt number indicates energy transfer from the solid surface boundary to the flowing fluid and across its thickness in a normal to the surface direction. Prandtl number, on the other hand, focuses on the moving fluid and the interaction between it and heat dissipation. Nusselt values of unity indicate that heat dissipation from the surface is evenly distributed between conduction and convection, as seen in laminar flow. Convection is dominant in a turbulent flow, Nu will surpass 100 [13]. It is vital to note that the characteristic length of the body's surface is represented by Equation (7). Over the arc region, the Nusselt number will be determined to assist explain the primary mechanism of heat conduction. To determine the mean local Nusselt number, McAdams [10], Equation (8) and Churchill and Chu [12], Equation (9), offered two distinct correlation equations; both were employed and compared, as illustrated in Figure 5. The mean local Nusselt number from the disc are included in the CFD data. It includes analyses carried out at four temperatures. The effect of temperature of disc and Nusselt number will be determined to assist explain the primary mechanism of heat conduction can thus be studied and analysed in Figure 5.

$$\mathrm{Nu_m}^{1/2} = 0.825 + \frac{0.387\ \mathrm{Ra_L^{1/6}}}{[1 + (0.492/\mathrm{Pr})^{9/16}]^{8/27}} \tag{8}$$

According to Necati Ozisik [13], Equation (9) provided by McAdams [10] better matches results. The final Equation (9) is as follows.

$$\mathrm{Nu_m} = c\mathrm{Ra_L}^{n} \tag{9}$$

where c denotes a constant and Ra represents Rayleigh number, Table 3 shows these parameter values, which all rely on Ra.

Both ways of computing the Nusselt number generated over the thermal boundary layer mean Nusselt number values. The Churchill and Chu [12] technique was evaluated first, followed by a comparison of the two methods. Nusselt values above 100 denote a convection-dominated surface-to-fluid regime; values one and lower represent through the fluid and away from the surface, and conduction occurs. A value of 71 is predicted by the Churchill and Chu [12] Equation (9), as seen in Figure 4. This value falls in the middle of both crucial values, implying a state of transition in line with previous trends.

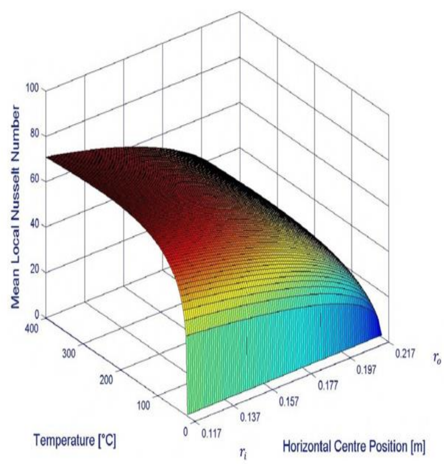

Figure 5. Temperature and horizontal position mean Nusselt number

TABLE 3. Mean Nusselt number parameters for McAdams [10]

Type of flow	Ra value	c	n
Laminar flow	10^4 to 10^9	0.6	0.25
Turbulent flow	10^9 to 10^{13}	0.11	0.667

The value remains high; while conduction still plays a part, the majority of the heat generated by the arc is dissipated through convection. The maximum estimated value was 72.25 when the temperature fell to 252 °C. The inner radius with the most extended characteristic length was discovered. The Nusselt number is affected by temperature and location as this nonlinear distinct declines. McAdams [10] produced a Nusselt number pattern that looks identical over the arc surface using his correlation equation (as seen in Churchill and Chu's [12] Figure 5. The McAdams [10] equation yields 14 percent better results, Nu values at maximum temperature were calculated to be 80.5 °C and 82.6 °C at 251.8 °C. The heat transmission from the arc surface isn't entirely conventional, even with a significant rise in Nu. The McAdams [10] Equation (9), according to Necati Ozisik [13], is a more accurate representation of the actual value; as a result, all subsequent vertical wall heat transfer calculations will be based on it.

Convective heat transfer coefficient can be calculated after determining that convection transports most heat from the arc surface to the surrounding air. Any h_{conv} estimate must account for the effect of conduction from the surface to the atmosphere. Figure 6 shows the locally computed mean h_{conv} values derived from Equation (5) at various positions around the disc arc area. The convective heat transfer coefficient values vary, ranging from zero to 14.4 W/m^2 K at the highest temperature.

In the region for reference, the appearance of apex h_{conv} value, similarly to the Nusselt number, is prevented by a rise in thermal conductivity with temperature. The magnitude drop as characteristic length decreases towards the outer disc radius exhibits a similar pattern. This is an expected outcome since the thermal boundary layer's typical length shortens, reducing heat transfer. Equation (10) linking convective HTC to temperature and location might be created. Because the goal was to create a total surface relationship for a convective HTC, it was unnecessary to build such a complicated Equation (10). To determine a single average h_{conv} value for the entire arc area, Equation (10) was employed.

$$\mathrm{h_{conv}} = \frac{\sum_{i=r_i}^{r_o} \mathrm{h_{conv_i} A_{arc_i}}}{\mathrm{k_{arc}}} \tag{10}$$

In Figure 5, Equation (10) outcomes regarding the temperature, h_{conv} decreases nonlinearly with cooling. The results were put through a regression analysis to see if there was a link between h_{conv} and temperature. The best estimate was found to be a natural logarithm adjustment term in a quadratic relationship, which caught roughly 98 percent of the data in Equation (11).

$$\mathrm{h_{conv}} = \mathrm{a_1} + \mathrm{a_2 T_d} + \mathrm{a_3 T_d^2} + \mathrm{a_4} \ln(\mathrm{T_d}) \tag{11}$$

The natural logarithm term was used to account for the drop in temperature as it approached ambient. When higher-order terms were added to Equation (11), a

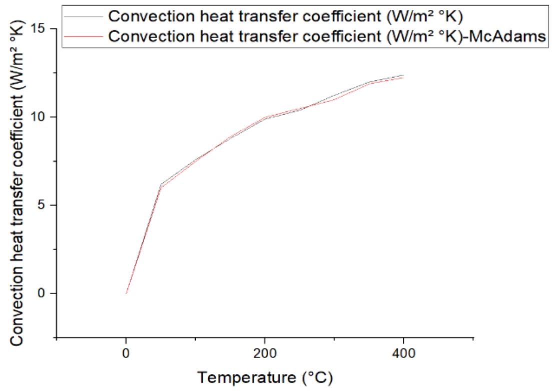

Figure 6. Mean convective heat transfer coefficient values across the arc area for various temperatures

regression equation that described almost 99 percent of the data was obtained, but the improved accuracy was deemed not justifiable due to the additional computational time required. For the arc section, coefficients for Equation (10) have been obtained and are listed in Table 4. The sole limitation to utilizing this Equation (11) is that it does not exactly pass through zero at ambient temperature. As a result, the user must explicitly provide ambient temperature has a h_{conv} value of zero and then let Equation (11) estimate the remainder.

Figure 7 depicts the flow chart analysis of the heat dissipation of the stationary disc brake. The first part of the analytical-numerical modeling is the topic of research on the expected temperatures of the discs over an extended period. In second part investigates air movement, convective heat transfer coefficients, and velocities, validations based on CFD modeling.

5. RESULTS AND DISCUSSION

It was uncertain how much convective heat transfer occurred between the two rectangular zones on the reduced disc brake friction surface shape. Regarding the arc areas, "h_{conv}" equation for a friction surface on a disc brake might be obtained using a similar technique. The capacity to take on a rectangular form has the advantage of allowing the boundary layer on the surface is expected to develop equally in the horizontal direction throughout the entire surface. Results have been discussed considering convective heat transfer in a rectangle, convection transfer of heat during friction as the whole

TABLE 4. Coefficients for the arc area according to Equation (11)

a1	a_2	a_3	a_4
-10.65	-0.025	3.4×10^{-5}	4.55

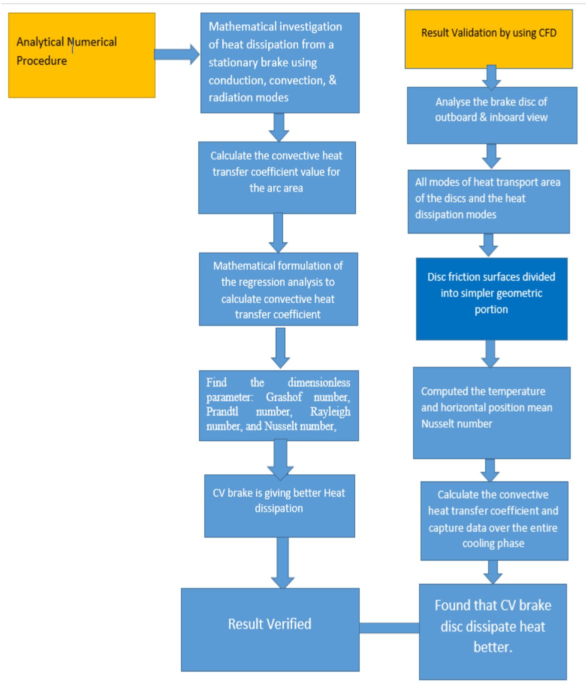

Figure 7. Flow chart for computation of heat transfer of the stationary disc brake

area of the disc, and convective heat transfer over the hat section.

5. 1. Convective Heat Transfer in a Rectangle

As a result, the airflow and heat transmission properties would be uniform across segments, significantly simplifying the operation. As per the design, the rectangle's base lengths equal twice the inner radius dimension. By equating the disc surface area to the four sectors and then adjusting for yr, the height of the rectangle could be calculated analytically. As a result, the size of the reduced geometry was the same as that of the conventional geometry, making them equivalent. The rectangle height was calculated using Equation (12), determined to be 114 mm.

$$y_r = \frac{\frac{\pi\left(r_o^2-r_i^2\right)}{4}-2A_{rec}}{2r_i} \tag{12}$$

The characteristic wall length and dimensionless quantities for the rectangle were determined. The temperature range that will be investigated may remain constant. The temperature range under investigation will be consistent, ranging from 20°C to 400°C, and will have equivalent temperature-dependent air characteristics. Figure 9 shows the change in Grashof, Prandtl, Rayleigh, and Nusselt numbers as a function of temperature. Because air is still fluid, Prandtl values decrease as temperature rises; the values are identical to those in the arc region. The Rayleigh, Grashof, and Nusselt numbers all began at zero and grew nonlinearly to a peak value before vanishing; For the three different dimensionless numbers, 1.15 x10^7, 1.685 x10^7, and 34.6 were the peak values, respectively. The convective HTC result for the rectangle region (shown in Figure 9) displays a pattern similar to the arc area since the same equations and fluid parameters were used (shown in Figures 8-11).

The h_{conv} value was 4.1 percent lower than the arc region; at 400°C, the most significant value was 11.5 W/m^2 K. Table 5 shows the coefficients for Equation (11) to create a regression equation for predicting h_{conv} values.

5. 2. Convection Transfer of Heat Over the Entire Friction Area of the Disc Since the brake disc geometries was simplified, two independent investigations of the disc friction surface and heat transmission zones could be developed. The result is a weighted average comparable measurement that was used to obtain a broad comprehension of the whole disc brake surface's heat transmission variation as a function of temperature. The arc surface area accounts for half of the surface total contact face area, giving it a weight

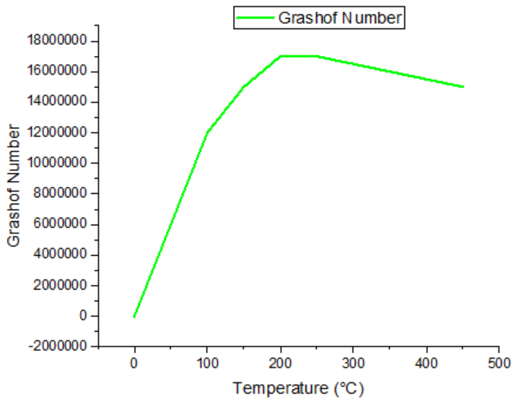

Figure 8. Grashof number vs temperature for the rectangular area

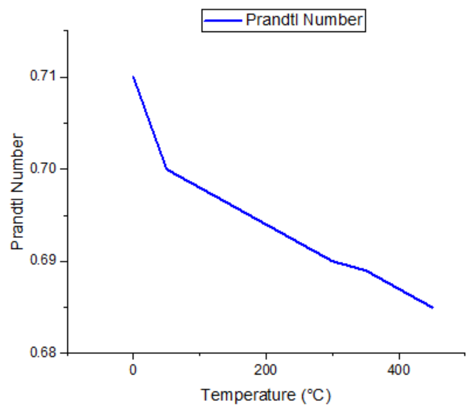

Figure 9. Prandtl number vs temperature for the rectangular area

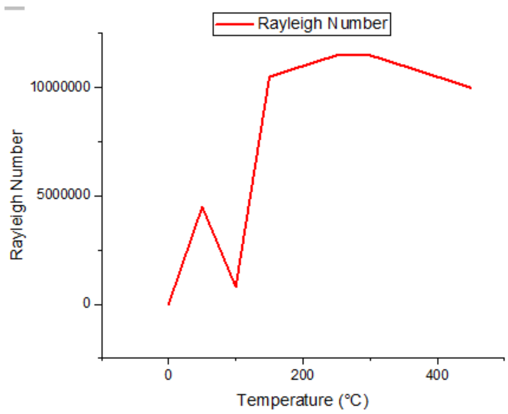

Figure 10. Rayleigh number vs temperature for the rectangular area

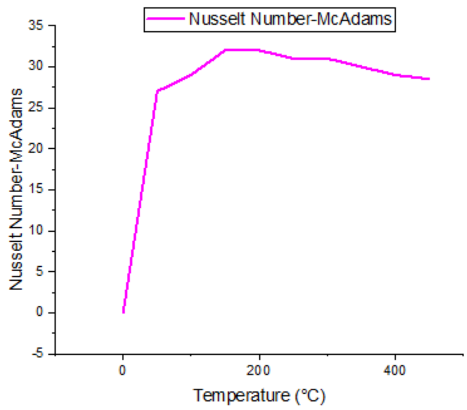

Figure 11. Nusselt number vs temperature for the rectangular area

TABLE 5. Coefficients for the rectangle area according to Equation (11)

a_1	a_2	a_3	a_4
-10.225	- 0.0245	3.3x10^{-7}	4.35

TABLE 6. Coefficients equivalent Equation (11) to friction area

a_1	a_2	a_3	a_4
-8.08	-0.019	2.55x10^{-5}	3.47

function of 0.51 and a weighted rectangle function of 0.49. The final disc surface regression equation adjusted quadratic equation represents roughly 98 percent of the data; Table 6 has the coefficient values.

Obtaining an Equation (11) that illustrates convective heat transfer from the friction surfaces of disc brakes was the subject of the preceding sections. However, four terms in the equation indicate the relative complexity of behavior. Several elements that influence the h_{conv} value must be simplified to create the relationship. It was claimed, for example, that the surface's relative position was not taken into account. The flow over the surface is affected by the hat part's presence on the outboard side. For example, the air passing through the top rectangle would be hotter than the air passing through the bottom rectangle, which was a final consequence that was overlooked. The heat transfer values in the rectangles at the top and bottom were calculated using identical figures.

On the other hand, this method substantially improves the current temperature estimate for disc brakes in parked conditions. In addition, the convective heat transfer capabilities of a general disc shape geometry oriented vertically in free air have been examined thus far. As a result, this method can now be used to acquire the hat section's h_{conv} value.

5. 3. Convective Heat Transfer Over Hat Section

In the CV brake disc convection research, an identical dimensionless number inquiry was performed on the hat part as it was on the disc friction surface. The buoyant air flow around cylindrical structures has also gotten much attention. For example, a CV brake disc's cylinder-shaped hat section has a high length and diameter; this allows for a lot of heat escape through convection. A pattern in Nusselt numbers for cylinders was observed by Churchill and Chu [12], similar to vertically placed flat walls in free air. For flow across cylindrical bodies, only isothermal surfaces with Rayleigh numbers in the 104 to 1012 range can use their correlation Equation (13).

$$Nu^{1/2} = 0.6 + \frac{0.387\ Ra_D^{1/6}}{[1+(0.6/Pr)^{9/16}]^{8/27}} \quad (13)$$

Morgan [11] also proposed a vertical wall correlation Equation (14), which is comparable to the McAdams [10] equation. However, the coefficient values matching flows across a circular surface to the relevant Ra value range.

$$Nu = \frac{h_{conv}D}{k} = cRa_D^n \quad (14)$$

As a result, the dimensionless numbers should all have the same profile, with the scale shifting as the duration of the characteristic varies in Table 7.

TABLE 7. Morgan [11] Equation (14), the Ra_D range values

Ra_D	c	n
10^{-10} to 10^{-2}	0.68	0.06
10^{-2} to 10^{2}	1.025	0.15
10^{2} to 10^{4}	0.851	0.19
10^{4} to10^{7}	0.482	0.252
10^{7} to 10^{12}	0.128	0.33

By averaging the findings, h_{conv} Equation was constructed. Because it fits Equation (11), the equation format was kept consistent; Table 8 presents the coefficients.

For emissivity calculations, the temperatures range from 0°C to 350°C and 200°C to 1000°C. Given that the temperature range under investigation in this project varies from 20° to 400° C, the cooling test had to be repeated twice to capture data over the entire cooling phase and to ensure consistent values were obtained.

Figure 12 depicts the emissivity result; Emissivity varies with temperature because a body's ability to accept electromagnetic waves decreases as it heats up. Figure 12 shows this pattern, but the decrease in temperature is so minor that the difference in the calculation is negligible. As a result, the emissivity of the grey cast iron disc brake can be assumed constant throughout the stationary parking application.

Previous studies concentrated on determining the thermal distortion and stress levels of a brake rotor [29], reducing the vonmises stresses and displacement vector sum and mass of the brake disc [30], increasing the velocity of mass movement through the passage [31], and calculating deformation and temperature [32].

According to Newcomb [33], Newcomb and Millner [34] the cooling rates of automobile drum and disc brakes. The drums or disc brakes were heated to maintain a consistent temperature using drag braking, and they were timed to see how quickly they cooled while the vehicle was moving at a constant speed. The shape and scale of the disc or drum have been shown to influence cooling rates. Front brake cooling rates are

TABLE 8. HTC coefficients for the hat area in relation to Equation (11)

a_1	a_2	a_3	a_4
-7.37	- 0.0100	1.22x10^{-5}	3.13

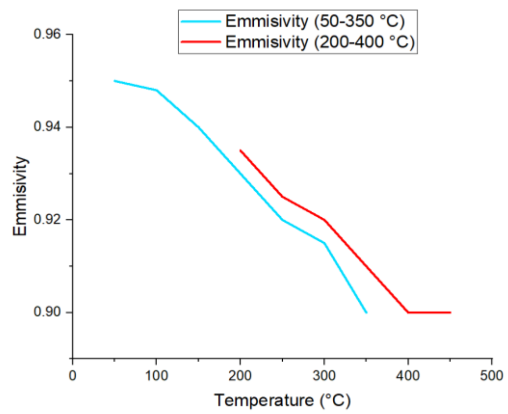

Figure 12. Entire cooling phase, emissivity results

approximately 18% higher than rear brake cooling rates, and front discs cool approximately 22 % faster than the optimum drum size for the same car, according to the results. The cooling rate of the front discs did not change when wire wheels were used instead of solid wheels. There was also a comparison of solid and vented discs. Dust shields on disc brakes have been found to reduce cooling rates by approximately 20%. The effect of disrupting airflow in other ways was investigated.

6. VALIDATION

In this section, analytically predicted temperature has been compared to computed values. A comparison of the three numerical analysis results to CFD data is shown in Figure 13, with error bars of 5% added to show the necessary degree of accuracy.

Cases 2 and 3 anticipated temperature profiles are highly similar to case 1, and the temperature is definitely over-predicted by more than the acceptable margin. After the hour mark, the main difference between cases 2 and 3 becomes apparent. When the two profiles parted ways when the disc brake temperature dropped below 125°C in case 2. Using a constant h_{conv} resulted in a slower change in the temperature profile gradient than in case 3. Both approaches are accurate to within a 5 percent margin of error. However, because of the flexibility of convection, case 3 more closely resembles the cooling profile than case 2. It may be determined that a variable coefficient of convection is required to maintain the cooling profile's surface temperature integrity during a temperature change from higher to lower.

Since only a tiny amount of energy may be emitted at temperatures close to ambient, at low temperatures, the increase in h_{conv} can be due to radiation variation. In the previous example, keeping radiation constant resulted in underestimating convection and overestimating emitted radiation energy. As a result, the variation in radiative heat transfer as a function of temperature must be taken into account because it was included in the cooling 1st order differential equation, and the numerical results were improved.

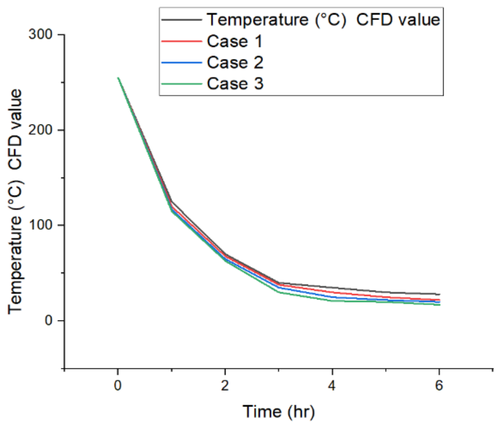

Figure 13. Comparison of the expected (Cases 1, 2 and 3) and measured temperatures CFD value

7. CONCLUSIONS

In the automotive industry, the research provided has two uses: Commercial vehicle EPB development which is both resilient and accurate, allowing temperature predictions, and EPB management on real-world automobiles. Following interferences can be reported.

- Estimating disc temperatures during the cooling process at 400°C, the value of Ra as 3.5 x10^8 indicates a turbulent flow.
- A Nusselt number pattern that appears identical over the arc surface produces 13.38 percent better performance. Nu values at maximum temperature were calculated to be 80.5 and 82.6 at 251.8 °C, respectively.
- When examining a single point along the horizontal center line, the size of the Grashof number increases as temperature falls, peaking at 255.6°C. The kinematic viscosity affects thermal gradient and a temperature of 255.6°C or higher, lowering the Gr value.
- The h_{conv} value was 4.1 percent lower than the arc zone, with a maximum of 11.5 W/m^2 K at 400°C.

Research limitations/ implications - Correct answers for complex processes such as heat transport and particle tumbling have been achieved using CFD software.

Social implications - The event of automated driving offers a number of possible benefits both on an individual level as well as to the society, such as improved safety and fuel economy, increased heat dissipation and reduced problems with congestions etc.

Findings - It is evident from the findings that convective heat transfer coefficient in all regions improves the disc brake thermal stability.

The expected and measured disc temperatures were relatively close, falling below the 5% tolerance for error. According to numerical solutions produced in heat transfer, coefficients and temperatures were averaged over the main disc surfaces to grasp a CV brake disc heat dissipation better. CFD modeling has helped to evaluate flow patterns and h_{conv} fluctuation throughout the entire disc brake surface area. In addition, the investigation has helped to assess appropriate modeling methodologies for calculating heat transfer coefficients for all disc regions.

The CFD software have been used so that correct solutions for complex processes, such as heat transmission and particle tumbling, may be achieved.

Regarding the outlook, there are three recommendations for the expansion of future work

related to disc brake that can be done to further understand the effects of the thermal stability of the disc brake, the recommendations are as follows:
1. Experimental study to verify the accuracy of the numerical model developed.
2. Tribological and vibratory study of the contact disc – pads;
3. Study of dry contact sliding under the macroscopic aspect (macroscopic state of the surfaces of the disc and pads).

8. REFERENCES

1. Slosarczyk, K., Linden, J., Burnham, K., Cockings, K. and Capolongo, R., "Implementation of an electronic park brake feature with limited data availability", in 2008 19th International Conference on Systems Engineering, IEEE., (2008), 254-259.
2. Peng, Y.-q. and Li, W., "Research on fuzzy control strategies for automotive epb system with amesim/simulink co-simulation", in 2009 Chinese Control and Decision Conference, IEEE., (2009), 1707-1712.
3. Lee, C., Chung, H., Lee, Y., Chung, C., Son, Y. and Yoon, P., "Fault detection method for electric parking brake (epb) systems with sensorless estimation using current ripples", ***International Journal of Automotive Technology***, Vol. 11, No. 3, (2010), 387-394.
4. Galindo-Lopez, C. and Tirovic, M., "Understanding and improving the convective cooling of brake discs with radial vanes", ***Proceedings of the Institution of Mechanical Engineers, Part D: Journal of Automobile Engineering***, Vol. 222, No. 7, (2008), 1211-1229.
5. Voller, G., Tirovic, M., Morris, R. and Gibbens, P., "Analysis of automotive disc brake cooling characteristics", ***Proceedings of the Institution of Mechanical Engineers, Part D: Journal of Automobile Engineering***, Vol. 217, No. 8, (2003), 657-666.
6. McPhee, A.D. and Johnson, D.A., "Experimental heat transfer and flow analysis of a vented brake rotor", ***International Journal of Thermal Sciences***, Vol. 47, No. 4, (2008), 458-467.
7. Liang, L., Jian, S. and Xuele, Q., *Study on vehicle braking transient thermal field based on fast finite element method simulation*. 2005, SAE Technical Paper.
8. Bagnoli, F., Dolce, F. and Bernabei, M., "Thermal fatigue cracks of fire fighting vehicles gray iron brake discs", ***Engineering Failure Analysis***, Vol. 16, No. 1, (2009), 152-163.
9. Tirovic, M. and Voller, G., "Interface pressure distributions and thermal contact resistance of a bolted joint", ***Proceedings of the Royal Society A: Mathematical, Physical and Engineering Sciences***, Vol. 461, No. 2060, (2005), 2339-2354. doi.
10. McAdams, W., "Heat transfer", ***McGraw-Hill, New York***, Vol. 1, No. 51, (1954), 3.
11. Morgan, V.T., The overall convective heat transfer from smooth circular cylinders, in Advances in heat transfer. 1975, Elsevier.199-264.
12. Churchill, S.W. and Chu, H.H., "Correlating equations for laminar and turbulent free convection from a horizontal cylinder", ***International journal of heat and mass transfer***, Vol. 18, No. 9, (1975), 1049-1053.
13. Ozisik, M.N., "Heat transfer: A basic approach, McGraw-Hill New York, Vol. 780, (1985).
14. Richardson, P. and Saunders, O., "Studies of flow and heat transfer associated with a rotating disc", ***Journal of Mechanical Engineering Science***, Vol. 5, No. 4, (1963), 336-342.
15. Fletcher, L., "Recent developments in contact conductance heat transfer", (1988).
16. Bergman, T.L., Lavine, A.S., Incropera, F.P. and DeWitt, D.P., "Introduction to heat transfer, John Wiley & Sons, (2011).
17. Moffat, R.J., "Describing the uncertainties in experimental results", ***Experimental Thermal and Fluid Science***, Vol. 1, No. 1, (1988), 3-17.
18. Moffat, R.J., "Using uncertainty analysis in the planning of an experiment", (1985).
19. Nakos, J.T., *Uncertainty analysis of thermocouple measurements used in normal and abnormal thermal environment experiments at sandia's radiant heat facility and lurance canyon burn site*. 2004, Sandia National Laboratories (SNL), Albuquerque, NM, and Livermore, CA
20. Taylor, J., "Introduction to error analysis, the study of uncertainties in physical measurements, (1997).
21. Taylor, J.R., *University science books*. 1982, Mill Valley California.
22. Stevens, K. and Tirovic, M., "Heat dissipation from a stationary brake disc, part 1: Analytical modelling and experimental investigations", ***Proceedings of the Institution of Mechanical Engineers, Part C: Journal of Mechanical Engineering Science***, Vol. 232, No. 9, (2018), 1707-1733.
23. Stevens, K., Leiter, R. and Taylor, M., "Thermal aspects in electronic parking braking of commercial vehicles", in European conference on braking., (2010).
24. Noroozi, M.J., "Investigation of the effects of non-linear and non-homogeneous non-fourier heat conduction equations on temperature distribution in a semi-infinite body", ***International Journal of Engineering, Transactions C: Aspects***, Vol. 28, No. 12, (2015), 1802-1807. doi: 10.5829/idosi.ije.2015.28.12c.14.
25. Goudarzi, K., Shojaeifard, M. and Fazelpour, M., "Effect of contact pressure and frequency on contact heat transfer between exhaust valve and its seat", ***International Journal of Engineering, Transactions B: Applications*** Vol. 21, No. 4, (2008), 401-408.
26. Viviani, A. and Pezzella, G., "Heat transfer analysis for a winged reentry flight test bed", ***International Journal of Engineering***, Vol. 3, No. 3, (2009), 329-345.
27. Kostikov, Y.A. and Romanenkov, A.M., "Approximation of the multidimensional optimal control problem for the heat equation (applicable to computational fluid dynamics (CFD))", ***Civil Engineering Journal***, Vol. 6, No. 4, (2020), 743-768. doi: 10.28991/cej-2020-03091506.
28. Abderrahmane, B., Naima, B., Tarek, M. and Abdelghani, M., "Influence of highway traffic on contamination of roadside soil with heavy metals", ***Civil Engineering Journal***, Vol. 7, No. 8, (2021), 1459-1471. doi: 10.28991/cej-2021-03091736.
29. Valvano, T. and Lee, K., "An analytical method to predict thermal distortion of a brake rotor", ***SAE Transactions***, (2000), 566-571.
30. Kumar, G.R., Thriveni, S., Reddy, M.R. and Gowd, G.H., "Design analysis & optimization of an automotive disc brake", ***International Journal of Advanced Engineering Research and Science***, Vol. 1, No. 3, (2014), 24-29.
31. More, A.V. and Sivakumar, R., "Cfd analysis of automotive ventilated disc brake rotor", ***Int. Journal of Engineering Research and Applications, ISSN***, Vol., No. 2248-9622.
32. Jaligama, S.K., Choudhary, P., Kumar, K.C., Prashanth, B. and Sreekanth, D., "Cfd and thermal analysis of atv disc brake", ***International Journal of Research and Technology***, Vol. 7, (2020), 1511-1516.

33. Newcomb, T., "Transient temperatures in brake drums and linings", ***Proceedings of the Institution of Mechanical Engineers: Automobile Division***, Vol. 12, No. 1, (1958), 227-244.

34. Newcomb, T. and Millner, N., "Cooling rates of brake drums and discs", ***Proceedings of the Institution of Mechanical Engineers: Automobile Division***, Vol. 180, No. 1, (1965), 191-205.

Persian Abstract

چکیده

هدف مطالعه حاضر توسعه ترمز دستی الکتریکی (EPB) برای وسایل نقلیه تجاری (CVs) است. رزومه‌هایی با برنامه‌های EPB در حال حاضر در مجموعه‌ای کاملاً متفاوت از برنامه‌های EPB در خودروهای سواری که در حال حاضر به طور گسترده استفاده می‌شوند، در دسترس هستند. پارک ایمن نیاز به تمرکز بسیار بیشتری با مرتبه بزرگی، ظرفیت حرارتی بیشتر، جرم ترمز و فشار گیره دارد. در مرحله اول، تلفات حرارتی از دیسک ترمز برآورد شد. بررسی‌ها همچنین امکان پیش‌بینی دقیق اتلاف حرارت تشعشعی را با تعریف گسیل سطحی فراهم کردند. پارامترهای حرکت هوا، ضرایب انتقال حرارت همرفتی و سرعت مورد بررسی قرار گرفت و اعتبارسنجی با مدل CFD انجام شد. هنگامی که دما به ۲۵۲ درجه سانتیگراد کاهش یافت، حداکثر مقدار تخمینی عدد ناسلت ۷۲/۲۵ بود. الگوی عدد ناسلت که روی سطح قوس یکسان به نظر می رسد، ۱۳/۳۸ درصد نتایج بهتری به همراه دارد. مقادیر Nu در حداکثر دما ۸۰/۵ و ۸۲/٦ در ۲۵۱/۸ درجه سانتیگراد محاسبه شد. مقدار "h_{conv}" ٤/۱ درصد کمتر از ناحیه قوس بود، با بالاترین مقدار در ٤۰۰ درجه سانتیگراد ۱۱.۵ W/m^2 °K. مطالعه حاضر رویکرد منحصر به فردی را اتخاذ کرد و دمای دیسک ترمز و ضریب انتقال حرارت همرفتی را روی سطوح اصطکاک دیسک و مناطق کلاه به دست آورد. مدل سازی CFD در طول فاز خنک کننده برای ارزیابی الگوهای جریان و نوسانات "h_{conv}" در کل سطح ترمز دیسکی انجام شد. مدل‌سازی ریاضی و روش اتخاذ شده برای محاسبه ضرایب انتقال حرارت برای مناطق مختلف دیسک به درک بهتر اتلاف حرارت دیسک ترمز CV کمک کرده است.

International Journal of Engineering

Journal Homepage: www.ije.ir

Probabilistic Damage Analysis of Isolated Steel Tub Girder Bridge Excited by Near and Far Fault Ground Motions

M. A. Baig*, M. I. Ansari, N. Islam, M. Umair

Jamia Millia Islamia, Department of Civil Engineering, New Delhi, India

PAPER INFO

Paper history:
Received 27 September 2022
Received in revised form 14 November 2022
Accepted 18 November 2022

Keywords:
Tub Girder Bridge
Friction Pendulum Isolator
Damage State
Probabilistic Demand Model
Fragility Curve

ABSTRACT

Friction Pendulum Bearing (FPB) has emerged as a popular solution for damage protection of bridges under seismic events. The study presents the probabilistic damage analysis for the isolated tub girder continuous bridge under the near and the far fault earthquakes using fragility analysis. The steel tub girder continuous bridge is considered with friction pendulum isolator as the seismic isolation mechanism. In order to represent the hysteretic behavior of friction pendulum isolators, a bilinear force-deformation model was used. Fragility curves are developed for various damage measures namely rotational ductility of pier and girder displacement with the peak ground acceleration (PGA) as an intensity measure (IM). Incremental dynamic analyses (IDA) were performed to develop the fragility curves and probabilistic damage model considering the four threshold damage states. The results suggest that in the case of low PGA level, the near fault earthquake leads to the high probability of exceedance in the case of isolated tub girder bridge. Damage model for piers and girder were developed to correlate component responses levels to overall bridge deterioration states. Finally, recommendations for the bridge developers in the stage of the early bridge seismic isolation design utilizing friction pendulum isolators are discussed.

***doi**: 10.5829/ije.2023.36.02b.09*

1. INTRODUCTION

In recent years, it is observed that the long-period displacement and velocity pulse motion of the near-fault earthquakes may severely influence the bridge seismic performance and design. Major earthquakes can inflict damage to them, which can have a large direct or indirect economic impact. The seismic isolation is considered to provide the layer of flexibility between the bent and the superstructure isolating the structure from the destructive force from the ground motion. Additional energy dissipation devices may also be utilized for increasing seismic response and reducing the damage to the bridges. The source of seismic excitation determines the dynamic response of the bridge structure and the designer must take this effect into consideration in order to produce a successful design [1].

The application of the friction pendulum dampers and the rubber bearings can prolong the superstructure vibration in response to earthquake motion leading to the increase the fundamental time period and lowering the likelihood that the structure will resonate when an earthquake occurs. During the swing of the friction pendulum back and forth, the friction between the wear plates may absorb some seismic energy [2].

Energy conservation was used in the numerical simulations for vibrations of continuous bridge using friction pendulum bearing (FPB) caused by the earthquakes. The multi-hazard source excitations (such as Taft and El Centro earthquake) with various dominating time- period and duration on an isolated bridge energy response, the impact of friction coefficient and the FPB isolation period was investigated [3].

Nonlinear dynamic history studies are performed to explore the sensitivity impacts of isolation duration, friction coefficient, limits on sliding deformation and the bridge reactions. The analysis shows that by employing proper friction coefficients, the drift and ductility may be

*Corresponding Author Institutional Email: aamirmirzagarri@gmail.com (M. A. Baig)

Please cite this article as: M. A. Baig, M. I. Ansari, N. Islam, M. Umair, Probabilistic Damage Analysis of Isolated Steel Tub Girder Bridge Excited by Near and Far Fault Ground Motions, ***International Journal of Engineering, Transactions B: Applications***, Vol. 36, No. 02, (2023), 289-298

reduced [4]. The ensemble of horizontal components of actual earthquake ground motions are studied in order to determine the seismic effect of multi-span continuous bridges decoupled by sliding isolators and elastomeric bearings. Different mathematical models of bridges isolated by various isolation techniques are provided with the mathematical framework for seismic response analysis [5].

Varied-sized seismic activity produces different levels of intensity in various seismic areas, and the severity of the damage to bridges caused by an earthquake directly relates to the intensity level. 1516 girder bridges and 612 arch bridges that were damaged to varying degrees by May 12, 2008 earthquake in Wenchuan County, China, were studied. The parameters of vulnerability assessment include sample number (SN), failure ratio (FR), and exceeding probability (EP) [6].

The empirical seismic damage probability matrix model together with a mean seismic damage index (MSDI) matrix model were computed in order to obtain a more realistic picture of the overall damage condition of various bridge segments. It was decided to use MSDI as the vulnerability parameter in a regional vulnerability matrix probability model [7].

The copula approach is used to create seismic fragility curves for isolated continuous girder bridges made of reinforced concrete, taking into account indices of earthquake damage such drift limit, isolated bearing, and main girder impact damage [8].

This study employs PSDM and the fragility analysis to investigate the probabilistic seismic damage analysis of a steel tub girder influenced by the ground vibrations from the near and the far faults. For parametric analysis, a benchmark bridge in New Delhi, India, that exhibits the essential features of a typical continuous girder bridge, was used. A nonlinear analytical model in three dimensions was created in the CSI Bridge software using bridge data to account for the inelastic behaviour of substructure. The IDA approach was utilized to compute damage for demand factors such as pier ductility and girder displacement, whereas seismic intensity parameters such as PGA were considered. The current study seeks to create an effective methodology for estimating the likelihood of collapse throughout the design and retrofit phases of bridges exposed to seismic risks.

2. GROUND MOTION CHARACTERISTIC AND SELECTION

Near-fault earthquakes (which are typically focused at a range of 10-20 km) include a substantial fraction of the fault energy appears as pulses. Far-field motions are defined as ground motions with an epicentral distance of greater than 10 miles [9]. When compared to higher frequencies of ground motions caused by the far-faults, near-fault ground motions have higher acceleration and more restricted frequencies. Seismic waves from such earthquakes often show lengthy pulse durations of large ranges in the beginning of earthquake records, particularly when they exhibit progressive direction effects. A significant amount of the fault energy is transferred to the site with a significant pulse that appears at the beginning of the seismic waves when the fault is propagating toward a site with a velocity that is similar to that of the shear wave [10].

Near-fault ground motions, according to Somerville are ones that frequently include pulses of long period velocity and persistent ground displacement. Most of the near-fault earthquake pulses have a maximum Fourier spectrum in a narrow range of periods, in contrast to far-field seismic events have a maximum Fourier spectrum throughout a wide range of periods [11].

The level of energy input to a structure is influenced by the seismic record rather than the structure's parameters [12]. To investigate the isolated bridge's behavior, 8 near-fault and 8 far-fault records of seismic events were selected from the Pacific Earthquake Engineering Research Center (PEER) database depicted in Table 1. Based on references, the following specific rules for choosing near-fault ground motion records were developed: (i) the nearest source-to-site distance to rupture in the chosen data were less than 10 km, which is typically thought to be within a near-fault region ; and (ii) the moment magnitude levels (Mw) were between 6 and 7.5 [13]. The epicentral distance of the far-field recordings taken into consideration was more than 20 km, and their magnitudes (Mw) ranged from 6 to 7.5. The response spectra for 5% damping for corresponding earthquakes is shown in Figure 1.

3. ISOLATION SYSTEM MODELING AND DESIGN

The Friction Pendulum (FPB) bearing has a spherical sliding interface and a spherical bearing (for the rotating

TABLE 1. Records of Near and Far Fault Earthquakes

Seismic Record	PGA	Near-fault Rjb	PGA	Far-fault Rjb	Mag.
	(g)	(Km)	(g)	(Km)	
Imperial	0.16	8.54	0.128	23.17	6.48
Irpinia	0.13	8.14	0.027	44.82	6.88
San Fernando	0.23	6.78	0.075	25.58	6.61
Loma Prieta	0.29	10.27	0.078	52.39	6.89
Northridge	0.41	0	0.047	53.71	6.69
Landers	0.73	2.19	0.115	69.21	7.28
Kobe Japan	0.35	3.31	0.068	69.04	6.86
Tabas Iran	0.62	1.46	0.105	24.07	7.35

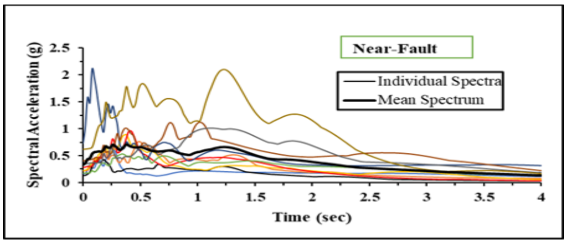

(a)

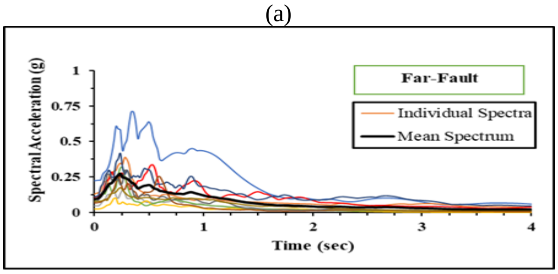

(b)

Figure 1. Response spectrums: (a) Near fault; (b) Far fault earthquakes

component). It functions very similarly to a spherical bearing having higher lateral stiffness as a result of the sliding interface curvature [14]. Such isolators may be made to have lengthy durations of vibration (5 or more seconds) and significant lateral displacement capabilities. The majority of friction pendulum bearings are made up of a concave spherical steel plate, an articulate slider, and a housing plate [5].

Two distinct processes work together to supply the bearing with resistance to horizontal loads that act to increase displacement. The first of these is the frictional resistance, F_f produced at the point where the articulated slider and concave surface meet. This force is determined by multiplying the weight component normal to the concave surface by the dynamic friction coefficient. A bilinear hysteresis model can roughly represent the (lateral) force- displacement behavior of an FPB, as shown in Figure 2. Figure 2 presents the representation of the equivalent linear stiffness (ke), which is determined by Equation (6). Equation (5) was used to calculate the period of vibration (Tp) that occurs after an FPB isolator is activated, where D_0 is the greatest value of the FPB horizontal displacement during the cyclic movement. Thus:

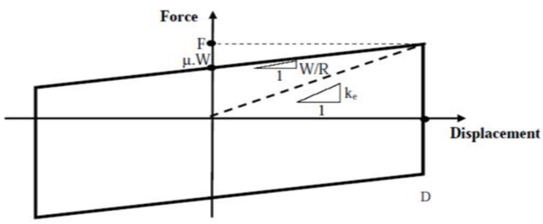

Figure 1. Idealized Bi-linear curve for Friction Pendulum Isolator

$$F_f = \mu W \cos\theta \tag{1}$$

The second mechanism of resistance is the bearing's restoring force, which is caused more by weight's tangential component and is provided by:

$$F_f = W \sin\theta \tag{2}$$

The following factors determine the bearing's horizontal resistance to displacement:

$$F = \mu W + \frac{W}{R} D \tag{3}$$

$$F = Q_d + K_d D \tag{4}$$

where μ = coefficient of friction; W = design load; R = Radius of concave sliding surface; Q_d = characteristic strength of isolator; D = design displacement and K_d = post yield stiffness of isolator.

The time period, while sliding is given by following expression:

$$T = 2\pi\sqrt{\frac{R}{g}} \tag{5}$$

By dividing the horizontal force, F, by the appropriate bearing displacement D, the effective isolator stiffness, ke, is determined as follows:

$$K_e = \frac{\mu W}{D} + \frac{W}{R} \tag{6}$$

The area of the hysteretic loop is given by Equation (7):

$$\text{Area} = 4\mu WD \tag{7}$$

The effective damping of the isolator is given by Equation (8):

$$\beta_e = \frac{2}{\pi}\left[\frac{\mu}{\mu+\frac{D}{R}}\right] \tag{8}$$

where β_e = effective damping of isolator.

4. METHODOLOGY FOR FRAGILITY FUNCTION

Bridges may sustain damage during an earthquake, especially if they were not constructed with proper seismic design and details. The uncertainty regarding a number of contributing variables and its capacity to sustain demands before incurring damage, it is appropriate to express the probability of experiencing various levels of damage using a probabilistic approach [15].

Fragility curves are classified into two types (i.e., empirical and analytical). Post-earthquake surveys are used to generate empirical fragility curves, which support to offer a broad understanding of correlation for the various structural damage limits and the ground motion indices [16]. This technique is impractical for creating fragility curves for bridges that have been modified because damage state definitions are arbitrary and there is a scarcity of damage data. Analytical fragility curves that represent the seismic sensitivity of a structure have been developed using probabilistic seismic demand model (PSDM) that employ a Bayesian method and nonlinear time-history studies [17]. If the seismic demand and capacity were characterized by a log-normal distribution, the likelihood of attaining a certain damage state will also be distributed log-normally, as calculated by a cumulative log-normal probability density function as follows:

$$P\left[\frac{LS}{IM}\right] = \Phi\left[\frac{ln(IM) - ln\,(IM_n)}{\beta_{total}}\right] \tag{9}$$

where IMn = intensity measure median; ln (IM) logarithmic median of selected damage state; and Φ = standard cumulative normal distribution.

$$\beta_{total} = \sqrt{{\beta_C}^2 + {\beta_D}^2} \tag{10}$$

where β_C indicates the uncertainty of structural capacity and β_D indicates the uncertainty in ground motion.

In this study, the uncertainties in modelling, material characteristics, damping and concrete strength variations were not taken into account. The uncertainty due to earthquake ground vibrations was anticipated to be significantly larger than the uncertainties in structural capacity.

HAZUS specifies a value of βc of 0.3 for the isolated structure [18]. Based on these findings, a value of βc equal to 0.3 was used to create the fragility curves in this investigation.

A probabilistic seismic analysis was performed using a nonlinear time-history response analysis of the chosen bridge for the 16 ground motions. The PGA of the seismic records was scaled from 0.1g to 1.2g at intervals of 0.1g in this study to perform the IDA, which was utilized to construct the fragility curves. To identify the nonlinear behavior produced by the ground motions and to determine the variables of the conditional probability distribution of the demand measure, data from a total of 192 analyses were collated (i.e., pier ductility and the girder displacement). When predicated on the intensity measure, the demand measure data are considered to follow a lognormal distribution [19]. While the conditional demand dispersion is constant, the conditional mean of the given demand and (PGA) was linear in log-log space [20]. As a result, the resultant probabilistic seismic demand model (PSDM) was expressed by Equation (11):

$$\text{Demand Measure (DM)} = a\,(IM)^{b} \tag{11}$$

where DM = demand measure; IM = Intensity measure.

$$\ln DM = a + b \ln (PGA) \tag{12}$$

where a and b are regression coefficients on PGA and demand measure.

The suggested technique enables engineers to choose wisely by taking into account the likelihood of each restoration scenario reducing collapse[21].

5. DAMAGE METRICS AND THRESHOLD LIMITS

A limit state is the range beyond which the structure can no longer sustain the necessary level of performance. The most crucial damages for continuous girder seismically isolated bridges are the bridge piers and displacement of girder, which are frequently compelled to enter an inelastic range of deformation during earthquakes [22]. The seismic vulnerability evaluation of engineering structures often adopts the four HAZUS damage states of mild, modest, severe, and collapse damages [18]. The explanations behind the various damage states and the accompanying damage criteria that may be found in the literature are compiled in TABLE 2. Mild state depicts the structure yield point, past which plastic deformations occur to the structure, severe denotes the degree of damage to a bridge beyond which it would not be economically possible to rebuild it.
Collapse is the maximum load that a structure can bear before losing stability and perhaps collapsing completely or partially [23].

When considering earthquake-related bridge damage, excessive plastic rotation of the plastic hinges formed at the bridge pier is most frequently used. Inelastic rotation has been found to gradually reduce the stiffness and rigidity of the pier when they are subjected to seismic loads. It is thought that a reliable indicator of the damage is the ductility that results from inelastic rotation in the plastic hinge generated at the fixity points of piers [24]. The column ductility requirement is, by definition, stated as follows:

$$\varphi = \frac{\theta}{\theta_y} \tag{13}$$

where θy represents the equivalent rotation at the yield point and θ represents the rotation of pier in its plastic hinge.

The equivalent rotation at the yield point can be calculated as:

$$\theta_y = L_P * \varphi_y \tag{14}$$

$$Lp = 0.08L + 0.022\, fy * d \geq 0.044fy \tag{15}$$

where L_P depicts the length of plastic hinge, L depicts distance from inflection point to plastic hinge, d depicts steel bar diameter.

Using moment-curvature analysis, the plastic hinge length (Lp) was determined to be 0.765 m and ϕy to be 0.00025.

A bridge collapse will occur when the girder reaches its maximum seat length, which is determined by the superstructure movement from the abutment. Due to the deck's longitudinal motion, girders may fall loose from the bearing pads, resulting in structural failure. From AASHTO-LRFD, the minimum seat width will be determined as follows [25]. The damage thresholds for mild, modest, severe, and collapse were considered with respect to the minimum seat width [26].

$$N = 1.5 \times \{8 + 0.002L + 0.008H\}\ \{1 + 0.000125\ S^2\} \qquad (16)$$

where N depicts minimum length of support length, L depicts deck length, and H depicts height of pier.

The damage limit state, which includes (i) pier ductility, which displays the inelastic rotations of bridge pier, and (ii) girder displacement, which displays the dislocation of girder from bearing, are regarded to correctly assess the vulnerability of the tub girder bridge. Four commonly utilized damage levels are employed in the seismic risk assessment of a chosen bridge:

TABLE 2. Damage Limit Definition

Damage Metrics	Damage Limits			
	Mild	**Modest**	**Severe**	**Collapse**
	DL-1	DL-2	DL-3	DL-4
Pier Ductility	2.01	3.14	5.90	9.42
Girder displacement	25% N	50% N	75% N	100% N

6. FINITE ELEMENT MODELLING OF BRIDGE

The multi-span continuous (MSC) steel tub girder bridge used for this investigation has a continuous composite deck supported by concrete column bents. The bridge, which has four spans measuring 32.6, 38.7, 41.2, and 28.2 meters, as shown in Figure 3. The bridge's superstructure is made up of a continuous composite girder deck that is 10 m wide and 0.3 m thick, and it is supported by two tub girders that are 5 m apart [27]. The twin column bents made of reinforced concrete support the girders with height of pier 6.6m. The pier has a diameter of 1.6m and a 1.6 m by 1.25 m cap beam make up the concrete column bent. Each column is strengthened with 25 dia. #32 vertical bars and 150 mm-spaced #10 spiral hoops. The abutments support the girders at the ends of the bridge. Figure 3 depicts the cross sections of the tub girder, pier and cap beam.

For the purpose of simulating the superstructure and substructure of the bridge, the lumped mass approach was used. In the structural modelling of a steel box girder bridge, elastic beam elements were used to represent the girder, while nonlinear elements were used to simulate the bearings and piers [18]. Rigid links were used to connect the girder and piers with bearings, while fiber-based nonlinear links were used to represents the piers plastic hinge [28] . The ends of the columns are where plastic hinges are most likely to develop, as shown in Figure 8, and they are modelled using the lumped plasticity model [29]. The steel model uses the Menegotto-Pinto model of steel to replicate the reinforcing bars for the piers [30]. The characteristic strengths of steel reinforcing yield stress (415 MPa), confined concrete (45 MPa), and unconfined concrete (40 MPa). The bridges are simulated in three dimensions while taking into account geometrical and material nonlinearities utilizing a finite element programmed CSI Bridge.

The bents were assumed to be fixed at the base due to the stiff site consideration, and the effect of soil interaction was not considered [25].

6. 1. Model for Friction Pendulum Isolator

The element non-linear links of the Isolator property type, which exhibit bilinear hysteretic behavior, were used to model the friction pendulum in the CSI Bridge. For the two shear directions, this element exhibits coupled bilinear hysteretic behavior, whereas the other four degrees of freedom (axial deformation and three rotations) are linear [31]. For friction isolator connections, the force-deformation curve characteristics are manually entered into the CSI Bridge data sheet depicted in Table 3. The isolator characteristics used in the study of isolated bridges determine effective stiffness. The fundamental period of a taken for isolated bridge is 2 seconds, whereas the period of a non-isolated bridge is 0.37 seconds.

7. RESULTS AND DISCUSSION

The Probabilistic damage analysis of a four-span continuous steel tub bridge isolated by a friction

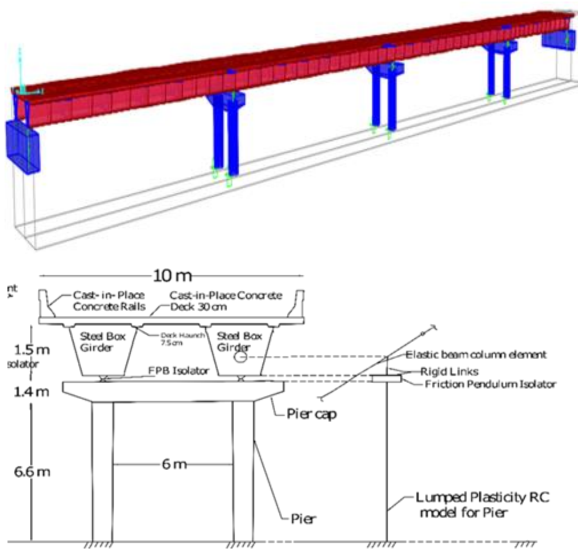

Figure 2. Finite element model of Tub girder bridge

TABLE 3. Friction pendulum Design parameters

Location	Radius	Eff. stiffness	Post slip stiffness	Coff. of Friction	Coff. of Friction	Eff. damping
	(m)	K_{eff} (KN/m)	K1 (KN/m)	μ fast	μ slow	β_{eff}
Abutment	1.2	848.2	669.16	0.04	0.02	0.134
Bent	1.2	2759.2	2176.6	0.04	0.02	0.134

pendulum isolator is assessed by developing bridge component fragility curves (pier and girder). The near and far fault earthquake records were scaled to a PGA of 0.1 g to 1.2 g, with 0.1g increments to perform time domain response history analysis. The bi-linear backbone curve of the isolator is taken into consideration while doing a nonlinear time history analysis since the bridge may experience inelastic excursion under various earthquake types (near and far fault).

The responses of the bridge are expressed in terms of pier ductility and girder displacement in the abutment, which are considered to be lognormally distributed.

Figure 4 shows the typical IDA curve and mean for displacement ductility for both near and far fault earthquakes for PGA of 0.1 g to 1.2 g. As Figure 4 shows, the response displacement ductility of the near fault earthquakes is very different from that of far fault earthquakes. The bridge begins in inelastic state at 0.42g for near fault earthquakes and 0.58g for far fault earthquakes. Also, Figure 4 shows that at PGA = 0.2g which is design level, the difference in displacement ductility requirements between near fault and far fault earthquakes are not significant. Figure 4 shows that the difference between the ductility requirements for near fault and the far fault is more noticeable when PGA = 0.6 g.

Figure 5 shows the maximum girder displacement responses and their corresponding median values for different groups of earthquakes. The peak deck displacements for the near fault are roughly three times larger than those for the far fault.

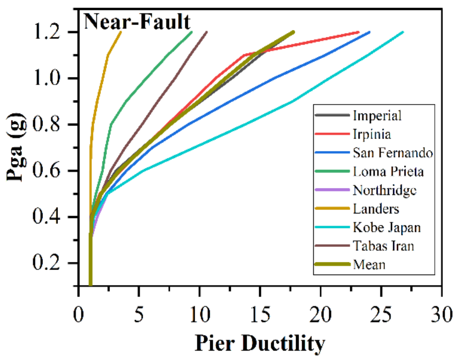

(a)

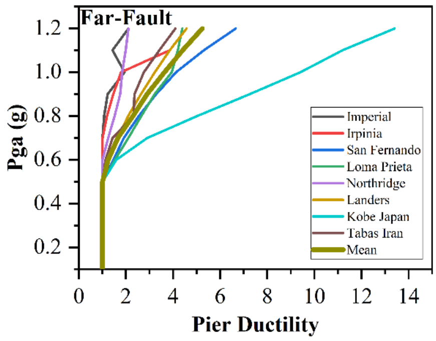

(b)

Figure 4. IDA curves for Pier Ductility: (a) Near fault; (b) Far-fault Earthquakes

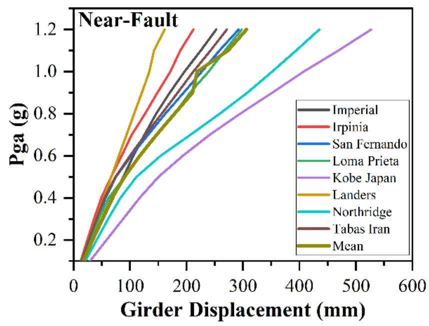

(a)

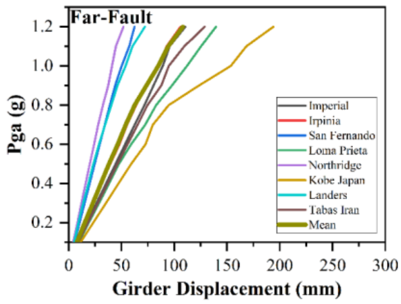

(b)

Figure 3. IDA curves for girder displacement: (a) Near fault; (b) Far-fault Earthquakes

The responses to near fault earthquakes diverge completely from those far-field earthquakes. Additionally, the pier ductility was significantly higher in

Near-fault earthquakes and exceeds the collapse damage state at 0.6 g while for the far-fault earthquakes, the bridge begins to collapse at 1g as shown in Figure .

The girder displacement responses for various earthquake types are shown in Figure 7. When compared to records from the far fault, the peak girder displacement for the close fault is approximately 2.72 times greater. When compared to the far fault effect, the amplifying response for the close fault ground motion is demonstrated to be 2.72. With a PGA of 0.8 g in the near-fault earthquake the bridge reaches a condition of collapse, as depicted in Figure 7.

A PSDM was employed in this research to construct the fragility curves from the bridge nonlinear time-history analyses. The PSDM creates a correlation between demand measures and intensity measure. The structural responses were distributed using the cloud approach, and a PSDM was created based on the results of the nonlinear time-history analysis. By employing the power-law that creates a logarithmic correlation between the median demand and chosen measure, regression analysis was utilized to obtain the mean and standard deviation for each limit condition. Figure 8 depicts a log-log plot of pier ductility and girder displacement with respect to PGA (96 data points). The structural median demands, R^2 and standard logarithmic deviation for pier and deck are listed in Table 4.

Using the described technique, fragility functions for bridges were built for the different damage measures and PGA as an intensity measure. The probability of reaching the limit states DS-1 (mild), DS-2 (modest), DS-3 (severe), and DS-4 (collapse) is depicted by the fragility curves in Figure 9.

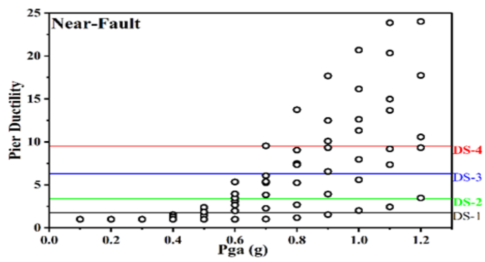

Figure 6. Response distribution for Pier Ductility: a) Near fault; b) Far-fault Earthquakes

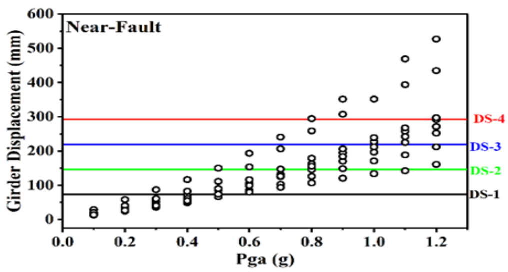

Figure 7. Response distribution for Girder Displacement: (a) Near fault; (b) Far-fault Earthquakes

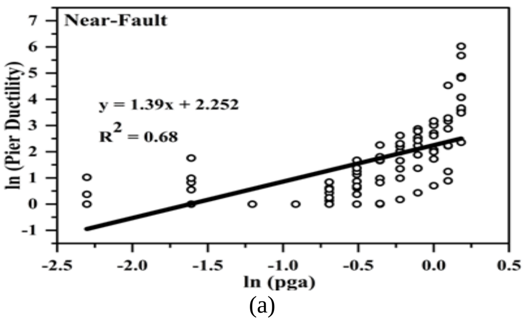

(b)

Figure 4. Logarithmic Regression Analysis for Pier Ductility: (a) Near fault; (b) Far-fault Earthquakes

TABLE 4. Proposed Damage Model for damage measures

Damage Measure	Earthquake	Damage Model	β_D	R^2
Pier Ductility	Near Fault	ln 9.50 + 1.39 ln (PGA)	1.21	0.68
Pier Ductility	Far Fault	ln 5.87 + 1.18 ln (PGA)	1.07	0.76
Girder Displacement	Near Fault	ln 340.3 + 1.38 ln (PGA)	1.12	0.85
Girder Displacement	Far Fault	ln 131.6 + 1.30 ln (PGA)	1.02	0.77

For mild (DS-1) damage scenarios related to various damage indicators, the probability of Exceedance (POE) varies substantially less between ground motions. The difference in the probability of exceedance becomes large as the damage condition advances from DS-3 to DS-4 as shown in Figure 10.

For the near-fault earthquakes, the rotational pier ductility has the POE, with 8% at 0.2g, 23% at 0.4g, and 51 % at 0.8g in severe (DS-3) damage and 5% at 0.2g, 17% at 0.4g, and 31% at 0.8g in collapse (DS-4) damage. The POE for girder displacement was 6% at 0.2g, 27% at 0.4g, and 62 % at 0.8g in severe (DS-3) damage and 3% at 0.2g, 18% at 0.4g, and 44% at 0.8g in collapse (DS-4) damage as depicted in Figure 5.

According to the current study, the POEs for far-fault earthquake for DS-3 were 1 to 5% corresponding to extreme level (PGA of 0.4g), and substantially (within 28%) at extreme-level (PGA of 0.8g), with severe and

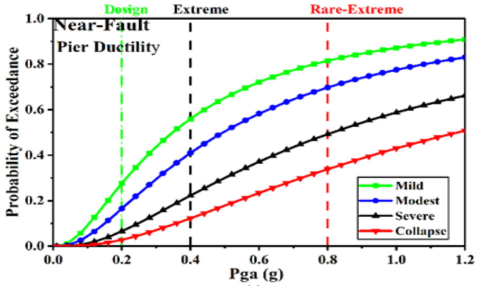

(a)

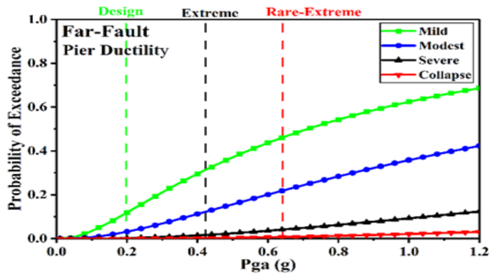

(b)

Figure 5. Fragility curve for Pier Ductility: a) Near fault; b) Far-fault Earthquakes

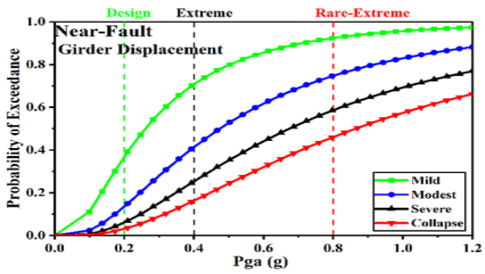

(a)

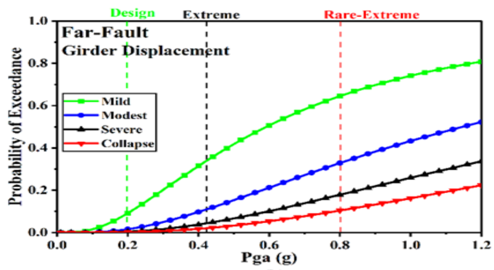

(b)

Figure 6. Fragility curve for Girder Displacement: a) Near fault; b) Far-fault Earthquakes

collapse (DS4) damage only being significant at the rare extreme-level (PGA of 0.8g) as shown in Figure 10.

8. CONCLUSIONS

To illustrate the differences in the performance of the bridge features, the performance of a tub girder bridge was examined for the near- and far-fault seismic data. The selected bridge's behavior was indicated by (i) pier ductility and (ii) girder displacement. Furthermore, the nonlinear fluctuation of the friction pendulum bearing and the plastic rotation of the bridge isolated with FPB under various forms of seismic events are explored. The analytical results of this study on a particular steel-tub girder bridge leads to the following conclusions:

- Pier ductility and girder displacement are reduced significantly in far-fault ground motions.
- Seismic isolation using friction pendulum is highly efficient in lowering ductility and girder displacement in far-field earthquakes, but it is less efficient in near-fault earthquakes.
  At a higher PGA of 0.4g, Inelastic excursions occurs on the isolated bridge.
- The highway bridge fragility curves were designed to account for four damage limit conditions. The fragility curve for the collapse damage limit condition was substantially influenced by the relative displacement of the superstructure. In contrast, the ductility requirements of the piers dominated the fragility curves for the severe and collapse damage limit states.
- Because these fragility curves were more trustworthy, it emerged that the analyses ground motion (PGA) had an accurate correlation with the seismic damage suffered by bridge components. As a result, it was found that the fragility curves produced using PGA were more accurate for evaluating the damage limit condition of the bridges.
- Even for greater PGA levels with severe and collapse damage states, the probability of exceedance for the ground motions remains significant. In the severe damage state, the POE is 24% at 0.4g and 52% at 0.8g and nearly 65% in the collapse damage state.

The information above should make it apparent that the friction pendulum bearing developed for bridges sensitive to far-fault earthquakes should not be employed in the case of near-fault earthquakes. When an earthquake occurs close to a fault, the isolator must withstand much more seismic force; for instance, the pier's ductility begins to deteriorate at a level of 0.7 g PGA. The girder displacements suffered collapse when the level of PGA was 0.8 g earthquake levels. For the peak ground acceleration of 0.6g the bridge suffers mild to moderate damage under near-fault ground motions. Therefore, the friction pendulum isolator is feasible up to 0.6g under near-fault earthquakes higher levels of PGA it is necessary to develop additional type of isolators. To allow for such large pier ductility and girder displacement without causing system instability, the pier ductility must be controlled to a lower value, necessitating a hybrid control method.

9. REFERENCES

1. Khan, B. L., Azeem, M., Usman, M., Farooq, S. H., Hanif, A., and Fawad, M. "Effect of near and far field earthquakes on performance of various base isolation systems." ***Procedia Structural Integrity***, Vol. 18, (2019), 108-118. https://doi.org/10.1016/j.prostr.2019.08.145
2. Xu, J., Li, Y., Liu, K., and Qiao, W. "Seismic Design of Tied Arch Bridge in High Earthquake Region Based on Friction Pendulum Seismic Isolation Bearing." ***IOP Conference Series: Earth and Environmental Science***, Vol. 787, No. 1, (2021). https://doi.org/10.1088/1755-1315/787/1/012172
3. Li, B., Wang, B., Wang, S., and Wu, X. "Energy response analysis of continuous beam bridges with friction pendulum bearing by multihazard source excitations" ***Shock and Vibration***, Vol. 2020, (2020). https://doi.org/10.1155/2020/3724835
4. Zhang, Y., Li, J., Wang, L., and Wu, H. "Study on the Seismic Performance of Different Combinations of Rubber Bearings for Continuous Beam Bridges." ***Advances in Civil Engineering***, Vol. 2020, (2020). https://doi.org/10.1155/2020/8810874
5. Kunde, M. C., and Jangid, R. S. "Effects of Pier and Deck Flexibility on the Seismic Response of Isolated Bridges." ***Journal of Bridge Engineering***, Vol. 11, No. 1, (2006), 109121. https://doi.org/10.1061/(asce)10840702(2006)11:1(109)
6. Li, S. Q., and Liu, H. B. "Comparison of vulnerabilities in typical bridges using macroseismic intensity scales." ***Case Studies in Construction Materials***, Vol. 16, (2022). https://doi.org/10.1016/j.cscm.2022.e01094
7. Li, S. Q., and Liu, H. B. "Analysis of probability matrix model for seismic damage vulnerability of highway bridges." ***Geomatics, Natural Hazards and Risk***, Vol. 13, No. 1, (2022), 1395–1421. https://doi.org/10.1080/19475705.2022.2077146
8. Liu, Q., and Yang, C. "Seismic damage probability assessment of isolated girder bridges based on performance under near-field earthquakes." ***Applied Sciences (Switzerland)***, Vol. 11, No. 20, (2021). https://doi.org/10.3390/app11209595
9. Afreen, A., Ahmed, A., and Moin, K. "Effect of near-field earthquake on masonry structure." ***Asian Journal of Civil Engineering***, No. 0123456789, (2021). https://doi.org/10.1007/s42107-021-00353-4
10. Bhagat, S., Wijeyewickrema, A. C., and Subedi, N. "Influence of Near-Fault Ground Motions with Fling-Step and Forward-Directivity Characteristics on Seismic Response of Base-Isolated Buildings." ***Journal of Earthquake Engineering***, Vol. 25, No. 3, (2021), 455-474. https://doi.org/10.1080/13632469.2018.1520759
11. Bhandari, M., Bharti, S. D., Shrimali, M. K., and Datta, T. K. "The Numerical Study of Base-Isolated Buildings Under Near-Field and Far-Field Earthquakes." ***Journal of Earthquake Engineering***, Vol. 22, No. 6, (2018), 989-1007. https://doi.org/10.1080/13632469.2016.1269698
12. Yadav, K. K., and Gupta, V. K. "Near-fault fling-step ground motions: Characteristics and simulation." ***Soil Dynamics and Earthquake Engineering***, Vol. 101, (2017), 90-104. https://doi.org/10.1016/j.soildyn.2017.06.022
13. Shang, J., Tan, P., Han, J., Zhang, Y., and Li, Y. "Performance of seismically isolated buildings with variable friction pendulum bearings under near-fault ground motions." ***Journal of Building Engineering***, Vol. 45, (2022), 103584. https://doi.org/10.1016/j.jobe.2021.103584
14. Sreeman, D., and Kumar Roy, B. "Optimization Study of Isolated Building using Shape Memory Alloy with Friction Pendulum System under Near-fault Excitations." ***International Journal of Engineering, Transactions A: Basics***, Vol. 35, No. 11, (2022), 2176-2185. https://doi.org/10.5829/ije.2022.35.11b.12
15. Siqi, L., Tianlai, Y., and Junfeng, J. "Empirical Seismic Vulnerability and Damage of Bottom Frame Seismic Wall Masonry Structure: A Case Study in Dujiangyan (China) Region." ***International Journal of Engineering, Transactions C: Aspects***, Vol. 32, No. 9, (2019), 1260-1268. https://doi.org/10.5829/ije.2019.32.09c.05
16. Nair, S. S., Hemalatha, G., Raja, S. R., and Stephen, E. A. "Seismic vulnerability studies of a G+17 storey building in Abu Dhabi - UAE using fragility curves." ***International Journal of Engineering, Transactions B: Applications***, Vol. 34, No. 5, (2021), 1167-1175. https://doi.org/10.5829/ije.2021.34.05b.10
17. Avşar, Ö., Yakut, A., and Caner, A. "Analytical fragility curves for ordinary highway bridges in Turkey." ***Earthquake Spectra***, Vol. 27, No. 4, (2011), 971-996. https://doi.org/10.1193/1.3651349
18. Federal Emergency Management Agency. "Hazus Earthquake Model Technical Manual ." ***Federal Emergency Management Agency***, (2020), 1-436.
19. Razmkhah, M. H., Kouhestanian, H., Shafaei, J., Pahlavan, H., and Shamekhi Amiri, M. "Probabilistic seismic assessment of moment resisting steel buildings considering soft-story and torsional irregularities." ***International Journal of Engineering, Transactions B: Applications***, Vol. 34, No. 11, (2021), 2476-2493. https://doi.org/10.5829/IJE.2021.34.11B.11
20. Shinozuka, M., Banerjee, S., and Kim, S.-H. "Statistical and Mechanistic Fragility Analysis of Concrete Bridges," (2007), 214. Retrieved from c:%5CCS%5Call refs%5Ctechnical%5CMCEER reports%5C07-0015.pdf
21. Ranjkesh, S. H., Asadi, P., and Hamadani, A. Z. "Seismic collapse assessment of deteriorating RC bridges under multiple hazards during their life-cycle." ***Bulletin of Earthquake Engineering***, Vol. 17, No. 9, (2019), 5045-5072. https://doi.org/10.1007/s10518-019-00647-8
22. Asadi, P., Nikfar, D., and Hajirasouliha, I. "Life-cycle cost based design of bridge lead-rubber isolators in seismic regions." ***Structures***, Vol. 27, (2020), 383-395. https://doi.org/10.1016/j.istruc.2020.05.056
23. Pan, Y., Agrawal, A. K., Ghosn, M., and Alampalli, S. "Seismic Fragility of Multispan Simply Supported Steel Highway Bridges in New York State. I: Bridge Modeling, Parametric Analysis, and Retrofit Design." ***Journal of Bridge Engineering***, Vol. 15, No. 5, (2010), 448-461. https://doi.org/10.1061/(asce)be.1943-5592.0000085
24. Wang, Q., Wu, Z., and Liu, S. "Seismic fragility analysis of highway bridges considering multi-dimensional performance limit state." ***Journal of Earthquake Engineering and Engineering Vibration***, Vol. 11, No. 2, (2012), 185-193. https://doi.org/10.1007/s11803-012-0109-1
25. Deepu, S. P., Prajapat, K., and Ray-Chaudhuri, S. "Seismic vulnerability of skew bridges under bi-directional ground motions." ***Engineering Structures***, Vol. 71, (2014), 150-160. https://doi.org/10.1016/j.engstruct.2014.04.013
26. Chaudhary, D., Bahadur, G., and Krishna, R. "Performance Evaluation of Seismically Isolated Bridge," Vol. 8914, (2020), 513-518.
27. Baig, M. A., Ansari, I., Islam, N., and Umair, M. "Materials Today : Proceedings Effect of lead rubber bearing on seismic performance of steel box girder bridge." ***Materials Today: Proceedings***, (2022). https://doi.org/10.1016/j.matpr.2022.04.953
28. Ghosh, G., Singh, Y., and Thakkar, S. K. "Seismic response of continuous bridge with isolation bearings." ***Proceedings of the Institution of Civil Engineers: Bridge Engineering***, Vol. 164, No. 4, (2011), 211-225. https://doi.org/10.1680/bren.2011.164.4.211
29. Phan, V., Saiidi, M. S., Anderson, J., and Ghasemi, H. "Near-

Fault Ground Motion Effects on Reinforced Concrete Bridge Columns." ***Journal of Structural Engineering***, Vol. 133, No. 7, (2007), 982-989. https://doi.org/10.1061/(asce)0733-9445(2007)133:7(982)

30. Lee, T. H., and Nguyen, D. D. "Seismic vulnerability assessment of a continuous steel box girder bridge considering influence of LRB properties." ***Sadhana - Academy Proceedings in Engineering Sciences***, Vol. 43, No. 1, (2018), 1-15. https://doi.org/10.1007/s12046-017-0774-x

31. Landi, L., Grazi, G., and Diotallevi, P. P. "Comparison of different models for friction pendulum isolators in structures subjected to horizontal and vertical ground motions." ***Soil Dynamics and Earthquake Engineering***, Vol. 81, (2016), 75-83. https://doi.org/10.1016/j.soildyn.2015.10.016

Persian Abstract

چکیده

یاتاقان آونگ اصطکاکی (FPB) به عنوان یک راه حل محبوب برای محافظت از آسیب پل ها تحت رویدادهای لرزه ای ظهور کرده است. این مطالعه تحلیل آسیب احتمالی را برای پل پیوسته تیر وان جدا شده تحت زمین لرزه های گسل نزدیک و دور با استفاده از تحلیل شکنندگی ارائه می دهد. پل پیوسته تیر وان فولادی با جداساز آونگی اصطکاکی به عنوان مکانیزم جداسازی لرزه ای در نظر گرفته می شود. به منظور نشان دادن رفتار هیسترتیک جداسازهای آونگ اصطکاکی، از یک مدل نیرو-تغییر شکل دوخطی استفاده شد. منحنی‌های شکنندگی برای اندازه‌گیری‌های آسیب مختلف از جمله شکل‌پذیری چرخشی جابجایی پایه و تیر با پیک شتاب زمین (PGA) به عنوان اندازه‌گیری شدت (IM) ایجاد شده‌اند. تحلیل‌های دینامیکی افزایشی (IDA) برای توسعه منحنی‌های شکنندگی و مدل آسیب احتمالی با در نظر گرفتن چهار حالت آسیب آستانه انجام شد. نتایج نشان می دهد که در مورد سطح PGA پایین، زلزله نزدیک به گسل منجر به احتمال زیاد بیش از حد در مورد پل تیر وان جدا شده می شود. مدل آسیب برای پایه ها و تیرها برای همبستگی سطوح پاسخ اجزا به حالت کلی خرابی پل ایجاد شد. در نهایت، توصیه هایی برای توسعه دهندگان پل در مرحله طراحی جداسازی لرزه ای پل اولیه با استفاده از جداسازهای آونگ اصطکاکی مورد بحث قرار می گیرد.

IJE TRANSACTIONS B: Applications Vol. 36, No. 02, (February 2023) 299-310

International Journal of Engineering

Journal Homepage: www.ije.ir

A Multi-objective Cash-in-transit Pollution-location-routing Problem Based on Urban Traffic Conditions

M. Mazinani[a], R. Tavakkoli-Moghaddam*[b], A. Bozorgi-Amiri[b]

[a] *Department of Industrial Engineering, Alborz Campus, University of Tehran, Tehran, Iran*
[b] *School of Industrial Engineering, College of Engineering, University of Tehran, Tehran, Iran*

PAPER INFO

Paper history:
Received 18 July 2022
Received in revised form 21 September 2022
Accepted 02 October 2022

Keywords:
Cash-in-transit
Pollution-location-routing Problem
PROMETHEE Method
Genetic Algorithm

ABSTRACT

Cash transfer from the central treasury to the bank branches and automated teller machines (ATMs) all over the city is one of the vital processes in a banking system. There are multiple factors (e.g., location of the treasury, transportation fleet, geographic distribution of the branches and ATMs, the demand for cash, customer satisfaction, and traffic that influence the efficiency of the cash transfer). Moreover, environmental issues, and in particular the issue of greenhouse gas (GHG) emissions are given weight. In this paper, a new mathematical model for a location-routing problem with transport vehicles in the banking system is developed based on urban traffic in such a way that three objectives of decreasing greenhouse emissions, reducing location and routing costs, and increasing customer satisfaction are taken into consideration simultaneously. Furthermore, a new multi-objective genetic algorithm hybridized with a PROMETHEE method, namely the multi-objective genetic-PROMETHEE algorithm (MOGPA), is developed to tackle the proposed model. The efficiency of the proposed algorithm is examined by comparing it with the non-dominated sorting genetic algorithm (NSGA-II) and multi-objective imperialist competitive algorithm (MOICA) for the real-case issue of Saman Bank. Because management assumptions are considered in the preference functions of the proposed algorithm, the results show that the solutions of the proposed algorithm are more efficient and closer to reality.

doi: *10.5829/ije.2023.36.02b.10*

NOMENCLATURE

Indices:			
$N_\circ=\{1,\ldots,m\}$	Set of treasuries	$K=\{1,\ldots,k\}$	Set of vehicles
$N_c=\{1,\ldots,n\}$	Set of customers	$T=\{1,\ldots,t\}$	Set of periods
$N_T=N_\circ \cup N_c$	Set of nodes	$R=\{1,2,3\ldots r\}$	Set of speeds
$A=\{(i,j)\}$	Set of arcs		
Parameters:			
$K_\circ$	Engine friction factor		
N	Engine speed	C_i	Capacity of treasury i
V	Engine displacement	Q_k	Capacity of vehicle k
β	Vehicle-specific constant	G_i	Fixed cost of building a treasury i
α	Vehicle-arc specific constant	$PLDT$	Maximum possible travel time
M_k^w	Total vehicle weight	ET	Earliest time to start the cash transfer process
M^f	Weight of one million Rials	LT	Latest CIT vehicle return time
PR	Total salary of driver, cashier, and law enforcement officer (per second)	d_{ij}	Distance between two nodes i and j

* Corresponding Author's Email: tavakoli@ut.ac.ir
(R. Tavakkoli-Moghaddam)

Please cite this article as: M. Mazinani, R. Tavakkoli-Moghaddam, A. Bozorgi-Amiri, A Multi-objective Cash-in-transit Pollution-location-routing Problem Based on Urban Traffic Conditions, ***International Journal of Engineering, Transactions B: Applications***, Vol. 36, No. 02, (2023), 299-310

H_k	Variable CIT vehicle costs	q_j	Demand of customer *j*
F_k	Fixed cost for CIT vehicles *k*	s_j	Service time of customer *j*
$\left[e_j, l_j\right]$	Soft time window for costumer *j*	ts_t	Start time for traffic time interval *t*
$\left[EET_j, ELT_j\right]$	Hard time window for costumer *j*	v_{ij}^{tr}	Discretized speed defined by *r* non-decreasing speed levels in period *t*
Decision variables:			
f_{ij}^k	Amount of commodity on board of vehicle *k* traverses from *i* to *j*	y_i	1 if treasury *i* is opened; 0, otherwise
p_{ij}^k	Travel time from node *i* to node *j* by vehicle *k*	u_{ij}	1 if treasury *i* serves customer *j*; 0, otherwise
tt^k	Total travel time for vehicles *k*	x_{ij}^k	1 if vehicle *k* traverses from i to *j*; 0, otherwise
a_j	Start time to customer service *j*	z_{ij}^{ktr}	1 if vehicle *k* traverses from i to *j* in the period *t* with speed *r*; 0, otherwise
w_{il} , o_{il}	Variables of piece linear functions	SL_j	Satisfaction for customer *j*

1. INTRODUCTION

As the main body of the modern financial system, the banking system plays a significant role in sustainable growth as well as organizational adjustment and sustainable development of the economy. Cash transfer from the central treasury to the customers (branches of the bank, automated teller machines (ATMs), and large retailers) is among the vital processes of the banking system. On a global size, cash keeps being the common medium of payment in transactions. This instrument is the final source to finance transactions, especially in low-value purchases. The recent report by the Federal Reserve on the payment and business habits of the people in the United States shows that 26% of the total transactions and 40% of the payments ranging from \$10 to \$25 in 2019 were in cash [1]. Despite the support of the legislators in the usage and propagation of non-cash transactions, cash in circulation has experienced consistent growth in recent years. The amount of cash swirling in the United States has increased by 80%, between 2010 to 2019 [1]. In Iran, cash circulation is high and six of ten transactions are performed by cash. The issue of cash-in-transit (CIT) is generally one of the application areas in vehicle routing problems (VRPs) for the transportation of valuable goods including cash in areas such as populated cities or metropolitans; hence it has been a popular topic in various recent studies.

The high volume of cash and valuable goods which are in demand every day should be transferred between the treasury of the bank branches, the ATMs, and large retailers. The main limitation of the cash transit network is in the delivery and collection of cash within the timeframe. Bank branches have a limited time in the working day and security rules of the Central Bank further limit this process within the set timeframe. On top of that, we are faced with the issue of a VRP with a time window (VRPTW). Regular delivery has to happen before 12:30 and its collection before 3:00. Thus, we are faced with a hard time window. On the other hand, should the required amount of cash be not provided within the desired timeframe, apart from a loss in the fee, the bank will suffer from customer dissatisfaction with the services. So, we have also faced a soft timeframe window. Customers of the treasury are categorized into three groups; i.e., bank branches, ATMs, and large retailers. ATMs have demands for cash, retailers request for the delivery of the surplus cash and the branches can have either of these two from the treasury. It is noteworthy that on a typical day a branch can ask for cash pick-up or delivery of the surplus cash.

Traffic congestion is an important issue for logistics companies in urban areas. This growing phenomenon increasingly influences the pace of traveling during peak times. Traffic congestion usually happens in key traffic nodes, e.g., intersections, overpasses, and tunnels which can result in serious challenges for the routing optimization of the vehicles. To capture the impact of traffic congestion, the time-dependent VRP (TDVRP) is introduced in the literature. This problem considers traffic patterns throughout the day in which the pattern of alternating speed according to a predictable rhythm is exerted; this is aimed to determine the average speed of movement from one period to another. There have been few studies on the transfer of valuable commodities regarding traffic conditions. This underestimation of traffic congestion may result in inexact planning decisions as the significance of the time factor in traffic is disregarded.

In bigger banks due to the wider distribution of branches in megacities, cash delivery is handled through multiple treasuries to various branches so deciding on the proper location of the treasuries is one of the most important decisions in the process of any cash delivery [2]. The location of the treasury is selected from several nominated points which are the very branches of the bank. Each treasury possesses several CIT vehicles and independent facilities so we are faced with a location-routing problem (LRP). As the name suggests, making decisions on the facilities (e.g., factories, storehouses, and distribution centers) have been amalgamated with the decision-making on routing. It goes without saying that if any of these matters are studied independently and separately from the other ones, it may lead to inefficient results. The LRP has various applications in the supply chain network design, tactical planning, and healthcare systems [3-5].

The objective of most banks so far has been to minimize risk, cost, and time. Every day gargantuan volumes of cash are transferred to delivery vehicles, which has multiple risks including robbery. To control this risk, special security standards are put in place for the transfer of cash in local, regional, and national statutes. In other words, the process of cash delivery must be done through routes verified by the police, and the vehicles, which carry the cash must enjoy certain standards. Banks also need to ensure the cash delivery vehicles through insurance companies to control the risk (cash is usually carried by armored vehicles). It is worth noting that in this process, the volume of the cash must not exceed the set cap which is determined by the insurer. Hence if something happens through the process of cash delivery, the insurance company will sustain the risk. Regarding what has been said so far and because of outsourcing the risk of the cash delivery process to insurance companies, in this study unlike many previous ones, the risk objective function has not been used.

In recent years, social demand has been on the increase regarding environmental issues. In Iran, the most outstanding crisis in the discussion about pollution is the suspended particles with a size of fewer than 2.5 microns, which take the biggest share of the pollutants in cities, which in turn mostly emanate from older vehicles, which are in demand of renovation and repair. Recently the Environment Organization passed the clean air rule some parts of which have not yet been enforced, e.g., upgrading the obligatory standard of vehicles to Euro 5, and renovating the old transport fleet of the country which could have affected air pollution conspicuously. In addition, as air pollution increases daily due to its effects on social health passing such legislation shortly is not far-fetched. So, amelioration and renovation of the cash delivery fleet is not only a social responsibility but also represents a futuristic measure. Thus, in this article, the matter of cash delivery has been reviewed regarding the existing environmental issues and corresponding green objectives have been incorporated. Apart from the futuristic attitude to social responsibility, customer orientation in banks is an inevitable principle which all the more highlights the need to pace up providing services, like the cash delivery process.

In this paper, a multi-objective model of a location-routing problem is presented after considering the traffic conditions and with the objectives of reducing costs, as well as greenhouse emissions and increasing customer satisfaction (along with decreasing the time of cash delivery), which is considered a valuable commodity. To solve this model, a novel and metaheuristic algorithm with various objectives has been presented by hybridizing the PROMETHEE method and genetic algorithm.

The remaining parts of this paper are organized as follows. In section 2, the studies in this regard for the identification of key points and a study gap are reviewed. In section 3, the mathematical model is explicated through traffic conditions. In section 4, the solution method is offered. In section 5, the proposed problem-solving methodology is analyzed via a real-life case of cash distribution. Finally, in section 6 the key findings of this research plus grounds for future ones are touched on.

2. LITERATURE REVIEW

The vehicle routing problem with time windows is a kind of a classical VRP. Considering time windows in routing is one of the methods which contributes to making this closer to real life. This problem when was first offered by Bodin et al. [6] in 1983. In cases where there are time windows, giving services to each customer must be done within a specific time frame. This becomes all the more important considering the importance of time in providing a solution in practice. Among its applications is cash transfer in banks as well as transportation of valuable commodities. A cash-in-transit VRP (CTVRP) has derived from the traditional VRPTW, yet enjoys its unique characteristics. As CIT vehicles carry cash and other valuables, there have been many studies on them. Talarico et al. [7] solved a case of VRPTW and limitations related to the risk of cash transfer via two metaheuristic algorithms. General limitation guarantees that the overall risk does not exceed the threshold of risk. Talarico et al. [8] suggested a risk-constrained CTVRP (RCTVRP) and defined the risk of the route as the function related to the probability of a robbery, the probability of a successful robbery, and the quantitative loss after the robbery happens.

Talarico et al. [9] put forth a CVRP model with a risk limitation, in which risk was dependent on the transferred cash as well as the covered distance. For smaller samples, the model was using CPLEX and for bigger ones, two metaheuristic methods were exploited. Talarico et al. [10] developed a VRP model with two objectives minimizing costs as well as minimizing the maximum risk for solving the model, they used a combination of a metaheuristic method and a multi-criteria decision-making (MCDM) method. Bozkaya et al. [11] offered a model to decrease valuables transfer risk considering two criteria of socioeconomic risk as well as risk based on using a link. This model is solved by an adaptive large neighborhood search (ALNS) algorithm. To solve the RCTVRP, Radojičić et al. [12] designed a greedy randomized adaptive search procedure hybridized with path relinking methodology and constructed a new data structure to reduce the time complexity. Ghannadpour and Zandiyeh [13] developed a new multi-objective game theory-based model to increase the security of cash-in-transit. For this objective and to reduce transportation costs, a bi-objective vehicle routing problem with a time window (VRPTW) is developed where the risk of transfers and the distance traveled by vehicles is minimized. To better estimate the robber's performance, the probability of a robber's ambush is calculated by the game theory approach. Moreover, a new multi-objective hybrid genetic algorithm incorporated with some new heuristics and operators is developed. Fallahtafti et al. [14] suggested a location-routing framework with two objectives based on risk and the cost of transport and to solve it they used various precise and metaheuristic methods.

Although the aforementioned studies reached useful results regarding the CTVRP, they had not considered road traffic especially traffic networks inside cities, so developing a model that can encompass urban traffic is a pre-requirement. Also, there are researches in which there is a presupposition that time is not a definite factor in solving CTVRP traveling between traffic nodes. Chang [15] proposed a CTVRP model with stochastic travel time to formulate the variant distribution plans and to reduce the risk of robbery by using the time-space network flow technique. Within the same context, Yan et al. [16] established an RCTVRP model by using the time-space network technology. Mathematical programming software and decomposition/collapsing technology were employed to solve the model.

Boonsam et al. [17] studied assignment problems and VRPTW, taking Bangkok bank (Thailand) as an example. Three heuristic algorithms were used to address the problems, aiming to improve distribution efficiency by utilizing existing resources. Tikani et al. [18] offered a new model for CIT which put forth that as transport risk is proportional to the travel time of the vehicle, a formula for measuring the transport risk of traffic congestion was needed. To solve this model, they suggested flexible restricted dynamic programming and a self-adaptive caching genetic algorithm. Tikani et al. [19] came up with three objectives, including completion times, risk of robbery, and customers' satisfaction level considering the effects of traffic congestion as a daily phenomenon. Jin et al. [20] improved a bi-objective model of the CTVRP, including both the economic and environmental objectives based on real-time traffic data, and designs the nearest neighbor-first iterated local search-second (NN-ILS) algorithm.

These studies considered road traffic conditions solely based on routing. Regarding traffic conditions, the proper location of the treasuries can have a considerable impact on valuable commodities and cash transfers. Simultaneous study of the location of the treasuries and proper routing for valuables and cash about the traffic can be deemed as a gap in research in this area.

In recent years, environmental issues have attracted more attention as above said and as road transport is among the biggest producers of greenhouse gases which in turn contribute to CO_2 emissions, which trigger global warming and all this is in direct connection with fuel consumption of the vehicles, special attention has been and needs to be given this issue [21-23]. The amount of fossil fuel consumed by vehicles is dependent on factors such as velocity, acceleration, workload, quality of the road, type of vehicles, as well as traffic issues. A Pollution and Routing Problem (PRP) was initially introduced by Bektas and Laporte [24] which was a boosted version of the classical VRP within a time window that comprised routing for vehicles that are used for giving services to a group of customers and determining the speed of which is of significant importance to lower fuel costs, driver fees as well as the dissemination of greenhouse gases (GHGs). In this paper, a location-routing model with multiple objectives aiming at decreasing GHGs as well as costs on the one hand, and increasing customer satisfaction through considering traffic matters on the other are presented while weighing the issue of valuables' transport. Among the most important innovations of this paper are the modeling and the presentation of a meta-heuristic algorithm enjoying multiple objectives for the problem solutions.

3. PROBLEM DEFINITION

3. 1. Problem Description

In this section, the problem will be clarified initially through the definition of the suppositions that have been considered.

- The problem has been designed as a discrete network in which the locations of the treasuries must be close to the branches; branches, ATMs, and large retailers are considered nodes.
- The customers of the treasury are three groups (i.e., branches, ATMs, and large retailers).
- Two main activities, which are cash delivery and surplus cash collection, are done through cash transit vehicles.
- The demands of the customers are considered as clear and definite.
- Each cash transit vehicle starts moving from treasury and after going through a certain route, returns to its original location. It is noteworthy that deficiency is not allowed and that the demands of each of the customers must be met by one vehicle and within one visit. Cash transit vehicles are all the same and sustain fuel costs, depreciation costs, maintenance costs as well as manpower expenditures. Typically,

when a cash transit vehicle is used, there should be a driver, two cash deliverers, and two police officers.

- The treasuries and the vehicles do not have capacity limitations as cash is not bulky. However, because of the limitations of the demand that customers can have as well as the insurer's defined cap, plus security considerations, the maximum amount of cash, which can be transferred through each vehicle must be determined and clarified.
- Soft and hard time windows should be defined for each customer. Giving services outside the hard time window is not viable; nevertheless, doing so outside the soft time vehicle window is allowed but can result in customer dissatisfaction .
- To take route traffic into account, cash delivery is divided into t timeframes. As traffic is deemed consistent by Bektas and Laporte [24], the alternative speed for each timeframe has been regarded as r. The model is defined in a way that only one alternative of speed within the timeframe of t is passed by a vehicle over a specific arc.

3. 2. Mathematical Model In this section, a routing and location model is offered to reduce costs, decrease GHG emissions, and increase customer satisfaction by decreasing the time of cash delivery within the cash transfer network of Saman Bank. To do this, capacity limitations and soft and hard time windows have been taken into account for each of the customers of the bank treasury.

$$\begin{aligned}\text{Min } OF_1 = NVK_\circ\lambda \sum_{i\in N_T}\sum_{j\in N_T}\sum_{k\in K}\sum_{t\in T}\sum_{r\in R} d_{ij} z_{ij}^{ktr} / v_{ij}^{tr} \\ + \beta\gamma\lambda \sum_{i\in N_T}\sum_{j\in N_T}\sum_{k\in K}\sum_{t\in T}\sum_{r\in R} d_{ij} z_{ij}^{ktr} / (v_{ij}^{tr})^2 \\ + \gamma\lambda \sum_{k\in K}\sum_{i\in N_T}\sum_{j\in N_T} M_k^w \alpha_{ij} d_{ij} x_{ij}^k \\ + \gamma\lambda \sum_{k\in K}\sum_{i\in N_T}\sum_{j\in N_T} M^f \alpha_{ij} d_{ij} f_{ij}^k\end{aligned} \quad (1)$$

$$\begin{aligned}\text{Min } OF_2 = \sum_{i\in N_\circ} G_i y_i + \sum_{k\in K}(PR + H_k) tt^k \\ + \sum_{k\in K}\sum_{j\in N_c}\sum_{i\in N_\circ} F_k x_{ij}^k\end{aligned} \quad (2)$$

$$\text{Max } OF_3 = \sum_{j\in N_c} SL_j \quad (3)$$

s.t.

$$SL_j = w_{j2} + w_{j3} \qquad \forall j\in N_c \quad (4)$$

$$\begin{aligned}a_j = EET_j \times w_{j1} + e_j \times w_{j2} \\ + l_j \times w_{j3} + ELT_j \times w_{j4}\end{aligned} \qquad \forall j\in N_c \quad (5)$$

$$\sum_{l=1}^{4} w_{jl} = 1 \qquad \forall j\in N_c \quad (6)$$

$$\sum_{l=1}^{4} o_{jl} = 1 \qquad \forall j\in N_c \quad (7)$$

$$w_{j1} \le o_{j1} \qquad \forall j\in N_c \quad (8)$$

$$w_{j2} \le o_{j1} + o_{j2} \qquad \forall j\in N_c \quad (9)$$

$$w_{j3} \le o_{j2} + o_{j3} \qquad \forall j\in N_c \quad (10)$$

$$w_{j4} \le o_{j3} + o_{j4} \qquad \forall j\in N_c \quad (11)$$

$$\sum_{i\in N_\circ} u_{ij} = 1 \qquad \forall j\in N_c \quad (12)$$

$$\sum_{j\in N_c}\left(\frac{q_j + |q_j|}{2}\right) u_{ij} \le C_i y_i \qquad \forall i\in N_\circ \quad (13)$$

$$\sum_{j\in N_c}\left(\frac{|q_j| - q_j}{2}\right) u_{ij} \le C_i y_i \qquad \forall i\in N_\circ \quad (14)$$

$$\sum_{j\in N_c}\left(\frac{q_j + |q_j|}{2}\right) u_{ij} = \sum_{k\in K}\sum_{j\in N_c} f_{ij}^k \qquad \forall i\in N_\circ \quad (15)$$

$$\sum_{j\in N_c}\left(\frac{|q_j| - q_j}{2}\right) u_{ij} = \sum_{k\in K}\sum_{j\in N_c} f_{ji}^k \qquad \forall i\in N_\circ \quad (16)$$

$$\sum_{k\in K} x_{ij}^k \le u_{ij} \qquad \forall i\in N_\circ, j\in N_c \quad (17)$$

$$\sum_{k\in K} x_{ji}^k \le u_{ij} \qquad \forall i\in N_\circ, j\in N_c \quad (18)$$

$$\sum_{k\in K} x_{ij}^k + u_{kj} + \sum_{\substack{m\in N_\circ \\ m\ne k}} u_{mj} \le 2 \qquad \forall k\in N_\circ, i, j\in N_c, i\ne j \quad (19)$$

$$\sum_{k\in K}\sum_{i\in N_T} x_{ji}^k = 1 \qquad \forall j\in N_c \quad (20)$$

$$\sum_{k\in K}\sum_{i\in N_T} x_{ij}^k = 1 \qquad \forall j\in N_c \quad (21)$$

$$\sum_{j\in N_c}\sum_{i\in N_\circ} f_{ij}^k = \sum_{\substack{m\in N_T \\ m\ne j}}\sum_{j\in N_c} x_{mj}^k \left(\frac{q_j + |q_j|}{2}\right) \qquad \forall k\in K \quad (22)$$

$$\sum_{j\in N_c}\sum_{i\in N_\circ} f_{ji}^k = \sum_{\substack{m\in N_T\\ m\neq j}}\sum_{j\in N_c} x_{mj}^k\left(\frac{|q_j|-q_j}{2}\right) \qquad \forall k\in K\,. \tag{23}$$

$$\sum_{k\in K}\sum_{i\in N_T} f_{ij}^k - \sum_{k\in k}\sum_{i\in N_T} f_{ji}^k = q_j \qquad j\in N_c \tag{24}$$

$$\left(\frac{q_j+|q_j|}{2}\right)x_{ij}^k \le f_{ij}^k \qquad \forall i\in N_T, j\in N_c, k\in K \tag{25}$$

$$\left(\frac{|q_j|-q_j}{2}\right)x_{ji}^k \le f_{ji}^k \qquad \forall i\in N_T, j\in N_c, k\in K \tag{26}$$

$$\left(Q_k - \left(\frac{q_j+|q_j|}{2}\right)\right)x_{ji}^k \ge f_{ji}^k \qquad \forall j\in N_c, i\in N_T, k\in K \tag{27}$$

$$\left(Q_k - \left(\frac{|q_j|-q_j}{2}\right)\right)x_{ij}^k \ge f_{ij}^k \qquad \forall j\in N_c, i\in N_T, k\in K \tag{28}$$

$$Q_k x_{ij}^k \ge f_{ij}^k \qquad \forall i\in N_\circ, j\in N_c, k\in K \tag{29}$$

$$Q_k x_{ji}^k \ge f_{ji}^k \qquad \forall i\in N_\circ, j\in N_c, k\in K \tag{30}$$

$$\sum_{\substack{h\in K\\ h\neq k}}\sum_{\substack{m\in N_T\\ m\neq j}} x_{jm}^h + x_{ij}^k \le 1 \qquad \forall i\in N_\circ, j\in N_c, i\neq j, k\in K \tag{31}$$

$$\sum_{t\in T}\sum_{r\in R} z_{ij}^{ktr} = x_{ij}^k \qquad \forall (i,j)\in A, k\in K \tag{32}$$

$$\sum_{r\in R}\sum_{t\in T}\sum_{k\in K}\sum_{i\in N_T}\frac{d_{ij}}{v_{ijtr}} z_{ij}^{ktr} + \sum_{k\in K}\sum_{i\in N_T} p_{ij}^k \le a_j \qquad \forall j\in N_c \tag{33}$$

$$\sum_{k\in K}\sum_{i\in N_T} p_{ji}^k \ge a_j + s_j \qquad \forall j\in N_c \tag{34}$$

$$ts_{t+1}\sum_{r\in R} z_{ij}^{ktr} + PLDT\left(1-\sum_{r\in R} z_{ij}^{ktr}\right) \ge p_{ij}^k \qquad \forall (i,j)\in A,\ k\in K, t\in T \tag{35}$$

$$ts_t\sum_{r\in R} z_{ij}^{ktr} \le p_{ij}^k \qquad \forall (i,j)\in A, k\in K, t\in T \tag{36}$$

$$p_{ij}^k \ge ET\times x_{ij}^k \qquad \forall i\in N_\circ, j\in N_c, k\in K \tag{37}$$

$$EET_j \le a_j \le ELT_j \qquad \forall j\in N_c \tag{38}$$

$$p_{ij}^k \le PLDT\times x_{ij}^k \qquad \forall (i,j)\in A, k\in K \tag{39}$$

$$\sum_{r\in R}\sum_{t\in T}\sum_{i\in N_\circ}\frac{d_{ji}}{v_{ijtr}} z_{ji}^{ktr} + \sum_{i\in N_\circ} p_{ji}^k \le tt^k \qquad \forall j\in N_c, \forall k\in K \tag{40}$$

$$tt^k \le LT \qquad \forall k\in K \tag{41}$$

$$x_{ij}^k \in \{0,1\} \qquad \forall (i,j)\in A, k\in K \tag{42}$$

$$z_{ij}^{ktr} \in \{0,1\} \qquad \forall (i,j)\in A, k\in K, t\in T, r\in R \tag{43}$$

$$y_i \in \{0,1\} \qquad \forall i\in N_\circ \tag{44}$$

$$u_{ij} \in \{0,1\} \qquad \forall i\in N_\circ, j\in N_c \tag{45}$$

$$f_{ij}^k, p_{ij}^k \ge 0 \qquad \forall (i,j)\in A, k\in K \tag{46}$$

$$a_j \ge 0 \qquad \forall j\in N_c \tag{47}$$

$$tt^k \ge 0 \qquad \forall k\in K \tag{48}$$

$$w_{jl} \ge 0 \qquad \forall j\in N_c, l\in\{1,2,3,4\} \tag{49}$$

$$o_{jl} \in \{0,1\} \qquad \forall j\in N_c, l\in\{1,2,3,4\} \tag{50}$$

In the mathematical model of the problem, the first objective function (1) minimizes the emission of greenhouse gases. The objective function of fuel consumption is based on the comprehensive model of distribution which was professed by Demir et al. [25]. What is considered the second objective function (2) as a whole is defined as the stable costs of the treasury, operational costs within the cash transfer team, as well as stable and alternating costs of using cash transfer vehicles which have to be minimized. The third objective function (3) is considered to be customer satisfaction, which must be maximized. In this paper, by using a trapezoidal fuzzy function, hard and soft time windows are changing to the concept of customer satisfaction in a way that exceeds the time defined through these time windows resulting in customer dissatisfaction; Figure 1 displays this concept.

Constraints (4) to (11) represent the linearization constraints of the customer satisfaction function using Piece Linear Functions (PLFs). Constraint (12) guarantees that only one treasury is allotted to each customer. Constraints (13) and (14) state that the cash demands of the customers who are being catered for through one treasury must be lower than its capacity.

Moreover, the collected cash from the branches must be less than the capacity of the treasury. It is noteworthy that a positive demand for cash illustrates the demand for receiving cash from the treasury and a negative level of it displays cash surplus return to the treasury. Constraint (15) shows that the cash that is taken out of a treasury through all its specialized CIT vehicles is equal to the demand of all the customers from the treasury, which they had asked requested. This is all not to mention that Constraint (16) that presents the cash which enters it through all its specialized vehicles, is equal to the demands of all the customers that are specifically dealing with that treasury and have asked for the pickup of surplus cash.

Constraints (17) to (19) depict that cash transfer operations start from one treasury and finish at the same place. Constraints (20) and (21) are used to make sure that each node is met only once; in other words, the demands of one customer are catered for all at once and by the same vehicle. Constraints (22) and (23) show that the total load that exits a typical treasury is equal to the aggregate of all the demands of the customers that asked for cash and are being given services by that vehicle. Constraint (24) is the difference between the entrance and the exit of the nodes which is equal to the demand; in other words, this limitation balances commodity flow in each node and in this way discards the sub-tours to make sure that the request of the customer is met accordingly. Constraints (25) and (26) state that once a customer asks for cash, the amount of cash that is transferred by the cash transit vehicle must be more or equal to the specific customer's demand, and should the customer want to return any surplus cash, the cash, which is transferred by the vehicle on the next trip should be more or equal to the cash that was initially provided with.

Constraints (27) to (30) put forth that each customer must be allocated to one vehicle and it must be guaranteed and checked that the amount of cash that is carried through a specific vehicle does not ever exceed the insurance limit. Constraint (31) states that each customer must be linked to one cash transfer vehicle. Constraint (32) states that each parabola just uses dimension j of speed. Constraint (33) states that if node j is met after node i, the time of meeting node j is equal to the total time of movement from node i to node j and the time spent between i and j. Constraint (34) displays that the time spent from node i to node j, is bigger than the

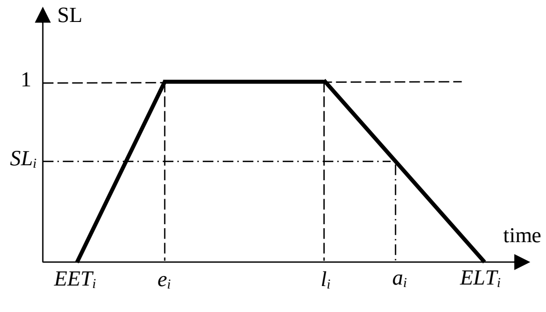

Figure 1. Satisfaction level for fuzzy time windows

entrance time to node i, and the time of giving service at node i. Constraints (35) and (36) display that the time of movement is proportionate to the time frame spent in traffic. Constraint (37) states that the time of departure for every vehicle from the treasury must be bigger than the earliest time of service provision by the treasury.

Constraint (38) is a hard time window constraint. In other words, it delimits the time of service to the customer more stringently. Constraint 39 guarantees that the time of movement from i to j by vehicle k has a non-zero amount only if its corresponding determining alternative is tantamount to 1 and the maximum level of the time of movement is commensurate to the stable quantity of PLDT. Constraint (40) shows that the time spent by vehicle k is equal to the aggregate time of moving from the last customer toward the treasury and the time spent on the way. Constraint (41) ensures that the return time of each vehicle to the treasury is before the last service is done. Constraints (42) to (50) determine the type of variables used in the model.

4. SOLUTION APPROACH

The location and pollution-routing problem is an NP-hard problem that cannot be solved through typical optimization methods and the situation persists even for the smaller and simpler samples. One solution for such problems is using metaheuristic algorithms. In this section, a new multi-objective meta-heuristic algorithm for the defined problem is proposed.

4. 1. Multi-objective Genetic-PROMETHEE Algorithm Genetic algorithms have one objective by essence. Some researchers have developed this algorithm for multi-objective problems out of which we can name NSGA-II, NRGA, and AFDGA [26-28]. Through blending the genetic and meta-heuristic algorithm with the PROMETHEE method, we are after undominated solutions which can comprise some of the decision-making characteristics within them. Such characteristics include the weight of the objectives and the function of their preference. The PROMETHEE method, as a functional one, has two words of preference and indifference it in, is after the best options. This method was first suggested by Brans [29]. In this paper, the PROMETHEE-II method is used, which rates discrete options thoroughly. In the suggested method, like the genetic algorithm, some solutions are initially generated randomly that are called first-generation parents.

The problem is a multi-objective one. The parents are assessed and rated by the PROMETHEE method. Afterward, based on the roulette wheel some of the parents are chosen to reproduce children and do the intersection operation. Upon the reproduction of the children, the population of the parents will be mixed with them and then the nondominated population will be added to the archive which will be in turn updated. The population inside the archive will be studied in terms of prominence and the solutions which can dominate others are eliminated. Moreover, in the population of the archive, the operation of eliminating similar solutions is exerted. If the size of the archive is bigger than the defined size, the solutions will be arrayed within it by using the PROMETHEE method and redundant solutions will be eliminated. In this algorithm, the size of the archive will be shown via nArchive. Furthermore, the blended population will be rated by the PROMETHEE method, the best will be transferred to the next generation only in proportionate to the initial population. This process will carry on until the precondition is reached. The stages of the multi-objective genetic-PROMETHEE algorithm (MOGPA) are shown in Figure 2.

As it is clear the functionality of an algorithm and the quality of the output solutions are completely dependent on the way the solutions are displayed in the possible area. Moreover, solution representation must be in a way that the audience can easily and freely search through them. In this paper, there has been the best use of a continuous representation for location and routing. In this representation and a simultaneous fashion of the location of the treasuries, the way customers are allotted to them, and also the route for service provision for each customer via the CIT vehicles have been shown. While the nominated location for the treasury is shown as *m*, the customer is represented by *n* with the transit vehicle being labeled as *k*.

Should the solution be shown as two lines, then *n* would be an integer. The first chain of integers is in the range of [l, *k*+1). The integer in each figure presents the way each customer is served via a vehicle and the decimal part shows the sequence of the services in a way that smaller numbers have a higher priority. As for the way treasuries are built and the point from which each vehicle should set out, there is a need to calculate all the numbers, whose integer parts are equal so that we can come up with a mean number. Then, the decimal part of them may show the position of the treasury. If the decimal part is within the range of $[0,1/m)$, it is the first treasury and if it is in the range of $[1/m,2/m)$, it will be the second treasury. Likewise, if it is within the range of $[(m-1)/m,1)$, *m* will be the starting point of the vehicles.

It shows after the vehicle delivers its required services, what speed will it use to reach customer *n*. So, the decimal segment of the figure is divided into *r* equal parts each of which represents a separate speed. In Figure 3, the solution along with its schematic form for a problem of 10 customers, 4 nominated locations for the treasury, and 5 CIT vehicles is shown.

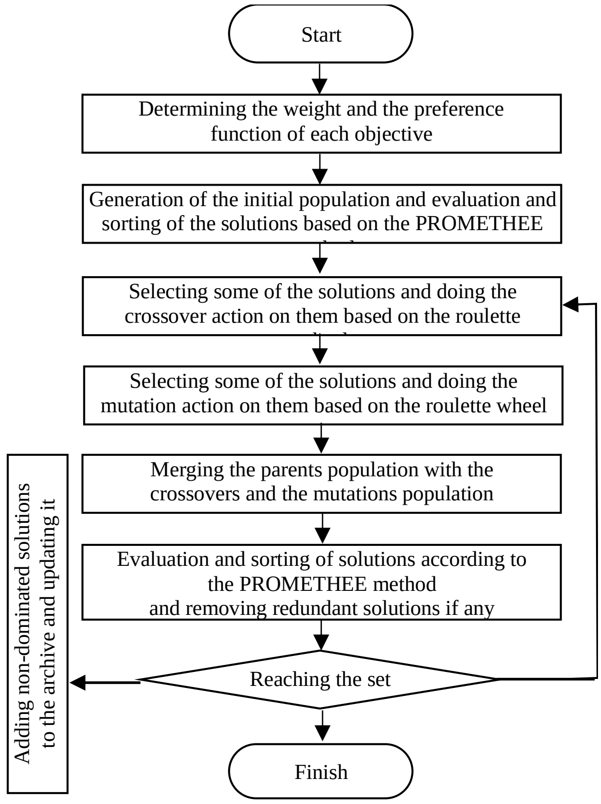

Figure 2. Flowchart of the MOGPA

The second line of integers will be in the range of $[1,r+1)$, in which the integer part shows if the vehicle leaves to any customer, which of the discrete part of speed will be used within that time.

In the suggested algorithm, three crossover operators (i.e., one-point, two-point, and uniform) are used to solve the problem. Moreover, four methods of insertion, swap, reversion, and perturbation for genetic mutation are used. The condition to halt the algorithm is to reach a certain number of function evaluations (NFE's).

1	2	3	4	5	6	7	8	9	10
3.09	5.72	2.69	1.56	2.21	1.66	3.88	2.77	1.22	4.66
4.69	1.28	1.42	4.21	2.03	2.51	2.37	2.52	1.45	2.83

	Average	Treasury
Vehicle 1	1.48	2
Vehicle 2	2.56	3
Vehicle 3	3.49	2
Vehicle 4	4.66	3
Vehicle 5	5.72	3

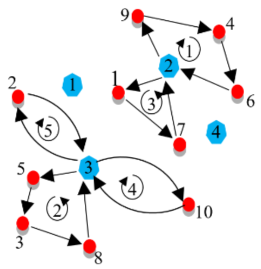

Figure 3. Solution representation and its schematic form

4. 2. Comparison Metrics for Algorithm Evaluation Studying the function of multi-objective algorithms is much more complicated than that of single-objective algorithms in a way that one assessment indicator alone will not suffice to study all the acquired responses for the presented algorithms. Hence, in this paper, to assess the quality of the solutions for the suggested algorithms, Pareto solutions attained from the suggested algorithm are compared with NSGA-II [26] and multi-objective imperialist competitive algorithm (MOICA) [30] algorithms having six indices of quality metric, mean ideal distance [31], spacing metric, diversification metric, data envelopment metric [32], and PROMETHEE metric [29].

4. 3. Parameters Tuning the design and adjustments of its parameters in a way that different quantities of the algorithm parameters may result in different solutions with totally different qualities. So, if the parameters are not tuned correctly, we cannot reach optimal solutions. In this paper, to tune the parameters, a response surface methodology (RSM) is used. The related parameters and their levels are shown in Table 1. Then, the selected parameters are summarized in Table 2.

5. COMPUTATIONAL RESULTS

To assess the functionality of the suggested algorithm, three problems with various scales based on real-life situations of Saman Bank are used (Table 3), which were in congruence with the real data of the bank. All these matters are related to cash delivery to Rial (local currency) branches of Isfahan, Mashhad, and Tabriz. All through the project the maps of the afore-cited cities which entailed the required information - for instance, potential locations to established treasuries, the locations of the branches, the ATMs, and the retailers of the bank along with the routes among the nodes - were made use of. Generally, the cash balance of the branches and the ATMs were systematically monitored and if at the end of the working day the balance or one of the centers was lower than the required minimum, the order to request cash would be put in place at the beginning of the next working day. Furthermore, the surplus liquidity of the branches and their sales points (retailers) would be collected regarding the security issues of cash transport. The bank did not allow for the disclosure of the details of the amounts of the study; to solve this issue, the suggested algorithms were programmed into the software of MATLAB 2019a. Also, other sample matters were tested in a computer with a processor of 8.1 GHz core i5 and the main hard drive of 6 GHz in the operating system of Windows 10.

In the banking industry, the most important objective is customer satisfaction so, in the method of PROMETHEE, an ordinary function is used to reach this objective which shows that even a fractional improvement in this objective enjoys high significance. The U- and the V-shaped functions are also used to minimize the cost function and to emit GHG, respectively. Because in CIT, the small difference in the cost can be ignored as long as other objectives have significant improvements. In this paper, for solution algorithms to be comparable, the weight of the objectives is deemed equal. After the implementation of the algorithms on the objectives, the six metrics mentioned above are calculated, whose results are presented in Tables 4 to 6.

Regarding the presented results, it is visible that the MOGPA algorithm is more functional than algorithms NSGA-II and MOICA. The important point in this regard is that the Pareto solutions of the MOGPA outmatch those of others all through, which shows the higher quality of solutions in this algorithm. As an example, the comparison between the Pareto solutions of the three algorithms, whose results are inserted in Figure 4, clearly supports this claim.

TABLE 1. MOGPA parameter levels

Factor	Symbol	Level		
		-1	0	1
NFE	X_1	100000	200000	300000
nPop	X_2	80	100	120
p_c	X_3	0.6	0.7	0.8
p_m	X_4	0.3	0.35	0.4
nArchive	X_5	80	100	120

TABLE 2. MOGPA parameter setting values

Factor	Symbol	Coded value	Optimal level
NFE	X_1	0.6	26000
nPop	X_2	0.061	101
p_c	X_3	0.49	0.705
p_m	X_4	0.11	0.355
nArchive	X_5	0.72	101

TABLE 3. General information on sample issues

No. of problems	City	No. of treasuries	No. of branches	No. of ATMs	No. of retailers
1	Isfahan	5	6	53	6
2	Mashhad	5	5	49	5
3	Tabriz	5	5	47	3

TABLE 4. Computational results of the QM and MID metrics

	QM			MID		
	NSGA-II	MOICA	MOGPA	NSGA-II	MOICA	MOGPA
1	0.093	0.148	0.759	0.637	0.485	0.354
2	0	0.073	0.927	0.685	0.493	0.268
3	0.017	0.124	0.859	0.847	0.732	0.349

TABLE 5. Computational results of the DM and SM metrics

	DM			SM		
	NSGA-II	MOICA	MOGPA	NSGA-II	MOICA	MOGPA
1	0.842	0.878	1.245	0.784	0.641	0.508
2	0.849	0.904	1.368	0.860	0.607	0.492
3	1.101	0.937	1.073	0.827	0.580	0.372

TABLE 6. Computational results of the DEA and PM metrics

	DEA			PM		
	NSGA-II	MOICA	MOGPA	NSGA-II	MOICA	MOGPA
1	0.837	0.952	0.954	0.308	0.392	0.731
2	0.811	0.908	0.976	0.212	0.391	0.783
3	0.875	0.917	0.956	0.294	0.303	0.642

The most important characteristics of the algorithm MOGPA are management presuppositions which are neglected by other algorithms. In other words, through blending a metaheuristic and genetic algorithm with the PROMETHEE method, non-dominated solutions are gained which entail some of the characteristics which are targeted by the decision maker comprising the weight of the objectives as well as their preference function. In this regard, customer satisfaction, as well as costs, enjoy a higher priority than the pollution objective. Moreover, a little improvement in costs is not of high priority to the bank; for instance, when the cost of transport is high, expenses with a difference of lower than 1,000,000 Rials are deemed as the same to the bank and are not privileged by the tester. On the other hand, and in non-dominated sorting even one Rial saving in costs can dominate a response. In other words, using the PROMETHEE method in rating responses has caused data optimization of the location and – in the view of the manager - also closer condition to the reality, who is taking the threshold of indifference in the preference function. Because of this, the results emanating from the MOGPA are more functional.

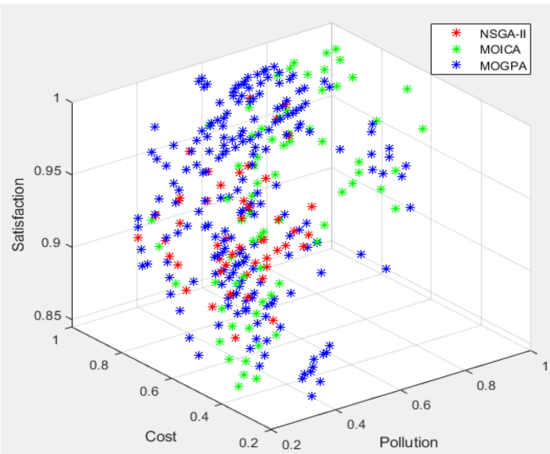

Figure 4. Pareto solutions for each algorithm

6. CONCLUSION

The model presented in this paper is a homogeneous one in the area of CIT for banks which considers both location and routing consistently and interrelatedly. In our presented model apart from minimizing cash transfer costs, we are after minimizing greenhouse emissions as well as increasing customer satisfaction. This model also takes into consideration the effects of traffic and its controlling impact on speed. As said earlier, this matter is an NP-hard one so solving bigger issues through exact optimization is not functional; as a result, a metaheuristic, multi-objective and novel algorithm in companionship with the genetic algorithm and PROMETHEE method were offered, together as the solution model. To assess the functionality of the presented algorithm, its Pareto solutions were compared with those of NSGA-II and MOICA in terms of six metrics of quality metric, mean ideal distance, spacing metric, diversification metric, data envelopment metric, and PROMETHEE metric; it was witnessed that in five indices of the quality metric, mean ideal distance, spacing metric, data envelopment metric and PROMETHEE metric, our suggested model surpassed the other algorithms with a wide margin and in terms of diversification metric, still its results were more acceptable than the other two.

For future potential research:

- We can view this problem as a simulation having in mind the demands of the customers so that in indefinite conditions, we can all the more get closer to real-life situations.
- Based on the opinions of the banking elite, significant and effective parameters can be transport costs, treasury construction costs, permitted capacity of cash transfer in the CIT vehicles, and the soft time window for each customer. As a result, through alterations in the number of parameters, we can evaluate the amount of creditability and sensitivity of the parameters, which are of more significance to the model.

7. REFERENCES

1. Federal Reserve., "Findings from the diary of consumer payment choice" Accessed September 2020. (2020) https://www.frbsf.org/cash/files/2020-findings-from-the-diary-of-consumer-payment-choice-july2020.pdf
2. Prodhon, C., and Prins, C., "A survey of recent research on location-routing problems", ***European Journal of Operational Research***, Vol. 238, (2014), 1-17. https://doi.org/10.1016/j.ejor.2014.01.005
3. Tian, G., Fathollahi-Fard, A.M., Ren, Y., Li, Z., Jiang, X., "Multi-objective scheduling of priority-based rescue vehicles to extinguish forest fires using a multi-objective discrete gravitational search algorithm", ***Information Sciences***, Vol. 608, (2022), 578-596. https://doi.org/10.1016/j.ins.2022.06.052
4. Pasha, J., Nwodu, A.L., Fathollahi-Fard, A.M., Tian, G., Li, Z., Wang, H., Dulebenets, M.A., "Exact and metaheuristic algorithms for the vehicle routing problem with a factory-in-a-box in multi-objective settings", ***Advanced Engineering Informatics***, Vol 52, (2022), 101623. https://doi.org/10.1016/j.aei.2022.101623
5. Fathollahi-Fard, A.M., Ahmadi, A., Karimi, B., "Sustainable and Robust Home Healthcare Logistics: A Response to the COVID-19 Pandemic", ***Symmetry***, (2022), Vol. 14, No. 2, 193. https://doi.org/10.3390/sym14020193
6. Bodin, L., Golden, B., Assad, A., and Ball, M., "Routing and scheduling of vehicles and crews: The state of the art", ***Computers and Operations Research***, Vol. 10, No. 2, (1983), 63-211.
7. Talarico, L., Sörensen, K., and Springael, J., "The risk-constrained cash-in-transit vehicle routing problem with time window constraints", In 14th Workshop of the EURO Working Group "EU/ME: the Metaheuristics Community," Hamburg, Germany, (2013), 104-109.
8. Talarico, L., Sörensen, K. and Springael, J., "Metaheuristics for the risk-constrained cash-in-transit vehicle routing problem", ***European Journal of Operational Research***, Vol. 244, (2015), 457-470. https://doi.org/10.1016/j.ejor.2015.01.040
9. Talarico, L., Sörensen, K., and Springael, J., "A biobjective decision model to increase security and reduce travel costs in the cash-in-transit sector", ***International Transactions in Operational Research***, Vol. 24, No. 1-2, (2015), 59-76. https://doi.org/10.1111/itor.12214
10. Talarico, L., Springael, J., Sörensen K. and Talarico, F., "A large neighbourhood metaheuristic for the risk-constrained cash-in-transit vehicle routing problem", ***Computers and Operation Research***, Vol. 78, (2017), 547-556. https://doi.org/10.1016/j.cor.2016.04.003
11. Bozkaya, B., Salman, F. S. and Telciler, K., "An adaptive and diversified vehicle routing approach to reducing the security risk of cash-in-transit operations", ***Networks***, Vol. 69, No. 3, (2017), 256-269. https://doi.org/10.1002/net.21735
12. Radojičić, N., Djenić, A. and Marić, M., "Fuzzy GRASP with Path Relinking for the risk-constrained cash-in-transit vehicle routing problem", ***Applied Soft Computing***, Vol. https://doi.org/10.1016/j.asoc.2018.05.022
13. Ghannadpour, S. F., and Zandiyeh, F., "A new game-theoretical multi-objective evolutionary approach for cash-in-transit vehicle routing problem with time windows (A Real life Case)", ***Applied Soft Computing***, Vol. 93, (2020), 106378. https://doi.org/10.1016/j.asoc.2020.106378
14. Fallahtafti A., Ardjmand E., Young W.A., and Weckman G.R., "A multi-objective two-echelon location-routing problem for cash logistics: A metaheuristic approach", ***Applied Soft Computing***, Vol. 111, (2021), 107685. https://doi.org/10.1016/j.asoc.2021.107685
15. Chang Y.H., "The Cash Pick-up and Delivery Vehicle Routing/Scheduling under Stochastic Travel Times", National Central University, Taiwan, 2011.
16. Yan, Sh., Wang, S.S., and Wu, M.W., "A model with a solution algorithm for the cash transportation vehicle routing and scheduling problem", ***Computers & Industrial Engineering***, Vol 63, (2012). 464-473. https://doi.org/10.1016/j.cie.2012.04.004
17. Boonsam, P., Suthikarnnarunai, N., Chitphaiboon, W., "Assignment problem and vehicle routing problem for an improvement of cash distribution", Proceedings of the World Congress on Engineering and Computer Science, (2011), 19-21.
18. Tikani H., Setak M., and Demir E. "A risk-constrained time-dependent cash-in-transit routing problem in multigraph under uncertainty", ***European Journal of Operational Research,*** Vol. 293, No. 2, (2021), 703-730. https://doi.org/10.1016/j.ejor.2020.12.020
19. Tikani H., Setak M., Demir E. "Multi-objective periodic cash transportation problem with path dissimilarity and arrival time variation", ***Expert Systems with Applications***, Vol. 164, (2021), 114015. https://doi.org/10.1016/j.eswa.2020.114015
20. Jin Y., Ge X., Zhang L., and Ren J., "A two-stage algorithm for bi-objective logistics model of cash-in-transit vehicle routing problems with economic and environmental optimization based on real-time traffic data". ***Journal of Industrial Information Integration***, Vol. 26, (2022), 100273. https://doi.org/10.1016/j.jii.2021.100273
21. Fallah, M., Tavakkoli-Moghaddam, R., Salamatbakhsh-Varjovi, A. and Alinaghian, M., "A green competitive vehicle routing problem under uncertainty solved by an improved differential evolution algorithm", ***International Journal of Engineering, Transactions A: Basics***, Vol. 32, No. 7, (2019), 976-981. doi: 10.5829/ije.2019.32.07a.10.
22. Esmaili M. and Sahraeian, R., "A new bi-objective model for a two-echelon capacitated vehicle routing problem for perishable products with the environmental factor", ***International Journal of Engineering, Transactions A: Basics***, Vol. 30, No. 4, (2017), 523-531. doi: 10.5829/idosi.ije.2017.30.04a.10.
23. Nozari, H., Tavakkoli-Moghaddam, R., Gharemani-Nahr, J., "A Neutrosophic Fuzzy Programming Method to Solve a Multi-depot Vehicle Routing Model under Uncertainty during the COVID-19 Pandemic", ***International Journal of Engineering, Transactions B: Applications***, Vol. 35, No. 02, (2022), 360-371. doi: 10.5829/IJE.2022.35.02B.12
24. Bektas, T. and Laporte, G., "The pollution-routing problem", ***Transportation Methodological***, Vol. 45, No. 8, (2011), 1232-1250. https://doi.org/10.1016/j.trb.2011.02.004
25. Demir, E., Bektas¸ T. and Laporte, G., "The bi-objective pollution-routing problem", ***European Journal of Operational Research***, Vol. 232, No. 3, (2014), 464-478. https://doi.org/10.1016/j.ejor.2013.08.002
26. Deb, K., Pratap, A., Agarwal, S. and Meyarivan, T., "A fast and elitist multiobjective genetic algorithm: NSGA-II", ***IEEE Transactions on Evolutionary Computation***, Vol. 6, No. 2, (2002), 182-197. doi: 10.1109/4235.996017
27. Al Jadaan, O., Rajamani, L. and Rao, C.R., "Non-dominated ranking genetic algorithm for solving multi-objective optimization problems: NRGA", ***Journal of Theoretical and Applied Information Technology***, (2008), 60-67.
28. Afruzi, E.N., Roghanian, E., Najafi, A.A., and Mazinani, M., "A multi-mode resource-constrained discrete time–cost tradeoff problem solving using an adjusted fuzzy dominance genetic algorithm". ***Scientia Iranica***, Vol. 20, No. 3, (2013), 931-944. https://doi.org/10.1016/j.scient.2012.12.024

29. Brans, J.P. L'ingénièrie de la décision; Elaboration d'instruments d'aide à la decision, La méthode PROMETHEE. In: Nadeau, R. and Landry, M., Eds., L'aide à la décision: Nature, Instruments et Perspectives d'Avenir, Presses de l'Université Laval, Québec, (1982), 183-213.

30. Afruzi, E.N,, Najafi, A.A., Roghanian, E., and Mazinani, M., "A Multi-Objective Imperialist Competitive Algorithm for solving discrete time, cost and quality trade-off problems with mode-identity and resource-constrained situations", ***Computers & Operations Research***, Vol. 50, (2014), 80-96. https://doi.org/10.1016/j.cor.2014.04.003

31. Fasihi, M., Tavakkoli-Moghaddam, R., Najafi, S. E., Hahiaghaei-Keshteli, M., "Developing a Bi-objective Mathematical Model to Design the Fish Closed-loop Supply Chain", ***International Journal of Engineering, Transactions B: Applications***, Vol. 34, No. 5, (2021), 1257-1268. doi: 10.5829/ije.2021.34.05b.19

32. Mazinani, M., Ghazi, S.E., Ghazi, N.E. and Ghaseminejad, A. "Proposing new models for finding the most efficient DMUs in DEA", ***International Journal of Management Science and Engineering Management***, Vol. 6, No. 6, (2011), 403-407. https://doi.org/10.1080/17509653.2011.10671189

Persian Abstract

چکیده

انتقال وجه نقد از خزانه مرکزی به شعب بانک و خودپردازهای موجود در سطح شهر، یکی از فرآیندهای حیاتی در نظام بانکی است. عوامل متعددی مانند محل خزانه، ناوگان حمل، مسیرهای انتقال، پراکندگی جغرافیایی شعب و خودپردازها، توزیع تقاضای پول، رضایت مشتریان و ترافیک در انجام بهینه فرآیند انتقال پول مؤثر است. همچنین امروزه مسائل زیست‌محیطی به‌خصوص مبحث انتشار گازهای گلخانه‌ای موردتوجه قرارگرفته است. در این مقاله، یک مدل جدید از مسئله مکان‌یابی – مسیریابی وسایل نقلیه برای شبکه پول‌رسانی بانک بر مبنای ترافیک شهری توسعه داده شده است به‌طوری‌که هم‌زمان سه هدف کاهش میزان انتشار گازهای گلخانه‌ای، کاهش هزینه‌های مکان‌یابی و مسیریابی و افزایش رضایت مشتریان را در نظر می‌گیرد. علاوه بر این، یک الگوریتم ژنتیک ترکیبی چند هدفه جدید که با روش پرومته ترکیب شده است برای حل مدل پیشنهادی توسعه داده شده است. کارایی و اثربخشی الگوریتم پیشنهادی از طریق مقایسه با الگوریتم ژنتیک برمبنای مرتب‌سازی نامغلوب برای مسائل واقعی بانک سامان مورد بررسی قرار گرفته است. از آنجایی که مفروضات مدیریتی در توابع ارجحیت الگوریتم پیشنهادی در نظر گرفته شده است، نتایج نشان می‌دهد که راه‌حل‌های الگوریتم پیشنهادی کارآمدتر و نزدیک‌تر به واقعیت هستند.

International Journal of Engineering

Journal Homepage: www.ije.ir

Development of a New Backward Directional Coupler Based on Perforated Substrates

H. Karimian-Sarakhs, M. H. Neshati*

Department of Electrical Engineering, Ferdowsi University of Mashhad, Mashhad, Iran

P A P E R I N F O

Paper history:
Received 27 July 2022
Received in revised form 2 December 2022
Accepted 04 December 2022

Keywords:
Directional Coupler
Perforated Substrate
Transmission Matrix

A B S T R A C T

In this paper, two wideband 10 dB backward directional couplers based on artificial perforated substrates over the frequency range of 25-35 GHz and 32-38 GHz are developed. An analytical method is proposed to design the coupler geometrical parameters. The theoretical modeling is established based on the coupled version of the transmission line (TL) theory using the extended version of the *ABCD* matrix for four ports microwave network. It is shown that using the proposed method, all required parameters of the directional coupler are determined using the per-unit-length of the applied lines. The geometrical parameters of primary designed couplers are optimized using the particle swarm optimization (PSO) procedure to improve the performance of couplers. The designed couplers are also simulated using High Frequency Structure Simulator (HFSS) software. Moreover, sensitivity analysis is carried out to investigate the effect of fabrication imperfections of the proposed couplers. The obtained results show that the simulated results agree well with the theoretical ones and a low insertion loss (*IL*) with high return loss is obtained over a wide frequency range bandwidth.

doi: *10.5829/ije.2023.36.02b.11*

1. INTRODUCTION

Directional couplers are developed as passive microwave structures consisting of three or four ports designed for arbitrary power dividing ratios, which have been used in various microwave systems including communication and measurement systems [1-5].

So far, a wide variety of waveguide or transmission line-based couplers have been developed and characterized providing a few advantages and disadvantages. Cao et al. [6] designed a directional coupler based on substrate-integrated waveguide (SIW) and stripline techniques; in which TE_{10} and TEM modes can be simultaneously transmitted. However, the operating bandwidth is only about 15%, and its size is too large. Ali et al. [7] designed a hybrid directional coupler based on the printed ridge gap waveguide (PRGW). The most important feature of the proposed coupler includes low signal distortion, low loss, and low size, meanwhile, it provides a limited bandwidth. A two-hole directional coupler consisting of different dielectric-loaded SIWs is introduced for Ka-band by Parment et al. [8]. This coupler provides a very good insertion loss lower than 0.3 dB, and the coupling factor is 20 dB with a flatness of 0.25 dB, but it can be only used for applications with high coupling. Zarifi et al. [9] introduced a variable coupling directional coupler based on a double-layer groove gap waveguide. The coupler size is very large, and also, a low coupling factor cannot be achieved using the proposed coupler. A wideband directional coupler using a dielectric overlay is presented by Peláez-Pérez et al. [10], which provides 15 dB coupling with a maximum flatness of 1 dB.

A 3 dB directional coupler based on periodic vias and multi-holes SIW is developed by Tavakoli and Mallahzadeh [11]. In order to achieve wide bandwidth, several sections are serially connected. However, insertion loss and flatness of the coupling factor are extremely affected by using the multi-holes technique, and these are about 5 dB and 2 dB, respectively. Zhao et al. [12] introduced a compact coupler with a symmetrical square feed for operating at Ka-band. Although the coupler flatness is about 0.5 dB, it provides a very low

*Corresponding Author Institutional Email: *neshat@um.ac.ir* (M. H. Neshati)

bandwidth of 7%. Moreover, its insertion loss is as high as 7 dB with the port's isolation around 10 dB.

Tabatabaeian et al. [13] designed a forward-wave directional coupler using periodic patterned ground structure in microstrip coupled lines with a 96% bandwidth, while the coupling flatness is 1 dB and return loss is not better than 10 dB. Tabatabaeian et al. [14] proposed a directional coupler using periodic shunt short-circuited stubs. Although this coupler is compact and the ripple of the final responses is about 1 dB, it shows a very low bandwidth of about 11.7%.

In this paper, an analytical procedure is proposed to design a backward directional coupler based on the coupled version of transmission line (TL) equations. The modified *ABCD* matrix of a four ports microwave network is developed and it is shown that using the introduced matrix, any multi-sections coupled structures can be analyzed. Using the proposed model, the important parameters of a directional coupler, including insertion loss, return loss, coupling level, and isolation factor are determined closed-form expressions are developed for these parameters. Then, two microstrip directional couplers based on one and the two-dimensional perforated substrate is designed. The designed coupler covers the frequency range of 25-35 GHz and 32-38 GHz with a 10 dB coupling level, a maximum flatness of 0.5 dB, and a return loss (*RL*) better than 15 dB. The simulated results show that the fractional bandwidth of the couplers is about 17% and 34%.

2. THEORETICAL MODELLING

A single-section coupled line coupler is shown in Figure 1. In the general case, this four-port coupler is terminated by impedances Z_L, Z_N, and Z_F at three different ports, and driven with a voltage source V_S and internal impedance Z_S at the exciting port.

It is assumed that the coupled lines convey Quasi-TEM waves. Therefore, based on TL theory, the current waves along the lines are given by equations (1a) and (1b) [15], in which I_{10}, I_{20}, and γ are the amplitude of propagating waves of the lines at z=0, and propagation constant given by $\gamma=\alpha+j\beta$, and α, β are the attenuation and phase constant, respectively.

$$I_1(z)=I_{10}\cosh(\gamma z)+k_1\sinh(\gamma z) \tag{1a}$$

$$I_2(z)=I_{20}\cosh(\gamma z)+k_2\sinh(\gamma z) \tag{1b}$$

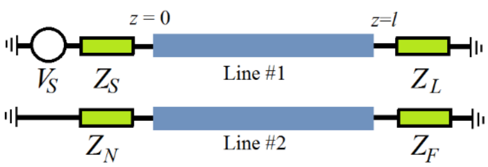

Figure 1. The geometry of a directional coupler

Also, k_1 and k_2 are constant parameters related to the amplitude of the waves of the two lines at $z=l$, respectively given by Equations (2a) and (2b), in which I_{1l}, I_{2l} are the value of the current waves of the two lines at $z=l$, respectively.

$$k_1=\frac{I_{1l}-I_{10}\cosh(\gamma l)}{\sinh(\gamma l)} \tag{2a}$$

$$k_2=\frac{I_{2l}-I_{20}\cosh(\gamma l)}{\sinh(\gamma l)} \tag{2b}$$

The corresponding voltage waves propagating on the lines are also determined using the coupled version of TL modeling given by Equations (3a) and (3b) [16].

$$I_1'(z)=-Y_1V_1(z)+Y_mV_2(z) \tag{3a}$$

$$I_2'(z)=-Y_2V_2(z)+Y_mV_1(z) \tag{3b}$$

in which

$$Y_1=G_1+j\omega C_1 \tag{4a}$$

$$Y_2=G_2+j\omega C_2 \tag{4b}$$

$$Y_m=-G_m-j\omega C_m \tag{4c}$$

C_1, C_2, C_m, ω are self and mutual per-unit-length capacitance, and angular frequency, respectively. Also, G_1, G_2, and G_m show self and mutual per-unit-length conductance. By substituting the derivatives of Equation (1) into Equation (3), the voltage waves can be expressed by the following equations.

$$\begin{aligned}&-Y_1V_1(z)+Y_mV_2(z)=\\&\qquad\gamma I_{10}\sinh(\gamma z)+\gamma k_1\cosh(\gamma z)\end{aligned} \tag{5a}$$

$$\begin{aligned}&-Y_2V_2(z)+Y_mV_1(z)=\\&\qquad\gamma I_{20}\sinh(\gamma z)+\gamma k_2\cosh(\gamma z)\end{aligned} \tag{5b}$$

Here, it is desired to extend using the *ABCD* matrix for a 4-port coupled structure as shown in Figure 1. To this end, Equations (6a) and (6b) is defined, in which **T** is a 4×4 matrix of the coupled transmission line.

$$\begin{bmatrix}V_{10}\\I_{10}\\V_{20}\\I_{20}\end{bmatrix}=\mathbf{T}\begin{bmatrix}V_{1l}\\I_{1l}\\V_{2l}\\I_{2l}\end{bmatrix} \tag{6a}$$

$$\mathbf{T}=\left[T_{nm}\right]_{4\times4} \tag{6b}$$

Also, pairs (V_{n0}, I_{n0}), (V_{nl}, I_{nl}); n=1, 2 show that the value of voltage and current for the input port at z=0, and the output port at $z=l$, and l is the length of the coupled lines, respectively. Using four Equations (1), (2), (5) and (6) the components of matrix **T** are obtained.

$$\mathbf{T}=\begin{bmatrix}\mathbf{T}_{11} & \mathbf{T}_{12}\\ \mathbf{T}_{21} & \mathbf{T}_{22}\end{bmatrix} \tag{7a}$$

$$\mathbf{T}_{11}=\begin{bmatrix}\cosh\gamma l & \frac{\gamma Y_2}{\Delta}\sinh\gamma l\\ \frac{Y_1}{\gamma}\sinh\gamma l & \cosh\gamma l\end{bmatrix} \tag{7b}$$

$$\mathbf{T}_{12}=\begin{bmatrix}0 & \frac{\gamma Y_m}{\Delta}\sinh\gamma l\\ \frac{-Y_m}{\gamma}\sinh\gamma l & 0\end{bmatrix} \tag{7c}$$

$$\mathbf{T}_{21}=\begin{bmatrix}0 & \frac{\gamma Y_m}{\Delta}\sinh\gamma l\\ \frac{-Y_m}{\gamma}\sinh\gamma l & 0\end{bmatrix} \tag{7d}$$

$$\mathbf{T}_{22}=\begin{bmatrix}\cosh(\gamma l) & \frac{\gamma Y_1}{\Delta}\sinh(\gamma l)\\ \frac{Y_2}{\gamma}\sinh(\gamma l) & \cosh(\gamma l)\end{bmatrix} \tag{7e}$$

$$\Delta=Y_1Y_2-Y_m^2 \tag{7f}$$

After specifying matrix **T**, the value of voltage and current of the coupled lines at four ports have to be calculated. To this end, four boundary conditions at the input and output terminals of the coupled lines are regarded as follows.

$$V_{10}+Z_S I_{10}=V_S \tag{8a}$$

$$V_{1l}-Z_L I_{1l}=0 \tag{8b}$$

$$V_{20}+Z_N I_{20}=0 \tag{8c}$$

$$V_{2l}-Z_F I_{2l}=0 \tag{8d}$$

By considering the mentioned boundary conditions, and four equations in matrix form Equations (7) and (8), the eight unknowns can be calculated by following matrix representation [17].

$$\mathbf{AX}=\mathbf{B} \tag{9a}$$

$$\mathbf{X}=\mathbf{A}^{-1}\mathbf{B} \tag{9b}$$

in which

$$\mathbf{X}=\begin{bmatrix}\mathbf{X}_1 & \mathbf{X}_2\end{bmatrix}^T \tag{10a}$$

$$\mathbf{X}_1=\begin{bmatrix}V_{10} & I_{10} & V_{1l} & I_{1l}\end{bmatrix} \tag{10b}$$

$$\mathbf{X}_2=\begin{bmatrix}V_{20} & I_{20} & V_{2l} & I_{2l}\end{bmatrix} \tag{10c}$$

$$\mathbf{B}=\begin{bmatrix}V_S & 0 & 0 & 0 & 0 & 0 & 0 & 0\end{bmatrix}^T \tag{10d}$$

and

$$\mathbf{A}=\begin{bmatrix}\mathbf{A}_{11} & \mathbf{A}_{12}\\ \mathbf{A}_{21} & \mathbf{A}_{22}\end{bmatrix} \tag{11a}$$

$$\mathbf{A}_{11}=\begin{bmatrix}1 & Z_S & 0 & 0\\ 0 & 0 & 1 & -Z_L\\ 0 & 0 & 0 & 0\\ 0 & 0 & 0 & 0\end{bmatrix} \tag{11b}$$

$$\mathbf{A}_{12}=\begin{bmatrix}0 & 0 & 0 & 0\\ 0 & 0 & 0 & 0\\ 1 & Z_N & 0 & 0\\ 0 & 0 & 1 & -Z_F\end{bmatrix} \tag{11c}$$

$$\mathbf{A}_{21}=\begin{bmatrix}1 & 0 & -T_{11} & -T_{12}\\ 0 & 1 & -T_{21} & -T_{22}\\ 0 & 0 & 0 & -T_{32}\\ 0 & 0 & -T_{41} & 0\end{bmatrix} \tag{11d}$$

$$\mathbf{A}_{22}=\begin{bmatrix}0 & 0 & 0 & -T_{14}\\ 0 & 0 & -T_{23} & 0\\ 1 & 0 & -T_{33} & -T_{34}\\ 0 & 1 & -T_{43} & -T_{44}\end{bmatrix} \tag{11e}$$

For a symmetrical microstrip directional coupler, in which all ports are matched, insertion loss (*IL*), return loss (*RL*), coupling factor (*CF*), and isolation factor (*IF*) are approximately determined by the following closed-form formulas.

$$RL\approx\left(V_{10}-Z_S I_{10}\right)/\left(V_{10}+Z_S I_{10}\right) \tag{12a}$$

$$IL\simeq\exp(-\gamma l)\cosh\left[\left(k_1+k_2\right)l/2\right] \tag{12b}$$

$$CF\approx\frac{k_2-k_1}{4\gamma}\left\{1-e^{-2\gamma l}\left[\cosh\left(k_1+k_2\right)l-\frac{k_1-k_2}{j2\gamma}\sinh\left(k_1+k_2\right)l\right]\right\} \tag{12c}$$

$$IF \approx -\exp(-\gamma l)\sinh\left[\left(k_1+k_2\right)l/2\right] \tag{12d}$$

in which

$$k_1 = \frac{Y_m}{u}\sqrt{\frac{j\omega C_1}{Y_1(C_1C_2-C_m^2)}} \tag{13a}$$

$$k_2 = \frac{j\omega C_m}{u}\sqrt{\frac{Y_2}{j\omega C_1(C_1C_2-C_m^2)}} \tag{13b}$$

u in the above equations is wave velocity. It is worth noting that the accuracy of the obtained equations severely depends on the per unit length parameters of the coupled lines. For a symmetrical coupled microstrip line, Equations (14a) and (14b) present an approximation value of per-unit-length parameters [18].

$$\frac{C_1}{\varepsilon} \simeq \left[1.15\left(\frac{W}{H}\right)^{0.963}+1.07\left(\frac{T}{H}\right)^{0.049}\right]+ \mathrm{e}^{-3.52\frac{S}{H}}\left[0.75\left(\frac{W}{H}\right)^{0.25}+2.7\left(\frac{T}{H}\right)^{1.36}\right] \tag{14a}$$

$$\frac{C_m}{\varepsilon} \simeq 1.17\left(\frac{W}{H}\right)^{0.083}\left(\frac{S}{H}+0.402\right)^{-0.78}+ \left(\frac{S}{H}+1.32\right)^{-0.8}\left[-1.36\left(\frac{W}{H}\right)^{-0.037}+0.227\left(\frac{T}{H}\right)^{0.98}\right] \tag{14b}$$

3. MICROSTRIP LINE COUPLER DESIGN

In this section, the design process of a backward coupler using a microstrip line placed on a perforated substrate is reported. As stated by Karimian-Sarakhs et al. [19], any two-dimensional perforated substrate is modeled by its equivalent one-dimensional perforated substrate. To this end, the equivalent propagation constant $\gamma_e=\alpha_e+j\beta_e$ is determined by equations (15a) and (15b) [19].

$$\gamma_e = \frac{1}{L_1+L_2}\cosh^{-1}\left[\frac{1-\Lambda}{2}\cosh\left(\sum_{i=1}^{2}(-1)^{i-1}\gamma_i L_i\right) + \frac{1+\Lambda}{2}\cosh\left(\sum_{i=1}^{2}\gamma_i L_i\right)\right] \tag{15a}$$

$$\Lambda = \frac{\varepsilon_1+\varepsilon_2}{\sqrt{\varepsilon_1\varepsilon_2}} \tag{15b}$$

in which (L_1, ε_1, γ_1), (L_2, ε_2, γ_2) are the length, dielectric permittivity, and the propagation constant of dielectric and air sections along the *x*-direction of the perforated substrate, respectively. The α_e and β_e are the equivalent attenuation and phase constant of the substrate. Additionally, the introduced transformation can be applied to any 2-D substrate with arbitrary shapes of air holes. More details are discussed by Karimian-Sarakhs et al. [19].

A microstrip directional coupler based-on 1-D perforated substrate can be regarded as a multi-section directional coupler. For each section, transmission matrix **T** is calculated using Equation (7). Since the coupler is divided into a few series of sub-sections, the total transmission matrix of the coupler is determined by multiplying the transmission matrix of the sub-sections given by Equation (16) [20].

$$\mathbf{T}_t = \prod_{n=1}^{N}\mathbf{T}_n \tag{16}$$

in which $\mathbf{T}_t$, $\mathbf{T}_n$, and N are the total transmission matrix, the transmission matrix of the *n*th section, and the total number of series sections, respectively. By specifying $\mathbf{T}_t$, the required parameters of the coupler including coupling factor, directivity, insertion loss, and return loss can be evaluated using the provided equations. Since the proposed method is an analytical approach, the desired parameters of the directional coupler can be straightforwardly optimized using well-known algorithms such as genetic algorithm (GA), particle swarm optimization (PSO), and the other methods.

4. RESULTS AND DISCUSSION

The microstrip line on the artificial perforated substrate provides several band gaps in its frequency response, due to existing of air holes in the structure [21]. Hence, the directional couplers established on the perforated substrate have typically low-frequency bandwidth. However, by selecting the proper value of the ratio of the dielectric section length to the air section length (L_1/L_2), the band-gaps is shifted to the undesired frequency band. Figure 2 shows the phase constant of a perforated substrate for different values of ratio L_1/L_2. It can be seen that by increasing the value of L_1/L_2, the first band gaps will be shifted to the lower frequencies. Also, the number of band gaps will be increased with the arising value of L_1/L_2.

Another factor influencing the band-gap properties of a perforated substrate is the length of the dielectric and air sections. Figure 3 shows the phase constant of a perforated substrate for different values of L_1, and L_2. It is worth noting that in this figure, the length of air and dielectric sections are equal. It can be seen that similar to Figure 2, by increasing the length of dielectric and air sections, the first band gap has appeared at lower frequencies. Additionally, the number of band gaps will be also increased by arising the length of dielectric and air sections. As a result, to design a directional coupler based on the perforated substrate, not only L_1 and L_2

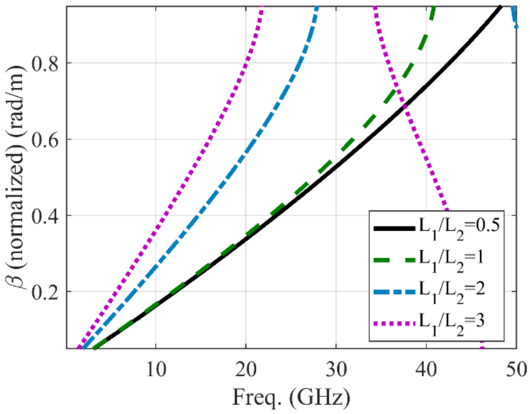

Figure 2. Phase constant of the perforated substrate for different values of ratio L_1/L_2

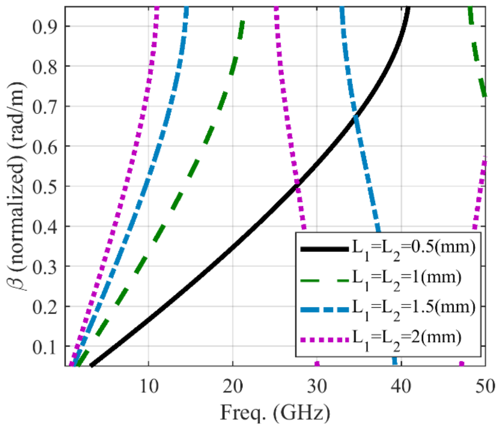

Figure 3. Phase constant of the perforated substrate for different values of L_1, and L_2

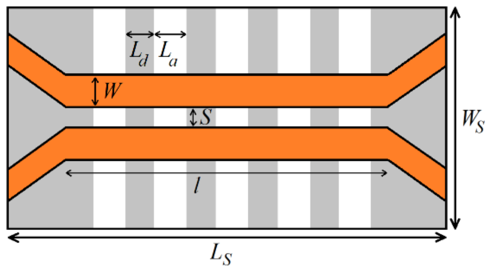

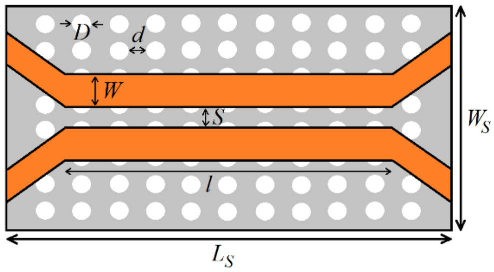

Figure 4. Microstrip backward directional coupler based on (a) 1-D perforated substrate (b) a 2-D perforated substrate

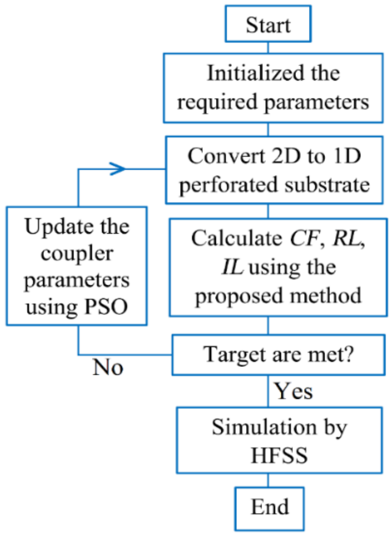

Figure 5. Flowchart of the designed coupler procedure

should be a small value, but also, L_1, and L_2 should be as small as possible. It should be noted that values of L_1, L_2 should be physically acceptable.

Considering the aforementioned limitations, a microstrip backward directional coupler with a coupling level of 10 dB is designed and investigated based on a perforated substrate with a dielectric permittivity of 10.2, a thickness of 0.635 mm, tangent loss of 0.0035, and conductor thickness 17 µm. The dimensions of the proposed coupler are W_S=3.2 mm, and L_S=2.9 mm as defined in Figures 4(a) and 4(b) including the other geometrical parameters of the two couplers. The primary design is done using the presented formulas in section II, and the final geometrical parameters of determined using an optimization procedure by PSO implemented by MATLAB code. Figure 5 shows the flowchart of the optimization procedure. In the optimization process, a 10 dB coupling level with a maximum ripple of 0.5 dB, and return loss better than 15 dB are considered as the objective and constrains. Also, the minimum and maximum values of the substrate parameters (L_d, L_a, D, d) are determined according to Figures 2, 3, and corresponded expressions. The maximum length of the couplers is considered equal to $\lambda_g/2$. The maximum variations for W and S are about of ±10% around their initial values.

Figure 6 shows the equivalent attenuation and phase constant of the 1-D and 2-D perforated substrate using the introduced method by Karimian-Sarakhs et al. [19], which confirms that the first band gap is far from the desired frequency band. For the designed couplers, the isolated port is terminated to a 50 Ω load to obtain good return loss. The initial and optimized parameters of the couplers are summarized in Tables 1 and 2.

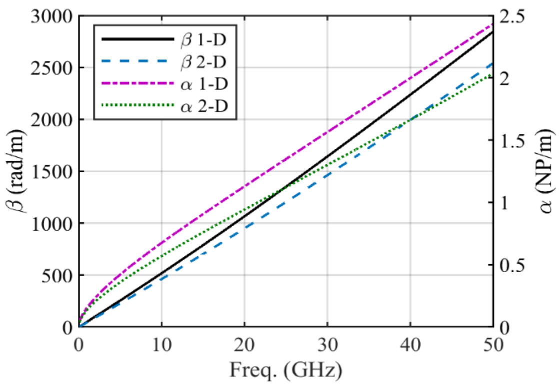

Figure 6. The equivalent attenuation and phase constant of the 1-D and 2-D perforated substrate

TABLE 1. The initial and optimized parameters of the coupler based on a 1-D perforated substrate. (All values in mm)

Parameter	Initial Value	Optimized Value
L_d	0.25	0.1
L_a	0.3	0.1
W	0.5	0.58
S	0.25	0.2
l	1.5	1.1

TABLE 2. The initial and optimized parameters of the coupler based on a 2-D perforated substrate (All values in mm)

Parameter	Initial Value	Optimized Value
D	0.3	0.2
d	0.1	0.3
W	0.5	0.58
S	0.25	0.15
l	1	3

Figure 7 shows the simulation results of scattering parameters of the designed backward coupler using a 1-D perforated substrate. It can be seen that the obtained *RL* is better than 15 dB, while the maximum *IL* is 0.8 dB, and the coupling level is 10 dB. Moreover, the coupling ripple is lower than 0.5 dB in a wide frequency range from 25 GHz to 35 GHz. The coupler bandwidth is 34%. Figure 8, the simulation results of the phase of S_{21}, and S_{31} are depicted, which are linear along the operating bandwidth. Figures 9 and 10 show the results of the designed 10 dB coupler on a non-perforated substrate. These figures show does not provide good performance for the directional coupler on a non-perforated substrate compared to the designed coupler using a perforated substrate.

Figure 11(a) shows the simulation results of the scattering parameters of the designed backward coupler using a 2-D perforated substrate. It can be seen that *RL* is better than 15 dB, and the maximum *IL* is 1 dB. Figure 11(b) also shows that the coupler flatness is less than 0.5 dB in the wide frequency range from 32 GHz to 38 GHz.

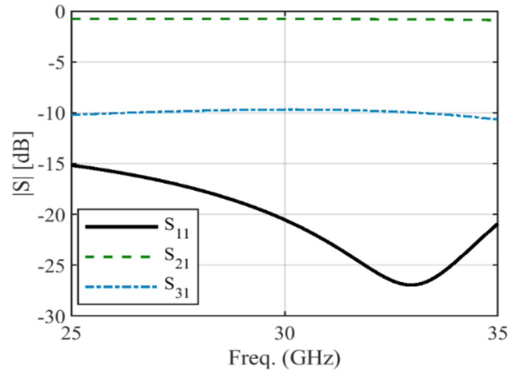

Figure 7. The simulation results of scattering parameters of the designed backward coupler using a 1-D perforated substrate

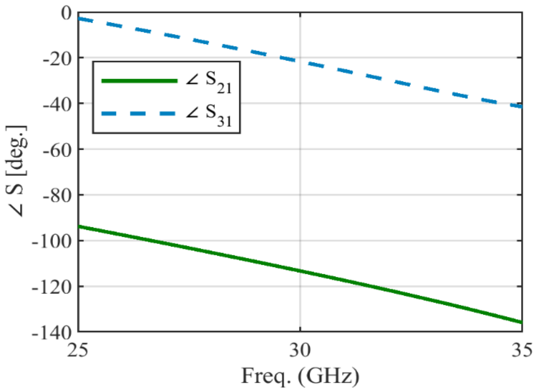

Figure 8. The simulation results of the phase of *S*-parameters of the proposed coupler using a 1-D perforated substrate

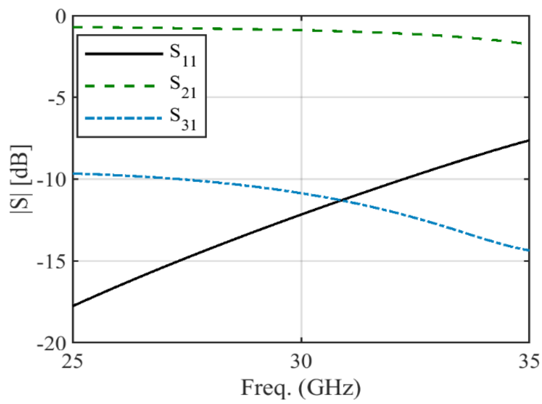

Figure 9. The simulation results of scattering parameters of the designed backward coupler using a non-perforated substrate.

The obtained bandwidth is about 17% at a center frequency of 35 GHz. Figure 12, also, shows the simulation results of the phase of the scattering parameters including S_{21} and S_{31} versus frequency. It can be seen that the phases of S_{21}, and S_{31} are linear along the operating bandwidth. Furthermore, Figures 13 and 14 show the results of the same 2-D coupler using a non-

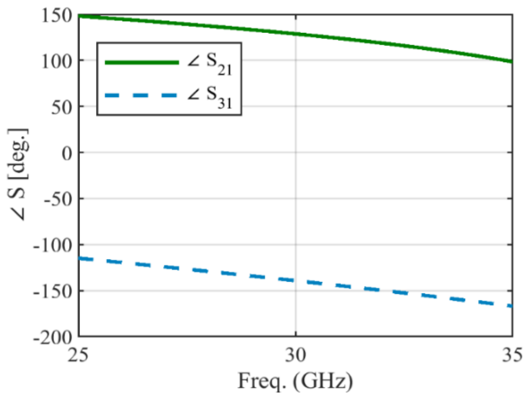

Figure 10. The simulation results of the phase of *S*-parameters of the coupler using the non-perforated substrate

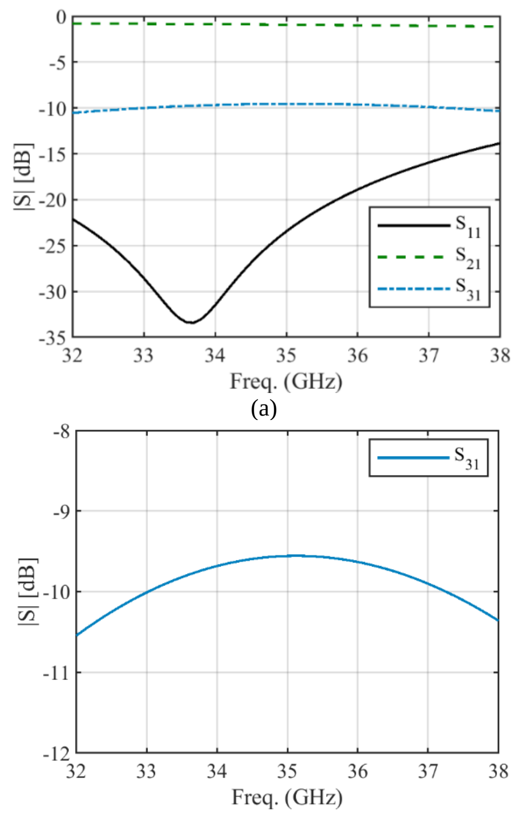

(a)

(b)

Figure 11. The simulation results **a.** scattering parameters of the designed backward coupler using a 2-D perforated substrate **b.** S_{31} and flatness of the designed backward coupler using a 2-D perforated substrate

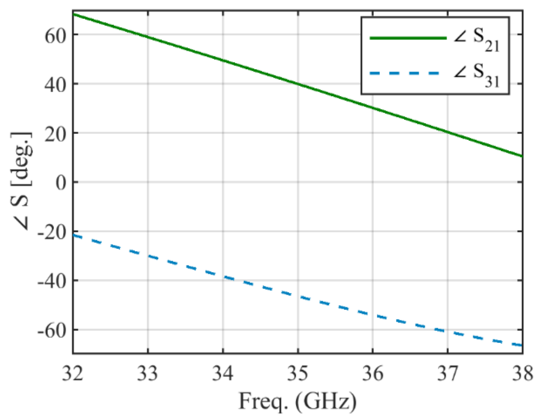

Figure 12. The simulation results of the phase of *S*-parameters of the proposed coupler using a 2-D perforated substrate

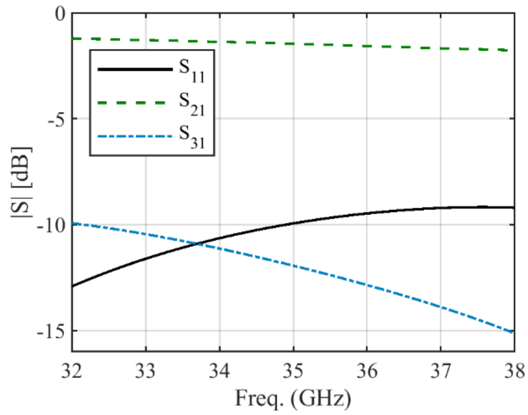

Figure 13. The simulation results of the same 2-D coupler using a non-perforated substrate

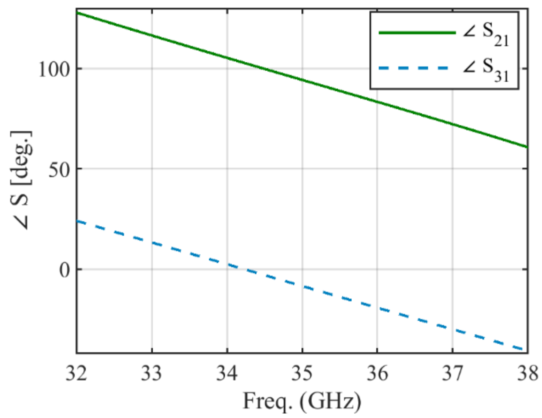

Figure 14. The simulated results of the phase of S-parameters for a coupler using a non-perforated substrate

perforated substrate. It can be seen that the performance of the directional coupler on a non-perforated substrate is weaker than the designed coupler using a perforated substrate.

The detailed performance of the proposed couplers and the simulated results of the recently published research, including center frequency f_0, coupling level *CF*, coupling ripple in pass band, total size, coupler bandwidth *BW*, average *IL*, and maximum *RL* are reported in Table 3. This table confirms that for a 10 dB level of coupling, the proposed coupler using the 2-D perforated substrate provides the lowest *IL* with a 17% bandwidth while the coupler size is only $0.32\times0.29\lambda^2_g$.

5. SENSITIVITY ANALYSIS

In order to study the effects of fabrication imperfection on the performance of the proposed couplers, a sensitivity analysis is carried out using random error by uniform distribution with 0 average for the geometrical parameters of the structure in Tables 1 and 2. The standard deviation is chosen in such a way that these parameters are changed over a maximum variation range of ±10% around the central value. To this end, the introduced method by Trinchero et al. [22] is employed. Figures 15, and 16 show the obtained results for the 1-D and 2-D couplers based on the perforated substrate. In these figures, the uncertain area is depicted by gray color. Also, the simulation results of S_{11}, S_{21}, and S_{31} are shown by back, blue and red lines, respectively. For the 1-D coupler, the maximum deviation of S_{11}, S_{21}, and S_{31} from the simulation ones are about 3.1 dB, 0.1 dB, and 0.52 dB, respectively. Also, for the 2-D coupler, the maximum deviation of S_{11}, S_{21}, and S_{31} from the simulation ones are about 6.9 dB, 0.1 dB, and 0.53 dB, respectively. It is seen that the value of S_{11} is more affected.

6. CONCLUSION

In this paper, at first, the coupled version of the transmission line equation of two microstrip lines is derived and then, the extended version of the *ABCD* matrix of a four ports microwave network is introduced using the closed-form expression. Two low-profile microstrip backward directional couplers placed on a 1-D and 2-D artificial perforated substrate are designed using the proposed analytical method. Using an optimization procedure by PSO, the optimum

TABLE 3. The detailed simulated performances of the proposed couplers and those recently published in literature

	Number of Layers	f_0 (GHz)	Ripple (dB)	*CF* (dB)	*IL* (dB)	*RL* (dB)	*BW* (%)	Coupler size ($\lambda_g\times\lambda_g$)
[6]	2	26	2	5	5	11	15.7	3.8×0.5
[7]	3	30	2.3	5	2.5	15	26	1.2×1.2
[9]	2	60	1	10	0.5	20	33	9.8×4.8
[11]	1	35	1.2	3	5	17	28	3.55×1.92
[12]	2	30	1.4	5	5	7	14	1.12×1.12
	1 (1-D*)	30	0.6	10	0.8	15	34	0.5×0.11
This work	1 (2-D*)	30	1	10	0.9	17	27	0.32×0.29
	1 (2-D)	35	0.5	10	1	15	17	0.32×0.29

*) These couplers are used without connectors or bending.

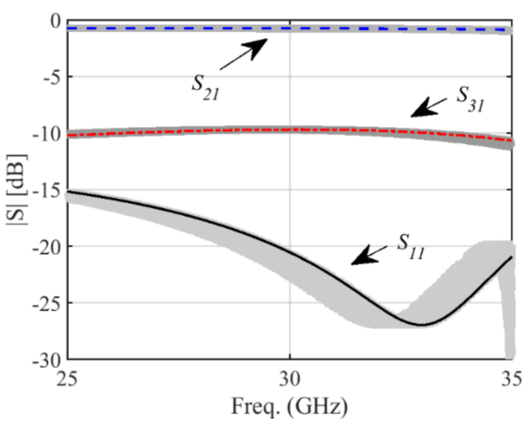

Figure 15. The sensitivity analysis of 1-D couplers based on the perforated substrate

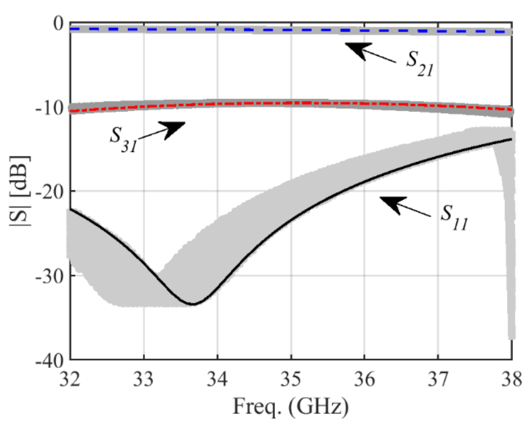

Figure 16. The sensitivity analysis of 2-D couplers based on the perforated substrate

geometrical dimensions of both couples are determined. The proposed couplers are simulated using HFSS software and their performances including scattering parameters, insertion loss, and coupler flatness are reported. Results show that the operating frequency band of the couplers are 25-35 GHz and 32-38 GHz for 1-D and 2-D substrates, respectively. The obtained results of the couplers show a good performance with low insertion, high return loss, and wide operating bandwidth.

7. REFERENCES

1. Fonseca, N. J. G., Angevain, J. C., "Waveguide Hybrid Septum Coupler," ***IEEE Transactions on Microwave Theory and Techniques***, Vol. 69, No. 6, (2021), 3030-3036. https://doi.org/ 10.1109/TMTT.2021.3074194
2. Tabatabaeian, Z. S., Neshati, Mohammad H., "Sensitivity Analysis of a Wideband Backward-wave Directional Coupler Using Neural Network and Monte Carlo Method," ***International Journal of Engineering Transaction B Applications***, Vol. 31, No. 5, (2018), 729-733.
3. Alcep, A., Tokan, F., "Perforated Dielectric Lens Antenna Design," ***International Journal on Future Revolution in Computer Science & Communication Engineering***, Vol. 4, No. 12, (2018), 12-15.
4. Wang, Z.B., Wei, X., Fang, H.P., Zhang, H.M., Zhang, Y.R., "A Compact and Broadband Directional Coupler for High-Power Radio Frequency Applications," ***IEEE Microwave and Wireless Components Letters***, Vol. 30, No. 2, (2020), 164-166. https://doi.org/ 10.1109/LMWC.2020.2964672
5. Sedaghat, M., Firouzeh, Z.H., Aliakbarian, H., "Development of a Non-Iterative Macro-Modelling Technique by Data Integration and Least Square Method," ***International Journal of Engineering Transaction B Applications***, Vol. 34, No. 11, (2021), 2408-2417. https://doi.org/ 10.5829/ije.2021.34.11b.04
6. Cao, Y., Wu, Y., Jiang, Z., Hao, Z., "A Compact Millimetre-Wave Planar Directional Coupled Crossover with a Wide Bandwidth," ***IEEE Microwave and Wireless Components Letters***, Vol. 30, No. 7, (2020), 661-664. https://doi.org/ 10.1109/LMWC.2020.2998780
7. Ali, M. M. M., El-Gendy, M. S., Al-Hasan, M., Mabrouk, I. B., Sebak, A., Denidni, T.A., "A Systematic Design of a Compact Wideband Hybrid Directional Coupler Based on Printed RGW Technology," ***IEEE Access***, Vol. 9, (2021), 56765-56772. https://doi.org/ 10.1109/ACCESS.2021.3071758
8. Parment, F., Ghiotto, A., Vuong, T., Duchamp, J., Wu, K., "Air-to-Dielectric-Filled Two Hole Substrate-Integrated Waveguide Directional Coupler," ***IEEE Microwave and Wireless Components Letters***, Vol. 27, No. 7, (2017), 621-623. https://doi.org/ 10.1109/LMWC.2017.2711525
9. Zarifi, D., Farahbakhsh, A., Zaman, A. U., "Design and Fabrication of Wideband Millimetre-Wave Directional Couplers with Different Coupling Factors Based on Gap Waveguide Technology," ***IEEE Access***, Vol. 7, (2019), 88822-88829. https://doi.org/ 10.1109/ACCESS.2019.2926233
10. Peláez-Pérez, A. M., Almorox-Gonzalez, P., Alonso, J.I., González-Martín, J., "Ultra-Broadband Directional Couplers Using Microstrip with Dielectric Overlay in Millimetre-Wave Band," ***Progress in Electromagnetics Research***, Vol. 117, (2011), 495-509. https://doi.org/ 10.2528/PIER11042703
11. Tavakoli, M. J., Mallahzadeh, A., "Wideband Directional Coupler for Millimetre Wave Application based on Substrate Integrated Waveguide," ***Emerging Science Journal***, Vol. 2, No. 2, (2018). https://doi.org/ 10.28991/esj-2018-01132
12. Zhao, Z., Denidni, T. A., "Millimetre-Wave Printed-RGW Hybrid Coupler with Symmetrical Square Feed," ***IEEE Microwave and Wireless Components Letters***, Vol. 30, No. 2, (2020), 156-159. https://doi.org/10.1109/LMWC.2019. 2960475
13. Tabatabaeian, Z. S., Neshati, Mohammad H., "Development of broadband forward-wave directional couplers loaded by periodic patterned ground structure," ***International Journal of RF and Microwave Computer-Aided Engineering***, Vol. 27, No. 8, (2017), 1-9. https://doi.org/ 10.1002/mmce.21135
14. Tabatabaeian, Z.S., Neshati, Mohammad H., "Development of Forward-wave Directional Couplers Loaded by Periodic Shunt Shorted Stubs," ***International Journal of Engineering Transaction C Aspect***, Vol. 30, No. 3, (2017), 344-350. https://doi.org/10.5829/idosi.ije.2017.30.03c.03
15. Pozar, D. M., Microwave Engineering. John Wiley & Sons, 4th e, 2011.
16. Paul, C. R., Introduction to Electromagnetic Compatibility. 2nd ed., 2006.
17. Strang G., Introduction to Linear Algebra. Cambridge Press, 2016.
18. Sohn, Y. S., Lee, J,C., Park, H.J., Cho, S.I., "Empirical equations on electrical parameters of coupled microstrip lines for crosstalk estimation in printed circuit board," ***IEEE Transactions on Advanced Packaging***, Vol. 24, No. 4, (2001), 521–527. https://doi.org/ 10.1109/6040.982839
19. Karimian-Sarakhs, H., Neshati, Mohammad H., and Alijani, M. G. H., "Development of an analytical method to determine the propagation characteristics of microstrip line on artificial perforated substrates," ***AEU-International Journal of Electronics and Communications***, Vol. 140, (2021), 1-8. https://doi.org/ 10.1016/j.aeue.2021.153951
20. Alijani-Ghadikolae, M., Neshati, Mohammad H., "Developing an accurate and simple dispersion analysis of TE10 mode of substrate integrated waveguides," *21st Iranian Conference on Electrical Engineering (ICEE)*, (2013), 1-4. https://doi.org/ 10.1109/IranianCEE.2013.6599879
21. Méndez-Jerónimo, G., Wu, K., "Effects of Unshielded Air Holes Periodically Perforated in Substrate Integrated Waveguides," ***IEEE Microwave and Wireless Components Letters***, Vol. 30, No. 11, (2020), 1049-1052. https://doi.org/ 10.1109/LMWC.2020.3022973.
22. Trinchero, R., Manfredi, O., Stievano, I.S., Canavero, F.G., "Machine Learning for the Performance Assessment of High-Speed Links," ***IEEE Transactions on Electromagnetic Compatibility***, Vol. 60, No. 6, (2018), 1627-1634. https://doi.org/ 10.1109/TEMC.2018.2797481.

Persian Abstract

چکیده

در این مقاله، دو تزویج کننده جهتی معکوس پهن باند با ضریب تزویج ۱۰ دسی بل مبتنی بر زیرلایه حفره دار در محدوده فرکانس ۲۵–۳۵ گیگاهرتز و ۳۲–۳۸ گیگاهرتز توسعه داده شده است. یک روش تحلیلی برای طراحی پارامترهای هندسی کوپلر پیشنهاد شده است. مدل سازی نظری بر اساس تئوری خط انتقال با استفاده از نسخه توسعه یافته ماتریس ABCD برای شبکه مایکروویو چهار پورت ارائه شده است. نشان داده شده است که با استفاده از روش پیشنهادی، تمام پارامترهای مورد نیاز کوپلر جهتی را می توان با استفاده از پارامترهای واحد طول خط تعیین کرد. برای بهبود عملکرد کوپلرهای طراحی شده از الگوریتم بهینه سازی ذرات برای بهینه سازی پارامترهای هندسی کوپلرها استفاده شده است. همچنین، کوپلرهای طراحی شده با استفاده از شبیه ساز ساختار فرکانس بالا (HFSS) شبیه سازی شده اند. علاوه بر آن، برای بررسی تاثیر ناکاملی در فرآیند ساخت، تحلیل حساسیت نیز به کار گرفته شده است. نتایج به‌دست‌آمده نشان می‌دهد که نتایج شبیه‌سازی به خوبی با نتایج نظری مطابقت دارد و تلفات تعبیه کم به همراه تلفات بازگشتی زیاد در پهنای باند فرکانسی وسیع به‌دست می‌آید.

IJE TRANSACTIONS B: Applications Vol. 36, No. 02, (February 2023) 321-334

International Journal of Engineering

Journal Homepage: www.ije.ir

A New Mechanism for Detecting Shilling Attacks in Recommender Systems Based on Social Network Analysis and Gaussian Rough Neural Network with Emotional Learning

R. Moradi, H. Hamidi*

Department of Industrial Engineering, K. N. Toosi University of Technology, Tehran, Iran

PAPER INFO

Paper history:
Received 18 September 2022
Received in revised form 04 December 2022
Accepted 06 December 2022

Keywords:
Recommender System
Shilling Attack
Collaborative Filtering
Fake Profiles
Social Network

ABSTRACT

A recommender system is an integral part of any e-commerce site. Shilling attacks are among essential challenges in recommender systems, which use the creation of fake profiles in the system and biased rating of items, causing the accuracy to decrease and the correct performance of the recommender system in providing recommendations to users. The target of attackers is to change the rank of content or items corresponded to their interests. Shilling attacks are a threat to the credibility of recommender systems. Therefore, detecting shilling attacks it necessary to in recommender systems to maintain their fairness and validity. Appropriate algorithms and methods have been so far presented to detect shilling attacks. However, some of these methods either examine the rating matrix from a single point of view or use low-order interactions or high-order interactions. This study aimed to propose a mechanism using users' rating matrix, rating time, and social network analysis output of users' profiles by Gaussian-Rough neural network to simultaneously use low-order and high-order interactions to detect shilling attacks. Finally, several experiments were conducted with three models: mean attack, random attack, and bandwagon attack, and compared with PCA, Semi, BAY, and XGB methods using precision, recall, and F1-Measure. The results indicated that the proposed method is more effective than the comparison methods regarding attack detection and overall detection, which proves the effectiveness of the proposed method.

***doi**: 10.5829/ije.2023.36.02b.12*

1. INTRODUCTION

A recommender system can be defined as a program that recommends appropriate items by predicting user preference for an item based on information related to items, users, and interaction between the two [1]. In the past 25 years, the personalization of e-services by recommender systems has received much attention [2, 3]. The growing importance of the web as a medium for electronic and commercial transactions has created a strong impetus in the development of recommender systems. One of the key factors in this regard is that the web allows users to provide feedback about their taste [4].

One of the challenges of life today is making the right choice when buying a product. This challenge is compounded due to the increasing volume, variety and velocity of product-related data [5]. Although the vast increase in the number of options has given consumers the opportunity to choose the most interesting products; it has also caused choice overload. This problem occurs when there are an infinite number of options to choose from that do not significantly differ from each other [6].

Recommender systems are primarily developed and integrated into e-commerce websites and have largely been able to help users make decisions. However, recommender systems have found applications beyond e-commerce websites and are used in almost every field from social networks to medical science [7, 8].

Recommender systems have improved user decisions when interacting with the system, and their effectiveness has been proven. For example, recommender systems

*Corresponding Author Institutional Email: h_hamidi@kntu.ac.ir (H. Hamidi)

Please cite this article as: R. Moradi, H. Hamidi, A New Mechanism for Detecting Shilling Attacks in Recommender Systems Based on Social Network Analysis and Gaussian Rough Neural Network with Emotional Learning, ***International Journal of Engineering, Transactions B: Applications***, Vol. 36, No. 02, (2023), 321-334

allow users to discover surprising items that may be unknown to them by receiving recommendations from unexplored parts of goods [9]. For this purpose, recommender systems observe user behaviors carefully and collect different forms of users to understand users' personal preferences [10, 11].

Recommender systems are currently used in various areas where there are various options to choose from, such as watching movies, reading books, buying goods, listening to music, visiting tourist areas, eating at restaurants [12].

Research on recommender systems was initially focused on the goal of providing accurate recommendations, but now, other goals such as novelty, diversity, reliability, etc., have also emerged beyond accurate recommendations [13]. Recommender systems are a powerful personalization tool that uses user behaviors to provide personalized options or adapt the user interface [2]. Currently, two factors, high dependence of users on recommender systems and the great interest of companies to provide user-friendly recommendations, have contributed to the success of recommender systems [12].

Providing recommendations in recommender systems in a set of cases such as products, business services and news can lead to significant changes such as increasing business profits or influencing public opinion. Due to the great importance of these systems, there is a strong interest in influencing the output of recommender systems. Part of the efforts to influence the output of recommender systems are done through legal and authorized actions such as advertising, enriching the information of the presented items, but another part is carried out by using illegal and deceptive actions such as attacking the recommender systems.

Collaborative filtering based recommender systems are currently known to be the most popular and successful approach in recommender systems and are widely used in e-commerce websites [14]. By finding neighbors similar to a user's profile, collaborative filtering algorithms provide taste-based recommendations of neighbors that are thought to represent different people's interests. In most of these websites, anyone can submit and post their opinion about a specific item. Interactivity of the collaborative filtering on the one hand has created power and on the other hand has caused the vulnerability of this type of recommender system [15].

These issues have left collaborative filtering-based recommender systems vulnerable to various types of shilling attacks by profit-seeking people, which are one of the most common attacks in these systems. These attacks usually come into two forms in recommender systems. In the first case, the beneficiary posts positive feedback in favor of the desired product, and in the second case, the beneficiary posts negative feedback against the product or competing products [16, 17]. Posting fake feedback in recommender systems can alter the results and reduce the accuracy of the system's recommendations. Therefore, it seems essential to detect shilling attacks and neutralize their effects in recommender systems.

several methods and algorithms have been developed in this regard. Some of these methods either examine the rating matrix from a single point of view or use low-order interactions or high-order interactions. The rating patterns of fake users and normal users become similar when an attacker uses obfuscation techniques. Shilling attacks cannot be detected by methods that only examine a single monitor's user's rating matrix. However, Schilling attack detection methods based on another unitary view of only low-order interactions or high-order interactions also suffer from low accuracy. This research provides a mechanism based on social network analysis for better detection and a lower error percentage to detect shilling attacks and better results.

Injection of fake profiles for shilling attack by the adversary with certain strategies and patterns are injected into the system. Therefore, there are certain relationships between the characteristics of fake profiles, the rating time by fake profiles, and the rating matrix, which can greatly distinguish these profiles from normal profiles. In this article, the social network between profiles was drawn to find hidden patterns between fake profiles. Since fake profiles are created in almost identical ways, connections between fake profiles are denser than real profiles. Then, social network output information, rating time, and users' rating matrix were used to discover low-order and high-order information simultaneously.

Finally, a powerful tool is needed to detect and predict fake profiles and normal profiles from low-order and high-order information. Gaussian-Rough neural network was used in this study because neural networks are powerful modeling tools with unique properties and can solve nonlinear and complex problems, pattern classification, pattern recognition, and prediction. Gaussian-Rough neural networks can classify complex patterns and remove noise. In addition, the emotional learning method was used in the neural network training process. This method can properly affect network learning by considering the errors of the previous moments.

The basic concepts are introduced in section 2. In section 3, the background is reviewed. In section 4, the proposed mechanism is presented, and then in section 5, an experimental evaluation is done to check the results. Finally, in section 6 the conclusion is presented.

2. BASIC CONCEPTS

In this section, we will introduce and briefly explain the common definitions and terms in shilling attacks, then we will examine the model and types of shilling attacks.

2. 1. Common Definitions And Terms

- Adversary: a person or persons who intend to attack a recommender system.
- Shilling attack: an attack carried out by the adversary to post fake feedback and alter the result of the recommender system.
- Profile: a set of points given by a user to different items in the recommender system.
- Fake profiles: profiles that are injected into the system by the adversary to achieve the desired results.
- Attack intent: each type of shilling attack may have various intents, but the final intent of the adversary may be one of the following [16, 17]. The two main targets are push and nuke. In push, the adversary injects fake profiles into the system to post positive feedback to increase the probability of an item to be seen, and in nuke, the adversary injects fake profiles into the system to post negative feedback to reduce the probability of the item or competing items to be seen. Another goal of the shilling attack is random sabotage [17], which is done by disrupting recommendation algorithms to reduce users' trust in the recommender system.
- Filler size: the number of points given by the fake profile to the items in the recommender system [18]. Adding the number of points costs relatively less than creating a fake profile for the adversaries. Since normal users do not rate all the items of the recommender system, usually the filler size is between 1 and 20% of the total items.
- Attack size: the number of fake profiles injected into the recommender system by the adversary. The number of profiles injected into a recommender system is usually set between 1 and 15% [18].
- Target item: The item that the adversary intends to minimize or maximize its rating in the recommender system depending on the attack type [19].
- Low knowledge attacks: These types of attacks require little knowledge about the recommender system (such as the rating range of items).
- High knowledge attacks: These types of attacks require a high level of knowledge about the recommender system.

2. 2. Shilling Attack Model The adversary performs the shilling attack by injecting fake profiles, which was first defined in the research by Bhaumik et al. [20] and Mobasher et al. [21] to misguide collaborative filtering-based recommender systems. Figure 1 shows the overall diagram of fake profiles in the recommender system in attacks with a single target item. But in practice, the adversary can attack several target items at the same time. Yang et al. [22] and Chung et al. [23] suggested creating attacks with several target items simultaneously. Figure 2 shows the overall diagram of the fake profiles in the recommender system in this case. In fact, the attack model can be considered as an approach to create fake profiles rely on the existing knowledge of the recommender system [20, 21].

As shown in Figures 1 and 2, the fake profiles of a recommender system in the shilling attack include an n-dimensional vector of ratings, where n represents the number of items in the system. This vector contains a set of target items i_t along with a rating function γ that assigns a rating value to it and γ_{max} rates push and γ_{min}rates nuke according to the attack intent. I_S is a set of selected items with specific characteristics determined by the adversary and typically used for group attacks. I_F is a set of filler items that are usually randomly selected along with a rating function σ to map the filler items to the rating value. The filler items are created to normalize the appearance of fake profiles and increase the difficulty of identifying them. $I_\emptyset$ is a set of items that are not rated in the fake profile. In fact, the main difference among different shilling attack models is in the selection of the set of filler items, the selected items and their rating strategies.

2. 3. Types of Shilling Attacks According to the shilling attack model explained in the previous section, fake profiles with specific strategies and patterns are injected into the recommender system. Table 1 summarized the types of known attacks [15, 24] and their strategies against recommender systems with a collaborative refinement approach. In addition, the attack type and category, as well as I_S ،I_F ،$I_\emptyset$ و I_t rating for

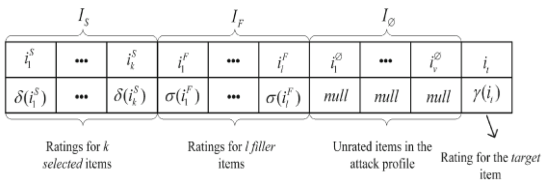

Figure 1. General diagram of fake profiles in attacks with a target item

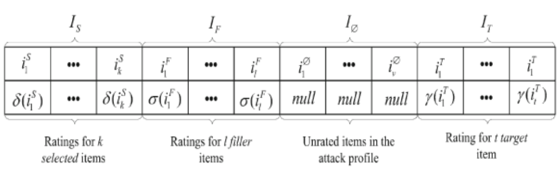

Figure 2. General diagram of fake profiles in attacks with multiple target items

famous shilling attacks are stated in Table 1. For example, I_S items are not rated in a random attack which is a basic attack category. The I_F items are randomly rated with a normal distribution around the average rating value in the entire database. $I_\emptyset$ are also not rated, and the I_F item(s) are rated according to the target of the attack, γ_{max} for push and γ_{min} for nuke.

TABLE 1. Types of shilling attacks and their strategies

Attack Model	Attack Group	Reference	I_S	I_F	$I_\emptyset$	I_T
Random attack	Basic attacks	[25, 26]	Null	Random rating with a normal distribution around the mean rating in the entire database	Null	$\gamma_{max}/\gamma_{min}$
Average attack	Basic attacks	[26]	Null	Random rating with a normal distribution around the mean rating for item i in I_F	Null	$\gamma_{max}/\gamma_{min}$
Bandwagon attack	Low-knowledge attacks	[27]	Popular items are rated with γ_{max}	Random rating with a normal distribution around the mean rating in the entire database	Null	γ_{max}
Segment attack	Low-knowledge attacks	[28]	Popular items are rated with γ_{max}	γ_{min}	It is determined based on the size of the filler item	γ_{max}
Love/hate attack	Nuke attack	[18]	Null	γ_{max}	Null	γ_{min}
Reverse bandwagon attack	Nuke attack	[21]	The least popular items are rated with γ_{min}	Random rating with a normal distribution around the mean rating for item i in I_F	Null	γ_{min}
Sampling attack	High-knowledge attacks	[29]	Null	Copy of an existing profile	It is determined based on the size of the filler item	$\gamma_{max}/\gamma_{min}$
Noise injection	Obfuscated attacks	[30]	$R_{u,i} = r_{u,i} + (\text{random number} \times \alpha)$	$R_{u,i} = r_{u,i} + (\text{random numbr} \times \alpha)$	Null	$\gamma_{max}/\gamma_{min}$
Target shifting	Obfuscated attacks	[30]	$R_{u,i} = r_{u,i}$	$R_{u,i} = r_{u,i}$	Null	$\gamma_{max} - 1$ $/\gamma_{min} + 1$
User shifting	Obfuscated attacks	[30]	$R_{u,i} = r_{u,i} + \text{shift}(u, O_s)$	$R_{u,i} = r_{u,i} + \text{shift}(u, O_s)$	Null	$\gamma_{max}/\gamma_{min}$
Mixed attack	Obfuscated attacks	[31]	Simultaneous injection of fake profiles of all kinds of shilling attacks			
Average over popular items (AOP) attack	Obfuscated attacks	[32]	Null	Equally likely to be selected from the top X% of most popular items.	Null	$\gamma_{max}/\gamma_{min}$
Power User Attack (PUA) attack	Other attacks	[33]	Items and ratings are copied from powerful user profiles.	Null	Null	$\gamma_{max}/\gamma_{min}$
Power Item Attack (PIA) attack	Other attacks	[34]	Powerful items are rated with a normal distribution adjusted around the item mean.	Null	Null	$\gamma_{max}/\gamma_{min}$
Bandwagon and average hybrid attack	Other attacks	[35]	Bandwagon items selected and rated with γ_{max}; Mean items are rated with a normal distribution around the item mean	Random rating with a normal distribution around the system mean	Null	$\gamma_{max}/\gamma_{min}$
Random vandalism attack	Other attacks	[17]	Random number between $[\gamma_{min}, \gamma_{max}]$	Random number between $[\gamma_{min}, \gamma_{max}]$	Null	$\gamma_{max}/\gamma_{min}$

3. BACKGROUND

Collaborative filtering-based recommender system designs are commonly developed and publicly available by e-commerce sites for customer acquisition. These systems are not sufficiently resistant to shilling attacks or fake profile injection due to their open nature [36, 37]. In general, shilling attacks cause push and nuke attacks on specific items or by injecting fake profiles to damage the performance of the recommender system.

Fraudulent behavior such as fake rating was first proposed by Dellarocas [38]. The attack on collaborative filtering-based recommender system was first introduced by O'Mahony et al. [39]. This paper defined the robustness of recommender systems and various vulnerabilities of the collaborative filtering approach against shilling attacks to promote specific recommendations.

So far, various attack detection algorithms have been presented by researchers, each of which strives to maintain the overall validity of the recommender system. In general, there are three main approaches in research including supervised learning, unsupervised learning, and semi-supervised learning.

Chirita et al. [25] presented the first shilling attack detection algorithm based on supervised classification. They introduced some factors that may be useful in analyzing the patterns of fake profiles insert for shilling attacks. They proposed two features to detect attacks: they are rating deviation from average agreement and the highest degree of similarity with neighbors. This algorithm is capable of detecting random, average and bandwagon attacks, but is unable to detect fragment and friend/hate ones.

Burke et al. [40] derived two new features based on the deviation of rates from the mean agreement. These features include the weighted deviation from the average agreement and the weighted degree of agreement. They then combined the extracted features with the KNN to do the attack detection. Williams et al [41] used machine learning algorithms including SVM to detect attacks.

Tong and Tang [42] proposed a model using interval analysis of the user ratings to detect suspicious behavior regarding the most popular items in recommender systems. They considered such features as fixed interval, frequency, and span based on the user's temporal behavior.

Xia et al. [43] presented a new dynamic interval segmentation method based on item anomaly detection to detect shilling attacks. Yang et al. [44] proposed three new features that focus on a number of specific rates (such as maximum rate, minimum rate, and average rate) in the selected items to deal with the imbalanced classification problem. This method attempts to identify all fake profiles from the real ones.

Using classic machine learning algorithms, Wu et al. [45] selected two attack detection methods based on highest performance features. Li et al. [46] used a statistical analysis method based on item popularity. This method compares and examines the popularity distribution among attack and normal profiles.

As with the semi-supervised learning methods, Wu et al. [47] presented a hybrid shilling attack detector to detect more complex shilling attacks. First, this algorithm collects the criteria of well-known shilling attacks in order to select the feature through an overlay. The algorithm then uses simple semi-supervised Bayes classification to group labeled and unlabeled users.

In the unsupervised learning approach, Mehta [48] proposed a method called PCASelectUsers. To identify fake profiles, this method requires obtaining certain information. Yang et al. [22] proposed a method based on graph mining. In this method, they used a clustering algorithm to calculate the similarity of normal users and suspicious users.

Shao and Sun [49] proposed a method named XGB-SAD to detect the shilling attack by binary combination of gradient boosting schematics. They analyzed the rating matrix with a binary schematic of time and item with using eXtreme Gradient Boosting.

The methods mentioned above either examine the rating matrix from a single point of view or use low-order interactions or high-order interactions. In this article, social network output information (in order to find hidden patterns), users' rating time and rating matrix were simultaneously used to use low-order and high-order information in discovering shilling attacks. The proposed mechanism and its details are explained in the next sections.

4. PROPOSED MECHANISM

This section presents the details of the proposed mechanism in five stages, including the Injection of Shilling Attacks, Creating a Social Network of Users, Neural Network Inputs, Building a Gaussian Rough Neural Network With Emotional Learning and Detection of Fake Profiles according to Figure 3. Table 2 shows the actions and objectives of the above steps.

4. 1. Injection of Shilling Attacks The first step of the proposed method is to inject the shilling attack(s) into the recommender system. Since there is no data set containing types of shilling attacks of different attack sizes, this issue can lead to wrong injection of shilling attacks into the system. If shilling attacks are mistakenly injected into the system, they can interfere with the evaluation of the proposed method and make it difficult to recognize fake profiles and detect shilling attacks.

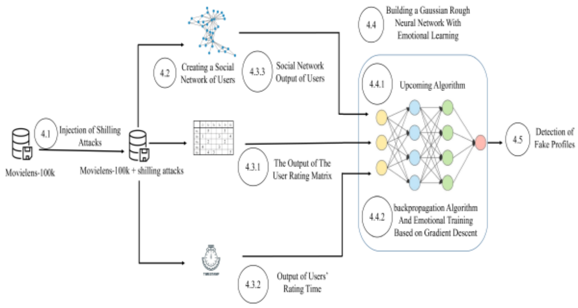

Figure 3. General diagram of the proposed mechanism

Therefore, the first stage of the proposed method is particularly important, and the implementation of the following stages depends on the precise implementation of this stage.

At this stage, fake profiles were injected into the data set using the shilling attack model, and the resulting rating matrix including fake and normal profiles was used as input for the next step.

4. 2. Creating a Social Network of Users A social network is a social structure that consists of a number of social actors and there are binary relationships (social relationships) among these social actors. Social actors are not necessarily human and a group of any gender may form a community. For example, a group of humans, a group of buffaloes, a group of computers and a group of robots are examples of community. Social relations may also exist in various forms between social actors. For example, friendship, interest, trust, cooperation, etc. are considered as social relationships. One of the main goals of social network mapping is to study collective behavior.

In other words, there are patterns in the structure of social networks, by using these patterns we are able to discover knowledge from the network and predict the future of the network. A series of recent discoveries show us the amazing truth that a number of simple and inaccessible rules govern the structure and evolution of social networks, although these rules are very complex until they are not known.

One of the best ways to model social networks is to use graph theory because social actors can be imagined as vertices and social relationships between them as edges [50]. In fact, the starting point of social networks can be traced back to 1735 with the emergence of graph theory.

In this step, a social network is drawn using user profiles, then based on this social network, information is sent to the neural network as an input. At first, according to the profile of users represented by P, which is the output of stage 1 and includes real and fake profiles, an undirected user-user network G = (V, E, W) is formed, where V is a set of vertices and E represents the set of edges between vertices, W is a weight matrix where each element wij ∈ W shows the weight corresponding to the edge eij. For example, Iu and Iv are two item vectors

TABLE 2. Actions and objectives of the proposed mechanism

Stage		Action	Objective
Injection of shilling attacks		Injects fake profiles into the data set using the shilling attack model	Creating a dataset including fake and normal profiles
Creating a social network of users		Creating a social network using relationships between items and profiles	Discover knowledge from the network and finding hidden patterns between profiles
Neural network inputs	The output of the user rating matrix	Calculate Boolean values of user rating, The coefficient of item Boolean, Mean index of user Boolean, The number of max and min rating and Max-1 and min+1 rating number	Reducing the negative effects of obfuscation techniques and using low-order interactions to detecting shilling attacks
	Output of users' rating time	Calculate Collection of user rating time, The max interval of user rating time, Aggregation index of user rating time and Relative aggregation index of user rating time	Using rating intervals to detecting shilling attacks
	Social network output of users	Calculate Degree centrality, Closeness centrality, Eigenvector centrality and Local clustering coefficient	Using high-order interactions to detecting shilling attacks
Building a gaussian rough neural network with emotional learning	Upcoming algorithm		
	Backpropagation algorithm and emotional training based on gradient descent	Training weights, cluster centers, and standard deviation	Reducing the error between the network output and the desired output
detection of fake profiles		Using the proposed model with test data	Separation normal and fake profiles

rated by users u and v, respectively. An edge is created between vertices u and v if $| I_u \cap I_v | > t$, where t is an empirical threshold. Additionally, the weight of each edge is set to 1 due to its undirected graph (as described in Figure 4).

Since fake profiles are created in almost identical ways, it means that the communication between attackers is denser than that of real users. During the process of building a social network, it is very important how to choose the threshold t to detect all attackers and filter out more real users at the same time. Yang et al.'s paper [22] has been used to determine how to choose the threshold t.

4. 3. Neural Network Inputs According to Figure 3, the inputs of the neural network are provided by the outputs of users' rating matrix, users' rating time and users' social network. At this stage, these items will be reviewed.

4. 3. 1. The Output of The User Rating Matrix The attacker can design attacks by using the knowledge gained from the recommender system and obfuscation methods and insert profiles into the system that are similar to the existing normal profiles. Therefore, attack detection methods that use low-order features (user rating matrix) make mistakes in evaluating normal and fake users. To reduce the effects of this issue, in addition to analyze the rating matrix, Boolean values of user ratings are also considered.

- Boolean values of user rating

In this method, instead of considering the value of user rating to an item, only the user's rating to an item is considered. So we make the user's rating values (R_{ij} reprsents the rating value of $user_i$ to $item_j$ in the rating matrix $R_{m\times n}$).

```
Input:
    User Profile P;
    Empirical threshold t;

Out Put:
    Undirected Social Network G;

Process:
    for each pair of users u, v ∈ P do;
      if | I u ∩ I v | > t then
        Create an edge e u v between vertexes u and v , set w u v = 1 ;
      end if
    end for

Construct an undirected Social Network G;
return G ;
```

Figure 4. Algorithm of social network construction

$$\mathrm{BVUR_{ij}} = \begin{cases} 0\ , & \mathrm{R_{i,j}} = 0 \\ 1\ , & \mathrm{R_{i,j}} \neq 0 \end{cases} \tag{1}$$

- The coefficient of item Boolean

Coefficient of item Boolean is equal to the sum of BVUR values of all users in a column. This coefficient shows the number of times each item is rated as well as the acceptance rate of the item. TCIB value for item j is defined as follows:

$$\mathrm{TCIB_j} = \sum_{i=1}^{n} \mathrm{BVUR_{ij}} \tag{2}$$

- Mean index of user Boolean

First, the product of the coefficient of item Boolean and the Boolean value of the user's rating to the items are added from the beginning to the end, respectively. Then the accumulated value is divided by the total number of users (m refers to the total number of users and n refers to the total number of items). This index is used to reduce the negative effects of obfuscation techniques.

$$MIUB_{user_i} = \frac{1}{m}\sum_{j=1}^{n} TCIB_j \times BVUR_{i,j} \tag{3}$$

- The number of max and min rating

In order to achieve their attack goals, attackers attack one or more target items with the lowest or highest ratings, which means that if the attackers want to downgrade or upgrade the items in the recommendation list, will focus on these items frequently [51-53]. The number of maximum and minimum ratings of the user is also sent to the neural network as a parameter.

- Max-1 and min+1 rating number

In some attacks, attackers may attack one or more target items with min+1 or max-1 ratings with target change attacks. The number of max-1 and min+1 rates of the user is also sent to the neural network as a parameter.

4. 3. 2. Output of Users' Rating Time A shilling attack by an attacker occurs by inserting fake profiles in a certain time unit. A shilling attack on recommender systems is a short-range action which is highly evident in the rating intervals of fake profiles. The rating interval for fake profiles is significantly different from normal profiles [54, 55]. Based on this, the following items are extracted from users' rating time according to the following equations:

- Collection of user rating time

In this collection, there are user rating time tags for items, which are arranged in descending order (u refers to a specific user and n refers to n items rated by this user).

$$\mathrm{CURT_u} = \{\mathrm{t_1, t_2, t_3, \ldots, t_n}\} \tag{4}$$

- The max interval of user rating time

$$\mathrm{MIURT_u} = \mathrm{CURT_n} - \mathrm{CURT_1} \tag{5}$$

- Aggregation index of user rating time

$$\mathrm{AIURT_u} = \frac{\mathrm{MIURT_u}}{\mathrm{N_u}} \tag{6}$$

- Relative aggregation index of user rating time

$\overline{\mathrm{MIURT}}$ is the mean MIUTR values of the users in the database and $\overline{\mathrm{N}}$ is the mean of all user-rated items.

$$\mathrm{RAIURT_u} = \frac{|\mathrm{MIURT_u} - \overline{\mathrm{MIURT}}|}{|\mathrm{N_u} - \overline{\mathrm{N}}|} \tag{7}$$

4. 3.3. Social Network Output of Users

- Degree centrality

This measure calculates the number of neighbors of a vortex. In fact, this index determines the degree of connection of a vortex with other vortices, which expresses the social connections of a vortex. This measure is calculated by dividing the degree of each vortex k_i by N-1, where N is the number of vortices in the entire network [56].

$$\mathrm{C_D(i)} = \frac{\mathrm{k_i}}{\mathrm{N-1}} \tag{8}$$

- Closeness centrality

A vortex is located in the center of a network when it can quickly interact with other vortices. This measure calculates the average length of the shortest path from the desired vortex to other vortices of the network (d_{ij} refers to the length of the shortest path from vortex i to vortex j) [56].

$$\mathrm{C_C(i)} = \frac{\mathrm{N-1}}{\sum_{\mathrm{i \neq j}}^{\mathrm{N}} \mathrm{d_{ij}}} \tag{9}$$

- Eigenvector centrality

Eigenvector centrality is one of the measures that shows the importance of a vortex. This index calculates the relative rating of all vortices according to a general rule. In fact, the vortex connected to high-rating vortices rates more than the vortex connected to low-rating vortex. This measure is calculated using the neighborhood matrix and according to the following equation [56]:

$$\mathrm{C_E(i)} = \frac{1}{\lambda} \sum_{\mathrm{j}} \mathrm{A_{i,j} C_E(i)} \tag{10}$$

- Local clustering coefficient

This measure examines the relationship between the neighbors of a vortex. According to the following equation, the local clustering coefficient for vortex i is calculated as the result of dividing the number of links between friends of vortex i by the number of possible edges between friends of vortex i [56].

$$\mathrm{C_i} = \frac{2\mathrm{e_i}}{\mathrm{k_i(k_i-1)}} \tag{11}$$

4. 4. Building a Gaussian Rough Neural Network With Emotional Learning

Neural network is a branch of computational intelligence that tries to solve problems based on abstract structure. The performance of neural networks is based on training and information sampling. The important factor in neural networks are neuronal units. Although neurons are a simple computational transformation function, the network structure by combining these neurons can be used in simple and complex systems that can solve small and large problems. As a result, neural networks are able to solve problems with different behavior and dynamics. Neural networks are widely used with the aim of human-like performance these days. These networks are composed of a number of non-linear computing elements that operate in parallel [57, 58].

At this stage, Gaussian rough neural network has been used to classify profiles and detect shilling attacks. Gaussian neural networks are usually used in function approximation, interpolation and classification. In general, the method that the RBF neural network uses to classify complex patterns is based on a non-linear mapping from the n_0 dimensional space (the number of input parameters) to the larger m dimensional space (the number of intermediate layer neurons). According to Cover's theorem, after a nonlinear mapping to a higher dimensional space, complex patterns can be linearly classified better than the initial space with lower dimensions. On the other hand, real data is always associated with uncertainty and neural networks do not perform well in the presence of noisy data. One of the noise-resistant neural networks is the rough neural network.

According to Figure 5, a Gaussian rough neural network has been used to classify normal and fake profiles. If we consider the input vector as follows:

$$\mathrm{x} = [\mathrm{x_1, x_2, \dots, x_{n0}}] \tag{12}$$

4. 4. 1. Upcoming Algorithm

$$\|\mathrm{x} - \mathrm{c_j}\| = \sqrt{(\mathrm{x_1} - \mathrm{c_1^1})^2 + \cdots + (\mathrm{x_{n0}} - \mathrm{c_{n0}^1})^2} \tag{13}$$

$$\mathrm{o_j^1} = \varphi_{\mathrm{j}}(\mathrm{net_j^1}) = \exp\left[-\frac{1}{2}\left[\frac{\|\mathrm{x-c_j}\|}{\sigma_{\mathrm{j}}}\right]^2\right] \tag{14}$$

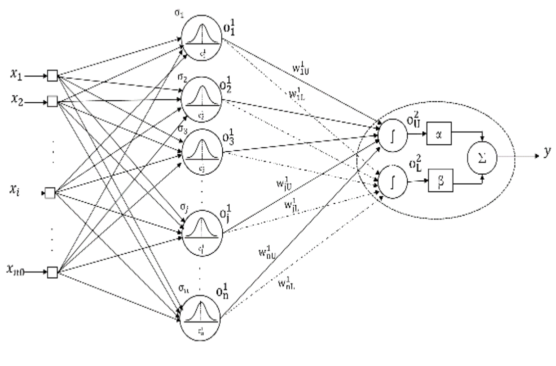

Figure 5. Gaussian rough neural network design for problem solving

$$o_j^1 = \exp\left[-\frac{1}{2(\sigma_j)^2}\sum_{p=1}^{n_0}(x_p - c_{pj})^2\right] \quad (15)$$

The output of Gaussian rough network for the upper and lower limit is as:

$$o_U^2 = \max\,[w_U^T(k)o^1(k), w_L^T(k)o^1(k)] \quad (16)$$

$$o_L^2 = \min\,[w_U^T(k)o^1(k), w_L^T(k)o^1(k)] \quad (17)$$

And the output of the network is finally as:

$$y(k) = \propto o_L^2 + \beta o_U^2 \quad (18)$$

4. 4. 2. Backpropagation Algorithm And Emotional Training Based on Gradient Descent In this section, using the error between the network output and the desired output, neural network parameters, including weights, cluster centers, and standard deviation, are taught. For better learn these parameters, emotional training algorithm and gradient descent have been used. We define the total error relation as follows:

$$E(k) = \frac{1}{2}\sum_{i=1}^{N}(r)^2(k) = \frac{1}{2}\sum_{i=1}^{N}(k_1 e_i(k) + k_2 \dot{e_i}(k))^2 \quad (19)$$

$$E(k) = \frac{1}{2}\sum_{i=1}^{N}((k_1 + k_2)e_i(k) - k_2 e_i(k-1))^2 \quad (20)$$

First mode if $w_U^T(k)o^1(k) \geq w_L^T(k)o^1(k)$:

$$w_U(k+1) = w_U(k) + \eta_w(k_1 + k_2)r(k) \propto o_j^1(k) \quad (21)$$

$$w_L(k+1) = w_L(k) + \eta_w(k_1 + k_2)r(k)\beta o_j^1(k) \quad (22)$$

$$c_j(k+1) = c_j(k) + \eta_c(k_1 + k_2)r(k)\left[\propto w_{Uj}(k) + \beta w_{Lj}(k)\right]\frac{(x - c_j(k))}{(\sigma_j(k))^2} o_j^1(k) \quad (23)$$

$$\sigma_j(k+1) = \sigma_j(k) + \eta_\sigma(k_1 + k_2)r(k)\left[\propto w_{Uj}(k) + \beta w_{Lj}(k)\right]\frac{(x - c_j(k))}{(\sigma_j(k))^2} o_j^1(k) \quad (24)$$

Second mode if $(k)o^1(k) < w_L^T(k)o^1(k)$:

$$w_U(k+1) = w_U(k) + \eta_w(k_1 + k_2)r(k)\beta o_j^1(k) \quad (25)$$

$$w_L(k+1) = w_L(k) + \eta_w(k_1 + k_2)r(k)\alpha o_j^1(k) \quad (26)$$

$$c_j(k+1) = c_j(k) + \eta_c(k_1 + k_2)r(k)\left[\beta w_{Uj}(k) + \alpha w_{Lj}(k)\right]\frac{(x - c_j(k))}{(\sigma_j(k))^2} o_j^1(k) \quad (27)$$

$$\sigma_j(k+1) = \sigma_j(k) + \eta_\sigma(k_1 + k_2)r(k)\left[\beta w_{Uj}(k) + \alpha w_{Lj}(k)\right]\frac{(x - c_j(k))}{(\sigma_j(k))^2} o_j^1(k) \quad (28)$$

4. 5. Detection of Fake Profiles The process of detecting shilling attacks in the proposed model is done in four stages. In the first step, fake profiles are inserted into the system using the shilling attack model and attack parameters. The resulting rating matrix, after injecting shilling attacks, is used as input for the next steps.

Then, in the second stage, the social network of users is created to find patterns between users and discover knowledge. The purpose of creating a social network of users is to discover latent relationships between profiles in the network.

In the third stage, parameters are extracted from the users' social network, the users' rating matrix and the users' rating time and are used as input for the next stage.

Finally, in the fourth stage, the construction of Gaussian rough neural network is done by determining forward and back error propagation algorithms, determining the parameters of the neural network, such as determining the number of neurons, training rate, initializing the weights and biases, the number of IPACs, and determining the volume of training data, evaluation and testing. After learning the network with training data and selecting the best trained weights, the network output is checked with test data to evaluate the performance of the proposed model.

5. EXPERIMENTAL EVALUATION

5. 1. Preliminaries In this section, we will discuss the pre-test preparations containing the data set used, attack size, filler size, attack model and comparison algorithms. Movielens-100k dataset is used in this research [59]. The Movielens-100k dataset includes rating information for 1682 items from 943 users. Table 3 summarized the user-item rating table for the Movielens-100k dataset. In the rating matrix, the user's rating values for the items are from 1 to 5. 0 indicates no rate, 1 indicates the lowest rate, and 5 indicates the highest user rate for an item.

The parameters of the attack size and the filler size should be determined during shilling attack injection. The attack size parameter indicates how many fake profiles are injected into the system and the filler size

TABLE 3. User-item rating table for Movielens-100k dataset

User /item	$item_1$	$item_2$	$item_3$	$item_4$	…	$item_{1682}$
$user_1$	5	3	4	3	…	0
$user_2$	4	0	0	0	…	0
$user_3$	0	0	0	0	…	0
$user_4$	0	0	0	0	…	0
…	…	…	…	…	…	0
$user_{943}$	0	5	0	0	…	0

indicates the number of items rated by fake profiles. Attack size and padding size are defined as follows.

The attack size equal to the number of fake profiles injected into the system refers to the total number of profiles in the system database and is calculated as follows:

$$\text{Attack Size} = \frac{N_{\text{fake profiles}}}{N_u} \quad (29)$$

The filler size equal to the number of points given by fake profiles injected into the system to the items in the recommender system refers to the total number of items in the system database and is calculated as follows:

$$\text{Filler Size} = \frac{N_{IF}}{N_{item}} \quad (30)$$

This mechanism is compared with four methods used in the experiments: PCA [48], Semi [60] and BAY [61] and XGB [49] to compare the performance of the proposed mechanism.

PCA is a method that uses unsupervised learning method PCA-SelectUsers to identify malicious fake users. Semi is a semi-supervised learning method. BAY combines several sets of base classifiers and uses the combined output to detect the shilling attack. XGB is a method that utilizes binary combination of gradient boosting to detect shilling attacks. Also, average attack, random attack and bandwagon attack models are used in this research.

5. 2. Evaluation Criteria In this research, three efficiency measures of shilling attack detection schemes are used. These criteria are:

- Precision

expressed as the percentage of fake profiles actually detected divided by all fake profiles [20].

$$\text{Precision} = \frac{TP}{TP+FP} \quad (31)$$

- Recall

expressed as the percentage of fake profiles actually detected divided by all fake profiles [20].

$$\text{Recall} = \frac{TP}{TP+FN} \quad (32)$$

- F1-Measure

combines precision and recall rate [20].

$$\text{F1} - \text{Measure} = 2 * \frac{\text{Precision} * \text{Recall}}{\text{Precision} + \text{Recall}} \quad (33)$$

5. 3. Evaluation Results In this section, we test three models of average attack, random attack and bandwagon attack with parameters of 10% filler size and 3, 5, 7, 10, 12 and 15% attack size after neural network learning. Figures 6, 7, and 8 show the performance of the proposed mechanism for precision, recall, and F1 criteria, respectively.

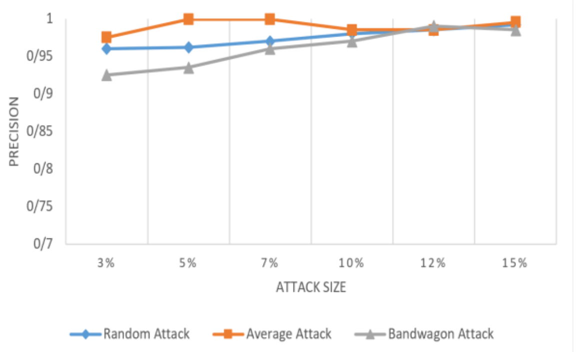

Figure 6. Performance of the proposed mechanism for precision

Figure 6 shows a view of the changes in the precision. As it is clear from the graph, in general, the precision of the proposed mechanism is improving as the attack size increases. Also, the precision in small and large attacks is above 0.9 and is at an acceptable level.

Figure 7 shows a view of the recall changes. According to the figure, the proposed mechanism in the random attack model, compared to the average and bandwagon attack, works weaker in small-sized attacks, but with an increase in the size of the attack, the recall in the proposed mechanism is generally increased.

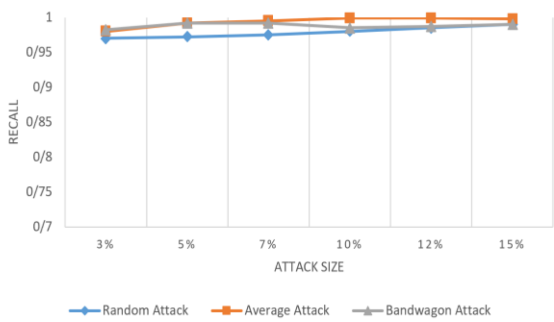

Figure 7. Performance of the proposed mechanism for recall

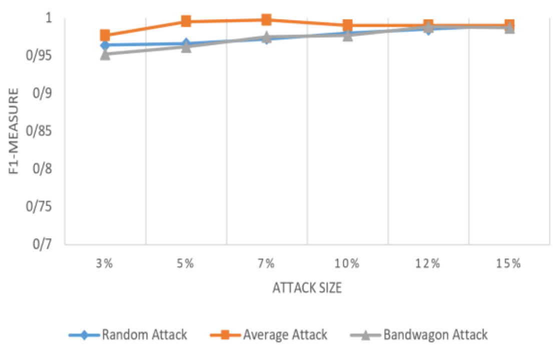

Figure 8. Performance of the proposed mechanism for F1-Measure

Figure 8 shows a view of the changes in the F1. F1 is generally improving as the attack size increases and is almost above 0.95 and is at an acceptable level. based on the experiments the comprehensive detection effectiveness of the algorithm is better in average attacks.

After checking the results of the proposed mechanism, the performance of the proposed mechanism is compared with the four methods used in PCA, Semi, BAY and XGB experiments. For this purpose, three models of random, average and bandwagon attacks were tested with parameters like 10% filler size and 3, 5, 7, 10, 12 and 15% attack size for the mentioned methods. Figures 9, 10, and 11 show the performance of the proposed mechanism for random attack, average attack, and bandwagon attack model, respectively, for F1.

As can be seen in Figures 9, 10 and 11, the proposed mechanism is clearly more effective in detecting attacks in random, average and bandwagon attack models.

6. DISCUSSION AND CONCLUSION

A growing number of e-commerce sites are implementing recommender systems to solve the selection overhead problem. The open and interactive

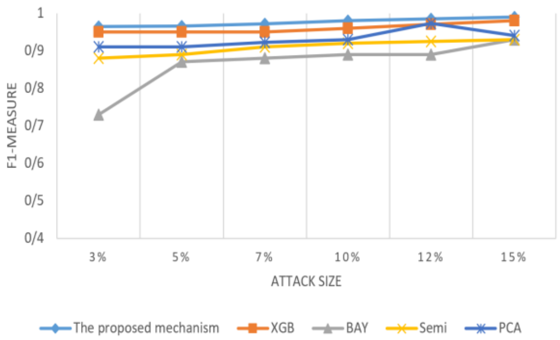

Figure 9. Performance of comparison methods under F1-Measure evaluation criterion for random attack

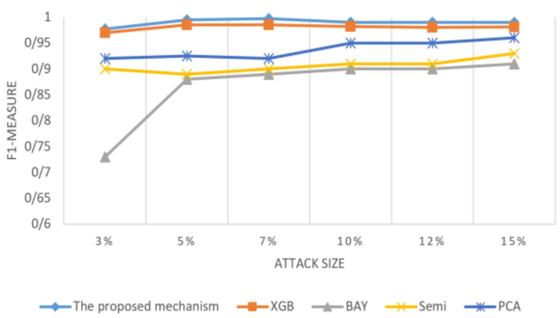

Figure 10. Performance of comparison methods under F1-Measure evaluation criterion for average attack

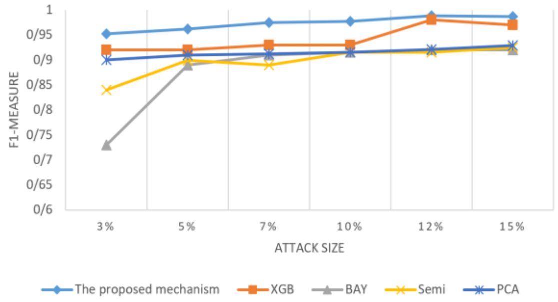

Figure 11. Performance of comparison methods under F1-Measure evaluation criterion for bandwagon attack

nature of recommender systems has made it possible for adversaries to disrupt their proper functioning by recording fake feedback through shilling attacks. Thus, the early detection of hose attacks in recommender systems plays a very important role in maintaining the stability of the recommender system and, along with it, maintaining its credibility.

This paper presented a new mechanism for detecting shilling attacks using social network analysis and Gaussian-Rough neural network. Fake profiles with specific strategies and patterns are injected into the recommender system, and identifying the characteristics of these strategies and patterns detects shilling attacks and discover fake profiles. The three outputs of users' rating matrix, rating time, and analysis of users' social networks were used to discover low and high order information after modeling their profiles and features in the form of a network of vertices, and edges, and building a social network at the same time. This type of neural network was used to detect fake profiles due to the high ability of Gaussian-Rough neural networks to classify complex patterns and noise resistance.

The proposed mechanism overcomes the limitations of previous methods and analyzes user profiles from different perspectives, as well as uses low-order interactions and high-order interactions to detect malicious attackers. The experimental results show that the proposed mechanism in the mean and bandwagon random attack model is more effective in detecting attacks compared to the four methods PCA, Semi, BAY, and XGB.

The proposed mechanism can be used as a practical method in recommender systems based on collaborative filtering in e-commerce sites to detect standard attacks. The main challenge facing the proposed mechanism is group shilling attacks. The proposed mechanism for detecting group shilling attacks is considered in future research because the shilling attack detection algorithms mainly focus on identifying individual attackers in online recommender systems and rarely deal with group shilling attacks.

7. REFERENCES

1. Bobadilla, J., Ortega, F., Hernando, A. and Gutiérrez, A., "Recommender systems survey", ***Knowledge-based systems***, Vol. 46, (2013), 109-132. doi: 10.1016/j.knosys.2013.03.012.
2. Resnick, P. and Varian, H.R., "Recommender systems", ***Communications of the ACM***, Vol. 40, No. 3, (1997), 56-58. doi: 10.1145/245108.245121.
3. Adomavicius, G. and Tuzhilin, A., "Toward the next generation of recommender systems: A survey of the state-of-the-art and possible extensions", ***IEEE transactions on knowledge and data engineering***, Vol. 17, No. 6, (2005), 734-749. doi: 10.1109/TKDE.2005.
4. Aggarwal, C.C., "Recommender systems, Springer, Vol. 1, (2016).
5. Moghaddam, F.B. and Elahi, M., Cold start solutions for recommendation systems, in Big data recommender systems: Recent trends and advances. 2019, IET.
6. Bollen, D., Knijnenburg, B.P., Willemsen, M.C. and Graus, M., "Understanding choice overload in recommender systems", in Proceedings of the fourth ACM conference on Recommender systems., (2010), 63-70.
7. Ricci, F., Rokach, L. and Shapira, B., Introduction to recommender systems handbook, in Recommender systems handbook. 2011, Springer.1-35.
8. Jannach, D., Zanker, M., Felfernig, A. and Friedrich, G., "Recommender systems: An introduction, Cambridge University Press, (2010).
9. Rubens, N., Elahi, M., Sugiyama, M. and Kaplan, D., Active learning in recommender systems, in Recommender systems handbook. 2015, Springer.809-846.
10. Su, X. and Khoshgoftaar, T.M., "A survey of collaborative filtering techniques", ***Advances in Artificial Intelligence***, Vol. 2009, (2009). https://doi.org/10.1155/2009/421425
11. Burke, R., "Hybrid recommender systems: Survey and experiments", ***User Modeling and User-adapted Interaction***, Vol. 12, No. 4, (2002), 331-370.
12. Alonso, S., Bobadilla, J., Ortega, F. and Moya, R., "Robust model-based reliability approach to tackle shilling attacks in collaborative filtering recommender systems", ***IEEE Access***, Vol. 7, (2019), 41782-41798. doi: 10.1109/ACCESS.2019.2905862.
13. Kaminskas, M. and Bridge, D., "Diversity, serendipity, novelty, and coverage: A survey and empirical analysis of beyond-accuracy objectives in recommender systems", ***ACM Transactions on Interactive Intelligent Systems (TiiS)***, Vol. 7, No. 1, (2016), 1-42. doi: 10.1145/2926720.
14. Jia, C.-X. and Liu, R.-R., "Improve the algorithmic performance of collaborative filtering by using the interevent time distribution of human behaviors", ***Physica A: Statistical Mechanics and its Applications***, Vol. 436, (2015), 236-245. doi: 10.1016/j.physa.2015.05.060.
15. Si, M. and Li, Q., "Shilling attacks against collaborative recommender systems: A review", ***Artificial Intelligence Review***, Vol. 53, No. 1, (2020), 291-319. doi: 10.1007/s10462-018-9655-x.
16. Mobasher, B., Burke, R., Bhaumik, R. and Williams, C., "Toward trustworthy recommender systems: An analysis of attack models and algorithm robustness", ***ACM Transactions on Internet Technology (TOIT)***, Vol. 7, No. 4, (2007), 23-es. doi: 10.1145/1278366.1278372.
17. Burke, R., O'Mahony, M.P. and Hurley, N.J., Robust collaborative recommendation, in Recommender systems handbook. 2015, Springer.961-995.
18. Williams, C.A., "Thesis: Profile injection attack detection for securing collaborative recommender systems", (2012).
19. O'Mahony, M.P., Hurley, N.J. and Silvestre, G.C., "Recommender systems: Attack types and strategies", in AAAI., (2005), 334-339.
20. Bhaumik, R., Williams, C., Mobasher, B. and Burke, R., "Securing collaborative filtering against malicious attacks through anomaly detection", in Proceedings of the 4th workshop on intelligent techniques for web personalization (ITWP'06), Boston. Vol. 6, (2006), 10.
21. Mobasher, B., Burke, R., Bhaumik, R. and Sandvig, J.J., "Attacks and remedies in collaborative recommendation", ***IEEE Intelligent Systems***, Vol. 22, No. 3, (2007), 56-63. doi: 10.1109/MIS.2007.45.
22. Yang, Z., Cai, Z. and Guan, X., "Estimating user behavior toward detecting anomalous ratings in rating systems", ***Knowledge-based Systems***, Vol. 111, (2016), 144-158. doi: 10.1016/j.knosys.2016.08.011.
23. Chung, C.-Y., Hsu, P.-Y. and Huang, S.-H., "Bp: A novel approach to filter out malicious rating profiles from recommender systems", ***Decision Support Systems***, Vol. 55, No. 1, (2013), 314-325. doi: 10.1016/j.dss.2013.01.020.
24. Rezaimehr, F. and Dadkhah, C., "A survey of attack detection approaches in collaborative filtering recommender systems", ***Artificial Intelligence Review***, Vol. 54, No. 3, (2021), 2011-2066. doi: 10.1007/s10462-020-09898-3.
25. Chirita, P.-A., Nejdl, W. and Zamfir, C., "Preventing shilling attacks in online recommender systems", in Proceedings of the 7th annual ACM international workshop on Web information and data management., (2005), 67-74.
26. Lam, S.K. and Riedl, J., "Shilling recommender systems for fun and profit", in Proceedings of the 13th international conference on World Wide Web., (2004), 393-402.
27. O'Mahony, M.P., Hurley, N.J. and Silvestre, G.C., "Detecting noise in recommender system databases", in Proceedings of the 11th international conference on Intelligent user interfaces., (2006), 109-115.
28. Mobasher, B., Burke, R., Bhaumik, R. and Williams, C., "Effective attack models for shilling item-based collaborative filtering systems", in Proceedings of the WebKDD Workshop, Citeseer., (2005), 13-23.
29. Burke, R., Mobasher, B. and Bhaumik, R., "Limited knowledge shilling attacks in collaborative filtering systems", in Proceedings of 3rd international workshop on intelligent techniques for web personalization (ITWP 2005), 19th international joint conference on artificial intelligence (IJCAI 2005)., (2005), 17-24.
30. Williams, C., Mobasher, B., Burke, R., Sandvig, J. and Bhaumik, R., "Detection of obfuscated attacks in collaborative recommender systems", in Proceedings of the ECAI'06 Workshop on Recommender Systems. Vol. 94, (2006).
31. Bhaumik, R., Mobasher, B. and Burke, R., "A clustering approach to unsupervised attack detection in collaborative recommender systems", in Proceedings of the International Conference on Data Science (ICDATA), Citeseer. (2011), 1.
32. Hurley, N., Cheng, Z. and Zhang, M., "Statistical attack detection", in Proceedings of the third ACM conference on Recommender systems., (2009), 149-156.
33. Wilson, D.C. and Seminario, C.E., "When power users attack: Assessing impacts in collaborative recommender systems", in Proceedings of the 7th ACM conference on Recommender systems., (2013), 427-430.
34. Seminario, C.E. and Wilson, D.C., "Nuking item-based collaborative recommenders with power items and multiple targets", in The Twenty-Ninth International Flairs Conference. (2016).

35. Zhang, F., "Analysis of bandwagon and average hybrid attack model against trust-based recommender systems", in 2011 Fifth International Conference on Management of e-Commerce and e-Government, IEEE., (2011), 269-273.
36. O'Mahony, M., Hurley, N., Kushmerick, N. and Silvestre, G., "Collaborative recommendation: A robustness analysis", ***ACM Transactions on Internet Technology (TOIT)***, Vol. 4, No. 4, (2004), 344-377. doi: 10.1145/1031114.1031116.
37. Mobasher, B., Burke, R. and Sandvig, J.J., "Model-based collaborative filtering as a defense against profile injection attacks", in AAAI. Vol. 6, (2006), 1388.
38. Dellarocas, C., "Immunizing online reputation reporting systems against unfair ratings and discriminatory behavior", in Proceedings of the 2nd ACM Conference on Electronic Commerce., (2000), 150-157.
39. O'Mahony, M.P., Hurley, N.J. and Silvestre, G., "Promoting recommendations: An attack on collaborative filtering", in International Conference on Database and Expert Systems Applications, Springer., (2002), 494-503.
40. Burke, R., Mobasher, B., Williams, C. and Bhaumik, R., "Classification features for attack detection in collaborative recommender systems", in Proceedings of the 12th ACM SIGKDD international conference on Knowledge discovery and data mining., (2006), 542-547.
41. Williams, C.A., Mobasher, B. and Burke, R., "Defending recommender systems: Detection of profile injection attacks", ***Service Oriented Computing and Applications***, Vol. 1, No. 3, (2007), 157-170. doi: 10.1007/s11761-007-0013-0.
42. Tang, T. and Tang, Y., "An effective recommender attack detection method based on time sfm factors", in 2011 IEEE 3rd International Conference on Communication Software and Networks, IEEE., (2011), 78-81.
43. Xia, H., Fang, B., Gao, M., Ma, H., Tang, Y. and Wen, J., "A novel item anomaly detection approach against shilling attacks in collaborative recommendation systems using the dynamic time interval segmentation technique", ***Information Sciences***, Vol. 306, (2015), 150-165. doi: 10.1016/j.ins.2015.02.019.
44. Yang, Z., Xu, L., Cai, Z. and Xu, Z., "Re-scale adaboost for attack detection in collaborative filtering recommender systems", ***Knowledge-based Systems***, Vol. 100, (2016), 74-88. doi: 10.1016/j.knosys.2016.02.008.
45. Wu, Z.-A., Zhuang, Y., Wang, Y.-Q. and Cao, J., "Shilling attack detection based on feature selection for recommendation systems", ***Acta Electonica Sinica***, Vol. 40, No. 8, (2012), 1687. doi: 10.3969/j.issn.0372-2112.2012.08.031.
46. Li, W., Gao, M., Li, H., Zeng, J., Xiong, Q. and Hirokawa, S., "Shilling attack detection in recommender systems via selecting patterns analysis", ***IEICE Transactions on Information and Systems***, Vol. 99, No. 10, (2016), 2600-2611. doi: 10.1587/transinf.2015EDP7500.
47. Wu, Z., Wu, J., Cao, J. and Tao, D., "Hysad: A semi-supervised hybrid shilling attack detector for trustworthy product recommendation", in Proceedings of the 18th ACM SIGKDD international conference on Knowledge discovery and data mining., (2012), 985-993.
48. Mehta, B., "Unsupervised shilling detection for collaborative filtering", in AAAI., (2007), 1402-1407.
49. Shao, C. and zhong yi Sun, Y., "Shilling attack detection for collaborative recommender systems: A gradient boosting method", ***Mathematical Biosciences and Engineering***, Vol. 19, No. 7, (2022), 7248-7271. doi: 10.3934/mbe.2022342.
50. Ajzen, I., "The theory of planned behavior", ***Organizational Behavior and Human Decision Processes***, Vol. 50, No. 2, (1991), 179-211. doi: 10.1016/0749-5978(91)90020-T.
51. Zhou, W., Koh, Y.S., Wen, J., Alam, S. and Dobbie, G., "Detection of abnormal profiles on group attacks in recommender systems", in Proceedings of the 37th international ACM SIGIR conference on Research & development in information retrieval., (2014), 955-958.
52. Zhou, W., Wen, J., Koh, Y.S., Alam, S. and Dobbie, G., "Attack detection in recommender systems based on target item analysis", in 2014 International Joint Conference on Neural Networks (IJCNN), IEEE., (2014), 332-339.
53. Zhou, W., Wen, J., Koh, Y.S., Xiong, Q., Gao, M., Dobbie, G. and Alam, S., "Shilling attacks detection in recommender systems based on target item analysis", ***PloS One***, Vol. 10, No. 7, (2015), e0130968. doi: 10.1371/journal.pone.0130968.
54. Zhang, S., Chakrabarti, A., Ford, J. and Makedon, F., "Attack detection in time series for recommender systems", in Proceedings of the 12th ACM SIGKDD international conference on Knowledge discovery and data mining., (2006), 809-814.
55. Oestreicher-Singer, G. and Sundararajan, A., "Recommendation networks and the long tail of electronic commerce", ***Mis Quarterly***, (2012), 65-83. doi: 10.2139/ssrn.1324064.
56. Kong, X., Shi, Y., Yu, S., Liu, J. and Xia, F., "Academic social networks: Modeling, analysis, mining and applications", ***Journal of Network and Computer Applications***, Vol. 132, (2019), 86-103. doi: 10.1016/j.jnca.2019.01.029.
57. Liao, H., Ding, S., Wang, M. and Ma, G., "An overview on rough neural networks", ***Neural Computing and Applications***, Vol. 27, No. 7, (2016), 1805-1816. doi: 10.1007/s00521-015-2009-6.
58. Salehi, S. and Pouyan, A., "Detecting overlapping communities in social networks using deep learning", ***International Journal of Engineering, Transactions C: Aspects*** Vol. 33, No. 3, (2020), 366-376. doi: 10.5829/IJE.2020.33.03C.01.
59. Harper, F.M. and Konstan, J.A., "The movielens datasets: History and context", ***ACM Transactions on Interactive Intelligent Systems (TiiS)***, Vol. 5, No. 4, (2015), 1-19.
60. Cao, J., Wu, Z., Mao, B. and Zhang, Y., "Shilling attack detection utilizing semi-supervised learning method for collaborative recommender system", ***World Wide Web***, Vol. 16, No. 5, (2013), 729-748. https://doi.org/10.1007/s11280-012-0164-6
61. Bhebe, W. and Kogeda, O.P., "Shilling attack detection in collaborative recommender systems using a meta learning strategy", in 2015 International Conference on Emerging Trends in Networks and Computer Communications (ETNCC), IEEE., (2015), 56-61.

Persian Abstract

چکیده

یک سیستم توصیه‌گر بخش جدایی ناپذیر از سایت‌های تجارت الکترونیکی است. یکی از چالش‌های مهم در سیستم‌های توصیه‌گر حملات شیلینگ هستند هستند که با استفاده از ایجاد پروفایل‌های جعلی در سیستم و امتیازدهی مغرضانه به آیتم‌ها سبب کاهش دقت و از بین رفتن عملکرد صحیح سیستم توصیه‌گر در ارائه توصیه به کاربران می‌شود. هدف اصلی حمله‌کنندگان، تغییر رتبه محتوا یا آیتم‌ها متناسب با منافعشان می‌باشد. حملات شیلینگ تهدیدی علیه اعتبار سیستم‌های توصیه‌گر است بنابراین تشخیص حملات شیلینگ در سیستم‌های توصیه‌گر برای حفظ عدالت و اعتبار آن‌ها امری ضروری به نظر می‌رسد. تاکنون الگوریتم‌ها و روش‌های خوبی برای تشخیص حملات شیلینگ ارائه شده است اما برخی از این روش‌ها یا ماتریس امتیازدهی را از یک دیدگاه واحد بررسی می‌کنند و یا از تعاملات مرتبه پایین و یا تعاملات مرتبه بالا استفاده می‌کنند. با توجه به این مورد این مقاله سازوکاری را با استفاده از ماتریس امتیازدهی کاربران، زمان امتیاز دهی کاربران و خروجی تحلیل شبکه‌های اجتماعی پروفایل کاربران با استفاده از شبکه عصبی گاوسی راف به منظور استفاده همزمان از تعاملات مرتبه پایین و مرتبه بالا برای تشخیص حملات شیلینگ ارائه می‌کند. در نهایت، ما چندین آزمایش را با سه مدل حمله میانگین، حمله تصادفی و حمله باندواگن انجام می‌دهیم و با استفاده از معیارهای دقت، فراخوانی و معیار-F1 با روش‌های PCA، Semi، BAY و XGB مقایسه می‌کنیم. نتایج نشان می‌دهد که روش پیشنهادی از روش‌های مقایسه از نظر تشخیص حمله و تشخیص کلی موثرتر عمل می‌کند، که کارایی روش ما را ثابت می‌کند.

IJE TRANSACTIONS B: Applications Vol. 36, No. 02, (February 2023) 335-347

International Journal of Engineering

Journal Homepage: www.ije.ir

Gender Identification of Mobile Phone Users based on Internet Usage Pattern

F. Negaresh, M. Kaedi*, Z. Zojaji

Faculty of Computer Engineering, University of Isfahan, Azadi Sq., Hezarjarib St., Isfahan, Iran

PAPER INFO

Paper history:
Received 30 September 2022
Received in revised form 29 November 2022
Accepted 02 December 2022

Keywords:
Gender Identification
Internet Usage Pattern
User Modeling
Machine Learning
Feature Selection

ABSTRACT

Gender is an important aspect of a person's identity. In many applications, gender identification is useful for personalizing services and recommendations. On the other hand, many people today spend a lot of time on their mobile phones. Studies have shown that the way users interact with mobile phones is influenced by their gender. But the existing methods for identify the gender of mobile phone users are either not accurate enough or require sensors and specific user activities. In this paper, for the first time, the internet usage patterns are used to identify the gender of mobile phone users. To this end, the interaction data, and specially the internet usage patterns of a random sample of people are automatically recorded by an application installed on their mobile phones. Then, the gender identification is modeled using different machine learning classification methods. The evaluations showed that the internet features play an important role in recognizing the users gender. The linear support vector machine was the superior classifier with the accuracy of 85% and F-measure of 85%.

doi: *10.5829/ije.2023.36.02b.13*

NOMENCLATURE

FP	False Positive	TP	True Positive
FN	False Negative	TN	True Negative

1. INTRODUCTION

Nowadays, the benefits of having a smartphone are undeniable, and almost everyone uses it almost constantly. For this reason, these devices contain rich sources of information about users and are powerful tools for better understanding of the user [1]. But different people use mobile phones differently. Various factors such as age, level of education, job, personality characteristics, and gender affect the people's mobile phones usage and internet usage patterns. Actually, studies have shown that the way users interact with mobile phones is influenced by their gender [2-4]. In particular, the internet usage patterns in male and female users are not the same.

On the other hand, user gender identification can play an important role in personalizing e-commerce services. For example, from the marketing perspective, the analysis of preferences and target items of each gender provides effective marketing strategies and profitable offers for companies [5, 6]. If a mobile application can identify the users gender and then provides personalized services according to the users gender, the experience of people interacting with smartphones will be more enjoyable, which increases customer satisfaction and loyalty and, consequently, the profitability of businesses.

Due to the importance of automatic gender identification of mobile phone users, this field has been considered in several studies. However, some of the methods suffer from low accuracy [3], some require the use of special sensors [4] (e.g., accelerometers and gyroscopes), and some others necessitate specific user activities such as high-speed walking that are not applicable to users who have been sedentary.

The objective of this study is to use the internet usage pattern of mobile phone users to identify their gender. The hypothesis that has been examined in this study is that the use of users internet usage patterns, alone or along with other features, can lead to the accurate users gender identification. In this paper, we intend to propose

*Corresponding Author Institutional Email: kaedi@eng.ui.ac.ir (M. Kaedi)

Please cite this article as: F. Negaresh, M. Kaedi, Z. Zojaji, Gender Identification of Mobile Phone Users based on Internet Usage Pattern, ***International Journal of Engineering, Transactions B: Applications***, Vol. 36, No. 02, (2023), 335-347

a method that predicts the users gender by investigating their Internet usage pattern, while it does not require special sensors on the mobile phone and does not depend on the specific user activities.

In the proposed method, a sample of 99 mobile phone users were randomly selected. Then, by installing an application on their mobile phone, their daily interactions with the mobile phone were automatically recorded. The obtained data were then analyzed and several classification models were built to predict the users gender. Finally, the results of gender classification for different scenarios were evaluated using standard evaluation criteria.

In the rest of the paper, in section 2, an overview of the related work is presented. Then, in section 3, the proposed method is discussed in details. Section 4 describes the results obtained, and section 5 presents the conclusions and future work.

2. LITERATURE REVIEW

In this section, the related work are reviewed in three categories.

The first category which is the most relevant to the current study includes studies that identifies the gender of mobile phone users. Jane and Kanhangad [4, 7] performed gender classification using user's gait information recorded by smartphone internal sensors. The authors recorded the user's gait data, including the data collected by accelerometer and gyroscope sensors, using an Android application. They then used gradients to extract several features from this data. Finally, by applying the decision tree learning algorithm to pre-processed data, they identified the user gender with 90% accuracy. In another study, Jane and Kanhangad [3] developed an approach to gender recognition in smartphones using user touch screen gestures. They used some classification algorithms to recognize the finger gestures pattern of - males and females. The K-nearest neighbor classification algorithm showed the highest accuracy in identifying user gender. In their study, Sarraute et al. [8] investigated whether the differences in smartphone usage between males and females are reflected in their call and SMS patterns. They were interested to find out the difference between the use of mobile phones in different age groups. Afterwards, they predicted the age and gender of users using several algorithms including Naïve Bayes, support vector machine (SVM), and logistic regression algorithms, which at the best resulted in 62.3% accuracy. Choi et al. [9] collected user data from messengers and social media platforms and investigated the wrodsets preferred by male and female users to predict their gender. They identified a set of representative wordsets for men and women and identified the gender of writers based on the presence of representative words in the texts. They used several measures, such as: term frequency–inverse document frequency (TF-IDF), mutual information and chi-square to calculate the similarity of the words in the text with the representative words. They examined Naive Bayes classifiers, logistic regression, and SVM with a linear kernel. They showed that SVM performed better than the others. Miguel-Hurtado et al. [10] presented an approach to identify the user gender based on touch gestures and keystroke dynamics. They collected touch data on both the horizontal and vertical axes, and the feature vectors were defined as the mean of the collected touch features. The dataset included 57 men and 59 women, and the evaluation was performed through 10-fold cross validation .

Despite the success of the studies of the first category, they suffer from significant limitations and weaknesses. Methods based on the user gait information pattern require specific user activity. They are also device-dependent due to their dependence on accelerometer and gyroscope sensors, and generalizing them to other devices with different versions of sensors is a challenging task. Also, the accuracy of these methods depends significantly on the walking speed. In addition, signals received from gyroscope and accelerometer sensors produce large volumes of data that cannot be easily be stored and processed by the mobile phone. Therefore, processing these signals and recognizing the gender accordingly may not be easily achievable in real-time. The large volume of data received for touch gestures-based methods is also an important challenge that makes it difficult to be used in a real-time gender recognition model. Also, accessing messages sent by mobile users can violate user privacy, and many users are reluctant to give permission to an application for accessing their messages. Unlike previous methods, using the Internet connection pattern presented in our study considers higher-level data, which, in addition to using a much lower volume of data than sensor signals, is not dependent on specific devices or specific sensors and preserves the user's privacy.

The second category includes studies on how females and males use the internet. Ramirez-Correa et al. [11] studied the pattern of internet usage between females and males and found that the pattern of internet usage is influenced by gender. In their study, the use of the internet by smartphone users was analyzed. The results show that males who have smartphones are more inclined to use mobile Internet. Su et al. [12] investigated the pattern of internet traffic volume and usage duration of men and women. By analyzing 204,352 mobile phone users from 34 countries, they found that men spend more time online than women and their use of the internet has a direct impact on their health, alcohol use, and smoking. In another study, Okazaki and Hirose [13] examined the impact of gender on the use of smartphones by Japanese men and women to search for travel information. They used an online questionnaire and collected 992 responses. They observed that women were more likely to use the mobile internet to search for travel information. In addition, the structural equation model showed that men are more likely to use mobile phone than traditional personal computers. Also, mobile internet usage is more popular among females than males. Even thought studies reviewed in this category investigate the difference in the volume and manner of internet usage between men and women, they have not provided a model for gender identification; they presented only the difference analysis.

In the third category, studies are introduced that identify the gender of users in social networks regardless of the device used. Vashisth and Meehan [14] categorized the gender of the Twitter users based on the text of their tweets. They first extracted features from tweets using natural language processing techniques. Then, common machine learning methods (e.g., logistic regression, SVM, and Naïve Bayes) were applied to the extracted features. The results showed that the traditional Bag of Words models could not produce accurate results in gender recognition; however, word embedding models can work better than several machine learning methods. Therefore, in their study, word embedding models have been introduced as the most efficient method in gender classification based on Twitter textual data. Abadin et al. [15] showed that the way that social media users use language can reflect their gender. They concluded that to identify the writer's gender, texts should be analyzed from both psycholinguistic and semantic aspects. After extracting various features, they used different classification methods such as Random Forest, AdaBoost, and LightGBM [16] to identify the gender. Finally, they reported the performance of each of the three classification methods using different feature categories, with and without feature selection. Results showed that using all types of features, regardless of the feature selection step, leads to the best results. Kowsari et al. [17] used ensemble deep learning to categorize the profiles of Twitter and Facebook users into male and female groups. They utilized Random Multimodel Deep Learning, which consists of several deep neural networks and a convolutional neural network in which the architecture and the number of nodes are generated randomly. Safara et al. [18] employed the Whale optimization algorithm as a metaheuristic method to find latent patterns of the text in combination with a two-hidden-layer neural network to identify the gender of the users. The Enron dataset, containing half a megabyte of e-mail texts from social network users, was adopted to evaluate their proposed method. studies reviewed in this category have identified gender on social media generally regardless of considering specific limitations of mobile phones such as limited processing power and privacy issues. These studies have mainly identified gender based on the content of posts shared on social networks and sometimes based on user profiles on social networks, which cannot be accessed on mobile phones without the user's privilege. Furthermore, the gender classification error is often relatively high in these methods, which threatens their usefulness in real-world applications .

3. PROPOSED METHOD

This study presents a gender identification system for mobile phone users based on user interactions, especially their internet usage pattern. The architecture of the proposed method shown in Figure 1 includes the following steps.

- Data acquisition from users interactions with mobile phones along with the users gender
- Data processing and feature extraction
- Feature selection to detect the features that are effective in identifying the gender of users
- Training the gender classification models by applying machine learning algorithms to the training data
- Applying the models to test data to evaluate their gender prediction accuracy

As it is shown in Figure 1, user-mobile interaction data is first collected by an Android application. After preprocessing, the features affected by the user gender are extracted from the raw data, and then, significant features are selected. After splitting the data into training and test subsets, modeling is performed on the training data. Finally, the test data is used to evaluate the performance of gender prediction models. The details of each step are described in the following sections.

3. 1. Data Acquisition In order to collect data, a random sample of 99 mobile phone users from different strata of the society was selected. The set included 47 men and 52 women. The age of these people was between 17 and 41 years, with the mean of 24.3, the median of 22, and the standard deviation of 5.8 years. These users were asked to install a specific Android application called Mobisense [19], designed to collect data on user-mobile phone interactions. Participants gradually joined in and installed the android application. The data acquisition process took eight months. After installation, the application does not require direct user intervention but implicitly records user behavioral data. This application records two types of data :

-User gender which is first asked directly from the user when installing the application. This data is used as the class labels in the model training process.

-Behavioral data such as internet usage, call, and SMS history, which is automatically collected by the application to be used as the inputs for classification models.

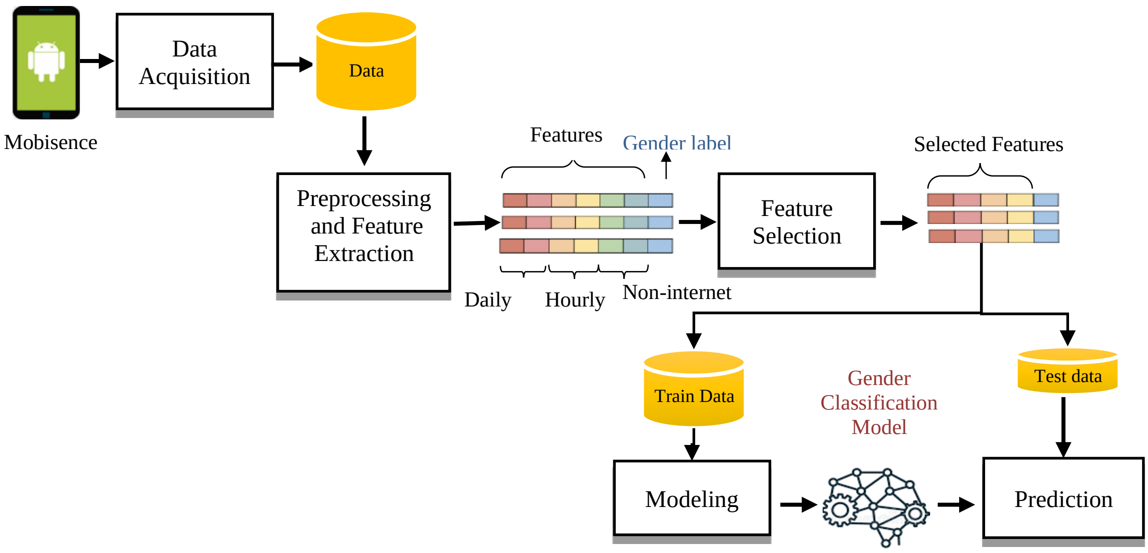

Figure 1. The architecture of the proposed method

In previous methods, the questionnaire has been used to collect data. However, data collected by questionnaire is influenced by the moods and situations of the participant at the time of completing the questionnaire. In addition, it is not possible to collect data continuously using a questionnaire. Unlike previous methods, the proposed method uses Android application to collect data implicitly and continuously, without being biased by the user's moods.

3. 2. Preprocessing Some users were excluded from future analysis in the preprocessing step because insufficient data was collected from them. To be more precise, users whose data was collected for less than one day, did not use mobile internet, or used multi-user phones were excluded from the list. Finally, 60 users remained, including 28 men and 32 women. Therefore, the final data included the user gender and behavioral features of individuals whose mobile phone interactions were recorded within an acceptable time frame, who used the mobile internet during that period, and all interactions belonged to only one user of a specific gender.

3. 3. Feature Extraction After data collection and data preprocessing, the data were stored as application logs in the SQL database to perform the feature extraction step. In this step, the significant features are extracted and calculated based on the raw data. Ninety-three features were extracted for each user, including cumulative and partial internet-based features and other features related to user interactions with the mobile phone (hereinafter referred to as "non-Internet-based" features).

3. 3. 1. Internet-based Features As shown in Table 1, two categories of internet-based features were extracted in this step. The first category is cumulative Internet-based features that describe the overall Internet usage of user throughout the day. Cumulative features do not indicate the distribution of Internet usage at different hours of the day, while Internet usage at different hours can differentiate the gender of the user. Therefore, the detailed internet-based features is defined as the second category of features. This category includes 12 detailed features (reffered to as D1, …, D12) indicating the percentage of daily internet connection at two-hour intervals throughout the day.

TABLE 1. Internet-based features

Feature Category	Feature Name	Description
Cumulative	C1	The average number of times the mobile data network is turned on per day
	C2	The average number of times Wi-Fi is turned on per day
	C3	The average number of network connections per day
	C4	The average duration of network connection per day
Detailed	D1	What percentage of the user's daily connection was between 24 and 2 o'clock.
	D2	What percentage of the user's daily connection was between 2 and 4 o'clock.
	…	…
	D12	What percentage of the user's daily connection was between 22 and 24 o'clock.

The following equation shows how to calculate the D1:

D1=100×(Internet connection duration from 24 to 2 o'clock) / (Internet connection duration per day) (1)

Other features, including D2 to D12, are calculated in a similar way for their respective periods.

3. 3. 2. Non-internet-based Features In addition to internet-based features, other behavioral features of user interactions with mobile phones have also been recorded and used. These features are called non-internet-based features in this study. They fall into 14 categories related to the following topics: call logs, hands-free usage logs, GPS usage logs, user profiles, applications installation, update, and uninstallation logs, airplane mode setting logs, Bluetooth usage logs, language change logs, battery level logs, power supply logs, sound and vibrate setting logs, touch screen turn on/off logs, SMS logs, and time zone change logs.

3. 4. Feature Selection Some features may not be important in determining the gender of a mobile phone user; The presence of such features in the training phase can cause bias in the model or reduce the accuracy. Therefore, using a feature selection step before applying classification models can lead to the selection of useful information, thus increasing the accuracy of model. For feature selection, the random forest algorithm was employed. In this method, after creating a random forest, an importance factor is calculated for each feature according to its average ability to increase the pureness of the leaves over the trees of the forest. Then, the most important features are selected [20].

3. 5. Training The set of features extracted for each user forms a feature vector that can be used to train a binary classifier. Classification is a supervised learning algorithm that, given a set of feature vectors and labels, models the input-output relationship and classifies new data based on the obtained model (male = 1and female =0). In this study, seven machine learning classification algorithms, including LSVM with Radial basis kernel, KNN, Naïve Bayes, CART [21] decision tree, random forest, and Adaboost [22, 23] have been used. The reason for choosing these algorithms was to use and compare the performance of different types of classifiers. Some of these algorithms are linear, and some others are nonlinear. Also, some are stochastic and some are deterministic. In addition, random forest and Adaboost are ensemble learning methods utilizing multiple learning algorithms to obtain better performance. In general, modeling the data by various algorithms gives a more comprehensive view of the problem at hand; therefore, a more accurate comparison and evaluation can be made. The set of candidate classifiers was selected the same as what was used by the related work so that the proposed method could be comparable to the literature. Hence, the effect of using internet-based features is determined purely.

4. EXPERIMENTAL RESULTS AND DISCUSSIONS

To evaluate the performance of the proposed method, different classification algorithms were applied and evaluated through 10-fold cross-validation [24]. In this evaluation method, the set of all users was randomly divided into ten folds. In each iteration, a fold is considered as the test data, and the model was trained using the remaining folds. This process was repeated for each of the ten folds, and the final evaluation criteria were calculated by averaging the performance over all iterations. Moreover, different scenarios were designed to investigate the effect of different feature sets on the performance of the gender identification models. In the rest of this section, after introducing the evaluation criteria and hyperparameter settings, different feature selection scenarios are evaluated and compared.

4. 1. Evaluation Criteria The evaluation criteria used in the current study include accuracy, precision, recall, and F-measure, which are expressed in Equations (2) to (5) based on the confusion matrix shown in Table 2. Male and female are considered as the positive and negative classes, respectively. Due to the trade-off between precision and recall, modifying the models to increase precision usually results in reducing the recall and vice versa. To balance these two criteria, the F-measure criterion was introduced to reflect the harmonic mean of precision and recall. Therefore, the F-measure is a more important criterion than precision and recall because it includes both.

$$\text{Accuracy}= (TP+TN)/(TP+TN+FP+FN) \quad (2)$$

$$\text{Precision}= TP/(TP+FP) \quad (3)$$

$$\text{Recall}= TP/(TP+FN) \quad (4)$$

$$\text{F-meaure}=(2\times\text{Precision}\times\text{Recall})/(\text{Precision}+\text{Recall}) \quad (5)$$

4. 2. Hyperparameter Setting Each of the classification algorithms, enumerated in section 3.5,

TABLE 2. Confusion matrix for gender identification

		Actual gender	
Predicted gender		**Male**	**Female**
	Male	True Positive (TP)	False Positive (FP)
	Female	False Negative (FN)	True Negative (TN)

requires one or more hyperparameters. Changing the hyperparameters greatly impacts the performance of the models; therefore, they must be adjusted carefully. In this research, we employed grid search for optimizing the hyperparameters. The optimal values of the hyperparameters obtained by the grid search are given in Table 3.

Depending on the features collected from users, various scenarios were conducted for evaluating the proposed method. In the following section, we use a unified notation for referring to different feature sets. Symbols C and D denote cumulative and detailed internet-based features, respectively, and symbol O indicates the other features (i.e., non-internet based features). Also, the asterisk at the top of these notations means that the feature selection step (i.e., random forest) is also performed. The remaining section describes scenarios one by one and provides the gender identification result, accordingly.

4. 3. Various Feature Sets Utilization Scenarios

- **Using cumulative Internet-based features**

In this scenario, different machine learning algorithms are applied and evaluated on the cumulative internet-based features. Table 4 shows the evaluation results of these classifiers.

As indicated in the table, these methods have not performed very well. This may be due to the lack of detailed internet features. The four applied features just show how the internet-based is used during the overall day, neglecting the details of using it within the day. The best performance of Table 4 is 0.53 in terms of precision. This prediction is not much different from the random guess. SVM with the radial basis kernel function has relatively high accuracy in comparison to others, but the other criteria of this method are not so high. On the other hand, the KNN outperformed other classifiers in terms of all criteria, which may be due to the simplicity of this classifier.

TABLE 3. The hyperparameter setting

Classifier	Hyperparameters value description
SVM	Regularization parameter = 0.025
SVM (Radial basis kernel)	Kernel variance = 10^{-7} Regularization parameter= 1
KNN	K=3
Decision Tree	Splitting criterion = gini-index
Random Forrest	Number of trees = 100, Splitting criterion = Gini-index, Number of features to consider for the best split = Sqrt of the number of features
AdaBoost	Number of weak classifiers = 100, Base classifier = Decision Tree
Naïve Bayes	Kernel = Gaussian

TABLE 4. Performance of gender identification on cumulative Internet-based features (FSC)

Algorithm	Accuracy	Recall	Precision	F-measure
LSVM	0.41	0.35	0.38	0.38
SVM (RBF)	**0.54**	0.4	0.4	0.4
KNN	**0.54**	**0.45**	**0.53**	**0.53**
Naïve Bayes	0.48	0.37	0.43	0.43
Decision Tree	0.48	0.38	0.43	0.43
Random forest	0.5	0.4	0.41	0.41
Adaboost	0.44	0.39	0.41	0.41

- **Using detailed Internet-based features**

In this scenario, classification algorithms are applied and evaluated on detailed internet-based features. The results are reported in Table 5. This table shows that among the various machine learning methods, Naïve Bayes has superior performance in predicting the gender of individuals according to 12 detailed internet-based features. After that, the decision tree obtaied the second-best place. In addition, by comparing Table 5 with Table 4, it can be concluded that the use of detailed internet-based features rather than cumulative ones provided more accurate information about the gender of individuals. This may be due to the use of more features providing more accurate information in the detailed internet-based features.

- **Using cumulative and detailed Internet-based features**

This scenario studies the effect of utilizing both detailed and cumulative internet-based feature sets in modeling. Table 6 shows the results of gender identification under this scenario.

According to this table, the performance of Naïve Bayes and decision tree have been better than other methods, in terms of accuracy. This result is consistent with the result of the second scenario reported in Table 5. Also, comparing Tables 5 and 6, indicates that the union of cumulative features and detailed ones has increased

TABLE 5. Performance of gender identification on detailed Internet-based features (FSD)

Algorithm	Accuracy	Recall	Precision	F-measure
LSVM	0.57	0.56	0.52	0.54
SVM (RBF)	0.52	0.3	0.2	0.24
KNN	0.55	0.48	0.6	0.53
Naïve Bayes	**0.72**	**0.68**	**0.65**	**0.66**
Decision Tree	0.62	0.67	0.5	0.57
Random forest	0.55	0.53	0.48	0.51
Adaboost	0.57	0.56	0.55	0.55

TABLE 6. Performance of gender identification on both cumulative and detailed Internet-based features (FSC+D)

Algorithm	Accuracy	Recall	Precision	F-measure
LSVM	0.57	0.56	0.52	0.54
SVM(RBF)	0.55	0.22	0.33	0.17
KNN	0.63	0.59	0.58	0.59
Naïve Bayes	**0.73**	**0.73**	**0.74**	**0.73**
Decision Tree	0.65	0.67	0.5	0.57
Random forest	0.6	0.57	0.55	0.56
Adaboost	0.57	0.55	0.57	0.56

TABLE 8. Performance of gender identification on all features (FSC+D+O)

Algorithm	Accuracy	Recall	Precision	F-measure
LSVM	**0.83**	**0.88**	**0.78**	**0.83**
SVM(RBF)	0.53	0.41	0.42	0.41
KNN	0.68	0.68	0.68	0.67
Naïve Bayes	0.73	0.73	0.7	0.72
Decision Tree	0.7	0.69	0.7	0.7
Random forest	0.71	0.6	0.57	0.58
Adaboost	0.65	0.63	0.63	0.63

the predictability and, consequently, the accuracy of the classifiers.

- **Using non-Internet-based features**

This scenario was conducted so that only non-internet-based features contribute to modelling the gender. Table 7 shows the results of this evaluation. It illustrates that Naïve Bayes has the highest accuracy among the classification algorithms, followed by random forest, LSVM, and Adaboodt, respectively.

- **Using All features**

In this scenario, all features, including cumulative internet-based, detailed internet-based, and non-internet-based features involved in the training phase. Table 8 reveals the performance evaluation of different classifiers under this scenario.

As it is inferred from Table 8, LSVM performed better than the other methods for all criteria, and Naïve Bayes is in second place. Furthermore, comparing Tables 7 and 8, it is apparent that the accuracy of all the classification algorithms has been improved by considering the internet features. This improvement determines the effect of using internet-based features along with other ones.

- **Summary of evaluating different feature sets**

To summarize the impact of applying different feature sets on the performance of gender identification models, we compared the best accuracy obtained for each of the enumerated scenarios. Figure 2 provides the result of this comparison. The chart shows that the detailed internet-based feature set gives better results than the cumulative one since it provides more accurate information. The use of all internet-based features has a better result than the use of detailed or cumulative internet features alone. Finally, the highest accuracy was achieved by utilizing all of the internet and non-internet-based features.

TABLE 7. Performance of gender identification on non-Internet-based features (FSO)

Algorithm	Accuracy	Recall	Precision	F-measure
LSVM	0.63	0.63	0.63	0.63
SVM(RBF)	0.53	0.53	0.26	0.35
KNN	0.51	0.51	0.49	0.47
Naïve Bayes	**0.70**	**0.70**	**0.70**	**0.70**
Decision Tree	0.55	0.55	0.54	0.54
Random forest	0.65	0.65	0.64	0.65
Adaboost	0.63	0.63	0.63	0.63

4. 4. Various Feature Sets Utilization Scenarios Along with Feature Selection

Applying the feature selection methods to the dataset before data modeling may improve the model's performance. Several experiments were conducted for evaluating the impact of feature selection on the model's performance over different feature set utilizations. Experimental results are reported in subsequent sections.

- **Using Internet-based features with feature selection**

This scenario applies feature selection on the set of internet-based features (both cumulative and detailed) to select the impressive features for modeling the users gender. After performing the feature selection step, C1, C2, C3, C4, D3, D4, D5, D7, D10, and D1 were selected as the most important features. This indicates that all the

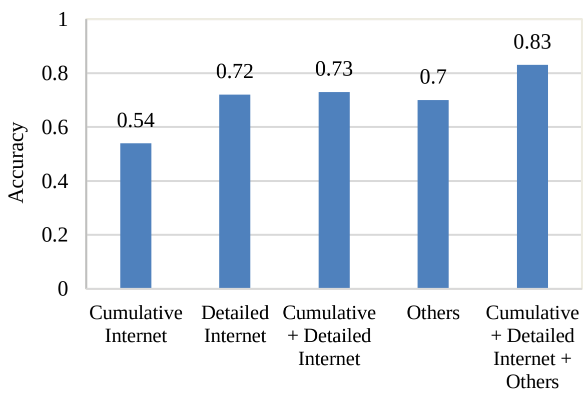

Figure 2. Summary of feature sets utilization

features of the cumulative set, including the average number of times the network data and Wi-Fi are turned on per day the average number of times Wi-Fi is turned on per day, the average number of network connections per day, the average duration of network connection per day, along with some detailed internet-based features including the average hours of internet use between 24 to 2 o'clock, 4 to 10 o'clock, 12 to 2 o'clock and 6 to 8 o'clock are important features for gender identification. Table 9 shows the evaluation results of the classification algorithms for the selected internet-based features.

Again, similar to the previous two scenarios, the Naïve Bayes method has superior performance by obtaining the accuracy of 0.70 in this scenario. Comparing Tables 9 and 6 indicates that the performance of Naïve Bayes has improved by applying the feature selection step. Moreover, the performance of Adaboost and decision tree have been slightly reduced. Random forest and KNN did not perform much differently. However, the performance of LSVM, SVM, and Naïve Bayes improved after applying the feature selection phase.

- **Using all features with feature selection**

This scenario includes feature selection applied to the whole set of features, including internet-based and non-Internet ones, prior to modeling. The feature selection algorithms suggested some non-internet-based features as well as D10 and D5 from the internet-based set. This selection reveals the duration of users' connection between 24 and 2 o'clock, and between 8 to 10 o'clock is affected by the user gender more than other features. The best obtained result is for LSVM in terms of accuracy, precision, recall, and F-measure. Table 10 shows the results of this evaluation. As inferred by the table, LSVM performed better than other classifiers and obtained the accuracy of 0.85. After that, random forest provided the best results with the 0.83 accuracy.

- **Summary of applying feature selection**

To analyze the effect of feature selection on gender identification accuracy, we compared the best accuracy

TABLE 9. Performance of gender identification on Internet-based features selected by the feature selection method (FS*C+D)

Algorithm	Accuracy	Recall	Precision	F-measure
LSVM	0.62	0.59	0.58	0.59
SVM(RBF)	0.55	0.48	0.28	0.36
KNN	0.62	0.63	0.53	0.58
Naïve Bayes	**0.7**	**0.71**	**0.65**	**0.68**
Decision Tree	0.57	0.55	0.5	0.52
Random forest	0.59	0.53	0.57	0.55
Adaboost	0.55	0.62	0.45	0.52

TABLE 10. Performance of gender identification on all features selected by the feature selection method (FS*C+D+O)

Algorithm	Accuracy	Recall	Precision	F-measure
LSVM	**0.85**	**0.85**	**0.85**	**0.85**
SVM(RBF)	0.64	0.57	0.68	0.62
KNN	0.7	0.7	0.71	0.69
Naïve Bayes	0.79	0.74	0.77	0.75
Decision Tree	0.66	0.55	0.67	0.56
Random forest	0.83	0.83	0.84	0.83
Adaboost	0.76	0.77	0.76	0.76

obtained for each scenario. Figure 3 illustrates this comparison through a bar chart. As shown in this figure, applying feature selection on the Internet-based feature set has not resulted in significant improvement. But when all the features are used, applying feature selection has increased the accuracy by 0.02. Since the total number of features is large in this scenario and, irrelevant features may also exist, especially in the non-internet set, feature selection has positively affected the performance.

4. 5. Summary of Various Scenarios of the Proposed Method

To sum up, by comparing the four criteria of accuracy, recall, precision, and F-measure calculated for different machine learning methods in different scenarios, it can be concluded that LSVM has the best performance on all feature sets. These comparisons are presented in Figures 4 to 7 for different criteria and scenarios.

It can be concluded that if only the cumulative internet-based features are used, KNN is the best machine learning method for gender identification. But, if the detailed Internet-based features are provided, Naïve Bayes has the best performance. Moreover, if the non-internet-based features are considered in addition to

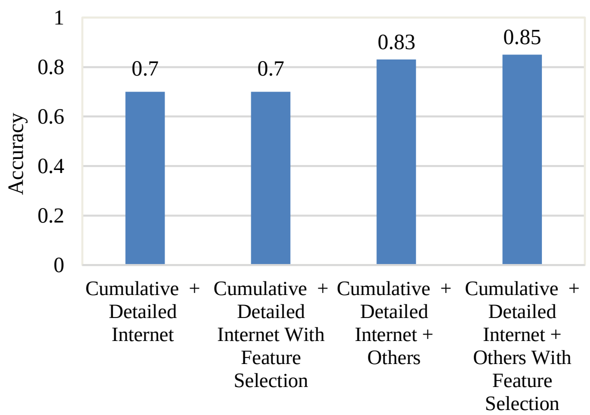

Figure 3. The effect of feature selection on gender identification accuracy for different feature sets

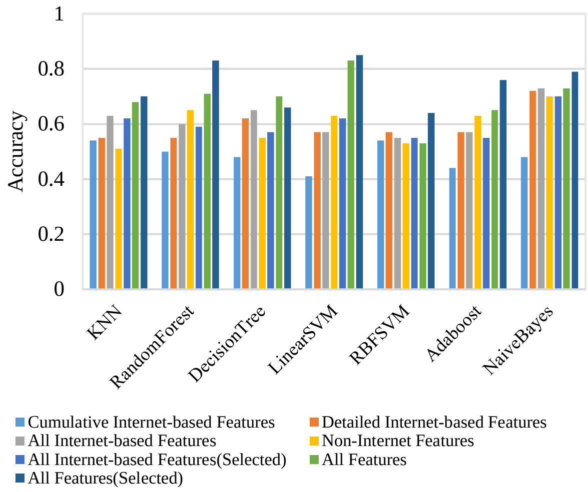

Figure 4. Accuracy of different classifiers in different scenarios

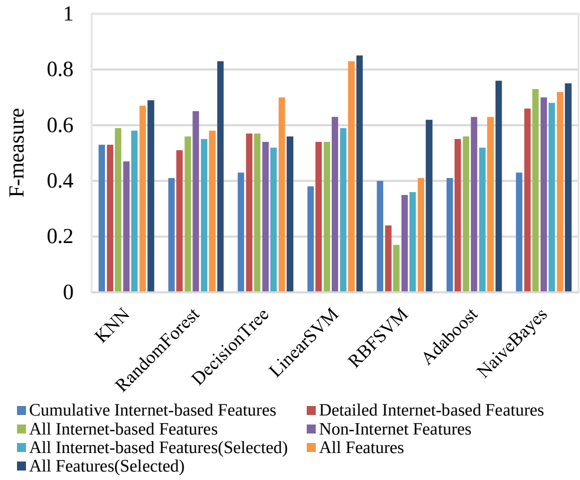

Figure 7. F-measure of different classifiers in different scenarios

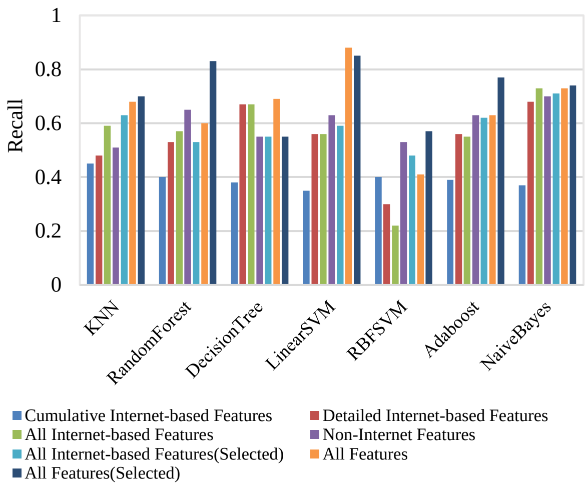

Figure 5. Recall of different classifiers in different scenarios

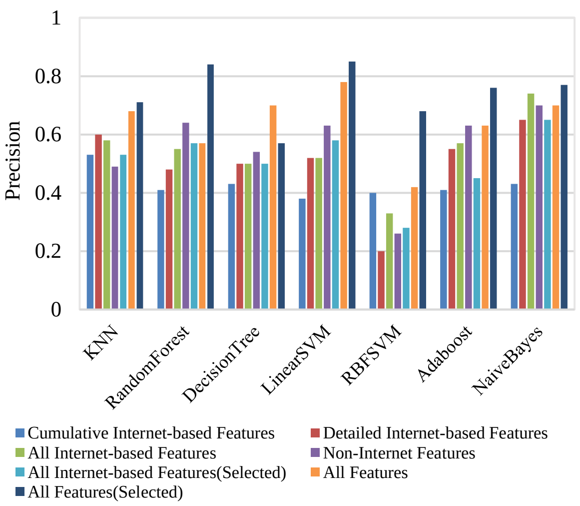

Figure 6. Precision of different classifiers in different scenarios

internet-based ones, LSVM can better identify the individuals' gender. In addition, it can be inferred from the figures that applying the feature selection step improves the classification performance in most cases. The presence of internet-based features among the selected features shows that internet-based features have played a significant role in identifying the gender of individuals.

Finally, by comparing the present study with previous studies that used the same classifiers on a set of other features, it can be concluded that our utialized features have improved the performance of machine learning methods in gender identification. Therefore, the use of internet-based features along with other behavioural information of mobile phone users can lead to more accurate gender identification.

4. 6. Summary of Various Machine Learning Techniques This section aims to compare the ability of various machine learning techniques in classifying genders over different feature selection scenarios. The average performance of each classifier over different scenarios is depicted in Figures 8 to 11, in terms of four performance criteria of accuracy, recall, precision, and F-measure. From these figures, it can be concluded that Naïve Bayes has the best and RBFSVM has the worst performances in gender detection for all criteria. The superiority of the Naïve Bayes method may be due to the simplicity of this classifier which leads to more regularization and generalization ability.

4. 7. Comparison with Related Works on Social Networks To better evaluate the performance of the proposed method, it was compared with some important previous studies. To our best knowledge, no study has utilized internet usage data for gender identification. Therefore, the performance of the

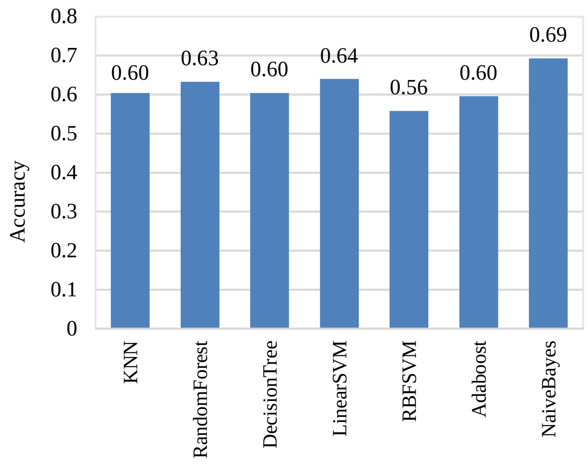

Figure 8. The overall accuracy of different machine learning techniques

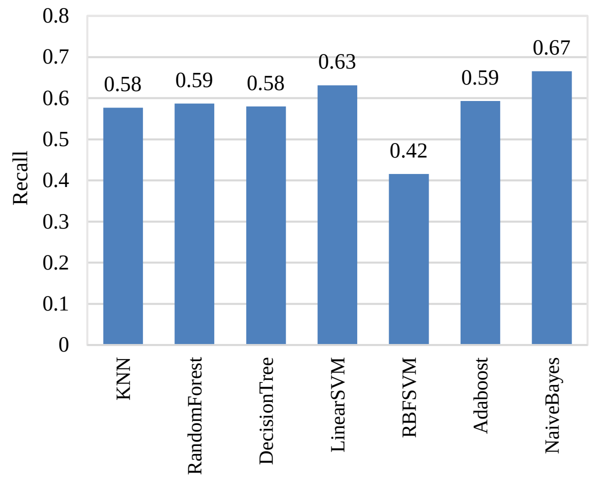

Figure 9. The overall recall of different machine learning techniques

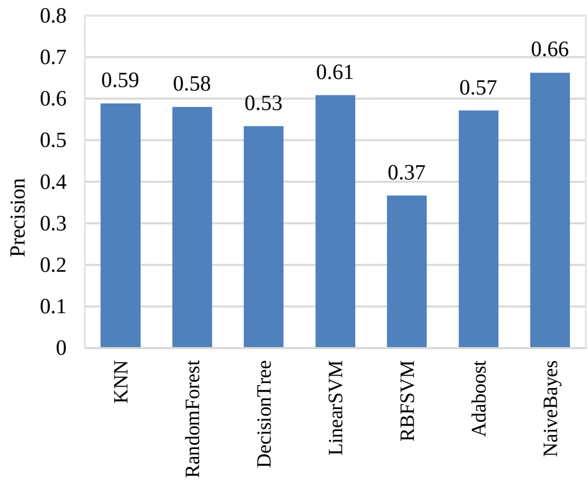

Figure 10. The overall precision of different machine learning techniques

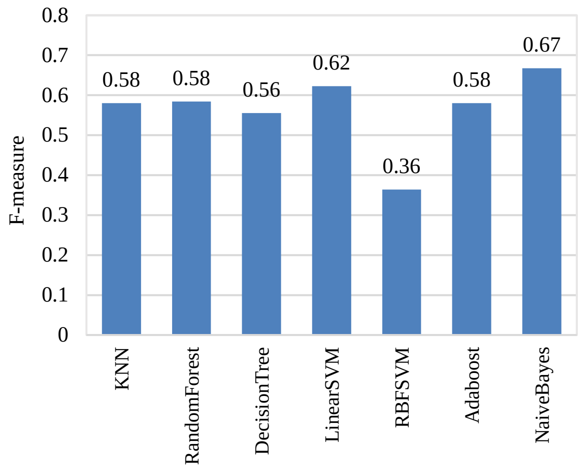

Figure 11. The overall F-measure of different machine learning techniques

proposed method is compared with the works that used other features for this task. This section compares the proposed method to gender identification studies in social networks. We choose machine learning classifiers the same as those used in the related studies to facilitate the comparison. But the dataset used in the proposed method is different from the datasets used in the previous studies. Related work contributed to the comparison includes Vashisth and Meehan [14] that determined the gender of individuals from individuals' tweets. Abadin et al. [15], which identified the gender of social network users using their posts on social networks. Table 11 reveals the results of the comparison. Since this section aims to compare with other studies, only the results related to the classifiers used in one of these two studies have been considered. Also, because previous studies have reported only the accuracy criterion, the results are reported in terms of accuracy in the table.

As mentioned earlier, in the proposed method, the best performance was achieved by applying the LSVM to all internet and non-internet-based features along with the use of feature selection. As shown in Table 11, the accuracy of this method is far better than the accuracies of the related works reported in literature [14, 15]. The same is true for Naïve Bayes, random forest and Adaboost classifiers. As a result, it can be inferred that the use of internet and non-internet data collected in this study has increased the efficiency of machine learning methods in identifying users gender.

4. 8. Comparison with Related Work on Mobile Phone Data To have a fair and comprehensive comparisons, in addition to studies that use social media information to identify the gender, the results of the proposed method is compared with other methods that use mobile phone information. Important studies from recent years have been selected to compare with the

TABLE 11. Comparing the accuracy of the proposed method with the related work in social networks

Method/Classifier	LSVM	Random Forest	Adaboost	Naïve Bayes
Proposed method (FS_{C+D})	0.57	0.6	0.57	0.73
Proposed method (FS^*_{C+D})	0.62	0.59	0.55	0.7
Proposed method (FS_{C+D+O})	0.83	0.71	0.65	0.73
Proposed method (FS^*_{C+D+O})	0.85	**0.83**	**0.76**	**0.79**
Abadin et al.[15] (all features)	-	0.6	0.55	-
Abadin et al.[15] (all features except text topic)	-	0.66	0.65	-
Abadin et al.[15] (less important features)	-	0.67	0.65	-
Abadin et al.[15] (selected features)	-	0.65	0.65	-
Vashisth et al. [14] (TF-IDF)	0.52	0.47	0.55	0.53
Vashisth et al. [14] (W2Vec)	0.52	0.47	0.55	-
Vashisth et al. [14] (GloVe)	0.52	0.48	0.52	-

proposed method. Jain and Kanhangad [4] used collected signals from smartphone accelerometer and gyroscope sensors to predict gender. This method was evaluated in different scenarios based on the walking speed, the underlying device, and the sensors type. The accuracy for fast, normal, and slow walking as well as the two devices S-II and Note-II, in the case of using all sensors are averaged and reported in Table 12.

In another study [3], the same authors used touch screen gesture information along with various machine learning methods. They showed that the KNN obtains the best performance in this regard. Also, some researchers [10] used the information of sweep gestures to identify the gender. The accuracy of the best presented model has been considered in Table 12.

It is evident that the proposed method using all the features and feature selection could reach a higher accuracy than the work of Jain and Kanhangad [3] with the KNN model and the method of Miguel-Hurtado et al. [10]. But the best performance was achieved in another work of Jain and Kanhangad [4] among the compared studies. However, their presented model requires the use of accelerometer and gyroscope sensors and walking activity which threats the generality and universality of the deployment of the method. For example, the method does not apply to users who have been idle for a long time or on sensorless mobile phones. They are also device-dependent, and their generalizability to other devices

TABLE 12. Comparing the accuracy of the proposed method with the related work on mobile phone data

Method	Accuracy
Proposed method(FS^*_{C+D+O})	0.85
Jain and Kanhangad [4]	**0.90**
Jain and Kanhangad [3]	0.82
Miguel-Hurtado et al.[10]	0.69

with different sensors can be quite challenging. On the other hand, in their proposed method a high volume of data is recorded from gyroscope and accelerometer sensors that are not easy to store and process for the mobile phone as a small processing unit.

4. 9. Analysis of Gender-related Characteristics on Internet Usage

The evaluation results of the proposed method confirm that it is possible to identify the gender of users based on their internet usage. This result is in line with psychological studies conducted in this regard.

The gender-related characteristics which distinguish the internet usage pattern in females and males have been investigated in former studies [12]. Some of these distinguishing features that have been mentioned in psychological studies are as follows:

- The amount of family supervision is often more for female teenagers than males, which prevents them from spending too much time on the internet [28].
- Internet availability is higher for males than for females approximately all over the world [29].
- According to FMRI image analysis [30], males' and females' brains have different susceptibilities to internet gaming addiction.
- Sociocultural customs and norms cause different types of behaviour in females and males for example by imposing more restrictions on females for using the internet [31]. Again, Becker et al. [32] claimed that the effect of social and legal constraints on females is usually greater than on males.
- It was also stated [33] that excessive internet usage in males can be interpreted as an escape into cyberspace. It is a kind of self-medication behaviour for them in reaction to depression.

5. CONCLUSION

In this study, gender identification according to internet usage patterns was investigated. To this aim, two sets of Internet-based features (i.e., cumulative internet-based features and detailed internet-based features) were introduced to be used beside the non-internet-based features. Then, several models were obtained to predict the gender of mobile phone users based on internet and non-internet based feature sets. Various experiments were conducted to investigate the effect of cumulative and detailed internet-based features on the performance of gender identification models. From the experiments, it was inferred that using internet-based features along with other interaction-based ones can improve the performance of the models. The results of applying machine learning algorithms on the collected phone interaction data suggested that LSVM with the accuracy of 85% obtained the best results in identifying the gender of users. One of the limitations of this work is related to mobile phone computing power. Because of this limitation, it may not be possible to process the features on some types of smartphones and the features need to be sent to the server to be processed. Another considerable limitation of the presented work is that the collected dataset is limited in terms of both records and features. For future studies, more diverse feature sets (e.g., the data volume transferred in each connection or period, applications used by the users, etc.) can be introduced to represent the internet usage pattern of users. Other feature selection methods and machine learning algorithms can also be examined on the collected data to investigate if the results improve. In addition, the data extracted from social media can be combined with the smartphone usage data to improve the accuracy of the models. In addition to gender, the usefulness of internet usage features to identify other user characteristics such as the age and education level can be examined.

6. REFERENCES

1. Daneshvar, S. and Inkpen, D., "Gender identification in twitter using n-grams and lsa.", in Proceedings of the Ninth International Conference of the CLEF Association (CLEF 2018), (2018).
2. Giannakopoulos, O., Kalatzis, N., Roussaki, I. and Papavassiliou, S., "Gender recognition based on social networks for multimedia production." in 2018 IEEE 13th Image, Video, and Multidimensional Signal Processing Workshop, IVMSP 2018 - Proceedings. Institute of Electrical and Electronics Engineers Inc, (2018).
3. Jain, A. and Kanhangad, V., "Gender recognition in smartphones using touchscreen gestures." ***Pattern Recognition Letters***, Vol. 125, (2019), 604-611. https://doi.org/10.1016/j.patrec.2019.06.008
4. Jain, A. and Kanhangad, V,, "Gender classification in smartphones using gait information." ***Expert Systems & Application*s**, Vol. 93, (2018), 257-266. https://doi.org/10.1016/j.eswa.2017.10.017
5. Meena, T. and Sarawadekar, K., "Gender recognition using in-built inertial sensors of smartphone.", in IEEE Region 10 Annual International Conference, Proceedings/TENCON. Institute of Electrical and Electronics Engineers Inc., (2020), 462-467.
6. Nguyen-Quoc, H. and Hoang, VT., "Gender recognition based on ear images: A comparative experimental study.", in 2020 3rd International Seminar on Research of Information Technology and Intelligent Systems, ISRITI 2020. Institute of Electrical and Electronics Engineers Inc., (2020), 451-456.
7. Jain, A. and Kanhangad, V., "Investigating gender recognition in smartphones using accelerometer and gyroscope sensor readings", in 2016 international conference on computational techniques in information and communication technologies (ICCTICT). IEEE, (2016), 597-602.
8. Sarraute, C., Blanc, P. and Burroni, J., "A study of age and gender seen through mobile phone usage patterns in mexico.", in 2014 IEEE/ACM international conference on advances in social networks analysis and mining (ASONAM 2014). IEEE, (2014), 836-843.
9. Choi, Y., Kim, Y., Kim, S., Park, K. and Park, J., "An on-device gender prediction method for mobile users using representative wordsets". ***Expert Systems & Applications***, Vol. 64, (2016), 423-433. https://doi.org/10.1016/j.eswa.2016.08.002
10. Miguel-Hurtado, O., Stevenage, S. V., Bevan, C. and Guest. R. "Predicting sex as a soft-biometrics from device interaction swipe gestures." ***Pattern Recognition Letters***, Vol. 79, (2016), 44-51
11. Ramirez-Correa, P.E., Rondan-Cataluña, F.J. and Arenas-Gaitán, J. "Predicting behavioral intention of mobile Internet usage." ***Telemat Informatics***, Vol. 32, (2015), 834-841. https://doi.org/10.1016/j.tele.2015.04.006
12. Su, W., Han, X., Jin, C., Yan, Y. and Potenza, M.N., "Are males more likely to be addicted to the internet than females? A meta-analysis involving 34 global jurisdictions." ***Computers in Human Behavior***, Vol. 99, (2019), 86-100. https://doi.org/10.1016/j.chb.2019.04.021
13. Okazaki, S. and Hirose, M., "Does gender affect media choice in travel information search? On the use of mobile Internet.", ***Tourism Management***, Vol 30, (2009), 794-804. https://doi.org/10.1016/j.tourman.2008.12.012
14. Vashisth, P. and Meehan, K., "Gender classification using Twitter text data.", in 2020 31st Irish Signals and Systems Conference (ISSC). IEEE, (2020), 1-6.
15. Piot-Perez-Abadin, P., Martín-Rodilla, P. and Parapar, J., "Experimental analysis of the relevance of features and effects on gender classification models for social media author profiling." in ENASE., (2021), 103-113.
16. Ke, G., Meng, Q., Finley, T., Wang, T., Chen, W., Ma, W., Ye, Q. and Liu, T.Y., "Lightgbm: A highly efficient gradient boosting decision tree" ***Advances in Neural Information Processing Systems***, Vol. 30, (2017).
17. Kowsari, K., Heidarysafa, M., Odukoya, T., Potter, P., Barnes, L.E. and Brown, D.E., "Gender detection on social networks using ensemble deep learning.", in Proceedings of the Future Technologies Conference. Springer, (2020), 346-358.
18. Safara, F., Mohammed, A.S., Potrus, M.Y., Ali, S., Tho, Q.T., Souri, A., Janenia, F. and Hosseinzadeh, M., "An author gender detection method using whale optimization algorithm and artificial neural network.", ***IEEE Access***, Vol. 8, (2020), 48428-48437
19. Sadeghian, A. and Kaedi, M.. "Happiness recognition from smartphone usage data considering users' estimated personality traits.", ***Pervasive and Mobile Computing***, Vol. 73, (2021), 101389
20. James, G., Witten, D., Hastie, T. and Tibshirani, R., An introduction to statistical learning, Springer, (2013).
21. Breiman, L., Classification and regression trees, Wadsworth Stat Ser 358, 1984.
22. Han, J., Pei, J. and Kamber, M., Data mining: concepts and techniques, Elsevier, 2011.
23. Jo, T., Machine Learning Foundations: Supervised, Unsupervised, and Advanced Learning, Springer Nature, (2021).
24. Yadav, S. and Shukla, S., "Analysis of k-fold cross-validation over hold-out validation on colossal datasets for quality

classification.", in 2016 IEEE 6th International conference on advanced computing (IACC). IEEE, (2016), 78-83.

25. Hamidi, H. and Rafebakhsh, M. S. "Analyzing factors influencing mobile social media marketing acceptance among customers.", ***International Journal of Engineering, Transactions C: Aspects***, Vol. 35, No. 6, (2022), 1209-1216. DOI: 10.5829/IJE.2022.35.06C.13

26. Yavari, A., Hassanpour, H., Rahimpour Cami, B. and Mahdavi, M. "Election Prediction Based on Sentiment Analysis using Twitter Data." ***International Journal of Engineering, Transactions B: Applications***, Vol. 35, No. 2, (2022), 372-379. DOI: 10.5829/IJE.2022.35.02B.13

27. Jaderyan, M. and Khotanlou, H. "Automatic hashtag recommendation in social networking and microblogging platforms using a knowledge-intensive content-based approach.", ***International Journal of Engineering, Transactions B: Applications***, Vol. 32, No. 8, (2019), 1101-1116. doi: 10.5829/ije.2019.32.08b.06

28. Yu, L. and Shek, D. T. L.. "Internet addiction in Hong Kong adolescents: A three-year longitudinal study." ***Journal of Pediatric and Adolescent Gynecology***, Vol. 26, No. 3, (2013), 10-17. https://doi.org/10.1016/j.jpag.2013.03.010.

29. International Telecommunication Union "ICT facts and figures 2016". (2016), from https://www.itu.int/en/ITU-D/Statistics/Documents/facts/ICTFactsFigures2016.pdf.

30. Wang, Z., Hu, Y., Zheng, H., Yuan, K., Du, X. and Dong, G. "Females are more vulnerable to Internet gaming disorder than males: Evidence from cortical thickness abnormalities." ***Psychiatry Research: Neuroimaging***, Vol. 283, (2019), 145-153. https://doi.org/10 .1016/j.pscychresns.2018.11.001.

31. Hafkin, N. J. and Huyer, S. "Women and gender in ICT statistics and indicators for development." ***Information Technologies and International Development***, Vol. 4, No. 2, (2007), 25-41.

32. Becker, J. B., McClellan, M. and Reed, B. G. "Sociocultural context for sex differences in addiction." ***Addiction Biology***, Vol. 21 No. 5, (2016), 1052-1059. https://doi.org/10.1111/adb.12383.

33. Jang, M. H. and Ji, E. S. "Gender differences in associations between parental problem drinking and early adolescents' Internet addiction." ***Journal for Specialists in Pediatric Nursing***, Vol. 17, No. 4, (2012), 288-300. https://doi.org/10.1111/j.1744-6155.2012.00344.x

Persian Abstract

چکیده

جنسیت افراد بخش مهمی از هویت افراد را تشکیل می‌دهد. تشخیص جنسیت کاربران سیستم‌ها، برای شخصی‌سازی خدمات و پیشنهادات در بسیاری از کاربردها مفید واقع می‌گردد. از طرف دیگر، امروزه اغلب افراد ساعات زیادی را با تلفن همراه خود سپری می‌کنند. پژوهش‌ها نشان داده است که نحوه تعامل کاربران با تلفن همراه، تحت تاثیر جنسیت آنها است. اما سیستم‌هایی که تا کنون برای تشخیص جنسیت کاربران بر اساس تعاملات آنها با تلفن همراه ارائه شده‌اند، یا دقت کافی در تشخیص ندارند و یا نیاز به سنسورها و فعالیت خاص کاربر برای تشخیص جنیست دارند و بنابرین قابلیت استفاده در حالت کلی و عمومی را ندارند. در این پژوهش، برای اولین بار به تشخیص جنسیت افراد بر اساس تعاملات آن‌ها با تلفن همراه، و به‌طور ویژه بر اساس ویژگی‌های مربوط به الگوهای استفاده آنها از اینترنت پرداخته شده است. بدین منظور با در نظر گرفتن یک نمونه تصادفی از افراد جامعه، اطلاعات دموگرافیک، الگوهای استفاده از اینترنت و همچنین ویژگی‌های مربوط به تعامل کاربران با تلفن همراه به صورت خودکار توسط یک برنامه کاربردی ثبت شده است. سپس جنسیت کاربران بر اساس ویژگی‌های استخراج شده و با به کارگیری روش‌های مختلف یادگیری ماشین مدل‌سازی شده است. نتایج ارزیابی‌ها نشان داد که ویژگی‌های اینترنتی نقش مهمی در شناسایی جنست کاربران تلفن های همراه دارند و روش ماشین بردار پشتیبان خطی با اجرا بر روی تمام ویژگی‌ها با اعمال انتخاب ویژگی با صحت 85% و شاخص-اف ٪۸۵ بالاترین عملکرد را در شناسایی جنسیت کاربران داشته است.

IJE TRANSACTIONS B: Applications Vol. 36, No. 02, (February 2023) 348-359

International Journal of Engineering

Journal Homepage: www.ije.ir

Integrated Dynamic Cellular Manufacturing Systems and Hierarchical Production Planning with Worker Assignment and Stochastic Demand

H. Bakhshi-Khaniki, S. M. T. Fatemi Ghomi*

Department of Industrial Engineering, Amirkabir University of Technology, 424 Hafez Avenue, Tehran, Iran

PAPER INFO

Paper history:
Received 23 October 2022
Received in revised form 14 November
Accepted 15 November 2022

Keywords:
Stochastic Demand
Dynamic Cellular Manufacturing
Hierarchical Production Planning
Mixed Integer Programming
Multi-period Cellular Manufacturing
Worker Assignment

ABSTRACT

This study deals with the interaction of dynamic cellular manufacturing (DCM) and hierarchical production planning (HPP) problems with stochastic demands for the first time. Each of these alone does not consider the system factors such as stochastic demands and dynamic cellular formation separately. Accordingly, to fill this gap, this paper presents an integrated optimized model incorporating the most comprehensive design of DCM systems and HPP problems with stochastic demands. This model helps administrators get the optimal size and number of cells to decrease costs. Also, the model applies the principles of HPP to reduce the complexity of the integrated model. Since demands are uncertain, they need to be accurately predicted. Therefore, this study aims to combine the most precise decision variables with the most realistic conditions. A case study from an agriculture mechanization and industrial development company shows that an integrated model can provide managers with a feasible solution to meet demand, reconfigure cells in each period, provide new machinery to increase the required production capacity, and adjust production capacity to help them cope with demand fluctuations. A sensitivity analysis was performed and the results show that increase in forecast error and inter-cell move cost cause less significant changes in total cost but the total cost is sensitive to intra-cell move cost, available time capacities and cell quantity. It is also shown that the total cost was very sensitive to available regular time and available over time and the system should try to increase the time capacity.

***doi**: 10.5829/ije.2023.36.02b.14*

1. INTRODUCTION

Cellular manufacturing (CM) is a well-known just-in-time manufacturing process which aims to increase production efficiency by assigning multi-skilled workers, parts, and machines into cells significantly cheaper than other kinds of producing processes [1-4]. CM systems can produce medium-volume and medium-variety parts to decrease setup cost, lead time, inventory cost, worker allocation cost, worker salary cost, and inventory cost and improve material flow and product quality [5, 6]. Production planning models create production schedules that minimize inventory and worker costs in response to changing demand over time. In order to develop a comprehensive production plan, uncertain parameters (especially market demand) must be paid attention. CM and production planning are connected and solved simultaneously and need to be integrated [7]. Production planning requires complex selections from a large number of attributes. One of the best options to simplify this complexity is the hierarchical production planning (HPP) approach. This approach aggregates items into three steps including aggregate production planning for product types to assign capacity among product types, class (or family) disaggregation to allocate product types into classes, and item disaggregation to preserve items with inventory [7].

2. LITERATURE REVIEW

Production planning is a novel topic studied by many researchers for different industries [8-10]. Many studies

*Corresponding Author's Email: fatemi@aut.ac.ir
(S. M. T. Fatemi Ghomi)

Please cite this article as: H. Bakhshi-Khaniki, S. M. T. Fatemi Ghomi, Integrated Dynamic Cellular Manufacturing Systems and Hierarchical Production Planning with Worker Assignment and Stochastic Demand, ***International Journal of Engineering, Transactions B: Applications***, Vol. 36, No. 02, (2023), 348-359

in the literature assume that in the planning period, demand is constant. However, in real conditions, demands can alter rapidly and variations over different periods cause different optimal fabrication cells [11]. Hence, the cellular formation has to change over periods. Accordingly, predicting demand is an undeniably important topic which needs to be addressed. CM systems research has been extended to the development of integrated models and methods, as discussed by Song and Choi [12].

CM systems have been employed and implemented with many other techniques for studying the current status, possible improvement and barriers of different organizations. Ebrahimi et al. [13] studied the scheduling and cell loading in CM systems, considering the consumption of speed power together with the price elasticity of demand. Sharma et al. [14] presented a fuzzy analytic hierarchy process model of CM systems to improve success in an organization. Kumar et al. [15] employed the interpretative structural modelling technique to investigate and define the barriers/enablers in the implementation of CM systems in sports industries. Saraçoğlu et al. [16] presented a parallel multi-stage CM model and improved the cell loading efficiency using a genetic algorithm (GA). Guo et al. [17] employed a CM digital twin-based flexible model for optimizing the performance of air conditioner lines. Akturk and Turkcan [18] presented an algorithm that solves the problem of part family and machine cell configuration problems using a holistic approach that considers inter-cell movement and independent cells. In another research, Mahdavi et al. [19] presented a model for cell configuration in CM systems to minimize the exceptional elements and increase cell utilization.

For cell formation, Defersha and Chen [20] present a comprehensive model for dynamic cell formation derived from tools accessible on the machine and the tool necessity of the products. Computational results appeared that a critical cost saving can be accomplished by considering cell formation and system adaptability. Feng et al. [21] presented an integrated model of cell formation and worker allocation problems. The model was solved with a hybrid approach and swarm optimization, taking into account workload balancing and production planning. Alimian et al. [7] presented a novel production planning in the DCM model that integrates four attributes including production planning, maintenance planning, cell formation and group scheduling. They argue that there is a contradiction between the total integrated cost and the total availability of the system. They did not incorporate workers and uncertain environments. Saxena and Jain [22] proposed an integrated model of supply chain design and DCM considering attributes like multiple markets, multiple plant locations and multiple periods customized for strategic, tactical and operational decisions. Chen and Cao [23] presented an integrated model for the production planning of cell production systems, including features such as inter-cell material handling and cell relocation. They applied the tabu search method to solve the model and compared it with the traditional model. However, their model uses only production and inventory to meet the demand. Defersha and Chen [24] have studied the effect of lot sizing on production quality by developing a mathematical model which integrates CM systems, cell relocation and lot sizing. As the model was NP-hard, a real size problem could not be solved and GA was developed to solve it.

In another study, Safaei and Tavakkoli-Moghaddam [25] extended the model as reported in the literature [26]. They proposed a multi-period mathematical model that integrates CM systems and production planning which focuses on the impact of subcontracting and production trade-off on cell relocation. Their results showed that subcontracting can lead to spasmodic behaviour on cell relocation.

A novel model that integrates HPP and DCM in a deterministic environment was recently proposed by Xue and Offodile [27]. The model was solved with a simple branch and bound approach but the model ignores worker allocation and uncertainty in demand. Mahdavi et al. [28] proposed a multi-objective model that integrates production planning and dynamic virtual CM with a fuzzy approach. The proposed model takes into account changes in demand and part variation over multiple planning periods with employee flexibility.

TABLE 1. List of attributes in integration of cellular manufacturing and production planning

Attributes	Definition	Attributes	Definition	Attributes	Definition
1	Worker salary	9	Backordering cost	17	Intra-cell material handling cost
2	Worker over allocation cost	10	Outsourcing cost	18	Production cost
3	Worker hiring cost	11	Stochastic demand	19	Cell capacity
4	Worker training cost	12	Deterministic demand	20	Dynamic cell formation
5	Procurement cost	13	Setup cost	21	Robust cell formation
6	Cell reconfiguration cost	14	Inventory holding cost	22	Tool consumption
7	Machine operation cost	15	Lot splitting		
8	Maintenance and overhead cost	16	Inter-cell material handling cost		

Koopman and Lit [29] developed a score-driven model based on the predictive probability function score. This model has similar prediction accuracy compared to a correctly specified parameter-driven model. There are many attributes that impact the integration of production planning and cellular manufacturing, as summarized in Table 1. Table 2, gives a review and comparison of these attributes in earlier studies and this paper.

This paper develops a mathematical model that integrates dynamic cellular manufacturing (DCM) and HPP with stochastic demand and worker allocation with attributes like worker salary, operation cost, material movement cost, outsourcing and backordering. Accordingly, this paper is structured as follows. Section 2, gives a literature review showing a gap in analyzing real-world demands. Section 3 presents a novel mathematical model for integrated multi-period DCM systems and HPP problems with dynamic stochastic demand. Section 4 explains the solution procedure via an introduction of a case study on an agricultural mechanization and industrial development company. Section 5 deals with a detailed sensitivity analysis of the proposed model for cell quantities, inter and intra-cell movement cost, setup cost, demands and capacity. Finally, section 6 gives a conclusion to highlight the benefits of employing the developed model.

From Tables 1 and 2, it can be seen that this paper covers the gaps in previous works by including both worker assignment and stochastic demand and providing a detailed analysis of cell quantity, costs, demand, setup time and time capacity.

3. DEVELOPMENT OF THE MODEL

3. 1. Mathematical model

The mathematical model includes two phases. Phase 1 presents a model for forecasting probabilistic [29]. Then in phase 2, a novel mathematical model is developed to integrate multi-period DCM systems with aggregate production planning, class disaggregation, and item disaggregation model with dynamic stochastic demand is presented. The following describes the two cited phases

Phase 1:

In an observation-driven model, time series demands are extracted as a function of past demand data. X_T denotes unobserved demands and Y_T denotes observed demands.

$$X_T = \xi + b_1 X_{T-1} + b_2 Z_{T-1} \tag{1}$$

$$Z_T = -E_{T-1}\left[\frac{\partial^2 \ln P(y_T \mid Y_{T-1}, X_T; P)}{\partial X_T X_T'}\right]^{-1/2} \times \left[\frac{\partial \ln P(y_T \mid Y_{T-1}, X_T; P)}{\partial X_T}\right] \tag{2}$$

The mechanism for updating demands is given by an autoregressive equation where ξ is a constant vector and $b_1$and b_2 are unknown coefficients estimated using the maximum likelihood estimation (MLE) method for simulated series. Z_T in Equation (2) is a function of the past. When an observation demand is realized, X_T will be updated to the next period using Equation (1).

Phase 2:

Sets:

t = 1, 2, 3, …, T (set of periods)
w = 1, 2, 3, …, W (set of worker types)
m = 1, 2, 3, …, M (set of machine types)
c = 1, 2, 3, …, C (set of cells)
p = 1, 2, 3, …, P (set of product types)
$o(p)$ = 1, 2, 3,…,O_p (set of operations for product p)
$j(m)$ = 1,2,3,…,J_m (set of worker that can operate machine type m)
$k(p,o)$ = 1,2,3,…,K_{po} (set of machine types to process operation o for product type p)
f = 1, 2, 3, …, F (set of classes)
$PF(f)$ = 1, 2, 3, …, PF_f (set of product p classified in f)

TABLE 2. Attributes used in literature of the integrated cellular manufacturing and production planning problems

Models	Attributes																					
	1	2	3	4	5	6	7	8	9	10	11	12	13	14	15	16	17	18	19	20	21	22
Alimian et al. [7]						*				*		*	*	*		*		*	*	*		
Safaei & Tavakkoli-Moghaddam [25]					*	*	*		*	*		*		*		*	*			*		
Xue & Offodile [27]					*	*	*	*	*	*		*	*	*		*	*	*	*	*		
Mahdavi et al. [28]	*						*		*			*		*						*		
Feng et al. [21]	*	*	*	*	*					*		*			*	*		*	*		*	
Defersha & Chen [24]					*	*	*			*		*	*	*	*	*			*	*		
Defersha & Chen [20]					*	*	*	*		*		*			*	*			*	*		*
Saxena & Jain [22]					*	*	*	*		*		*	*	*		*	*		*	*		*
Chen and Cao [23]					*	*	*	*	*	*		*	*	*		*	*	*	*	*		
Present study	*	*			*	*	*	*	*	*	*		*	*		*	*	*	*	*		

Parameters:
wc_w: salary cost for worker type w
$arw_w(t)$: Available regular time of worker w in period t
$aow_w(t)$: Available overtime of worker w in period t
$arm_m(t)$: Available regular time of machine type m
$aom_m(t)$: Available overtime of machine type m
owc_w: Overtime cost of worker type w per unit time
$D_f(t)$: Forecasted demand for class f in period t
mhc_p^{inter}: Inter-cell material handling cost of product p
mhc_p^{intra}: Intra-cell material handling cost per product p
$moc_m(t)$: Maintenance and overhead costs of machine m
rc_m: Relocation cost of machine type m
oc_m: Operating cost of machine type m per unit time
pc_p: Production cost of product per unit type p
tp_{pmow}: Time to process product type p on machine type m for operation o by worker type w
$hc_f(t)$: Holding cost of class f in period t
$oc_f(t)$: Outsourcing cost of class f in period t
$bc_f(t)$: Backordering cost of class f in period t
$cp_m(t)$: Procurement cost of machine type m in period t
st_{pmo}: Setup time for production p on machine type m for operation o
$sc(t)$: Unit setup cost in period t
$LF_f(t)$: Lower bound proportion of product type p classified in class f in period t
$UF_f(t)$: Upper bound proportion of product type p classified in class f in period t
LM_c: Lower bound of the number of machines in cell c
UM_c: Upper bound of the number of machines in cell c
Decision variables:
$NW_{wc}(t)$: Number of worker type w allocated to cell c
$NM_{mc}(t)$: Number machines type m allocated to cell c
$NP_{pmcow}(t)$: Number of product p on machine type m in cell c processed by operation o by worker type w
$NMA_{mc}(t)$: Number machine type m added to cell c
$NMR_{mc}(t)$: Number machine m removed from cell c
$NAI_f(t)$: Number of available Inventory of class f
$NO_f(t)$: Number of class f outsourced in period t
$NB_f(t)$: Number of backordering in class f in period t
$NPF_f(t)$: Number of production of class f in period t
$U_p(t)$: 1 (if product p is processed), and 0 otherwise

The objective function is defined as:

$$\begin{aligned}
\min Z = & \sum_{w\in W}\sum_{c\in C}\sum_{t\in T} wc_w.NW_{wc}(t) \\
& +\sum_{t\in T}\sum_{w\in j(m)}\sum_{c\in C} owc_w \max\{\sum_{o\in O(p)}\sum_{m\in K(p,o)}\sum_{p\in P} tp_{pmow}.NP_{pmcow}(t) - NW_{wc}(t).arw_w(t),0\} \\
& +\sum_{t\in T}\sum_{c\in C}\sum_{o\in O(p)}\sum_{m\in K(p,o)}\sum_{p\in P} mhc_p^{\text{intra}}[\min\{\sum_{w\in J(m)}\sum_{m\in(p,o+1)} NP_{pmc,o+1,w}(t), \sum_{w\in J(m)}\sum_{m\in(p,o)} NP_{pmcow}(t)\}] \\
& +\sum_{t\in T}\sum_{c\in C}\sum_{o\in O(p)}\sum_{p\in P} \frac{1}{2} mhc_p^{\text{inter}} \left| \sum_{w\in J(m)}\sum_{m\in K(p,o+1)} NP_{pmc,o+1,w}(t) - \sum_{w\in J(m)}\sum_{m\in K(p,o)} NP_{pmcow}(t) \right| \\
& +\sum_{t\in T}\sum_{c\in C}\sum_{m\in M} N_{mc}(t).moc_m(t) + \sum_{t\in T}\sum_{c\in C}\sum_{m\in M} rc_m.(NMA_{mc}(t)+NMR_{mc}(t)) \\
& +\sum_{t\in T}\sum_{c\in C}\sum_{o\in O(p)}\sum_{m\in K(p,o)}\sum_{p\in P}\sum_{w\in J(m)} oc_m.tp_{pmow}.NP_{pmcow}(t) \\
& +\sum_{t\in T}\sum_{c\in C}\sum_{m\in K(p,1)}\sum_{p\in P}\sum_{w\in J(m)} pc_p.NP_{pmc1w}(t) + \sum_{t\in T}\sum_{f\in F} hc_f(t).NAI_f(t) \\
& +\sum_{t\in T}\sum_{f\in F} oc_f(t).NO_f(t) + \sum_{t\in T}\sum_{f\in F} bc_f(t).NB_f(t) \\
& +\sum_{t\in T}\sum_{m\in M} cp_m(t)(\sum_{c\in C} NM_{mc}(t) - NM_{mc}(t-1)) + \sum_{t\in T}\sum_{p\in P}\sum_{m\in K(p,o)}\sum_{o\in O(p)} U_p(t).sc(t).st_{pmo}
\end{aligned} \tag{3}$$

where Equation (3), as the objective function, minimizes the total cost. The first term of this equation represents worker salary cost. The second term represents overtime cost; this cost occurs when the available regular time of workers finishes and the model uses available overtime of workers. The third term denotes intra-cell material handling cost. The fourth term represents inter-cell material handling cost. The fifth term represents the maintenance and overhead costs. The sixth term denotes configuration cost. The seventh term represents operation cost. The eighth term denotes production cost. The ninth term represents inventory holding cost. The tenth term represents outsourcing costs. The eleventh term represents backordering cost. The twelfth term denotes procurement cost and the last term denotes setup cost.

This objective function is subjected to constains shown as follows:

$$\begin{aligned}
& \sum_{c\in C}\sum_{m\in k(p,o)}\sum_{p\in P}\sum_{o\in O(p)} tp_{pmow}.NP_{pmcow}(t) + \qquad \forall t\in T, \forall w\in W \\
& \sum_{p\in P}\sum_{m\in K(p,o)}\sum_{o\in O(p)} U_P(t).st_{pmo} \le \sum_{c\in C} NW_{wc}(t).(arw_w(t)+aow_w(t))
\end{aligned} \tag{4}$$

where constraints (4) are regular and over available time limitations for workers,

$$\begin{aligned}
& \sum_{c\in C}\sum_{p\in P}\sum_{o\in O(p)}\sum_{w\in J(m)} tp_{pmow}.NP_{pmcow}(t) \qquad \forall t\in T, \forall m\in M, \forall c\in C \\
& +\sum_{p\in P}\sum_{o\in O(p)} U_P(t).st_{pmo} \le NM_{mc}(t).(arm_m(t)+aom_m(t))
\end{aligned} \tag{5}$$

where constraints (5) are regular and over available time limitations for machines,

$$\begin{aligned}
& D_f(t) = NPF_f(t) - (NAI_f(t) - NAI_f(t-1)) \\
& + NO_f(t) + (NB_f(t) - NB_f(t-1)) \qquad \forall t\in T, \forall f\in F
\end{aligned} \tag{6}$$

where constraints (6) ensures that all forecast demand for classes will be satisfied by production, inventory, backordering or outsourcing,

$$\sum_{p\in PF(f)}\sum_{c\in C}\sum_{m\in K(p,1)}\sum_{w\in J(m)} NP_{pmc1w}(t) = NPF_f(t) \qquad \forall t\in T, \forall f\in F \tag{7}$$

where the set of constraints (7) ensures that the number of product types in each class is equal to the number of productions in that class,

$$\sum_{c\in C}\sum_{m\in K(P,1)}\sum_{w\in J(m)} NP_{pmc1w}(t) \le UF_f(t).NPF_F(t) \qquad \forall t\in T, \forall P\in PF(f) \tag{8}$$

$$\sum_{c\in C}\sum_{m\in K(P,1)}\sum_{w\in J(m)} NP_{pmc1w}(t) \ge LF_f(t).NPF_F(t) \qquad \forall t\in T, \forall P\in PF(f) \tag{9}$$

where the set of constraints (8) and (9) are the upper and lower bounds of the production level, respectively. Besides,

$$\sum_{m\in M} NM_{mc}(t) \ge LM_c \qquad \forall t\in T, \forall c\in C \tag{10}$$

$$\sum_{m\in M} NM_{mc}(t) \le UM_c \quad \forall t\in T, \forall c\in C \tag{11}$$

where the set of constraints (10) and (11) are the lower and upper bounds of the cell size is lower bound of cell size, respectively. Moreover

$$NM_{mc}(t+1) - NM_{mc}(t) - NMA_{mc}(t) + NMR_{mc}(t) = 0 \quad \forall t\in T, \forall c\in C, \forall m\in M \tag{12}$$

where the set of constraints (12) ensures that the number of machines removed and added is equal to the difference between the total machines in this period and the next period.

$$\sum_{c\in C}\sum_{m\in K(p,o)}\sum_{w\in J(m)} NP_{pmcow}(t) = \sum_{c\in C}\sum_{m\in K(p,o+1)}\sum_{w\in J(m)} NP_{pmc,o+1,w}(t) \quad \forall t\in T, \forall p\in P, \forall o\in O(p) \tag{13}$$

where the set of constraints (13) ensures that the total number of products for an operation is equal to the total number of products for the next operation.

$$\sum_{c\in C}\sum_{m\in K(p,o)}\sum_{w\in J(m)} NP_{pmcow}(t) = \sum_{c\in C}\sum_{m\in K(p,o+1)}\sum_{w\in J(m)} NP_{pmc,o+1,w}(t) \quad \forall t\in T, \forall p\in P, \forall o\in O(p) \tag{14}$$

$$\sum_{c\in C}\sum_{m\in K(P,1)}\sum_{w\in J(m)} NP_{pmc1w}(t) \le M.U_p(t) \quad \forall t\in T, \forall p\in P \tag{15}$$

Sets of constraints (14) and (15) indicate that if product type *p* is produced, the binary variable of *Up*(*t*) will be 1 if product *p* is processed, otherwise 0.

$$NW_{WC}(t) >= 0 \text{ and integer } \forall t\in T, \forall c\in C, \forall w\in W \tag{16}$$

$$NM_{mc}(t) >= 0 \text{ and integer } \quad \forall t\in T, \forall c\in C, \forall m\in M \tag{17}$$

$$\sum_{m\in M} NM_{mc}(t) \le UM_c \quad \forall t\in T, \forall c\in C$$
$$NMA_{mc}(t) >= 0 \text{ and integer } \quad \forall t\in T, \forall c\in C, \forall m\in M \tag{18}$$

$$\sum_{m\in M} NM_{mc}(t) \le UM_c \quad \forall t\in T, \forall c\in C$$
$$NMR_{mc}(t) >= 0 \text{ and integer } \quad \forall t\in T, \forall c\in C, \forall m\in M \tag{19}$$

$$\sum_{m\in M} NM_{mc}(t) \le UM_c \quad \forall t\in T, \forall c\in C$$
$$NP_{pmcow}(t) >= 0 \text{ and integer } \quad \forall t\in T, \forall c\in C, \forall m\in M, \forall p\in P, \forall o\in O, \forall w\in W \tag{20}$$

$$NAI_F(t) >= 0 \text{ and integer } \quad \forall t\in T, \forall f\in F \tag{21}$$

$$NO_F(t) >= 0 \text{ and integer } \quad \forall t\in T, \forall f\in F \tag{22}$$

$$NB_F(t) >= 0 \text{ and integer } \quad \forall t\in T, \forall f\in F \tag{23}$$

$$NPF_F(t) >= 0 \text{ and integer } \quad \forall t\in T, \forall f\in F \tag{24}$$

$$U_p(t) \in (0,1) \quad \forall t\in T, \forall p\in P \tag{25}$$

and finally, constraints (16-25) ensure that variables are positive and integer and Up(t) is binary.

3. 2. Linearization of the model The developed model is not linear due to the second, third and fourth terms of Equation (3). Hence, the model is simplified as follows:

To linearize the second term of Equation (3), one can define:

$$\alpha_{wc}(t) = \max\{\sum_{o\in O(p)}\sum_{m\in K(p,o)}\sum_{p\in P} tp_{pmow}.NP_{pmcow}(t) - NW_{wc}(t).arw_w(t), 0\} \tag{26}$$

with additional constraints as:

$$\alpha_{wc}(t) \ge \sum_{o\in O(p)}\sum_{m\in K(p,o)}\sum_{p\in P} tp_{pmow}.NP_{pmcow}(t) - NW_{wc}(t).arw_w(t) \quad \forall w\in W, \forall c\in C, \forall t\in T \tag{27}$$

$$\alpha_{wc}(t) \ge 0 \quad \text{and integer } \forall w\in W, \forall c\in C, \forall t\in T \tag{28}$$

To linearize the third term of Equation (3), one can define

$$\beta_{pco}(t) = \min\{\sum_{w\in J(m)}\sum_{m\in(p,o+1)} NP_{pmc,o+1,w}(t), \sum_{w\in J(m)}\sum_{m\in(p,o)} NP_{pmcow}(t)\} \tag{29}$$

with additional constraints as:

$$\beta_{pco}(t) \le \sum_{w\in J(m)}\sum_{m\in(p,o+1)} NP_{pmc,o+1,w}(t) \quad \forall p\in P, \forall c\in C, \forall o\in O, \forall t\in T \tag{30}$$

$$\beta_{pco}(t) \le \sum_{w\in J(m)}\sum_{m\in(p,o)} NP_{pmcow}(t) \quad \forall p\in P, \forall c\in C, \forall o\in O, \forall t\in T \tag{31}$$

$$\beta_{pco}(t) \ge 0 \quad \text{and integer } \forall p\in P, \forall c\in C, \forall o\in O, \forall t\in T \tag{32}$$

To linearize the fourth term of Equation (3), one can define:

$$\theta_{pco}(t) + \vartheta_{pco}(t) = \left|\sum_{w\in J(m)}\sum_{m\in K(p,o+1)} NP_{pmc,o+1,w}(t) + \sum_{w\in J(m)}\sum_{m\in K(p,o)} NP_{pmcow}(t)\right| \tag{33}$$

and the following constraints are added.

$$\theta_{pco}(t) - \vartheta_{pco}(t) = \sum_{w\in J(m)}\sum_{m\in K(p,o+1)} NP_{pmc,o+1,w}(t) - \sum_{w\in J(m)}\sum_{m\in K(p,o)} NP_{pmcow}(t) \quad \forall p\in P, \forall c\in C, \forall o\in O, \forall t\in T \tag{34}$$

$$\theta_{pco}(t) \ge 0 \text{ and integer } \forall p\in P, \forall c\in C, \forall o\in O, \forall t\in T \tag{35}$$

$$\vartheta_{pco}(t) \ge 0 \text{ and integer } \forall p\in P, \forall c\in C, \forall o\in O, \forall t\in T \tag{36}$$

4. CASE STUDY

This section employs the production data of an agricultural mechanization and industrial development

TABLE 3. Data of the products of case study

Product type	Machine	Processing time (minute)	Setup time (min)	Inter cell move cost	Intra cell move cost
1	1	30	10	100	20
	4	10	5		
	3	25	10		
	2	35	10		
	5	20	10		
2	1	35	10	110	25
	2	10	15		
	3	20	10		
	5	20	5		
3	1	35	15	100	20
	4	20	5		
	1	25	10		
	2	20	5		
4	1	40	10	90	15
	4	10	15		
	5	20	10		
5	1	35	15	100	20
	4	20	5		
	1	20	10		
	5	10	5		

company, as a case study, to validate the proposed model. There are five product types classified into two classes. Class 1 includes product types 1, 2 and 3 and class 2 includes product types 4 and 5. Also, five types of machines including cutting machines, hydraulic pressing machines, welding machines, assembling machines and spray machines are used for manufacturing their hatchery and incubation products.

Table 3 provides product information from a case study. As can be seen, the minimum processing time of this case is 10 minutes and the maximum is 40 minutes. Also, setup times are between 5 and 15 minutes, and the unit cost of intra cell move cost is less than inter cell move cost, since intra cell movement travels less distance.

Table 4 shows the relationship between machines and workers, and each worker, based on their skills, has the ability to work with specific machines. Table 5 provides information on workers. Available regular time and available over time are the same in each period. Besides, workers receive a bonus for overtime in addition to salary costs.

TABLE 4. The ability of worker types to work with machines

		Machine types				
		1	2	3	4	5
Worker types	1		*			*
	2	*		*		
	3		*		*	
	4	*		*		

Moreover, Table 6 contains information about machines such as available regular time, available over time, reconfiguration cost, procurement cost, operation cost, maintenance and overhead cost.

5. RESULTS AND DISCUSSION

This section analyses the proposed model in four subsections including sensitivity analysis of cell quantity, sensitivity analysis of setup time and inter- and intra-cell move costs, sensitivity analysis of demands and sensitivity analysis of capacity. The results include the application of the HPP system and DCM system in five periods and in each period, production decisions are made and the model is updated. The model is solved with GAMS on a computer with 8 GB of RAM and Core-i5 CPU.

TABLE 5. Time capacity and costs of workers of case study

	Worker type			
	1	2	3	4
Available regular time	300	300	300	300
Available over time	100	100	100	100
Salary costs	4000	3000	3000	3000
Over time cost per unit time	40	30	30	30

TABLE 6. Time capacity and costs of machines of case study

	Machine type				
	1	2	3	4	5
Available regular time	300	300	300	300	300
Available over time	100	100	100	100	100
Reconfiguration cost	300	250	300	400	250
Procurement cost	15000	10000	15000	20000	10000
Operation cost	20	10	20	15	10
Maintenance and overhead cost	400	500	400	600	550

5. 1. Sensitivity Analysis of Cell Quantity In this study, three cells, five types of machines, five types of products and two types of classes are taken for the mathematical modelling. However, other production control parameters may affect cell size and quantity. This subsection first analyzes the effect of different numbers of cells on the objective function and then determines the optimal number of cells under the assumption that the number of machines and the cost of displacement are constant. For this analysis, the number of cells is assumed to vary from three to eight. For the given range of cells, the corresponding focused values are shown in Table 7. It may be visible that the complexity of the answer will increase with the number of cells. Besides, for the case study concerned in this paper, it is shown that the ideal optimal cell amount is eight as it gives the lowest total cost. As result, managers should increase the number of cells in order to reach optimal total cost.

5. 2. Sensitivity Analysis of Setup Time and Inter- and Intra-cell Move Cost This subsection first, studies the effect of setup cost on the total cost by three different approaches. In the first approach, the condition is the same as the baseline condition and does not change. In the second approach, the setup time is five times higher and in the third approach, the setup time is 10 times higher. As can be seen from Table 8, although the total cost has significantly increased, there is no significant difference in inventory holding cost and overtime cost, indicating that changes in setup cost do not have much effect on production decisions.

In the next study, to analyze the effect of inter-cell move cost and intra-cell move cost, four different situations have been considered. In the first situation, intra-cell move costs are fixed and inter-cell move costs are considered twice as normal. In the second situation, intra-cell move costs are fixed and inter-cell move costs are considered four times higher than normal. In the third situation, intra-cell move costs are considered twice as normal and inter-cell move costs are fixed. In the fourth situation, the intra-cell move costs are considered four times higher than normal and the inter-cell move costs are fixed.

As shown in Table 9, the results are as follows. In the first and second situations, it is observed that the total cost does not change significantly with increases in inter-cell move cost. The reason is that due to the dynamics of

TABLE 7. Total cost changes according to the different total number of cells

	Total number of cells				
	3	4	5	6	7
Total cost	84738600	84254600	83961800	82523100	80974500

TABLE 8. Costs according to the different setup times

	Product type	Machine	Setup time (minute)
Approach: 1 Overtime cost: 6314500 Inventory holding cost: 8649100 Total cost: 84738600	1	1	10
		4	5
		3	10
		2	10
		5	10
	2	1	10
		2	15
		3	10
		5	5
	3	1	15
		4	5
		1	10
		2	5
	4	1	10
		4	15
		5	10
	5	1	15
		4	5
		1	10
		5	5
Approach: 2 Overtime cost: 6430100 Inventory holding cost: 8716400 Total cost: 104112400	1	1	50
		4	25
		3	50
		2	50
		5	50
	2	1	50
		2	75
		3	50
		5	25
	3	1	75
		4	25
		1	50
		2	25
	4	1	50
		4	75
		5	50
	5	1	75
		4	25
		1	50
		5	25

Approach: 3 Overtime cost: 6491200 Inventory holding cost: 8781000 Total cost: 12819700	1	1	100
		4	50
		3	100
		2	100
		5	100
	2	1	100
		2	150
		3	100
		5	50
	3	1	150
		4	50
		1	100
		2	50
	4	1	100
		4	150
		5	100
	5	1	150
		4	50
		1	100
		5	50

TABLE 9. Total costs change according to the different inter and intra-cell move costs

Situations	Product type	Inter cell move cost (per unit)	Intra cell move cost (per unit)	Total cost
1	1	200	20	84829400
	2	220	25	
	3	200	20	
	4	180	15	
	5	200	20	
2	1	400	20	84964300
	2	440	25	
	3	400	20	
	4	360	15	
	5	400	20	
3	1	100	40	89711300
	2	110	50	
	3	100	40	
	4	90	30	
	5	100	40	
4	1	100	80	93122100
	2	110	100	
	3	100	80	
	4	90	60	
	5	100	80	

the cells of the model, with increasing inter-cell move cost, the model avoids intercellular displacement as much as possible. In order to reduce inter-cell movement, managers could increase machines in cells.

Besides, it is observed in the third and fourth situations that with an increase in intra-cell move cost, the total cost also changes significantly. This is because intra-cell movement naturally has to be performed and the model cannot reduce the total cost. Therefore, managers should reduce inter-cell movement as much as possible.

5. 3. Sensitivity Analysis of Demands For sensitivity analysis of demands, demands for two types of classes are accurately forecasted using historical factory data of an agricultural mechanization and industrial development company. For each of these products, demand fluctuations are determined by solving datasets shown in Figure 1. Historical data sets with moderate demand fluctuations follow the Poisson distribution. In Figures 2-4, the demand for each period is calculated based on different error rates.

Table 10 shows the results of running these four scenarios, which denote that the change in the error rate does not have a significant impact on the periodic demand trend of these products and higher forecasting errors do not necessarily lead to higher backordering cost and total cost. Even if the company has a higher demand fluctuation in their planning horizon, leading to a higher total cost of production planning, and even under 20% forecast errors, the integrated model developed in this paper performs reasonably. As result, the proposed model adapts to demand fluctuations to avoid total cost increases and helps managers in production decisions.

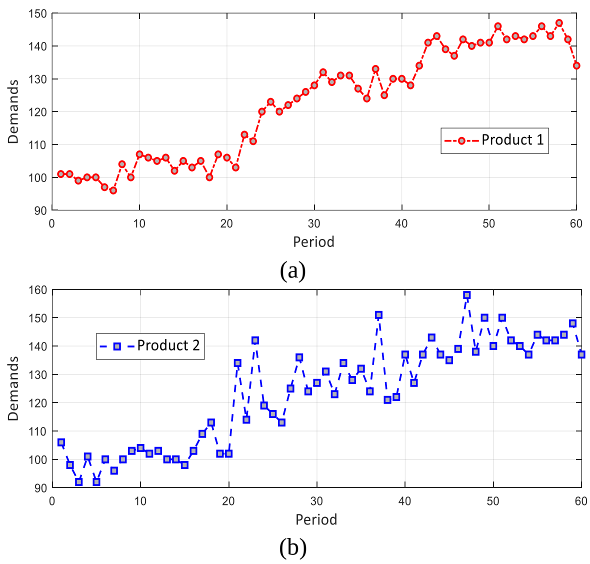

Figure 1. Demand-period for (a) product class 1, (b) product class 2

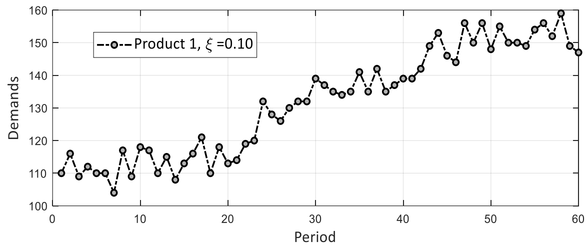

(a)

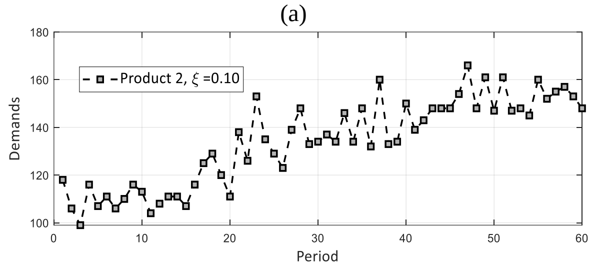

(b)

Figure 2. Demand-period with ξ=0.1 for (a) product class 1, (b) product class 2

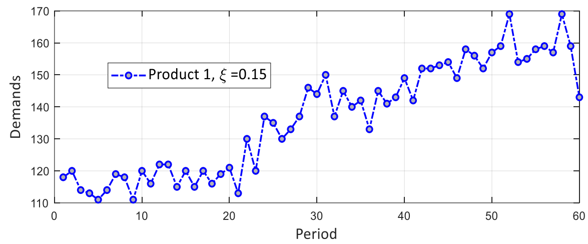

(a)

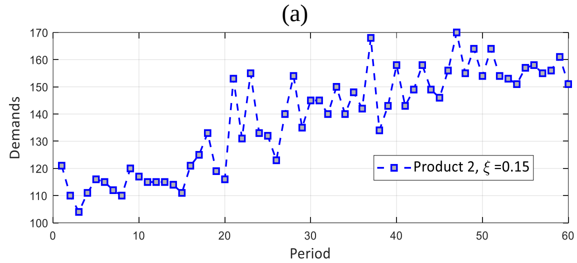

(b)

Figure 3. Demand-period with ξ=0.15 for (a) product class 1, (b) product class 2

TABLE 10. Total costs changes according to different forecasting errors

Forecasting errors	0%	10%	15%	20%
Total cost	84738600	85021300	85534800	86174900

TABLE 11. Total costs change according to different available regular and over times

Mods	Available regular time	Available over time	Total cost
1	150	50	1190322300
2	450	150	67447600

5. 4. Sensitivity Analysis of Time Capacity This subsection, examines the impact of available regular time and available over time on total cost is examined by considering two modes. In the first mod, the amount of available regular time and available over time have decreased, and in the second model, the amount of available regular time and available over time have increased. As can be seen from Table 11, when the cited times decrease, the total cost increases, and when the cited times increase, the total cost decreases. This indicates that the total cost is very sensitive to available regular time and available over time and the system managers should try to increase the time capacity.

It is noteworthy that this study primarily used an exact optimization approach to solve the problem. For large instances, one may employ different optimization algorithms. There are many different domains where advanced optimization algorithms have been applied as solution approaches, such as online learning, scheduling, multi-objective optimization, transportation, medicine, data classification, and others [30-34]. Moreover, there are many studies on manufacturing, remanufacturing, assembly, and disassembly operations including the research performed by Zhang et al. [35], Yuan et al. [36], Golmohammadi et al. [37] and Yazdani et al. [38] which provided detailed analysis using different algorithms.

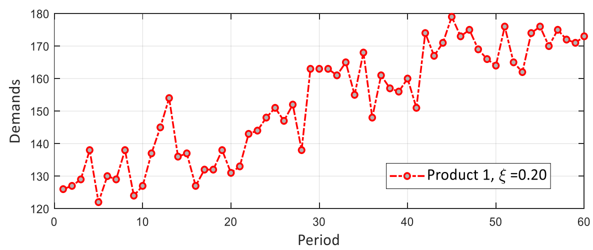

(a)

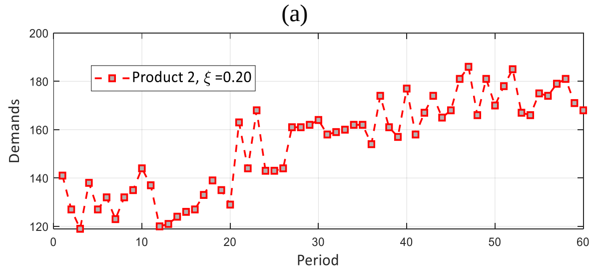

(b)

Figure 4. Demand-period with ξ=0.2 for (a) product class 1, (b) product class 2

6. CONCLUSION

In this paper, a new model was developed to integrate a dynamic cellular manufacturing system, hierarchical production planning problem under stochastic demands and several other features such as multiple periods and worker assignment. The purpose of this study is to combine the most precise decision variables with the most realistic conditions by considering stochastic demand and worker assignment. Using some linearization techniques, this nonlinear model was converted to an integer linear model. The model is capable of determining the optimal cell design and production plan for any type of product in each period for all the planning horizons. A real case study of an agricultural mechanization and industrial development company was given to validate the model and the integrated linear optimization model was solved in GAMS. It was shown that:

- Historical data on the company's demands were recorded and demands for the desired periods were predicted using the autoregressive model. It was shown that demand for the products of this company follows the bivariate Poisson distribution.
- By varying the total number of cells, it was shown that the optimal situation is when eight cells were selected, and this amount depends on the capacity of the factory and the total number of machines.
- An increase in forecast errors causes less significant changes in total cost. The results showed that aggregate forecasts can be more precise and give a significant explanation to the model.
- For the studied case, it is observed that the total cost does not change significantly with increasing inter-cell move cost. The reason is that due to the dynamic cells of the model, with increasing inter-cell movement cost, the model avoids intercellular movement as much as possible.
- For the studied case, it is observed that with increasing intra-cell move cost, the total cost also changes significantly. This is because intracellular movement naturally has to be performed and the model cannot reduce the total cost. Therefore, managers should reduce intercellular movement as much as possible.
- There was no significant difference in inventory holding cost and overtime cost indicating that changes in setup cost do not have much effect on production decisions.
- The total cost was very sensitive to available regular time and available over time and the system should try to increase the time capacity.

7. STATEMENTS AND DECLARATIONS

The authors declare that they have no known competing financial interests or personal relationships that could have appeared to influence the work reported in this paper.

8. REFERENCES

1. Arkat, J., Rahimi, V. and Farughi, H., "Reactive scheduling addressing unexpected disturbance in cellular manufacturing systems", ***International Journal of Engineering, Transactions A: Basics***, Vol. 34, No. 1, (2021), 162-170. doi: 10.5829/IJE.2021.34.01A.18
2. Bagheri, F., Safaei, A.S., Kermanshahi, M. and Paydar, M.M., "Robust design of dynamic cell formation problem considering the workers interest", ***International Journal of Engineering, Transactions C: Aspects***, Vol. 32, No. 12, (2019), 1790-1797. doi: 10.5829/IJE.2019.32.12C.12
3. Tajdin, A., Mahdavi, I. and Hashemoghli, A., "A novel interactive possibilistic mixed integer nonlinear model for cellular manufacturing problem under uncertainty", ***International Journal of Engineering, Transactions C: Aspects***, Vol. 30, No. 3, (2017), 384-392. doi: 10.5829/idosi.ije.2017.30.03c.08
4. Mirgorbani, S., Jolai, F., Javadi, B. and Tavakkoli-Moghaddam, R., "An efficient algorithm to inter and intra-cell layout problems in cellular manufacturing systems with stochastic demands", ***International Journal of Engineering***, Vol. 19, No. 1, (2006), 67-78.
5. Cakir, M., Guvenc, M.A. and Mistikoglu, S., "The experimental application of popular machine learning algorithms on predictive maintenance and the design of iiot based condition monitoring system", ***Computers & Industrial Engineering***, Vol. 151, (2021), 106948. doi: 10.1016/j.cie.2020.106948
6. Sharifi, S., Chauhan, S. and Bhuiyan, N., "Part-level sequence dependent setup time reduction in cms", ***Journal of Industrial and Systems Engineering***, Vol. 5, No. 3, (2011), 142-153. doi: 20.1001.1.17358272.2011.5.3.2.0
7. Alimian, M., Ghezavati, V. and Tavakkoli-Moghaddam, R., "New integration of preventive maintenance and production planning with cell formation and group scheduling for dynamic cellular manufacturing systems", ***Journal of Manufacturing Systems***, Vol. 56, (2020), 341-358. doi: 10.1016/j.jmsy.2020.06.011
8. Sadjadi, S. and Makui, A., "An algorithm to compute the complexity of a static production planning (research note)", ***International Journal of Engineering***, Vol. 16, No. 1, (2003), 57-60.
9. Aghajani-Delavar, N., Tavakkoli-Moghaddam, R. and Mehdizadeh, E., "Design of a new mathematical model for integrated dynamic cellular manufacturing systems and production planning", ***International Journal of Engineering, Transactions B: Applications***, Vol. 28, No. 5, (2015), 746-754. doi: 10.5829/idosi.ije.2015.28.05b.13
10. Sakhaii, M., Tavakkoli-Moghaddam, R. and Vatani, B., "A robust model for a dynamic cellular manufacturing system with production planning", ***International Journal of Engineering, Transactions A: BAsics***, Vol. 27, No. 4, (2014), 587-598. doi: 10.5829/idosi.ije.2014.27.04a.09
11. Balakrishnan, J. and Cheng, C.H., "Dynamic cellular manufacturing under multiperiod planning horizons", ***Journal of Manufacturing Technology Management***, (2005). doi: 10.1108/17410380510600491
12. Song, S.-J. and Choi, J.-H., "Integrated autonomous cellular manufacturing-a new concept for the 21st century", ***International Journal of Manufacturing Technology and Management***, Vol. 3, No. 3, (2001), 293-307. doi: 10.1504/IJMTM.2001.001412
13. Ebrahimi, H., Kianfar, K. and Bijari, M., "Scheduling a cellular manufacturing system based on price elasticity of demand and time-dependent energy prices", ***Computers & Industrial Engineering***, Vol. 159, (2021), 107460. doi: 10.1016/j.cie.2021.107460

14. Sharma, V., Kumar, S. and Meena, M., "Key criteria influencing cellular manufacturing system: A fuzzy ahp model", ***Journal of Business Economics***, Vol. 92, No. 1, (2022), 65-84. doi: 10.1007/s11573-021-01043-y

15. Kumar, S., Gupta, M., Suhaib, M. and Asjad, M., "Current status, enablers and barriers of implementing cellular manufacturing system in sports industry through ism", ***International Journal of System Assurance Engineering and Management***, Vol. 12, No. 3, (2021), 345-360. doi: 10.1007/s13198-021-01052-8

16. Saraçoğlu, İ., Süer, G.A. and Gannon, P., "Minimizing makespan and flowtime in a parallel multi-stage cellular manufacturing company", ***Robotics and Computer-Integrated Manufacturing***, Vol. 72, (2021), 102182. doi: 10.1016/j.rcim.2021.102182

17. Guo, H., Chen, M., Mohamed, K., Qu, T., Wang, S. and Li, J., "A digital twin-based flexible cellular manufacturing for optimization of air conditioner line", ***Journal of Manufacturing Systems***, Vol. 58, (2021), 65-78. doi: 10.1016/j.jmsy.2020.07.012

18. Akturk, M.S. and Turkcan, A., "Cellular manufacturing system design using a holonistic approach", ***International Journal of Production Research***, Vol. 38, No. 10, (2000), 2327-2347. doi: 10.1080/00207540050028124

19. Mahdavi, I., Javadi, B., Fallah-Alipour, K. and Slomp, J., "Designing a new mathematical model for cellular manufacturing system based on cell utilization", ***Applied mathematics and Computation***, Vol. 190, No. 1, (2007), 662-670. doi: 10.1016/j.amc.2007.01.060

20. Defersha, F.M. and Chen, M., "A comprehensive mathematical model for the design of cellular manufacturing systems", ***International Journal of Production Economics***, Vol. 103, No. 2, (2006), 767-783. doi: 10.1016/j.ijpe.2005.10.008

21. Feng, H., Da, W., Xi, L., Pan, E. and Xia, T., "Solving the integrated cell formation and worker assignment problem using particle swarm optimization and linear programming", ***Computers & Industrial Engineering***, Vol. 110, (2017), 126-137. doi: 10.1016/j.cie.2017.05.038

22. Saxena, L.K. and Jain, P., "An integrated model of dynamic cellular manufacturing and supply chain system design", ***The International Journal of Advanced Manufacturing Technology***, Vol. 62, No. 1, (2012), 385-404. doi: 10.1007/s00170-011-3806-4

23. Chen, M. and Cao, D., "Coordinating production planning in cellular manufacturing environment using tabu search", ***Computers & Industrial Engineering***, Vol. 46, No. 3, (2004), 571-588. doi: 10.1016/j.cie.2004.02.002

24. Defersha, F.M. and Chen, M., "A linear programming embedded genetic algorithm for an integrated cell formation and lot sizing considering product quality", ***European Journal of Operational Research***, Vol. 187, No. 1, (2008), 46-69. doi: 10.1016/j.ejor.2007.02.040

25. Safaei, N. and Tavakkoli-Moghaddam, R., "Integrated multi-period cell formation and subcontracting production planning in dynamic cellular manufacturing systems", ***International Journal of Production Economics***, Vol. 120, No. 2, (2009), 301-314. doi: 10.1016/j.ijpe.2008.12.013

26. Safaei, N., Saidi-Mehrabad, M. and Jabal-Ameli, M., "A hybrid simulated annealing for solving an extended model of dynamic cellular manufacturing system", ***European Journal of Operational Research***, Vol. 185, No. 2, (2008), 563-592. doi: 10.1016/j.ejor.2006.12.058

27. Xue, G. and Offodile, O.F., "Integrated optimization of dynamic cell formation and hierarchical production planning problems", ***Computers & Industrial Engineering***, Vol. 139, (2020), 106155. doi: 10.1016/j.cie.2019.106155

28. Mahdavi, I., Aalaei, A., Paydar, M.M. and Solimanpur, M., "Multi-objective cell formation and production planning in dynamic virtual cellular manufacturing systems", ***International Journal of Production Research***, Vol. 49, No. 21, (2011), 6517-6537. doi: 10.1080/00207543.2010.524902

29. Koopman, S.J. and Lit, R., "Forecasting football match results in national league competitions using score-driven time series models", ***International Journal of Forecasting***, Vol. 35, No. 2, (2019), 797-809. doi: 10.1016/j.ijforecast.2018.10.011

30. Zhao, H. and Zhang, C., "An online-learning-based evolutionary many-objective algorithm", ***Information Sciences***, Vol. 509, (2020), 1-21. doi: 10.1016/j.ins.2019.08.069

31. Dulebenets, M.A., "An adaptive polyploid memetic algorithm for scheduling trucks at a cross-docking terminal", ***Information Sciences***, Vol. 565, (2021), 390-421. doi: 10.1016/j.ins.2021.02.039

32. Pasha, J., Nwodu, A.L., Fathollahi-Fard, A.M., Tian, G., Li, Z., Wang, H. and Dulebenets, M.A., "Exact and metaheuristic algorithms for the vehicle routing problem with a factory-in-a-box in multi-objective settings", ***Advanced Engineering Informatics***, Vol. 52, (2022), 101623. doi: 10.1016/j.aei.2022.101623

33. Kavoosi, M., Dulebenets, M.A., Abioye, O.F., Pasha, J., Wang, H. and Chi, H., "An augmented self-adaptive parameter control in evolutionary computation: A case study for the berth scheduling problem", ***Advanced Engineering Informatics***, Vol. 42, (2019), 100972. doi: 10.1016/j.aei.2019.100972

34. Rabbani, M., Oladzad-Abbasabady, N. and Akbarian-Saravi, N., "Ambulance routing in disaster response considering variable patient condition: Nsga-ii and mopso algorithms", ***Journal of Industrial & Management Optimization***, Vol. 18, No. 2, (2022), 1035. doi: 10.3934/jimo.2021007

35. Zhang, X., Yuan, J., Chen, X., Zhang, X., Zhan, C., Fathollahi-Fard, A.M., Wang, C., Liu, Z. and Wu, J., "Development of an improved water cycle algorithm for solving an energy-efficient disassembly-line balancing problem", ***Processes***, Vol. 10, No. 10, (2022), 1908. doi: 10.3390/pr10101908

36. Yuan, G., Yang, Y., Tian, G. and Fathollahi-Fard, A.M., "Capacitated multi-objective disassembly scheduling with fuzzy processing time via a fruit fly optimization algorithm", ***Environmental Science and Pollution Research***, (2022), 1-18. doi: 10.1007/s11356-022-18883-y

37. Golmohammadi, A.-M., Honarvar, M., Hosseini-Nasab, H. and Tavakkoli-Moghaddam, R., "A bi-objective optimization model for a dynamic cell formation integrated with machine and cell layouts in a fuzzy environment", ***Fuzzy Information and Engineering***, Vol. 12, No. 2, (2020), 204-222. doi: 10.1080/16168658.2020.1747162

38. Yazdani, M., Kabirifar, K., Fathollahi-Fard, A.M. and Mojtahedi, M., "Production scheduling of off-site prefabricated construction components considering sequence dependent due dates", ***Environmental Science and Pollution Research***, (2021), 1-17. doi: 10.1007/s11356-021-16285-0

Persian Abstract

چکیده

این مطالعه به تعامل سیستم تولید سلولی پویا و برنامه ریزی تولید سلسله مراتبی با تقاضاهای غیرقطعی می پردازد. هر یک از این مسائل به تنهایی پارامترهایی مانند تقاضای غیرقطعی و تشکیل سلولی پویا را به طور جداگانه در نظر نمی گیرند. بر این اساس، برای پر کردن این شکاف، این مقاله یک مدل بهینه‌سازی یکپارچه را ارائه می‌کند که جامع‌ترین طراحی سیستم‌های تولید سلولی پویا و مسائل برنامه ریزی تولید سلسله مراتبی با تقاضای غیرقطعی را در خود جای داده است. این مدل به مدیران کمک می کند تا سایز و تعداد سلول های بهینه را برای کاهش هزینه ها بدست آورند. این مدل همچنین از اصول برنامه‌ریزی تولید سلسله مراتبی استفاده می‌کند تا جابه‌جایی مواد بین سلولی و درون‌سلولی و تخصیص کارگر برای هر قسمت را برای کاهش پیچیدگی مدل یکپارچه تسهیل نماید. در بسیاری از مطالعات قبلی، محققان تقاضای دوره ای را قطعی فرض میکردند، اما در واقعیت، از آنجایی که تقاضا غیر قطعی است، نیاز به پیش بینی دقیق دارد. بنابراین، این مطالعه با هدف ترکیب دقیق ترین متغیرهای تصمیم گیری با واقعی ترین شرایط، انجام شده است. یک مطالعه موردی از یک شرکت توسعه صنعتی و مکانیزاسیون کشاورزی نشان می‌دهد که مدل یکپارچه می‌تواند راه‌حلی عملی برای پاسخگویی به تقاضا، پیکربندی مجدد سلول‌ها در هر دوره، ارائه ماشین‌آلات جدید برای افزایش ظرفیت تولید مورد نیاز و تنظیم ظرفیت تولید برای کمک به مدیران ارائه دهد. مقابله با نوسانات تقاضا تجزیه و تحلیل حساسیت بر روی کمیت سلول، زمان راه اندازی، هزینه های جابجایی بین سلولی و درون سلولی، تقاضاها و ظرفیت زمانی انجام شده است و نتایج نشان می دهد که افزایش خطای پیش بینی و هزینه جابجایی بین سلولی باعث تغییرات کمتری در هزینه کل می شود اما هزینه کل به جابجایی درون سلولی ، ظرفیت های زمانی موجود و کمیت سلول حساس است.

International Journal of Engineering

Journal Homepage: www.ije.ir

An Experimental Study to Predict a New Formula for Calculating the Deflection in Wide Concrete Beams Reinforced with Shear Steel Plates

A. S. Mohammed[a], A. S. J. Al-Zuheriy*[a], B. F. Abdulkareem[b]

[a] *Civil Engineering Department, University of Technology – Iraq, Baghdad, Iraq*
[b] *Civil Engineering Department, Al-Mansour University College, Baghdad, Iraq*

PAPER INFO

Paper history:
Received 10 October 2022
Received in revised form 27 October 2022
Accepted 28 October 2022

Keywords:
Moment of Inertia
Shear Failure
Stirrups
Beams Strengthening

ABSTRACT

A conventional stirrup is widely used in all concrete beams as shear reinforcement to prevent shear failure that happens suddenly and unexpectedly without previous warning. It is a great challenge to figure out another type of stirrup and establish a new formula to calculate the deflection. This article offers an experimental study that predicts a novel formula for calculating deflection in concrete beams reinforced with shear steel plates as a stirrup. The experimental work was established and consists of 16 wide reinforced concrete beams with 216x560x1800 mm dimensions. Instead of the conventional reinforcing stirrups, steel plates with 3.0, 4.0, and 5.0 mm thickness in longitudinal and transverse dimensions and for one-half of the samples, recycled PVC round bubbles were used as the variables explored in this study. In addition, the variables include an examination of the opening form of shear steel plates with varying distances between them. For calculating the deflection of wide beams, a new formula for the effective moment of inertia is proposed, and it yields excellent agreement for several investigations, with a coefficient of variation of 5.48 percent. The formulae for calculating the maximum deflection are established using ACI 318M-14 and EC 2.

doi: *10.5829/ije.2023.36.02b.15*

1. INTRODUCTION

In recent years, the use of large concrete beams in structural framing systems has increased. This modification addresses the need for low-cost keys that minimize the structural height and architectural complexity. Broad beams may offer enough cross-sectional areas to perform the needed function at a shorter depth than a system of narrower beams with parallel spacing in the plan; when coupled with reinforced concrete broad beam-column connections. It is very effective at resisting earthquake stresses.

Sherwood et al. [1] conducted an experimental investigation to determine the shear behavior of broad beams and thick slabs, as well as the effect of element width. In their investigation, they examined five specimens of standard-strength concrete ranging in width from 250 to 3005 mm and nominal thickness from 470 mm. Their research revealed that the shear failure stresses of narrow beams and broad beams are very comparable.

Adam et al. [2] studied the effect of shear reinforcement spacing on the unidirectional shear capacity of broad reinforced concrete components. A set of thirteen concrete examples of typical strength were constructed and tested. The spacing of shear reinforcements was the key test variable. The specimens' shear reinforcement ratios were in close proximity to ACI 318-11 [3] minimum standards. To ensure that the shear strength of all elements with shear reinforcement produced in accordance with ACI 318-11 is adequate. The study advises restricting the transverse spacing of web reinforcement to the lesser of the effective element depth or 600 mm.

Hanafy [4] noted that the test findings show the relevance of web reinforcement in strengthening the shear capacity and ductility of narrow broad beams, which conform to globally recognized norms and standards.

*Corresponding Author's Email: *ahmed.sh.jeber@uotechnology.edu.iq* (A. S. J. Al-Zuheriy)

Please cite this article as: A. S. Mohammed, A. S. J. Al-Zuheriy, B. F. Abdulkareem, Experimental Study to Predict a New Formula Calculating the Deflection in Wide Concrete Beams Reinforced with Shear Steel Plates ***International Journal of Engineering, Transactions B: Applications***, Vol. 36, No. 02, (2023), 360-371

The deflection, strain, and fracture patterns of four examined full-scale reinforced concrete beams are estimated using theoretical and experimental analysis in this paper. Said and Elrakib [5] examined the shear behavior of broad beams. The testing program had 9 beams of 29.0 MPa concrete strength, each measuring 700.0 mm in width, 250.0 mm in depth, and 1750.0 mm in length, with a 650 mm shear span. The research demonstrates that the contributions of stirrups to shear strength are substantial and directly related to the quantity and spacing of stirrups. Compared to the reference beam, the maximum shear stress of the range of tested beams increased by between 32% and 132%. Broad beams' shear resistance was more effectively contributed to by high-grade steel.

Mohammadyan-Yasouj et al. [6] studied six broad beams with inner column specimens, one sample for each of the following conditions: without web reinforcement, with web reinforcement. According to the findings, independent bent bars enhanced the shear capacity and ductility of broad beams. Although independent strait bars enhanced the shear strength to some degree, it was determined that the beam was less ductile upon failure. In addition, the findings revealed that the beam with banded primary longitudinal reinforcement attained a higher failure load.

The risk management and earthquake research and applications center [7] showed a new technology. An experimental evaluation of reinforced concrete broad beams strengthened with lattice girders, commonly known as one-way slabs, are subjected to low-rate (static) concentrated loads at their midspan. To determine the impact of lattice girders on load-bearing capability, tests were performed on lattice girder-reinforced and conventionally reinforced beam-type specimens. Six beams with two distinct reinforcing configurations were evaluated. The examined beams were supported by a simple 2250.0 mm span. All specimens were subjected to static loading tests, and mid-span deflections were measured using displacement transducers. The lattice girder-reinforced and conventionally reinforced beams exhibited comparable stiffness, while the lattice girder-reinforced beams exhibited a better resisting capacity.

Ibrahim et al. [8] investigated the strength of bubbling broad reinforced concrete beams with various shear steel plate kinds. A total of eight specimens were examined. The factors examined concern the replacement of stirrups with shear steel plates of the comparable cross-sectional area for stirrups at mid-leg height with circular openings of varying thicknesses (3, 4, and 5 mm). Four specimens lacked bubbles, whereas the remaining specimens included bubbles. This research revealed that shear steel plates are a viable replacement for stirrups; since they increased yield, ultimate load, and deflection (at service load) by an average of 5%, 15%, and 9% as compared to utilizing bubbles. The yield deflection is enhanced by 24%, 37%, and 27% for 3, 4, and 5mm thick shear steel plates, respectively, as compared to 10mm stirrups, and it was within 8% for all samples when utilizing bubbles.

Eklou et al. [9] looked at how steel plate pieces and regular stirrups worked as shear reinforcement in beams. In this experiment, two full-size reinforced concrete beams were made to fail in shear. The types of shear reinforcement were used as the test parameters for this study. By looking at the crack configurations, load-deflection relationship, and shear capacities of the samples, the shear resistance of the beams was discussed. The values predicted by the Modified Truss Theory were compared to the shear capacities that were found through experiments. The proportion of the evaluated shear strength to the predicted shear capacity in the steel plate RC beams and the reference beam showed that they were pretty close. The findings of this research demonstrate that the global behavior of the steel plate beam and the control beam using traditional stirrups is only slightly different.

Hamoda et al. [10] look into how engineered cement composite (ECCO) and stainless steel plates can make concrete members stronger. For samples strengthened with an ECCO layer, non-linear 3D finite element models were made. When the lab tests were compared to the model, it was discovered to be accurate. Depending on the results of the experiments and the numeracy data, new shear strength formulas were made.

Due to the importance of shear failure in reinforced concrete members which is happened suddenly without warning, Alferjani et al. [11] and Abdollahi et al. [12] presented the experimental and analytical studies for reinforced concrete members to evaluate the shear capacity. Rahmani et al. [13], Faez et al. [14] and Mohsenzadeh et al. [15] studied the reinforced concrete beams strengthening due to the importance of this topic.

Aydin et al. [16] investigated the various effects of using steel diagonal elements and dampers as strengthening materials on the structural responses as well as the best placement locations in terms of different structural response parameters. They found that both viscous dampers and steel diagonal braces reduce the top story displacement.

Aydin et al. [17] showed the concepts and the principles of using the steel plate systems and studied the effects of steel plates on 5-story and 10-story steel buildings to strengthen frames.

The novelty of this work is to predict a novel formula for calculating deflection in concrete beams reinforced with shear steel plates as a stirrup. The objectives of this research are represented by offering an experimental study that included testing 16 concrete beams with 33.0 MPa as nominal compressive strength under the four-point loading test with studied different variables consist steel plates with 3.0, 4.0, and 5.0 mm thickness in longitudinal and transverse dimensions, instead of the conventional reinforcing stirrups and for one-half of the samples, recycled PVC round bubbles. In addition, the variables include an examination of the opening form of shear steel plates with varying distances between them.

In this study, the main goal of the study is to find a new way to figure out how much W-reinforced concrete (RC) beams with steel shear plates bend and to predict the new equation to estimate the deflections in these types of beams. In fact, using a steel plate is a new way to deal with a lot of stirrups in a broad (RC) beam because concrete's shear portion is very tiny when compared to high-depth concrete beams.

2. EXPERIMENTAL TEST DETAILS

The experimental work included testing 16 concrete beams with 33.0 MPa as nominal compressive strength (SCC - Self Compacting Concrete) under the four-point loading test. All of the samples had a width of 560mm and a height of 216mm. The beam's effective depth is 170mm. All of the beams were made stronger by adding 10 ø 16.0 mm bars in tension and 2 ø 10.0 mm bars in the compression zone. This steel ratio is greater than the minimum and larger than the maximum ratios that the ACI M-318-14 says should be used [3]. In the middle of the beam, there were no stirrups. Table 1 shows details and notes about each of the sixteen beam specimens. The last number, -1, -2, or -3, tells you how far apart the steel plates are: 125 mm, 166 mm, or 250 mm. The symbol shows the diameter of the steel bars that run lengthwise.

Figure 1 shows the typical sizes and details of the reinforcing bars of the specimens that were tested. Figures 2 and 3 show cross-sections of the same specimens. Figure 4 shows where the bubbles go, and Figure 5 shows where the longitudinal main reinforcement and the steel shear plate are located.

3. RESULTS AND DISCUSSION

3. 1. Result of Beam Specimens

Table 2 lists the f'_c, cracks, yielding stress, ultimate loads, deflections at the crack, and ultimate loading, as well as the ductility factor for each specimen. The load at which the first crack appeared was carefully noted. Load-deflection graphs were used to figure out the experimental results of the cracking loads.

TABLE 1. Specimens' details

Beam Name	B * H (mm)	a /d	Reinforcing of main Bars		Shear Rein.	Plate thicknesses (mm)	Spacings (mm)	Bubbles Diam. (mm)
			Ten.	Comp.				
BWS	560x216	3.529	10 ϕ 16.0	2 ϕ 10.0	Double stirrups ϕ 10	---	125.0	--
BWBS	560x216	3.529	10 ϕ 16.0	2 ϕ 10.0	Double stirrups ϕ 10	---	125.0	85.0
BWP3-1	560x216	3.529	10 ϕ 16.0	2 ϕ 10.0	--	3.0	125.0	--
BWBP3-1	560x216	3.529	10 ϕ 16.0	2 ϕ 10.0	--	3.0	125.0	85.0
BWP3-2	560x216	3.529	10 ϕ 16.0	2 ϕ 10.0	--	3.0	167.0	--
BWBP3-2	560x216	3.529	10 ϕ 16.0	2 ϕ 10.0	--	3.0	167.0	85.0
BWP3-3	560x216	3.529	10 ϕ 16.0	2 ϕ 10.0	--	3.0	250.0	--
BWBP3-3	560x216	3.529	10 ϕ 16.0	2 ϕ 10.0	--	3.0	250.0	85.0
BWP4	560x216	3.529	10 ϕ 16.0	2 ϕ 10.0	--	4.0	125.0	--
BWBP4	560x216	3.529	10 ϕ 16.0	2 ϕ 10.0	--	4.0	125.0	85.0
BWP5	560x216	3.529	10 ϕ 16.0	2 ϕ 10.0	--	5.0	125.0	--
BWBP5	560x216	3.529	10 ϕ 16.0	2 ϕ 10.0	--	5.0	125.0	85.0
BWPR4	560x216	3.529	10 ϕ 16.0	2 ϕ 10.0	--	4.0	125.0	--
BWBPR4	560x216	3.529	10 ϕ 16.0	2 ϕ 10.0	--	4.0	125.0	85.0
BWPL3	560x216	3.529	10 ϕ 16.0	2 ϕ 10.0	--	--	--	--
BWBPL3	560x216	3.529	10 ϕ 16.0	2 ϕ 10.0	--	--	--	85.0

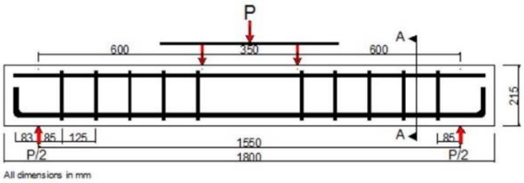

Figure 1. Loading details

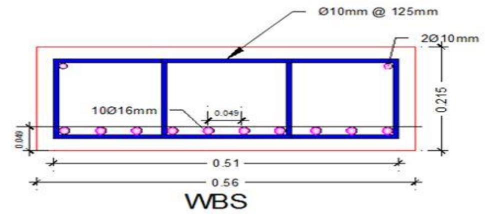

Figure 2. Section A-A stirrups (BWS beam)

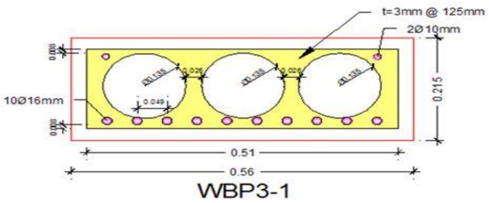

Figure 3. Section A-A for plates (BWP3-1 beam)

Figure 4. Preparation of the molded specimen and placing the reinforcement

Figure 5. Preparation and lying the bubles on the right side of the specimen

TABLE 2. The examined specimens' strength characteristics

Beam Name	Compressive Strength f'_c (MPa)	Measured Cracking load P(kN)	Measured Δ_{cr} (mm)	Yielding load P(kN)	Measured Δ_y (mm)	Ultimate Load P (kN)	Measured Δ_u (mm)	Ductility= $\frac{\Delta_u}{\Delta_y}$	Failure mode
BWS	36.60	50.0	1.730	400.0	10.830	440.0	18.930	1.750	Flexural
BWBS	33.20	40.0	1.500	361.0	13.400	378.0	25.700	1.920	Flexural
BWP3-1	33.50	50.0	1.530	420.0	13.450	431.0	36.450	2.710	Flexural
BWBP3-1	33.10	60.0	2.100	421.0	12.30	446.0	22.500	1.830	Flexural
BWP3-2	34.00	60.0	2.900	400.0	13.150	441.0	23.100	1.760	Flexural
BWBP3-2	32.50	50.0	2.100	410.0	16.850	430.0	35.750	2.120	Flexural
BWP3-3	32.80	40.0	1.760	370.0	11.330	376.0	22.820	2.010	Shear
BWBP3-3	32.90	40.0	1.750	410.0	14.800	431.0	28.600	1.930	Shear
BWP4	32.40	50.0	2.050	420.0	14.550	441.0	30.350	2.090	Flexural
BWBP4	32.60	50.0	1.900	420.0	14.080	441.0	21.280	1.510	Flexural
BWP5	32.40	50.0	1.900	410.0	13.750	419.0	17.750	1.290	Flexural
BWBP5	33.40	50.0	2.130	410.0	13.750	431.0	20.050	1.460	Flexural
BWPR4	33.20	50.0	2.250	370.0	13.000	380.0	17.600	1.350	Flexural
BWBPR4	32.60	50.0	2.200	400.0	15.900	420.0	18.900	1.190	Flexural
BWPL3	32.320	40.0	2.350	400.0	11.350	450.0	22.450	1.980	Flexural
BWBPL3	32.80	80.0	2.800	400.0	14.050	431.0	25.250	1.800	Flexural

3. 2. The Deflection Comparison Computed by ACI 318-14 and EC 2 Codes The experimental deflection computed from load-deflection curves at service load which is assumed 60.0 % of the ultimate loads and the analytical deflection outcomes at service load of all specimens computed by ACI-318-14 [3] codes are presented in Table 3. It can be noticed that the analytical deflections of wide beams computed by ACI-318-14 [3] codes were on average 24% and 25% lower than the experimental deflection, respectively. This increase in experimental deflection is due to the ability of the dial gauge to catch the readings of deflection at the center of wide beams in both directions (longitude and transverse) while the dial gauge cannot catch the readings of deflection at the edges of the center of the beam.

By Saint-Venant's principle, this case makes sense. Saint-Venant's theorem says that when a system of forces is imposed on a small part of a body's boundary, the stresses and strains caused by such forces in that other part of the body, which is far away from the region where the forces are applied, do not depend on how the forces are implemented, but only on what happens as a result. Most of the time, this huge distance can be thought of as the largest dimension of the area where the forces are implemented [18].

Take the prismatic bar shown in Figure 6 as an example. The stresses at a length farther than the transverse dimension (2*b) from the top of the steel bar can be considered equal in all three cases when three systems of forces have the same effect.

TABLE 3. Experimental deflections compared with deflections computed by ACI 318-14 [18] codes at service load

Beam Name	Deflections at Service Load, Δ_s (mm)				
	Measured	Predicted			
		ACI-318M-14		EC-2	
			%Differences		%Differences
BWS	3.50	3.010	-13.930	3.000	-14.260
BWBS	3.60	2.6000	-27.640	2.600	-27.520
BWP3-1	3.10	2.9600	-4.2840	2.9640	-4.3740
BWBP3-1	3.70	3.070	-16.810	3.070	-16.870
BWP3-2	4.40	3.000	-31.700	3.000	-31.660
BWBP3-2	4.50	3.000	-33.270	3.000	-33.270
BWP3-3	3.60	2.610	-27.290	2.610	-27.340
BWBP3-3	4.10	3.000	-26.700	2.990	-26.840
BWP4	4.10	3.040	-25.840	3.040	-25.710
BWBP4	4.00	3.070	-23.170	3.060	-23.280
BWP5	3.60	2.920	-19.960	2.920	-19.990
BWBP5	4.20	2.960	-29.430	2.960	-29.420
BWPR4	4.10	2.590	-36.710	2.590	-36.580
BWBPR4	4.30	2.900	-32.370	2.900	-32.380
BWPL3	4.10	3.180	-22.350	3.170	-22.510
BWBPL3	4.00	3.010	-24.740	3.000	-24.830

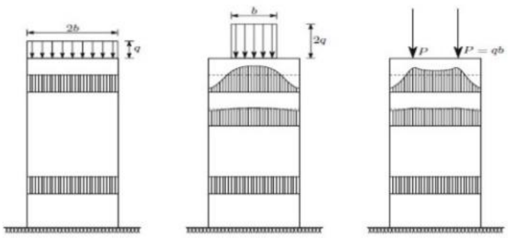

Figure 6. The distributions of stree due to three force systems with the same resultant for several bar cross-sections [3]

3. 3. Deflection Suggestion Models The cracked and uncracked section characteristics of the tested beams were used to look at the deflections of the flexural tests. The goal was to come up with a system design for checking the deflection of a broad beam under the effect of service load. The following equations were given by ACI-318-14 [3] codes to figure out the maximum deflection.

3. 3. 1. Deflection Calculation According to ACI 318M-14 By adding up the curves along the length of a beam, you can figure out how it will bend. For an elastic beam, the curvature, 1/r, is equal to M/EI, where (EI) is the stiffness of the flexural member of the cross-section. If EI stays the same, this is a normal thing to do. But three different EI values should be thought about for reinforced concrete. Figure 7 shows moment-curvature diagrams for a beam with many cracks. The following diagram shows how these things work [19]. The uncracked inertia moment EI_u refers to the moment of inertia of any section before it cracks. And the radial O-A in Figure 7 shows how the conformable EI_u works. After a crack happens, the section's inertia moment is called the “cracked moment of inertia,” EI_{cr}, and it is smaller than the uncracked moment of inertia. There are intermediate values of EI between where the steel breaks (point A) and where it gives way (point B).

The transition from I_{gt} to I_{cr} that is noticed in the experimental data was derived in the following equation by James et al. [19]:

$$I_e = \left(\left(\frac{M_{cr}}{M_a}\right)^3 I_g\right) + \left(1 - \left(\frac{M_{cr}}{M_a}\right)^3\right) I_{cr} \quad (1)$$

In Figure 8, the four-point-loaded beam deflection was predicted using the formula given in Equation (2):

$$\Delta_{\max} = \left(\frac{Pa\left(3L^3 - 4a^2\right)}{48 E_c I_{effective}}\right) \quad (2)$$

where L is the beam length, P is the applied load, E is the elastic modulus, and a is the length between the point load and the beam's edge.

3. 3. 2. Deflection Calculation According to EC 2 Model

An equation was used to figure out how much a structure bends; this equation was used by EC 2.

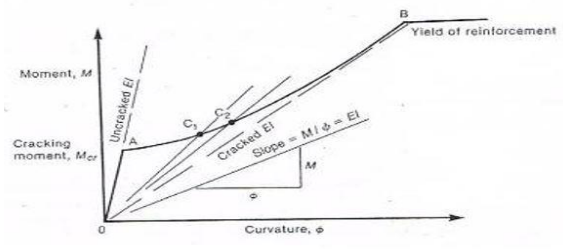

Figure 7. Moment-curvature diagram

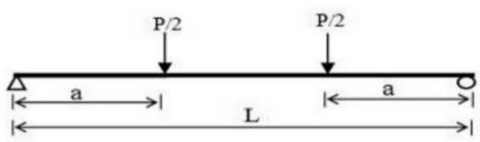

Figure 8. Testing set up

$$M_{cr} = \frac{0.9 f_{ctm}.I_u}{h - x_u} \quad (3)$$

where f_{ctm} is the rupture modulus, I_u is the inertia moment of gross sectional area, h is the height of the sample, and x_u is the distance of the level of the uncracked section neutral axis from the tension face.

$$\xi = 1 - 0.5\left(\frac{M_{cr}}{M_a}\right)^2 \quad (4)$$

$$\frac{1}{r_n} = \xi\left(\frac{M_{QP}}{EI_c}\right) + (1-\xi)\left(\frac{M_{QP}}{EI_u}\right) \quad (5)$$

$$\frac{1}{r_{t,QP}} = \left(\frac{1}{r_n}\right) + \left(\frac{1}{r_{cs}}\right) \ (i.e\ \Phi) \quad (6)$$

$$\delta_{QP} = kl^2 \frac{1}{r_{t,QP}} \quad (7)$$

$$k = \left(0.125 - \frac{(a/l)^2}{6}\right) \quad (8)$$

3. 3. 3. Modified Stiffness Equation for Wide Beams

In the preceding section, it was made clear that the equations used do not ensure a good job of predicting deflection for broad beams. So, a new equation is needed to anticipate how much the beam will bend. The moment of inertia that works I_e is the most important factor in figuring out how much beams bend. By applying the displacement equation based on the structural analysis and the elastic bending theory, the next method is according to an analysis of all the information about displacement readings at mid-span. Equation (9) is used to calculate the bending stiffness.

$$E_c I_{effective} = \left(\frac{Pa(3L^2 - 4a^2)}{48\ \Delta_{\max}}\right) \quad (9)$$

Where: Δ_{max} represents the experimental deflection value. Upon removing the service load (approximately 250 kN).
It is possible that the increased experimental deflection and reduced stiffness of the broad beam are because the deflection at the end of the transverse direction is smaller than at the center point of the beam according to the Sant Venant principle. Bending stiffness may also be measured in terms of curvature, as shown in Figure 9 and represented by Equation (10).

In Figure 9, the values of ε_c, ε_s, k_d, and d-k_d are compression concrete strains in the top fiber, tensile steel strains, depth of the neutral axis at the service stage, and depth of the neutral axis at the ultimate stage, respectively.

$$E\ I_{\exp} = \frac{M}{\Phi} \quad (10)$$

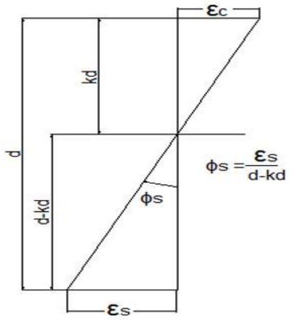

Figure 9. service-curvature (φy) in bending sections

With Equation (11) and the strain in concrete and steel measured during loading, we can calculate the curvature.

$$\Phi = \frac{\varepsilon_s}{d - kd} \qquad (11)$$

Table 4 describes the $I_{\exp}$ values calculated by Equation (10) that were based on the $M_{service}$ equals 60.0 % of $M_{ultimate}$ and curvatures Φ that are based on the experimental strain of longitudinal bars and depth of neutral axis on the service load state. Also, Table 4 demonstrates the $I_{\exp}$ values calculated by Equation (9) based on the experimental deflection at the service state.

The difference in average between Equation (10)'s EI_{exp} and Equation (9)'s EI_{eff} value was 1.50 %, so the two values were very close to each other. In this paper, the values of curvature were used to figure out the effective inertia moment.

Tables 5 and 6 show how the effective moment of inertia from Equation (10) compares to the completely dependent deflection at the service stage from ACI-318-14 [3]. It is obvious that 138.6% and 138.26% were the difference in the average of (I_{exp} / I_{eff}) for ACI 318M-14 [3] and for EC 2, respectively. As well, -74.07% and -74.12% were the average deflection differences for ACI 318M-14 [3] and -73.96% for EC 2, respectively.

To determine the deflection and the ductility index, load section stiffness and load-neutral axis depth diagrams were used by Mohammad [20]. Then according to ACI 318M-14 [3] and EC 2 for wide beams, a new equation (Equation (12)) was modified to predict the deflection depending on the experimental stiffness values and the experimental curvature values calculated from Equations (9) and (10), respectively.

$$I_e = 0.740\left(\left((\frac{M_{cr}}{M_a})^3 I_g\right) + \left(1 - (\frac{M_{cr}}{M_a})^3\right) I_{cr}\right) \qquad (12)$$

At the service load, the deflection results computed by the modified Equation (12) compared with the experimental deflection are shown in Table 7. It was obvious that the difference between the actual deflection and what ACI-318-14 [3] and EC 2 calculated was 1.40 % and 1.30 %, respectively.

TABLE 4. Bending and curvature stiffness Equations (10) and (11)

Beam Name	From Equation (10)					From Equation (11)	$\frac{EI_{effective}}{EI_{\exp}}$ %
	ε_s	(d-kd) mm	Φ x10^{-5} (mm^{-1})	$M_{service}$ (kN.m)	$EI_{\exp}$ (x10^{12})	$EI_{effective}$ (x10^{12})	
BWS	0.00150	110.0	1.3630	79.200	5.8080	5.4360	93.6010
BWBS	0.00160	104.0	1.5380	68.040	4.4230	4.5410	102.670
BWP3-1	0.00130	112.0	1.1600	77.580	6.6840	6.0120	89.9550
BWBP3-1	0.00160	108.0	1.4810	80.280	5.4190	5.2130	96.2000
BWP3-2	0.00180	92.0	1.9560	79.380	4.0570	4.3340	106.840
BWBP3-2	0.00180	87.0	2.0680	77.400	3.7410	4.1320	110.470
BWP3-3	0.00140	87.0	1.6090	67.680	4.2060	4.5160	107.390
BWBP3-3	0.00150	88.0	1.7040	77.580	4.5510	4.5460	99.8900
BWP4	0.00160	95.0	1.6840	79.380	4.7130	4.6510	98.6990
BWBP4	0.00150	90.0	1.6660	79.380	4.7630	4.7680	100.110
BWP5	0.00150	98.0	1.5300	75.420	4.9270	4.9640	100.750
BWBP5	0.00170	95.0	1.7890	77.580	4.3350	4.4380	102.370
BWPR4	0.00180	94.0	1.9140	68.400	3.5720	4.0080	112.210
BWBPR4	0.00170	87.0	1.9540	75.600	3.8690	4.2240	109.180
BWPL3	0.00160	97.0	1.6490	81.000	4.9110	4.7460	96.6640
BWBPL3	0.00140	87.0	1.6000	77.580	4.8210	4.6600	96.6600
C.O.V.							1.50 %

TABLE 5. The comparison of Equation (10) with ACI-318-14 [3] at the service stage for the moment of inertia and deflection

Beam Name	From Equation (10)		From Equation (2)		$I_{\exp} / I_{eff}$ (%)	$\frac{\Delta_{s(equation2)}}{\Delta_{s(equation10)}}$ (%)
	$I_{\exp}$ x10^8	Δ_s (mm)	$I_{eff.}$ x10^8	Δ_s (mm)		
BWS	1.85	3.310	2.046	3.01	110.59	90.936
BWBS	1.51	3.731	2.178	2.60	144.23	69.686
BWP3-1	2.22	2.823	2.111	2.96	95.090	104.85
BWBP3-1	1.81	3.594	2.126	3.07	117.45	85.420
BWP3-2	1.28	4.735	2.038	3.00	159.21	63.357
BWBP3-2	1.34	5.005	2.253	3.00	168.13	59.940
BWP3-3	1.50	3.901	2.246	2.61	149.73	66.905
BWBP3-3	1.60	4.130	2.216	3.00	138.50	72.639
BWP4	1.59	4.081	2.143	3.04	134.77	74.491
BWBP4	1.67	4.039	2.210	3.07	132.33	76.008
BWP5	1.75	3.712	2.236	2.92	127.77	78.663
BWBP5	1.43	4.334	2.112	2.96	147.69	68.297
BWPR4	1.16	4.635	2.099	2.59	180.94	55.879
BWBPR4	1.32	4.729	2.172	2.90	164.54	61.323
BWPL3	1.87	3.997	2.365	3.18	126.47	79.559
BWBPL3	1.85	3.901	2.241	3.01	121.13	77.159
COV					+138.6%	-74.07%

TABLE 6. The comparison of Equation (10) with EC 2 at the service stage for the effective moment of inertia and deflection

Beam Name	From Equation (10)		EC 2		$\Phi_{\exp} / \frac{1}{r_{t,QP}}$ %	$\frac{\Delta_{s\,EC2}}{\Delta_{s(equation10)}}$ %
	$\Phi_{\exp}$ x10^{-5}(mm^{-1})	Δ_s (mm)	$\frac{1}{r_{t,QP}}$ x10^{-5} mm^{-1}	Δ_s (mm)		
BWS	1.363	3.310	1.234	3.000	110.3	90.63
BWBS	1.538	3.731	1.071	2.609	143.0	69.92
BWP3-1	1.160	2.823	1.219	2.964	95.24	104.9
BWBP3-1	1.481	3.594	1.266	3.075	116.8	85.55
BWP3-2	1.956	4.735	1.237	3.006	157.5	63.48
BWBP3-2	2.068	5.005	1.235	3.002	166.7	59.98
BWP3-3	1.609	3.901	1.074	2.615	149.1	67.03
BWBP3-3	1.704	4.130	1.234	2.999	137.71	72.61
BWP4	1.684	4.081	1.253	3.045	134.0	74.61
BWBP4	1.666	4.039	1.263	3.068	131.6	75.95
BWP5	1.530	3.712	1.201	2.920	127.1	78.66
BWBP5	1.789	4.334	1.219	2.964	146.2	68.38
BWPR4	1.914	4.635	1.068	2.599	178.3	56.07
BWBPR4	1.954	4.729	1.196	2.907	162.6	61.47
BWPL3	1.649	3.997	1.308	3.177	125.8	79.48
BWBPL3	1.600	3.901	1.237	3.006	129.7	77.05
COV					+138.26%	-74.12%

TABLE 7. Comparing the experimental deflection to the calculated deflection at the service load stage using Equation (12)

Beam Name	Modified Equation (12)					
	From Equation (2)			EC 2		
	I_{eff} x10⁸	Δ_s (Equation (2)) (mm)	$\frac{\Delta_{s(eq.2)}}{\Delta_{exp}}$ x100	$\frac{1}{r_{t,QP}}$ x10⁵ (mm⁻¹)	Δ_s EC 2 (mm)	$\frac{\Delta_{s\,EC2}}{\Delta_{s\,exp}}$ x100
BWS	2.0460	4.0580	115.90	1.6680	4.0420	115.50
BWBS	2.1780	3.5080	97.440	1.4480	3.5130	97.600
BWP3-1	2.1110	3.9970	128.90	1.6480	3.9930	128.80
BWBP3-1	2.1260	4.1470	112.00	1.7100	4.1440	112.00
BWP3-2	2.0380	4.0480	92.000	1.6720	4.0510	92.070
BWBP3-2	2.2530	4.0450	89.880	1.6690	4.0450	89.900
BWP3-3	2.2460	3.5240	97.880	1.4520	3.5220	97.850
BWBP3-3	2.2160	4.0480	98.730	1.6670	4.0410	98.560
BWP4	2.1430	4.0960	99.900	1.6940	4.1030	100.00
BWBP4	2.2100	4.1400	103.50	1.7060	4.1340	103.30
BWP5	2.2360	3.9350	109.30	1.6230	3.9340	109.20
BWBP5	2.1120	3.9930	95.070	1.6480	3.9930	95.080
BWPR4	2.0990	3.4940	85.210	1.4430	3.5010	85.400
BWBPR4	2.1720	3.9170	91.090	1.6160	3.9170	91.090
BWPL3	2.3650	4.2890	104.60	1.7670	4.2810	104.40
BWBPL3	2.2410	4.0550	101.30	1.6710	4.0500	101.20
C.O.V			1.40 %			1.30 %

3. 4. Comparison of the Modified Stiffness Equation for Wide Beams with Other Researches

The forty-three broad beams accessible in the literature and used in this work were split into five groups based on the literature [1, 2, 5-7] and tabulated in Table 8 to determine the range of the revised stiffness formula for broad beams.

Table 8 compares experimental data of deflections on the service loads (60 percent of the ultimate loads) for forty-three broad beams with findings of deflections on the service load estimated using the revised stiffens Equation (12) for these broad beams.

All forty-three specimens used to assess the applicability of the modified Equation (12) were broad beams, a/d >1, simply supported beams with rectangular sections.

Table 8 summarized the analytical data of all samples. It is obvious that -11.20%, -4.530%, -11.400%, 12.600%, and -12.900% represent the coefficient of variation [COV] for Said and Elrakib [5], Mohammadyan [6], Tapan [7], Edward [1], and Adam [2], respectively as well as the 5.480% represents the average of all COV of all beams. All of the reported data in literature [2, 5-7] unless Edward [1] showed that the deflections calculated by the revised Equation (12) were too low, which means the revised Equation (12) remain a conservative formula.

This comparison validates the adjusted Equation (12) used to calculate the effective inertia moment for wide beams.

TABLE 8. A comparison of the revised stiffness equation with other studies [5-7], [1-2]

Researcher	Experimental Results of Researcher													Δ Eq. (12)	Def. %	Point - load	Failure
	Spe.	L (mm)	B (mm)	H (mm)	a (mm)	a/d	S (mm)	f'_c	ρ_l %	ρ' %	P service	Δ_s					
M. Said [5]	SB1	1750.0	700.0	250	650	3	-	29	1.72	0.29	270	**3.0**	**3.06**	**2.15**	2.0	shear	
	SB2	1750.0	700.0	250	650	3	φ6-200	29	1.72	0.29	358	**3.6**	**3.57**	**-0.77**	2.0	shear	
	SB3	1750.0	700.0	250	650	3	φ8-200	29	1.72	0.29	392	**5.2**	**3.76**	**-27.5**	2.0	shear	

	SB4	1750.0	700.0	250	650	3	φ6-150	29	1.72	0.29	374	**4.6**	**3.66**	**-20.3**	2.0	shear
	SB5	1750.0	700.0	250	650	3	φ8-150	29	1.72	0.29	406	**4.2**	**3.84**	**-8.34**	2.0	shear
	SB6	1750.0	700.0	250	650	3	φ6-100	29	1.72	0.29	390	**3.9**	**3.75**	**-3.66**	2.0	shear
	SB7	1750.0	700.0	250	650	3	φ8-100	29	1.72	0.29	416	**4.1**	**3.90**	**-4.70**	2.0	shear
	SB8	1750.0	700.0	250	650	3	φ10-200	29	1.72	0.29	484	**5.0**	**4.29**	**-14.0**	2.0	shear
	SB9	1750.0	700.0	250	650	3	φ10-100	29	1.72	0.29	556	**6.2**	**4.71**	**-23.9**	2.0	shear
COV														**-11.20**		
S. E. M. [6]	WB-1	1820.0	751	251	551	2.60	-	28	1.420	0.080	241.0	**1.10**	**1.210**	**10.60**	1.0	shear
	WB-2	1820.0	751	251	551	2.60	φ10-150	28	1.420	0.080	362.0	**2.20**	**1.820**	**-17.20**	1.0	shear
	WB-3	1820.0	751	251	551	2.60	804-H	28	1.420	0.080	304.0	**1.70**	**1.530**	**-9.860**	1.0	shear
	WB-4	1820.0	751	251	551	2.60	-	28	1.420	0.080	288.0	**1.40**	**1.450**	**3.740**	1.0	shear
	WB-5	1820.0	751	251	551	2.60	φ11-150	28	1.420	0.080	349.0	**2.10**	**1.970**	**-5.720**	1.0	shear
	WB-6	1820.0	751	251	551	2.60	φ11-150	28	1.420	0.080	381.0	**2.10**	**1.910**	**-8.800**	1.0	shear
COV														**-4.530**		
M. T. [7]	KD--1	2250.0	500.0	251	1126	4.90	φ8-300a	38	0.360	0.2	71.0	**4.0**	**3.38**	**-15.00**	1.0	shear
	KD--2	2250.0	500.0	251	1126	4.90	φ8-300b	38	0.360	0.2	60.0	**3.0**	**3.07**	**2.990**	1.0	shear
	KD--3	2250.0	500.0	251	1126	4.90	φ8-300c	38	0.360	0.2	74.0	**4.0**	**3.5**	**-12.30**	1.0	shear
	ND--1	2250.0	500.0	251	1126	4.90	φ8-200a	38	0.360	0.2	103	**5.0**	**4.38**	**-12.60**	1.0	shear
	ND--2	2250.0	500.0	251	1126	4.90	φ8-200b	38	0.360	0.2	94.0	**5.0**	**4.12**	**-17.30**	1.0	shear
	ND--3	2250.0	500.0	251	1126	4.90	φ8-200c	38	0.360	0.2	132	**6.0**	**5.16**	**-14.00**	1.0	shear
COV														**-11.40**		
E. G. [1]	AT-250A	2601	251	468	1301	2.96	--	37.8	0.92	--	138	**1.60**	**1.38**	**-13.90**	1.0	shear
	AT-250B	2601	253	470	1301	2.96	--	38.6	0.91	--	135	**1.30**	**1.35**	**3.680**	1.0	shear
	AT-1000A	2601	1003	470	1301	2.96	--	39.1	0.92	0.2	566	**2.50**	**1.93**	**-23.00**	1.0	shear
	AT-1000B	2601	1003	471	1301	2.96	--	37.8	0.92	0.2	529	**2.10**	**1.86**	**-11.50**	1.0	shear
	AT-3000	2601	3006	471	1301	2.96	--	40.5	0.92	0.2	1539	**2.20**	**1.86**	**-15.80**	1.0	shear
	AT--3A	2081	698	338	1041	3.38	--	37.4	0.94	--	286	**1.40**	**2.09**	**49.00**	1.0	shear
	AT--3B	2081	701	337	1041	3.38	--	37.7	0.94	0.2	305	**1.450**	**2.18**	**49.70**	1.0	shear
	AT--3C	2081	707	337	1041	3.38	--	37.2	0.94	--	311	**1.650**	**2.2**	**33.10**	1.0	shear
	AT--3D	2081	707	338	1041	3.38	--	37.2	0.94	0.2	299	**1.500**	**2.15**	**42.90**	1.0	shear
COV														**12.60**		
Ada [2]	AW-2	3701	1173	592	1851	3.66	φ15-300E	39.4	1.680	0.050	492	**4.0**	**2.98**	**-25.10**	1.0	shear
	AW-3	3701	1166	594	1851	3.66	φ15-300I	37.3	1.690	0.050	503	**5.1**	**3.05**	**-39.80**	1.0	shear
	AW-4	3701	1169	591	1851	3.66	--	39.8	1.690	0.080	436	**2.0**	**2.72**	**36.50**	1.0	shear
	AW-5	3701	1171	591	1851	3.66	φ15-300D	34.7	1.670	0.100	579	**3.0**	**3.37**	**12.80**	1.0	shear
	AW-6	3701	1170	594	1851	3.66	φ15-300E	43.8	1.680	--	506	**4.0**	**3.00**	**-24.70**	1.0	shear
	AW-7	3701	1171	592	1851	3.66	φ15-300D	35.9	1.670	0.100	645	**3.5**	**3.63**	**4.220**	1.0	shear
	AW-8	3701	1169	592	1851	3.66	--	39.5	1.690	0.100	481	**1.5**	**2.90**	**94.10**	1.0	shear
	AX-1	2081	704	340	1851	3.66	φ10-300E	42.0	1.720	0.050	277	**7.0**	**2.91**	**-58.20**	1.0	shear
	AX-2	2081	704	337	1851	3.66	φ4-300E	42.0	1.740	0.050	205	**7.5**	**2.38**	**-68.00**	1.0	shear
	AX-3	2081	708	336	1851	3.66	φ6-300D	42.0	1.740	0.080	272	**5.0**	**2.86**	**-42.40**	1.0	shear

	AX-4	2081	699	336	1851	3.66	φ8-300D	42.0	1.760	0.10	251	**3.0**	**2.70**	**-9.530**	1.0	shear
	AX-5	2081	698	336	1851	3.66	φ10-300	41.0	1.770	0.10	218	**5.5**	**2.47**	**-54.80**	1.0	shear
	AX-6	2081	704	339	1851	3.66	--	41.0	1.730	--	171	**2.0**	**2.12**	**6.980**	1.0	shear
COV														**-12.90**		
								Cumulative COV						**-5.480**		

E: Just Externally—legs.
I: Just Internally--legs
D: Both Externally, and Internally legs

4. CONCLUSIONS

1. Except for one specimen, there is not a big difference between the measured crack loads of the rest, and the difference does not go above 20% for the rest. This is because concrete and longitudinal reinforcing use the same properties.
2. By replacing the shear steel plate (with a round hole) with shear reinforcement (stirrups), there was only a 5% difference in yield load and ultimate load. Yield and ultimate loads for the rectangular opening were about 7.5% and 13.6% different. When bubbles are used, the yield load and ultimate load of a shear steel plate don't change much, but the yield load and ultimate load of a stirrup specimen go down by 10% and 14%, respectively.
3. When matched with experimental data from five different researchers, a new equation is projected to calculate the deflection in a RC broad beam based on the revised effective inertia moment, with a coefficient of variations of 5.48 percent.
4. Deflection at yield and ultimate load were both raised by an average of 20% and 28% when the shear steel plate was used in place of the stirrups. The 10% increase in deflection seen with the use of the current bubbles for the identical specimens is significant.
5. Using bubbles resulted in a 4.7% average reduction in sample weight and switching to shear steel plate from reinforcing steel of stirrups resulted in further reductions of 2.30%, 1.30%, and 1.0% for thicknesses of 3.0, 4.0, and 5.0mm, respectively.

5. REFERENCES

1. Sherwood, E.G., Lubell, A.S., Bentz, E.C. and Collins, M.P., "One-way shear strength of thick slabs and wide beams", ***ACI Structural Journal***, Vol. 103, No. 6, (2006), 794.
2. Lubell, A.S., Bentz, E.C. and Collins, M.P., "Shear reinforcement spacing in wide members", ***ACI Structural Journal***, Vol. 106, No. 2, (2009).
3. ACI, *Building code requirements for structural concrete and commentary*. 2011.
4. Hanafy, M.M., Mohamed, H.M. and Yehia, N.A., "On the contribution of shear reinforcement in shear strength of shallow wide beams", ***Life Science Journal***, Vol. 9, No. 3, (2012), 484-498.
5. Said, M. and Elrakib, T., "Enhancement of shear strength and ductility for reinforced concrete wide beams due to web reinforcement", ***Hbrc Journal***, Vol. 9, No. 3, (2013), 235-242. https://doi.org/10.1016/j.hbrcj.2013.05.011
6. Mohammadyan-Yasouj, S.E., Marsono, A.K., Abdullah, R. and Moghadasi, M., "Wide beam shear behavior with diverse types of reinforcement", ***ACI Structural Journal***, Vol. 112, No. 2, (2015), 199-208.
7. Tapan, M., "Structural response of reinforced concrete wide beams reinforced with lattice girders", ***Iranian Journal of Science and Technology. Transactions of Civil Engineering***, Vol. 38, No. C2, (2014), 337.
8. Ibrahim, A.M., Mansor, A.A., Salman, W.D. and Hamood, M.J., "Strength and ductility of bubbled wide reinforced concrete beams with diverse types of shear steel plates", ***International Journal of Engineering & Technology***, Vol. 7, No. 4.20, (2018), 502-506.
9. Eklou, R.J., Yani, M.B., Saifullah, H.A., Sangadji, S. and Kristiawan, S.A., "Experimental study: Shear behaviour of reinforced concrete beams using steel plate strips as shear reinforcement", in IOP Conference Series: Materials Science and Engineering, IOP Publishing. Vol. 1144, (2021), 012040.
10. Hamoda, A., Ahmed, M. and Sennah, K., "Experimental and numerical investigations of the effectiveness of engineered cementitious composites and stainless steel plates in shear strengthening of reinforced concrete beams", ***Structural Concrete***, (2022).
11. Mohamed, N., Elrawaff, B., Abdul Samad, A.A. and Alferjani, M., "Experimental and theoretical investigation on shear strengthening of rc precraced continuous t-beams using cfrp strips", ***International Journal of Engineering, Transactions B: Applications***, Vol. 28, No. 5, (2015), 671-676. doi: 10.5829/idosi.ije.2015.28.05b.04.
12. Ilbegyan, S., Ranjbar, M. and Abdollahi, S.M., "Shear capacity of reinforced concrete flat slabs made with high-strength concrete: A numerical study of the effect of size, location, and shape of the opening", ***International Journal of Engineering, Transactions B: Applications***, Vol. 30, No. 2, (2017), 162-171. doi: 10.5829/idosi.ije.2017.30.02b.02.
13. Rahmani, I., Maleki, A. and Lotfollahi-Yaghin, M.A., "A laboratory study on the flexural and shear behavior of rc beams retrofitted with steel fiber-reinforced self-compacting concrete jacket", ***Iranian Journal of Science and Technology, Transactions of Civil Engineering***, Vol. 45, No. 4, (2021), 2359-2375. doi: 10.1007/s40996-020-00547-x.
14. Faez, A., Sayari, A. and Manei, S., "Retrofitting of rc beams using reinforced self-compacting concrete jackets containing aluminum oxide nanoparticles", ***International Journal of Engineering, Transactions B: Applications***, Vol. 34, No. 5, (2021), 1195-1212. doi: 10.5829/ije.2021.34.05b.13.
15. Mohsenzadeh, S., Maleki, A. and Lotfollahi-Yaghin, M.A., "Strengthening of rc beams using scc jacket consisting of glass fiber and fiber-silica fume composite gel", ***International Journal of Engineering, Transactions B: Applications***, Vol. 34, No. 8, (2021), 1923-1939. doi: 10.5829/ije.2021.34.08b.14.

16. Aydin, E., Ozturk, B. and Duzel, E., "Rehabilitation of planar building structures using steel diagonal braces and dampers", ***rehabilitation***, Vol. 16, No. 17, (2012), 18.
17. Aydin, E., Öztürk, B., Çetin, H. and Gasir, M., "Strengthening plane frames with steel plates", (2018).
18. Johnston, F.P.B.E.R., "Jr. John t. De wolf, "Mechanics of Materials, Lecture Notes: J. Walt Oler Texas Tech University, (2009).
19. MacGregor, J.G., Wight, J.K., Teng, S. and Irawan, P., "Reinforced concrete: Mechanics and design, Prentice Hall New Jersey, Vol. 3, (1997).
20. Mohammad, M., Mohd, Z.B.J., Ali, A.M., Shatirah, A., Mohamed, J., Rafiepour, N., Mohammadhassani, A., Sinaei, H., Heydar, R.E. and Ghanbari, F., "Bending stiffness and neutral axis depth variation of high strength concrete beams in seismic hazardous areas: Experimental investigation", ***International Journal of Physical Sciences***, Vol. 6, No. 3, (2011), 482-494.

Persian Abstract

چکیده

رکاب معمولی به طور گسترده در تمام تیرهای بتنی به عنوان تقویت کننده برشی برای جلوگیری از شکست برشی که به طور ناگهانی و غیرمنتظره بدون هشدار قبلی رخ می دهد، استفاده می شود. کشف نوع دیگری از رکاب و ایجاد یک فرمول جدید برای محاسبه انحراف، چالش بزرگی است. این مقاله یک مطالعه تجربی را ارائه می‌کند که فرمول جدیدی را برای محاسبه انحراف در تیرهای بتنی تقویت‌شده با صفحات فولادی برشی به عنوان رکاب پیش‌بینی می‌کند. کار آزمایشی ایجاد شد و شامل ١٦ تیر بتن مسلح عریض با ابعاد ٢١٦x560x1800 میلی متر است. به جای رکاب های تقویت کننده معمولی، صفحات فولادی با ضخامت های ٣.٠، ٤.٠ و ٥.٠ میلی متر در ابعاد طولی و عرضی و برای نیمی از نمونه ها، حباب های گرد PVC بازیافتی به عنوان متغیرهای مورد بررسی در این مطالعه استفاده شد. علاوه بر این، متغیرها شامل بررسی فرم بازشوی صفحات فولادی برشی با فواصل متفاوت بین آنها می باشد. برای محاسبه انحراف پرتوهای عریض، فرمول جدیدی برای ممان اینرسی موثر پیشنهاد شده است و با ضریب تغییرات ٥.٤٨ درصد، تطابق عالی را برای چندین بررسی به دست می‌دهد. فرمول های محاسبه حداکثر انحراف با استفاده از ACI 318M-14 و EC 2 ایجاد شده است.

IJE TRANSACTIONS B: Applications Vol. 36, No. 02, (February 2023) 372-383

International Journal of Engineering

Journal Homepage: www.ije.ir

Potential Applications of Ginger Rhizomes as a Green Biomaterial: A Review

N. Akhlaghi*, G. Najafpour-Darzi

Biotechnology Research Laboratory, Faculty of Chemical Engineering, Babol Noshirvani University of Technology, Babol, Iran

PAPER INFO

Paper history:
Received 02 November 2022
Received in revised form 01 December 2022
Accepted 04 December 2022

Keywords:
Ginger Rhizome
Herbal Medicine
Food Packaging
Metal Nanoparticles
Biodiesel Preservation

ABSTRACT

The rhizome of ginger (*Zingiber officinale Roscoe*), usually known as ginger, is one of the most popular species used in food and traditional medicine. Ginger is rich of various hydrophobic and hydrophilic active compounds with diverse properties. Having fresh aroma, pungent taste, and various health benefits, along with being readily available and inexpensive are the advantages of ginger rhizome. In addition to herbal medicine perspective along with utilization as flavoring agent in foods and beverages, ginger rhizome demonstrated potential application in different fields. In this review, the current evidence of main potential applications of ginger, including its usage in preservation of food and food packaging systems, tenderization of meat product, medical properties, acting as an inhibitor of metal corrosion, biodiesel preservation from oxidation, and its role in the synthesis of metal nanoparticles were discussed. Overall, this review provides valuable information about ginger rhizome as a plant-based material, beyond its role in herbal medicine and imparting flavor to our food.

doi: *10.5829/ije.2023.36.02b.16*

Contents

Graphical abstract

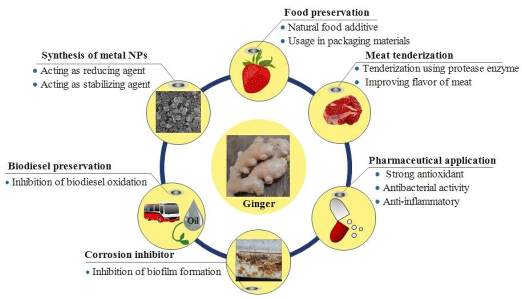

1. INTRODUCTION

Ginger is the rhizome of *Zingiber officinale Roscoe*, a perennial herb of the *Zingiberaceae* family [1]. The plant of *Zingiber officinale* was named by an English botanist, William Roscoe in 1807. The name of Zingiber is from the Greek word of 'zingiberis' meaning deer's antlers like shape, while the *officinale* refers to the medical properties of ginger [2]. The ginger plant is indigenous to South-East Asia and then introduced to various parts of globe [3]. Nowadays, it is cultivated in commercial scale throughout the world and is a common crop in Africa, Latin America, and Asia [2].

The rhizome or root of ginger is tuberous and perennial, and the stems are round, erect, oblique and annual [3]. Ginger rhizome was used as condiment to flavor beer throughout middle ages [2]. The flavor of ginger rhizome is combination of spicy, sweet, and peppery along with a very pungent characteristic [4]. Ginger rhizome is commonly consumed as a dried powder, fresh paste, candy, or slices preserved in tea for flavoring as a natural additive [3, 4]. Owing to powerful aroma, the rhizome of ginger is one of the most popular

*Corresponding Author Email: Nedaakhlaghi4@gmail.com
(N. Akhlaghi)

Please cite this article as: N. Akhlaghi, G. Najafpour-Darzi, Potential Applications of Ginger Rhizomes as a Green Biomaterial: A Review, ***International Journal of Engineering, Transactions B: Applications***, Vol. 36, No. 02, (2023), 372-383

worldwide used spices [5]. Moreover, ginger has been widely used in traditional medicine due to its valuable hydrophilic and hydrophobic bioactive compounds [6]. Ginger possesses advantages of inexpensive and nontoxic bioactive compound. The main hydrophobic metabolites of ginger were found to be safe for up to doses of 2000 mg, which is below the guidelines of the U.S. National Cancer Institute Common Toxicity Criteria [2]

Ginger bioactive constituent differ depending on the plant source, extraction method, and the storage conditions [7]. In case of separation and extraction processes, Soxhlet and steam distillation approaches are known as traditional extraction methods, which are widely used for the extraction of bioactive compounds from ginger [8]. Needing hazardous solvents, being tedious to operate, and in some cases operating at high temperature are their limitation [8]. In addition to traditional methods, various advanced extraction methodologies such as supercritical fluid extraction [9], subcritical water extraction [10], microwave-assisted extraction [11], and ultrasound assisted extraction [5] have also been employed to solve the problem associated with traditional extraction methods, mostly the thermal degradation of the desired bioactive compounds [8, 9]. For additional information on extraction processes, one can refer to literature [12].

There are several review articles on various aspects of ginger rhizome. Choi et al. [13] reviewed pharmacotherapeutic potential of ginger rhizome in age-related neurological disorders. Srinivasan [14] published review on ginger rhizome having focused on multiple health properties of ginger. Mao et al. [15] reviewed bioactive compounds of ginger and their mechanisms of action in biomedical applications. Shukla and Singh [3] studied anticancer activities of ginger. Ali et al. [16] reviewed pharmacological and toxicological properties of ginger. Nevertheless, a comprehensive review article on the all-potential applications of ginger rhizome is limited in literature to the authors' best of knowledge.

Considering the advantages of ginger rhizome as a green biomaterial, herein, at first the chemical constituents of ginger rhizome were briefly reviewed. Then, various potential applications of ginger rhizome including its application in food industry for food preservation and meat tenderization, pharmaceutical, metallurgy as metal corrosion inhibitor, fuel industry for biodiesel preservation, and nanotechnology for metal nanoparticle synthesis were comprehensively reviewed.

2. CHEMICAL CONSTITUENTS OF GINGER RHIZOMES

In fresh ginger rhizome, gingerols are the major compounds. The pungency level of fresh ginger is attributed to the concentration of gingerols, which vary depending on the growing conditions, harvesting, and extraction process [18].

Gingerols comprise a series of structural analogs differentiated by the length of their alkyl chains, including [6]-,[8]-and [10]-gingerol [3, 19]. Of these, [6]-gingerol is the most abundant phenolic ketones compound in gingerols (50-70%) with high biological activities [17, 18]. Meanwhile, the hydrophobicity property of [6]-gingerol limits its application [17].

Ginger contains more than 200 different compounds including pungent and active ingredients [17]. Generally, the constituents of ginger can be classified into two groups: volatile oils and non-volatile pungent compounds, which induce aroma and hot sensation in the mouth, respectively. Over 50 compounds of ginger's oil have been characterized, which are mainly sesquiterpenoids (α-zingiberene, α-farnesene, zingiberol, β-bisabolene, and β-sesquiphellandrene) and monoterpenoids (terpineol, borneol, curcumene, and geraniol) zingeberene, [3, 16]. The odor of ginger is mainly associated with these volatile oils [16]. The non-volatile pungent constituents are biologically active phenolic compounds, including gingerols, shogaols, zingerone, and paradols [3]. The chemical structures of the major constituents of ginger are shown in Figure 1.
Zingerones, as pungent constituents of ginger, cannot be found in fresh ginger. It produced from gingerols through reverse aldolization reaction when fresh ginger is heated [13]. After dehydration, gingerols can be transformed to shogaols, which are spicier than gingerols [18, 20]. In fact, the pungency of dried ginger is related to the presence of shogaols [16]. Besides, paradols are also other constituents of ginger formed from hydrogenation of shogaols [3]. In addition to the above mentioned compounds, ginger contains carbohydrates, lipids, waxes, raw fibers, organic acids, vitamins, and minerals. Moreover, proteolytic enzyme named as zingibain was also identified as ginger constituents [15].

3. APPLICATIONS OF GINGER RHIZOMES

In this section, the main applications of ginger rhizomes are discussed. Based on mostly recent publication, they

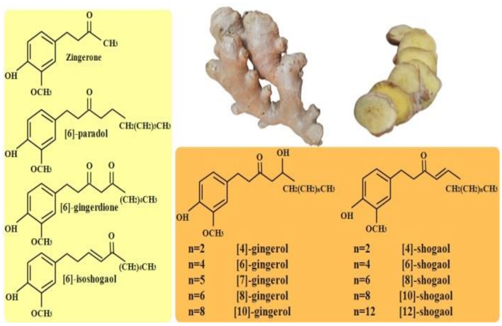

Figure 1. Chemical structure of major components of ginger

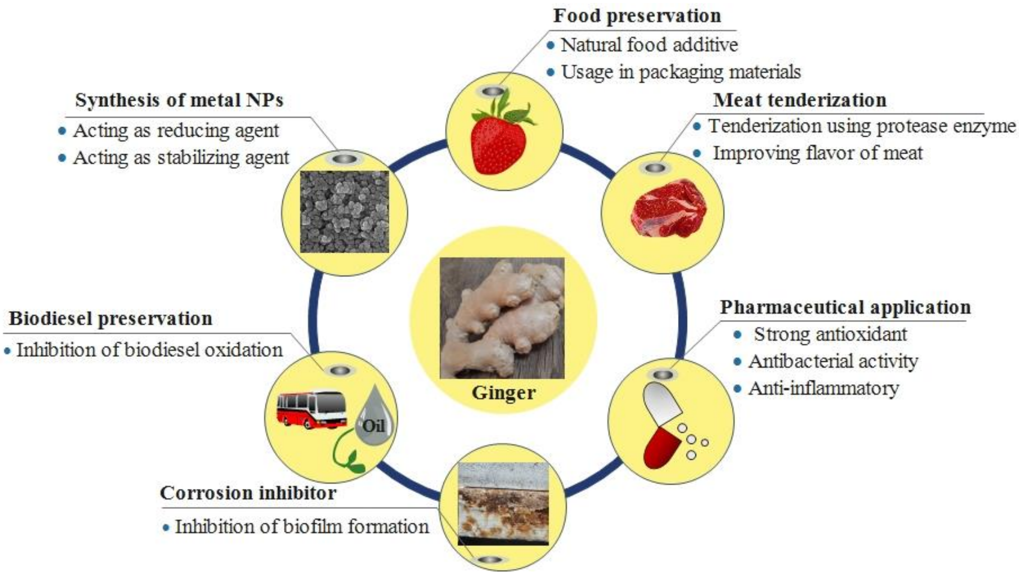

Figure 2. Main overall applications of ginger rhizomes

were classified into six independent categories, as illustrated in Figure 2.

3. 1. Food Preservation The oxidation of lipid and protein along with microbial contamination are the main causes of changes in the food quality [21]. For extending the shelf-life of food products, appropriate intervention is needed. Antioxidant compounds have the capability to terminate the chain reaction mechanism in oxidation process, owing to their ability to capture free radicals and donors electrons [22].

Ginger extract composed of essential oils, volatile odoriferous oil, gingerol, paradol, shogaol, α-zingiberene, α-curcumene, and β-sesquiphellandrene with strong antioxidant and antimicrobial activities. These can act as natural radical scavenger in food and food products instead of synthetic preservatives like butylated hydroxytoluene (BHT) and butylated hydroxyanisole (BHA) [21-23].

Thiobarbituric acid reactive substances (TBARS) assay is a common method for the detection of lipid oxidation in cells and tissues. Addition of ginger extract to Muscovy duck breast muscle [24], sheep muscle [24], and camel meat burger patties [25] reduced TBARS value of samples in compare to control sample (without extract), confirming retardation of lipid oxidation in muscle. This retardation could be attributed to the activities of peroxide-scavenging enzyme and polyphenol compounds in ginger extract [24, 25]. Besides, ginger extract demonstrated positive effect on the quality of canola oil even at temperatures of 60, 90, and 120 °C owing to its strong antioxidant activities [23].

The application of biobased materials that are derived from biological sources instead of petroleum-based polymers is ideally suited to develop sustainable packaging system. For improving the quality, safety, and prolong the shelf-life of the food, ginger essential oil can be incorporated into packaging materials [26, 27]. Chaijan et al. [28] observed an increase in shelf-life of Asian sea bass steak during chilled storage from 8 days for control sample to 15 days for the meat coated with whey protein isolate-polyphenol, containing phenolic extract from ginger, mostly due to the antimicrobial activity of ginger extract.

Zhang et al. [21] investigated the preservation of fresh beef using active coating by agar/sodium alginate film containing ginger essential oil. According to the results of lipid oxidation and antimicrobial assays, the coating extended the shelf-life of the chilled beef by 9 days compare to the uncoated sample (control). Addition of ginger essential oil to the agar/sodium alginate film not only reduced microorganism growth and inhibited lipid oxidation but also delayed the oxidation of myoglobin in meat tissues through acting as a barrier between the beef sample and the oxygen presence in the environment. It is worth mentioning that, the color of uncoated meat changed to brownish red, while the color of the chilled meat did not changed. Amalraj et al. [26] reported synthesis of polyvinyl alcohol/gum Arabic/chitosan film incorporated with ginger essential oil through solvent casting methods. In fact, addition of ginger essential oil to the film, improved its resistance to breakage, increased heat stability of the film, and showed antibacterial activity against pathogens like *Bacillus cereus, Staphylococcus aureus, Escherichia coli*, and *Salmonella typhimurium*.

Direct application of essential oils in packaging films is limited owing to their poorly solubility nature in water, as a common used solvent [29]. Moreover, most ingredient of essential oils may be oxidized and deteriorated when exposed to light, heat, and atmospheric oxygen [26]. The encapsulation of essential oils could solve such problems. In fact, through encapsulation, not only the bioavailability of the encapsulated ingredients increased but also enable controlled release of the bioactive compounds. In addition, intense flavors and odors of essential oils would be minimized [30]. Silva et al. [31] investigated the encapsulation of ginger essential oil at concentration of 12% (v/v) in the ultrafine fibers composed of soy protein isolate, polyethylene oxide, and zein through electrospinning for preservation of fresh Minas cheese. Based on antibacterial assays, addition of ginger essential oil to the composite fibers resulted in decrease in the growth of *Listeria monocytogenes* from 4.39 log CFU/g for control (fiber less package) to 3.62 CFU/g for stored cheeses in the package containing ginger essential oil and fiber after 9 days storage.

Taken together, owing to antibacterial and antioxidant properties, essential oils extracted from ginger can be used directly in various food products as natural food additive for preservation of lipid from oxidation and retardation of bacterial growth. Besides, indirectly application of ginger essential oil for food preservation could be carried out through incorporation of ginger essential oil into packaging material.

3. 2. Meat Tenderization Meat constituents are connective tissue like collagen and elastin, as well as myofibrils composed of four main proteins including myosin, actin, tropomyosin, and troponin. The hard texture of meat is related to the arrangement pattern and chemical structure of these proteins [32]. In tenderization process, degradation of the structural proteins of meat and collagen is carried out in order to reduce meat toughness.

Various mechanical (physical), chemical, and enzymatic methodologies have been employed for the meat tenderization [32]. In this context, exogenous proteolytic enzymes from plant sources like papain, bromelain, and ficin have been demonstrated meat tenderization activity [33]. In fact, exogenous proteases have the potential to digest connective tissue and myofibrillar proteins [25].

Ginger (*zingiber officinalae*) is a potential source of plant proteolytic enzyme. Ginger extract proved meat tenderization activity through hydrolysis of structural myofibrillar proteins and connective tissue, mainly of collagen [33]. The main protease responsible for the tenderization properties of ginger extract is zingibain [32]. Zingibain or ginger protease is a thiol proteinase with a molecular weight of 33.8 kDa. It has optimal proteolytic activity at 60 °C and pH 7 [34]. This proteolytic enzyme was isolated for the first time from ginger rhizome by Thompson and his co-workers in 1973 [35]. It is worth to be mentioned that, ginger proteases contained two main isoforms including GP-I and GP-II [36]. These two isoforms are 83% similar in amino-acid sequence, having homologies with papain [24].

It is well demonstrated that ginger extract has specific proteolytic activity against collagen as meat connecting tissue protein [32, 33]. Addition of ginger extract to camel meat burger patties [25], *M. pectoralis profundus* isolated from the beef brisket cut [33], and tough buffalo meat [35] led to increase in collagen solubility and noticeable reduction in shear force values; consequently, an increase in the tenderness. In fact, to break the meat samples with less resistance to cutting, low shear force is needed. Cruz et al. [37] reported 37.7% reduction in the shear force of chicken breast meat by addition of 5% ginger extract, indicating significant changes in the sample tenderness.

Myofibrillar fragmentation index (MFI) is a useful indicator of meat tenderization associated with the proteolysis of myofibrillar protein [36]. Through enzymatic tenderization, breakdown of Z-lines of meat resulted in reducing the length of myofibril and consequent increase in MFI value [36]. Owing to the proteolytic activity of ginger extract, the MFI value of chicken breast increase from 23.82 to 76.5 for the control (without extract) and treated sample with 5% of crude enzymatic ginger after 24 h storage at 4 °C, respectively [37]. He et al. [36] also reported 23% increase in MIF value of the marinated duck breast muscles with 30% ginger extract in compare to control (no extract) after 72 h of margination, mostly due to the degradation of myofibrillar proteins.

A comparative study was conducted by Naveena et al. [35] on the tenderization properties of cucumis extract, ginger extract, and papain against tough buffalo meat. In compare to control sample (no enzymatic treatment), significant increase in collagen and myofibrillar protein solubility, and reduction in shear force was reported for all enzyme-treated meats. Meanwhile, the sample treated with ginger extract demonstrated better flavor, appearance and tenderness. Besides, higher cooking yield was observed using ginger extract and papain compare to cucumis-treated meat.

In summary, ginger's protease enzyme could be used as an alternative of the most popular commercial enzyme like papain in meat tenderization. From the above section, it can be concluded that incorporation of zingibain with meat product not only enhances the tenderness, but also has the ability to improve the flavor and juiciness of meat products.

3. 3. Pharmaceutical Applications Ginger rhizome has a long history of application in traditional medicine for its performance in stopping vomiting and bleeding, acting as diaphoretics, and treating phlegm/cough [13]. Extract from ginger demonstrated therapeutic potential to ameliorate various disorders such as atherosclerosis [38], metabolic dysfunction (e.g. diabetes) [13], cardiovascular, gastrointestinal symptoms [15], treating vascular disorders (e.g. hypertension), and bone disorders (e.g. rheumatoid arthritis) [13].

Modern science revealed ginger extract composed of valuable bioactive compounds like terpenes, polysaccharides, lipids, phenolic, and organic acids [15]. Multiple biological activities associated to these bioactive compounds have been reported for ginger, including anti-inflammatory, anti-rheumatic, antibacterial, antifungal, hypolipidaemic, anti-obesity, anti-carcinogenic (e.g. lung, liver, ovarian, pancreatic, and colon cancer), and strong antioxidant activity, as well [9, 39-41].

Bernard et al. [42] compared the ability of bioactive components of ginger rhizome extract, including [6]-gingerol, [8]-gingerol, and [10]-gingerol in inhibition of human and mouse mammary carcinoma cells growth. Based on reported results, the [10]-gingerol was more effective than [6]-gingerol and at least as potent as [8]-gingerol in inhibition of human (MDA-MB-231, MDA-MB-468) and mouse (4T1, E0771) cell growth. In fact, the growth of MDA-MB-231 cells was influenced by the inhibitory effect of [10]-gingerol that reduces the number of rounds of cell division and induction of apoptosis through mitochondrial outer membrane permeabilization.

To inhibit the generation of oxidative stress and consequent occurrence of diseases such as cancers, diabetes, and cardiovascular, the balance between antioxidant molecules and free radicals is necessary. In fact, antioxidants act as free radical scavengers through chemical prevention of electron transformation from other molecules to the free radicals [43]. Zingerones, which belongs to pungent constituents of ginger suppressed the oxidative stress through the addition of C=O at the C_3 position [13]. Ginger extract also demonstrated antioxidant protective affects against BPA-induced thyroid oxidative damage through increasing the synthesis of thyroid hormones and activating the expression of Nrf-2/HO-1 gene [44].

The pharmaceutical properties of ginger extract are mostly related to its phytochemicals such as 6-gingerol, 8-gingerol, 10-gingerol, and 6-shogaol [45]. Fajrin et al. [46] revealed the role of 6-shogaol in alleviating hyperalgesia and allodynia in painful diabetic neuropathy in a mice model. Another work performed by Simon et al. [47] used a parallel artificial membrane permeability assay to investigate the effect of ginger extract on the central nervous system. Their results demonstrated that 6-gingerol, 8-gingerol, and 6-shogaol are able to penetrate blood-brain barrier through passive diffusion. This finding support the fact ginger extract possesses anti-neuroinflammatory activity *via* prevention of neurodegenerative diseases like Alzheimer's and Parkinson's [47].

Contaminated food and feed with Aflatoxin B_1 is the main causes of hepatocellular carcinoma [48]. The phenolic rich extract from ginger, mostly composed of 6-gingerol and 6-shogaol, exhibited hepatoprotective activity in treatment of Aflatoxin B_1 induced toxicity of liver through reducing lipid peroxidation along with improving the activities of antioxidant enzymes [48]. Moreover, the bioactive compounds of ginger extract like 6-gingerol, 6-shogaol, 6-paradol, and zingerone were found effective in treatment of age-related neurological disorders. In such disorders, the risk of diseases increases with aging *via* modulating signaling molecules of cell death or cell survival (e.g. stroke, multiple sclerosis (MS), migraine, and epilepsy) [13].

In brief, ginger possesses active compounds with therapeutic potential in various diseases mostly due to their antibacterial activity and efficiency as reducing oxidative stress.

3. 4. Corrosion Inhibitor Corrosion is a natural process in which alloys and metals interact with certain elements presence in their surroundings to form more stable compounds named as corrosion product [49]. In this process, loss of metal happen and the surface of metals become corroded [50].

Metals, with the exception of gold and platinum are found in nature in impure form mostly as oxides or sulfides, in stable state. For having pure metals, energy is consumed which lead to the formation of pure metals that are in higher energy state than the ore, in unstable state. So, corrosion is the easiest and fastest way for unstable metals to reach to the lowest energy state with stable thermodynamic form [51]. Different factors like temperature, acidic or bases environment, hazardous gases, salts, moisture, and formation of bacterial biofilm on the metals and alloys surface accelerate the corrosion phenomena [50, 51]. Use of corrosion inhibitors is an effective, economic, and convenient strategy to minimize corrosion related issues in many systems such as boiler, oil and gas production units, cooling systems, and refinery units [52].

Electrochemical analyses revealed the inhibitory function of ginger extract as green biocide in reducing chloride-induced corrosion of reinforcing steel. As the chloride threshold value (CTV) improved from 0.02 mol/L to 0.08 mol/L by using ginger root extract at optimum dosage of 2% [53]. Another work performed by Gadow and Motawea [54], investigated the effect of concentration and temperature on the inhibitory activity of ginger extract against corrosion of carbon steel in HCl (1M) solution. The results of weight loss (WL) measurement of carbon steel in 1M HCl solution revealed the positive effect of rise in concentration of ginger extract as inhibitor on inhibition efficiency (IE), as the WL reduced by increasing the concentration of ginger extract. On the other hand, high temperature demonstrated negative effect on IE. According to the reported results, the IE reduced from 94.9 to 62.8% at temperature of 25 °C and 55 °C, respectively [54]. This phenomena could be related to the fact that the electrostatic force that induce adsorption of plant extract on metal surface weaken at high system temperature [51].

The presence of water along with bacterial biofilm formations are two important reasons for the corrosion of materials in cooling towers systems. In fact, microorganisms provide an electrolytic environment that stimulate the anodic or cathodic reaction, causing metal surface corrosion [55]. Use of ginger extract, the WL value of mild steel 1010 in a cooling water system reduced from 992 mg (control sample) to 41 mg. Ginger extract at optimum concentration of 20 mg/L showed 80% IE on microbial corrosion of mild steel in the cooling water system. This can be explained by the fact that, ginger extract with high antibacterial activity prevented bacterial growth on metal surface. In addition, ginger extract affected on the composition of extracellular polymeric substances produced by the bacteria. As, by using ginger extract as inhibitor, the amount of protein and carbohydrates formed in the biofilm on the metal surface decreased from 44% and 18% to 27% and 9%, respectively [55].

Plant extracts as natural corrosion inhibitors composed of various phytochemicals like flavonoids, alkaloids, phytosterol, tannins, glycosides, and phenolic compounds with polar functional groups such as amino, ester, hydroxyl, carboxylic acids, and amid which facilitate their adoption on metal surface [56]. The above mentioned bioactive molecules can be served as the center of interaction with the surface of metals [51, 57]. In corrosion inhibition process using inhibitors, the adsorption of inhibitors onto the metal surface decreases the diffusion rate of reactants, consequently; reducing metal corrosion rate [52]. In fact, the interaction between inhibitor and heteroatoms of metal surface like sulphur, nitrogen, phosphorous, and oxygen led to the blockage of binding sites on the surface of metal [55]. According to Figure 3, the presence of phenolic constituents and lots of aromatic ring functional groups that contain oxygen atom and π-electrons in ginger extract could possibly be responsible for its inhibitory performance [53, 55].

The inhibition mechanism of plant extract is based on the adsorption including physisorption and chemisorption or both, which named as mixed-type adsorption inhibition mechanism (Figure 3) [50, 51]. The mixed-type inhibitors demonstrated the highest protection owing to the effecting on both cathodic and anodic reactions [50]. According to the literature [53, 54, 59], ginger extract was classified as a mixed-type corrosion inhibitor, demonstrating inhibition effect *via*

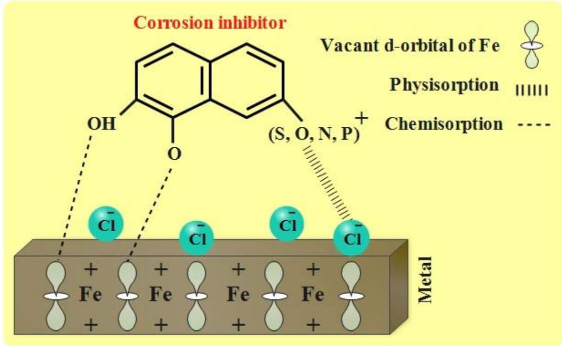

Figure 3. Mechanism of corrosion inhibition by ginger extract; physisorption through electrostatic interaction and chemisorption between heteroatoms of aromatic ring and vacant d-orbital of metal [58]

the formation of carbonaceous organic film on the metal surface. Base on analyses of liquid chromatography-mass spectrometry (LCMS), X-ray photoelectron spectroscopy (XPS), and attenuated total reflection Fourier transform infrared spectroscopy (ATR-FTIR); the carbonaceous film could be composed of different phenolic compounds like 6-gingerol and curcumin [53]. Coordination bonds between oxygen atoms in C=O or N=O bonds of the phenolic constituents and empty d-orbital of metal elements were believed to be as a mechanism of ginger extract adsorption on the steel surface (see Figure 3). As a result, the corrosion reactions of both cathodic and anodic areas were restrained [53, 59].

In short, corrosion is harmful to the human health and environment. Ginger extract as a green inhibitor can control and prevent corrosion. It possesses numerous phenolic compounds that enable its adsorption on metal surface, acting as a barrier for biofilm formation through blocking the binding sites on the surface of metal.

3. 5. Biodiesel Preservation Biodiesel is a biofuel that is generated from nonpetroleum sources. In fact, it is short-chain alkyl (methyl or ethyl) ester produced *via* the transesterification of fats and vegetable oils as renewable energy sources in the presence of appropriate catalyst [60]. In compare to diesel obtained from fossil fuels, biodiesel demonstrated negligible toxicity with low contents of sulfur and aromatic hydrocarbon. However, owing to the presence of allylic and bis-allylic groups in the chains of fatty acid esters in oil feedstock, which is used for biodiesel production, biodiesel faced the problem of oxidation degradation during long-term storage [61].

Factors like light, heat, transition metals, water, and presence of oxygen can cause fuel oxidation during storage [62]. As a consequence, the quality of biodiesel reduced due to the changes in fuel properties like increasing its viscosity, acidity, and water content which can damage the engine [63].

Use of antioxidant additives is an efficient method for preventing or delaying the oxidation of biodiesel during long storage periods. For improving biodiesel oxidation stability, natural antioxidants are better choice in compare to synthetic antioxidants owing to the biodegradability and nontoxicity [60]. In this context, ginger extract as a green antioxidant has potent to improve the quality of biodiesel by increasing its oxidative stability [62]. In fact, owing to the presence of high non-polar compounds in ginger extract as well as low water content, it has good miscibility in biodiesel for acting as an natural antioxidant [1].

The oxidation stability of biodiesel can be determined by induction period (IP). The IP is known as the time of delay, from the beginning of oxidation upon sudden increase in oxidation rate [64]. Devi et al. [1] investigated the effect of different concentrations of ginger extract on IP value of biodiesel obtained from *Pongamia pinnata* oil. The IP of *Pongamia pinnata* biodiesel increased from 4.03 h (without ginger extract) to 17.24 and 23.99 h after addition of ginger extract at concentration of 1000 and 2000 ppm to the *Pongamia pinnata* biodiesel, respectively.

It is worth mentioning that, by addition of ginger extract at concentration of 250 ppm (IP of 8.01 h) complied with American (ASTMD-6751) and European (ENE 14214) standard specifications for oxidation stability of biodiesel.

According to the reported results, ginger extract demonstrated antioxidant activities in a concentration dependent manner in preservation of *Pongamia pinnata* biodiesel. As oxidation stability of biodiesel enhanced at higher percentages of ginger extract. This phenomenon could be attributed to the presence of more number of –OH groups in ginger extract at high concentration. These –OH groups can block or retard the formation of free radicals; consequently, increasing the IP value of biodiesel sample. The overall probable mechanism of 2,2-diphenyl-1-picrylhydrazyl (DPPH) radicals scavenging by ginger extract is illustrated in Figure 4. In this process, the lipids oxidation chain reactions of free DPPH radicals stopped by donating hydrogen atoms from phenolic compounds of ginger extract; consequently, forming stable DPPH [1]. In another work by Rial et al. [62], the performance of dichloromethane extract from ginger on oxidation stability of soybean methyl biodiesel was studied. The IP value of soybean methyl biodiesel increased from 3.8 h (without addition of antioxidant) to 6.1 h using ginger extract at concentration of 1000 ppm during 90 days storage.

Taken together, ginger extract with high content of antioxidant compounds can interface with the biodiesel oxidation process and enhances oxidative stability of this biofuel, which is one of the important criterions for fuel quality determination.

3. 6. Synthesis of Metal Nanoparticles

Nanoparticles (NPs) composed of inorganic or organic materials. They are submicron molecules with size-dependent properties [65]. Owing to the advantages of plant-based biomaterials like being cost-effective, biocompatibility, and straight forward preparation process [66], the biologically synthesis of NPs using plant extract is an alternative for the large scale green production of NPs and specially metal NPs [67].

Plant extract contains various bioactive compounds like flavonoids, polyphenols, and other biomolecules that enable them to act as reducing agent for the reduction of metal ions to metal NPs [68]. Besides, plant extract can be used as stabilizing agents to prevent metal NPs agglomeration and oxidation, as well [68].

The mechanism of metal NPs synthesis using metal ions and plant extract in our case ginger extract is shown in Figure 5. In this process, ginger extract contains aromatic compounds including zingiberene, amino acids, vitamins, and protein, as well as phenolic compounds like

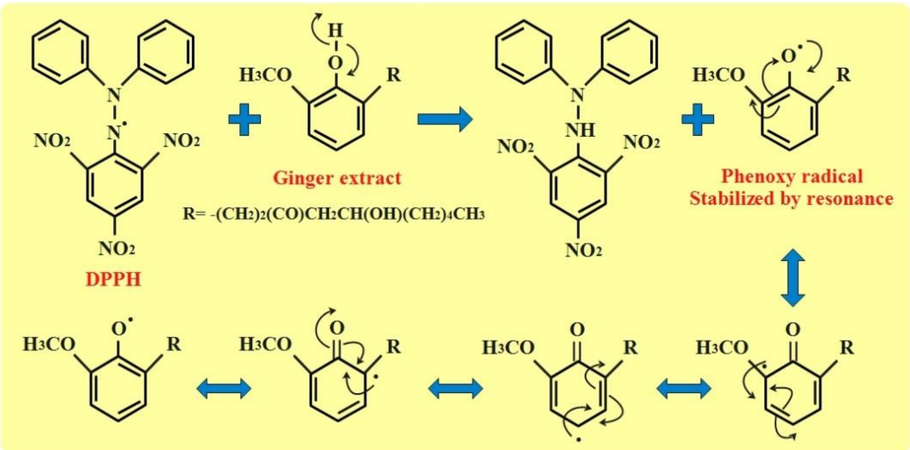

Figure 4. Mechanism of DPPH radicals scavenging by ginger extract [1]

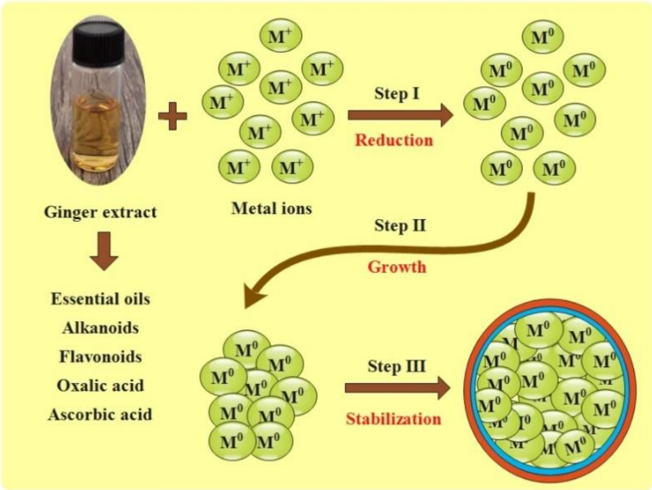

Figure 5. Mechanism of metal NPs synthesis using phytochemicals of ginger extract [70]

6-gingerol and 6-shogaol that acted as both reducing and stabilizing agent. In fact, the mechanism of the formation of metal NPs use of ginger extract could be reduction of metal ions due to the changing enol form to keto form of the alcoholic groups in phytochemicals. Besides, the electrostatic interaction between carboxylic (-COOH) and amine ($-NH_2$) groups of enzyme present and metal ions supports the stabilization of metal NPs [69].

Various exciting studies have been carried out using ginger extract for the synthesis of metal NPs (summarized in Table 1).

Both water soluble and hydrophobic compounds of ginger extract can be used for the synthesis of metal NPs. Kumar et al. [71] demonstrated that the water soluble compounds of ginger rhizome extract including heterocyclic compounds like flavonoids and alkaloids are responsible for the reduction and stabilization of gold (Au) NPs. In addition, ginger rhizome extract possess chemicals like oxalic acid and ascorbic acid that represented as reducing agents in the synthesis of Au NPs and silver (Ag) NPs [72].

A comparative study was conducted by Yaqub et al. [73] on evaluation of anticancer activities of green and chemical synthesized copper (Cu) NPs using ginger rhizome extract and ascorbic acid as stabilizing agents, respectively. Based on the results of transmission electron microscope (TEM), the spherical NPs were synthesized through chemical and green synthesis approaches, with average size of 22.7 and 35 nm, respectively. According to the reported results, the green synthesized Cu NPs demonstrated higher anticancer activity against HeLa and HepG2 cells compared to the chemical synthesized Cu NPs. This could be attributed to the presence of biomolecules such as curcumin, 6-shogaol, 6-paradol, and 6-gingerol on/in the green synthesized Cu NPs.

TABLE 1. Summary of studies on the green synthesized metal NPs using extract of ginger rhizomes

Nanostructure	Synthesis method	Size (nm)	Shape	Application/significance	Ref.
Ag NPs	Bio-chemical reduction	20-51 (D_{TEM})	Spherical	Anti-cancer activity against human colon carcinoma (HT-29) cells with IC_{50}: 150.8 (μg/mL)	[75]
Ag NPs	Ball milling	11-24 (D_{TEM})	Semi-spherical	Catalytic activities in degradation of 4-nitrophenol and methylene blue	[76]
Ag/iron oxide NPs	Co-precipitation	50-150 (SEM)	Hydrocolloids	Antibacterial activities at concentration of 100 (μg/mL) against Gram-positive and Gram-negative bacteria; contrast enhancing in magnetic resonance imaging	[77]
Ag NPs	Microwave irradiation	~10 (D_{TEM})	Spherical	Antibacterial activities against Gram-positive and Gram-negative bacteria	[78]
Au NPs	Bio-chemical reduction	5-15	Semi-spherical	NPs exhibited bio stability and blood compatibility	[71]
Se NPs	Bio-chemical reduction	100-150 (D_{AFM})	Spherical	Antibacterial activity against *Proteus* sp	[79]
Cu NPs	Bio-chemical reduction	20-100 (D_{TEM})	Spherical	Antibacterial activity against *Staphylococcus aureus*	[80]

In case of participation of hydrophobic compounds of ginger extract in the synthesis of metal NPs, Azizi et al. [74] reported one-pot process for the synthesis of zinc oxide-silver core-shell (ZnO-Ag) nanocomposite using essential oils of ginger extract. The essential oils were obtained by hydro-distillation method and were used as a basic medium for the synthesis of ZO NPs. Besides, the essential oil extracted from ginger acted as reducing agent in the formation of Ag NPs from Ag^+ ions. According to the literature, *zerumbone*, *humulene*, and *camphene* compounds in the essential oil of ginger were known responsible for the reduction of Ag^+ ions and synthesis of Ag NPs.

In brief, heterocyclic compounds of ginger rhizome extract, as hydrophilic constituents, can act as reducing and stabilizing agent in the synthesis of metal NPs. In addition to hydrophilic compounds, essential oils of ginger rhizome extract also demonstrated positive effect in metal NPs synthesis by acting as reducing agent. Owing to the presence of bioactive compounds with antioxidant activity in ginger extract, the green synthesized metal NPs showed more anticancer activity in compare to chemical synthesized NPs.

4. CONCLUSIONS

The present treatise reviewed chemical constituents and all potential applications of ginger rhizome. This review revealed the role of ginger rhizome extract in food preservation through acting as an antioxidant agent in protection of lipid and protein ingredients of food from oxidation. The presence of proteolytic enzyme like zingibain in ginger rhizome supports its further application in meat tenderization by hydrolyzing meat structural proteins and connective tissue and consequent reducing shear force in meat cutting. Besides, ginger extract exert promising multiple health beneficial like anticancer and anti-inflammatory owing to its volatile oils. Demonstrating inhibitory effect in metal corrosion by forming carbonaceous organic film on metal surface makes ginger extract as a promising natural mixed type corrosion inhibitor. Acting as a green antioxidant in increasing antioxidation stability of biodiesel was other potential applications of ginger rhizome. Considering the role of both hydrophobic and hydrophilic compounds of ginger rhizome extract as reducing and stabilizing agent in the synthesis of metal NPs, make a claim on its multiple applications.

5. REFERENCES

1. Devi, A., Das, V.K., Deka, D., "Ginger extract as a nature based robust additive and its influence on the oxidation stability of biodiesel synthesized from non-edible oil", ***Fuel***, Vol. 187, (2017), 306-314. doi.org/10.1016/j.fuel.2016.09.063
2. Semwal, R.B., Semwal, D.K., Combrinck, S., Viljoen, A.M., "Gingerols and shogaols: Important nutraceutical principles from ginger", ***Phytochemistry***, Vol. 117, (2015), 554-568. doi.org/10.1016/j.phytochem.2015.07.012
3. Shukla, Y., Singh, M., "Cancer preventive properties of ginger: A brief review", ***Food and Chemical Toxicology***, Vol. 45, (2007), 683-690. doi:10.1016/j.fct.2006.11.002.
4. Mancini, S., Paci, G., Fratini, F., Torracca, B., Nuvoloni, R., Bosco, A.D., Roscini, V., Preziuso, G., "Improving pork burgers quality using *Zingiber officinale* Roscoe powder (ginger)", ***Meat Science***, Vol. 129, (2017), 161-168. doi.org/10.1016/j.meatsci.2017.03.004
5. Kou, X., Ke, Y., Wang, X., Rahman, M.R.T., Xie, Y., Chen, S., Wang, H., "Simultaneous extraction of hydrophobic and hydrophilic bioactive compounds from ginger (*Zingiber officinale* Roscoe)", ***Food Chemistry***, Vol. 257, (2018), 223-229. doi.org/10.1016/j.foodchem.2018.02.125
6. Liao, D.W., Cheng, C., Liu, J.p., Zhao, L.Y., Huang, D.C., Chen, G.T., "Characterization and antitumor activities of polysaccharides obtained from ginger (*Zingiber officinale*) by different extraction methods***", International Journal of Biological Macromolecules***, Vol. 152, (2020), 894-903. doi.org/10.1016/j.ijbiomac.2020.02.325
7. Kiyama, R., "Nutritional implications of ginger: chemistry, biological activities and signaling pathways", ***The Journal of Nutritional Biochemistry***, Vol. 86, (2020), 108486. doi.org/10.1016/j.jnutbio.2020.108486
8. Khaw, K.Y., Parat, M.O., Shaw, P.N., Falconer, J.R., "Solvent Supercritical Fluid Technologies to Extract Bioactive Compounds from Natural Sources: A Review", ***Molecules***, Vol. 22, (2017), 1186. doi. 10.3390/molecules22071186
9. Mesomo, M.C., Scheer, A.P., Perez, E., Ndiaye, P.M., Corazza, M.L., "Ginger (*Zingiber officinale R*.) extracts obtained using supercritical CO_2 and compressed propane: Kinetics and antioxidant activity evaluation" , ***The Journal of Supercritical Fluids***, Vol. 71, (2012), 102-109. doi.org/10.1016/j.supflu.2012.08.001
10. Nourbakhsh Amiri, Z., Najafpour, G., Mohammadi, M., Moghadamnia, A., "Subcritical Water Extraction of Bioactive Compounds from Ginger (*Zingiber officinale Roscoe*)", ***International Journal of Engineering***, ***Transactions C: Aspects***, Vol. 31, (2018), 1991-2000. doi: 10.5829/ije.2018.31.12c.01
11. Teng, H., Seuseu, K.T., Lee, W.Y., Chen, L., "Comparing the effects of microwave radiation on 6-gingerol and 6-shogaol from ginger rhizomes (*Zingiber officinale* Rosc)", ***PLoS One***, Vol. 10, (2019), p. e0214893. doi.org/10.1371/journal.pone.0214893
12. Zhang, Q.W., Lin, L.G., Ye, W.C., "Techniques for extraction and isolation of natural products: a comprehensive review", ***Chinese Medicine***, Vol. 13, (2018). doi.org/10.1186/s13020-018-0177-x
13. Choi, J.G., Kim, S.Y., Jeong, M., Oh, M.S., "Pharmacotherapeutic potential of ginger and its compounds in age-related neurological disorders", ***Pharmacology and Therapeutics***, Vol. 182, (2017), 56-69. doi.org/10.1016/j.pharmthera.2017.08.010
14. Srinivasan, K., "Ginger rhizomes (*Zingiber officinale*): A spice with multiple health beneficial potentials", ***PharmaNutrition***, Vol. 5, (2017), 18-28. dx.doi.org/10.1016/j.phanu.2017.01.001
15. Mao, Q.Q., Xu, X.Y., Cao, S.Y., Gan, R.Y., Corke, H., Beta, T., Li, H.B., "Bioactive Compounds and Bioactivities of Ginger (*Zingiber officinale* Roscoe)", ***Foods***, Vol. 8, (2019), 185. doi:10.3390/foods8060185.
16. Ali, B.H., Blunden, G., Tanira, M.O., Nemmar, A., "Some phytochemical, pharmacological and toxicological properties of ginger (*Zingiber officinale* Roscoe): A review of recent research", ***Food and Chemical Toxicology***, Vol. 46, (2008), 409-420. doi.org/10.1016/j.fct.2007.09.085

17. Wang, Q., Wei, Q., Yang, Q., Cao, X., Li, Q., Shi, F., Tong, S.S., Feng, C., Yu, Q., Yu, J., Xu, X., "A novel formulation of [6]-gingerol: Proliposomes with enhanced oral bioavailability and antitumor effect", ***International Journal of Pharmaceutics***, Vol. 535, (2017), 308-315. doi.org/10.1016/j.ijpharm.2017.11.006

18. Chaisiwamongkhol, K., Ngamchuea, K., Batchelor-McAuley, C., Compton, R.G., "Electrochemical detection and quantification of gingerol species in ginger (*Zingiber officinale*) using multiwalled carbon nanotube modified electrodes", ***Analyst***, Vol. 141, (2016), 6321-6328. doi: 10.1039/c6an02254e

19. Silva, J.A., Becceneri, A.B., Mutti, H.S., Martin, A.C.B.M., Silva, M.F.G.F., Fernandes, J.B., Vieira, P.C., Cominetti, M.R., "Purification and differential biological effects of ginger-derived substances on normal and tumor cell lines", ***Journal of Chromatography B***, Vol. 903, (2012), 157-162. doi.org/10.1016/j.jchromb.2012.07.013

20. Gajic, J.S., Cvetanovic, A., Segura-Carretero, A., Mašković, P., Jakšić, A., "Functional coffee substitute prepared from ginger by subcritical water", ***The Journal of Supercritical Fluids***, Vol. 128, (2017), 32-38. doi.org/10.1016/j.supflu.2017.05.008

21. Zhang, B., Liu, Y., Wang, H., Liu, W., Cheong, K.L., Teng, B., "Effect of sodium alginate-agar coating containing ginger essential oil on the shelf life and quality of beef", ***Food Control***, Vol. 130, (2021), 108216. doi.org/10.1016/j.foodcont.2021.108216

22. Bonilla, J., Poloni, T., Lourenço, R.V., Sobral, P.J.A., "Antioxidant potential of eugenol and ginger essential oils with gelatin/chitosan films", ***Food Bioscience***, Vol. 23, (2018), 107-114. doi.org/10.1016/j.fbio.2018.03.007

23. Si, W., Chen, Y.P., Zhang, J., Chen, Z.Y., Chung, H.Y., "Antioxidant activities of ginger extract and its constituents toward lipids", ***Food Chemistry***, Vol. 239, (2018), 1117-1125. doi.org/10.1016/j.foodchem.2017.07.055

24. Tsai, L.L., Yen, N.J., Chou, R.G.R., "Changes in Muscovy duck breast muscle marinated with ginger extract", ***Food Chemistry***, 130, (2012), 316-320. doi:10.1016/j.foodchem.2011.07.044

25. Abdel-Naeem, H.H.S., Mohamed, H.M.H., "Improving the physico-chemical and sensory characteristics of camel meat burger patties using ginger extract and papain", ***Meat Science***, Vol. 118, (2016), 52-60. doi: 10.1016/j.meatsci.2016.03.021

26. Amalraj, A., Haponiuk, J.T., Thomas, S., Gopi, S., "Preparation, characterization and antimicrobial activity of polyvinyl alcohol/gum arabic/chitosan composite films incorporated with black pepper essential oil and ginger essential oil", ***International Journal of Biological Macromolecules***, Vol. 151, (2020), 366-375. doi.org/10.1016/j.ijbiomac.2020.02.176

27. Tongnuanchan, P., Benjakul, S., "Essential Oils: Extraction, Bioactivities, and Their Uses for Food Preservation", ***Journal of Food Science***, Vol. 79, (2014), doi: 10.1111/1750-3841.12492

28. Chaijan, S., Panpipat, W., Panya, A., Cheong, L.Z., Chaijan, M., "Preservation of chilled Asian sea bass (Lates calcarifer) steak by whey protein isolate coating containing polyphenol extract from ginger, lemongrass, or green tea", ***Food Control***, Vol. 118, (2020), 107400. doi.org/10.1016/j.foodcont.2020.107400

29. Alexandre, E.M.C., Lourenco, R.V., Bittante, A.M.Q.B., Moraes, I.C.F., Sobral, P.J.d.A., "Gelatin-based films reinforced with montmorillonite and activated with nanoemulsion of ginger essential oil for food packaging applications", ***Food Packaging and Shelf Life***, Vol. 10, (2016), 87-96. doi.org/10.1016/j.fpsl.2016.10.004

30. Reis, D.R., Ambrosi, A., Luccio, M.D., "Encapsulated essential oils: A perspective in food preservation", ***Future Foods***, Vol. 5, (2022), 100126. doi.org/10.1016/j.fufo.2022.100126

31. Silva, F.T., Cunha, K.F., Fonseca, L.M., Antunes, M.D., Hala, S.L.M.E., Fiorentini, A.M., Zavareze, E.R., Dias, A.R.G., "Action of ginger essential oil (*Zingiber officinale*) encapsulated in proteins ultrafine fibers on the antimicrobial control in situ", ***International Journal of Biological Macromolecules***, Vol. 118, (2018), 107-115. doi:10.1016/j.ijbiomac.2018.06.079.

32. Madhusankha, G.D.M.P., Thilakarathna, R.C.N., "Meat tenderization mechanism and the impact of plant exogenous proteases: A review", ***Arabian Journal of Chemistry***, Vol. 14, (2021), 102967. doi.org/10.1016/j.arabjc.2020.102967

33. Moon, S.S., "Effect of Proteolytic Enzymes and Ginger Extract on Tenderization of M. pectoralis profundus from Holstein Steer", ***Korean Journal for Food Science of Animal Resources***, Vol. 38, (2018), 143-151. doi.org/10.5851/kosfa.2018.38.1.1437

34. Gagaoua, M., Dib, A.L., Lakhdara, N., Lamri, M., Botinestean, C., Lorenzo, J. M., "Artificial meat tenderization using plant cysteine proteases", ***Current Opinion in Food Science***, Vol. 38, (2020), 177-188. doi.org/10.1016/j.cofs.2020.12.002

35. Naveena, B.M., Mendiratta, S.K., Anjaneyulu, A.S.R., "Tenderization of buffalo meat using plant proteases from Cucumis trigonus Roxb (Kachri) and *Zingiber officinale* roscoe (Ginger rhizome)", ***Meat Science***, Vol. 68, (2004), 363-369. doi:10.1016/j.meatsci.2004.04.004

36. He, F.Y., Kim, H.W., Hwang, K.E., Song, D.H., Kim, Y.J., Ham, Y.K., Him, S.Y., Yeo, I.J., Jung, T. J., Kim, C.J., "Effect of Ginger Extract and Citric Acid on the Tenderness of Duck Breast Muscles", ***Korean Society for Food Science of Animal Recources***, Vol. 35, (2015), 721-730. doi.10.5851/kosfa.2015.35.6.721

37. Cruz, P.L., Panno, P.H.C., Giannotti, J.D.G., Carvalho, R.V., Roberto, C.D., "Effect of proteases from ginger rhizome on the fragmentation of myofibrils and tenderness of chicken breast", ***LWT - Food Science and Technology***, Vol. 120, (2020), 108921. doi.org/10.1016/j.lwt.2019.108921

38. Toma, L., Raileanu, M., Deleanu, M., Stancu, C.S., Sima, A.V., "Novel molecular mechanisms by which ginger extract reduces the inflammatory stress in TNFα – activated human endothelial cells; decrease of Ninjurin-1, TNFR1 and NADPH oxidase subunits expression", ***Journal of Functional Foods***, Vol. 48, (2018), 654-664. doi.org/10.1016/j.jff.2018.08.011

39. Yeh, H., Chuang, C.H., Chen, H.C., Wan, C.J., Chen, T.L., Lin, L.Y., "Bioactive components analysis of two various gingers (*Zingiber officinale* Roscoe) and antioxidant effect of ginger extracts", ***LWT - Food Science and Technology***, Vol. 55, (2014), 329-334. doi.org/10.1016/j.lwt.2013.08.003

40. Ghafoor, K., Juhaimi, F.A., Özcan, M.M., Uslu, N., Babiker, E.E., Ahmed, I.A.M., "Total phenolics, total carotenoids, individual phenolics and antioxidant activity of ginger (*Zingiber officinale*) rhizome as affected by drying methods", ***LWT - Food Science and Technology***, Vol. 126, (2020), 109354. doi.org/10.1016/j.lwt.2020.109354

41. Svarc-Gajic, J., Cvetanovic, A., Segura-Carretero, A., Linares, I.B., Mašković, P., "Characterisation of Ginger Extracts Obtained by Subcritical Water", ***Journal of Supercritical Fluids***, Vol. 123, (2017), 92-100. doi.org/doi:10.1016/j.supflu.2016.12.019

42. Bernard, M.M., McConnery, J.R., Hoskin, D.W., "[10]-Gingerol, a major phenolic constituent of ginger root, induces cell cycle arrest and apoptosis in triple-negative breast cancer cells", ***Experimental and Molecular Pathology***, Vol. 102, (2017), 370-376. doi: 10.1016/j.yexmp.2017.03.006

43. Akhlaghi, N., Najafpour, G.D., "Phytochemical analysis, antioxidant activity, and pancreatic lipase inhibitory effect of ethanolic extract of *Trigonella foenumgraceum L.* leaves", ***Biocatalysis and Agricultural Biotechnology***, Vol. 32, (2021), 101961. doi.org/10.1016/j.bcab.2021.101961

44. Mohammed, E.T., Hashem, K.S., Ahmed, A.E., Aly, M.T., Aleya, L., Abdel-Daim, M.M., " Ginger extract ameliorates Bisphenol A (BPA)-induced disruption in thyroid hormones synthesis and metabolism: Involvement of Nrf-2/HO-1 pathway", ***Science of the Total Environment***, Vol. 703, (2020), 134664. doi.org/10.1016/j.scitotenv.2019.134664

45. Ogino, M., Yakushiji, K., Suzuki, H., Shiokawa, K., Kikuchi, H., Seto, Y., Sato, H., Onoue, S., "Enhanced pharmacokinetic behavior and hepatoprotective function of ginger extract-loaded supersaturable self-emulsifying drug delivery systems", ***Journal of Functional Foods***, Vol. 40, (2018), 156-163. doi.org/10.1016/j.jff.2017.08.035

46. Fajrin, F.A., Nugroho, A.E., Nurrochmad, A., Susilowati, R., "Ginger extract and its compound, 6-shogaol, attenuates painful diabetic neuropathy in mice via reducing TRPV1 and NMDAR2B expressions in the spinal cord", ***Journal of Ethnopharmacology***, Vol. 249, (2020), 112396. doi.org/10.1016/j.jep.2019.112396

47. Simon, A., Darcsi, A., Kéry, Á., Riethmüller, E., "Blood-brain barrier permeability study of ginger constituents", ***Journal of Pharmaceutical and Biomedical Analysis***, Vol. 177, (2020), 112820. doi.org/10.1016/j.jpba.2019.112820

48. Vipin, A.V., Raksha, R.K., Kurrey, N.K., Appaiah, K.A.A., Venkateswaran, G., "Protective effects of phenolics rich extract of ginger against Aflatoxin B1-induced oxidative stress and hepatotoxicity", ***Biomedicine & Pharmacotherapy***, Vol. 91, (2017), 415-424. doi.org/10.1016/j.biopha.2017.04.107

49. Ebrahimi, N., A. Hosseinzadeh, S.A., Vaezi, M., Mozafari, M., "Evaluation of Corrosion Resistance of Bi-layered Plasma-sprayed Coating on Titanium Implants", ***International Journal of Engineering***, Vol. 35, (2022), 635-643. doi. 10.5829/IJE.2022.35.04A.03

50. Salleh, S.Z., Yusoff, A.H., Zakaria, S.K., Taib, M.A.A., Seman, A.A., Masri, M.N., Mohamad, M., Mamat, S., Sobri, S.A., Ali, A., Teo, P.T., "Plant extracts as green corrosion inhibitor for ferrous metal alloys: A review", ***Journal of Cleaner Production***, Vol. 304, (2021), 127030. doi.org/10.1016/j.jclepro.2021.127030

51. Umoren, S.A., Solomon, M.M., Obot, I.B, Suleiman, R.K., "A critical review on the recent studies on plant biomaterials as corrosion inhibitors for industrial metal", ***Journal of Industrial and Engineering Chemistry***, Vol. 76, (2019), 91-115. doi.org/10.1016/j.jiec. 2019.03.057

52. Raja, P.B., Sethuraman, M.G., "Natural products as corrosion inhibitor for metals in corrosive media — A review", ***Materials Letters***, Vol. 62, (2008), 113-116. doi.org/10.1016/j.matlet.2007.04.079

53. Liu, Y., Song, Z., Wang, W., Jiang, L., Zhang, Y., Guo, M., Song, F., Xu, N., "Effect of ginger extract as green inhibitor on chloride-induced corrosion of carbon steel in simulated concrete pore solutions", ***Journal of Cleaner Production***, Vol. 214, (2019), 298-307. doi.org/10.1016/j.jclepro.2018.12.299

54. Gadow, H. S., Motawea, M.M., "Investigation of the corrosion inhibition of carbon steel in hydrochloric acid solution by using ginger roots extract", ***RSC Advances***, Vol. 7, (2017), 24576-24588. doi.org/10.1039/C6RA28636D

55. Narenkumar, J., Parthipan, P., Nanthini, A.U.R., Benelli, G., Murugan, K., Rajasekar, A., "Ginger extract as green biocide to control microbial corrosion of mild steel", ***3 Biotech***, Vol. 133, (2017), 1-11. https://doi.org/10.1007/s13205-017-0783-9

56. Zakeri, A., Bahmani, E., Aghdam, A.S.R., "Plant extracts as sustainable and green corrosion inhibitors for protection of ferrous metals in corrosive media: A mini review", ***Corrosion Communications***, Vol. 5, (2022), 25-35. doi.org/10.1016/j.corcom.2022.03.002

57. Nikitasari, A., Priyotomo, G., Royani, A., Sundjono, S., "Exploration of Eucheuma Seaweed Algae Extract as a Novel Green Corrosion Inhibitor for API 5L Carbon Steel in Hydrochlorid Acid Medium", ***International Journal of Engineering, Transactions C: Aspects***, Vol. 35, (2022), 596-603. doi.10.5829/IJE.2022.35.03C.13

58. Bhardwaj, N., Sharma, P., Kumar, V., "Phytochemicals as steel corrosion inhibitor: an insight into mechanism", ***Corrosion Reviews***, Vol. 39, No. 1, (2021), 27-41. doi.org/10.1515/corrrev-2020-0046

59. Wang, W., Song, Z., Guo, M., Jiang, L., Xiao, B., Jiang, Q., Chu, H., Liu, Y., Zhang, Y., Xu, N., "Employing ginger extract as an eco-friendly corrosion inhibitor in cementitious materials", ***Construction and Building Materials***, Vol. 228, (2019), 116713. doi.org/10.1016/j.conbuildmat.2019.116713

60. Ahanchi, M., Tabatabaei, M., Aghbashlo, M., Rezaei, K., Talebi, A.F., Ghaffari, A., Khoshnevisan, B., Khounani, Z., "Pistachio (Pistachia vera) wastes valorization: enhancement of biodiesel oxidation stability using hull extracts of different varieties", **Journal of Cleaner Production**, Vol. 185, (2018), 852-859. doi.org/10.1016/j.jclepro.2018.03.089

61. Medeiros, M.L., Cordeiro, A.M.M.T., Queiroz, N., Soledade, L.E.B., Souza, A.L., Souza, A.G., "Efficient Antioxidant Formulations for Use in Biodiesel", ***Energy & Fuels***, Vol. 28, (2014), 1074-1080. doi.org/10.1021/ef402009e

62. Rial, R.C., Freitas, O.N.d., Santos, G.D., Nazario, C.E.D., Viana, L.H., "Evaluation of the oxidative and thermal stability of soybean methyl biodiesel with additions of dichloromethane extract ginger (*Zingiber officinale* Roscoe)", ***Renewable Energy***, Vol. 143, (2019), 295-300. doi.org/10.1016/j.renene.2019.04.164

63. Sousa, L.S.D., Moura, C.V.R.D., Moura, E.M.D., "Action of natural antioxidants on the oxidative stability of soy biodiesel during storage", ***Fuel***, Vol. 288, (2021), 119632. doi.org/10.1016/j.fuel.2020.119632

64. Romola, C.V.J., Meganaharshini, M., Rigby, S.P., Moorthy, I.G., Kumar, R.S., Karthikumar, S., "A comprehensive review of the selection of natural and synthetic antioxidants to enhance the oxidative stability of biodiesel", ***Renewable and Sustainable Energy Reviews***, Vol. 145, (2021), 111109. doi.org/10.1016/j.rser.2021.111109

65. Akhlaghi, N., Najafpour, G.D., "Manganese ferrite ($MnFe_2O_4$) Nanoparticles: From synthesis to application -A review", ***Journal of Industrial and Engineering Chemistry***, Vol. 103, (2021), 292-304. doi.org/10.1016/j.jiec.2021.07.043

66. Akhlaghi, N., "Hemp Fibres as Novel Green Support Material for Immobilization of Acidithiobacillus ferrooxidans", ***International Journal of Engineering, Transactions C: Aspects***, Vol. 32, (2019), 1225-1230. doi: 10.5829/ije.2019.32.09c.01

67. Bayee, P., Amani, H., Najafpour, G.D., Kariminezhad, H., "Experimental Investigations on Behaviour of Rhamnolipid Biosurfactant as a Green Stabilizer for the Biological Synthesis of Gold Nanoparticles", ***International Journal of Engineering, Transactions C: Aspects*** Vol. 33. (2020), 1054-1060. doi:10.5829/IJE.2020.33.06C.02

68. Akhlaghi, N., Najafpour, G.D., Younesi, H., "Facile and green synthesis of cobalt oxide nanoparticles using ethanolic extract of Trigonella foenumgraceum (Fenugreek) leaves", ***Advanced Powder Technology***, Vol. 31, (2020), 3562-3569. doi.org/10.1016/j.apt.2020.07.004

69. Mehata, M.S., "Green route synthesis of silver nanoparticles using plants/ginger extracts with enhanced surface plasmon resonance and degradation of textile dye", ***Materials Science & Engineering B***, Vol. 273, (2021), 115418. doi.org/10.1016/j.mseb.2021.115418

70. Mittal, A.K., Chisti, Y., Banerjee, U.C., "Synthesis of metallic nanoparticles using plant extracts", ***Biotechnology Advances,*** Vol. 31, (2013), 346-356. doi.org/10.1016/j.biotechadv.2013.01.003

71. Kumar, K.P., Paul, W., Sharma, C.P., "Green synthesis of gold nanoparticles with Zingiber officinale extract: Characterization and blood compatibility", ***Process Biochemistry***, Vol. 46, (2011), 2007-2013. doi:10.1016/j.procbio.2011.07.011

72. Velmurugan, P., Anbalagan, K., Manosathyadevan, M., Lee, K.J., Cho, M., Lee, S.M., Park, J.H., Oh, S.G., Bang, K.S., Oh, B.T., "Green synthesis of silver and gold nanoparticles using Zingiber officinale root extract and antibacterial activity of silver nanoparticles against food pathogens", ***Bioprocess and Biosystems Engineering***, Vol. 37, (2014), 1935-1943. doi: 10.1007/s00449-014-1169-6

3. Yaqub, A., Malkani, N., Shabbir, A., Ditta, S.A., Tanvir, F., Ali, S., Naz, M., Kazmi, S.A.R., Ullah, R., "Novel Biosynthesis of Copper Nanoparticles Using Zingiber and Allium sp. with Synergic Effect of Doxycycline for Anticancer and Bactericidal Activity", ***Current Microbiology***, Vol. 77, (2020) 2287-2299. doi.org/10.1007/s00284-020-02058-4

74. Azizi, S., Mohamad, R., Rahim, R.A., Moghaddam, A.B., Moniri, M., Ariff, A., Saad, W.Z., Namvab, F., "ZnO-Ag Core Shell Nanocomposite Formed by Green Method using Essential Oil of Wild Ginger and Their Bactericidal and Cytotoxic Effects", ***Applied Surface Science***, Vol. 384, (2016), 517-524. dx.doi.org/doi:10.1016/j.apsusc.2016.05.052

75. Venkatadri, B., Shanparvish, E., Rameshkumar, M.R., Arasu, M.V., Al-Dhabi, N.A., Ponnusamy, V.K., Agastian, P., "Green synthesis of silver nanoparticles using aqueous rhizome extract of Zingiber officinale and Curcuma longa: In-vitro anti-cancer potential on human colon carcinoma HT-29 cells", ***Saudi Journal of Biological Sciences***, Vol. 27, (2020), 2980-2986. doi.org/10.1016/j.sjbs.2020.09.021

76. Eisa, W.H., Zayed, M.F., Anis, B., Abbas, L.M., Ali, S.S.M., Mostafa, A.M., "Clean production of powdery silver nanoparticles using Zingiber officinale: The structural and catalytic properties", ***Journal of Cleaner Production***, Vol. 241, (2019), 118398. doi.org/10.1016/j.jclepro.2019.118398

77. Ivashchenko, O., Gapinski, J., Peplińska, B., Przysiecka, L., Zalewski, T., Nowaczyk, G., Jarek, M., Gapinska, A.M., Jurga, S., "Self-organizing silver and ultrasmall iron oxide nanoparticles prepared with ginger rhizome extract: Characterization, biomedical potential and microstructure analysis of hydrocolloids", ***Materials & Design***, Vol. 133, (2017), 307-324. doi: 10.1016/j.matdes.2017.08.001

78. Judith Vijaya, J., Jayaprakash, N., Kombaiah, K., Kaviyarasu, K., John Kennedy, L., Jothi Ramalingam, R., Al Lohedan, H.A., Mansoor.Ali. V.M., Maaza, M., "Bioreduction potentials of dried root of Zingiber officinale for a simple green synthesis of silver nanoparticles: Antibacterial studies", J***ournal of Photochemistry & Photobiology, B: Biology***, Vol. 177, (2017), 62-68. doi:10.1016/j.jphotobiol.2017.10.007

79. Menon, S., Shrudhi Devi, K.S., Agarwal, H., Shanmugam, V.K., "Efficacy of Biogenic Selenium Nanoparticles from an Extract of Ginger towards Evaluation on Anti-Microbial and Anti-Oxidant Activities", ***Colloid and Interface Science Communications***, Vol. 29, (2019), 1-8. doi.org/10.1016/j.colcom.2018.12.004

80. Varghese, B., Kurian, M., Krishna, S., Athira, T.S., "Biochemical synthesis of copper nanoparticles using Zingiber officinalis and Curcuma longa: Characterization and antibacterial activity study", ***Materials Today: Proceedings***, Vol. 25, (2020), 302-306. doi.org/10.1016/j.matpr.2020.01.476

Persian Abstract

چکیده

ریشه زنجبیل، که معمولا با نام زنجبیل شناخته می¬شود، یکی از گونه¬های رایج در غذا و طب سنتی است. زنجبیل غنی از انواع ترکیبات آب دوست و آبگریز است که خواص متفاوتی دارند. دارا بودن عطر تازه، طعم تند، و انواع خواص مفید برای سلامتی، و همچنین ارزان قیمت و در دسترس بودن از مزایای ریشه زنجبیل است. علاوه بر جنبه¬های درمانی در طب گیاهی و مصرف به عنوان یک طعم دهنده در غذا، ریشه زنجبیل توانایی بالقوه برای کاربرد در دیگر زمینه¬ها دارد. در این مقاله مروری، انواع کاربردهای زنجبیل، شامل استفاده از آن برای محافظت از غذا و بسته بندی محصولات غذایی، نرم کننده محصولات گوشتی، خواص درمانی، کاربرد آن به عنوان مهار کننده خوردگی فلزات، محافظت از بیودیزل در مقابل اکسید شدن، و نقش آن در ساخت نانو ذرات فلزی مورد بحث و بررسی قرار می¬گیرد. در کل، این مقاله مروری اطلاعات ارزشمندی در مورد ریشه زنجبیل به عنوان یک ماده با منشا گیاهی، علارغم کاربرد آن به عنوان یک گیاه داروی و طعم دهنده فراهم آورده است.

IJE TRANSACTIONS B: Applications Vol. 36, No. 02, (February 2023) 384-397

International Journal of Engineering

Journal Homepage: www.ije.ir

Determination of Blast Impact Range and Safe Distance for a Reinforced Concrete Pile Under Blast Loading

M. Khodaparast*, S. H. Hosseini, H. Moghtadaei

Faculty of Engineering, University of Qom, Qom, Iran

P A P E R I N F O

Paper history:
Received 14 November 2022
Received in revised form 06 December 2022
Accepted 10 December 2022

Keywords:
Reinforced Concrete Pile
Blast Loading
Damage
Coupled Eulerian-lagrangian Method
Clayey Soil
Sandy Soil

A B S T R A C T

Piles transfer structural loads to the hard layers of the soil or rock; thus, any damage to the pile foundations could have irreparable consequences. A surface blast can create a ground shock that transmits the blast energy along the surface and at depths. Explosion research necessitates technical design to mitigate the adverse effects on nearby structures and facilities. The blast impact range and the safe distance at which the pile will avoid structural damage are two critical parameters for the design of a pile under blast loading. Therefore, this study used the coupled Eulerian-Lagrangian method to determine the blast impact range and safe distance for reinforced concrete piles (RC piles) subjected to blast loading. The results for clayey and sandy soils revealed that an increase in the explosive depth had no significant effect on the safe distance, despite a decrease in the compressive and tensile damage to the pile. Increasing the mass and depth of the blast decreased the ultimate compressive bearing capacity of the pile and increased the blast impact range. Sandy soil performed better than clayey soil against blast loading. The findings of this study can be applied to various projects, including critical structures near gas transmission lines or vulnerable to terrorist attacks.

doi*: 10.5829/ije.2023.36.02b.17*

1. INTRODUCTION

Pile foundations are used in civil structures to transfer the structural load to the depth of the soil or rock layers. It is critical to consider soil behavior in dynamic load presence [1, 2]. Any damage to the pile foundations can lead to failure of the structure [3]. The shockwave from a surface explosion will transfer the blast energy along the ground surface and to the underlying layers. One potential source of damage which can lead to failure of a pile from blast loading is an explosion at the surface or in the depths. As a pile collapses under blast loading, the upper structure will become vulnerable and collapse; therefore, it is necessary to evaluate the damage factors in a pile subjected to blast loading [4].

The studies conducted on this subject have used both field and laboratory experiments as well as analytical and numerical methods for their investigations. However, because of the difficulties and security issues associated with field and laboratory experiments, numerical methods more often are used. Therefore, many numerical studies have been prepared in this field.

Prasanna and Boominathan [5] conducted a numerical study on the factors influencing the response of underground tunnels subjected to internal blasts using the finite element method. They studied the effect of the blast on variables that included the material, thickness and shape of the lining. They also found that box-shaped tunnels were more vulnerable to blasts than horseshoe-shaped and circular tunnels.

Problems related to numerical modeling of the blast load include the large deformation caused by the blast load and consideration of the soil-structure interaction. Qiu et al. [6] applied the coupled Eulerian-Lagrangian method (CEL) to geotechnical problems with large deformations. They found that the CEL method was suitable for solving problems caused by major deformations, such as severe distortion and contact problems. They also found this method suitable for investigation of the soil-structure interaction in

*Corresponding Author Institutional Email: khodaparast@qom.ac.ir (M. Khodaparast)

Please cite this article as: M. Khodaparast, S. H. Hosseini, H. Moghtadaei, Determination of Blast Impact Range and Safe Distance for a Reinforced Concrete Pile Under Blast Loading, ***International Journal of Engineering, Transactions B: Applications***, Vol. 36, No. 02, (2023), 384-397

geotechnical problems with large deformations, such as explosions.

Other researchers also have investigated the impact of the blast load on the pile foundations. The behavior of pile foundations in saturated sandy soil under blast loading was investigated by Jayasinghe et al. [7] by considering the soil-pile interaction in FE software using LS-DYNA. They studied the distribution of the blast waves in the soil, vertical deformation of the pile, and effective stresses on the pile. The results showed that the pile head was more vulnerable to blast waves and that the effect of the blast on the pile decreased as the distance between them increased.

Huang et al. [8] developed a numerical dynamic analysis approach in LS-DYNA to evaluate the soil-pile interaction under blast loading. They found that the maximum shear stress on the head of the pile was greater than at the tip and that the stress distribution along the pile length showed an inverted triangular model. They also found that the maximum contact pressure between the soil and pile was concentrated at the pile head.

Jayasinghe et al. [9] studied the blast response of RC piles in saturated sandy soil. They reported that sufficient longitudinal reinforcement and proper detailing of transverse reinforcement could reduce the vulnerability of RC piles.

Chakraborty [10] carried out a numerical study in Abaqus to analyze the performance of a hollow steel pile exposed to an explosion at depth. It was concluded that the lateral deformation increased with an increase in the lateral load. It was also found that, in loose soil, the maximum velocity in the soil particles increased as the elastic modulus, specific gravity, and friction angle decreased.

Jayasinghe et al. [11] used a numerical study to evaluate the response and possible damage to a rock-socketed pile near the soil-rock interface when subjected to ground shock excitation in LS-DYNA. They found that the pile was relatively vulnerable and the soil properties significantly influenced the response of the pile when subjected to blast loading.

Jayasinghe et al. [12] carried out a field test on the pile response to blast-induced ground motion in Singapore. They calculated the structural and geotechnical bearing capacity of the pile using experimental methods and the pile bearing capacity. The results showed that, in a fixed-head pile, the maximum bending moment occurred at the pile head. The free-head pile recorded higher bending moments at the mid-height of the pile and zero bending moment at the pile head due to the absence of restraints at the top. In all cases, the maximum axial force was applied to the pile head.

Ibrahim and Nabil [13] evaluated the risk of a surface blast load on pile foundations. They reported that wall barriers containing expanded polystyrene between the pile and blast load reduced the blast effect better than other types of wall barriers.

Bakhshandeh Amnieh et al. [14] used numerical and field analysis to investigate the vibrations caused by explosions in oil pipelines. This research records explosion vibrations in the Izeh-Karun 3 main road project using four three-component seismographs. The stresses applied to the oil pipeline were measured using a static analysis of the stress caused by the oil pipeline's internal pressure and a dynamic analysis of the ground vibration. The results showed that the vibrations caused by the blasting operation did not damage the oil pipeline and that the pipelines near the blasting operation were at a safe distance.

The results of research done on the destructive effects of blasts at the ground surface and at depth indicate that it is necessary to take into account their effects and the pressure distribution during the design of structures, especially piles. Explosion research necessitates technical design to mitigate the adverse effects on nearby structures and facilities. The blast impact range and the safe distance at which the pile will avoid structural damage are two critical parameters for the design of a pile under blast loading. Therefore, this study used the coupled Eulerian-Lagrangian method to determine the blast impact range and safe distance for reinforced concrete piles (RC piles) subjected to blast loading. In the present study, the safe distance has been considered to be the minimum distance of an explosive from a pile for which the tension and compression damage values for the concrete are lower than the final tension and compression damage values so that the pile does not experience structural damage.

The blast impact range has been defined as the shortest safe distance to the pile after which the effect of blast loading on the pile becomes negligible. The blast impact range and safe distance are important parameters that can be used to determine the effect of the impact of blast loading on the pile and anticipate aspects of the design that will become necessary to reduce the effects of the blast wave to a suitable range and distance from the pile.

Despite the importance of the effect of blast loading on the design of piles, only a small number of studies have investigated the effect of blast impact range and safe distance under blast loading. The current research investigated the effect of blasts on determining the safe distance and blast impact range for an RC pile using a three-dimensional numerical model in Abacus software.

The results for clayey and sandy soils were compared. To determine the safe distance, 50 to 500 kg of TNT were used beginning at the shortest allowable distance from the pile (1 m) at the ground surface and at depths of 1 to 6 m. The safe distance for each explosive weight was determined so as not to exceed maximum damage to the

RC pile using the tensile and compressive damage values.

The blast impact range also was determined in order to comprehend the influence of the blast length and depth on the RC pile. The blast impact range for Q2/Q1 (ratio of ultimate compressive bearing capacity of pile after the blast to ultimate compressive bearing capacity of pile before the blast) and Ql2/Ql1 (ratio of ultimate lateral bearing capacity of pile after the blast to ultimate lateral bearing capacity of pile before the blast) were investigated for a TNT blast using 50 to 500 kg at the ground surface and at a depth of 6 m from the ground surface.

2. NUMERICAL MODELING

Abaqus version 6.13 uses the FE method and has applications in civil engineering analysis, especially geotechnical engineering. It is also used for analysis of nonlinear dynamic problems, especially blast loading. In Abaqus/Explicit, the effect of blast loading on structures can be analyzed using CEL technique [15].

2. 1. FE Modeling of Soil A 3D FE model for clayey and sandy soils using Lagrangian elements is presented. The dimensions considered were 30 × 30 × 30 m to prevent boundary effects. The stress-strain response of sandy soil has been modeled using the Drucker-Prager plastic model [10-16]. Because there is no time for drainage to occur under impact blast loading, the soil mass can be considered as a single-phase material under these conditions and total stress analysis can be carried out. In this study, the behavior of clayey soil was simulated using an elasto-plastic Drucker-Prager cap model. This was originally developed to predict the plastic deformation of soil under compression [16,17].
Table 1 lists the characteristics of the sandy soil [10]. The stress-strain curve for Ottawa sand was taken from Chakraborty [10]. Figure 1 shows the curve and stress-strain relationship of Ottawa sand at a strain rate of 1000/s [10]. Table 2 summarized the properties of clayey soil [17].

The mesh for the FE model was generated using eight-node brick elements (C3D8R) with reduced integration and hourglass control. Finer mesh was generated such that the minimum size of the elements near the blast was 10 mm and the maximum size at a distance from the blast was 10 cm [10]. In order to model the soil-pile interaction, the general contact option in Abaqus was used with hard contact in the normal direction and frictional contact in the tangential direction (δ=1/3ø [6]).

Boundary conditions constrained the bottom of the model to prevent movement in all directions [10]. In this model, the boundaries were considered to be practically non-reflective [6, 18]. The dimensions of the soil model were such that the blast wave did not reach the boundaries of the soil space; therefore, it had no effect on the boundaries and returned to the soil space. The vertical, front, and rear boundaries of the soil provided horizontal and rotational fixity to constrain displacement perpendicular to the planes (Ux, Uy, Uz) and rotations (URx = URy = URz = 0), respectively (Figure 2). The FE

TABLE 1. Sandy soil properties [10]

Parameter	Value
modulus of elasticity (*E*)	28 MPa
Poisson's ratio (ν)	0.2
density (ρ)	1560 kg/m^3
cohesion (*d*)	0 MPa
angle of internal friction (ϕ)	30°
dilation angle (ψ)	5°

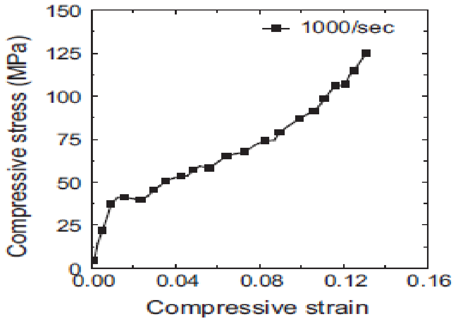

Figure 1. Stress–strain curve of Ottawa sand at 1000/s strain rate [10]

TABLE 2. Clayey soil properties [17]

Parameter	Value	
Modulus Of Elasticity (*E*)	51.7 MPa	
Poisson's Ratio (ν)	0.45	
Density (P)	1920 kg/m^3	
Cohesion (*D*)	0.036 MPa	
Angle Of Internal Friction (ϕ)	24°	
Cap Eccentricity Parameter (*R*)	0.3	
Initial Cap Yield Surface Position (ε_v)	0.02	
Transition Surface Radius Parameter (*A*)	0	
Cap Hardening Behavior	Stress	PVS
(Stress- Plastic Volumetric Strain (Pvs))	2.75 MPa	0
	4.83 MPa	0.02
	5.15 MPa	0.04
	6.20 MPa	0.08

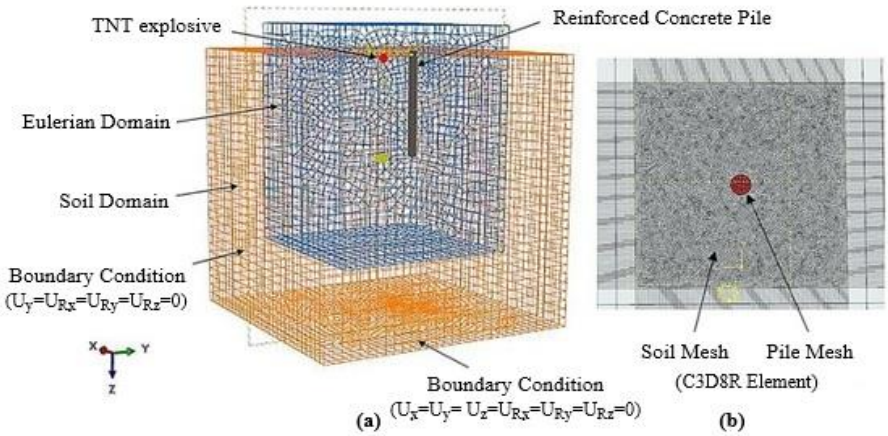

Figure 2. (a) FE model and boundary conditions; (b) soil and pile mesh with types of element

model, mesh, and boundary conditions are shown in Figure 2.

2. 2. FE Modeling of Explosive The TNT was modeled as a Eulerian element using ABAQUS/CEL. Three-dimensional eight-node continuous elements were used to model the explosives with reduced integration (EC3D8R). The Eulerian elements containing explosive were filled with explosive material and the remainder of the Eulerian grid was a void. In Eulerian analysis, the material is tracked by means of the Eulerian volume fraction (EVF) as it flows through the mesh. The EVF represents the ratio to which each Eulerian element is filled with material; thus, EVF = 1 represents an element that is completely filled with material and EVF = 0 represents a complete void [15]. Eulerian and Lagrangian elements were considered to be in contact (using the general contact option) according to the explosive depth, pile and soil values. In order to avoid reflection of the blast wave into the Eulerian environment, free-flow boundary conditions were considered. The explosive was modeled using the equation of state (JWL). This equation models the pressure created by the blast from a chemical explosive. The JWL equation of state (EOS) is [15]:

$$P = A\left(1-\frac{\omega\rho}{R_1\rho_0}\right)\exp\left(-R_1\frac{\rho_0}{\rho}\right)+B\left(1-\frac{\omega\rho}{R_2\rho_0}\right)\exp\left(-R_2\frac{\rho_0}{\rho}\right)+\omega\rho E_m \tag{1}$$

where A, B, R1, R2, and ω are material constants for the TNT. Parameters A and B represent the pressure magnitude, ρ0 is the explosive density in the solid state, ρ is the current density, and Em is the internal energy per unit of mass. The properties of the explosive for the JWL EOS are shown in Table 3. The explosive mass ranged from 50 to 500 kg of TNT and were modeled as a cubic element at distances of 1 to 4 m in accordance with the safe distance at each explosive mass at the surface and at depths of 1 to 6 m (Figure 3).

TABLE 3. TNT characteristics [10]

Parameter	Value
density (ρ)	1630 kg/m^3
detonation wave speed (v)	6930 m/s
A	373800 MPa
B	3747 MPa
ω	0.35
R_1	4.15
R_2	0.9
detonation energy density (E_m)	3680 kJ/kg

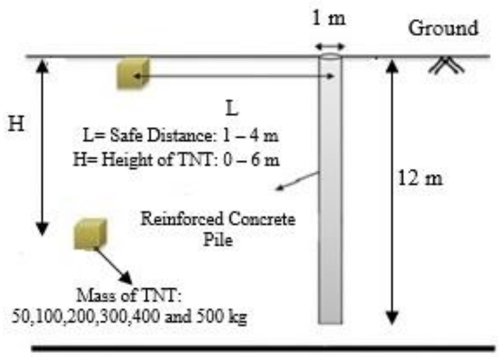

Figure 3. Explosive weight and position for modeling

2. 3. FE Modeling of RC Pile The piles and reinforcements were modeled using Lagrangian elements in ABAQUS/CAE. The diameter and the length of the piles were 1 and 12 m, respectively. The piles were reinforced with 16 tension-compression bars of 25 mm in diameter (16T25). Bars of 10 mm in diameter spaced 100 mm apart (T10@10cm) were used for shear reinforcement of the piles. The concrete and reinforcements of the piles were modeled using the concrete damage plasticity and Johnson-Cook hardening behavior models, respectively [19]. The properties of the modeled RC piles are shown in Table 4. Stress-strain curves for compression and tension and the damage versus compression and tension strain curves are shown in Figure 4 [19]. The stress-strain behavior of the steel reinforcing bars was defined using the Johnson-Cook (J-C) hardening behavior model. This model is usually used for high strain-rate materials, especially metals. The dynamic yield stress-strain equation of the J-C model with rate dependent strains is [15]:

$$\bar{\sigma}=\left[A+B(\bar{\varepsilon}^{pl})^{n}\right]\left[1+C\ln\varepsilon^{*}\right](1-\hat{\theta}^{m}) \quad (2)$$

where $\bar{\varepsilon}^{pl}$ is the equivalent plastic strain, ε* is plastic strain equal to $\varepsilon^{*}=\frac{\dot{\bar{\varepsilon}}^{pl}}{\dot{\varepsilon}_0}$, $\dot{\bar{\varepsilon}}^{pl}$ is the equivalent plastic strain rate, and $\dot{\varepsilon}_0=1/s$ is the reference strain rate. *A*, *B*, *C*, *m*, and *n* are the constant parameters of the model and $\hat{\theta}$ is the corresponding temperature. Parameters *C* and $\dot{\varepsilon}_0$ are related to the dependent strain rate. The properties of the modeled reinforcement bars are shown in Table 5 [10].

TABLE 4. Properties and parameters of RC pile [19]

Parameter	Value
modulus of elasticity (E)	27.4 GPa
poisson's ratio (ν)	0.2
density (ρ)	2400 kg/m^3
flow potential eccentricity (ε)	0.1
dilation angle (β)	36°
K_c	0.666
fb0/fc0	1.16

Note: Kc=The ratio of uniaxial tensile deflection stress to uniaxial compressive deflection stress; fb0/fc0=The ratio of biaxial compressive strength of concrete to uniaxial compressive strength.

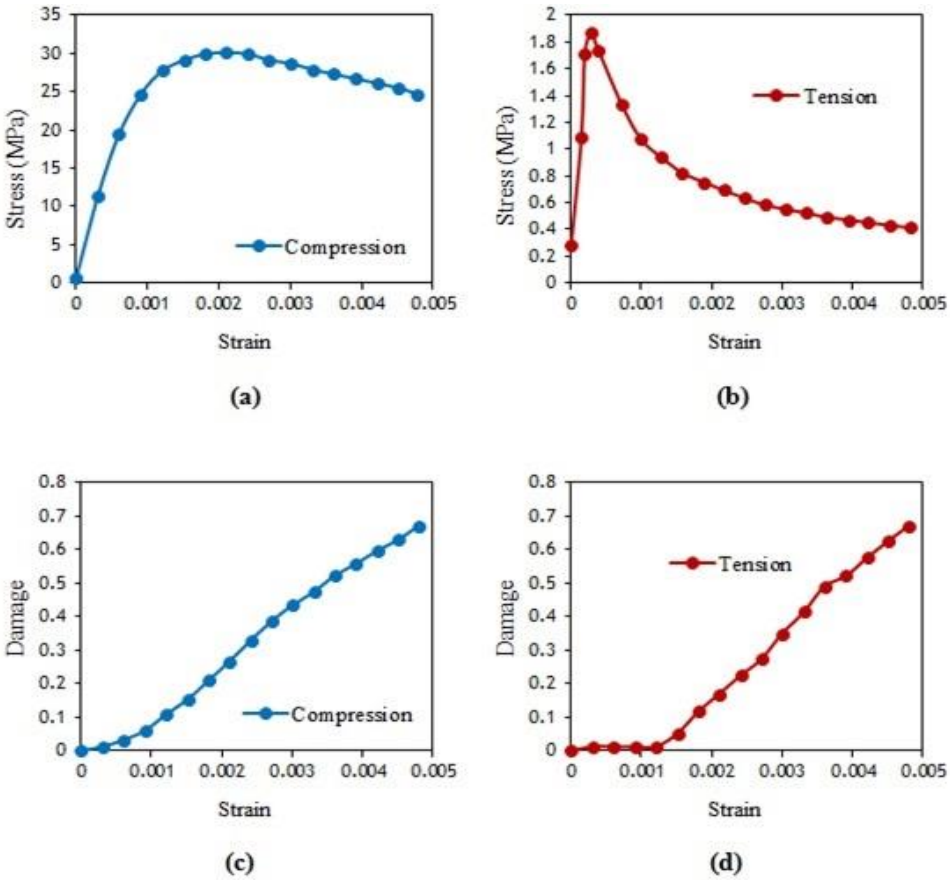

Figure 4. Concrete curves for: (a) compression stress-strain; (b) tension stress-strain; (c) compression damage-strain; (d) tension damage-strain [19]

TABLE 5. Properties and parameters of reinforcement [10]

Parameter	Value	
modulus of elasticity (E)	200 GPa	
Poisson's ratio (ν)	0.3	
density (ρ)	7800 kg/m^3	
yield strength (f_s)	350 MPa	
hardening parameters of J-C model	A	360 MPa
	B	635 MPa
	n	0.114
	C	0.075

The pile mesh was generated using an eight-node brick element (C3D8R) with reduced integration, hourglass control, and longitudinal and transverse reinforcement using a two-node element (T3D2). The size of the mesh elements was 10 cm for the pile and 1 cm for the reinforcement. The pile-reinforcement interaction was considered using the general contact option and embedment of the reinforcements in the pile was considered using the embedded region option in Abaqus [19]. Figure 5 shows the FE model of the pile and reinforcements.

2. 4. Model Analysis Explicit dynamic analysis was performed using the CEL and central difference integration methods in one step. The CEL method carries out both the Lagrangian and Eulerian methods in Abaqus [18]. In numerical analysis using the CEL method, the Euler materials along the mesh are calculated using EVF. Each Eulerian element represents a percentage that denotes its solidness. The contact between the Eulerian and Lagrangian materials is considered using the general contact option based on the penalty contact method. Lagrangian elements can move along the Eulerian mesh without resistance until they reach an EVF $\neq$ 0 element [6].

The central difference method uses a time difference (Δt) that is smaller than the current time frame. The time difference is represented as $\Delta t \leq l/c$, where l is smallest dimension of the element and c is the speed of sound of the distributed wave in the model. The total time required for analysis was 25 ms; thus, the wave created by the blast was able to spread and transmit throughout the pile. In order to properly distribute the compressive stress wave caused by the blast, artificial bulk viscosity was activated using the quadratic and linear functions and a volumetric strain rate with default values of 1.2 and 0.06 [10].

3. VRIFICATION OF NUMERICAL MODEL

The numerical model was validated in three parts and the results were compared with those from the experimental study by Jayasinghe et al. [7] numerical study using LS-DYNA, and Chakraborty [10] numerical study using Abaqus. Jayasinghe et al. [7] studied an aluminum hollow-pipe pile with a height of 14.3 cm in saturated sandy soil under blast loading in a 70g centrifuge test. The results of displacement along the pile and the maximum stress at different distances from the pile were compared with the results of the present study and the numerical model of Jayasinghe et al. [7]. Figure 6 shows the position of the pile and explosive in Jayasinghe et al. [7] model.

Table 3 shows the properties of the TNT. The sandy soil had a specific gravity of ρsoil = 1937 kg/m^3, elastic modulus of Esoil = 10 MPa, and internal friction angle of ϕ = 31.4° [7]. Figures 7(a) and 7(b), respectively, show displacement along the pile and the maximum soil stress at different distances from the pile from Jayasinghe et al. [7] and the numerical model developed in this study. As seen, the results showed good agreement with those of Jayasinghe et al. [7].

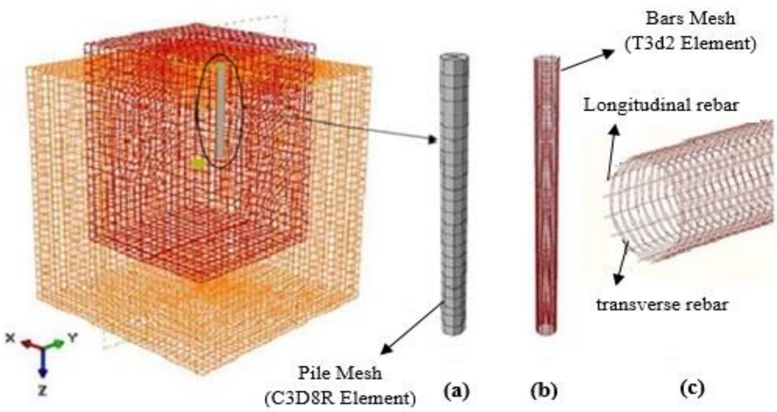

Figure 5. FE model of: (a) pile mesh; (b) bars mesh; (c) reinforcement

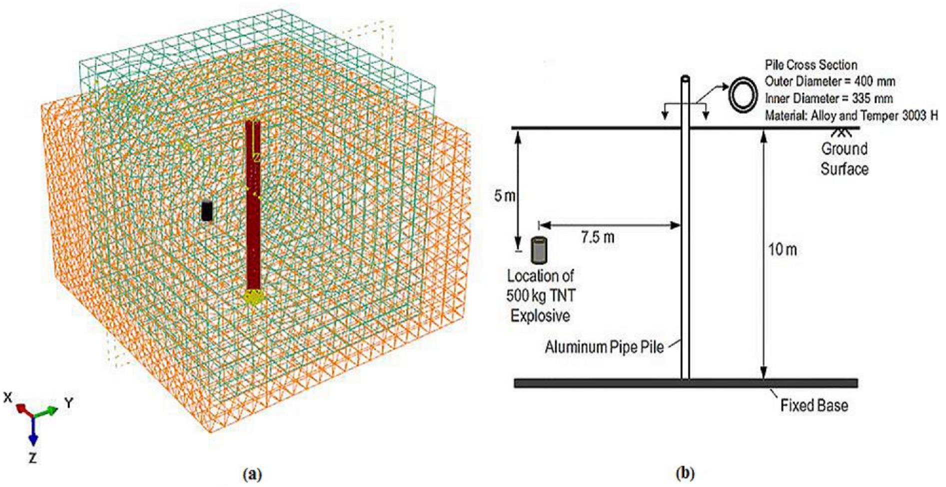

Figure 6. Jayasinghe et al. [7] model: (a) FE modeling for validation; (b) position of pile and explosives in soil

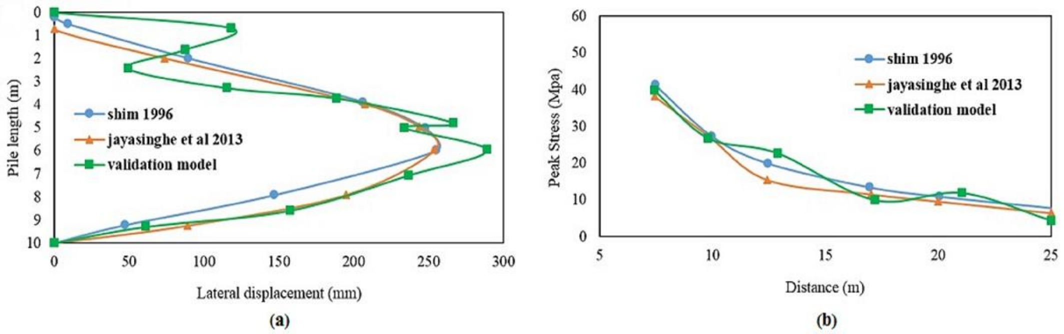

Figure 7. Verification of proposed numerical model using results from experimental model and numerical model [7]: (a) lateral displacement along pile; (b) maximum stress at different distances to the pile

Chakraborty [10] used Abaqus to model two thin steel piles buried in sandy soil exposed to blast loading at a distance of 3 m. A 3D environment of 20 × 20 × 20 m was considered for the soil. The pile was subjected to an axial force of 500 kN. The positions of the piles and explosives is shown in Figure 8. Tables 3 and 5 show the JWL model of the TNT and the properties of the steel pile, respectively. The sandy soil had a specific gravity of specific gravity of ρsoil = 1530 kg/m^3, elastic modulus of Esoil = 28 MPa, internal friction angle of ϕ = 30°, Poisson's coefficient of v = 0.2, and dilation angle of ψ = 5°. The stress-strain response of sandy soil at a strain rate of 1000/s is shown in Figure 1 [10].

Figure 9 compares the maximum lateral displacement of the pile head under blast loading and the results from Chakraborty [10]. As seen, there is an adequate agreement between the results of the current model and Chakraborty [10].

4. RESULTS AND DISCUSSION

4. 1. Determination of Safe Distance of RC Pile Under Blast Loading In this study, the safe distance is the minimum distance of an explosive from a pile for which the tension and compression damage values for the concrete are lower than the final tension and compression damage values. At this value, the pile does not experience structural damage. The safe distance of a pile in clayey and sandy soils was determined by comparing the tensile and compressive damage parameters of the RC pile. The concrete damage factor is defined as follows [15]:

$$\sigma = (1-d)E_0\varepsilon \tag{3}$$

where d is the dimensionless factor of concrete damage. This parameter is a criterion for determining the failure area in the concrete. The maximum amount of d denotes complete failure in the concrete. Equations (4) and (5) show the extent of damage to the concrete when exposed to tension and compression, respectively [15]:

$$\sigma_t = (1-d_t)E_0(\varepsilon_t - \varepsilon_t^{pl}) \tag{4}$$

$$\sigma_c = (1-d_c)E_0(\varepsilon_c - \varepsilon_c^{pl}) \tag{5}$$

where subscripts *t* and *c* denote tension and compression, respectively, d_t and d_c are the tension and compression

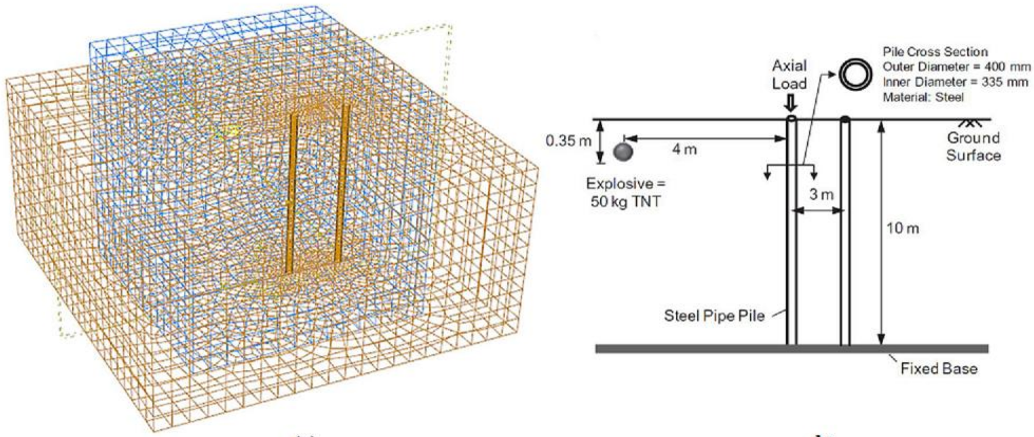

Figure 8. (a) Verified FE model; (b) location of pile and explosive in verified model [10]

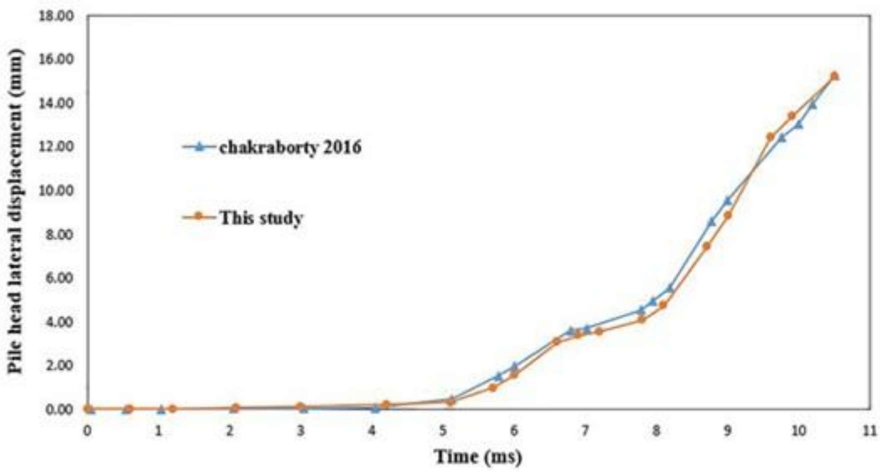

Figure 9. Comparison of pile head lateral displacement results from this study and Chakraborty [10]

damage factors, ε_t and ε_c are the total strains, ε_t^{pl} and ε_c^{pl} are the equivalent plastic strains, and E_0 is the initial (undamaged) elastic stiffness of the material.

A specific concrete damage factor can be defined for each point on the concrete stress-strain curve under compression or tension. Figure 4 shows that the final tension and compression damage values were 0.7437 and 0.7035, respectively. This means that the concrete failed at the final tension and compression damage values and lost effectiveness. This criterion can be used to obtain a safe distance from an explosion to avoid the structural failure of a pile. When the concrete damage factor exceeds the final values, the RC pile will fail; thus, the safe distance can be defined as the distance within which the structure of the pile will not fail under blast loading.

In order to determine the safe distance, initially, 50 kg of TNT was used at the distance nearest to the pile (1 m) and the tension and compression damage values were obtained. If those values exceeded the maximum concrete damage factor, the distance was increased by 1 m and analysis was repeated until the safe distance was obtained. Analysis was carried out for TNT at the surface of the ground and at depths of 1 to 6 m and for TNT mass of 100, 200, 300, 400 and 500 kg. Figure 10 compares the damage values at safe and unsafe distances for 300 kg of TNT at the surface of the ground in clayey soil. The color red on the pile represents exceedance of the damage value when exposed to tension and compression which resulted in structural failure of the pile. Figures 10(c) and 10(d) do not exceed the damage values for the pile when exposed to tension and compression. Figure 11 shows the tensile and compressive damage values for the RC pile in clayey soil at a distance of 3 m for explosive masses at the surface and at depths of 2, 4 and 6 m.

Figure 11 shows that the tension and compression damage values are below the maximum values (0.7437 and 0.7035, respectively) at a distance of 3 m for all explosive masses except for 500 kg of TNT. For the 500 kg explosive, these values had reached their final values, and the RC pile broke at this distance.

To obtain a safe distance for 500 kg of TNT, it was placed at a further distance than in the first step (4 m) to reduce the tensile and compressive damage to their ultimate values. Therefore, it can be concluded that a distance of 3 m for all explosive masses below 500 kg is the safe distance. The other tensile and compressive damage values for RC pile at all explosive masses at different depths in clayey soil.

Figure 11 also shows that the damage values decreased as the depth of the blast increased. For example, the tensile damage for 200 kg of TNT at the surface to a depth of 6 m decreased from 0.0755 to 0.0505, a change of 67%. Figure 12 evaluates the tensile and compressive damage to a RC pile in sandy soil at a distance of 3 m for all explosive masses at the surface and at depths of 2, 4, and 6 m.

Figure 12 shows that, unlike in clayey soil, the tension and compression damage in sandy soil was below the maximum values (0.7437 and 0.7035, respectively) at a distance of 3 m for all explosive masses. The effects of explosive mass and depth of blast on the tensile and compressive damage of the RC pile are similar to those for clayey soil. Comparison of Figures 11 and 12 indicate that the tensile and compressive damage values in sandy soil were lower than in clayey soil under similar conditions.

When a blast occurs, a shock wave propagates through the soil particles. The velocity of the wave depends on the modulus of elasticity (E) and density (ρ) of the soil. In sandy soil, the velocity of the blast wave usually is lower than in clayey soil because of the high values for E and ρ. Therefore, it can be said that sandy soil showed better resistance to blasting damage than did clayey soil.

Table 6 lists the safe distance values for tensile and compressive damage at different distances for masses of 100, 200, 300, 400 and 500 kg of TNT at the surface and at depths of 1 to 6 m. The safe distance for 50 kg of TNT was 1 m, which means that the pile was not damaged at

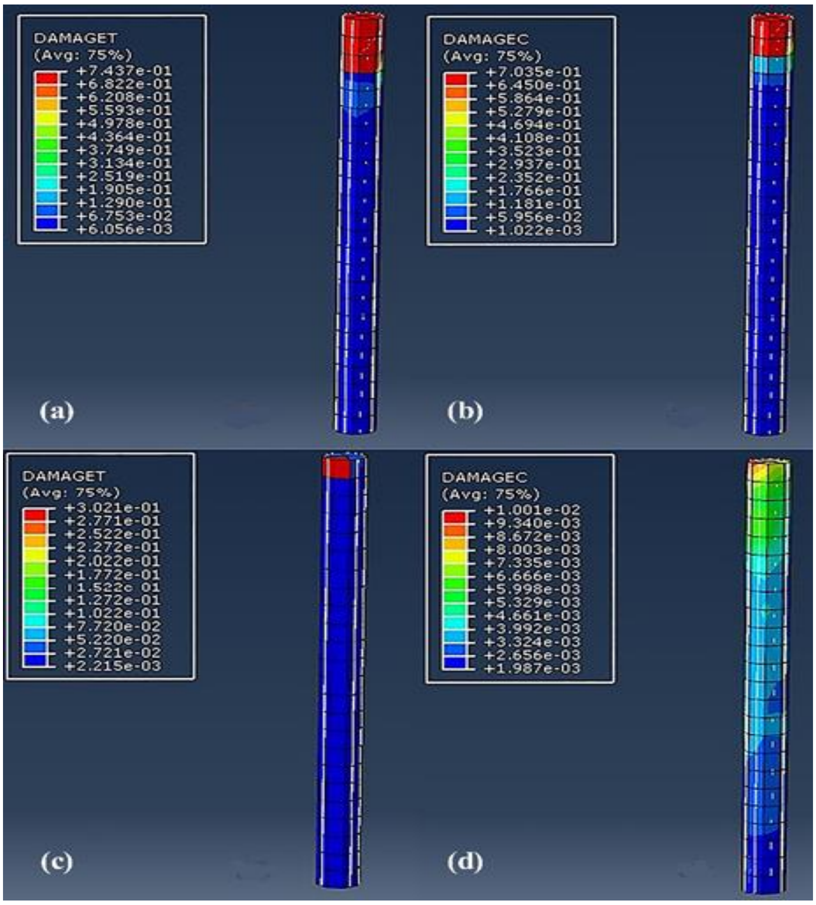

Figure 10. Comparison of damage for 300 kg TNT in clayey soil: (a) tension damage at an unsafe distance of 2 m; (b) compression damage at an unsafe distance of 2 m; (c) tension damage at a safe distance of 3 m; (d) compression damage at a safe distance of 3 m

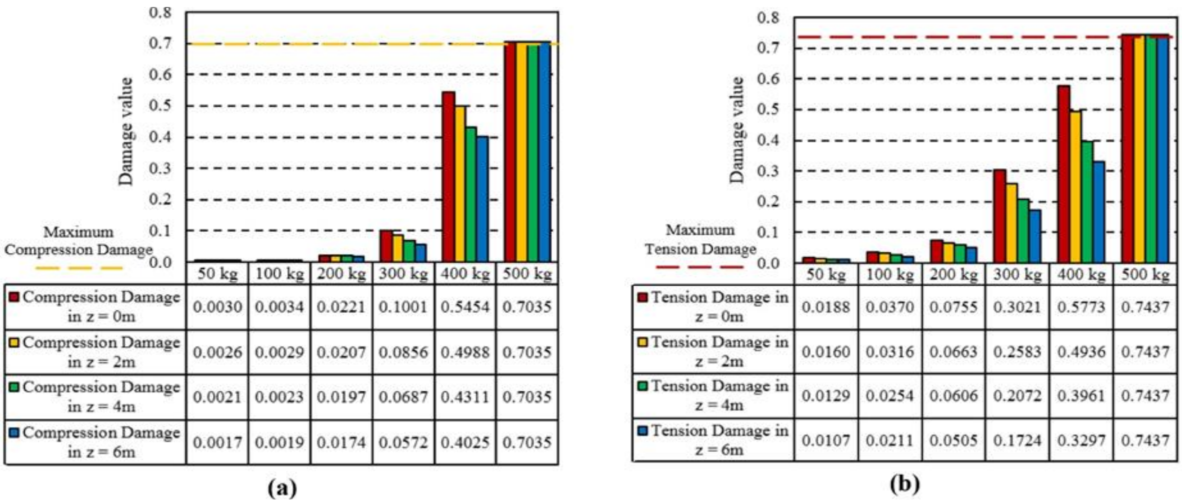

Figure 11. Tension and compression damage in RC piles in clayey soil for all explosive masses at 3 m at the surface and at depths of 2, 4 and 6 m: (a) compression; (b) tension

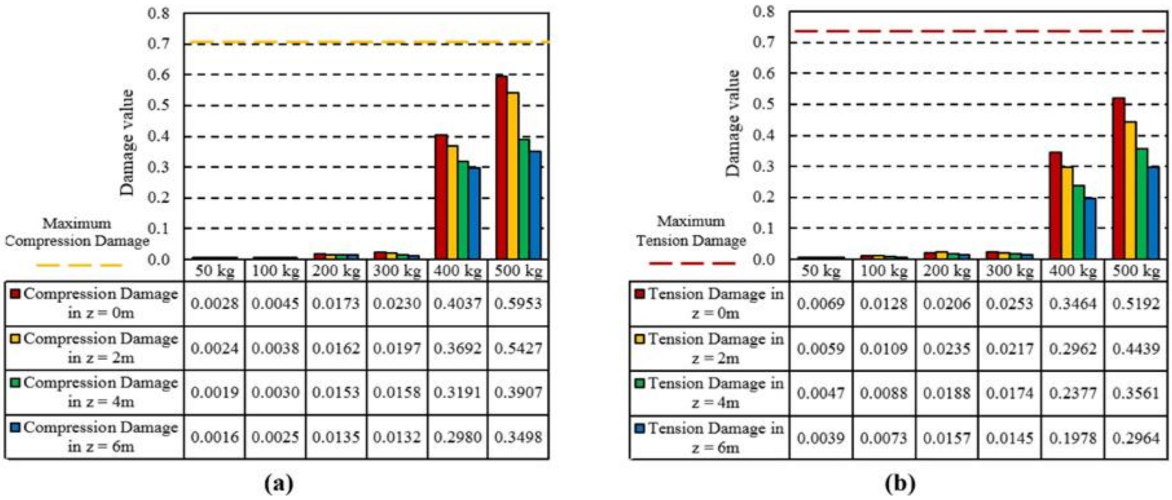

Figure 12. Tension and compression damage in RC piles in sandy soil for all explosive masses at 3 m at the surface and at depths of 2, 4 and 6 m: (a) compression; (b) tension

TABLE 6. Safe distances for all explosive masses at surface and at depths of 1 to 6 m in clayey and sandy soil

	Safe distance at all depths (m)	
Mass of TNT (kg)	**Clay**	**Sand**
50	1	1
100	2	1
200	2	2
300	3	2
400	3	3
500	4	3

the minimum distance. The safe distance for the RC pile for 100 kg of TNT was 2 m in clayey soil, but under such conditions, the sandy soil had a safe distance of 1 m, which means that the pile lost efficiency at a distance of 1 m. This suggests that a change in soil type from clay to sand will reduce the safe distance to about 1 m. The reason could be the lower density, lower Poisson's ratio and lower modulus of elasticity of sandy soil compared to clay soil, which better controlled the blast wave and reduced damage [13]. It can be stated that soil type plays a significant role in controlling damage and reducing the safe distance.

An increase in the TNT mass increased the safe distance. For example, the safe distance for 50 kg of TNT was 1 m and for 500 kg TNT was 4 m. The safe distances in clay soil for explosive masses of 100 and 200 kg, as well as for 300 and 400 kg, were the same. Table 6 reveals that the safe distance at different depths were constant in the numerical models and the safe distances in sandy soil did not change according to depth as they did in the clayey soil. Thus, an increase in explosive depth did not significantly reduce damage (especially tensile damage) at an unsafe distance or reduce the ultimate damage (rupture) in the pile.

Figure 13 shows the tension damage in a pile for 200 kg of TNT at an unsafe distance of 1 m at the surface in both clayey and sandy soil. The damage observed in clayey soil was much greater than that in sandy soil. The damage values in clayey soil exceeded the allowable maximum value (0.7437). In sandy soil, the damage values only reached the boundaries of the maximum value (0.7437). The destruction of the pile shell and reinforcements is shown in Figure 13(a) for clayey soil. It is clear that sandy soil was more effective in controlling damage and damping destructive excitation.

4. 2. Determination of Blast Impact Range in Clayey and Sandy Soil In this study, the blast impact range has been defined as the nearest safe distance of a pile after which the effect of blast loading on the pile becomes negligible. In order to determine the blast impact range, the nearest safe distance at the surface and at a depth of 6 m was determined for different TNT explosive masses.

This distance then was increased such that Q2/Q1 (the ratio of ultimate bearing capacity of pile after the explosion to ultimate compressive bearing capacity of pile before the explosion) and Ql2/Ql1 (the ratio of ultimate lateral bearing capacity of pile after the explosion to ultimate lateral bearing capacity of pile before the explosion) ratio values approached 1. In other words, the distance was increased until the blast wave no longer had an effect on the pile.

As prepared by Jayasinghe et al. [11] to determine the bearing capacity of piles under blast loading, in the present study, only the geotechnical bearing capacity of the pile was calculated after placing the pile at the safe distance. In order to calculate Q2/Q1 and Ql2/Ql1, the final compression capacity of the pile before the blast was calculated using the Meyerhof method as Q1 [20]. The maximum stress values for skin friction and the tip of the pile after the blast were obtained using the numerical model and were subtracted from the stress values for skin friction and the tip of the pile before the blast. The final compression capacity of the pile (Q2) after the explosion can be calculated as follows:

$$Q_1 = \left[(q_{p1})\times A\right] + \left[(q_{f1})\times PL\right] = \left[Q_{p1}\right] + \left[Q_{f1}\right] \quad (6)$$

$$Q_2 = \left[(q_{p1} - q_{p2})\times A\right] + \left[(q_{f1} - q_{f2})\times PL\right] = \left[Q_{p2}\right] + \left[Q_{f2}\right] \quad (7)$$

where Qp1 and Qp2 are the bearing capacity of the pile tip before and after the blast, respectively, and Qf1 and Qf2 are the bearing capacity of skin friction before and after the blast, respectively. Variables Qp1 and Qp2 are the maximum vertical stresses at the tip of the pile before and after the blast, respectively, and Qf1 and Qf2 are the maximum vertical stresses on the skin of the pile before and after the blast, respectively. Variables A, P and L are the cross-section, cross-section environment and pile length, respectively.

The lateral bearing capacity of the pile before the blast was calculated using the Broms method as Ql1 [20]. The maximum lateral stress after the explosion was calculated using the numerical model and was subtracted from the corresponding values before the blast. The final lateral bearing capacity of pile after the blast is denoted

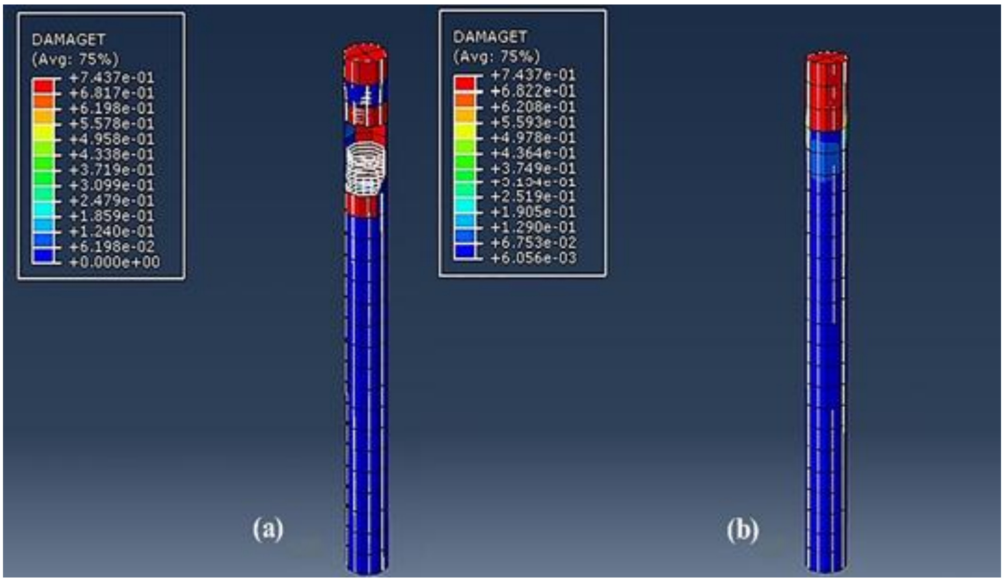

Figure 13. Comparison of tension damage in pile for 200 kg TNT at an unsafe distance of 1 m at the surface in: (a) clayey soil; (b) sandy soil

as Ql2. The blast impact range was obtained for the different explosive masses and is shown in Figure 14. As illustrated, Q2/Q1 increased with an increase in the distance from 50 kg of TNT at the surface in clayey soil. The blast impact range, Q2/Q1, and Ql2/Ql1 at the surface and at 6 m in depth for different explosive weights are presented in Table 7 for clayey and sandy soils. Table 7 summarizes that the blast impact range increased with an increase in the explosive mass. For example, the blast impact range for 500 kg of TNT at the surface was 23 m greater than for 50 kg of TNT. The corresponding difference at a depth of 6 m was only 1 to 3 m because Q2/Q1 increased as the depth increased. It is clear that the blast impact range was greater at the surface of than at depth. Also, the difference with the blast impact range at a higher explosive weight was greater because Q2/Q1 increased at depth compared to the corresponding value at the surface. The ratio of Ql2/Ql1 at a depth of 6 m was same for all explosive masses because the value of Ql2/Ql1 approached 1 for the nearest distance, which means that it did not need to be controlled at greater distances. Therefore, the only parameter that should be measured at depth is Q2/Q1.

Table 7 also shows that the blast impact range increased as the explosive mass increased in both sandy and clayey soils. At 500 kg of TNT in clayey and sandy soils, a difference of 1 to 2 m was detected. This was caused by the ability of the sandy soil to control the blast waves. The blast impact range in clayey soil was 4 to 34 m and in sandy soil was 3 to 32 m. The difference between the blast impact range at a depth of 6 m for the high TNT mass was greater than at the lower mass. The blast impact range in sandy soil at the surface was larger than at depth. In both soil types, the Ql2/Ql1 approached 1 at the nearest distance. This indicates that the only parameter that requires measurement at depth is Q2/Q1. It can be seen in Table 7 that the blast impact range decreased in sandy soil in comparison with clayey soil. This is due to the lower density, lower Poisson's ratio and lower modulus of elasticity of sandy soil compared to clay soil, which caused the generated wave to travel a shorter distance in sandy soil and caused less stress in the soil [13, 20]. Chakraborty [10] also has stated that the most influential soil parameters for blast loading are the internal friction angle and soil density.

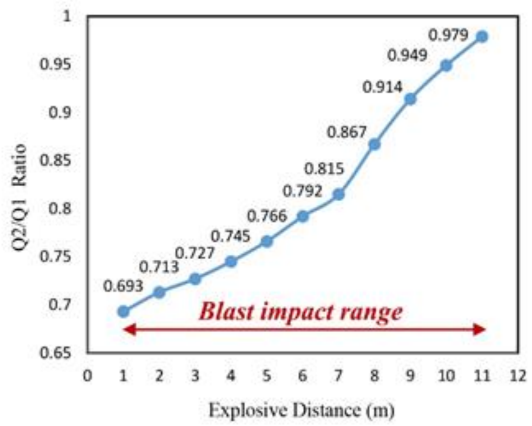

Figure 14. Q2/Q1 vs. distance for 50 kg of TNT at the surface in clayey soil

Table 7. Blast impact range for different explosive mass for blasts at the surface and at depths of 6 m for clayey and sandy soil

Clay					Sand				
Mass of explosive (kg)	**Depth of explosive (m)**	**Blast impact range (m)**	**Q_2/Q_1 in blast range**	**Ql_2/Ql_1 in blast range**	**Mass of explosive (m)**	**Depth of explosive (m)**	**Blast impact range (m)**	**Q_2/Q_1 in blast range**	**Ql_2/Ql_1 in blast range**
50	0	1-11	0.979–0.693	0.656- 0.980	50	0	1 -9	0.734 -0.982	0.950 -0.993
	6	1-12	0.635-0.960	0.980		6	1-10	0.721 -0.974	0.991
100	0	2-16	0.647- 0.971	0.743- 0.995	100	0	1 -14	0.705 -0.978	0.932 -0.997
	6	2-17	0.514- 0.954	0.985		6	1 -15	0.644 -0.963	0.988
200	0	2-20	0.602-0.965	0.576-0.996	200	0	2 -18	0.698 -0.978	0.913 -0.996
	6	2-22	0.417- 0.951	0.934		6	2 -20	0.634 -0.967	0.981
300	0	3-24	0.567- 0.968	0.649- 0.992	300	0	2 -22	0.658 -0.954	0.902 -0.995
	6	3-26	0.329- 0.962	0.955		6	2 -24	0.597 -0.961	0.977
400	0	3-29	0.452- 0.973	0.515- 0.994	400	0	3 -27	0.645 -0.952	0.896 -0.991
	6	3-32	0.290- 0.966	0.929		6	3 -30	0.588 -0.973	0.975
500	0	4-34	0.454- 0.965	0.601- 0.996	500	0	3 -32	0.612 -0.979	0.868 -0.994
	6	4-37	0.303- 0.951	0.962		6	3 -35	0.540 -0.963	0.968

5. CONCLUSION

Explosion research necessitates technical design to mitigate the adverse effects on nearby structures and facilities. The blast impact range and the safe distance at which the pile will avoid structural damage are two critical parameters for the design of a pile under blast loading. Therefore, in this research, 3D dynamic analysis of RC piles subjected to blast loading was numerically conducted in Abaqus. In order to determine the safe distance from the pile, different explosive masses were modeled at the closest possible distance, at the surface, and at different depths. The criteria were the maximum allowable tension and compression damage in the RC pile. In order to determine the blast impact range, the explosive masses were modeled at the closest safe distance from the pile to a distance at which Q2/Q1 and Ql2/Ql1 approached 1. The following conclusions were made:

- An increase in the mass and depth of the explosive increased the blast impact range. For example, in clayey soil, the blast impact range increased about 26 m when subjected to 50 to 500 kg of TNT at the ground surface. For 500 kg of TNT, the blast impact range increased from 34 to 37 m at a depth of 6 m because of the decrease in Q_2/Q_1. In both soil types, explosive loading increased as the depth and mass of the explosive increased.
- The safe distances were shorter for sandy soil than for clayey soil. The safe distance decreased 1 to 2 m when the geotechnical condition changed from clay to sand.
- The tensile and compressive damage and Q_2/Q_1 and Ql_2/Ql_1 of sandy soil were better than for clayey soil. In sandy soil, the maximum tension and compression damage decreased by 65% and 50%, respectively, and Q_2/Q_1 and Ql_2/Ql_1 increased by 25% and 14%, respectively. This indicates that the sandy soil had a higher capacity than clayey soil to resist the effects of blast loading.
- The blast impact range in sandy soil was less than in clayey soil. For example, under 500 kg of TNT at the ground surface, the blast impact range in clayey soil was 4 to 34 m and in the sandy soil was 3 to 32 m.
- If a pile is located at an unsafe distance, structural failure of the pile will occur prior to geotechnical failure. It is important in the design stage to control for structural sufficiency before controlling for the bearing capacity of the pile under blast loading.
- An increase in explosive depth had no significant effect on reducing the compression and tension damage (especially tension damage) at an unsafe distance.

Examining the effects of other parameters and conditions not addressed in this study can be significant and presented as a suggestion for future research. Among others, we can refer to the exploration of the impact of blast loading on piles in soils with different layers in depth, the investigation of the effect of changing soil parameters on the behavior of piles under blast load, and the investigation of the impact of the explosion on piles in saturated and unsaturated soils.

6. REFERENCES

1. Gorashi, S. M. S., Khodaparast, M., Rajabi, A. M., "Evaluation of Dynamic Probing Testing Effect in Hand Excavated Pit on Test Results Using Numerical Modeling", ***International Journal of Engineering, Transactions B: Applications,*** Vol. 33, No. 8, (2020), 1553-1559. doi: 10.5829/IJE.2020.33.08B.13
2. Gorashi, S. M. S., Khodaparast, M., Khodajooyan. Qomi, M., "Compaction quality control of coarse-grained soils using dynamic penetration test results through correlation with relative compaction percentages", ***International Journal of Engineering,*** Vol. 36, No. 3, (2023). https://www.ije.ir/article_160375.html
3. Liao, S., Li, W., Fan, Y., Sun, X. and Shi, Z, "Model Test on Lateral Loading Performance of Secant Pile Walls", ***Journal of Performance of Constructed Facilities,*** Vol. 28, No. 2, (2014), 391-401.https://doi.org/10.1061/(ASCE)CF.1943-5509.0000374
4. Dusenberry, D. O., "Handbook for Blast-Resistant Design of Buildings", ***John Wiley & Sons***, USA, 2010.
5. Prasanna, R. and Boominathan, A., "Finite-Element Studies on Factors Influencing the Response of Underground Tunnels Subjected to Internal Explosion", ***International Journal of Geomechanics,*** Vol. 20, No. 7, (2020), 04020089. https://ascelibrary.org/doi/10.1061/%28ASCE%29GM.1943-5622.0001678
6. Qiu, G., Henke, S. and Grabe, J., "Application of a Coupled Eulerian Lagrangian Approach on Geomechanical Problems Involving Large Deformations", ***Computers and Geotechnics*** Vol. 38, No. 1, (2011), 30-39. https://doi.org/10.1016/j.compgeo.2010.09.002
7. Jayasinghe, L. B., Thambiratnam, D. P., Perera, N. and Jayasoorya, J. H. A. R., "Computer Simulation of Underground Blast Response of Pile in Saturated Soil", ***Computers & Structures,*** Vol. 120, (2013), 86-95. https://doi.org/10.1016/j.compstruc.2013.02.016
8. Huang, B., Gao, Q., Wang, J., Jiang, X., Wang, X., Jiang, B. and Wu, W., "Dynamic Analysis of Pile-Soil-Structure Interaction System under Blasting Load", ***Applied Mechanics and Materials,*** Vol. 638-640, (2014), 433-436. https://doi.org/10.4028/www.scientific.net/AMM.638-640.433
9. Jayasinghe, L. B., Thambiratnam, D. P., Perera, N. and Jayasoorya, J. H. A. R., "Blast Response of Reinforced Concrete Pile Using Coupled Computer Simulation techniques", ***Computers & Structures,*** Vol. 135, (2014), 40-49. https://www.sciencedirect.com/science/article/abs/pii/S0045794914000285
10. Chakraborty, T., "Analysis of Hollow Steel Piles Subjected to Buried Blast Loading", ***Computers and Geotechnics,*** Vol. 78, (2016), 194-202. https://doi.org/10.1016/j.compgeo.2016.05.015
11. Jayasinghe, L. B., Zhou, H. Y., Goh, A. T. C., Zhao, Z. Y. and Gui, Y. L., "Pile Response Subjected to Rock Blasting Induced Ground Vibration Near Soil-Rock Interface", ***Computers and***

Geotechnics, Vol. 82, (2017), 1-15. https://doi.org/10.1016/j.compgeo.2016.09.015

12. Jayasinghe, L. B., Zhao, Z. Y., Goh, A. T. C., Zhao, H. Y., Gui, Y. L. and Tao, M., "A Field Study on Pile Response to Blast-Induced Ground Motion", ***Soil Dynamics and Earthquake Engineering,*** Vol. 114, (2018), 568-575. https://doi.org/10.1016/j.soildyn.2018.08.008
13. Ibrahim, Y. E. H. and Nabil, M., "Risk of Surface Blast Load on Pile Foundations", ***Magazine of Civil Engineering,*** Vol. 90, No. 6, (2019), 47-61. https://engstroy.spbstu.ru/en/article/2019.90.5/
14. Bakhshandeh. Amnieh, H., Mahdi. Mirabedi, S. M., Rahmanpour, M., Jafari, V., "A Study of Blast-induced Vibration on Oil Pipelines based on Numerical and Field Analysis", ***International Journal of Engineering, Transactions C: Aspects,*** Vol. 34, No. 9, (2021), 2116-2123. doi: 10.5829/IJE.2021.34.09C.09
15. Abaqus, ABAQUS/Explicit User's guide, Version 6.13, Providence, Dassault Systèmes Simulia Corp, Inc, USA, (2013).
16. Helwany, S., "Applied Soil Mechanics: with Abaqus Applications", ***John Wiley & Sons***, USA, 2007.
17. Nagy, N., Mohamed, M. and Boot, J. C., "Nonlinear Numerical Modelling for The Effects of Surface Explosions on Buried Reinforced Concrete Structures", ***Geomechanics and Engineering,*** Vol. 2, No. 1, (2010), 1-18. https://doi.org/10.12989/gae.2010.2.1.001
18. Abaqus, ABAQUS/Explicit User's manuals, Version 6.13, Providence, Dassault Systèmes Simulia Corp, Inc, USA, (2013).
19. Tiwari, R., Chakraborty, T., and Matsagar, V., "Dynamic Analysis of Twin Tunnels Subjected to Internal Blast Loading", ***Advances in Structural Engineering,*** Vol. 6, No. 30, (2015), 343-354. https://doi.org/10.1007/978-81-322-2190-6_30
20. Tomlinson, M., Woodward, J., "Pile Design and Construction Practice", ***Taylor & Francis Group***, UK, 2014.

Persian Abstract

چکیده

شمع‌ها بارهای سازه‌ای را به لایه‌های سخت خاک یا سنگ منتقل می‌کنند. بنابراین هرگونه آسیب به شمع‌ها می‌تواند عواقب جبران ناپذیری داشته باشد. یک انفجار سطحی می‌تواند یک شوک زمین ایجاد کند که انرژی انفجار را در امتداد سطح و در اعماق منتقل می‌کند. بررسی اثرات انفجار نیازمند طراحی فنی برای کنترل اثرات نامطلوب آن بر سازه‌ها و تاسیسات مجاور است. از جمله پارامترهای اساسی برای طراحی یک شمع تحت بارگذاری انفجار، محدوده تاثیر انفجار و فاصله ایمن است که در آن از آسیب سازه‌ای شمع جلوگیری می‌شود. لذا در این تحقیق مطالعه عددی شمع‌های بتن مسلح تحت بارگذاری انفجار با استفاده از روش کوپل اویلری-لاگرانژی جهت تعیین محدوده تاثیر انفجار و فاصله ایمن شمع‌ها انجام شد. نتایج برای خاک‌های رسی و ماسه‌ای نشان داد که افزایش عمق انفجار علیرغم کاهش آسیب فشاری و کششی به شمع، تأثیر قابل ملاحظه‌ای بر فاصله ایمن نداشت. افزایش جرم و عمق انفجار ظرفیت باربری فشاری نهایی شمع را کاهش و محدوده تاثیر انفجار را افزایش داد. خاک ماسه‌ای بهتر از خاک رسی در برابر بار انفجار عمل کرد. نتایج این پژوهش می‌تواند در پروژه‌های مختلف از جمله برای سازه‌های با اهمیت زیاد که در مجاورت خطوط انتقال گاز قرار گرفته و یا ممکن است در معرض حملات تروریستی قرار گیرند، استفاده شود.

IJE TRANSACTIONS B: Applications Vol. 36, No. 02, (February 2023) 398-407

International Journal of Engineering

Journal Homepage: www.ije.ir

Image Restoration by Projection onto Convex Sets with Particle Swarm Parameter Optimization

A. Rashno*[a], S. Fadaei[b]

[a] *Department of Computer Engineering, Engineering Faculty, Lorestan University, Khorramabad, Iran*
[b] *Department of Electrical Engineering, Faculty of Engineering, Yasouj University, Yasouj, Iran*

PAPER INFO

Paper history:
Received 13 September 2022
Received in revised form 11 December 2022
Accepted 17 December 2022

Keywords:
Image Restoration
Convex Sets
Particle Swarm Optimization

ABSTRACT

Image restoration is the operation of obtaining a high-quality image from a corrupt/noisy image and is widely used in many applications such as Magnetic Resonance Imaging (MRI) and fingerprint identification. This paper proposes an image restoration model based on projection onto convex sets (POCS) and particle swarm optimization (PSO). For this task, a number of convex sets are used as constraints and images are projected to these sets iteratively to reach restored image. Since relaxation parameter in POCS has a significant effect on restoration results, PSO is developed to find the best value for this parameter to be used in restoration process. The proposed scheme for image restoration is evaluated on three popular images with 4 configurations of noise, compared with 5 competitive restoration models. Results demonstrate that the proposed method outperforms other models in 32 out of 48 cases in images with different noise configurations with respect to relative error, ISNR, MAE and MSE measures.

doi: *10.5829/ije.2023.36.02b.18*

1. INTRODUCTION

Recovery a high-quality image from its degraded version, well-known as image restoration, is a fundamental and difficult problem in image processing field which is applicable in many fields such as Magnetic Resonance Imaging, identification of fingerprint, astronomy and so on [1]. As we know, the accuracy of image processing algorithms is depended to the quality of the input image, so, image restoration problem which improves the quality of image plays an important role in this field. To do this, variety of algorithms are introduced.

Li et al. [2] proposed an image restoration approach for fingerprint by manipulating nonlocal Cahn–Hilliard equation. In this paper, the damaged part is considered and the nonlocal CH equation is solved to restore the fingerprint image. A Generative Adversarial Network (GAN) can be used to eliminate the overfitting problem among the recent networks and then improve the image restoration performance [3]. A conjugate gradient algorithm is presented by Cao and Wu [4] to improve image restoration which possesses three properties: satisfaction of descent property; establishment of the trust region feature; convergence for nonconvex functions. A deep CNN referred as CU-Net is presented by Deng and Dragotti [5] to address the general multi-modal image restoration and multi-modal image fusion problems. The proposed network can split the common information automatically which can be shared among different modalities.

An extend and improved version of the Expected Patch Log Likelihood (EPLL) algorithm is proposed by Papyan and Elad [6] in which a multi-scale prior extracted from the target image is considered. Pang et al. [7] introduced a new model for image restoration based on minimizing surface regularization which is related to the classical ROF (Rudin, Osher and Fatemi) model [8]. By considering the support and sparsity prior together, a new method is presented by He et al. [1]. Also, the proximal alternating adaptive hard thresholding (PAAHT) algorithm is proposed to solve nonconvex

*Corresponding Author Institutional Email: rashno.a@lu.ac.ir (A. Rashno)

Please cite this article as: A. Rashno, S. Fadaei, Image Restoration by Projection onto Convex Sets with Particle Swarm Parameter Optimization, ***International Journal of Engineering, Transactions B: Applications***, Vol. 36, No. 02, (2023), 398-407

nonsmooth optimization problem. To address the problems of Rotating Synthetic Aperture (RSA) imaging system, an image restoration approach is presented by Zhi et al. [9]. In this work, the characteristics of image degradation analysis and mutual information are combined.

Zhang [10] has introduced a new restoration method by implementation of Expectation-Maximation algorithm using wavelet transform. A novel scheme is presented by Tanikawa et al. [11] based on weighted averaging of two images with different blur and noise artifacts. Indeed, the blur and noise artifacts are removed from the image by merging two degraded images. Although it is assumed that the image transformation be known in many methods, the transformation from the degraded image is estimated by Ševčík et al. [12] and this assumption is relaxed. A novel restoration algorithm is presented by Hu et al. [13] to remove both Gaussian noise and stripping artifacts. Some practical methods were proposed by Dar et al. [14] for image restoration when the degradation is an arbitrary form of known linear operator. Using the entropy constraint and the projection onto convex set algorithm, an effective restoration method based on super resolution is presented by Li et al. [15].

In case of the data with different scales, construction of a low-rank tensor is needed, so Lu et al. [16] proposed a model based on multi-band filters which are guided using low-rank tensor. An edge detection based on wavelet frame model is introduced by Choi et al. [17] to conduct image restoration by assuming that the image is a smooth function. Motohashi et al. [18] proposed a new method based on blind deconvolution to estimate the point spread function and improve the performance of restoration. A learning framework method based on Bayesian dictionary is introduced by Liu et al. [19] which the performance of image restoration is improved using the beta process of nonlocal structures. Image restoration is handled by using an effective neural network by Gou et al. [20]. A fitness-based multi-role particle swarm optimization was proposed Xia et al. [21]. Finally, convergence speed of a novel binary PSO was improved by fitness-based acceleration coefficients [22]. A new framework for image enhancement is proposed by Iravani and Ezoji [23] using optimization theorem. The quality of the image was improved by Tang et al. [24], Lin and Feng [25] based on image denoising. Mortezaei et al. [26] introduced an adaptive un-sharp masking algorithm to enhance image quality. An adaptive image dehazing approach was proposed by Azari Nasrabad et al. [27] based on dark channel prior. A higher resolution image was produced by Seyyedyazdi and Hassanpour [28, 29] using super resolution processing.

The main contributions of this paper are summarized as follows: 1) Image restoration is modeled by finding a common point to satisfy a set of convex sets constraints in Hilbert space, referred as projection onto convex sets (POCS); 2) In POCS, importance of relaxation parameter is investigated during restoration process and it is shown that how this parameter affects restoration quality; 3) A new schema for velocity update is proposed by first dividing particles to two groups based on their fitness and then applying velocity update rules to each group separately; 4) A new method for assigning particles inertia weight is finally proposed to control the process of exploration and exploitation.

The rest of the paper is organized as follows: Image restoration by projecting onto convex sets and particle swarm optimization algorithm are explained in sections 2 and 3. Section 4 introduces the proposed method. Implementation setup and results are reported in sections 5 and 6, respectively. Computation complexity of the fitness function in optimization process is discussed in section 7. Finally, the paper is concluded in section 8.

2. IMAGE RESTORATION BY PROJECTION ONTO CONVEX SETS

In the case of finding a common point *f* which satisfies a set of constraints as convex sets in Hilbert space *R*, POCS could be applied and used as follows:

$$f \in C = \cap_{i=1}^{m} C_i \tag{1}$$

where *m* is the number of convex sets and C_i is the *i*th closed convex set which is corresponding to *i*th constraint. The intersection vector f is found by successive projection onto convex sets started from any vector in R as initial guess f^0 with the following operator:

$$f^{t+1} = P_{C_m} P_{C_{m-1}} \dots P_{C_1} f^t \tag{2}$$

which means f at iteration $t+1$ is computed from projection of *f* at iteration *t* to convex set C_i by projection operator P_{C_i}.

It is worth mentioning that these projections converge to intersection point f in case that the intersection of convex sets is non-empty. The noise-free image restoration can be modeled as the following linear equation:

$$g = Hf \tag{3}$$

where *H* is PSF matrix, *f* is noise-free image and *g* is the degraded image. Each line of g is an equation that could be represented by a convex set. So, Equation (3) can be solved by POCS algorithms. Row-Action Projection (RAP) is a POCS method for solving Equation (3) [30]. The RAP equation which converges to intersection of hyperplanes is defined as follows [31]:

$$f^{(k+1)} = f^{(k)} + \lambda \frac{g_p - h_p^t f^{(k)}}{\|h_p\|^2} \tag{4}$$

where g_p and h_p^t are the pth element and pth row of vector g and matrix H respectively. λ is the relaxation parameter which is the main contribution of this paper. Since iteration index p is computed by $p = k(mod\ AB)$, each row is used multiple times in the iterations of the algorithm.

RAP can be reformulated for 2-D images. Each pixel of blurred image corresponds to Equation (4). The RAP in 2-dimensional space is proposed by the following equations.

$$\hat{f}^{(k+1)} = \begin{cases} \hat{f}^{(k)}(m,n) + \lambda \frac{\epsilon(i,j)}{\|h(i,j)\|^2} h(i-m, j-m), \\ \quad \text{for } \hat{f}^{(k)}(m,n) \epsilon S_{h(i,j)} \\ \hat{f}^{(k)}(m,n), \quad otherwise \end{cases} \tag{5}$$

where,

$$\epsilon(i,j) = g(i,j) - \sum_{m,n\epsilon S_{h(i,j)}} h(i-m, j-n; i,j)\, \hat{f}^{(k)}(m,n) \tag{6}$$

$$\|h(i,j)\|^2 = \sum_{m,n\epsilon S_{h(i,j)}} h(m,n;i,j)^2 \tag{7}$$

in Equations (6) and (7), $S_{h(i,j)}$ is the support of PSF centered at $g(i,j)$. At each iteration, projection operator is local which require only the pixels inside a window around each pixel [31, 32]. The lower and upper bounds for image pixels during iteration of restoration process are controlled by Limited Amplitude (LA) set as following:

$$C_{LA} = \{s : s \epsilon S \ and \ \alpha \le s(k,l) \le \beta \ \forall\, k,l \ \in \Omega\} \tag{8}$$

where Ω is the support region of the image, α and β are the upper and lower bounds, respectively and S is the Hilbert space. So, the projection operator can be defined as follows:

$$P_{C_{LA}} x(k,l) = \begin{cases} \alpha, & x(k,l) < \alpha \\ x(k,l), & \alpha \le x(k,l) \le \beta \\ \beta, & x(k,l) > \beta \end{cases} \tag{9}$$

In this transformation, bound $[\alpha\ \beta]$ is regulated based on image data. For example, in images with 8-bit precision, this bound is [0 255]. It means that the final restored image will be in the range of input image. In image restoration based on POCS, two convex sets including RAP-2D and LA are used in the restoration process. This procedure is followed by projection of restored image into hyperplanes as following:

$$f^{(k+1)} = P_{C_{RAP-2D}} P_{C_{LA}} \tag{10}$$

At each iteration, the image is projected first into RAP-2D using Equation (5). In this step, the qualification of the restoration is affected significantly by λ parameter which will be discussed in section 5. Afterward, $P_{C_{LA}}$ restrict the pixels values to be in the interval [0 255]. RAP-2D and LA projection are performed by $P_{C_{RAP-2D}}$ and $P_{C_{LA}}$ projection operators respectively [32].

3. PARTICLE SWARM OPTIMIZATION

Particle Swarm Optimization (PSO) [33] is a population-based meta-heuristic search optimization technique stem from the bird flocking behavior. The core of PSO is by the way that combine the global exploration and local exploitation strategies to find the optimum solution [34]. The main purpose of optimization problems is finding the optimum value of a cost function in D-dimensional space. In PSO, a population of particles is randomly initialized along the D-dimensional search space which each particle $p_i = (\vec{x}_i, \vec{v}_i) \in R^d$ is a point in this space with position ($\vec{x}_i$) and velocity ($\vec{v}_i$) properties. In the fist stage of the PSO, both position and velocity for all particles are randomly initialized. In the next step, each particle saves both the best position in its history as local optimum point and the best position among all particles as global optimum point. At each iteration, velocity and position of particles are updated as follows:

$$\vec{v}_i = w\vec{v}_i + c_1 r_1(\vec{\hat{x}}_i - \vec{x}_i) + c_2 r_2(\vec{\hat{s}} - \vec{x}_i) \tag{11}$$

$$\vec{x}_i = \vec{x}_i + \vec{v}_i \tag{12}$$

where $\vec{\hat{x}}_i$ and $\vec{\hat{s}}$ are respectively the local and global positions, w is the inertia weight, r_1 and r_2 are the random numbers in the interval [0 1] and finally c_1 and c_2 are the acceleration coefficients. Update equations show that particles follow the direction which is the combination of their current path, local and global paths [34].

4. PROPOSED POCS IMAGE RESTORATION BASED ON PSO

Relaxation parameter λ affect the result of POCS method in image restoration significantly. For declaring the effect of λ parameter, a sample image is blurred by Gaussian filter and then Gaussian noise is added to it. For different amounts of λs, POCS is applied to the image. The restored images results are shown in Figure 1 which shows that for the low amounts of λ, the restoration results are poor while by increasing the λ, although restored images are better visually, there are so many artifacts in high frequency regions of the image. This show that there is no any rule for expressing accuracy of the restoration results based on either increasing or decreasing the λ parameter.

With knowing the importance of λ parameter, empirical selection of this parameter is very difficult task since it is a variable in the continuous space. The main contribution of this paper is finding the optimal λ^* parameter which leads to the best restoration results. In this paper, a 1-dimensional continuous optimization algorithm is proposed which is an extension of classic PSO. In this optimization problem the cost function is the

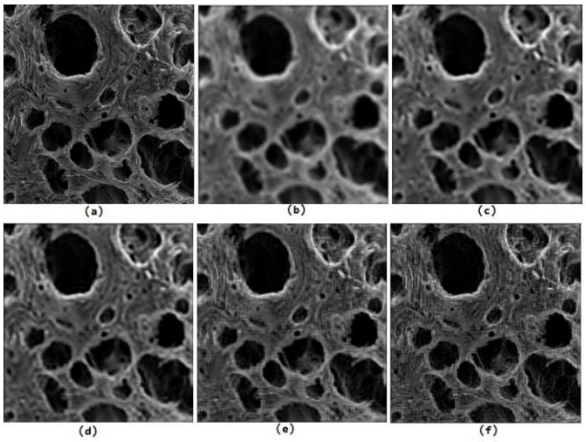

Figure 1. (a) Original image, (b) blurred and noised image, (c) restored image with $\lambda = 0.1$, (d) restored image with $\lambda = 1$, (e) restored image with $\lambda = 2.5$ and (f) restored image with $\lambda = 3.5$

accuracy of the restored image which must be maximized for the optimum solution λ^*. There are some measures for evaluating the restored image result. In this research we have used Improvement Signal to Noise Ratio (ISNR), Mean Absolute Error (MAE) and Mean Squared Error (MSE) measures which are computed as following:

$$ISNR = 10\log_{10}\left(\frac{\sum_{i,j}[g(i,j)-f(i,j)]^2}{\sum_{i,j}[\hat{f}(i,j)-f(i,j)]^2}\right) \quad (13)$$

$$MAE = \frac{\sum_{i,j}|\hat{f}(i,j)-f(i,j)|}{MN} \quad (14)$$

$$MSE = \frac{\sum_{i,j}|\hat{f}(i,j)-f(i,j)|^2}{MN} \quad (15)$$

where f, $\hat{f}$ and g are original image, restored image and degraded image respectively. Also, M and N are the image dimensions. It is worth mentioning that the higher amount of ISNR, the better restoration results are achieved while for MAE and MSE this relation is vice versa. Since our proposed algorithm maximize the above restoration measures, the cost functions for optimization problem are ISNR, $\frac{1}{MAE}$ and $\frac{1}{MSE}$.

In the optimization problem, each particle is a random number in the 1-dimensional search space which is the Lambda relaxation parameter. In the initial generation of particles, all particles are forced to be in the interval $[\lambda_{min}, \lambda_{max}]$ since there aren't appropriate restoration results for any amount of Lambda.

The velocity update is the core of PSO algorithm which is a sum of three parts include exploration, self-exploitation and social exploitation. The exploration part has inertia weight coefficient while self-exploitation and social exploitation have $c_1 r_1$ and $c_2 r_2$ coefficients respectively. In this paper the new schema for velocity update is proposed by the way that first particles are divided into two groups based on their fitness include the first B percent of the best particles and remained 1-B percent of other particles named as group 1 and group 2 respectively. Then, velocity update rules are applied to particles groups separately.

Inertia weight has important role in controlling the process of exploration and exploitation. In this paper, we have proposed the new method for assigning particles inertia weight. It is clear that the higher amount of inertia weight, the more exploration of search space is occurred by particles. So, inertia weights for particles in group 1 are increased to accelerate their search towards the global optimum. On the other hand, particles in group 2 try to have a balance between exploration and exploitation. So, they decrease their weights linearly. This idea is stem from self-regulating PSO algorithm which applied the above rule only for the best particle [35]. The inertia weight strategy for particles is proposed to be defined as following:

$$w_i(t) = \begin{cases} w_i(t-1) + \Delta w\,, if\ particle\ is\ in\ group 1 \\ w_i(t-1) - \Delta w, if\ particle\ is\ in\ group 2 \end{cases} \quad (16)$$

where $\Delta w = \frac{\eta}{IterationNumber}$ and η is a constant value.

For the self-exploitation and social exploitation, beside $c_1 r_1$ and $c_2 r_2$ two new coefficients are proposed as C_{se} and C_{So} respectively. In contrast with inertia weight, these two parts of velocity update rule highlight the exploitation property in the search space. As we mentioned in inertia weight rule, for the particles with the higher fitness, it is better that they have more ability for exploration of the search space rather than exploitation. So, for these particles we propose that their exploration weight be high in contrast with assigning the lower weights for exploitation. On the other hand, for other particles with lower fitness the exploitation property must be more highlighted since they must follow the direction of global and local particles to achieve the better fitness. Exploitation coefficients of the particles of group 1 and group 2 are defined as following:

$$C_{se}{}^{g1}(i) = \begin{cases} 1\,, & if\ a < P_1 \\ 0, & otherwise \end{cases} \quad (17)$$

$$C_{so}{}^{g1}(i) = \begin{cases} 1\,, & if\ a < P_2 \\ 0, & otherwise \end{cases} \quad (18)$$

$$C_{se}{}^{g2}(i) = \begin{cases} 1\,, & if\ a < P_3 \\ 0, & otherwise \end{cases} \quad (19)$$

$$C_{so}{}^{g2}(i) = \begin{cases} 1\,, & if\ a < P_4 \\ 0, & otherwise \end{cases} \quad (20)$$

These equations verify that particles with higher fitness update their velocity first based on their current direction as exploration of the search space, and second based on social exploitation and finally based on self-exploitation. For the particles with lower fitness this rule is implemented in equations vice versa. The flowchart of the proposed algorithm is depicted in Figure 2.

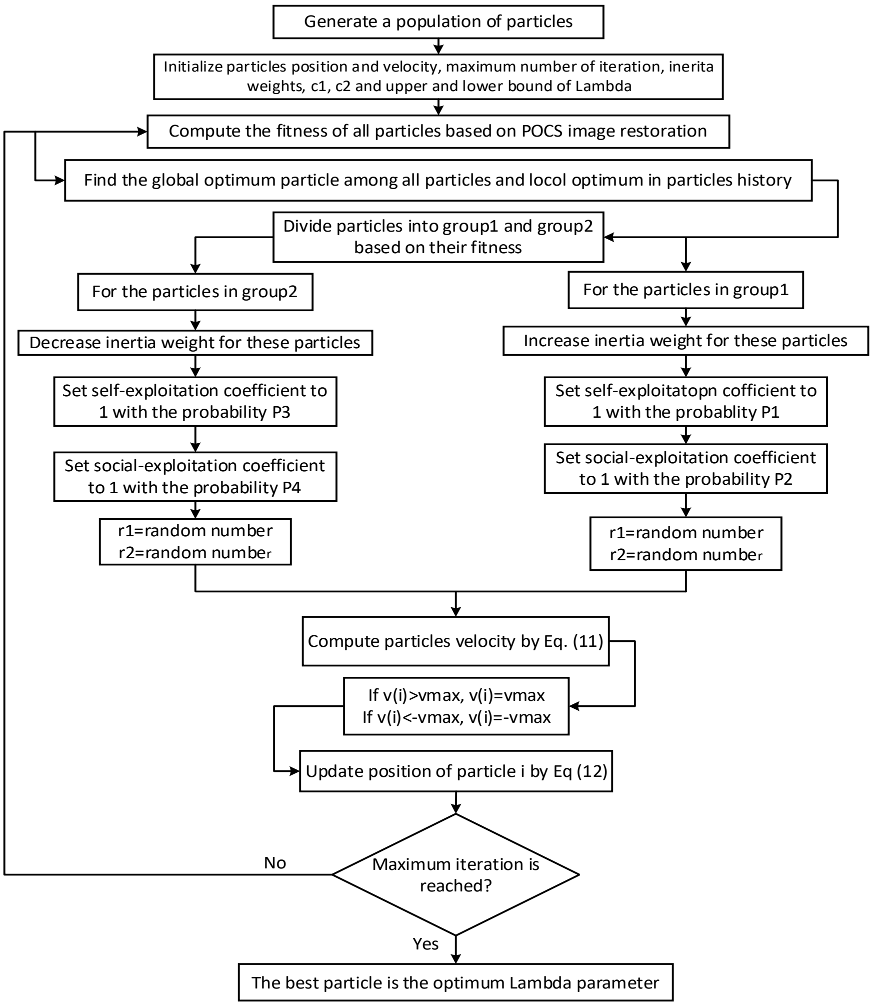

Figure 2. Flowchart of the proposed POS algorithm for finding optimum Lambda parameter

6. EXPERIMENTAL SETUP

To show the utility of the proposed algorithm a series of experiments is conducted. We implement our algorithm on a machine with 2.26 GHz Corei7 CPU and 6GB of RAM and windows 7. In these experiments, various parameter values were tested for PSO, POCS and our proposed optimization method in image restoration. According to our experiments, the highest performance is achieved by setting the parameters to values are shown in Table 1. For particles in group 1 with higher fitness, the self-exploitation and social exploitation considered in their velocity update with the probabilities of 0.3 and 0.6 respectively while these probabilities are both 0.8 for particles in group 2. Image restoration methods are evaluated on small number of well-known images. In this research, Cameraman, Fruits and Boats images are used for evaluation which is frequently used by image restoration researches.

TABLE 1. Parameter setting

Parameter	Value	Parameter	Value	Parameter	Value
Number of convex sets	20	C1 and C2	1	λ_{min}	-5
Maximum number of iterations	50	vmax	0.5	λ_{max}	+5
Number of particles	100	Initial weights	1.5	η	0.35
P1	0.3	P2	0.6	P3 and P4	0.8

6. EXPERIMENTAL RESULTS

To illustrate the effectiveness of proposed algorithm, it is evaluated by four measures Relative Error, ISNR, MSE and MAE. Three measures ISNR, MAE and MSE were defined previously in Equations (13)-(15) where they have been used as cost functions of PSO optimization. Relative error is defined as:

$$RelativeError(X) = \frac{\|\hat{X}-X\|_F}{\|\hat{X}\|_F} \tag{21}$$

where X is noised image, $\hat{X}$ is original noise-free image and $\|.\|_F$ is Frobenius norm.

The proposed method has been compared with 5 image restoration models which were proposed in [1, 7, 36-38]. To have variations in experiments, images are first blurred by blur matrix A which is Kronecker product of A_1 and A_2. These matrixes are calculated as following:

$$A_1(i,j) = A_2(i,j) = \begin{cases} \frac{1}{\sigma\sqrt{2\pi}} \exp\left(-\frac{(i-j)^2}{2\sigma^2}\right) & |i-j| \le r \\ o & otherwise \end{cases} \tag{22}$$

In the first round of comparison, the proposed model is compared with PSO for three images and two noise sets (σ, r, NV) including (4.4, 5, 2) and (8.4, 7, 2.5). The proposed method has lower relative error, MAE and MSE; and higher INSR in all images and all noise sets compared with PSO (Table 2). It means that the proposed method outperforms PSO in all experiments and restores images with higher qualities.

Then, the white Gaussian noise of mean 0 and variance NV are added to blurred noise-free image. For this task 4 configurations for noise parameters (σ, r, NV) including (1.4, 3, 1), (4.4, 5, 2), (8.4, 7, 2.5) and (12.4, 10, 5) are used as noise sets 1, 2, 3 and 4, respectively. Relative Error, ISNR, MSE and MAE of all methods for 4 noise sets are reported in Table 3. In relative error, the proposed method is the best method in Cameraman and Boats compared with all competitive models in which the best improvement of 24.93% was achieved in the last noise set 4. In Fruits, method by He et al. [1] outperforms all methods in all noise sets. With respect to ISNR, the proposed method achieves the highest results in Cameraman and Boats. Also, in the noise set 1, the proposed method has higher ISNR while in other noise sets [1] reaches to the best ISNRs. Promising results were achieved by the proposed method in MSE and MAE measures in which the proposed method is the best method in Cameraman and Boats while in Fruit image methods by Rashno et al. [38], Pang et al. [7] and He et al. [1] achieves lower values in different noise sets. The main conclusion from these experiments is that, the proposed method outperforms other methods in 32 cases out of 48 cases. Method proposed by He et al. [1] is the runner up model which is superior in 12 cases. Finally, methods developed by Rashno et al. [38] and Bouhamidi et al. [37] with 3 and 1 best cases are the third and fourth model, respectively.

As visual comparison, results of all models were shown for Boats and Fruits images in Figures 3 and 4, respectively. It is visually clear that the proposed restoration model restores images with better details.

7. COMPUTATIONAL COMPLEXITY OF FITNESS FUNCTION

During optimization process, restored images are compared with original images with respect to ISNR, MAE and MSE measures. For images with dimension ($M \times N$), computational cost of ISNR is

TABLE 2. Comparison between PSO and the proposed model

		Cameraman		Fruits		Boats	
Noise Sets	σ	4.4	8.4	4.4	8.4	4.4	8.4
	r	5	7	5	7	5	7
	NV	2	2.5	2	2.5	2	2.5
Relative Error	PSO	0.2312	0.0352	**0.2721**	**0.3318**	0.2231	0.2728
	Proposed	**0.2045**	**0.0315**	0.2481	0.3247	**0.1910**	**0.2548**
ISNR	PSO	0.0332	0.0110	**0.0382**	**0.0141**	0.0404	0.0122
	Proposed	**0.0415**	**0.0142**	0.0412	0.0168	**0.0442**	**0.0157**
MAE	PSO	7.3425	11.562	9.4560	13.878	10.122	11.342
	Proposed	**6.2549**	**9.2548**	**8.2549**	12.548	8.4587	**9.7854**
MSE	PSO	125.30	154.80	**139.10**	186.20	129.10	154.10
	Proposed	**120.50**	**142.80**	136.30	171.50	**124.10**	**145.50**

TABLE 3. Relative Error, ISNR, MSE and MAE of all methods for 4 noise sets

		Cameraman				Fruits				Boats			
	σ	1.4	4.4	8.4	12.4	1.4	4.4	8.4	12.4	1.4	4.4	8.4	12.4
	r	3	5	7	10	3	5	7	10	3	5	7	10
	NV	1	2	2.5	5	1	2	2.5	5	1	2	2.5	5
Relative Error	[36]	0.2065	0.2712	0.3283	0.5521	0.2354	0.2914	0.3467	0.4976	0.2147	0.2747	0.3157	0.4454
	[37]	0.1812	0.2634	0.3294	0.4834	0.2059	0.2848	0.3387	0.4453	0.1812	0.2798	0.3074	0.4056
	[38]	0.1831	0.2418	0.3243	0.4154	0.2123	0.2534	0.3341	0.3918	0.1956	0.2647	0.3086	0.3642
	[7]	0.1748	0.2315	0.0314	0.03514	0.2045	0.2457	0.3215	0.3854	0.1984	0.2214	0.2952	0.3547
	[1]	0.1758	0.2218	0.03215	0.03418	**0.2018**	**0.2348**	**0.3158**	**0.3315**	0.1874	0.2098	0.2857	0.3425
	Proposed	**0.1711**	**0.2045**	**0.03154**	**0.03028**	0.2084	0.2481	0.3247	0.3718	**0.1798**	**0.191**	**0.2548**	**0.3025**
ISNR	[36]	0.0432	0.0301	0.0104	-0.024	0.0382	0.0312	0.0091	-0.161	0.0357	0.0301	0.0084	-0.141
	[37]	0.0541	0.0304	0.0113	-0.073	0.0443	0.0356	0.0112	-0.067	0.0414	0.0325	0.0101	-0.054
	[38]	0.0514	0.0332	0.0118	-0.013	0.0412	0.0402	0.0184	-0.034	0.0401	0.0385	0.0136	-0.036
	[7]	0.0548	0.0321	0.0114	-0.025	0.0457	0.0451	0.0154	-0.031	0.0422	0.0418	0.0122	-0.029
	[1]	0.0568	0.0347	0.0121	-0.034	0.0469	**0.0445**	**0.0175**	**-0.033**	0.0435	0.0424	0.0141	-0.034
	Proposed	**0.0598**	**0.0415**	**0.0142**	**-0.026**	**0.0498**	0.0412	0.0168	-0.039	**0.0468**	**0.0442**	**0.0157**	**-0.022**
MAE	[36]	7.9786	10.873	14.653	28.873	8.8753	11.8912	14.874	25.543	6.1452	9.4456	12.452	21.475
	[37]	7.0134	10.234	13.873	21.453	7.9853	11.1546	14.165	18.843	6.4856	9.4562	11.475	19.365
	[38]	7.3421	9.1245	13.465	17.764	8.4633	10.1342	13.756	**16.345**	5.4253	9.7452	11.756	16.458
	[7]	7.5484	8.1256	12.548	17.256	7.2549	9.2548	**12.251**	19.254	5.7458	**8.1246**	10.785	16.485
	[1]	6.6589	7.1247	11.254	**14.254**	**7.2548**	9.2546	12.254	18.548	5.2154	8.4567	10.149	15.475
	Proposed	**6.1258**	**6.2549**	**9.2548**	15.254	7.4458	**8.2549**	12.548	19.541	**4.4785**	8.4587	**9.7854**	**13.456**
MSE	[36]	125.7	149.3	174.5	213.5	135.1	153.2	179.7	221.2	133.5	152.1	168.5	215.5
	[37]	118.3	141.9	168.6	205.3	125.6	146.4	172.1	209.9	120.7	142.5	165.7	201.9
	[38]	121.4	135.5	161.5	191.4	127.3	139.7	165.6	200.3	122.6	140.4	160.4	198.7
	[7]	120.2	129.2	160.5	182.6	125.6	135.4	**160.5**	186.3	121.1	140.6	154.3	192.1
	[1]	119.2	126.5	151.7	180.5	**124.8**	**133.5**	166.7	**185.2**	119.8	128.2	157.4	186.6
	Proposed	**111.2**	**120.5**	**142.8**	**152.7**	125.9	136.3	171.5	188.5	**115.4**	**124.1**	**145.5**	**174.1**

equivalent with by the following parameters:

$$ISNR \cong \left(\frac{\sum_{i=1}^{M}\sum_{j=1}^{N}[g(i,j)-f(i,j)]^2}{\sum_{i=1}^{M}\sum_{j=1}^{N}[\hat{f}(i,j)-f(i,j)]^2}\right) \quad (23)$$

There are $(M \times N)$ subtractin operations and $(M \times N)$ square operations, and 1 addition operation, the total $(M \times N) + (M \times N) + 1$ operations in numerator and denominator. Therefore, $2[(M \times N) + (M \times N) + 1] + 1$ operations are needed for ISNR computation. By the same way, for MAE and MSE, $[(M \times N) + (M \times N) + 1] + 2$ operations are needed.

$$MAE \cong \left(\frac{\sum_{i=1}^{M}\sum_{j=1}^{N}|\hat{f}(i,j)-f(i,j)|}{MN}\right) \quad (24)$$

$$MSE \cong \left(\frac{\sum_{i=1}^{M}\sum_{j=1}^{N}(\hat{f}(i,j)-f(i,j))^2}{MN}\right) \quad (25)$$

Since ISNR, MAE and MSE are used simultaneously as fitness function for particle evaluation, totally $6(M \times N) + 9$ Operations are needed for finness cmputation which is in complexity O(MN).

8. CONCLUSION

An image restoration model was presented by projection onto convex sets (POCS) and particle swarm optimization (PSO). Images were projected during restoration process and relaxation parameter was optimized by PSO. The proposed model was evaluated in several cases of images with different noise sets. Restored images were assessed by four criteria including Relative Error, ISNR, MSE and MAE which showed that

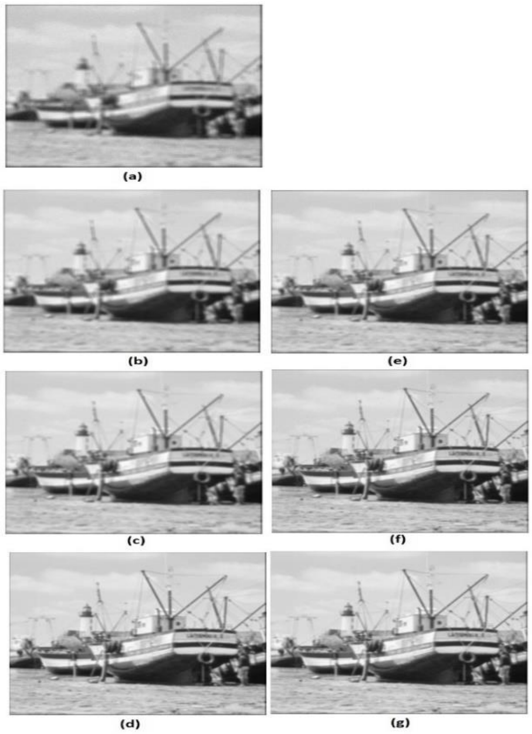

Figure 3. (a) Blurred and noised image, (b) restored image by [36], (c) restored image by [37], (d) restored image by [38], (e) restored image by [7], (f) restored image by [1], and (g) restored image by the proposed method

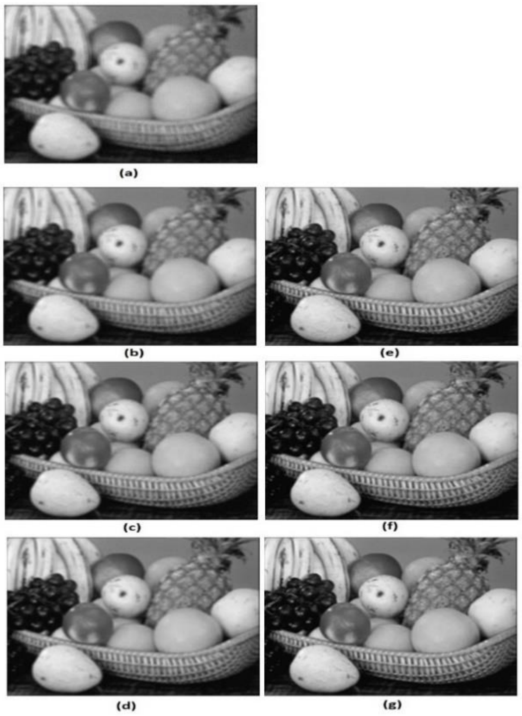

Figure 4. (a) Blurred and noised image, (b) restored image by [36], (c) restored image by [37], (d) restored image by [38], (e) restored image by [7], (f) restored image by [1], and (g) restored image by the proposed method

the proposed method is the best method among competitive methods. Suggested works will be directed to optimize more parameters of POCS by optimization methods. Finally, developing proposed restoration model for other noise types can be proposed as another future work.

9. REFERENCES

1. He, L., Wang, Y., Liu, J., Wang, C., and Gao, S., “Single image restoration through ℓ_2-relaxed truncated ℓ_0 analysis-based sparse optimization in tight frames”, ***Neurocomputing***, Vol. 443, (2021), 272-291, doi: 10.1016/j.neucom.2021.02.053.
2. Li, Y., Xia, Q., Lee, C., Kim, S., and Kim, J., “A robust and efficient fingerprint image restoration method based on a phase-field model”, ***Pattern Recognition***, Vol. 123, (2022), 108405, doi: 10.1016/j.patcog.2021.108405.
3. Kishore, A., Kumar, A., and Dang, N., “Enhanced image restoration by GANs using game theory”, ***Procedia Computer Science***, Vol. 173, (2020), 225-233, doi: 10.1016/j.procs.2020.06.027.
4. Cao, J., and Wu, J., “A conjugate gradient algorithm and its applications in image restoration”, ***Applied Numerical Mathematics***, Vol. 152, (2020), 243-252, doi: 10.1016/j.apnum.2019.12.002.
5. Deng, X., and Dragotti, P. L., “Deep convolutional neural network for multi-modal image restoration and fusion”, ***IEEE Transactions on Pattern Analysis and Machine Intelligence***, Vol. 43, No. 10, (2020), 3333-3348, doi: 10.1109/TPAMI.2020.2984244.
6. Papyan, V., and Elad, M., “Multi-scale patch-based image restoration”, ***IEEE Transactions on Image Processing***, Vol. 25, No. 1, (2015), 249-261, doi: 10.1109/TIP.2015.2499698.
7. Pang, Z. F., Guo, L. Z., Duan, Y., and Lu, J., “Image restoration based on the minimized surface regularization”, ***Computers & Mathematics with Applications***, Vol. 76, No. 8, (2018), 1893-1905, doi: 10.1016/j.camwa.2018.07.037.
8. Rudin, L. I., Osher, S., and Fatemi, E., “Nonlinear total variation based noise removal algorithms”, ***Physica D: Nonlinear Phenomena***, Vol. 60, No. 1-4, (1992), 259-268, doi: 10.1016/0167-2789(92)90242-F.
9. Zhi, X., Jiang, S., Zhang, L., Hu, J., Yu, L., Song, X., and Gong, J., “Multi-frame image restoration method for novel rotating synthetic aperture imaging system”, ***Results in Physics***, Vol. 23, (2021), 103991, doi: 10.1016/j.rinp.2021.103991.
10. Zhang, Y. “An EM-and wavelet-based multi-band image restoration approach”, In 2014 19th International Conference on Digital Signal Processing, (2014), 617-620, doi: 10.1109/ICDSP.2014.6900738.
11. Tanikawa, R., Fujisawa, T., and Ikehara, M., “Image restoration based on weighted average of multiple blurred and noisy images”, In 2018 International Workshop on Advanced Image Technology (IWAIT), (2018), 1-4, doi: 10.1109/IWAIT.2018.8369665.
12. Ševčík, J., Šmídl, V., and Šroubek, F., “A n adaptive correlated image prior for image restoration problems”, ***IEEE Signal Processing Letters***, Vol. 25, No. 7, (2018), 1024-1028, doi: 10.1109/LSP.2018.2836964.
13. Hu, T., Li, W., Liu, N., Tao, R., Zhang, F., and Scheunders, P., “Hyperspectral image restoration using adaptive anisotropy total variation and nuclear norms”, ***IEEE Transactions on Geoscience and Remote Sensing***, Vol. 59, No. 2, (2020), 1516-1533, doi: 10.1109/TGRS.2020.2999634.

14. Dar, Y., Elad, M., and Bruckstein, A. M., “Restoration by compression”, ***IEEE Transactions on Signal Processing***, Vol. 66, No. 22, (2018), 5833-5847, doi: 10.1109/TSP.2018.2871388.

15. Li, X. Q., Fang, K. L., and Jin, C., “Super-Resolution Restoration for Image Based on Entropy Constraint and Projection onto Convex Set”, ***In Advanced Materials Research***, Vol. 468, (2012), 1041-1048, doi: 10.4028/www.scientific.net/AMR.468-471.1041.

16. Lu, H., Li, S., Liu, Q., and Zhang, M., “MF-LRTC: Multi-filters guided low-rank tensor coding for image restoration”, ***Neurocomputing***, Vol. 303, (2018), 88-102, doi: 10.1016/j.neucom.2018.04.046.

17. Choi, J. K., Dong, B., and Zhang, X., “An edge driven wavelet frame model for image restoration”, ***Applied and Computational Harmonic Analysis***, Vol. 48, No. 3, (2020), 993-1029, doi: 10.1016/j.acha.2018.09.007.

18. Motohashi, S., Nagata, T., Goto, T., Aoki, R., and Chen, H., “A study on blind image restoration of blurred images using R-map”, In 2018 International Workshop on Advanced Image Technology (IWAIT), 1-4, 2018, doi: 10.1109/IWAIT.2018.8369650.

19. Liu, Z., Yu, L., and Sun, H., “Image restoration via Bayesian dictionary learning with nonlocal structured beta process”, ***Journal of Visual Communication and Image Representation***, Vol. 52, (2018), 159-169, doi: 10.1016/j.jvcir.2018.02.011.

20. Gou, Y., Li, B., Liu, Z., Yang, S., and Peng, X., “Clearer: Multi-scale neural architecture search for image restoration”, ***Advances in Neural Information Processing Systems***, Vol. 33, (2020), 17129-17140, doi: 10.48550/arXiv.2203.04313.

21. Xia, X., Xing, Y., Wei, B., Zhang, Y., Li, X., Deng, X., and Gui, L., “A fitness-based multi-role particle swarm optimization”, ***Swarm and Evolutionary Computation***, Vol. 44, (2019), 349-364, doi: 10.1016/j.swevo.2018.04.006.

22. Mehmood, Y., Sadiq, M., Shahzad, W., and Amin, F., “Fitness-based acceleration coefficients to enhance the convergence speed of novel binary particle swarm optimization”, In 2018 International Conference on Frontiers of Information Technology (FIT), 355-360, 2018, doi: 10.1109/FIT.2018.00069.

23. Iravani, S., and Ezoji, M., “A General Framework for 1-D Histogram-baesd Image Contrast Enhancement”, ***International Journal of Engineering***, ***Transactions A: Basics***, Vol. 29, No. 10. (2016), 1384-1391, doi: 10.5829/idosi.ije.2016.29.10a.09.

24. Tang, R., Zhou, X., and Wang, D., “Improved Adaptive Median Filter Algorithm for Removing Impulse Noise from Grayscale Images”, ***International Journal of Engineering***, ***Transactions A: Basics***, Vol. 30, No. 10, (2017), 1503-1509, doi: 10.5829/ije.2017.30.10a.11.

25. Lin, L., and Feng, L., “Comparative Analysis of Image Denoising Methods Based on Wavelet Transform and Threshold Functions”, ***International Journal of Engineering***, ***Transactions B: Applications***, Vol. 30, No. 2, (2017), 199-206, doi: 10.5829/idosi.ije.2017.30.02b.06.

26. Mortezaei, Z., Hassanpour, H., and Asadi Amiri, S., “Image Enhancement Using an Adaptive Un-sharp Masking Method Considering the Gradient Variation”, ***International Journal of Engineering***, ***Transactions B: Applications***, Vol. 30, No. 8, (2017), 1118-1125, doi: 10.5829/ije.2017.30.08b.02.

27. Azari Nasrabad, F., Hassanpour, H., and Asadi Amiri, S, “Adaptive Image Dehazing via Improving Dark Channel Prior”, ***International Journal of Engineering***, ***Transactions B: Applications***, Vol. 32, No. 2, (2019), 249-255, doi: 10.5829/ije.2019.32.02b.10.

28. Seyyedyazdi, S. J., and Hassanpour, H., “Improving Super-resolution Techniques via Employing Blurriness Information of the Image”, ***International Journal of Engineering***, ***Transactions B: Applications***, Vol. 31, No. 2, (2018), 241-249, doi: 10.5829/ije.2018.31.02b.07.

29. Seyyedyazdi, S. J., and Hassanpour, H., “Super-resolution of Defocus Blurred Images”, ***International Journal of Engineering***, ***Transactions A: Basics***, Vol. 33, No. 4, (2020), 539-545, doi: 10.5829/ije.2020.33.04a.04.

30. Mammone, R. J., “Computational methods of signal recovery and recognition”, ***John Wiley & Sons, Inc***., (1992), ISBN-13: 978-0471853848.

31. Kuo, S. S., and Mammone, R. J., “Image restoration by convex projections using adaptive constraints and the L/sub 1/norm”, ***IEEE Transactions on Signal Processing***, Vol. 40, No. 1, (1992), 159-168, doi: 10.1109/78.157191.

32. Papa, J. P., Fonseca, L. M., and de Carvalho, L. A., “Projections onto convex sets through particle swarm optimization and its application for remote sensing image restoration”, ***Pattern Recognition Letters***, Vol. 31, No. 13, (2010), 1876-1886, doi: 10.1016/j.patrec.2010.02.012.

33. Kennedy, J., and Eberhart, R., “Particle swarm optimization”, In Proceedings of ICNN'95-international conference on neural networks, Vol. 4, (1995), 1942-1948, doi: 10.1109/ICNN.1995.488968.

34. Eberhart, R. C., Shi, Y., and Kennedy, J. “Swarm intelligence”, ***Elsevier***, (2001), ISBN: 9781498741071.

35. Tanweer, M. R., Suresh, S., and Sundararajan, N., “Self-regulating particle swarm optimization algorithm”, ***Information Sciences***, Vol. 294, (2015), 182-202, doi: 10.1016/j.ins.2014.09.053.

36. B. Morini, M. Porcelli, and R. Chan, “A reduced Newton method for constrained linear least-squares problems”, ***Journal of Computational and Applied Mathematics***, Vol. 233, 2200–2212, 2010, doi: 10.1016/j.cam.2009.10.006.

37. Bouhamidi, Abderrahman, Rentsen Enkhbat, and Khalide Jbilou. “Conditional gradient Tikhonov method for a convex optimization problem in image restoration”, ***Journal of Computational and Applied Mathematics***, Vol. 255, (2014), 580-592, doi: 10.1016/j.cam.2013.06.011.

38. Rashno, Abdolreza, Foroogh Sadat Tabataba, and Saeed Sadri. “Image restoration with regularization convex optimization approach”, ***Journal of Electrical Systems and Signals***, Vol. 2, No. 2, (2014), 32-36, doi: 10.48550/arXiv.1902.02059.

Persian Abstract

چکیده

ترمیم تصویر عبارت است از به دست آوردن یک تصویر باکیفیت از تصویر نویزی یا خراب‌شده که در کاربردهای زیادی از جمله در MRI و تشخیص اثر انگشت استفاده می‌شود. در این مقاله یک مدل ترمیم تصویر مبتنی بر نگاشت بر مجموعه‌های محدب (POCS)و بهینه‌سازی ازدحام ذرات (PSO) ارائه شده است. برای این منظور، تعدادی مجموعه محدب به عنوان محدودیت‌ها استفاده شده و تصویر به این مجموعه نگاشت می‌شود تا تصویر ترمیم شده حاصل شود. از آنجاییکه پارامتر ریلکسیشن در POCS تاثیر بسزایی در نتایج ترمیم تصویر دارد برای تعیین مقدار بهینه‌ی آن از الگوریتم PSO استفاده شده است. روش پیشنهادی روی ۳ تصویر مشهور در چهار نویز مختلف پیاده‌سازی شده و با ۵ روش ترمیم تصویر مقایسه شده است. نتایج نشان می‌دهند که بر اساس معیارهای RelativeError، ISNR، MAE و MSE، مدل پیشنهادی در ۳۲ حالت از ٤۸ حالت بهتر از دیگر مدل‌ها بوده است.

IJE TRANSACTIONS B: Applications Vol. 36, No. 02, (February 2023) 408-419

International Journal of Engineering

Journal Homepage: www.ije.ir

Fabrication of Pebax/4A Zeolite Nanocomposite Membrane to Enhance CO_2 Selectivity Compared to Pure O_2, N_2, and CH_4 Gases

S. M. Faghih, M. Salimi*, H. Mazaheri

Department of Chemical Engineering, Arak Branch, Islamic Azad University, Arak, Iran

PAPER INFO

Paper history:
Received 28 May 2022
Received in revised form 21 November 2022
Accepted 22 November 2022

Keywords:
CO_2 Separation
PEBAX
Membrane
Polymer Morphology
4A Zeolite Nanoparticles

ABSTRACT

The separation of carbon dioxide is essential for the environment. Using membranes to separate this gas is economical, but the weakness in permeability and mechanical strength has prevented their commercialization. Robeson proved that permeability and selectivity have the opposite relationship and provided an upper limit for pairs of gases. Worth to be mentioned that any membrane placed above this limit could be commercialized. Scientists proposed mixed matrix membranes to overcome this problem. These membranes contain two phases, polymer, and inorganic. This research focuused on membrane technology and aimed to prepare a membrane that has a good performance for CO_2 separation and at the same time its cost is economical, so by adding a reasonable price zeolite available in the market named 4A to the Pebax1657 polymer and changing the operating conditions of the process, permeability and Selectivity was measured. Pebax polymer and 4A zeolite were selected as respectively the polymer and mineral phases for membrane fabrication. The fabricated membranes were evaluated by XRD, FT-IR, FE-SEM, BET, EDAX, TGA/DSC, and mechanical strength tests. Finally, the selectivity of CO_2 compared to N_2, O_2, and CH_4 improved by 53, 67, and 75%, respectively, and obtained a good position on the Robeson diagram.

***doi**: 10.5829/ije.2023.36.02b.19*

NOMENCLATURE

XRD	X-ray diffraction	$a_s BET$	Specific surface area based on BEt analysis ($m^2\ g^{-1}$)
FT-IR	Infrared Fourier transforms	L	Membrane thickness (cm)
FE-SEM	Field emission scanning electron microscopy	V	Tank volume after the membrane (cm^3)
BET	Brunauer-Emmett-Teller	P_o	Absolute input gas pressure (psia)
EDAX	X-ray energy scattering spectroscopy	A	Membrane area (cm^2)
TGA	Thermal balance analysis	V_m	Monolayer volume (cm^3(STP) g^{-1})
TPV	Total pore volume ($cm^3\ g^{-1}$)	*%Wt.*	Weight percent
P_A	Gas permeability A (Barrer)	*g*	Mass unit in grams
$\alpha_{A/B}$	The selectivity of A over B	*DMF*	Dimethylformamide solvent
μm	Micro metr (10^{-6} m)	*dP/dt*	Pressure changes in time (bar/s)

1. INTRODUCTION

The separation of carbon dioxide from the exhaust gases of chemical industries to preserve the environment and comply with standards has become an essential issue for industrial managers. When is not considered high purity in the separation of gases, membrane separation is the best technique [1,2]. The process of membrane separation requires small amount of energy [3-5].

Recently, researchers have for gases separation used Polyphosphazene, Polyamides, Cellulose acetate, Polyether-urethane, Polyamide-polyether-block copolymers, and Poly-vinylidene fluoride [2].

Lin et al. [6] concluded that using polar groups in polymers leads to a high selectivity for carbon dioxide

*Corresponding Author Institutional Email: m-salimi@iau-arak.ac.ir (S. M. Salimi)

Please cite this article as: S. M. Faghih, M. Salimi, H. Mazaheri, Fabrication of Pebax/4A Zeolite Nanocomposite Membrane to Enhance CO_2 Selectivity Compared to Pure O_2, N_2, and CH_4 Gases, ***International Journal of Engineering, Transactions B: Applications***, Vol. 36, No. 02, (2023), 408-419

compared to light gases. Copolymers containing ethylene oxides, such as polyether-block-amide or Pebax, are a very suitable proposal to achieve this aim [6]. Pebax is an elastomeric thermoplastic with a chemical structure as illustrated in Figure 1.

PA is an aliphatic polyamide that forms the hard part and PE polyether forms the soft part. The PA block provides mechanical resistance, and the passage of gas occurs from the PE phase. This polymer has good mechanical, and thermal stability [7].

Permeability and selectivity are two crucial actors in gas separation. Robeson reported a comprehensive analysis of gas pair permeability in polymer membranes. He proved that there is an inverse relationship between permeability and selectivity. In other words, these two factors have an opposite relationship [8]. Scientists are looking for a solution that increases permeability and selectivity simultaneously. One of their solutions is making composite membranes. These types of membranes include the polymer phase and filler phase [9-11]. With a combination of properties favorable to polymer membranes (high selectivity) and fillers (permeability and high mechanical stability), a stable and adjustable structure can be created, therewith expanding gas separation technology.

PEBA polymers provide the opportunity to produce membranes at a low cost. these polymers are commercially produced and can be converted into films with low thickness and excellent quality. The penetration, absorption, and permeability coefficients of films made from PEBA polymers vary due to their different chemical structure. Table 1 shows the chemical compositions and physical properties of some PEBA polymers. Among these polymers, the selectivity of

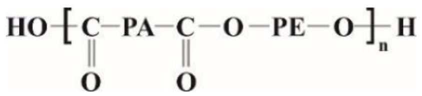

Figure 1. Chemical arrangement of PEBA polymers [7]

TABLE 1. Chemical compounds and physical properties of some PEBA polymers [7]

Type Polymer	Content PE (wt%)	Density (g/cm^3)	Melting temperature (°C)
2533	74.8 ,80	1.01	137, 126
3566	72.9 ,70	1.01	155, 142
4033	44,47	1.01	18, 159
5533	37.8	1.01	160
6333	42.2	-	170
1047	45	1.09	156
4011	43	1.14	201
1657	60	1.14	204

grade 1657 for CO_2 separation was the highest [12]. Zeolites have regular and tiny and controllable pores. They can act as a molecular sieve in the polymer membrane body [13]. Type A zeolite is a known synthetic example of the common compound Na1.[AlO_2.SiO_2]12.27H_2O [14].

This type of zeolite has three different groups, 4A, 3A, and 5A, which differ in the type of cations present in their internal structure [15,16].

Often, zeolite type 4A (Figure 2) is used to absorb water and hazardous gases. But due to its pore size, it can play an essential role as a CO_2 molecule sifting [17,18]. These excellent properties help us to commercialize this nanocomposite. In Table 2, a summary of carbon dioxide separation research by nanocomposite membrane is compiled.

The objective of this research is to solve the weaknesses in permeability and selectivity which gained a suitable position in the Robeson diagram. As mentioned in the introduction, the Robson diagram is presented as an indicator for the commercialization of membranes, so the data were marked on the Robson diagram, and in this way, the evaluation of the commercialization of the nanocomposite membrane was done.

2. EXPERIMENTAL

2. 1. Materials Required For Membrane Preparation

Pebax1657 was selected, made by French Arkema company with a density of 1.14 g/cm^3. Zeolite 4A powder made by Behdash Chemical Company of Iran was prepared. This material has a bulk density of 0.5 g/cm^3 and an average particle size of 250 to 500 nm. DMF solvent with a purity of 99% was sealed from Neutron Iran and standard hexane solvent was purchased from Merck (Darmstadt, Germany). Gases O_2, N_2, CH_4, and CO_2 with a purity of 99.9% were bought and used from Khorramshahr gas oxygen company.

2. 2. Devices Used In Membrane Preparation and Analysis

XRD analysis with XRD Philips pw1730 device, FE-SEM analysis with TESCAN MIRA3 device, FT-IR analysis with Thermo company model AVATAR. T hedevice, BET analysis with particular surface

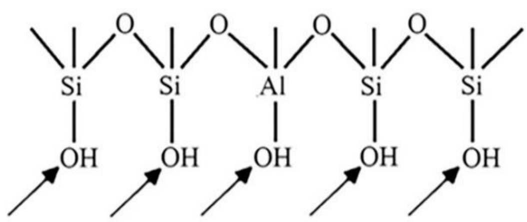

Figure 2. 4A zeolite structure [17]

TABLE 2. A selection of past research on membrane preparation with Pebax polymer and different nanoparticles

Ref.	Filler	Polymer	P_{CO2}	Selectivity
[24]	Zn/Co-ZIF	Pebax1657	102.5	16.4
[25]	Zeolite 13X	Pebax1657	168.59	45
[26]	ZIF-8	Pebax1074	144	72
[27]	ZnO	Pebax1074	152.27	13.52
[28]	TiO_2	Pebax1657	172	24.8
[29]	ZIF8	Pebax2533	727	63
[30]	Al_2O_3	Pebax1657	159.27	24.73
[31]	ZIF-8	Pebax1657/PE	758	16.1
[32]	DD3R	Pebax1074	188	38.5
[33]	ZIF-7	Pebax1657	150	40
[34]	NH2-CuBTC	Pebax1657	163	26.2
[35]	ZIF-7	Pebax1657	145	23
[36]	Zeolite NaY	Pebax1657	131.8	130.8
[37]	Zeolite NaX	Pebax1657/PES	45	121.5
[38]	ZIF-8	Pebax2533	1293	9
This work	4A	Pebax1657	115.5	CO_2/CH_4 32.3
This work	4A	Pebax1657	135.5	CO_2/O_2 20.53
This work	4A	Pebax1657	166.1	CO_2/N_2 75.19

measuring device: Belsorp mini II from Micro teach Bel Corp, Japan.

TGA/DSC analysis was done by TA company model Q600 device made in USA. To perform the mechanical resistance test was used Tensile Zwick device made in England, model CAT-350-56. The ultrasonic bath machine was manufactured by backer company vCLEAN1-L2. The thickness of the samples was measured by a digital thickness model GT-313-A1 made in Japan.

2. 3. Membrane Preparation And Synthesis Steps

Researchers have selected the membrane's thickness range between 60 and 120 µm [19-21]. Based on this, the amount of materials needed to prepare the membrane was roughly estimated according to the diameter of the petri dish and the thickness of 100 µm. Finally, after synthesizing the membranes, their thickness was measured using a thickness gauge. The nanocomposite was prepared by the solution mixing method.

To reach a concentration of 2.5 wt% of zeolite in the membrane, the first, 0.011 g of zeolite powder was placed at 70°C for 4 hours. In this way, the moisture was removed from the zeolite [22]. Then 12.076 g of DMF solvent (96.5%Wt. membrane) was added and placed on a magnetic stirrer at a temperature of 55°C for 4 hours [23].

The solution was placed in an ultrasonic bath for 15 minutes. In this way, we ensure the uniform distribution of nanoparticles and the removal of bubbles in the solution. This bath was set at a temperature of 50 °C, a frequency of 42 kHz, and a power of 50 W.

At this stage, the amount of 0.427 g of Pebax1657 granules was added to the solution and it was placed in an oil, and reflux bath at a temperature of 140 °C for 4 hours. To preserve the morphology of the nanocomposite and prevent damage to its structure, the bath was turned off 3 minutes before casting. In this way, the polymer was slightly cooled and ready for casting. Also, the glass petri dish was heated to 80 °C in the oven.

Then the obtained nanocomposite solution was poured into a Petri dish and immediately placed in the oven. The drying temperature and time were set at 40°C and 40 hours. During this time, the membrane was dehydrated. The Petri dish containing the membrane was removed from the oven, and a few drops of standard hexane solvent were poured on its surface.

So that its surface is free of any dust and undesirable particles. Then, for better drying and to ensure complete evaporation of the solvent, the petri dish containing the membrane was placed in a vacuum oven. The temperature of the oven was set at 45 °C. After 4 hours, the membrane was easily separated from the Petri dish and was ready for the permeability test.

In the same way, zeolite was made in the membrane for concentrations of 5, 8, 11.5, 16, and 22% Wt. The nanocomposite membranes prepared in this research were named Pebax1657/4A. Their thickness was measured and coded according to Table 3.

2. 4. Measurement of Permeability and Selectivity

The gas permeability measurement system was designed and built as a constant volume and according to Figure 3.

TABLE 3. Combination of polymer and nanoparticle in nanocomposite membranes

No	Pebax %Wt.	4A Zeolite wt%	ID
1	100	0	PA-0
2	97.5	2.5	PA-2.5
3	95	5	PA-5
4	92	8	PA-8
5	88.5	11.5	PA-11.5
6	84	16	PA-16
7	78	22	PA-22

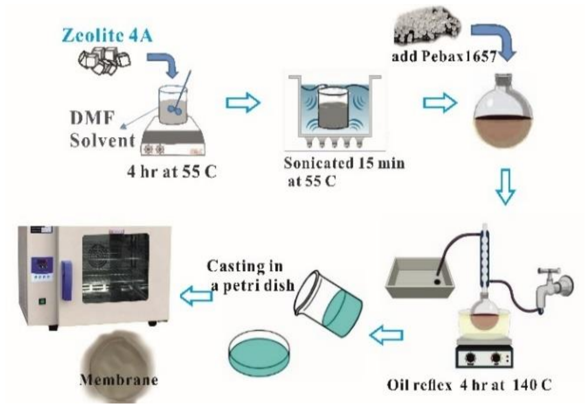

Figure 3. Nanocomposite membrane synthesis steps

This system can calculate gas permeability at different pressures and temperatures. The membrane cell is made of pure steel metal. To prevent gas leakage, rubber rings were installed on both sides of the membrane. The effective area of the membrane in this system is 17.71 cm^2.

Permeability experiments were performed at temperatures of 25, 35, 50, and 75 °C and pressures of 2, 5, 8 and 12 bars, each with three repetitions. Gas permeability was calculated using Equation (1) and reported in the Barrer unit.

$$P_{(Barrer)}=\frac{273.15\times10^{10}LV}{760\times76(AT\frac{P_0}{14.7})}\frac{dP}{dt} \quad (1)$$

1 Barrer $=10^{-10}$ cm^3 (STP)·cm/ (cm^2. s. cmHg)

In Equation (1), V (cm^3) is the volume of the reservoir after the cell, L (cm) is the thickness of the membrane, A (cm^2) is the effective area of the membrane, T (K) is the temperature, (psia) Po is the absolute pressure of the inlet gas and (bar/s) dP/dt is the pressure variation with time [39,40].

The selectivity of ideal gases was calculated using the equation 2 [41,42]. P_A and P_B are the permeability of gases A and B, respectively. The selectivity test results are discussed in the next sections; the selectivity expressed as ratio of P_A and P_B.

$$\alpha_{A/B}=\frac{P_A}{P_B} \quad (2)$$

Experimental set up for the gas permeabilty measurements is shown in Figure 4.

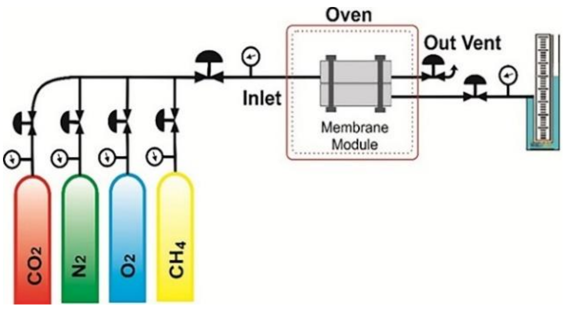

Figure 4. Permeability measurement system

3. RESULTS AND DISCUSSION

3. 1. Analysis of X-ray Diffraction (XRD)

XRD analysis was used to investigate the crystal structure of the synthesized membrane.

This analysis was performed from 10° to 80 ° with a step of 0.05° per second. The results of this analysis are shown in Figure 5. The zeolite phase is formed and has a crystal structure and favorable purity. The primary and significont peaks of the following particles after modification are related to X-ray reflection from planes 12.49, 20.09, 22, 27, 30, and 34 in the crystal structure of nanoparticles.

By comparing these figures with the results reported by other researchers [43], it can be said that the changes in the membrane structure are related to the addition of zeolite. In general, modifying the surface with non-crystalline agents reduces the crystallinity of the base particles. In this study, the size of the peaks in the central angles increased, which indicates an increase in membrane crystallinity and an increase in mechanical strength.

3. 2. Infrared Fourier Transforms (FT-IR)

This analysis was performed on membranes from 600 cm^{-1} to 4000 cm^{-1}. As shown in Figure 6, the prominent peaks of pure Pebax1657 membrane around 1089 cm^{-1} wave number were attributed to stretching vibration (C-O-C) of ether group in soft parts. The height at 1635 cm^{-1} is the stretching vibrations of (O=C) carbonyl in (H-N-O=C). The rise in the wave number of 1729 cm^{-1} was attributed to another carbonyl group (C=O-O), both of which are in the complex phase.

The peak at 1538 cm^{-1} is related to N-H bending vibration in polyamide parts and the peak at 3292 cm^{-1} is related to stretching vibration (N-H). Also, the elevation of 2861 cm^{-1} and the prak of 1460 cm^{-1} was related to C-H stretching and bending vibration, respectively.

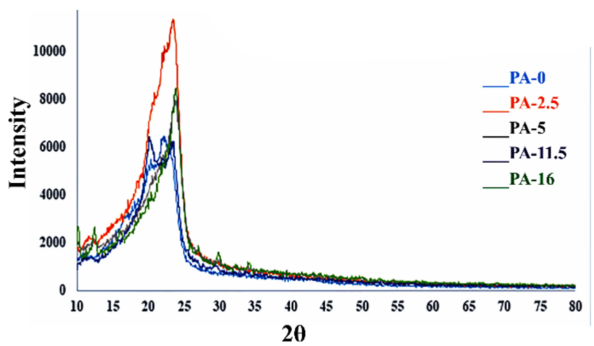

Figure 5. X-ray diffraction (XRD)

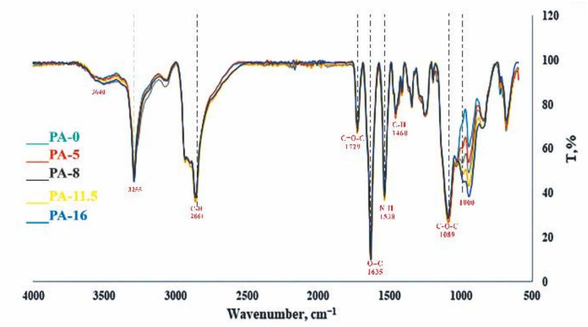

Figure 6. Fourier transform infrared spectroscopy

These results were in good agreement with another research [44]. In the spectrum of zeolite 4A, the broad absorption band in the wave number of 3255 cm^{-1} to 3640 cm^{-1} and the absorption band at 1650 cm^{-1} are related to hydroxyl (-OH) or silanol groups. Absorptions in wave number 1000 cm^{-1} are associated with O-Si or O-Al bending vibrations [45]. As the zeolite loading increased, the corresponding intensity of the peak at 3300 cm^{-1} also increased.

This significant change is attributed to filler phase loading. The absorption bands of zeolite overlap with the related bands in the Pebax spectrum. As the percentage of zeolite increases, the peak becomes higher at 1000 cm^{-1} due to the combined effect of Si-O or Al-O bonds in the zeolite. Finally, it can be said that the functional groups of Pebax and zeolite are placed next to each other with the help of physical bonds, and the formation of chemical bonds is ruled out.

3. 3. Imaging By Method Scanning Electron Microscopy (FE-SEM)

The behavior of polymeric membranes depends on their structure and morphology. Any defect in the membrane structure can cause poor performance in permeability. Therefore, FE-SEM photography was carried out to examine the morphology of the membranes. Figure 7 shows the FE-SEM images of the fabricated membranes.

The pure Pebax membrane (PA-0) has a uniform surface and shows that its preparation method is suitable. According to these images, it can be seen that by adding nano zeolite to the polymer, the morphology of the membrane surface changes.

By increasing the amount of zeolite, the intensity of these changes also increases. Tendency to aggregation and clumping has been observed in the 16% zeolite loading sample. The imaging of the cross-section of the pure Pebax membrane with 8% and 11.5% loading is shown in Figure 7 (G, H and I), respectively; their thicknesses was 82.3, 83.95, and 91.1 µm.

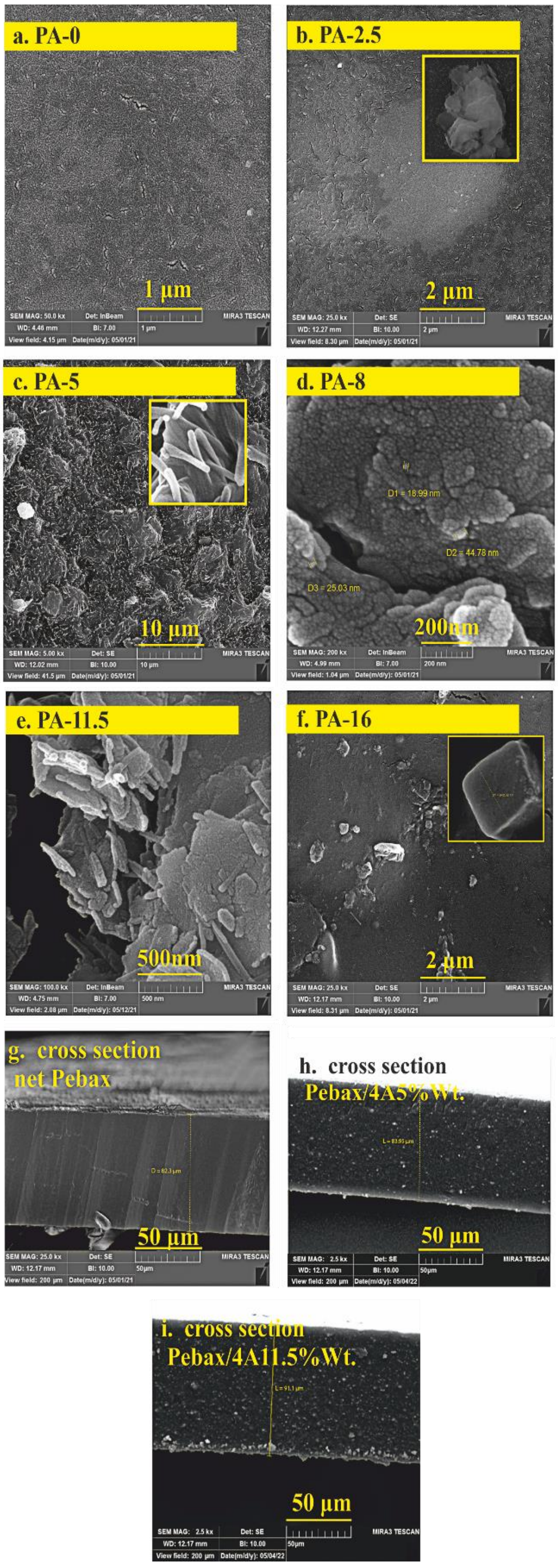

Figure 7. Scanning Electron Microscope (FE-SEM)

3. 4. X-ray Energy Scattering Spectroscopy (EDAX)

Al, Si, and Na are the main elements of zeolite 4A, making up about 70 Wt.% of its atoms. The results of this analysis, according to Table 4, show that the percentage of these atoms increases with an increase in the amount of zeolite in the membrane.

Also, Figures 8 and 9 show EDAX images for the the dispersion and proper distribution of elements on the surface of the membrane.

Still, the data of this analysis prove that the constructed membranes overcome this problem and the distribution of particles inside the polymer is uniform and acceptable. If the Si/Al ratio is less than 2, it indicates the hydrophilicity of the membrane [46]. In Table 4, this ratio for the PA-11.5 membrane is about 0.67. Membrane hydrophilicity can be an indicator of better CO_2 selectivity.

3. 5. Surface Measurement Specificity and Porosity (BET) BET analysis was performed to determine the physical properties of the synthesized membranes. In this specific surface area analysis, the total volume of specific pores, the size of the pore diameter and their distribution on the membrane surface were calculated.

TABLE 4. The percentage of the number of central atoms of zeolite in the samples of the constructed membranes

Na	Si	Al	ID
0.0	0.02	0.02	PA-0
0.11	0.16	0.22	PA-2.5
0.27	0.23	0.34	PA-5
0.47	0.52	0.94	PA-8
0.76	0.48	0.71	PA-11.5
0.82	0.76	1.06	PA-16

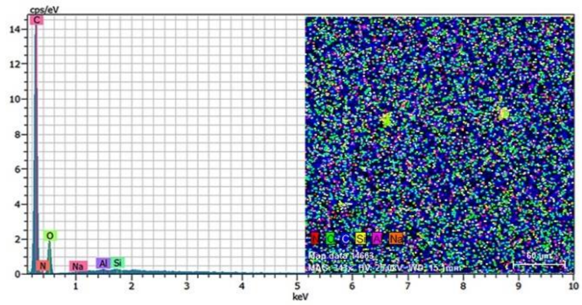

Figure 8. EDAX-Mapping PA-0

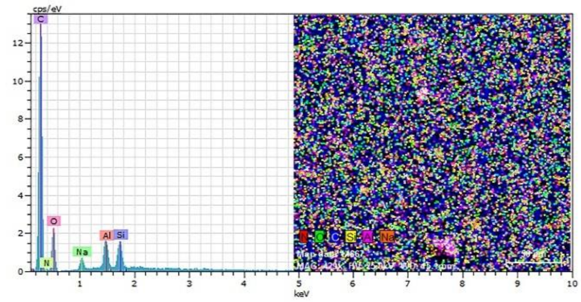

Figure 9. EDAX-Mapping PA-11.5

Table 5 summarized that after loading nanoparticles, the specific surface area of the membrane increased by 46%. Increasing this parameter affects gas absorption.

Figure 10 shows the absorption-desorption diagram of nitrogen at a temperature of 77 °K of the PA-11.5 membrane. This sample showed the best performance in permeability and selectivity. This diagram is similar to the isotherm of the sixth type of the IUPAC standard. According to this standard, a diameter of less than 2 nm is classified as non-porous.

For a more detailed investigation, the size distribution of the pores on the surface of the membrane was calculated by the BJH method. The results for pore size distribution by BJH method of PA-11.5 membrane is shown in Figure 11. The maximum number of the graph is 1.2nm and 1.8nm, which means that the size of the holes is mostly the same.

3. 6. Thermogravimetric Analysis (TGA) In this analysis, heating rate of 10 °C/min was applied to the samples. The TGA curves of PA-0 and PA-11.5 membranes were drawn in Figure 12. The noticeable weight loss in the samples up to 206 °C is about 1%, caused by the evaporation of the remaining solvent in the polymer [47].

TABLE 5. BET analysis results

ID	TPV	$a_{s,\,BET}$	Vm
PA-0	0.0044627	4.596	1.056
PA-11.5	0.0086457	6.694	1.538

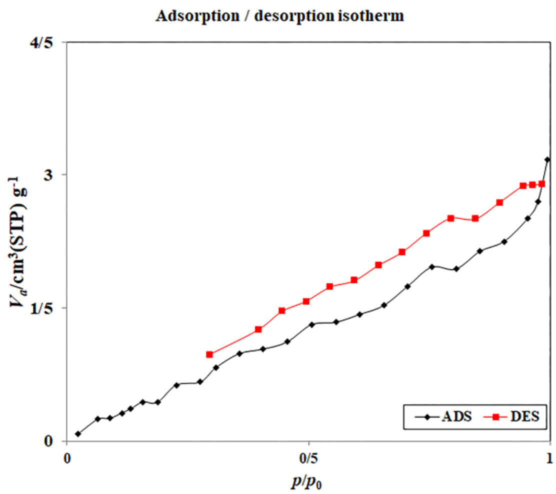

Figure 10. Isothermal absorption and desorption of nitrogen PA-11.5

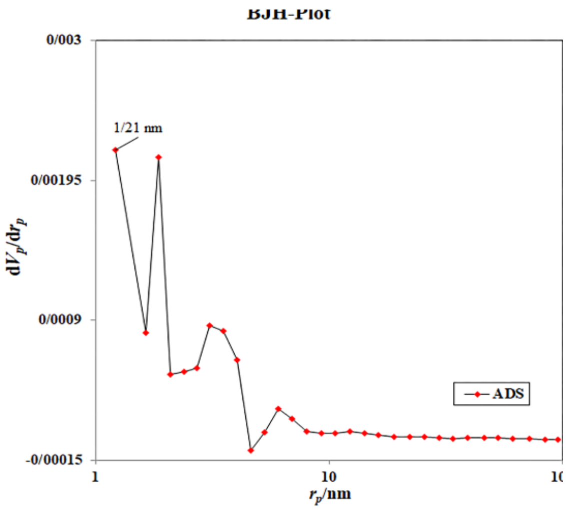

Figure 11. Pore size distribution by BJH method of PA-11.5 membrane

Weight loss in the PA-11.5 membrane started at about 328 °C. The reason is the beginning of the degradation of polymer chains. The DSC diagram shown the amount of energy required for this degradation. From about 361 to 446 °C, all polymer chains were destroyed. From about 450 °C, the polymer started to completely decompose and carbonate. After 525 °C, the weight did not change. But in the PA-0 membrane, the degradation started at 293 °C and at 450 °C, the chains were destroyed.

An increase in the destruction temperature in the nanocomposite membrane compared to the pure membrane is due to the physical bonds between nano zeolite and polymer. These bonds made the membrane strong. The formation of a strong covalent bond between them led to an increase in the energy required for destruction [48].

The DSC diagram shows the energy level needed to overcome these bonds. The TGA curve and the residual weight percentage confirm the presence of nano zeolite in the PA-11.5 membrane structure.

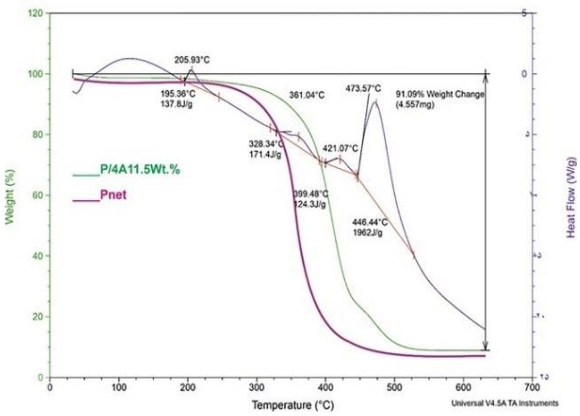

Figure 12. TGA/DSC analysis

3. 7. Analysis of Mechanical Strength

Mechanical strength analysis determines the tensile force a material can withstand before permanent damage. When a material is subjected to tensile force, it will withstand a certain amount of elongation before tearing. In this analysis, it was determined how strong the nanocomposite membrane is compared to the pure membrane.

The strip-shaped samples were placed between these two jaws of the machine and were drawn steadily at a speed of 5 mm/min. In this test, the temperature conditions and stretching rate remained constant. Table 6 shows the reaction of the manufactured membranes during the application of tensile force. In this table, it is shown that by addition of nanoparticles up to 11.5 wt%, the mechanical resistance of the composite membranes increased compared to the pure polymer membrane. The reason for that can be the proper physical bonding of nanoparticles and their coating by a polymer network. Also, this table shows that as the mass of particle increases, the membrane becomes denser. Excellent adhesion between nano zeolite and polymer, as well as their proper distribution on the surface of the membrane, increased the tensile strength.

The results of the EDAX analysis confirm that 4A particles are uniformly distributed in the polymer.The mechanical resistance of PA-16 and PA-22 membranes decreased. These two membranes cannot perform as well as the previous membranes. One of the reasons can be the clumping of nanoparticles in some places because clumping of nanoparticles causes their inability to interact with the polymer matrix and uneven stress distribution [48].

3. 8. Effect of Inlet Pressure

PA-11.5 nanocomposite membrane showed the best performance in permeability tests. For this reason, this membrane was chosen to investigate the effect of feed pressure on permeability and selectivity. By examining Figures 12, 13, and 14, the result of increasing the feed pressure on the permeability and selectivity of the membranes can be observed. As the pressure increased, the permeability of

TABLE 6. The mechanical performance of membranes

Loading Zeolite (Wt%)	Tensile strength (MPa)	Elastic modulus (MPa)	Elongation at break (%)
0	21.8	148.4	791 ± 2
2.5	23.1	135.3	812± 5
5	26.7	128.6	641 ± 5
8.5	29.3	118.5	598 ± 3
11.5	34.5	116.1	478 ± 3
16	19.9	95.8	251± 5
22.5	12.7	83.2	141 ± 5

CO_2 increased dramatically. at the same time, the permeability of other gases increased less. An increase in CO_2 permeability at higher pressures can be due to an increase in solubility due to the absorption of more CO_2 molecules in the polymer network [49]. Figure 12 demonstrates TGA/DSC analysis of the fabricated membrane

With an increase in pressure, the number of CO_2 molecules on the surface of the membrane increases. This increase creates a hydrogen bond between the O atom corresponding to the CO_2 molecule and the H of the amide groups on the surface of the polymer, for this reason, the selectivity of this gas increases. [6, 50]. Figure 13 shows the Robeson constraint chart for the selectivity of CO_2/CH_4 and CO_2/N_2 for the different Pebax 1657, Pebax 1657/4A and Pebax 1657/4A 11.5wt% of nanoparticles. In Figure 13, the performance of the optimized membrane in this study was marked on the Robeson diagram. This figure shows that the membrane was placed on the Robeson line. As a result, it can be considered a suitable option for separating carbon dioxide gas from other light gases in chemical industries.

3. 9. Effect of Operating Temperature The kinetic energy of gas molecules at high temperatures destroyed some of the polymer chains ,and the polymer network became more flexible. This flexibility in the polymer network can increase the molecular free volume coefficient in the membrane. Therefore, the membrane permeability increased, but the selectivity significantly decreased [51]. The reason for that can be the decrease in the solubility of CO_2 at temperatures higher than 35°C. If the solubility coefficient decreases, the selectivity of CO_2 also decreases compared to other gases [6]. Figure 14 shows CO_2 / N_2 selectivity at different temperatures and pressures; while Figure 15 illustrates CO_2 / CH_4 selectivity at different temperatures and pressures. In addition, the selectivity of CO_2/O_2 at different temperatures and pressures is shown in Figure 16.

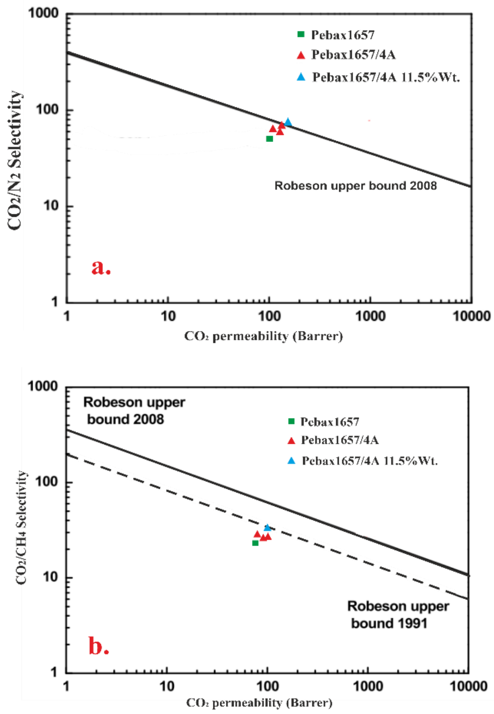

Figure 13. Robeson constraint chart

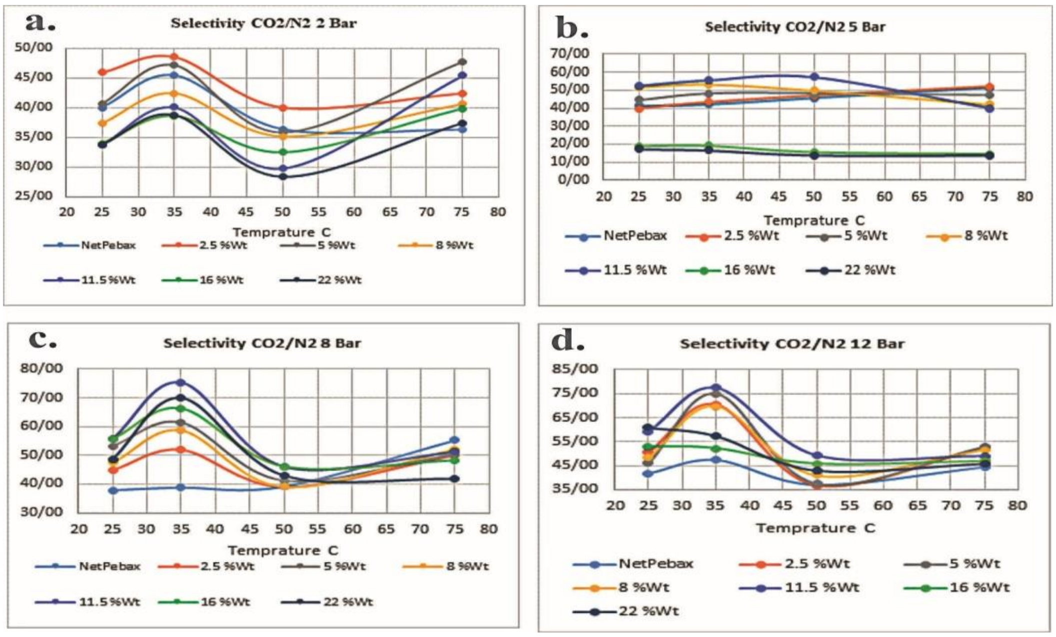

Figure 14. CO_2 / N_2 selectivity in different temperatures and pressures

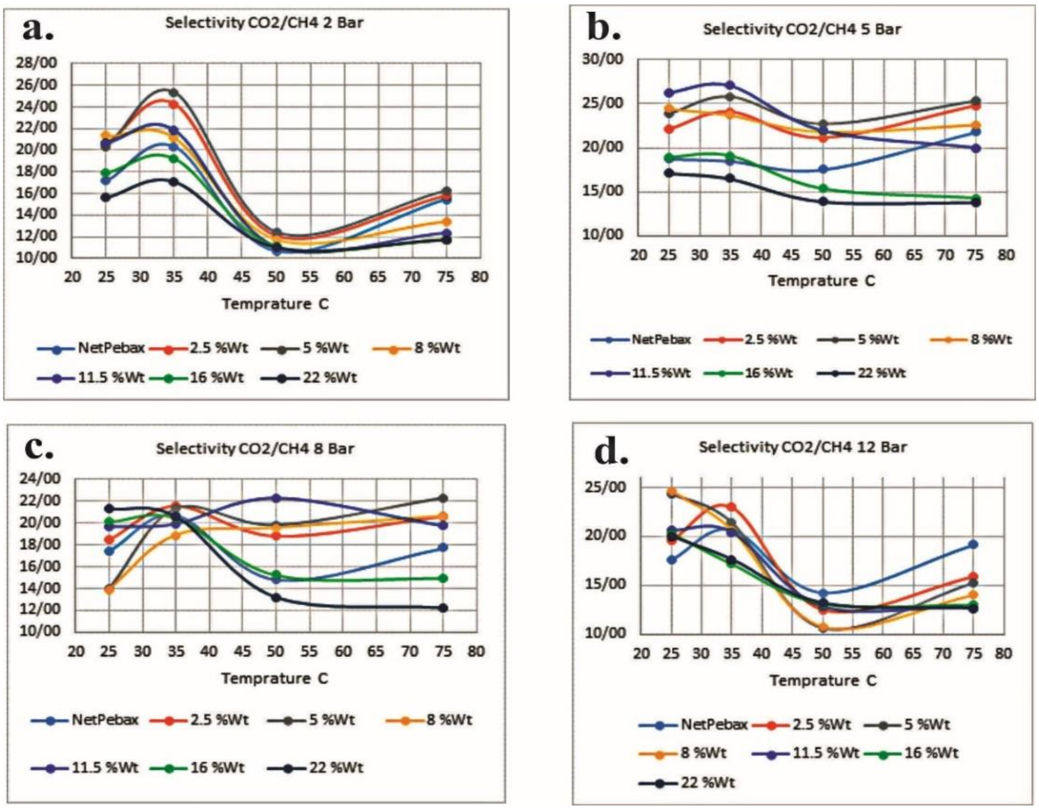

Figure 15. CO_2 / CH_4 selectivity in different temperatures and pressures

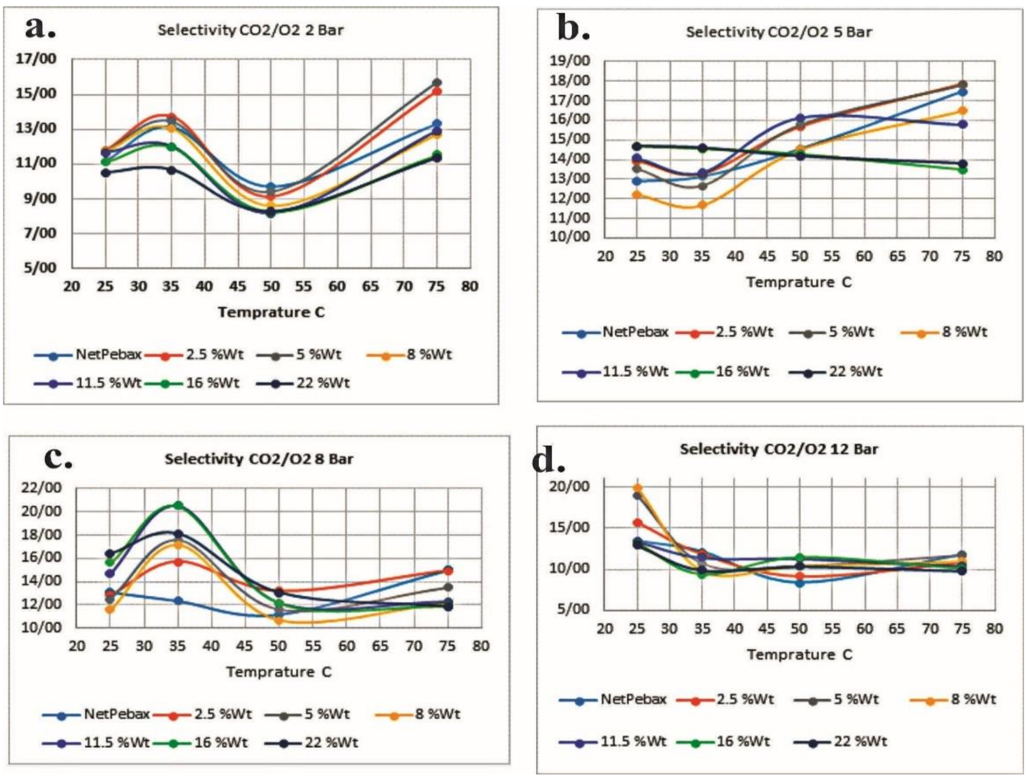

Figure 16. CO_2/ O_2 selectivity in different temperatures and pressures

4. CONCLUSION

In this research, Pebax 1657/4A zeolite nanocomposite membranes were prepared by casting and solvent evaporation. Their performance was investigated under operating conditions of 25 to 75 °C and pressures of 2 to 12 Bar for separating CO_2 gas relative to N_2, CH_4, and O_2. The results of FT-IR test denied the formation of a chemical bond between zeolite and polymer. FE-SEM images and EDAX analysis showed that the nano zeolites were well dispersed in the polymer, and a suitable nanocomposite membrane structure was obtained.

The TGA/DSC test showed that the thermal resistance of the nanocomposite membrane has increased compared to the polymer membrane. It also proved physical solid bonds between nano zeolite and polymer. CO_2 selectivity increased with increasing operating pressure. An increase in the operating temperature causes a significant increase in the permeability of gases due to an increase in their molecular kinetic energy and the polymer chains becoming more flexible. But the selectivity was significantly reduced. BET test showed that the pore size of nanocomposite membranes is less than 2 nm. This size is proportional to CO_2 molecules. These molecules can pass with less resistance than the pure polymeric membrane. Nanoparticle loading reduces the density of polymer chains and weakens the hydrogen bond between them. This factor increases the free volume between molecules and increases permeability.

The results of the gas permeability test showed that the best result was obtained at a temperature of 35 °C by adding 11.5% Wt. of zeolite to the polymer membrane. The best selectivity of CO_2 against N_2, O_2, and CH_4 was obtained at 12, 8, and 5 bar pressures, respectively.

Finally, the selectivity of the Pebax1657/4A nanocomposite membrane was 64, 67, and 45% better than pure Pebax in the mentioned operating conditions, respectively. As mentioned in the introduction, Robeson presented a limit in the permeability selectivity diagram, which was called Robeson's upper limit. The closer the polymer membrane is to this upper limit of the graph, the more suitable it is for industrialization.

Nowadays, the elimination of these gases has become a vital issue for researchers so that they can prevent the excessive heating of the earth.

5. REFERENCES

1. Othman, F.E.C., Yusof, N., Petrů, M., Nordin, N.A.H.M., Hamid, M.F., Ismail, A.F., Rushdan, A.I. and Hassan, S.A., "Polyethyleneimine-impregnated activated carbon nanofiber composited graphene-derived rice husk char for efficient post-combustion CO_2 capture", ***Nanotechnology Reviews***, Vol. 11, No. 1, (2022), 926-944. https://doi.org/10.1515/ntrev-2022-0055
2. A. Brunettia, F.S., G. Barbieria, E. Driolia,b, "Membrane technologies for CO_2 separation", ***Journal of Membrane Science***, Vol. 359, No. 1-2, (2010), 115-125. https://doi.org/10.1016/j.memsci.2009.11.040
3. Aghanezhad, M., Shafaghat, R., Alamian, R., Seyedi, S.M.A. and Raji Asadabadi, M.J., "Experimental study on performance assessment of hydraulic power take-off system in centipede wave energy converter considering caspian sea wave characteristics", ***International Journal of Engineering, Transactions B: Applications***, Vol. 35, No. 5, (2022), 883-899. https://doi.org/10.5829/ije.2022.35.05b.17
4. Jahanbakhsh, A., Hosseini, M., Jahanshahi, M. and Amiri, A., "Extraction of catechin as a flavonoid compound via molecularly imprinted polymers", ***International Journal of Engineering, Transactions B: Applications***, Vol. 35, No. 5, (2022), 988-995. https://doi.org/10.5829/ije.2022.35.08b.05
5. Mirhosseini, N., Davarnejad, R., Hallajisani, A., Cano-europa, E. and Tavakoli, O., "Sugarcane molasses as a cost-effective carbon source on arthrospira maxima growth by taguchi technique", ***International Journal of Engineering, Transactions C: Aspects***, Vol. 35, No. 3, (2022), 510-516. https://doi.org/10.5829/ije.2022.35.03C.13
6. Lin, H., Freeman, B.D., Kalakkunnath, S. and Kalika, D.S., "Effect of copolymer composition, temperature, and carbon dioxide fugacity on pure-and mixed-gas permeability in poly (ethylene glycol)-based materials: Free volume interpretation", ***Journal of Membrane Science***, Vol. 291, No. 1-2, (2007), 131-139. https://doi.org/10.1016/j.memsci.2007.01.001
7. Sheth, J.P., Xu, J. and Wilkes, G.L., "Solid state structure–property behavior of semicrystalline poly(ether-block-amide) pebax® thermoplastic elastomers", ***Polymer***, Vol. 44, No. 3, (2003), 743-756. https://doi.org/10.1016/S0032-3861(02)00798-X
8. Robeson, L.M., "The upper bound revisited", ***Journal of Membrane Science***, Vol. 320, No. 1-2, (2008), 390-400. https://doi.org/10.1016/j.memsci.2008.04.030
9. Kianfar, F. and Kianfar, E., "Synthesis of isophthalic acid/aluminum nitrate thin film nanocomposite membrane for hard water softening", ***Journal of Inorganic and Organometallic Polymers and Materials***, Vol. 29, No. 6, (2019), 2176-2185. https://doi.org/10.1007/s10904-019-01177-1
10. Kianfar, E., Salimi, M., Kianfar, F., Kianfar, M. and Razavikia, S.A.H., " CO_2/N_2 separation using polyvinyl chloride iso-phthalic acid/aluminium nitrate nanocomposite membrane", ***Macromolecular Research***, Vol. 27, No. 1, (2019), 83-89. https://doi.org/10.1007/s13233-019-7009-4
11. Salimi, M., Pirouzfar, V. and Kianfar, E., "Novel nanocomposite membranes prepared with pvc/abs and silica nanoparticles for C_2H_6/CH_4 separation", ***Polymer Science, Series A***, Vol. 59, No. 4, (2017), 566-574. https://doi.org/10.1134/S0965545X17040071
12. Embaye, A.S., Martínez-Izquierdo, L., Malankowska, M., Téllez, C. and Coronas, J., "Poly(ether-block-amide) copolymer membranes in CO_2 separation applications", ***Energy & Fuels***, Vol. 35, No. 21, (2021), 17085-17102. https://doi.org/10.1021/acs.energyfuels.1c01638
13. Salimi, M., Pirouzfar, V. and Kianfar, E., "Enhanced gas transport properties in silica nanoparticle filler-polystyrene nanocomposite membranes", ***Colloid and Polymer Science***, Vol. 295, No. 1, (2017), 215-226. https://doi.org/10.1007/s00396-016-3998-0
14. Padhi, P., Rout, S. and Panda, D., "Effect of modification of zeolite a using sodium carboxymethylcellulose (CMC)", ***Bulgarian Chemical Communications,*** Vol. 46, No.4, (2014), 777-783.

15. Shariatzadeh, S.M.R., Salimi, M., Fathinejad, H. and Hassani Joshaghani, A., "Nanostructured α-Fe_2O_3: Solvothermal synthesis, characterization, and effect of synthesis parameters on structural properties", ***International Journal of Engineering, Transactions C: Aspects***, Vol. 35, No. 6, (2022), 1186-1192. https://doi.org/10.5829/ije.2022.35.06c.10

16. Andami, P., Zinatizadeh, A.A., Feyzi, M., Zangeneh, H., Azizi, S., Norouzi, L. and Maaza, M., "Optimization of biodiesel production from sunflower oil transesterification using Ca-k/Al_2O_3 nanocatalysts", ***International Journal of Engineering, Transactions B: Applications***, Vol. 35, No. 2, (2022), 351-359. https://doi.org/10.5829/ije.2022.35.02b.11

17. Ahmad, J. and Hägg, M.-B., "Preparation and characterization of polyvinyl acetate/zeolite 4a mixed matrix membrane for gas separation", ***Journal of Membrane Science***, Vol. 427, (2013), 73-84. https://doi.org/10.1016/j.memsci.2012.09.036

18. Chung, T.-S., Jiang, L.Y., Li, Y. and Kulprathipanja, S., "Mixed matrix membranes (MMMS) comprising organic polymers with dispersed inorganic fillers for gas separation", ***Progress in Polymer Science***, Vol. 32, No. 4, (2007), 483-507. https://doi.org/10.1016/j.progpolymsci.2007.01.008

19. Saeedi Dehaghani, A.H. and Pirouzfar, V., "Preparation of high-performance membranes derived from poly (4-methyl-1-pentene)/zinc oxide particles", ***Chemical Engineering & Technology***, Vol. 40, No. 9, (2017), 1693-1701. https://doi.org/10.1002/ceat.201600693

20. Suhas, D.P., Aminabhavi, T.M. and Raghu, A.V., "Para-toluene sulfonic acid treated clay loaded sodium alginate membranes for enhanced pervaporative dehydration of isopropanol", ***Applied Clay Science***, Vol. 101, (2014), 419-429. https://doi.org/10.1016/j.clay.2014.08.017

21. Dharupaneedi, S.P., Anjanapura, R.V., Han, J.M. and Aminabhavi, T.M., "Functionalized graphene sheets embedded in chitosan nanocomposite membranes for ethanol and isopropanol dehydration via pervaporation", ***Industrial & Engineering Chemistry Research***, Vol. 53, No. 37, (2014), 14474-14484. https://doi.org/10.1021/ie502751h

22. Kianfar, E., Pirouzfar, V. and Sakhaeinia, H., "An experimental study on absorption/stripping CO_2 using mono-ethanol amine hollow fiber membrane contactor", ***Journal of the Taiwan Institute of Chemical Engineers***, Vol. 80, (2017), 954-962. https://doi.org/10.1016/j.jtice.2017.08.017

23. Saeedi Dehaghani, A.H., Pirouzfar, V. and Alihosseini, A., "Novel nanocomposite membranes-derived poly(4-methyl-1-pentene)/functionalized titanium dioxide to improve the gases transport properties and separation performance", ***Polymer Bulletin***, Vol. 77, No. 12, (2020), 6467-6489. https://doi.org/10.1016/j.jtice.2017.08.017

24. Cheng, J., Wang, Y., Liu, N., Hou, W. and Zhou, J., "Enhanced CO_2 selectivity of mixed matrix membranes with carbonized zn/co zeolitic imidazolate frameworks", ***Applied Energy***, Vol. 272, (2020), 115179. https://doi.org/10.1016/j.apenergy.2020.115179

25. Asghari, M., Mosadegh, M. and Harami, H.R., "Supported peba-zeolite 13x nano-composite membranes for gas separation: Preparation, characterization and molecular dynamics simulation", ***Chemical Engineering Science***, Vol. 187, (2018), 67-78. https://doi.org/10.1016/j.apenergy.2020.115179

26. Atash Jameh, A., Mohammadi, T. and Bakhtiari, O., "Preparation of pebax-1074/modified zif-8 nanoparticles mixed matrix membranes for CO_2 removal from natural gas", ***Separation and Purification Technology***, Vol. 231, (2020), 115900. https://doi.org/10.1016/j.seppur.2019.115900

27. Azizi, N., Mohammadi, T. and Behbahani, R.M., "Synthesis of a pebax-1074/zno nanocomposite membrane with improved CO_2 separation performance", ***Journal of Energy Chemistry***, Vol. 26, No. 3, (2017), 454-465. https://doi.org/10.1016/j.seppur.2019.115900

28. Azizi, N., Isanejad, M., Mohammadi, T. and Behbahani, R.M., "Effect of tio2 loading on the morphology and CO_2/ CH_4 separation performance of pebax-based membranes", ***Frontiers of Chemical Science and Engineering***, Vol. 13, No. 3, (2019), 517-530. https://doi.org/10.1016/j.seppur.2019.115900

29. Deng, J., Dai, Z. and Deng, L., "Effects of the morphology of the zif on the CO_2 separation performance of mmms", ***Industrial & Engineering Chemistry Research***, Vol. 59, No. 32, (2020), 14458-14466. https://doi.org/10.1021/acs.iecr.0c01946

30. Farashi, Z., Azizi, S., Arzhandi, M.R.-D., Noroozi, Z. and Azizi, N., "Improving CO_2/ CH_4 separation efficiency of pebax-1657 membrane by adding Al_2O_3 nanoparticles in its matrix", ***Journal of Natural Gas Science and Engineering***, Vol. 72, No., (2019), 103019. https://doi.org/10.1016/j.jngse.2019.103019

31. Jomekian, A., Behbahani, R.M., Mohammadi, T. and Kargari, A., "CO_2/ CH_4 separation by high performance co-casted zif-8/pebax 1657/pes mixed matrix membrane", ***Journal of Natural Gas Science and Engineering***, Vol. 31, (2016), 562-574. https://doi.org/10.1016/j.jngse.2016.03.067

32. Karamouz, F., Maghsoudi, H. and Yegani, R., "Synthesis of high-performance pebax®-1074/dd3r mixed-matrix membranes for CO_2/ CH_4 separation", ***Chemical Engineering & Technology***, Vol. 41, No. 9, (2018), 1767-1775. https://doi.org/10.1002/ceat.201800087

33. Khoshkharam, A., Azizi, N., Behbahani, R.M. and Ghayyem, M.A., "Separation of CO_2 from CH_4 using a synthesized pebax-1657/zif-7 mixed matrix membrane", ***Petroleum Science and Technology***, Vol. 35, No. 7, (2017), 667-673. https://doi.org/10.1080/10916466.2016.1273242

34. Khosravi, T., Omidkhah, M., Kaliaguine, S. and Rodrigue, D., "Amine-functionalized cubtc/poly (ether-b-amide-6)(pebax® mh 1657) mixed matrix membranes for CO_2/ CH_4 separation", ***The Canadian Journal of Chemical Engineering***, Vol. 95, No. 10, (2017), 2024-2033. https://doi.org/10.1002/cjce.22857

35. Li, T., Pan, Y., Peinemann, K.-V. and Lai, Z., "Carbon dioxide selective mixed matrix composite membrane containing zif-7 nano-fillers", ***Journal of Membrane Science***, Vol. 425, (2013), 235-242. https://doi.org/10.1002/cjce.22857

36. Zheng, Y., Wu, Y., Zhang, B. and Wang, Z., "Preparation and characterization of CO_2-selective pebax/nay mixed matrix membranes", ***Journal of Applied Polymer Science***, Vol. 137, No. 9, (2020), 48398. https://doi.org/10.1002/cjce.22857

37. Zarshenas, K., Raisi, A. and Aroujalian, A., "Mixed matrix membrane of nano-zeolite nax/poly (ether-block-amide) for gas separation applications", ***Journal of Membrane Science***, Vol. 510, (2016), 270-283. https://doi.org/10.1002/cjce.22857

38. Nafisi, V. and Hägg, M.-B., "Development of dual layer of zif-8/pebax-2533 mixed matrix membrane for CO_2 capture", ***Journal of Membrane Science***, Vol. 459, (2014), 244-255. https://doi.org/10.1002/cjce.22857

39. Hosseinzadeh Beiragh, H., Omidkhah, M., Abedini, R., Khosravi, T. and Pakseresht, S., "Synthesis and characterization of poly (ether-block-amide) mixed matrix membranes incorporated by nanoporous zsm-5 particles for CO_2/ch4 separation", ***Asia-Pacific Journal of Chemical Engineering***, Vol. 11, No. 4, (2016), 522-532. https://doi.org/10.1002/cjce.22857

40. mousavian, S., Faravar, P., Zarei, Z., azimikia, R., Ghasemi Monjezi, M. and kianfar, E., "Modeling and simulation absorption of CO_2 using hollow fiber membranes (HFM) with mono-ethanol amine with computational fluid dynamics", ***Journal of Environmental Chemical Engineering***, Vol. 8, No. 4, (2020), 103946. https://doi.org/10.1016/j.jece.2020.103946

41. Kianfar, E. and Cao, V., "Polymeric membranes on base of polymethyl methacrylate for air separation: A review", ***Journal***

of Materials Research and Technology, Vol. 10, (2021), 1437-1461. https://doi.org/10.1016/j.jmrt.2020.12.061

42. Kianfar, E., Pirouzfar, V. and Sakhaeinia, H., "An experimental study on absorption/stripping CO_2 using mono-ethanol amine hollow fiber membrane contactor", ***Journal of the Taiwan Institute of Chemical Engineers***, Vol. 80, No., (2017), 954-962. https://doi.org/10.1016/j.jtice.2017.08.017

43. Khoramzadeh, E., Mofarahi, M. and Lee, C.-H., "Equilibrium adsorption study of CO_2 and N2 on synthesized zeolites 13x, 4a, 5a, and beta", ***Journal of Chemical & Engineering Data***, Vol. 64, No. 12, (2019), 5648-5664. https://doi.org/10.1021/acs.jced.9b00690

44. Surya Murali, R., Ismail, A.F., Rahman, M.A. and Sridhar, S., "Mixed matrix membranes of pebax-1657 loaded with 4a zeolite for gaseous separations", ***Separation and Purification Technology***, Vol. 129, (2014), 1-8. https://doi.org/10.1016/j.seppur.2014.03.017

45. Zou, W., Bai, H., Zhao, L., Li, K. and Han, R., "Characterization and properties of zeolite as adsorbent for removal of uranium(vi) from solution in fixed bed column", ***Journal of Radioanalytical and Nuclear Chemistry***, Vol. 288, No. 3, (2011), 779-788. https://doi.org/10.1016/j.seppur.2014.03.017

46. Castillo, J.M., Silvestre-Albero, J., Rodriguez-Reinoso, F., Vlugt, T.J. and Calero, S., "Water adsorption in hydrophilic zeolites: Experiment and simulation", ***Physical Chemistry Chemical Physics***, Vol. 15, No. 40, (2013), 17374-17382.

47. Azizi, N., Isanejad, M., Mohammadi, T. and Behbahani, R.M., "Effect of TiO_2 loading on the morphology and CO_2/ CH_4 separation performance of pebax-based membranes", ***Frontiers of Chemical Science and Engineering***, Vol. 13, No. 3, (2019), 517-530. https://doi.org/10.1007/s11705-018-1781-0

48. Basu, S., Cano-Odena, A. and Vankelecom, I.F.J., "Mof-containing mixed-matrix membranes for CO_2/CH_4 and CO_2/N_2 binary gas mixture separations", ***Separation and Purification Technology***, Vol. 81, No. 1, (2011), 31-40. https://doi.org/10.1016/j.seppur.2011.06.037

49. Sridhar, S., Suryamurali, R., Smitha, B. and Aminabhavi, T.M., "Development of crosslinked poly(ether-block-amide) membrane for CO_2/CH_4 separation", ***Colloids and Surfaces A: Physicochemical and Engineering Aspects***, Vol. 297, No. 1, (2007), 267-274. https://doi.org/10.1016/j.colsurfa.2006.10.054

50. Saeedi Dehaghani, A.H., Pirouzfar, V. and Alihosseini, A., "Novel nanocomposite membranes-derived poly(4-methyl-1-pentene)/functionalized titanium dioxide to improve the gases transport properties and separation performance", ***Polymer Bulletin***, Vol. 77, No. 12, (2020), 6467-6489. https://doi.org/10.1016/j.colsurfa.2006.10.054

51. Rahman, M.M., Shishatskiy, S., Abetz, C., Georgopanos, P., Neumann, S., Khan, M.M., Filiz, V. and Abetz, V., "Influence of temperature upon properties of tailor-made pebax® mh 1657 nanocomposite membranes for post-combustion CO_2 capture", ***Journal of Membrane Science***, Vol. 469, (2014), 344-354. https://doi.org/10.1016/j.memsci.2014.06.048

Persian Abstract

چکیده

جداسازی دی اکسید کربن برای محیط زیست ضروری است. استفاده از غشاها برای جداسازی این گاز مقرون به صرفه است، اما ضعف در نفوذپذیری و استحکام مکانیکی مانع تجاری سازی آنها شده است. رابسون ثابت کرد که نفوذپذیری و گزینش پذیری رابطه معکوس دارند و حد بالایی برای جفت گازها ارائه کرد. وی اظهار داشت که هر غشایی که بالاتر از این حد قرار گیرد، قابل تجاری سازی است. دانشمندان برای غلبه بر این مشکل غشاهای ماتریس مخلوط را پیشنهاد کردند. این غشاها شامل دو فاز پلیمری و معدنی هستند. هدف از این تحقیق رفع نقاط ضعف ذکر شده و کسب جایگاه مناسب در نمودار رابسون می باشد. پلیمر Pebax و زئولیت 4A به ترتیب به عنوان فازهای پلیمری و معدنی برای ساخت غشا انتخاب شدند. غشاهای ساخته شده توسط تست های XRD، FT-IR، FE-SEM، BET، EDAX، TGA/DSC و استحکام مکانیکی مورد ارزیابی قرار گرفتند. در نهایت، گزینش پذیری دی اکسید کربن در مقایسه با نیتروژن، اکسیژن و متان به ترتیب ۵۳، ٦٧ و ۷۵ درصد بهبود یافت و موقعیت خوبی در نمودار رابسون به دست آورد.

IJE TRANSACTIONS B: Applications Vol. 36, No. 02, (February 2023) 420-432

International Journal of Engineering

Journal Homepage: www.ije.ir

Redesigning and Re-planning of Location, Pricing, Inventory and Marketing Decisions in a Multi-channel Distribution Network: A Case Study

H. Bagheri[a], M. H. Karimi Ghavareshki*[a], H. Fazlollahtabar[b], M. Abbasi[a]

[a] *Department of Industrial Engineering, Faculty of Engineering, Malek Ashtar University of Technology, Tehran, Iran*
[b] *Department of Industrial Engineering, School of Engineering Damghan University, Damghan, Iran*

PAPER INFO

Paper history:
Received 02 November 2022
Received in revised form 10 December 2022
Accepted 11 December 2022

Keywords:
Distribution Network
Location
Pricing
Marketing Decision

ABSTRACT

Discussion of distribution and distribution network design and planning, including location, pricing, optimal selection of distribution channels, as well as marketing decisions, is of great importance in the supply chain. Due to the changes and uncertainty of market demand, the design and planning of the distribution network and static sale have encountered many problems in practice. This article presents a nonlinear mathematical programming model for locating, inventory control, and marketing of manufactured products for a multi-activity organization that includes manufacturing, distribution, retail, and wholesale units. The model includes the localization of distribution centers and the corresponding inventory management, taking into account marketing-related parameters such as multi-channel pricing. A centralized decision support is developed to select the appropriate sales channel, to determine the quantity of products sold in each channel and the discounts granted for each specific channel using real data. In this model, the goal is to maximize profit while increasing customer value by considering competitors' price and choosing the best channel to deliver the product to the customer. Finally, for a small problem instance, the proposed model was solved using the GAMS 28.2.0 x64 optimization software package. Validation study and sensitivity analysis are performed to imply the effectiveness of the formulated mathematical model.

doi: *10.5829/ije.2023.36.02b.20*

NOMENCLATURE

Indices		P_K	Product lead time to reach distribution centers
l	Available distribution centers	$M_{m\gamma}$	Variance of product demand in normal distribution
m	The collection of sales channels of the company	CAP_γ	The cost of setting up a new warehouse at point k
k	Set of potential points for creating new distribution centers	$D_{\gamma r}$	The cost of transportation of each product unit from the warehouse of Lam to the sales channel of Mm
r	Areas of demand for the product	C_γ	The cost of transporting each product unit from the warehouse to the sales channel m
Parameters		**Decision variables**	
P	The speed of product production by the domestic manufacturer	φ_m	The selling price of the product in the m channel
$\mathbf{M_{m\gamma}}$	The average price of competitors for the product in the m distribution channel	γ_{mr}	If the product is allocated to the rth region through the mth channel, 1 otherwise 0
$\mathbf{CAP_\gamma}$	Domestic manufacturer's production capacity for the product	ω_{lmr}	The amount of product allocation from the L distribution centers through the m channel for the demand of the r region
$\mathbf{CAP_l}$	The capacity of distribution centers is L	ω'_{kmr}	The amount of product allocation from the kth potential distribution centers through the mth channel for the demand of the rth region
$\mathbf{h_\gamma}$	Cost of maintaining each product unit in distribution centers	α_m	The minimum percentage of net profit considered for the product in m channel
$\mathbf{T_{il\gamma}}$	The cost of transporting each product unit from domestic production to distribution centers is L	Q^*	The amount of the total order of the product by the decision-making system for allocation to the distribution centers

*Corresponding Author Institutional Email: mh_karimi@mut.ac.ir
(H. Karimi Ghavareshk)

Please cite this article as: H. Bagheri, M. H. Karimi Ghavareshki, H. Fazlollahtabar, M. Abbasi, Fabrication of Pebax/4A Zeolite Nanocomposite Membrane to Enhance CO_2 Selectivity Compared to Pure O_2, N_2, and CH_4 Gases, ***International Journal of Engineering, Transactions B: Applications***, Vol. 36, No. 02, (2023), 420-432

$\mathbf{T'_{jl\gamma}}$	The cost of transporting each product unit from the external manufacturer to the distribution centers is L, because it is delivered to the distributor's warehouse, and the cost of transportation is the responsibility of the supplier.	$EOQ_l = Q_{2l}$	The order amount of the L distribution center of the product
$\mathbf{T''_{lm\gamma}}$	The cost of transporting each product unit from domestic production to distribution centers is k	$EPQ_l = Q_{1l}$	The amount of product production order for L distribution center from the domestic supplier
$\mathbf{A_\gamma}$	The cost of transporting each product unit from the external manufacturer to the distribution centers is L, because it is delivered to the distributor's warehouse, and the cost of transportation is the responsibility of the supplier.	$EPQ_k = Q_{1k}$	The amount of product production order for the kth production center from the domestic supplier
$\mathbf{C'_\gamma}$	The cost of ordering the product from the manufacturer and supplier	$EOQ_k = Q_{2k}$	The order amount of the kth distribution centers of the product by the foreign supplier
$\mathbf{D_\gamma = \sum_r D_{\gamma r}}$	The amount of demand in the rth region of the product (with a normal distribution)	R^*	Reorder point for the product
$\mathbf{P_\gamma = \sum_i P_{i\gamma}}$	The purchase price of the product from a foreign supplier (outsourcing)	Pro_m	The amount of difference in the selling price of the manufactured product in the mth channel compared to competitors and the market
$\mathbf{l_\gamma}$	The set of demand of all regions for the p product	W_k	1 if a new warehouse is established at point k and zero otherwise

1. INTRODUCTION

In recent years, it is required to pay more attention to supply chain management; which has become more and more important. In order to improve and optimize the supply chain, special attention should be paid to the design and planning of distribution and sales. One of the tasks of the distribution and sales system is the transfer of goods from the producer level through the lower levels to the customer level. In addition, the distribution and sales systems can be seen as the eyes of the market observers, who are in direct contact with the customers and can transmit the customers' feedback and opinions to the producers in a timely manner. If producers can incorporate these opinions into their designs and planning, not only will the producers' profits increase, but so will the profits of all components of the supply chain. Distribution systems and sales channels can also collect returned goods and forward them to higher levels in the chain. Other tasks of distribution and sales systems are advertising, market research and competition analysis. A supply chain sales and distribution network typically consists of customers, warehouses, distribution centers, and distribution channels. When planning and designing such networks, decisions are made such as: B. Determining the location of distribution centers, capacity and location of facilities, inventory control policies in distribution center warehouses and determining the final price of the product. Various tools have been used to date to make such decisions, one of the most widespread of which is operations research, which dates back several decades. The design and planning of supply chain networks is one of the most important tasks of supply chain management. Due to the importance of the topic, many articles from different journals have been studied in Scopus and Web of Science databases. The number of reviewed articles was 76, out of which only 13 articles had conducted studies on the problem of joint optimization (location-inventory, location-inventory pricing). Out of 13 articles in the field of joint optimization, almost 61% investigated the problem of integrated optimization of inventory location and only 39% investigated the problem of joint optimization of inventory location and pricing. In this context, a review article has also been studied. The important point is that all these articles are related to the issue of production and distribution, and no article was found about the issue of distribution and sale.

One of the main areas of supply chain activity involves the distribution and sale of products. Due to the connection of the distribution network with the customer, the redesign and positioning of the network activities as well as the proper and correct planning of the distribution network has a significant impact on the cost, performance and flexibility of the supply chain network. The distribution and distribution network examined in this article reaches the customer through two types of suppliers, including internal manufacturers and external manufacturers, and through distribution and distribution centers to three distribution channels (retail, wholesale and e-commerce). There are several ways to distribute goods from production and supply points to demand points. The problem we are facing is the planning of the intelligent distribution and distribution network, which includes the placement of warehouses in distribution centers and the assignment of retailers to warehouses, as well as the selection of inventory and pricing policies for different distribution and distribution channels. In the studied distribution network, three retail and wholesale and internet channels were considered. The design and planning of the distribution and pricing network should be optimized to optimize the amount of demand allocation to each channel considering the profit from each channel. In the three-channel sales network to be examined, the prices and sales volumes should be determined in such a way that the conflict and competition between the two internal channels of the company, i.e. the retail and wholesale channels, is kept as low as possible and under control. In the considered model, product manufacturers are divided into two categories, which include suppliers within the organization and external manufacturers not connected to the holding company. In addition to the location of the distribution centers, this model also considered the inventory policy and pricing in different channels. It is worth noting that products are sold and delivered to customers through three main distribution channels, including retail, wholesale and internet.

Our goal in the studied model is to maximize the profit from Turnover in all three channels retail, wholesale and internet, which results from the difference between income and expenses and offers the maximum benefit for the customer, taking into account the availability and delivery time of the goods. In fact, the revenue is the revenue from the sale of products in all three retail and wholesale channels and the Internet, and the cost includes the cost of setting up a branch warehouse, inventory costs and transportation costs, including shipping from the main warehouse to the distribution centers, from the distribution centers to retailers and wholesalers. The distribution centers and production units affiliated with the holding company have limited capacities in this regard. Utilizing multiple capacities for distribution center storage has made the problem more practical. Further decisions are the optimal assignment of retailers and wholesalers to the established distribution centers, determining the product price and customer demand online for different sales channels. The pricing policy adopted in this edition attempts to manage the demand leakage in the retail, wholesale and internet channels by including restrictions on wholesale, retail and internet prices. If the demand leakage is not managed, the company's distribution channels will face internal competition (for the company's product), which will eventually lead to multi-priced goods.

Considering that the proposed model is presented for organizations that have different stores and a complete supply and value chain for each product, including delivery, production, distribution and sale, which requires simultaneous and coordinated planning for better and more accurate planning . It is between the variables of these 4 levels that we have attempted to use an integrated planning model for location, pricing, inventory management and marketing decisions. In the location discussion, we need to locate new warehouses or distribution centers during the implementation of the model since the demand for the product is variable and the capacity of the existing warehouses or distribution centers does not respond to it, and we need new locations for distribution centers during the implementation of the model.

2. LITERATURE REVIEW

Location, inventory, pricing and marketing decisions are important issue to address [1]. However, not much attention has been paid to this issue in the existing literature. The objective of classical location-inventory problems is simultaneously to decide on location allocation and to determine the amount of inventory storage in distribution centers [2]. Farahani et al. [3], provided a comprehensive review of the literature on location-inventory decision integration and explained its components and benefits.

Nasiri et al. [4] have presented a hierarchical model to combine production, distribution and inventory problems in a location-allocation problem with multi-capacity warehouses. Two Lagrangian methods and Genetic Algorithm (GA) have been used to achieve optimal solutions. Diabat et al. [5] presented an algorithm to solve a supply chain network that had three levels. They compared the obtained results from the output of the algorithm with the results of other research.

Ahmadi et al. [6] considered a distribution network with seasonal and non-seasonal products that had three levels. In this distribution network, joint decisions are made about location and inventory control, and it is assumed that movement between warehouses is allowed. The presented model has 2 objectives which are used by the fuzzy method. In another study, Puga and Tancrez [7] developed a heuristic algorithm to solve a large-scale inventory-location problem in a multilevel supply chain including retailers, distribution centers, and a central factory with uncertain customer demand. The goal was to minimize inventory, transportation, location, and allocation costs, as well as to provide a certain level of customer service.

Ross et al. [8] have investigated an inventory location problem in a multi-product, multi-level supply chain with uncertain demands under a continuous inventory policy.

A supply chain that has a number of products, several levels where the demand is uncertain and the policy of inventory control is continuous.The goal of this model is to minimize the total cost including allocation, location, transportation, inventory, and lost sales costs. The intended model was non-linear, and a heuristic algorithm was used to solve it. Correia and Melo [9] have developed a mixed integer linear programming model for a multi-period location-allocation-inventory problem where in which customers' treatment for delivery time is considered different. The desired model is presented as a mixed integer. Mousavi et al. [10] studied a multi-period and multi-product inventory location-allocation problem in a two-level buyer-seller supply chain in which shortages are not allowed and the policy of discounting the total unit amount for purchase. They used a particle swarm optimization algorithm to solve their model.

Rafie-Majd et al. [11] also presented a supply chain problem that had a number of products and in a multi-period manner with uncertain demand. Darvish and Coelho [12] investigated a production-distribution system. They showed that the integration of different decisions improves the results. In designing an integrated supply chain, in addition to determine the location of facilities, costs must also be considered. In some articles, decisions related to price and cost are integrated with production planning.

Fattahi et al. [13] stated that pricing decisions are important from two perspectives in the supply chain. First, they determine the revenue from the sale of a product unit to customers and affect the demand for the product and thus the total sales and revenue. Second, due to the non-uniformity of customer demand, regions depends on pricing decisions, they affect the number and capacity of facilities and the overall structure of the supply chain to adequately respond to demands. Ahmadzadeh and Vahdani [14], designed a three-level closed-loop supply chain in a correlated demand environment. The periodic review method has been used to control the buffer in the warehouse and in this model, the shortage has been allowed. 3 meta-heuristic algorithms have been used to solve the presented model. Fattahi et al. [15] considered a multi-period supply chain redesign problem for simultaneous pricing and supply chain redesign decisions where customers have stochastic price-dependent demand for products. They provided a model and then solved it using the Decom Benders method. The obtained results showed that the proposed algorithm has a good performance. Rabbani et al. [16] presented a combined location-inventory-routing model with pricing in the design of a distribution network that determines the number of trucks for each established distribution center and they also assigned customers to routes. Two meta-heuristic algorithms have been used to solve the proposed model. Nasiri et al. [17] presented a multi-layer distribution network design problem with pricing strategy in a stochastic environment, where location, inventory, and pricing decisions in retail and wholesale channels were made simultaneously. They considered network consists of a central warehouse, a set of distribution centers and a set of retailers and wholesalers. Nasiri et al. [18] presented a mixed integer nonlinear programming model to determine the optimal pricing of products in different sales and distribution channels. Decisions related to inventory location and control have been made in a unified and uncertaintly manner, distribution channels while integrating location allocation and inventory control decisions of distribution centers in a nondeterministic environment. A memetic algorithm has been used to solve the mixed integer nonlinear programming model. Shafaghizadeh et al. [19] addressed the allocation of inventory distribution for a distribution network, including a factory, a number of potential locations for distribution centers and a number of retailers. Customers demand is assumed to be certain and deterministic for all periods but time varying in the limited planning horizon. A meta-heuristic method is used to solve it. Moosavi and Seifbarghy [20] presented a new mathematical model for a green closed-loop supply chain (GCLSC) network with the objectives of maximizing profits, maximizing the number of jobs created, and maximizing reliability. Due to the uncertainty on some parameters such as demand and transportation costs, the new method of robust fuzzy programming model was utilized. Multi-objective Grey Wolf Optimizer (MOGWO) and Non-dominated Sorting Genetic Algorithm II (NSGA II) were used to tackle the problems for larger sizes. A number of instances of the problem in larger sizes were solved. Soleimani et al. [21] addressed the design of a sustainable closed-loop supply chain including suppliers, manufacturers, distribution centers, customer zones, and disposal centers considering the consumption of energy. In addition, the distribution centers play the roles of warehouse and collection centers. The problem involves three choices of remanufacturing, recycling, and disposing the returned items.

The general innovation of the article is that all the articles worked in this field include production-distribution planning, while in the proposed article decision-making and production-distribution-sale planning are presented. The general innovation of this article is divided into two parts, the first part includes supply: considering that this model is presented for organizations that have a complete value chain from supply to sales. In the proposed article, the product supply planning has been done in a combined way, that is, in the supply planning, both the economic order quantity EOQ and the economic production quantity EPQ have been presented in the model in a combined manne. The reason for this type of supply planning is because it is low and responsive. The lack of product production capacity inside the organization is why we sometimes need simultaneous planning from outside the organization. In the second part, innovation includes distribution and sales: in all the articles worked in this field, the amount of product demand in each sales channel is already known, while in the proposed article, the amount of demand in each channel is not known, only the amount of demand in each region. For the product, it is clear that decisions are made regarding the selection of distribution channels for each region, product pricing in each channel and the amount of demand coverage by each channel so that it has the most benefit for the organization and the most benefit for the customer. In short, the variables of marketing decisions are fully considered in this model.

3. PROPOSED PROBLEM AND MODELLING

The distribution and sales network investigated in this research is a forward distribution network, single period and single product, whose components include two types of producers inside and outside the organization, distributors, wholesalers and retailers, and internet sales, and the product is sold through three retail channels, wholesale and internet sales can reach the end customer. The investigated distribution network has a divergent structure, in the sense that we are facing a divergent structure during the process in which the goods are transported from the manufacturer to the distribution centers and from there to the wholesalers and retailers and even the final customer. In this network, the amount of total demand in a region has been uncertain, that the total demand of each region is supplied by three channels, that the amount of demand in each channel is not known, that after solving the model, the amount of demand met by each channel is determined, that is, the amount The fulfilled demand in each channel is a variable that is determined after solving the model.

The investigated supply chain is used for durable goods, which is multi-level, and the entities of this chain include internal and external production centers, distribution centers, and retailers and wholesalers. One of the assumptions of the model is that the investigated supply chain with its distribution centers in the country can cover all the desired areas of the country with three different channels and respond to all demands as soon as possible. After production in the factory, the product is transferred to the warehouse of the distribution centers and based on the optimal quantities and the optimal price, it is sent to wholesalers, retailers or even to the final customer in different regions. Investigated distribution network is shown in Figure 1. Figure 1 shows the sales distribution network of the proposed model. As can be seen, the proposed network has two types of internal production, external production (production outsourcing). The reason for outsourcing the production in some cases is due to the low production capacity of the product in relation to the demand, and in some cases the production is not able to meet the market demand due to the limited capacity, and to avoid lost sales, some of the production needs are forced to be outsourced. During the execution of the work, due to the limited capacity of the warehouses of the distribution centers, we need to locate and create new distribution centers, which is shown in Figure 1 with a red pentagon. According to Figure 1, the proposed sales network has 3 authorized sales channels (wholesale, retail and online sales) and also the total demand of each region is shown as the potential power for the total demand of the region.

3. 1. Proposed Optimization Model

As stated in the problem definition section, the problem in this

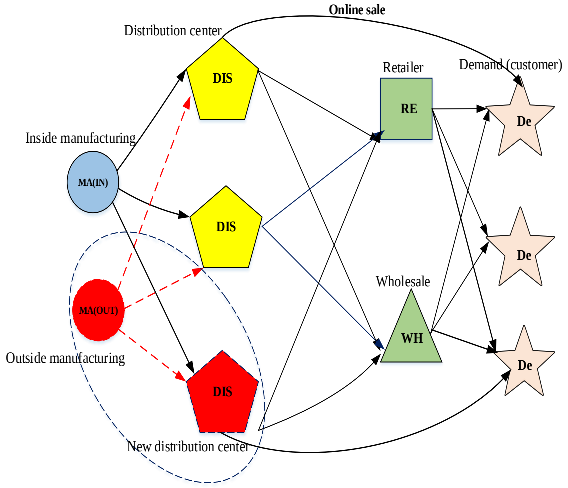

Figure 1. General shape of the investigated distribution network

article is that a multi-activity organization has production centers that have a wide market, which based on the market demand produces some of its demand in its centers and it prepares the rest of the demand in the form of supply (production outsourcing) from outside the organization. It sends its required production and supply products to the distribution centers for distribution. Based on the demand of each region, the relevant centers sell the most optimal quantity, channel and price through three channels of retail, wholesale and internet sales to the final customer. The amount of demand for each product in each region is specified as the input parameter of the model, but the amount of demand for the product, the price of the product and the amount of demand fulfilled by each channel are model variables in the field of distribution and sales. In this model, in the sales distribution department, we are looking for what product, at what price, in what volume, in which channel will be sold, which will be the most profitable for the organization and also the most favorable for the customer. In short, in this model, choosing the optimal channel is one of the main decision variables. Delivery, in this model, the variables of the problem are in what volume, at what price, in what channel, so that the demand of each region is covered in such a way that it has the most profit for the organization and also the best service to the customer. In terms of delivery time and price, it means that the desired model has two goals, the first goal of the model is to maximize the profit of the organization and the second goal is to maximize the customer's benefit from the two dimensions of the sales price in each channel and the service delivery time. In the presented model, the amount of demand of each region in a probabilistic manner (normal distribution) obtained through real online data should be covered by the three desired channels. In the previous models presented, the amount of demand in different channels is known, but in the model under review, the amount of demand in the region is possibly determined through online data, and this demand must be met by distribution centers, but in the model under review, the most optimal selection is made. The channel for the product, the amount of sales volume and the sales price in each channel are among the outputs of the model. In the mathematical model under investigation, the inventory policy is also considered, which product should be produced or supplied in what volume so that the costs of inventory control and ordering are minimal and increase the profit of the organization. The desired mathematical model is modeled in the scenario of unauthorized shortage, which will be explained below.

3. 2. Calculation of the Optimal Order Amount with Two Types of Suppliers in a Non-deterministic (Probable) State Inventory chart in the mode $D > P$ considering the definite demand is shown in Figure 2, in this case, the optimal amount of ordering is equal to the relationship $Q^* = EOQ + EPQ$ and because$D > P$, the amount of production is equal to the production capacity, that is, $EPQ = P$. In order to optimize the amount of production and the optimal order to satisfy the amount of demand, the relationship $Q^* = EOQ + P$ should be optimized. In the above relationship, considering that the amount of P is constant and some of the demand is met by production, the amount of the remaining demand, i.e. $D - P$, should be calculated by the order will be supplied.

$\frac{h}{2}QT + A + QC$	Total costs of a course
$K(Q) = \frac{h}{2}QTn + An + QCn$	Total annual costs
$K(Q) = \frac{h}{2}Q + A\frac{D-P}{Q} + CD$	To optimize the total annual cost, we derive K(Q) with respect to Q
$Q^* = \sqrt[2]{\frac{2(D-P)A}{h}}$	Optimal order quantity

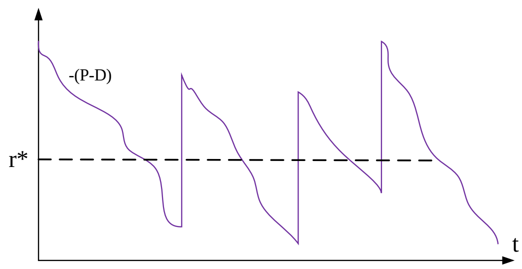

Figure 2. Inventory chart in the state $D > P$ considering the definite demand

Equation Q^*shows the amount of the desired order of the desired product from external producers

3. 3. The Proposed Mathematical Model The objective function of the model consists of two parts. The first is to minimize the completion time and the second is to minimize the average cost of maintenance and repairs per unit of time. Considering that in most of the previous mathematical models integrated planning has been worked in the field of production-distribution, but in the proposed model, due to the special conditions of some organizations, an integrated planning model of production-distribution-sales has been proposed, which according to the new discussion of sales, In the integrated planning model, marketing decision variables have been added to the mathematical model, and these decisions include what product with what volume $\omega'_{kmr} + \omega_{lmr}$ at what price φ_m in which channel γ_{mr} should be sold in the model. Also, the discussion of the new location variable of W_k distribution centers during the execution of the model is one of the topics and new variables of the proposed model. We hope the honorable reviewer will be convinced. The model is formulated as follows:

$$Q^* = EOQ^* + (\text{fix})P \quad \rightarrow \quad Q^* = EOQ^* \tag{1}$$

$$R^* = DL + Z_{1-\alpha}\sqrt[2]{L\,V} \;\rightarrow\; R^* = L\,(D-P) + Z_{1-\alpha}\sqrt[2]{L\,V} \tag{2}$$

$$D_{max} = DL + ss \;\rightarrow\; D_{max} = DL + ss \tag{3}$$

$$D \approx N(\mu, \sigma^2) \;\rightarrow\; Z_{1-\alpha} = \frac{(D-P)L+ss-(\mu-PL)}{\sqrt{var(D-P)L}} \tag{4}$$

3. 4. Calculation of the Order Point with Two Suppliers in Non-Deterministic (Probable) Mode Equation (5) shows the reorder point to supply the desired product from external suppliers.

$$ss = Z_{1-\alpha}\sqrt{var(D-P)L} \;\rightarrow ss = Z_{1-\alpha}\sqrt{L\,V} \tag{5}$$

$$R^* = (D-P)L + Z_{1-\alpha}\sqrt[2]{L\,V} \tag{6}$$

3. 5. Distribution and Sales Model

$$Max\ f_1 = \sum_l \sum_m \sum_r \varphi_m\, \gamma_{mr}\, \omega_{lmr} + \sum_k \sum_m \sum_r \varphi_m\, \gamma_{mr}\, \omega'_{kmr} - \left(\sum_l C\, Q_{1\,l} + \sum_k C\, Q_{1\,k}\right) - (C'Q^*) - \left(\frac{h}{2} \times \frac{Q^*}{T} + A\frac{D-P}{\frac{Q^*}{T}}\right) - \left(\sum_l T_{1\,l}\, Q_{1\,l} - \sum_l Q_{1\,k}\, T'_{1\,k} - \sum_l \sum_m \sum_r \omega_{lmr}\, T_{lm} - \sum_l \sum_m \sum_r \omega'_{kmr}\, T''_{km}\right) - \sum_i \sum_l p_k\, W_k \tag{7}$$

$$Max\ f_2 = \sum_m \left(\left(\frac{Pro_m}{M_m}\right) \sum_l \sum_r \boldsymbol{\omega_{lmr}}\right) + \sum_m \left(\left(\frac{Pro_m}{M_m}\right) \sum_k \sum_r \boldsymbol{\omega'_{kmr}}\right) \tag{8}$$

ST:

$$\sum_m \sum_r \omega_{lmr} = Q_{1\,l} + Q_{2\,l} \qquad \forall \quad l \tag{9}$$

$$\sum_m \sum_r W_k \omega'_{kmr} = Q_{1k} + Q_{2k} \qquad \forall \quad k \tag{10}$$

$$\sum_m \gamma_{mr} \leq 2 \qquad \forall \quad r \tag{11}$$

$$\sum_l \sum_m \gamma_{mr}\, \omega_{lmr} + \sum_k \sum_m \gamma_{mr}\, \omega'_{kmr} \leq D_r \qquad \forall \quad r \tag{12}$$

$$Q^* \leq \sum_l Q_{2l} + \sum_k Q_{2k} \qquad \forall \quad l \tag{13}$$

$$\varphi_m \geq \left(\frac{(\sum_l Q_{1l} + \sum_k Q_{1k}) \times C + \left(\frac{Q^*}{T} \times C'\right)}{\sum_l Q_{1l} + \sum_k Q_{1k} + \frac{Q^*}{T}} \right) \ \forall\, , m \tag{14}$$

$$\varphi_m \leq (1 + \alpha_m) \left(\frac{(\sum_l Q_{1l} + \sum_k Q_{1k}) \times C + \left(\frac{Q^*}{T} \times C'\right)}{\sum_l Q_{1l} + \sum_k Q_{1k} + \frac{Q^*}{T}} \right) \forall m \tag{15}$$

$$Q_{1l} + Q_{2l} \leq CAP_l \qquad \forall \ l \tag{16}$$

$$\sum_l Q_{1l} = CAP \tag{17}$$

$$Pro_m = (M_m - \varphi_m) \qquad \forall \ p \quad m \tag{18}$$

$$\varphi_m \ , \omega_{lmr} \ , \omega'_{kmr}, Q^*, R^*, Q_{1l} \ , Q_{2l}, Q_{2k}, Q_{1k}, Pro_m \geq 0 \quad Integer \tag{19}$$

$$\gamma_{mr} \ \ , W_k \quad 1 \ , 0 \qquad 0 \leq \alpha_m \leq 0.5 \tag{20}$$

The function of relation (7) seeks to maximize the net profit from the sale of the product; Equation (8) seeks to maximize the utility (price compared to competitors) for the customer. Equations (9) and (10) state that the amount of the product that entered the distribution center (existing distribution center and establishing new distribution centers) is equal to the amount of the product that left the distribution center and reached the customer through the sales channels. Equation (11) states that for better management and to prevent underselling, the sales channels for the product can be at most 2 channels. Equation (12) shows the amount of product allocated to customer through distribution centers and different channels. Equation (13) shows the method of allocating the product ordered from the supplier to the distribution centers. Equations (14) and (15) show the pricing range as well as the net profit of each product unit based on the cost price of the manufactured and purchased product. Equation (16) shows the capacity of distribution centers. Equation (17) shows the production capacity of production units for the desired product. Equation (18) ***s***hows the price difference of the desired product in sales channels compared to competitors. Equations (19) and (20) show the decision making variables of the model.

4. NUMERICAL EXAMPLES ANDDISCUSSIONS (ETKA ORGANIZATION)

The proposed model is presented for the Etka organization because it has a complete supply chain in the field of production, distribution and sales channels. In the next, 5 regions of Tehran province with data extracted from the Etka organization are given in Table 1. Each region will be solved using the GAMS software in the desired model and the results of each region have been analyzed and reviewed. In this case study, there are *l= 3* existing distribution centers in the west, east and center of tehran, *m=3* sales channels consist of wholesale,

TABLE 1. A summary of the literature review

Study	Joint Optimization	Marketing Decisions			Multiple Product	Demand Uncertainly	Multiple Channel	Solving Approach
		Product	Channel	Price				
Kaya and Urek [1]	Location- Inventory- pricing	-	-	✓	Yes	No	No	Meta -Heuristic
Zhang and Unnikrishnan [2]	Location - Inventory	-	-	-	No	Yes	Yes	Exact
Farahani et al. [3]	Location-inventory	-	-	-	No	No	Yes	Heuristic and meta-heuristic
Rafie-Majd et al. [11]	Location-inventory	-	-	-	No	Yes	No	Heuristic
Rabbani et al. [16]	Location-inventory- pricing	-	-	✓	No	No	No	Meta -Heuristic
Nasiri et al. [17]	Location- Allocation- Inventory-replenishment policy, Retail and wholesale prices			✓	No	Yes	Yes	Exact-Approximate Meta-heuristic
Nasiri et al. [18]	Location-Inventory-pricing			✓	Yes	Yes	Yes	Exact-Approximate Meta-heuristic
This work	Relocation- Inventory-Pricing- Marketing Decision	✓	✓	✓	Yes	Yes	Yes	Exact

retailing, online sale, $k=3$ potential centers (k=1 Southeast, k=2 Northweast, k=3 Southwest) for establishing new distribution centers in , $r=5$ demand areas for the product.

5. COMPUTATIONAL RESULTS

In Table 1 the parameters of the model for the case study of the ETKA organization are given. The case study is related to 5 demand centers (regions 9, 10, 14, 16, 17) and 3 existing distribution centers related to Tehran province. The amount of customer demand follows a normal probability distribution. Due to the capacity limitations, the existing distribution centers are not able to meet the demand.To solve the problem, we have to redesign the distribution centers as well as replining the distribution network, which is used in the model presented in this article. Table 2 summarizes the optimal values of inventory management variables as well as the optimal location of new distribution centers the optimal locations of new distribution centers are southeast and southwest. In Table 3, the optimal values of variables related to product pricing in different channels, the amount of product allocation from distribution centers to demand points are given. For more visibility and easier understanding of the model and the results obtained for the case study, the results of solving the model are briefly shown in Figure 3. Figure 3 shows all the variables related to inventory management in distribution centers as well as the optimal location of new distribution centers. Also, the variables of goods allocation from distribution centers to demand centers for areas 9 and 16 (to avoid crowding the figure) are shown as examples. As stated, there are 2 suppliers, including an internal supplier and an external supplier in Tehran province, for Etka organization. As mentioned, according to Table 2, the production capacity in the target network is limited, and sometimes the production capacity does not meet the demand of the regions, which is forced to outsource some of the demand to production units outside the organization, which are shown in the table of these two types of production units per unit. Production (internal and external) is given.

Table 3 shows the available distribution centers. In the continuation of Table 3, the potential locations for the creation of new distribution centers are also given. By solving the proposed model, any of them may be selected to create a distribution center. Table 3 consists of two parts, the first part shows the number of existing distribution centers and the second part shows the potential centers for creating new distribution centers during the execution of the model. In both sections, the exact location of existing distribution centers and the potential location for establishing distribution centers are given.

TABLE 2. The Information of Supplier

Supplier (Manufacuer)	Supplier Type	Location of Suplier
1	Intrnal of Etka	Tehran
2	External of Etka (Outsource)	Tehran

TABLE 3. Existing Distribution Centers and Potential Locations for establishing new Distribution Center

Indicator number (l)	Existing Distribution Center Location
L=1	West of Tehran
L=2	East of Tehran
L=3	South of Tehran
Indicator number (K)	Potential Location for Establishing new Distribution Centers
K=1	Southeast of Tehran
K=2	Northweast of Tehran
K=3	Southwest of Tehran

Table 4 shows the number and region name for customer j. For each region according to the table, it follows the normal distribution N(μ,δ). In Table 4, the total customer demands for 5 regions of Tehran, which had a normal distribution, are given according to the regions of Tehran.

Table 5, shows all the parameter values of the mathematical model in full detail for the case study. Table 6 shows the optimal values of the first and second objective functions. Table 7 shows the optimal values of the model variables resulting from the model solution in full detail. For example, the variable line related to $\boldsymbol{Q_{1k}}$ represents the amount of product allocation from the domestic production unit to the distribution centers, the variable line related to $\boldsymbol{\varphi_m}$ is the optimal price of the product in different channels, and the variable line related to $\boldsymbol{\omega_{lmr}}$ is the amount of optimal allocation of the product from the existing distribution centers to the regions It shows the demand.

TABLE 4. Indicator number and Region name for customer j

Customer indicator number r	Customer in regions	Demand Customer in region D_r
r=1	Region 9 of Tehran	N(80,4)
r=2	Region 10 of Tehran	N(95,5)
r=3	Region 14 of Tehran	N(75,5)
r=4	Region 16 of Tehran	N(120,6)
r=5	Region 17 of Tehran	N(80,3)

TABLE 5. Parameters of the model for ETKA case study

Parameters	Sets	l			k			m			r				
		1	2	3	1	2	3	1	2	3	1	2	3	4	5
$h = 0.5$	-	-	-	-	-	-	-	-	-	-	-	-	-	-	-
$A = 0.7$	-	-	-	-	-	-	-	-	-	-	-	-	-	-	-
$p = 40$	-	-	-	-	-	-	-	-	-	-	-	-	-	-	-
$C = 6$	-	-	-	-	-	-	-	-	-	-	-	-	-	-	-
C'=7	-	-	-	-	-	-	-	-	-	-	-	-	-	-	-
$\text{CAP} = 240$	-	-	-	-	-	-	-	-	-	-	-	-	-	-	-
LT	-	-	-	-	-	-	-	-	-	-	-	-	-	-	-
P_k	-	-	-	-	315	402	391	-	-	-	-	-	-	-	-
V_{va}	-	-	-	-	-	-	-	-	-	-	-	-	-	-	-
$D_r(hours)$	-	-	-	-	-	-	-	-	-	-	N(80,4)	N(95,5)	N(75,5)	N(120,6)	N(80,3)
CAP_l	-	100	100	100	-	-	-	-	-	-	-	-	-	-	-
M_m	-	-	-	-	-	-	-	9.2	9.7	9.9	-	-	-	-	-
T_{1l}	-	0.4	0.4	0.2	-	-	-	-	-	-	-	-	-	-	-
T_{2k}	-	-	-	-	0.6	0.4	0.4	-	-	-	-	-	-	-	-
T_{lm}	$l = 1$	-	-	-	-	-	-	0.4	0.6	0.4	-	-	-	-	-
	$l = 2$	-	-	-	-	-	-	0.2	0.4	0.4	-	-	-	-	-
	$l = 3$	-	-	-	-	-	-	0.6	0.2	0.4	-	-	-	-	-
T''_{km}	$k = 1$	-	-	-	-	-	-	0.4	0.4	0.4	-	-	-	-	-
	$k = 2$	-	-	-	-	-	-	0.4	0.4	0.8	-	-	-	-	-
	$k = 3$	-	-	-	-	-	-	0.4	0.2	0.6	-	-	-	-	-

TABLE 6. The results of solving the model

Objective Optimal	Optimal amount
Profit	138.2
Service desirability	84.23

By solving the proposed model with real data, the amount of profit and efficiency is obtained in Table 6.

The results of solving the proposed model are given in Table 7. For example, different values of 1 include (Q_{12}=61, Q_{11}=78, Q_{13}=50). These results are given for all variables and for all indices.

Figure 3 shows the results of solving the model shown in Table 7 on the proposed supply chain network. The results of solving the model are based on the parameters of Table 5. As can be seen from the network in Figure 3, we have two production methods (ETKA and Out source) in the proposed network. Production centers are shown as circles, distribution centers are shown as pentagons, and demand centers are shown as quadrilaterals in the figure. The values of variables $Q_{1k}Q_{2l}$ show the values of goods allocation from internal and external producers to distribution centers, the numbers on the vectors are the optimal values after solving the model. The values of the variables ω_{lmr} and ω'_{kmr} show the optimal values for the allocation of goods from existing and new distribution centers to the demand areas, for example, for two regions r=10 and r=16, which are given on the vectors, as well as 2 to pentagons that are shown inside a dashed ellipse are the optimal points selected for locating new distribution centers. In short, Figure 3 is given for a better understanding of the model solution and its results on the proposed network.

6. SENSITIVITY ANALYSIS

In this section, changes in the cost of transporting parameter have been investigated on the objective function where W_1 = 0.9, W_2 = 0.1.These changes are given in Table 8 and Figure 4. By reducing the cost of transportation, the amount of profit increases, the value of the second objective function does not change, but the value of the total objective function also decreases.

TABLE 7. The results of solving the model fo ETKA case study

Variables	**Sets**	l			k					$m=1$					$m=2$					$m=3$		
		1	**2**	**3**	**1**	**1**	**2**	**r=1**	**r=2**	**r=3**	**r=4**	**r=5**	**r=1**	**r=2**	**r=3**	**r=4**	**r=5**	**r=1**	**r=2**	**r=3**	**r=4**	**r=5**
Q_{1l}	-	61	78	50	-	-	-	-	-	-	-	-	-	-	-	-	-	-	-	-	-	-
Q_{2l}	-	23	17	35	-	-	-	-	-	-	-	-	-	-	-	-	-	-	-	-	-	-
Q_{1k}	-	-	-	-	36	0	0	-	-	-	-	-	-	-	-	-	-	-	-	-	-	-
Q_{2k}	-	-	-	-	54	0	96	-	-	-	-	-	-	-	-	-	-	-	-	-	-	-
W_k	-	-	-	-	1	0	1	-	-	-	-	-	-	-	-	-	-	-	-	-	-	-
γ_{mr}	-	-	-	-	-	-	-	0	1	1	1	0	1	1	0	1	1	1	0	0	0	1
ω_{lmr}	l = 1	-	-	-	-	-	-	0	9	19	8	0	7	9	0	6	9	7	0	0	0	10
	l = 2	-	-	-	-	-	-	0	10	19	25	0	6	8	0	21	0	6	0	0	0	0
	l = 3	-	-	-	-	-	-	0	13	13	8	0	7	9	0	6	7	10	0	0	0	12
ω'_{kmr}	k = 1	-	-	-	-	-	-	0	10	12	9	0	9	8	0	11	7	9	0	0	0	15
	k = 2	-	-	-	-	-	-	0	0	0	0	0	0	0	0	0	0	0	0	0	0	0
	k = 3	-	-	-	-	-	-	0	10	12	12	0	8	9	0	14	10	11	0	0	0	10
Variables	Sets	l			k					$m=1$					$m=2$					$m=3$		
φ_m	-	-	-	-	-	-	-			9.1					9.5					9.8		
α_m	-	-	-	-	-	-	-			0.23					0.25					0.26		
Pro_m	-	-	-	-	-	-	-			0.9					0.5					0.2		

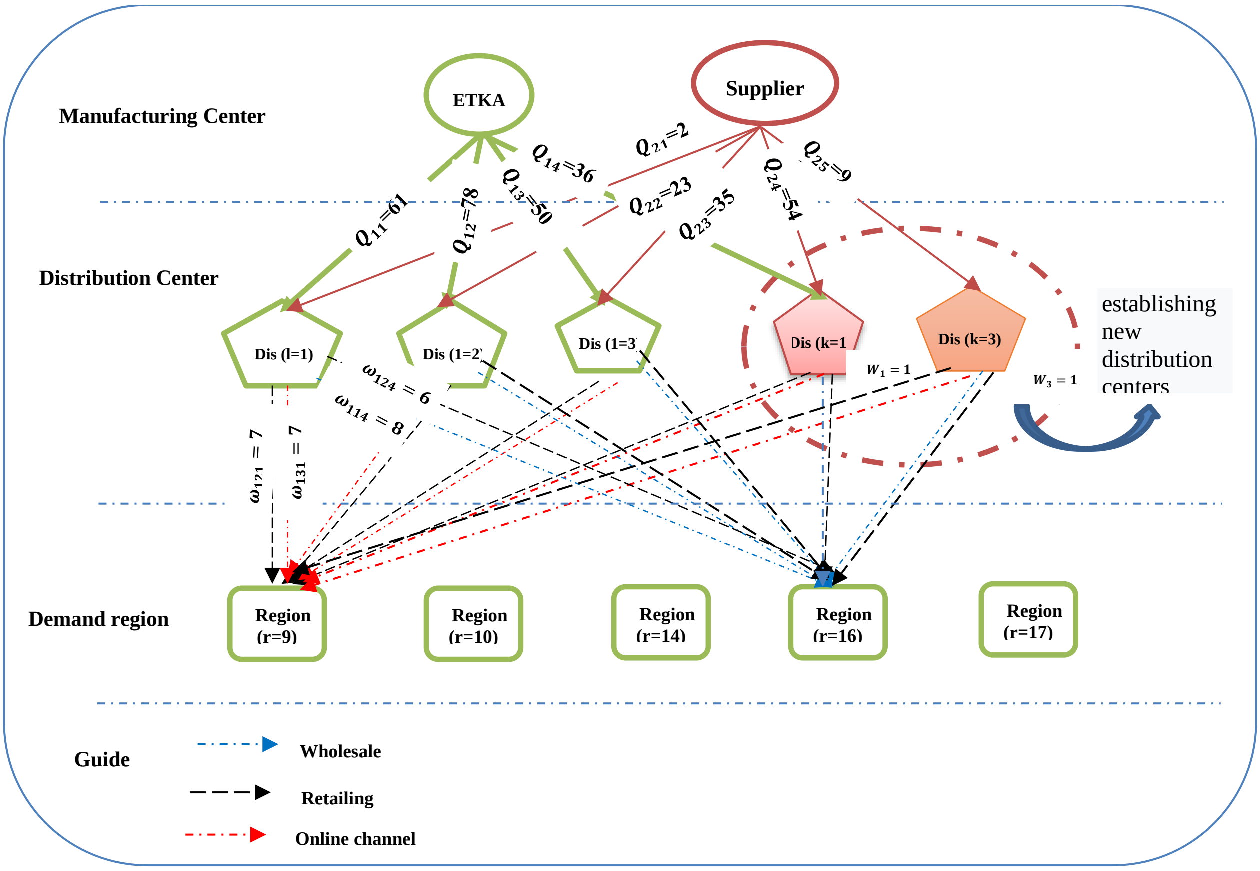

Figure 3. Solving the model using the real data of the Atka organization

TABLE 8. Variation of objective function with changes in cost of transporting

Cost of transporting	Profit objective functions (f_1)	Service desirability objective functions (f_2)	Objective function LP Metric model
50% increase	120/12	11/2	0/25
40% increase	118/01	11/2	0/24
30% increase	112/2	11/2	0/22
20% increase	108/8	11/2	0/21
10% increase	99/4	11/2	0/19
Normal	123/3	11/2	0/18
10% reduction	127/9	11/2	0/1
20% reduction	131/3	11/2	0/12
30% reduction	135/7	11/2	0/13
40% reduction	138	11/2	0/15
50% reduction	140/5	11/2	0/17

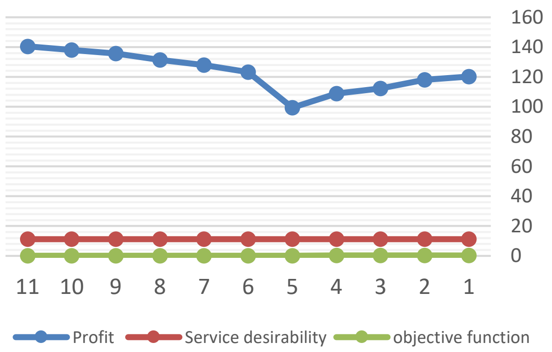

Figure 4. Variation of objective function with changes in cost of transporting

The proposed model is solved using the LP metric method and the results are shown in Table 7 and Figure 5. Considering that the objective function seeks to minimize, according to Table 9, the best situation is situation 1, where $W_1 = 0.9$, $W_2 = 0.1$.

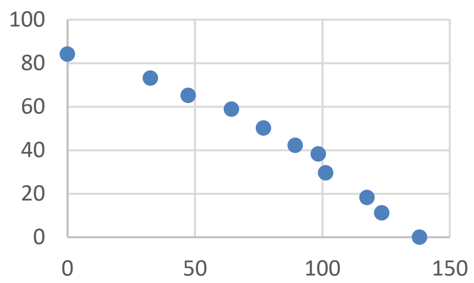

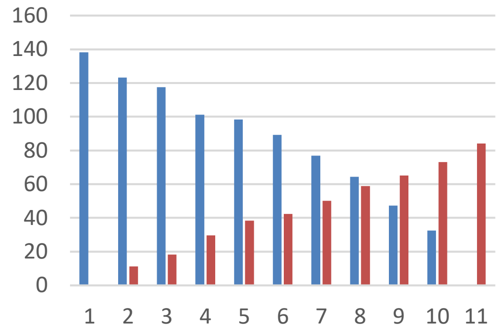

Figure 5. Pareto chart of results for different weights

TABLE 9. Weighing the objective functions and objective function of the LP metrice model

Status	Weight of objective functions	Profit objective functions (f_1)	Service desirability objective functions (f_2)	Objective function LP Metrice model
1	W_1=0.9 W_2=0.1	123.3	11.2	0.18
2	W_1=0.8 W_2=0.2	117.5	18.3	0.27
3	W_1=0.7 W_2=0.3	101.3	29.6	0.38
4	W_1=0.6 W_2=0.4	98.4	38.4	0.39
5	W_1=0.5 W_2=0.5	89.3	42.3	0.42
6	W_1=0.4 W_2=0.6	76.9	50.2	0.41
7	W_1=0.3 W_2=0.7	64.3	58.9	0.37
8	W_1=0.2 W_2=0.8	47.3	65.2	0.31
9	W_1=0.1 W_2=0.9	32.5	73.2	0.19

In addition to the above, Due to the fact that the solution method of the proposed model is exact, the solution time increases for problems with a large number of data. For future studies, it is suggested that in addition to exact solution algorithms, heuristic and meta-heuristic solution algorithms, for example, the algorithms used by Zhao and Zhang [22], where a learning-based algorithm is proposed with the aim of increasing generalization ability. The algorithm used by Dulebenets [23] is a new Adaptive Polyploid Memetic Algorithm (APMA); also similar algorithm were used by Pasha et al. [24], Kavoosi et al. [25] and Rabbani et al. [26].

7. CONCLUSIONS AND FUTURE RESEARCH

In this research, a non-linear planning model was presented to optimize economic goals, including the profit from product sales in the entire chain, as well as the desirability of providing services compared to competitors, which include maximizing product sales in sales channels, minimizing costs. Transportation, warehouse construction, inventory management and control, and finally choosing the most optimal sales channel based on the demand of the regions. The presented two-objective model was solved using the LP-Metrice technique and GAMS software. In the following, the sensitivity analysis on the importance and weight of the objective functions and the final impact on the objective function have been measured. Finally, each of the target functions was measured according to the real data as well as the importance of economic considerations, and the results and sensitivity analysis were presented in the form of tables and graphs. Computational results based on real data analysis for a furnicutre product are reported for Etka organization. The sample used includes two suppliers (1 internal, 2 external), three existing distribution centers and 3 potential locations for creating new distribution centers, and 5 demand areas (areas 9, 10, 14, 16, 17) for Tehran province.The solution of the proposed model leads to the selection of the most optimal distribution channel of the desired product in different areas of Tehran, as well as the creation of new distribution centers by optimizing the costs of creation, transportation and inventory management costs. The consequences of solving the model are as follows.

- Due to the fact that the existing distribution centers are not able to meet the demand of demand centers in terms of capacity, new distribution centers have been established in the southeast and southwest areas of Tehran.
- The most optimal channel for the distribution of goods in region 9 is retail and internet channels, for region 10 wholesale and retail, for region 14 only wholesale channels, for region 17 wholesale and retail channels and for region 18 retail and online sales is.
- The main motivation of Atta to use this model is to reduce system costs and provide better services than competitors. Distribution costs are reduced when the product reaches the customer through the best channel from the supplier.

In future works, modeling based on online data can be a good and accurate work. Considering the emergence of the 4th generation industry and the use of new technologies to collect data in real time and analyze them and use them in supply chain modeling can be a valuable work.

8. REFERENCES

1. Kaya, O. and Urek, B., "A mixed integer nonlinear programming model and heuristic solutions for location, inventory and pricing decisions in a closed loop supply chain", ***Computers & Operations Research***, Vol. 65, (2016), 93-103. https://doi.org/10.1016/j.cor.2015.07.005
2. Zhang, Z.-H. and Unnikrishnan, A., "A coordinated location-inventory problem in closed-loop supply chain", ***Transportation Research Part B: Methodological***, Vol. 89, (2016), 127-148. https://doi.org/10.1016/j.trb.2016.04.006
3. Farahani, R.Z., Rashidi Bajgan, H., Fahimnia, B. and Kaviani, M., "Location-inventory problem in supply chains: A modelling review", ***International Journal of Production Research***, Vol. 53, No. 12, (2015), 3769-3788. https://doi.org/10.1080/00207543.2014.988889
4. Nasiri, G.R., Zolfaghari, R. and Davoudpour, H., "An integrated supply chain production–distribution planning with stochastic demands", ***Computers & Industrial Engineering***, Vol. 77, (2014), 35-45. https://doi.org/10.1016/j.cie.2014.08.005
5. Diabat, A., Battaïa, O. and Nazzal, D., "An improved lagrangian relaxation-based heuristic for a joint location-inventory problem", ***Computers & Operations Research***, Vol. 61, (2015), 170-178.
6. Ahmadi, G., Torabi, S.A. and Tavakkoli-Moghaddam, R., "A bi-objective location-inventory model with capacitated transportation and lateral transshipments", ***International Journal of Production Research***, Vol. 54, No. 7, (2016), 2035-2056. https://doi.org/10.1080/00207543.2015.1082042
7. Puga, M.S. and Tancrez, J.-S., "A heuristic algorithm for solving large location–inventory problems with demand uncertainty", ***European Journal of Operational Research***, Vol. 259, No. 2, (2017), 413-423. https://doi.org/10.1016/j.ejor.2016.10.037
8. Ross, A., Khajehnezhad, M., Otieno, W. and Aydas, O., "Integrated location-inventory modelling under forward and reverse product flows in the used merchandise retail sector: A multi-echelon formulation", ***European Journal of Operational Research***, Vol. 259, No. 2, (2017), 664-676. https://doi.org/10.1016/j.ejor.2016.10.036
9. Correia, I. and Melo, T., "A multi-period facility location problem with modular capacity adjustments and flexible demand fulfillment", ***Computers & Industrial Engineering***, Vol. 110, (2017), 307-321. https://doi.org/10.1016/j.cie.2017.06.003
10. Mousavi, S.M., Bahreininejad, A., Musa, S.N. and Yusof, F., "A modified particle swarm optimization for solving the integrated location and inventory control problems in a two-echelon supply chain network", ***Journal of Intelligent Manufacturing***, Vol. 28, No. 1, (2017), 191-206. https://doi.org/10.1007/s10845-014-0970-z
11. Rafie-Majd, Z., Pasandideh, S.H.R. and Naderi, B., "Modelling and solving the integrated inventory-location-routing problem in a multi-period and multi-perishable product supply chain with uncertainty: Lagrangian relaxation algorithm", ***Computers & Chemical Engineering***, Vol. 109, (2018), 9-22. https://doi.org/10.1016/j.compchemeng.2017.10.013
12. Darvish, M. and Coelho, L.C., "Sequential versus integrated optimization: Production, location, inventory control, and distribution", ***European Journal of Operational Research***, Vol. 268, No. 1, (2018), 203-214. doi: 10.1016/j.ejor.2018.01.028.
13. Fattahi, M., Mahootchi, M., Govindan, K. and Husseini, S.M.M., "Dynamic supply chain network design with capacity planning

and multi-period pricing", ***Transportation Research Part E: Logistics and Transportation Review***, Vol. 81, (2015), 169-202. https://doi.org/10.1016/j.tre.2015.06.007

14. Ahmadzadeh, E. and Vahdani, B., "A location-inventory-pricing model in a closed loop supply chain network with correlated demands and shortages under a periodic review system", ***Computers & chemical Engineering***, Vol. 101, (2017), 148-166. https://doi.org/10.1016/j.compchemeng.2017.02.027
15. Fattahi, M., Govindan, K. and Keyvanshokooh, E., "A multi-stage stochastic program for supply chain network redesign problem with price-dependent uncertain demands", ***Computers & Operations Research***, Vol. 100, (2018), 314-332. https://doi.org/10.1016/j.cor.2017.12.016
16. Rabbani, M., Navazi, F., Eskandari, N. and Farrokhi-Asl, H., "A green transportation location-inventory-routing problem by dynamic regional pricing", ***Journal of Industrial Engineering and Management Studies***, Vol. 7, No. 1, (2020), 35-58. https://doi.org/10.22116/JIEMS.2020.110006
17. Nasiri, G.R., Deymeh, H., Karimi, B. and Miandoabchi, E., "Incorporating sales and marketing considerations into a competitive multi-echelon distribution network design problem with pricing strategy in a stochastic environment", ***Journal of Retailing and Consumer Services***, Vol. 62, (2021), 102646. https://doi.org/10.1016/j.jretconser.2021.102646
18. Nasiri, G.R., Kalantari, M. and Karimi, B., "Fast-moving consumer goods network design with pricing policy in an uncertain environment with correlated demands", ***Computers & Industrial Engineering***, Vol. 153, (2021), 106997. https://doi.org/10.1016/j.cie.2020.106997
19. Shafaghizadeh, S., Ebrahimnejad, S., Navabakhsh, M. and Sajadi, S., "Proposing a model for a resilient supply chain: A meta-heuristic algorithm", ***International Journal of Engineering, Transactions C: Aspects,*** Vol. 34, No. 12, (2021), 2566-2577. doi: 10.5829/IJE.2021.34.12C.01.
20. Moosavi, S. and Seifbarghy, M., "A robust multi-objective fuzzy model for a green closed-loop supply chain network under uncertain demand and reliability (a case study in engine oil industry)", ***International Journal of Engineering, Transactions C: Aspects,*** , Vol. 34, No. 12, (2021), 2585-2603. doi: 10.5829/IJE.2021.34.12C.03.
21. Soleimani, H., Chhetri, P., Fathollahi-Fard, A.M., Mirzapour Al-e-Hashem, S. and Shahparvari, S., "Sustainable closed-loop supply chain with energy efficiency: Lagrangian relaxation, reformulations and heuristics", ***Annals of Operations Research***, (2022), 1-26. https://doi.org/10.1007/s10479-022-04661-z
22. Zhao, H. and Zhang, C., "An online-learning-based evolutionary many-objective algorithm", ***Information Sciences***, Vol. 509, (2020), 1-21. https://doi.org/10.1016/j.ins.2019.08.069
23. Dulebenets, M.A., "An adaptive polyploid memetic algorithm for scheduling trucks at a cross-docking terminal", ***Information Sciences***, Vol. 565, (2021), 390-421. https://doi.org/10.1016/j.ins.2021.02.039
24. Pasha, J., Nwodu, A.L., Fathollahi-Fard, A.M., Tian, G., Li, Z., Wang, H. and Dulebenets, M.A., "Exact and metaheuristic algorithms for the vehicle routing problem with a factory-in-a-box in multi-objective settings", ***Advanced Engineering Informatics***, Vol. 52, (2022), 101623. https://doi.org/10.1016/j.aei.2022.101623
25. Kavoosi, M., Dulebenets, M.A., Abioye, O.F., Pasha, J., Wang, H. and Chi, H., "An augmented self-adaptive parameter control in evolutionary computation: A case study for the berth scheduling problem", ***Advanced Engineering Informatics***, Vol. 42, (2019), 100972. https://doi.org/10.1016/j.aei.2019.100972
26. Rabbani, M., Oladzad-Abbasabady, N. and Akbarian-Saravi, N., "Ambulance routing in disaster response considering variable patient condition: Nsga-ii and mopso algorithms", ***Journal of Industrial & Management Optimization***, Vol. 18, No. 2, (2022), 1035. doi: 10.3934/jimo.2021007.

Persian Abstract

چکیده

امروزه بحث طراحی و برنامه ریزی شبکه توزیع و فروش اعم از مکان‌یابی، قیمت‌گذاری، انتخاب بهینه ترین کانال فروش و همچنین تصمیمات بازاریابی از اهمیت بسزایی در زنجیره‌تامین می باشد باتوجه به تغییرات و عدم قطعیت مقدار تقاضا در بازار طراحی و برنامه‌ریزی شبکه توزیع و فروش ایستا در عمل با مشکلات زیادی مواجه گردیده است در این مقاله یک مدل برنامه‌ریزی ریاضی غیرخطی برای مکان‌یابی، کنترل موجودی و بازاریابی محصول تولیدی برای یک سازمان چند فعالیتی (سازمان که دارای واحد تولیدی، توزیع و خرده فروشی و عمده فروشی می باشد) با داده‌های آنلاین در زمان واقعی ارائه می‌گردد که در این مدل به دنبال ایجاد و مکان‌یابی مراکز توزیع جدید در حین فعالیت شبکه در صورت افزایش تقاضا، مدیریت موجودی در مراکز توزیع و همچنین تصمیمات بازاریابی اعم از قیمت‌گذاری محصولات در کانال‌ها (عمده فروشی، خرده فروشی، اینترنتی)، انتخاب بهینه‌ترین مقدار و کانال برای فروش محصول، میزان فروش در هر کانال و در نهایت قیمت‌گذاری برای محصول در کانال‌های مختلف با در نظر گرفتن داده‌های واقعی و سیستم پشتبان تصمیم‌گیر به صورت متمرکز می‌باشد. در این مدل هدف حداکثر کردن سود و همچنین افزایش مطلوبیت برای مشتری با در نظر گرفتن قیمت رقبا و انتخاب بهترین کانال برای ارائه محصول به مشتری می‌باشد. در نهایت مدل مورد نظر در حجم پایین‌تر با نرم افزار گمز حل گردیده و تحلیل حساسیت روی پارامترهای مختلف صورت گرفته است.

AIMS AND SCOPE

The objective of the International Journal of Engineering is to provide a forum for communication of information among the world's scientific and technological community and Iranian scientists and engineers. This journal intends to be of interest and utility to researchers and practitioners in the academic, industrial and governmental sectors. All original research contributions of significant value focused on basics, applications and aspects areas of engineering discipline are welcome.

This journal is published in three quarterly transactions: Transactions A (Basics) deal with the engineering fundamentals, Transactions B (Applications) are concerned with the application of the engineering knowledge in the daily life of the human being and Transactions C (Aspects) - starting from January 2012 - emphasize on the main engineering aspects whose elaboration can yield knowledge and expertise that can equally serve all branches of engineering discipline.

This journal will publish authoritative papers on theoretical and experimental researches and advanced applications embodying the results of extensive field, plant, laboratory or theoretical investigation or new interpretations of existing problems. It may also feature - when appropriate - research notes, technical notes, state-of-the-art survey type papers, short communications, letters to the editor, meeting schedules and conference announcements. The language of publication is English. Each paper should contain an abstract both in English and in Persian. However, for the authors who are not familiar with Persian, the publisher will prepare the latter. The abstracts should not exceed 250 words.

All manuscripts will be peer-reviewed by qualified reviewers. The material should be presented clearly and concisely:

- *Full papers* must be based on completed original works of significant novelty. The papers are not strictly limited in length. However, lengthy contributions may be delayed due to limited space. It is advised to keep papers limited to 7500 words.
- *Research* notes are considered as short items that include theoretical or experimental results of immediate current interest.
- *Technical notes* are also considered as short items of enough technical acceptability with more rapid publication appeal. The length of a research or technical note is recommended not to exceed 2500 words or 4 journal pages (including figures and tables).

Review papers are only considered from highly qualified well-known authors generally assigned by the editorial board or editor in chief. Short communications and letters to the editor should contain a text of about 1000 words and whatever figures and tables that may be required to support the text. They include discussion of full papers and short items and should contribute to the original article by providing confirmation or additional interpretation. Discussion of papers will be referred to author(s) for reply and will concurrently be published with reply of author(s).

INSTRUCTIONS FOR AUTHORS

Submission of a manuscript represents that it has neither been published nor submitted for publication elsewhere and is result of research carried out by author(s). Presentation in a conference and appearance in a symposium proceeding is not considered prior publication.

Authors are required to include a list describing all the symbols and abbreviations in the paper. Use of the international system of measurement units is mandatory.

- On-line submission of manuscripts results in faster publication process and is recommended. Instructions are given in the IJE web sites: www.ije.ir-www.ijeir.info
- Hardcopy submissions must include MS Word and jpg files.
- Manuscripts should be typewritten on one side of A4 paper, double-spaced, with adequate margins.
- References should be numbered in brackets and appear in sequence through the text. List of references should be given at the end of the paper.
- Figure captions are to be indicated under the illustrations. They should sufficiently explain the figures.
- Illustrations should appear in their appropriate places in the text.
- Tables and diagrams should be submitted in a form suitable for reproduction.
- Photographs should be of high quality saved as jpg files.
- Tables, Illustrations, Figures and Diagrams will be normally printed in single column width (8cm). Exceptionally large ones may be printed across two columns (17cm).

PAGE CHARGES AND REPRINTS

The papers are strictly limited in length, maximum 8 journal pages (including figures and tables). For the additional to 8 journal pages, there will be page charges. It is advised to keep papers limited to 3500 words.

Page Charges for Papers More Than 8 Pages (Including Abstract)	
For International Author ***	**$55 / per page**
For Local Author	**100,000 Toman / per page**

AUTHOR CHECKLIST

- Author(s), bio-data including affiliation(s) and mail and e-mail addresses).
- Manuscript including abstracts, key words, illustrations, tables, figures with figure captions and list of references.
- MS Word files of the paper.

International Journal of Engineering, P.O. Box 13145-1659, Tehran, I.R. Iran
Materials and Energy Research Center, 5 Ahuramazda St., Alvand Ave., Argentina Sq., Tehran, Islamic Republic of Iran
www.merc.ac.ir - www.emerc.ac.ir